

Dissociation, Recombination and the Character of Charge Transfer States in Organic Photovoltaics

Dissertation

Von der Universität Bayreuth
zur Erlangung des Grades eines
Doktors der Naturwissenschaften (Dr. rer. nat.)
genehmigte Abhandlung

von
Frank-Julian Cornelius Kahle

geboren in Münster, Deutschland

Erste Gutachterin: Prof. Dr. Anna Köhler
Zweiter Gutachter: Prof. Dr. Peter Strohrriegl

Tag der Einreichung: 15.08.2018
Tag des Kolloquiums: 09.11.2018

Die vorliegende Arbeit wurde in dem Zeitraum von Januar 2015 bis August 2018 am Lehrstuhl für Optoelektronik weicher Materie (Experimentalphysik II) der Universität Bayreuth unter der Betreuung von Prof. Dr. Anna Köhler angefertigt.

Amtierender Direktor der Graduiertenschule: Prof. Dr. Dirk Schüler

Dissertation eingereicht am: 15.08.2018

Datum des wissenschaftlichen Colloquiums: 09.11.2018

Prüfungsausschuss:

Erste Gutachterin:	Prof. Dr. Anna Köhler
Zweiter Gutachter:	Prof. Dr. Peter Strohsriegl
Drittprüfer:	Prof. Dr. Werner Köhler
Vorsitzender:	Prof. Dr. Stephan Gekle

Für meine Familie

*Zum Erfolg gibt es keinen Lift.
Man muss die Treppe benutzen.*

Emil Oesch (1894-1974)

Abstract

0.1. Deutsche Kurzzusammenfassung

Organische Solarzellen sind in den letzten Jahren durch die Entwicklung neuer Nicht-Fulleren-Akzeptoren erneut in den Fokus der Wissenschaft gerückt, nachdem das Interesse an ihnen zunächst stagnierte. Vor dieser Entwicklung wurden in effizienten organischen Solarzellensystemen mangels Alternative nahezu ausschließlich Fullerenakzeptoren eingesetzt und die Forschung war im Wesentlichen auf die Optimierung von Donormaterialien und deren Eigenschaften ausgerichtet. Mit der Erkenntnis, dass gegenwärtige Bauteileffizienzen, welche mit Fullerenen zu erreichen sind, durch das Verständnis der speziellen Eigenschaften von Elektronenakzeptoren und den Einsatz dieses Wissens für die systematische Entwicklung neuer Materialien erhöht werden können, wurde das Interesse an der Erforschung von Akzeptoren erneut geweckt. Wesentliche Voraussetzungen dafür sind es, zu verstehen, zum Einen welche Eigenschaften die Fullerene so einzigartig machen und zum Anderen, welche Mechanismen einer effizienten Dissoziation von Charge-Transfer-Zuständen in organischen Solarzellen zu Grunde liegen und diese antreiben.

Angesichts dessen widmet sich die vorliegende Doktorarbeit der grundlegenden Erforschung verschiedener Aspekte im Hinblick auf die Dissoziation, Rekombination und den Charakter von Charge Transfer Zuständen in organischen Materialien. Ein vielversprechender und vieldiskutierter Faktor, der für eine effiziente Dissoziation in organischen Solarzellen trotz mitunter fehlender „Driving force“ für die Ladungstrennung verantwortlich sein könnte, ist die Delokalisation der mit einem Ladungsträger assoziierten Wellenfunktion, im Hinblick auf obige Ausführungen speziell diejenige des Elektrons in der Akzeptorphase und an der Donor-Akzeptor-Grenzfläche. Aus diesem Grund beschäftigt sich Kapitel 9 dieser Dissertation mit dem Einfluss der Delokalisation der Elektronenwellenfunktion des Akzeptors auf den Dissoziationsprozess von Charge-Transfer-Zuständen an der Donor-Akzeptor-Grenzfläche. Dazu wurde eine systematische Studie an drei verschiedenen Fulleren-Akzeptoren durchgeführt, die sich in ihrem Ordnungsgrad, der Stärke der intermolekularen Kopplung sowie der Lokalisierung des niedrigsten unbesetzten Molekülorbitals (LUMO) unterscheiden. Diese wurden in einer Zweischichtarchitektur mit einem effizienten, vernetzten Donorpolymer kombiniert. Durch die Vernetzung der Donorschicht wurde eine wohldefinierte Grenzfläche erreicht, wodurch sich insgesamt ein gutes Modellsystem ergab, um Prozesse an der Donor-Akzeptor-Grenzfläche zu untersuchen. Durch die Korrelierung von Strukturinformationen aus Streuungsmessungen mit den Ergebnissen photophysikalischer und elektrischer Untersuchungen sowie theoretischer Modellierung fanden wir, dass ein hoher Ordnungsgrad und eine starke intermolekulare Kopplung innerhalb der Akzeptorphase mit einem höheren Grad an Delokalisation der Elektronenwellenfunktion verbunden sind. Besagter Zusammenhang wird schließlich durch die Anwendung eines Effektive-Masse-Modells auf feldabhängige Photostrommessungen unter Berücksichtigung von Grenzflächendipolen verifiziert. Die Dipolstärken wurden dabei mit Hilfe von Ultraviolettphotoelektronenspektroskopie (UPS)

bzw. Kelvin-Probe-Messungen bestimmt. Insgesamt ergibt sich damit die Aussage, dass eine Delokalisation der Elektronenwellenfunktion direkt mit einer höheren Dissoziationseffizienz der Charge-Transfer-Zustände verknüpft ist und somit eine positive Rolle im Prozess der Ladungsträgertrennung einnimmt. In diesem Zusammenhang kommt der Güte der lokalen Ordnung der Fullerschicht eine entscheidende Bedeutung zu. Unter Berücksichtigung früherer Arbeiten zur Delokalisation der Wellenfunktion des Loches in der Donorphase lässt sich somit schlussfolgern, dass eine Delokalisation beider „Ladungsträger“, Elektron und Loch, für die Entwicklung effizienter Donor-Akzeptor-Systeme in Betracht gezogen werden muss.

Weitere Faktoren, die großen Einfluss auf Dissoziations- und Rekombinationsprozesse und damit auch auf die Effizienz einer organischen Solarzelle haben, sind die Durchmischung an Grenzflächen in Schichtstrukturen sowie Phasenseparation in Blendmorphologien infolge von Diffusion. Die diffundierenden Spezies sind dabei entweder die für gewöhnlich in Solarzellen eingesetzten kleinen Akzeptormoleküle oder auch Dotanden aus einer angrenzenden Schicht. Phasenseparation kann dabei zu einer Verschlechterung der Perkulationspfade für die Ladungsträgerextraktion zu den Elektroden führen, sowie zu einer erhöhten Rekombinationswahrscheinlichkeit der Ladungsträger. Durchmischung wiederum könnte eine ungewollte Dotierung des photoaktiven Materials zur Folge haben, was mitunter zur Bildung von Fallenzuständen für den Ladungstransport führen kann. Hierbei handelt es sich um generelle Probleme kleiner Moleküle, welche in Kontakt mit einem weiteren Material stehen, sodass Diffusion in dieser Hinsicht einen wichtigen Einflussfaktor für die Stabilität von optoelektronischen Bauteilen darstellt.

Aus diesem Grund wurde ein neuartiger, zerstörungsfreier Ansatz zur Untersuchung von Diffusion in organischen Materialien entwickelt, welcher auf rein optischen Prinzipien beruht. Dieser wird in Kapitel 10 vorgestellt. Er basiert darauf, die Diffusion zeitabhängig mittels Photolumineszenzlöschung infolge von Energietransfer von dem untersuchten (Matrix-)Material auf das diffundierende kleine Molekül zu beobachten. Diese Methode ermöglicht es, den Diffusionskoeffizienten als Funktion der Temperatur zu bestimmen und zusätzlich mittels theoretischer Simulationen Informationen über die zeitliche Entwicklung des Konzentrationsprofils in der Probe zu erhalten. Diese Technik wurde schließlich eingesetzt, um die Diffusion von C_{60} -Molekülen in einer Polymermatrix in Beziehung zu der Glasübergangstemperatur T_g des Matrixmaterials zu untersuchen, da diese Größe von speziellem Interesse im Hinblick auf Durchmischung und damit Bauteilstabilität ist. Dabei fanden wir heraus, dass Diffusion in der Umgebung und speziell unterhalb von T_g eine Arrhenius-förmige Temperaturabhängigkeit aufweist. Dies bedeutet, dass die Diffusion in diesem Temperaturbereich durch lokale Bewegungen getrieben ist, die durch die Seitenketten vermittelt werden, und nicht durch kollektive Bewegung des Systems, welche üblicherweise mit einem Williams-Landel-Ferry-Gesetz assoziiert wird. Mit diesen Ergebnissen konnte ich besonders zu der anhaltenden Debatte über den Mechanismus beitragen, welcher der Diffusion unterhalb der Glastemperatur zu Grunde liegt.

Des Weiteren ergab sich, dass die Diffusion unterhalb T_g sehr langsam von Statten geht, sodass sich Materialien mit einem T_g oberhalb der gewöhnlichen Umgebungs- bzw. Betriebstemperatur als vorteilhaft im Hinblick auf langzeitstabile Morphologien in optoelektronischen Bauteilen erweisen. In zukünftigen Arbeiten könnte die vorgestellte Technik — eventuell in modifizierter Form — auch auf andere Materialklassen ausgedehnt werden, beispielsweise Perowskite. Bei diesen stellt Eindiffusion von Dotanden oder Molekülen aus angrenzenden Transportschichten — insbesondere im Hinblick auf Wasser aus der Umgebung — ein gravierendes Problem für die Bauteilstabilität dar.

Ein vielversprechender Ansatz im Feld der organischen Elektronik um die Morphologie in Blendstrukturen zu stabilisieren und Diffusion in Mehrschichtstrukturen zu unterdrücken, ist die Vernetzung einer der beiden aktiven Komponenten, Donor oder Akzeptor, oder gar die Verbindung zwischen ihnen. Mehrere Studien über Vernetzung in organischen Solarzellen behandeln den Einfluss der Netzwerkbildung auf die Gesamteffizienz oder die Langzeitstabilität, beziehen sich dabei aber hauptsächlich auf Aspekte der Prozessierung und der Bauteilarchitektur. Tiefer gehende Untersuchungen über den Einfluss der Vernetzung auf die Ladungsträgermobilität, einen Schlüsselparameter hinsichtlich der Bauteileffizienz, sind jedoch sehr selten, beziehungsweise existieren nicht im Hinblick auf organische Solarzellen. Vor diesem Hintergrund und insbesondere, da vernetzte amorphe Donorschichten eine essentielle Rolle in der präsentierten Studie über die Delokalisation der Elektronenwellenfunktion spielen, wird in Kapitel 11 eine systematische Untersuchung der Abhängigkeit der Lochmobilität von der Vernetzungsdichte in einem amorphen Modellsystem durchgeführt. Darüber hinaus wird in diesem Zusammenhang der Einfluss von Photoinitiatoren zur Aktivierung des Vernetzungsprozesses behandelt. Es stellte sich heraus, dass die Mobilität unter optimierten Prozessierungsbedingungen nicht durch den Vernetzungsprozess selbst negativ beeinflusst wird. Allerdings wird trotz allem eine leichte Abnahme der Mobilität mit steigendem Anteil an vernetzbaren Gruppen beobachtet, unabhängig davon, ob eine Vernetzung stattfand oder nicht. Dies lässt sich konformellen Veränderung zuschreiben, welche durch die zusätzlichen funktionellen Gruppen in den Seitenketten hervorgerufen werden. Da jedoch eine signifikante Stabilisierung bereits durch einen kleineren Anteil im Bereich von 25 % vernetzbarer Gruppen in den Seitenketten erzielt werden kann, wo die Reduktion der Mobilität lediglich einen Faktor 2-3 beträgt, ist ein vernünftiger Kompromiss durchaus erreichbar. Folglich konnte ich zeigen, dass der Einsatz von Vernetzung in optoelektronischen Bauteilen vom Standpunkt der Mobilität aus tatsächlich gerechtfertigt ist, sofern die Bedingungen sorgfältig gewählt werden.

Neben Faktoren, die die Dissoziation und die Rekombination von Charge-Transfer-Zuständen (CT-Zuständen) beeinflussen, wird in Kapitel 12 auch der Charakter dieser Zustände in organischen Solarzellen eingehender betrachtet. Dies umfasst insbesondere die Frage, wie wichtige Größen wie die Energie E_{CT} des CT-Zustandes sowie die mit dem Zustand assoziierte Reorganisationsenergie λ von experimentellen Daten abgeleitet werden können, hier im Speziellen von Photolumineszenz- (PL) und Photoströmspektren (EQE). Um zu identifizieren, welcher theoretische Rahmen für eine solche Analyse geeignet ist, wurden temperaturabhängige, zeitaufgelöste PL- sowie temperaturabhängige EQE-Spektren im Bereich von 5 K bis 295 K aufgenommen. Unsere Ergebnisse erwiesen sich als inkonsistent mit der Elektronentransfertheorie von Marcus sowie mit der ursprünglichen Marcus-Levich-Jortner-Theorie (MLJ). Stattdessen fanden wir, dass die mit einem CT-Zustand assoziierte Linienform zu gleichen Teilen von statischer Unordnung und niederfrequenten Schwingungen bestimmt wird. Das bedeutet, dass sich die CT-Spektren nur dann konsistent über den gesamten betrachteten Temperaturbereich modellieren lassen, wenn Unordnungseffekte berücksichtigt werden. Passende Modelle zur Analyse sind in diesem Fall entweder ein modifizierter MLJ-Fit unter Einbezug von Unordnung oder das gängige Franck-Condon-Modell. Aufgrund des Bildes, das sich aus dieser Studie ergibt, scheint der Ladungstransfer damit stark an intermolekulare Schwingungen zu koppeln, sodass eine beobachtete Stokesverschiebung mit der Reorganisationsenergie, welche mit niederfrequenten Phononen

assoziiert ist, identifiziert werden kann.

Inspiziert durch meine Studie zur Delokalisation der Elektronenwellenfunktion sowie durch frühere Arbeiten zu CT-Zuständen in Fullerenen, wird schließlich in Kapitel 13 von der effizienten Autoionisation von CT-Zuständen im Akzeptor selbst Gebrauch gemacht, um optoelektronische Bauteile mit ambipolarer Charakteristik zu erhalten. Dazu wurde C_{60} mit einem DPP-Monomer kombiniert und in einer einfachen Zweischichtarchitektur verbaut. Die resultierenden Bauteile weisen Charakteristiken eines bidirektionalen Phototransistors auf, der sowohl optisch als auch elektrisch schaltbar ist. Der zu Grunde liegende Mechanismus lässt sich im Sinne eines (photo-) verstärkten Rekombinationsstroms interpretieren, welcher durch die Autoionisationseigenschaft von C_{60} ermöglicht wird. Die Präsenz einer Injektionsbarriere garantiert zudem einen niedrigen Dunkelstrom, wodurch das Ein-Aus-Verhältnis des Bauteilaustragsstromes verbessert wird. Unter Ausnutzung des beschriebenen Verhaltens demonstrieren wir sogar die Realisierung von grundlegenden hybriden optisch/elektronischen logischen Elementen wie NICHT-, UND-, und ODER-Gattern, welche als Basis für fortgeschrittenere Analog- und Digitalanwendungen dienen könnten. Mit diesem Kapitel präsentiere ich damit abschließend ein bemerkenswertes Beispiel, wie effiziente Dissoziation von (delokalisierten) CT-Zuständen in der Akzeptorphase in einer etwas anderen Art und Weise als einer gewöhnlichen Solarzelle genutzt werden kann.

0.2. English abstract

Organic solar cells have recently regained attention upon the design of new non-fullerene acceptors. This happened after interest first had stagnated in the context of the (re)discovery of hybrid organic-inorganic perovskite materials for photovoltaics, which effectively started in the period between 2009 and 2012. Before this evolution, organic photovoltaics were largely restricted to the use of fullerene acceptors and research was more focused on the optimization of donor materials and their properties. Having realized that state-of-the-art efficiency limits with fullerenes can be extended when understanding the special properties of the electron accepting species and using this knowledge for a systematic design of new materials, research interest has turned back to the acceptors again. This requires understanding which properties made fullerenes so unique and which mechanisms actually govern the efficient dissociation of charge transfer states in organic solar cells.

In view of the above, this thesis is dedicated to fundamental research concerning various aspects of dissociation, recombination and the character of charge transfer states in organic materials. A promising factor that is currently under debate and could possibly account for efficient dissociation in organic solar cells despite an apparent lack of driving force for charge separation is charge carrier delocalization, in the view of the above especially delocalization of the electron in the acceptor phase and at the donor-acceptor interface.

For this reason, chapter 9 of this thesis deals with the influence of electron delocalization in the acceptor on the dissociation process of charge transfer states at donor-acceptor interfaces. We performed a systematic study on three different fullerene acceptors differing in their degree of order, intermolecular coupling and localization of the electron wavefunction in a bilayer configuration with an efficient, crosslinked donor polymer. By crosslinking the donor, a well-defined interface could be achieved resulting in a good model system for the investigation of processes happening at the donor-acceptor interface. Correlating information from scattering experiments with the results of photophysical and electrical investigations as well as theoretical modelling, we find that a higher degree of order and stronger intermolecular coupling within the acceptor phase is accompanied by a higher degree of electron delocalization. Said correlation is substantiated by theoretical modelling of field dependent photocurrent measurements applying an effective mass model taking into account interfacial dipoles determined from ultraviolet photoelectron spectroscopy (UPS) and Kelvin-Probe measurements. This analysis reveals that electron delocalization is directly coupled to an increase in charge transfer state dissociation efficiency. Consequently, our results substantiate the position that delocalization of electrons in the acceptor phase plays a positive role in the charge separation process and that high local order of fullerenes is crucial in this respect. Considering earlier works on delocalization of holes in the donor, I come to the conclusion that delocalization of both electron and hole should be taken into account when designing efficient donor-acceptor systems.

Further factors that largely affect dissociation and recombination, and with this efficiency of an organic solar cell, are intermixing at interfaces in layered architecture as well as phase separation in a blend morphology as a result of diffusion of the usually applied small molecular acceptor or in the former case a dopant from an adjacent layer. Phase separation may lead to a worsening of percolation paths of the charge carriers to the electrodes and increased recombination probability. Intermixing in turn could cause unwanted doping of the active material leading to traps for charge carriers. As this is a general problem of small molecules being in contact with another

material and as this represents an important factor in terms of device stability, we introduce a novel, non-destructive approach to study diffusion in organic materials by mere optical means in chapter 10. It is based on monitoring diffusion as a function of time via photoluminescence quenching associated with energy transfer from the investigated matrix material to the diffusing small molecular quenchers. Using this method allows studying the diffusion coefficient as a function of temperature and may additionally give information about the temporal evolution of the concentration profile in the sample from theoretical simulations. We applied the technique to study diffusion of C_{60} in a polymer matrix in relation to the glass transition temperature T_g of the matrix material as this quantity is of special interest with respect to intermixing and device stability. We find evidence that diffusion in the vicinity of and especially below T_g features an Arrhenius-type temperature dependence meaning that it is driven by local motions mediated by side chains and not collective motion as associated with a Williams-Landel-Ferry-type behaviour. With these results I could especially contribute to the ongoing debate about the mechanism behind sub- T_g diffusion.

Furthermore, diffusion is very slow below T_g , so materials with higher T_g than the usual ambient or operational temperatures are advantageous in terms of morphological long-term stability in organic electronic devices. In future work, our method could — maybe with some modifications — also be applied to other material classes like perovskites. There, diffusion of dopants or other molecules — especially water from the ambient atmosphere — into the active layer may cause severe stability problems .

A promising aspect introduced in the organic electronics community to stabilize bulk morphologies or suppress diffusion in multi-layer structures is crosslinking of either of the active materials or even to link them together. Several studies about crosslinking in organic solar cells address the influence of it on the overall device performance or its long-term stability, but mainly focus on processing or device architectures. Yet, more in-depth studies on the influence of crosslinking on charge carrier mobility, a key parameter of device performance, are very rare and especially lacking with respect to organic solar cells. Against this background and because crosslinked amorphous donor layers are an essential part of my work about electron delocalization, I performed a systematic study on the dependence of hole mobility on the degree of crosslinking in an amorphous hole transporting model system in chapter 11. Moreover, the impact of adding photoinitiators to activate the crosslinking process is addressed. When applying optimized conditions in terms of processing, i.e. small amounts of heavy metal free curing agents or even mere thermal activation, mobility is not negatively influenced by the crosslinking process itself. Nevertheless, a small decrease in mobility with increasing fraction of crosslinkable groups was observed independent of crosslinking, which is attributed to conformational changes mediated by these additional functional groups. But since a significant stabilization may be already achieved with smaller fractions in the order of 25 % of crosslinkable groups in the side chains, where mobility is only reduced by a factor of 2-3, a reasonable compromise can be achieved. Consequently, I could show that the use of crosslinking in optoelectronic devices is indeed justified from the mobility point of view, if conditions are chosen carefully.

Apart from factors influencing the dissociation or recombination of charge transfer (CT) states, I also had a more in-depth look into the character of the CT states in organic solar cells in chapter 12. This particularly includes the question of how important quantities like the CT energy E_{CT} as well as the reorganization energy λ can be derived from experimental data, namely

photoluminescence (PL) and photocurrent (i.e. external quantum efficiency [EQE]) spectra of CT states. In order to identify the appropriate framework for such an analysis, we recorded temperature dependent time-resolved PL as well as temperature dependent EQE spectra in the range from 5 K to 295 K. Our results are inconsistent with both Marcus' electron transfer theory and the original Marcus-Levich-Jortner (MLJ) theory. We rather find that the lineshape of a CT state is determined by both static disorder and low frequency vibrations by about equal contributions. Only when disorder effects are included, the CT spectra can be modelled consistently over the entire temperature range, either in terms of a modified MLJ-based fit or the common Franck-Condon model. In view of this, we suggest that charge transfer probably couples strongly to inter-molecular vibrations. In this interpretation, an observed Stokes' shift is then associated with the reorganization energy that is related to low-frequency phonons.

Finally, inspired by my work on electron delocalization and previous studies on CT states in fullerenes, I make use of the ability of comparably efficient autoionization of bulk CT states in acceptor itself, to obtain optoelectronic devices with ambipolar characteristics in chapter 13. Thereto, I combine C_{60} with a DPP monomer in a simple bilayer configuration. The resulting devices feature characteristics of a bidirectional phototransistor, that can be switched both optically and electrically. The underlying mechanism can be interpreted in terms of a (photo-) enhanced recombination current mediated by the intrinsic autoionization property of C_{60} . The presence of an injection barrier additionally ensures a low dark current and thereby a better on/off ratio. Eventually, I demonstrate the realization of basic hybrid optic/electronic logic elements like NOT-, AND-, and OR-Gates that could serve as a basis for advanced analog and digital applications. With this chapter, I eventually give a remarkable example of how efficient dissociation of (delocalized) CT states in the acceptor phase can be utilized in a kind of alternative way as compared to a conventional solar cell.

Contents

Abstract	IX
0.1. Deutsche Kurzzusammenfassung	IX
0.2. English abstract	XIII
I. Extended Abstract	1
1. Motivation	3
2. The working principle of organic solar cells	7
3. Charge transfer states at the donor-acceptor interface	13
3.1. The concept of Charge transfer states	13
3.2. Role of delocalization in the CT dissociation process	18
3.3. Further factors influencing CT state dissociation	23
4. Charge Transport and the role of mobility in the charge separation process	27
5. Fullerenes as electron acceptors in organic solar cells	35
6. Diffusion of small molecules in a polymer matrix	39
7. Excursus: Crosslinking in organic solar cells	43
8. Overview over the publications	47
8.1. Summary and overall context	47
8.2. Contents of the individual publications	55
8.2.1. Does Electron Delocalization Influence Charge Separation at Donor-Acceptor Interfaces in Organic Photovoltaic Cells?	55
8.2.2. Facile Method for the Investigation of Temperature-Dependent C_{60} Diffu- sion in Conjugated Polymers	60
8.2.3. Influence of Crosslinking on Charge Carrier Mobility in Crosslinkable Polyfluorene Derivatives	65
8.2.4. How to Interpret Absorption and Fluorescence Spectra of Charge Transfer States in an Organic Solar Cell	70
8.2.5. Organic Bidirectional Phototransistors Based on Diketopyrrolopyrrole and Fullerene	77
8.3. Author's contributions	81
8.4. Full list of Publications	83

II. Publications	117
9. Does Electron Delocalization Influence Charge Separation at Donor-Acceptor Interfaces in Organic Photovoltaic Cells?	119
10. Facile Method for the Investigation of Temperature-Dependent C_{60} Diffusion in Conjugated Polymers	157
11. Influence of Crosslinking on Charge Carrier Mobility in Crosslinkable Polyfluorene Derivatives	187
12. How to Interpret Absorption and Fluorescence Spectra of Charge Transfer States in an Organic Solar Cell	203
13. Organic Bidirectional Phototransistors Based on Diketopyrrolopyrrole and Fullerene	223
Appendix	245
A. Crosslinked Semiconductor Polymers for Photovoltaic Applications	245
B. List of abbreviations	257
C. Acknowledgements	259
D. Erklärung und Eidesstattliche Versicherung	263

Part I.

Extended Abstract

1 Motivation

The field of Photovoltaic has seen rapid developments in the past two decades (figure 1.1).²⁻⁶ Especially the (re)discovery of hybrid organic-inorganic perovskites as potential materials for solar cell application in the period between 2009 and 2012 has boosted research towards alternatives to the established Si-based technology, which features highly optimized device efficiencies of around 25 – 26 %, i.e. close the theoretically achievable Shockley-Queisser-limit for a bandgap of 1.1 eV.⁷⁻⁹ Hybrid organic-inorganic perovskite solar cells have undergone a rapid development in this respect, crossing the 20 % efficiency mark under optimized conditions with recent record values of nearly 24 %.¹⁰ Yet, these materials still feature some major drawbacks concerning their stability under ambient conditions and often decompose rapidly in the presence of humidity.^{11,12} Another disadvantage is the often discussed need of lead to achieve high efficiencies. Both factors actually could impede commercialization and are subject to current research.¹³⁻¹⁷

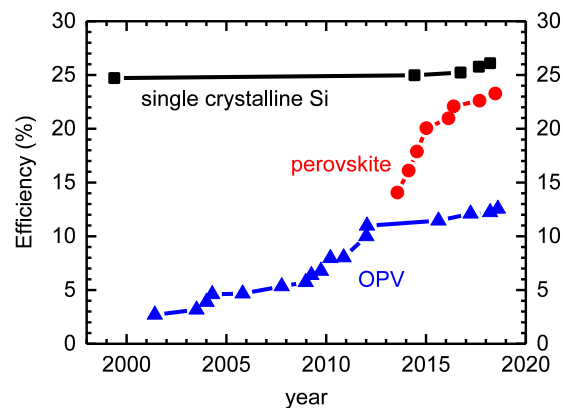


Figure 1.1.: Evolution of certified efficiencies for single crystalline Si solar cells (black squares), (non-stabilized) Perovskite solar cells (red circles) and organic photovoltaics (blue triangles) in the period between 1999 and 2018. Data were taken from Ref. [1].

This development at first seemed to turn research interest away from purely organic solar cells, where further improvements of device efficiency over 10–11 % were hard to achieve with the commonly used donor/acceptor systems based on polymeric donors and fullerene acceptors (figure 1.1).¹ Due to their outstanding properties like spherical aromaticity, three-dimensional charge transport, high electron mobility or their ability to aggregate to form pure domains in bulk heterojunction devices, fullerenes seemed to be the best choice as acceptor.^{3,18,19} Consequently, great effort has been put into the design of new donor materials, mainly conjugated low bandgap polymers like PCDTBT, PCPDTBT or PTB7, to complement the limited absorption of fullerenes in the VIS range of the electromagnetic spectrum and into the optimization and understanding of morphology formation.²⁰⁻²⁹ Yet, the tendency to diffuse and aggregate is at the same time one of the major drawbacks of fullerenes, as optimized morphologies are often not thermodynamically long-term stable under operating conditions.^{25,30,31} The resulting phase separation leads to a decrease in efficiency due to worsened percolation and increased recombination. This issue was addressed by developing bulkier fullerenes with less aggregation tendency or by crosslinking either or both of the active components to suppress diffusion and stabilize a certain morphology,

however often resulting in lower efficiencies.^{23,32-36}

The apparent stagnation in the field of organic solar cells has changed with the development of new non-fullerene acceptors (NFAs), which nowadays even surpassed fullerene based systems in terms of both efficiency and stability, with record values approaching 14%.^{2,37} Many of these NFA systems feature better tunability of their absorption spectrum as compared to fullerenes, less aggregation tendency - sometimes even too little - and easier synthesis and purification.^{3,18,38} Recent estimations even predict achievable efficiencies of up to 20% for an ideal non-fullerene acceptor.^{2,37} But nevertheless, NFAs are also organic semiconductors and as such feature the same basic properties as fullerenes or PDIs. Most importantly, they are extrinsic semiconductors where excitations results in bound electron-hole (e-h) pairs that have to be split before charges can be extracted.³⁹ Therefore, the critical factor for the performance of organic solar cells is the dissociation efficiency of these e-h-pairs, preferably residing at D/A interfaces in the form of CT states. Despite extensive research in the past decades, the relevant mechanisms and aspects of the dissociation process, including recombination before the actual separation, and the character of the CT states are still not fully understood and in some aspects even discussed controversial. Yet, these factors are critical in terms of further improvement of material design and overall device efficiency.

Against this background, the main part of this thesis is devoted to gain a deeper understanding of the character of the charge transfer state and its dissociation. In this context the focus is on the one hand laid on how the fundamental electron transfer process may be correctly described conceptually on a microscopic scale, which framework is actually suitable and what role static disorder plays in this respect. On the other hand, special attention is given to the influence of wavefunction delocalization and local order on the charge transfer dissociation process at a donor/acceptor interface, particularly with respect to the electron in the acceptor phase. This is because the latter aspect is among the most promising and controversially discussed candidates to account for efficient dissociation in the newly emerged NFA-based organic solar cells. This finally allows to better understand which factors are crucial in terms of material design and device architecture to achieve efficient dissociation in organic solar cells. Beside successful charge separation, device efficiency is also significantly affected by the probability of charge carrier recombination, be it geminately at the donor/acceptor interface where the e-h-pair was formed or non-geminately during extraction. The recombination process is largely determined by the mobility of the respective charge carriers. Here, the aspect of mobility is addressed in two contexts: First, through its connection with electron wavefunction delocalization and thus its direct influence on the dissociation process itself via geminate recombination; Second, via the influence of crosslinking on charge carrier mobility, because this is still a promising approach to stabilize morphologies for a long-term use and also to suppress interdiffusion of molecules from adjacent layers. The latter aspect may also have important implications in the field of perovskite solar cells, which rely on heavily doped hole transport layers to enable high efficiencies and are known to suffer from dopant diffusion into the perovskite layer.⁴⁰⁻⁴² In this respect, crosslinking is also an interesting approach to suppress diffusion of dopants. A part of this thesis is thus concerned with the diffusion at interfaces in layered architectures. Special attention is given to the temperature dependence of diffusivity in relation to the glass transition temperature, because it is an important quantity for a solar cell in terms of the long-term stability of morphology under

operating conditions. In the course of studying this topic I also take a deeper look into the influence of side chains in a polymeric matrix on the diffusion process. Moreover, I investigate the diffusion mechanism below the glass transition temperature. This aspect is still subject to current research and may have important implications for device stability and material design. In the end, I finally demonstrate an alternative usage of efficient charge transfer dissociation apart from organic photovoltaics by studying the applicability of fullerenes in hybrid optical and electrical logic elements.

The first part I of the thesis presents the theoretical background of the investigated topic as well as the current state of research with respect to the addressed issues. Chapter 2 gives a short introduction into the working principle of an organic solar cell with special focus on the different steps of charge generation and extraction. The critical steps of charge transfer state formation and particularly their dissociation are discussed in detail in chapter 3. Special attention is given to the factors that influence charge transfer dissociation, with particular focus on charge carrier delocalization. Chapter 4 addresses the role of charge carrier mobility in the charge separation process. The next three chapters summarize relevant information about the use of fullerenes as acceptors (5), diffusion of small molecules in a polymer matrix (6) and the application of crosslinking (7), all in the context of organic solar cells. Finally, part I is concluded by an overview over all my publications presented in this thesis (chapter 8). These publications are eventually reprinted in their original form in part II. Finally, the appendix contains my review on crosslinked semiconductor polymers for photovoltaic applications, which is not part of the dissertation, yet supplements it.

2 The working principle of organic solar cells

In contrast to inorganic semiconductors, photoexcitation in organic semiconductors leads to coulombically bound electron-hole (e-h)-pairs due to small screening with typical permittivities ϵ_r of about 3-4. Following the terminology known from inorganics these pairs are usually termed "excitons". They are often strongly localized on the excited chromophore with binding energies that are in the range of 0.3 – 0.5 eV ("Frenkel"-excitons).^{43,44} As (thermally activated) autoionization in a single organic materials is very inefficient there are basically no intrinsic charge carriers present.^{45,46} Therefore, the need of a combination of at least two materials, an electron-rich donor and an electron-deficient acceptor, arises in order to make a spatial separation of electron and hole via charge transfer energetically more favourable than for example mere energy transfer.⁴⁷ Accordingly, the electronic structure of the materials has to be chosen such that the resulting donor-acceptor heterojunction features both higher ionization energy and electron affinity of the acceptor with respect to the donor ("Type-II-Heterojunction", cf. figure 2.1(a)).¹ In this arrangement, either an electron may be transferred from the donor to the acceptor or a hole in the opposite direction, resulting in a positively charged donor and a negatively charged acceptor. Yet, both charges are still coulombically bound, now forming a so called Charge-Transfer exciton that still has to be split into free charges. The latter aspect is discussed in detail in chapter 3.

In general, there are two basic types of Donor-Acceptor-type organic solar cells. Both materials may be mixed in order to form a blend morphology and increase the interfacial area between them. This arrangement is called *Bulk heterojunction* device. Alternatively donor and acceptor may be deposited on top of each other in a bilayer architecture, which has the advantage of a defined percolation of generated charges to the respective electrodes. This structure is referred to as *Flat* or *Planar heterojunction* device (figure 2.1(b)).

The whole pathway of energy conversion from light absorption to charge carrier extraction from the device can be divided into five basic steps, each of which features a certain efficiency due to specific limitations and losses and therefore impacts on the resulting total efficiency of the solar cell.⁴⁸ These steps are illustrated in figure 2.1(b).

In the first step (i), photons are absorbed in the active materials of the solar cell to generate bound e-h-pairs. The efficiency η_A of this generation is directly linked to the absorption coefficient of the absorbing materials. Usually, organic molecules feature absorption bands widths in the order of 100 nm.⁹ For this reason, donor and acceptor are designed to preferably feature complementary absorption spectra to harvest a larger portion of the solar spectrum. Since in

¹ In this respect it should be noted that in literature the terms ionization energy and electron affinity are often replaced by and used equivalently with the energy levels of the HOMO and LUMO orbitals, respectively, although the latter actually refer to the orbital energies resulting from a one-electron approximation.

the last decades nearly exclusively fullerenes were used as acceptors, which only absorb significantly down to about 550 nm (see chapter 5), material design was mainly aimed at narrowing the bandgap of the mostly polymeric donors in order to extend the absorption of the device into the red part of the electromagnetic spectrum.^{20–24,49}

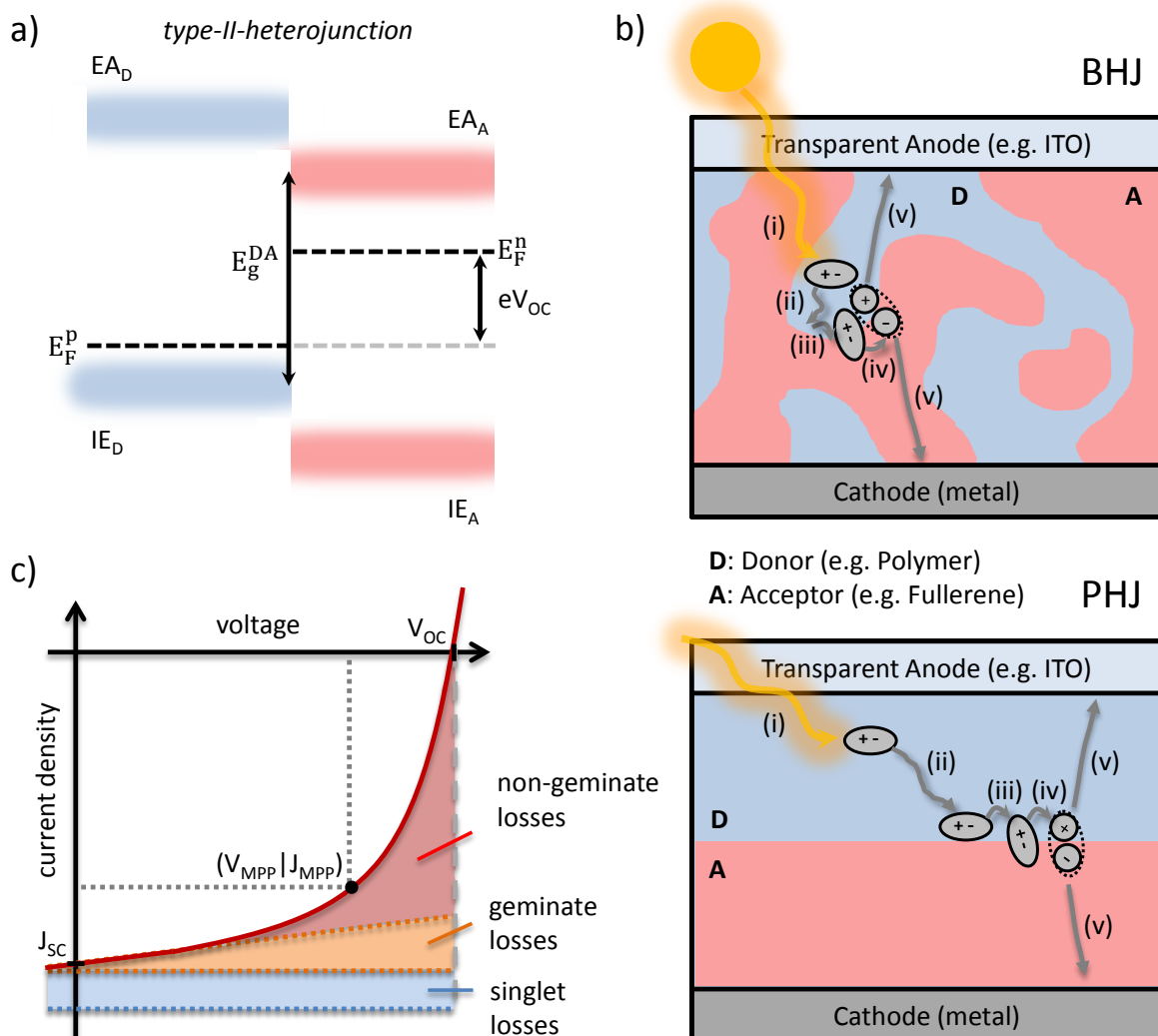


Figure 2.1.: (a) Schematic of a type-II Donor-Acceptor heterojunction along with the illustration of the relation between the effective Donor-Acceptor bandgap E_g^{DA} and the open-circuit voltage V_{OC} . E_F^p and E_F^n denote Quasi-Fermi levels for Donor and Acceptor, respectively. The broad coloured lines illustrate the respective density of states (DOS) of the HOMO ($\approx -IE$) and LUMO ($\approx -EA$) levels of donor (blue) and acceptor (red). (b) Schematic structures of a bulk heterojunction (BHJ, top) and a planar heterojunction (PHJ, bottom) device. The five basic steps of energy conversion from light to electric energy are depicted as roman numbers: (i) absorption, (ii) exciton diffusion, (iii) charge transfer, (iv) exciton dissociation, (v) charge extraction and collection. (c) Schematic of a typical J-V-characteristic of an organic solar cell. The different losses that impact on the shape of the curve are illustrated as coloured areas and are discussed in detail in the main text. V_{OC} and J_{SC} denote the open-circuit voltage and the short-circuit current density, respectively. The grey dot on the characteristic represents the point at which maximum power can be extracted from the device (MPP = Maximum Power Point)

With the discovery of efficient non-fullerene acceptors nowadays also attempts are made to tune the absorption spectra of acceptor materials.^{3,18,38} Apart from the actual absorption of the photoactive layer further losses might arise from parasitic absorption or reflection of additional transport or blocking layers or even the electrodes themselves.⁵⁰ As one of the electrodes is usually metallic, reflections at its backside may in turn increase the efficiency of light collection again, as the light passes through the photoactive layer a second time. Yet, due to active layer thicknesses in the order of 100 nm additional interference effects may arise so that possibly the optical field distribution inside the device has to be taken into account, when addressing the actual efficiency of charge generation inside the device.⁵⁰

In the second step (ii), the generated e-h-pairs need to diffuse to a Donor-Acceptor (D/A) interface. As the excited states feature a finite lifetime τ , the diffusion process naturally competes with the relaxation back to the ground state. With a certain diffusivity D of the respective exciton, its diffusion length x_D is simply given by $x_D = \sqrt{D \cdot \tau}$. Therefore, the probability η_{Diff} to reach a D/A interface is mainly determined by the mean distance the exciton has to overcome to get there.^{9,43,44} Typical exciton diffusion lengths x_D of singlet excitons in disordered (amorphous) organic materials like polymers are in the order of 6-10nm.^{9,48,51-53} In crystalline materials it can be considerably larger in the order of 50 – 100 nm (e.g. in naphthalene or anthracene).⁴⁵

Losses due to recombination prior to reaching the interface result in a reduction of the number of charges that could possibly be extracted and decrease the maximum extractable current of a solar cell (light blue area in figure 2.1(c)). Consequently, layers have to be either thin (PHJ), in which case absorption will be low, or both components have to be intermixed in a way that the mean spacing between different phases is in the order of twice times x_D (BHJ).^{36,52,54-56} Therefore, a lot of effort has been put into the optimization and especially the understanding of the formation and dynamics of device morphologies over the last years,^{25-31,57-59} yet a major problem of organic solar cells still remains: The morphologies in polymer-fullerene BHJ devices are not thermodynamically stable and prone to phase segregation under thermal stress as present under operating conditions. The driving force of this process is either crystallization of the polymeric donor or Ostwald ripening resulting in large fullerene clusters.^{23,35,36,60} A promising approach pursued in the organic electronics community to tackle with this problem is crosslinking to stabilize the morphology. This aspect is addressed in chapter 7 and especially appendix A.

In view of a more complex morphology in BHJ, PHJ devices, though they are not the most efficient, are better model devices to understand fundamental processes related to interfaces and disentangle them from device morphology. For example exciton diffusion lengths may be easier inferred from a variation of layer thicknesses than from an intermixed morphology where domain sizes may vary in size and are less easy to determine. Another aspect that may be well studied in PHJ devices is the dissociation of CT states at the D/A interface, as discussed below.

Having reached the interface, excitations may be transformed into charge transfer states with an efficiency η_{CT} via electron transfer from the donor to the acceptor or hole transfer from the acceptor to the donor (step iii). For this process to be efficient the energy of the CT state needs to be below the S_1 energy (and ideally also the T_1 -energy)⁶¹ of both donor and acceptor. Furthermore, it is commonly observed that the energetic offset of both IE and EA needs to be at least 0.1 – 0.2 eV in order to provide a sufficient driving force for the formation of a CT state.^{51,62}

Apart from that, very recent research implies that the process of CT formation is in fact independent on the actual strength of the driving force.⁶³ In general, the formation of CT states happens on an ultrafast timescale in the order of several tens to few hundreds of femtoseconds and was found to be very efficient for a number of donor-acceptor combinations,^{56,64–70} meaning that this step does not represent a limiting process regarding the efficiency of an organic solar cell.

After the formation of CT states at the D/A interface, these states may be dissociated into separate charges with a certain probability η_{Diss} or recombine geminately back to the ground state before any charges can be spatially separated (step iv). Losses via geminate recombination (GR) are more pronounced at low internal electric field as then no external force can assist the charges to overcome their mutual Coulomb potential (orange shaded area in figure 2.1(c)). In terms of efficiency, the step of CT dissociation is basically the most essential process in an organic solar cell. Yet, it is still not fully understood and the central question of how the mutual potential barrier for the charge carriers can be efficiently overcome or lowered and which mechanisms actually impact on the separation process is still under debate and subject to current research.^{44,71,72} This is especially important in the light of the emerging non-fullerene acceptors, where some recent studies suggest that efficient dissociation and charge separation may be also achieved in systems with negligible driving force and nearly resonant CT - and S_1 -energies.^{18,73} Several factors how the electrostatic potential may be modified at the interface or how the binding energy of the CT state could be lowered have been and still are under investigation. These include the presence of a strong internal electric field, dielectric effects and interfacial dipoles, application of excess energy to create vibrationally excited CT states, intra- and intermolecular delocalization, disorder and finally entropy, with the last three being the most promising candidates.⁷⁴ This is why the effect of delocalization of the electron wavefunction in the acceptor phase on CT dissociation efficiency is addressed in one of my publications (see chapters 8.2.1 and 9). In the course of this work we also make use of PHJ devices as model systems to study interfacial effects avoiding any morphological impact. More details about the concept of CT states and the factors that may impact on their dissociation efficiency are discussed in the next chapter (3).

Finally, charges that were separated at the D/A interface need to be transported across the active layer and eventually extracted at their respective electrode (step v). The only remaining loss mechanisms at this stage are the recombination between counter charges on their way out of the device or between a charge and a stationary trap. The recombination between charges may be still geminate between siblings at the D/A interface or non-geminate between different charges that meet in the bulk of the device. A lot of experimental and theoretical effort has been put into investigating the factors governing recombination as well as understanding the underlying mechanisms.^{75–82} A main factor that is especially relevant for BHJ solar cells is the presence of defined percolation pathways to the respective electrodes. This requires a bicontinuous network in these devices that is formed via spinodal decomposition.⁹ However, in such a morphology also the probability of an encounter between charges of different sign is significantly higher than in a bilayer structure, where the pathway to the electrodes is clearly defined. Furthermore, a blend morphology may readily feature dead ends for charge transport and apart from that, as already mentioned above, these morphologies are not thermodynamically stable and prone to coarsening and the formation of islands,^{23,35,36,47} which again increases the probability of non-geminate recombination (NGR). This type of recombination is enhanced at low internal electric

field and particularly in the case of flat energy levels as then carrier motion is only driven by diffusion and no longer by drift to the electrodes. This results in a pronounced field dependence of this process, particularly in the presence of high charge carrier densities (red shaded area in figure 2.1(c)). This is why often additional transport and blocking layers are incorporated at the electrodes to effectively separate the diffusive motion of electrons and holes.⁹

Another important factor beside morphology impacting on both geminate and non-geminate charge carrier recombination is the absolute mobility μ of the respective charges as well as the ratio of electron (μ_e) and hole mobilities (μ_h),^{76,83–85} because this basically determines how far a charge carrier can travel within its lifetime τ . Therefore, as a common measure for the efficiency of charge transport (η_μ) at a certain internal electric field one often refers to the mobility-lifetime ($\mu\tau$) product.⁴⁴ The role of mobility in the charge separation process and its influence on recombination in an organic solar cell is discussed in more detail in chapter 4.

When the charges have finally reached the electrodes they are collected with a certain efficiency η_{Coll} . This step is usually not a problem as long as selective contacts are employed. Only in the presence of extraction barriers a space charge may build up resulting in increased recombination and the occurrence of an S-shape in the J-V-characteristic of the device (see also chapter 4).⁸⁶

All the efficiencies related to the five basic steps finally combine to the total (external) quantum efficiency EQE of the device according to:⁴⁴

$$\begin{aligned} EQE(\lambda, V, T) &= \eta_A(\lambda)\eta_{Diff}(T)\eta_{CT}(T)\eta_{Diss}(F, T)\eta_\mu(F, T)\eta_{Coll}(F, T) \\ &= \eta_A(\lambda) \cdot IQE(\lambda, V, T) \end{aligned} \quad (2.1)$$

where λ is the wavelength, V the applied voltage, T the temperature and F the electric field. When the EQE is corrected for the absorption efficiency we arrive at the so called internal quantum efficiency (IQE) that is a measure of the number of electrons generated per photon that is actually absorbed in the active layer and not only incident on the device. The latter is a more useful quantity when assessing internal electric process of the device.⁵⁰

A helpful quantity to assess the geminate and non-geminate losses in a solar cell is the so called Fill-Factor (FF) (figure 2.1(c)). It is defined as:

$$FF = \frac{J_{MPP} \cdot V_{MPP}}{J_{SC} \cdot V_{OC}} \quad (2.2)$$

where J_{MPP} and V_{MPP} are the current density and the voltage at which the maximum power can be extracted from the device (MPP = Maximum Power Point; figure 2.1(c)). J_{SC} denotes the so called short-circuit current density, i.e. the current density that can be extracted from the device under short circuit conditions with no externally voltage applied. V_{OC} eventually is defined as the externally applied voltage at which the photogenerated current compensates parasitic leakage current (injected charge carriers) and recombination current (GR and NGR) so that the total current flow is zero. A quantity that is closely related to V_{OC} is the so called compensation voltage V_0 at which the photocurrent J_{Photo} , which is the difference between the total current under illumination J_{illu} and the current in the dark J_{dark} , vanishes. When calculating J_{Photo} as $J_{illu} - J_{dark}$ one has to keep in mind that above V_{OC} the total current is usually dominated by injected charge carriers unless an injection barrier is present.⁸⁷ In this case, the effect of the series resistance of the electrodes and the resulting voltage drop may

become significant⁸⁷⁻⁸⁹ for injection currents in the order of mA. In this case a correction for the associated voltage drop over the resistance is needed to determine the correct photocurrent in forward direction.⁸⁷

While J_{SC} is basically determined by all the efficiencies discussed above, the open-circuit voltage V_{OC} is determined by the energy levels of the applied donor and acceptor materials as long as it is not limited by the work function difference of the electrodes (figure 2.1(a)).^{44,90-92} Taking disorder at the interface into account, V_{OC} can be expressed as⁹³

$$e \cdot V_{OC} = E_F^n - E_F^p = E_g^{DA} - k_B T \ln \left(\frac{N_C \cdot N_V}{n \cdot p} \right) \quad (2.3)$$

with E_F^n and E_F^p being so called Quasi-fermi-levels that may be determined from the assumption that both holes and electrons are equilibrated in their respective density of states (DOS). Note that Quasi-fermi-levels are a well-defined quantity under illumination.⁹⁴ E_g^{DA} denotes the difference between the maxima of the HOMO and LUMO DOS, which are assumed to be Gaussian. This energy difference determines the energy E_{CT} of the charge transfer state.⁷² N_C and N_V eventually are the total densities of available states within HOMO and LUMO, respectively.⁴⁴

With the definition of the FF it is also possible to define an efficiency that is more relevant to application than EQE or IQE, which are usually recorded at short circuit conditions, where no power can be extracted, namely the power conversion efficiency η . It is given by the ratio of the maximum power P_{max} that can be extracted from the device (i.e. at the MPP) and the incident intensity $I(\lambda)$

$$\eta = \frac{P_{max}}{I(\lambda)} = \frac{FF(\lambda) \cdot J_{SC}(\lambda) \cdot V_{OC}(\lambda)}{I(\lambda)} \quad (2.4)$$

in the case of monochromatic illumination. For white light illumination the respective integrals over the wavelength have to be taken for each quantity.

For a detailed discussion of organic materials and the different steps in the charge generation process, the reader is referred to fundamental works on organic semiconductors and device physics like the books by Köhler/Bässler, Tress, Schwörer/Wolf or Brabec.⁹⁵⁻⁹⁸

3 Charge transfer states at the donor-acceptor interface

3.1. The concept of Charge transfer states

Meanwhile it has been unambiguously shown that charge generation in an organic solar cell takes place via the intermediate formation of a Coulomb-bound electron-hole pair on adjacent molecules or chromophores that fulfill the energetic requirements of a type-II-heterojunction (see chapter 2).^{69,82,99–103} The basic idea of the presence of such an intermediate charge transfer (CT) state with a finite lifetime has been first presented by Braun in 1984.¹⁰⁴ It is based on the observation that Onsager’s model from 1938,¹⁰⁵ which was developed to describe geminate pair dissociation in (weak) electrolytes and was successfully applied to single compound materials, predicts too large thermalization radii (2.5 – 3.5 nm) for an electron-hole pair as compared to the average donor-acceptor spacing $\lesssim 1$ nm when applied to donor-acceptor type solid materials. This was due to the fact that geminate pairs in Onsager’s model will certainly recombine and disappear if their separation reaches zero.^{43,71} Braun extended Onsager’s concept by introducing an additional intermediate CT state that has lower energy and a much longer lifetime than the singlet (or triplet) state of the donor or the acceptor. The electron-hole pair could now make several attempts to dissociate from this CT state during its lifetime before geminately recombining to the ground state (figure 3.1). The electric-field dependent dissociation yield $\phi(F)$ is then simply given by the balance between dissociation rate $k_d(F)$ and recombination rate k_f back to the ground state:

$$\phi(F) = \frac{k_d(F)}{k_d(F) + k_f} = k_d(F) \cdot \tau(F) \quad (3.1)$$

$\tau(F) = \frac{1}{k_d(F) + k_f}$ denotes the lifetime of the CT state (dependent on the electric field strength F). Adapting the mathematical framework of Onsager’s original work,¹⁰⁶ the field-dependent dissociation rate $k_d(F)$ may be written as:^{104,105}

$$k_d(F) = \frac{3\mu e}{4\pi\epsilon_0\epsilon_r r_0^3} \cdot \exp\left(\frac{-E_B}{k_b T}\right) \cdot \frac{J_1\left(2\sqrt{-2b}\right)}{\sqrt{-2b}} \quad \text{with} \quad b = \frac{e^3 F}{8\pi\epsilon_0\epsilon_r k_B^2 T^2} \quad (3.2)$$

where μ and ϵ_r are the effective mean mobility of both charge carriers and the averaged dielectric constants of both materials, respectively, J_1 denotes the Bessel function of the first kind and r_0 is the thermalisation radius of the electron-hole pair, i.e. the intra-pair separation after thermal relaxation. Eventually, $E_B = \frac{e^2}{4\pi\epsilon_0\epsilon_r r_0}$ is the Coulomb binding energy of the geminate pair. The first factor in equation (3.2) is derived from the concept of Langevin recombination of free charge carriers,^{107,108} the second factor is a measure of the ratio of free and coulomb-bound electrons and holes in the absence of an electric field¹⁰⁹ and the third term gives the relative increase of

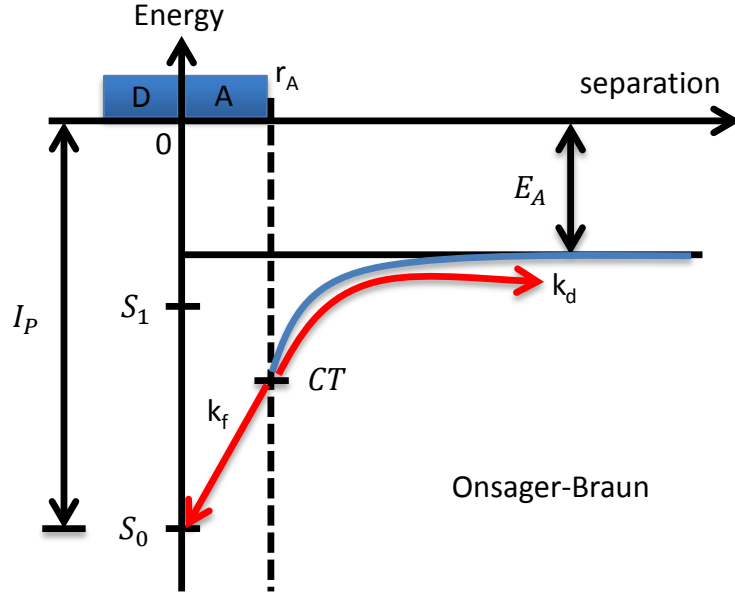


Figure 3.1.: Schematic of the Onsager-Braun model. An electron-hole pair can take several attempts to dissociate (with rate k_d) during its lifetime from an intermediate CT state before relaxing back to the ground state S_0 (with rate k_f). The CT state is energetically lower than the first excited state S_1 (in this case of the donor D) and features an initial intra-pair separation r_A . I_P and E_A denote the ionization potential of the donor (D) and the electron affinity of the acceptor (A), respectively. The blue line indicates the Coulomb potential the electron has to overcome in order to become a free charge (without any additional barrier lowering, e.g. via an applied electric field).

the dissociation with increasing electric field. According to this concept, electron-hole pairs are split with higher probability as compared to the original Onsager mode. Yet, strong electric fields ($10^7 \frac{V}{cm}$)⁷¹ are predicted to be necessary for efficient dissociation and Coulomb attraction is still much larger than the available thermal energy.^{71,110} With a typical dielectric constant of $\epsilon_r = 3 - 4$ for organic materials and a thermalisation radius of $r_0 = 1 nm$ ¹¹¹⁻¹¹³ E_B can be roughly estimated to be about $0.4 - 0.5 eV$, which is considerably larger than $k_B T \approx 0.025 eV$ at room temperature. This would result in a negligible dissociation rate k_d (\rightarrow second term in equation (3.2)). Since experimental observations prove that dissociation of CT states in organic solar cells can be very efficient — with internal quantum efficiencies reaching 100%^{114,115} — there has been and still is extensive research conducted on how the formation of charge transfer states can be properly described and how an efficient dissociation of them can actually take place.

Experimentally, CT states can be studied by spectroscopic means. As these states are usually lower in energy than excitonic states in the pristine materials, they appear as an additional broad absorption band below the bandgap of both donor and acceptor. Due to a small overlap of wavefunctions between different molecules, the absorption cross section of CT states is small so that sensitive techniques like photothermal deflection spectroscopy (PDS)¹¹⁶⁻¹²⁰ or EQE measurements (cf. equation (2.1)) using the Lock-In technique or Fourier-transform photocurrent spectroscopy (FTPS)^{44,118,121,122} are required. CT states may also be detected in sensitive photoluminescence (PL) or (voltage dependent) electroluminescence (EL) measurements,¹²³⁻¹²⁶ appearing

as broad red-shifted signal compared to the luminescence of the pristine materials.^{62,124,127–129} In well intermixed systems the original PL of the individual components might even be quenched due to efficient charge transfer which renders detection of the CT emission easier. Luminescence from CT states can be further identified via time resolved spectroscopy through different lifetimes^{130,131} as compared to the excitations of the donor or the acceptor or by the fact that they may be more easily dissociated when applying an electric field resulting in luminescence quenching.^{124,130,132,133} It is even possible to study the actual charge transfer process, i.e. the formation of charge transfer states, by using ultrafast pump-probe spectroscopy.^{63,69,134,135}

Commonly in literature, charge transfer in organic materials is assumed to follow the framework of Marcus' electron transfer theory,^{136–141} which was established in 1956 to describe electron transfer reactions in electrolytes^{142,143} and later used to model absorption and luminescence spectra of charge transfer states in such systems.¹⁴⁴

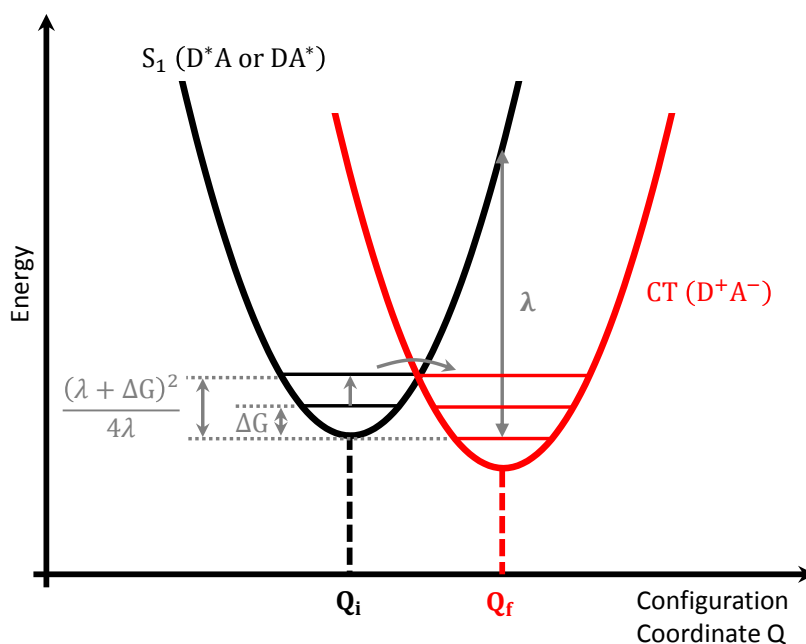


Figure 3.2.: Schematic potential energy diagram for Marcus theory of electron transfer from an excited donor (D^*A) or acceptor (DA^*) to the respective non-excited species resulting in a CT state (D^+A^-). A finite energetic offset ΔG between initial and final state alters the activation energy $E_A = \frac{(\lambda + \Delta G)^2}{4\lambda}$ needed to overcome the potential barrier.

In Marcus theory, electron transfer is described as a temperature activated process in which the system has to overcome a potential barrier to get from its initial state (i) where either donor or acceptor are excited (D^*A or DA^*) to the final state (f) where the charge transfer has taken place (D^+A^-). The potentials of the two states are usually taken to be identical parabolas, i.e. harmonic oscillators, that are shifted by a certain amount $\Delta Q = Q_f - Q_i$ in the configuration coordinate Q as a result of the reorganization needed for the system to adjust to the final geometry. The associated energy for this rearrangement is referred to as reorganization energy λ (figure 3.2). Yet, it is actually not necessary for the system to distort to this extent, as electron transfer already occurs when the system can overcome the barrier given by the intersection of the two parabolas. When there is no additional offset between the minima of the parabolas, this

barrier is $\frac{\lambda}{4}$. Taking internal (from the molecules themselves) and external phonon modes (from the surroundings) as well as a possible energetic offset ΔG (*driving force*) into account, the rate for electron transfer according to Marcus theory is given by:^{143,145}

$$k_{\text{Marcus}}(T) = \frac{|J_{DA}|^2}{\hbar} \cdot \sqrt{\frac{\pi}{\lambda k_B T}} \cdot \exp \left[-\frac{(\lambda + \Delta G)^2}{4\lambda k_B T} \right] \quad (3.3)$$

with J_{DA} being the electronic coupling strength between donor and acceptor, λ being the reorganization energy and $\Delta G = E_{CT} - E_{S1}$ being the driving force for charge transfer. The equation is based on thermal equilibrium and the assumption that the thermal energy of the system is much larger than the vibrational energy of the phonons.⁶³ This formulation implies that the rate $k_{\text{Marcus}}(T)$ features a maximum when $\Delta G = -\lambda$ and decreases again for larger ΔG (*Marcus inverted regime*), meaning that the driving force should have a large impact on the electron transfer rate.

Some works indeed report a correlation between driving force and charge transfer yield.^{136,146} For example, Ward et al. investigated a number of donor-acceptor blends with systematically varying LUMO energies and found an apparent correlation between driving force and charge transfer rate with a maximum rate at $\Delta G = -0.4 \text{ eV}$. As the rate decreased for higher and lower values of ΔG , their results were interpreted to be consistent with Marcus theory.¹³⁶ In contrast to this, recent studies on non-fullerene acceptors have shown that organic solar cells may be very efficient despite the lack of a significant driving force for charge transfer.^{73,147} In view of this, Unger et al. very recently performed another systematic study on the temperature dependence of the transfer rate in the range between 12 – 295 K in which the driving force was varied from $\Delta G \approx -\lambda$, i.e. in the normal regime where the rate should be maximal, to $\Delta G \approx -6.5\lambda$, i.e. far in the inverted regime, where the rate was expected to be several orders of magnitude lower according to Marcus electron transfer theory. In contrast to Ward et al., they found the rates as determined from Marcus theory to be inconsistent with their experimental observations. The actual rates of charge transfer were rather independent of both driving force and temperature. This observation is in line with the concept that, for charges, quantum mechanical tunneling between adjacent sites is more important in disordered systems than the thermally activated transfer process.^{148–150} For this reason, Unger et al. also investigated the applicability of an extension of the Marcus model, which was introduced by Levich and Jortner,^{145,151} and which takes the quantum mechanical nature of the internal phonon modes into account via an average effective mode $\hbar\omega$. This is especially necessary for electron transfer at low temperatures, i.e. when $\hbar\omega \geq k_B T$.^{43,63} With this modification equation (3.3) turns into

$$k_{\text{MLJ}}(T) = \frac{|J_{DA}|^2}{\hbar} \cdot \sqrt{\frac{\pi}{\lambda_0 k_B T}} \cdot \sum_{n=0}^{\infty} e^{-S} \frac{S^n}{n!} \cdot \exp \left[-\frac{(\lambda_0 + \Delta G + n\hbar\omega)^2}{4\lambda_0 k_B T} \right] \quad (3.4)$$

which is often referred to as *Marcus-Levich-Jortner (MLJ) expression*. S is the Huang-Rhys factor that is associated with the effective mode $\hbar\omega$ and λ_0 denotes the external reorganization energy. Unger et al. found that the observed transfer rates are formally tractable with equation 3.4 when additionally disorder is taken into account. This implies that indeed tunneling between initial and final states is of more importance. Yet they also note that the observed timescales for electron transfer are actually too short for the transfer process to be described in a theoretical

framework relying on the assumption of a non-adiabatic process and that coherent effects should be considered. In general, their results are in agreement with a rather activationless transfer observed also in other studies.^{115,135,152–155}

Marcus theory is often not only (mistakenly) used to describe the formation of the CT state, but also when determining the energy E_{CT} of a charge transfer state as well as the associated reorganization energy λ in an organic solar cell from sub-bandgap spectra. Most studies still rely on an extended Marcus-type model that was introduced by Gould in 1993 and which takes an energy dependence of the electronic transition dipole moment into account.¹⁵⁶ Yet, (static) disorder is not explicitly included. In this framework, Vandewal et al. suggested the nowadays widely used approach to simultaneously analyse EQE and EL spectra of an organic solar cell in the sub-bandgap region according to¹⁵⁷

$$rEQE(E) = EQE(E) \cdot E \propto \frac{1}{\sqrt{4\pi\lambda k_B T}} \cdot \exp\left[-\frac{(E_{CT} - E + \lambda)^2}{4\lambda k_B T}\right] \quad (3.5)$$

$$rEL(E) = \frac{EL(E)}{E} \propto \frac{1}{\sqrt{4\pi\lambda k_B T}} \cdot \exp\left[-\frac{(E_{CT} - E - \lambda)^2}{4\lambda k_B T}\right] \quad (3.6)$$

where $rEQE$ and rEL are referred to as *reduced* EQE and EL spectra, respectively.^{144,156} In this context, Vandewal et al. recently stated that the line shape of a CT absorption band is mainly determined by low-frequency temperature-activated intramolecular vibrations and that static disorder only takes a minor role in this respect. Therefore, the line shape could be described in terms of Marcus theory and geometric relaxation energies would be directly extractable from the corresponding spectra.¹⁴⁶

The apparent discrepancies between the works of Ward¹³⁶ and Vandewal¹⁴⁶ on the one side and the work of Unger⁶³ as well as the observations of activationless transfer by several other groups on the other side prompted us to further investigate, how CT spectra can be consistently described as a function of temperature and what role static disorder plays in determining the spectral line shape of a CT state. This is addressed in my work on absorption and fluorescence spectra of CT states in an organic solar cell (see chapters 8.2.4 and 12).

Apart from the formation of CT states via electron transfer, research on organic solar cells is especially dedicated to the understanding of the subsequent dissociation process and which factors may lower or modify the potential barrier or reduce the binding energy of the CT state. This is particularly essential for the systematic design and improvement of new materials, currently especially new non-fullerene acceptors. A promising factor that could be active in efficient systems that feature low to no actual driving force is the delocalisation of the wavefunctions associated with the charge transfer state. This aspect is addressed in the following section (3.2). Further possible contributing factors are discussed afterwards in section 3.3.

3.2. Role of delocalization in the CT dissociation process

The key idea behind the concept that delocalization may assist the CT dissociation process is the fact that delocalized wavefunctions of the geminate pair imply a reduction of the CT binding energy and an easier separation of charge carriers over a larger distance. On a conjugated segment of a polymer chain this also goes hand in hand with an enhanced local mobility on the chain segment.¹⁵⁸ All this is supposed to facilitate the dissociation of a CT state. An instructive model to illustrate the effects of delocalization on the dissociation process is the effective mass model which was originally introduced by Arkhipov et al.^{159,160} to model the effects of conjugation on a charge carrier located on a polymer chain and developed further later on by Nenashev et al. and Schwarz et al.^{161,162} This model was also applied in the framework of this thesis (see chapters 8.2.1 and 9).

After generation of an exciton via photoexcitation near a D/A interface, charge transfer occurs, resulting in Coulombically bound e-h-pair across the interface, i.e. a CT state. In the framework of this model, one of the charges is now considered to be immobile while its counterpart is allowed to delocalize to a certain extent. In the following, exemplarily the electron will be considered stationary, yet the concept of this one-dimensional model may also be applied to mobile, delocalized electrons oscillating within the Coulomb potential of a stationary hole. In the case of a polymeric donor, the hole is now delocalized coherently over a certain effective conjugation length meaning that it can carry out quantum mechanical zero-point oscillations within the Coulomb potential of the electron (figure 3.3(a)). These oscillations are associated with a kinetic energy that is determined by the effective mass m_{eff} of the hole and effectively lowers the binding energy of the CT state. m_{eff} is a measure of the electronic coupling within the polymer chain and basically indirectly proportional to it. The (one-dimensional) polymer chains (1...n) are arranged parallel to the D/A interface with a specific spacing r between them (figure 3.3) and the electric field acts orthogonal to the interface. The hole can now jump from site to site in x-direction and take several attempts to escape the Coulomb potential during the lifetime $\tau_0 = \frac{1}{k_r}$ of the CT state, where k_r is rate of recombination to the ground state. The dissociation yield $\phi(F)$ is then again given by the trade-off between recombination rate k_r and dissociation rate k_d .^{162,163}

$$\phi(F) = \frac{k_d}{k_d + k_r} = \frac{\tau_0}{\tau_0 + k_d^{-1}} = \frac{\tau_0}{\tau_0 + \sum_{n=1}^{N-1} a_{n \rightarrow n+1}^{-1} \exp\left(\frac{E_n - E_1}{k_B T}\right)} \quad (3.7)$$

where $a_{n \rightarrow n+1}$ is the well-known Miller-Abrahams hopping rate

$$a_{n \rightarrow n+1} = \nu_0 \exp(-2\gamma r) \begin{cases} \exp\left(-\frac{E_{n+1} - E_n}{k_B T}\right) & E_{n+1} > E_n \\ 1 & E_{n+1} \leq E_n \end{cases} \quad (3.8)$$

ν_0 is the attempt-to-hop frequency and γ is the inverse localization length that is a measure of the electronic coupling. Both the hopping and the dissociation process of the hole are essentially determined by the energy E_n of the hole on the n-th chain. E_n includes contributions from the potential energies due to Coulomb attraction of the electron as well as due to an applied electric field and eventually the kinetic energy associated with the zero-point oscillations of the hole. It

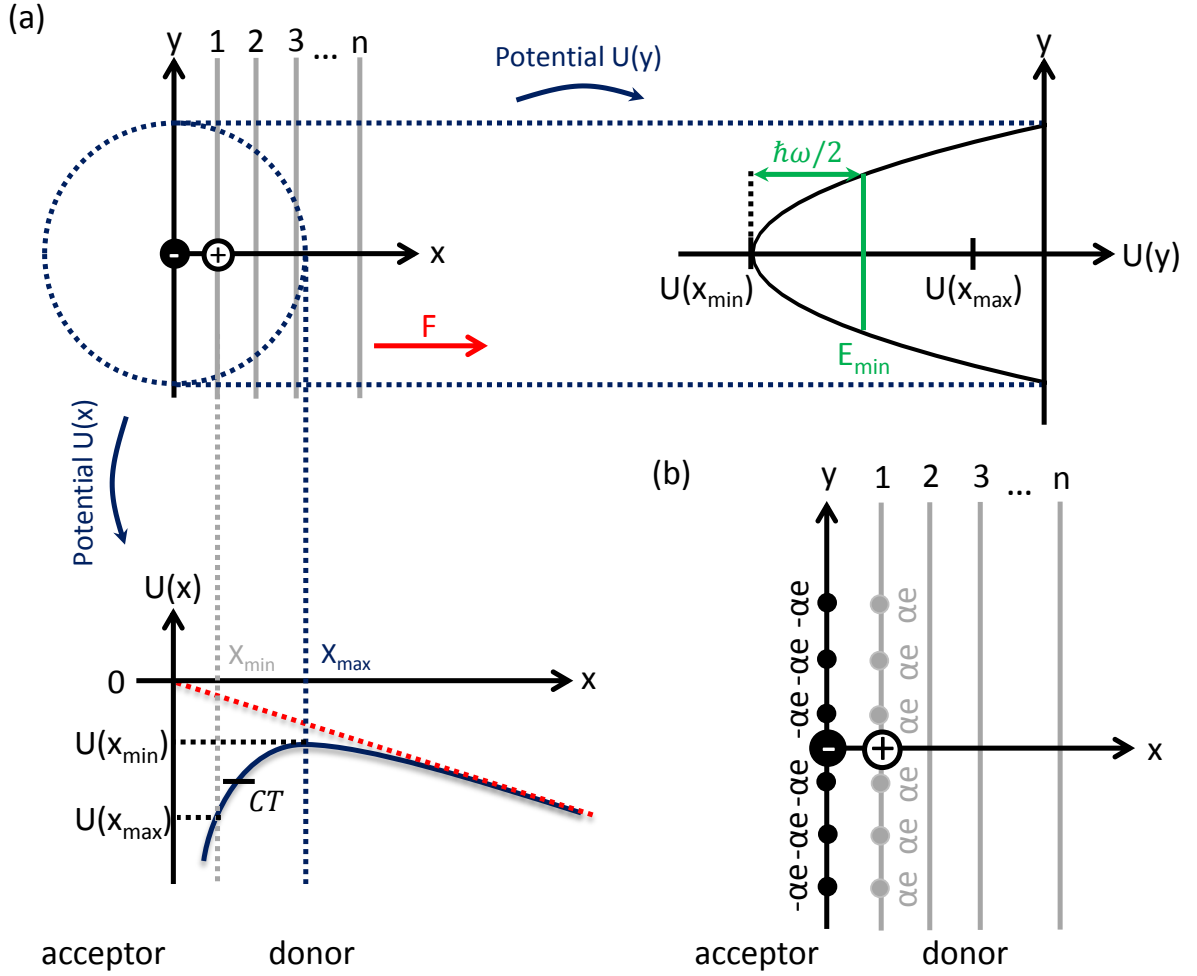


Figure 3.3.: (a) Schematic illustrating the effective mass model. An e-h-pair is located at interface of D/A bilayer architecture. The electron is considered stationary in this case and the hole is allowed to perform quantum mechanical zero-point oscillations in y-direction within the Coulomb potential $U(x, y)$ of the electron. These oscillations provide additional energy $\frac{\hbar\omega}{2}$ to raise the energy of the hole from $U(x_{min})$ to E_{min} thereby lowering the energy barrier to $U(x_{max}) - E_{min}$ and facilitating dissociation of the geminate pair. The polymer chains of the donor are aligned parallel to the interface and numbered consecutively from 1 to n. During the lifetime of the CT state, the hole may perform several hops in x-direction, which may be assisted by the presence of an electric field F that additionally lowers the potential barrier. (b) The dissociation process may be further facilitated by the presence of interfacial dipoles that modify the potential at the D/A interface. Within the model, these dipoles are evenly distributed along the interface. Adapted with permission from Christian Schwarz et al., *Phys. Rev. B* **87**, 155205, (2013). Copyright ©(2013) by the American Physical Society.

can be determined by solving the Schrödinger equation:¹⁶¹⁻¹⁶³

$$\frac{\hbar^2}{2m_{eff}} \frac{d^2\Psi}{dy^2} + U_n\Psi = E_n\Psi \quad \text{with} \quad (3.9)$$

$$U_n = \frac{e^2}{4\pi\epsilon_0\epsilon_r} \frac{1}{\sqrt{y^2 + x_n^2}} - eFx_n, \quad x_n = n \cdot r \quad (3.10)$$

Another factor that may alter the potential energy at the D/A interface is the presence of interfacial dipoles as a result of (partial) charge transfer even in the dark.¹⁶⁴ The shielding

induced by such dipoles eventually lowers the potential barrier and increases the dissociation yield. This concept has been already developed by Arkhipov et al. and further extended by Wiemer et al.^{159,165} Fractional interfacial dipoles α may be readily incorporated into the effective mass model by considering a modified potential instead of equation (3.10) (figure 3.3(b)):^{162,163}

$$\begin{aligned}
U(y, x_n) = & \frac{e^2}{4\pi\epsilon_0\epsilon_r} \frac{-1}{\sqrt{x_n^2 + y^2}} \\
& + \frac{e^2}{4\pi\epsilon_0\epsilon_r} \left(\sum_{j=-\frac{N}{2}}^{\frac{N}{2}} \frac{\alpha}{\sqrt{(x_n - r)^2 + \left(y - \left(j + \frac{1}{2}\right)r\right)^2}} + \sum_{i=-\frac{N}{2}}^{\frac{N}{2}} \frac{-\alpha}{\sqrt{(x_n)^2 + \left(y - \left(i + \frac{1}{2}\right)r\right)^2}} \right) \\
& - eFx_n
\end{aligned} \tag{3.11}$$

This model has been successfully applied to a series of conjugated (donor) polymers with different conjugation lengths in combination with C_{60} by Schwarz et al.¹⁶² In their work, they show that the Coulomb binding energy of the CT state scales inversely with the conjugation length and concomitantly effective mass m_{eff} . Differences in dissociation yield between the different polymers could be ascribed to a varying degree of hole delocalization as the acceptor was kept the same for all polymers. Apart from that, Schwarz et al. verified that e-h-pair dissociation may be facilitated by interfacial dipoles which screen the mutual Coulomb potential of the geminate pair.

The positive role of hole delocalization on CT dissociation is also substantiated by the works of several other groups.^{70,158,161,166–170} Deibel et al. for example performed Monte Carlo simulations on donor-acceptor blend systems and consistently found a higher CT dissociation yield for delocalized charge carriers within conjugated polymer chain segments.¹⁵⁸ The higher yield in this case was attributed to the larger intra-pair separation and the concomitant reduction in Coulomb binding energy as well as the higher local on-chain mobility within the conjugated segment. All in all, delocalization of the hole along a well conjugated polymer chain is now generally accepted to be an effective factor enhancing dissociation efficiency.

While it seems quite straightforward to see that coherent delocalization may occur for holes that are transported along a conjugated polymer chain with strong coupling between the conjugated segments,¹⁶² a comparable behaviour is less obvious for small molecules such as fullerene acceptors. In the latter case, the intermolecular coupling between adjacent molecules is expected to be smaller. Consequently, the bandwidth associated with an exciton or a charge carrier is usually smaller than the energetic disorder of the system meaning that transport rather takes place via incoherent hopping.⁴³ So although this issue has been addressed repeatedly in recent years,^{32,73,84,131,154,166–168,171–173} there is no full consensus up to now, whether electron delocalization in organic solar cells is of similar importance as hole delocalization.

Bredas and coworkers^{166,167} for example do only see a very small influence of electron delocalization on the charge transfer states in their MD- and DFT-calculations on the model system *pentacene*/ C_{60} . They attribute this to a smaller electronic coupling for electrons in C_{60} as compared to hole delocalization in the crystalline *pentacene*. Yet, they considered only a stack of at most 7 *pentacene* and 3 C_{60} molecules and did only take delocalization parallel to the interface into account. Furthermore, they point out that they expect the electron delocalization perpendicular to the interface to be larger due to the isotropic nature of C_{60} . Other works like

the ones by Zusan et al. or Murthy et al. suggest that aggregation of fullerenes may promote delocalization of the charge transfer state on the acceptor side of the D/A interface.^{135,154,171,174} Zusan et al. for example compare intercalated and non-intercalated polymer/fullerene blends and find the presence of a spatially extended neat fullerene phase to be responsible for a larger charge generation yield. This result is attributed to delocalization in the pure acceptor phase, which was suggested to be the major driving force for efficient photogeneration.¹⁷¹ In contrast to that, Athanasopoulos et al. point out that efficient charge separation may be also achieved via incoherent hopping, without necessarily having to consider a coherent process. Instead, from an entropic point of view, increased dimensionality, e.g. due to aggregation, could also account for a more efficient dissociation; Yet, though coherence is not the only possibility to increase the efficiency of a solar cell, they also emphasize that for the design of an efficient organic solar cell it is crucial for both donor and acceptor to feature ideally both high delocalization and high charge carrier mobility. Otherwise, performance will suffer if only one of the components is optimized in this respect.⁸⁴ Further studies that point to an important role of electron delocalization are the ones by Bernardo et al. and Larson et al.^{32,131}. Bernardo et al. studied BHJ devices with varying fraction of C_{60} and found that below a crystallite size of 4 nm the spatial extent of the CT state is reduced. This was verified by measurements of dipole moment and polarizability via electroabsorption. In this context, they point out that electron delocalization in the acceptor phase critically depends on the local crystallinity and therefore intermolecular coupling.¹³¹ The latter aspect is further substantiated by the work of Larson et al. who studied the correlation between molecular properties, driving force, intermolecular coupling and photogeneration yield.³² In contrast to that, Abramavicius et al. claim that already relatively weak coupling between PCBM molecules in the order of 10 meV is sufficient to facilitate electron delocalization and efficient charge separation at organic interfaces. According to their calculations, coherent electron transfer takes place up to about 500 fs after the excitation resulting in an initial e-h-pair separation of 2.5 nm before transition to classical incoherent hopping occurs. This was found to be in accordance with experimental data obtained from transient absorption spectroscopy.¹⁷³ A similar result was obtained by Gelinis et al. who state that initial charge separation distances of at least 4 nm are achieved in ordered fullerene regions of the acceptor phase within about 40 fs . This is attributed to the access to spatially coherent delocalized states present in ordered regions.¹⁷⁴

In contrast to all this, a very recent study on the general effect of delocalization on the barrier height for charge separation by Gluchowski et al. stated that from a thermodynamic point of view delocalization would even increase the free energy barrier for coupling strengths larger than about 10 meV . A positive effect from delocalization would then be only possible as a result of nonequilibrium kinetic effects, that are not covered within the framework of the study.¹⁷⁵ This would for example be the case in conjugated polymers due to a higher local mobility within the conjugated chain segments, which accompanies the delocalization of the charge carriers.¹⁵⁸ In view of this ongoing controversy and in order to contribute to the clarification of the actual role of electron delocalization, this issue is addressed in one of my publications (chapter 9) and discussed in detail in chapter 8.2.1.

Another aspect that is closely linked to the aspect of delocalization is the role of vibrational excess energy in the dissociation process. The idea behind this concept is that vibrational excitation may lead to more delocalized ("hot") CT states that very quickly dissociate into free

charges before thermally relaxing to stronger bound ("cold") CT states. The corresponding concept is illustrated in figure 3.4. In the case of a "hot" CT dissociation mechanism, lower, relaxed CT states would act as a trap so that for direct excitation of this lower energy state, a strong field dependence of dissociation would be expected. Therefore, IQE and its field dependence would depend on photon energy. If on the other hand a "cold" mechanism prevails, CT states first thermally relax quickly within the CT manifold (much faster than dissociation via higher energy states) meaning that all dissociation attempts start from the same energy level. In this case, the free carrier yield will be exclusively determined by competition between dissociation and recombination to the ground state and IQE and its field dependence will be independent of excitation energy. Charge generation will rather be determined by the binding energy of the relaxed CT state so that delocalization in donor and/or acceptor phase may act as "driving force" for charge separation.¹⁷¹ Although there were some studies that reported an effect of vibrational excess energy on the dissociation efficiency in organic solar cells,^{69,82,176–178} meanwhile there is consensus that dissociation nearly exclusively takes place via relaxed ("cold") CT states and that hot states do not really play a role.^{70,84,115,131,171,179–181} In this context, several groups have shown that the IQE is basically independent of excess energy so that there is no indication of any involvement of vibrationally excited CT states in the charge generation process in organic solar cells.^{115,171,179,180}

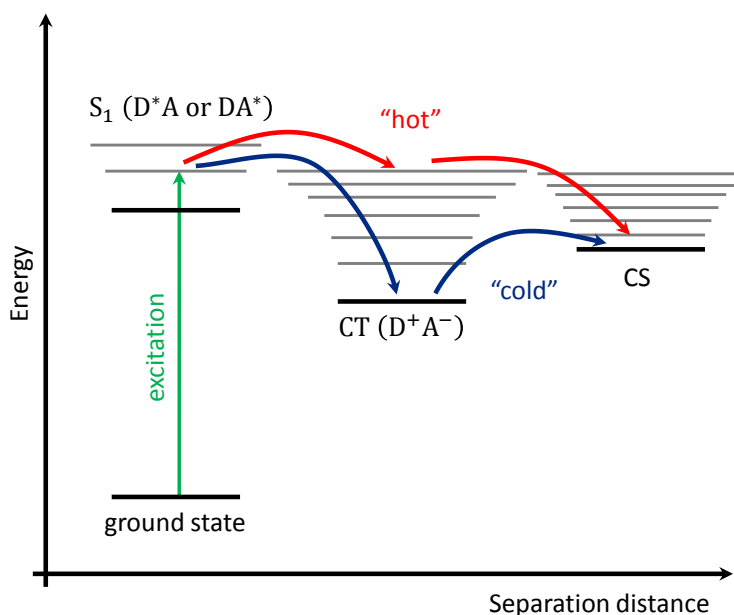


Figure 3.4.: Illustration of the two possible routes for CT dissociation via vibrationally excited ("hot") or via relaxed ("cold") CT states. CS denotes so-called charge separated states, i.e. states associated with free charge carriers.

3.3. Further factors influencing CT state dissociation

As already mentioned in chapter 2 a number of further factors may impact on the CT dissociation yield. Apart from delocalization and the closely related concept of vibrational excess energy discussed in the previous chapter, strong internal electric fields may readily assist CT dissociation by lowering the potential barrier a charge carrier has to overcome and also reducing the probability of geminate recombination by driving the charges apart (figure 3.5(a)).^{43,44,74} In the presence of an electric field, the Coulomb potential is modified to

$$U_{Coul} = \frac{-e^2}{4\pi\epsilon_0\epsilon_r r} - eFr \quad (3.12)$$

The field dependence of the dissociation rate has already been addressed implicitly in the context of the Onsager-Braun model and the effective mass model (chapters 3.1 and 3.2). One possibility to study the effect of an electric field on charge generation in an organic solar cell is the measurement of CT photoluminescence as a function of applied electric field. In this case, a correlation between the observed PL quenching and the extracted photocurrent indicates the generation of more charge carriers by field induced splitting of CT states as well as a possible reduction in geminate recombination.^{44,124,129,182} Another versatile method is the time-delayed-collection-field technique (TDCF) from which the different field-dependencies of CT-dissociation and subsequent separation processes may be determined.^{181,183–185} Finally, it is also possible to gain insight into the dependence of the dissociation process on the internal electric field by performing transient absorption measurements on actual devices.^{186,187} For example in a very recent work, Weu et al. argued that the internal electric field in an organic solar cell might even promote long-range charge separation in systems with low driving forces.¹⁴¹

Another factor that may modify the potential at the D/A interface is dielectric screening, i.e. (induced) electrostatic effects of the molecules surrounding the CT state.⁷⁴ This includes effects of chemical structure as well as position and orientation at the interface, e.g. face-on or edge-on alignment of polymers or crystalline small molecules,^{188,189} causing anisotropic polarizabilities and differences in charge distributions. These factors can have a large impact on the energetic landscape at the interface, but are only visible in case of a well controlled and aligned interface, not in randomly oriented amorphous systems.^{190–193} Further dielectric effects may be caused by permanent interfacial dipoles which may be present due to ground state charge transfer in the case of strong acceptors,^{159,162,164,165} as already discussed in the framework or the effective mass model above (cf. 3.2). Such dipoles may be determined from shifts in the ionization potential in UPS measurements when a layer is deposited on top of another one.^{162,194–198}

For a long time, also the energetic offset between the charge transfer energy and the lowest singlet energy of either donor or acceptor — the driving force for charge transfer $\Delta G = E_{CT} - E_{S1}$ — was believed to be an important factor in the charge separation process.^{133,136,146,199–201} But as it has already been discussed in chapter 3.1, nowadays there are also reports of very efficient organic solar cell systems with very low to nearly no driving force for charge transfer^{73,122,202,203} and there is growing evidence that the transfer process is rather activationless.^{63,115,135,152–155} Instead, several groups report an influence of the energetic offset between charge separated (CS) states and the lowest singlet of either donor or acceptor, the so called driving force for charge generation $\Delta G = E_{CS} - E_{S1} = (IE_D - EA_A) - E_{S1}$.^{71,138,176,179}

Finally, very recently much more fundamental considerations were made about how to describe

the actual energy barrier for charge separation and when a charge carrier may actually be considered as "free". The central aspects in this respect are the presence of disorder at the D/A interface and concomitantly the role of entropy in lowering the free energy barrier for the separation of bound e-h-pairs.^{71,110,175,204–207} A kind of pioneering position in this respect may be attributed to the work of Hood and Kassal about the role of entropy and disorder in the CT dissociation process.¹¹⁰ In their study they argue, that the barrier for charge separation is not only determined by the mutual Coulomb potential of the e-h-pair but that entropic contributions are important. The fundamental idea behind this concept is rather simple: Compared to the number of interfacial CT states, in a mostly ordered system there is a large number of available charge separated states of similar energy, that especially increases with increasing distance from the counter charge (figure 3.5(b)). So in this picture, dissociation is entropically favourable. Furthermore, disorder at the interface will lower the effective potential barrier by introducing lower energy sites at larger distances from the interface (figure 3.5(c)). In view of this, free energy ΔG is a more reasonable criterion to define energy barriers for charge separation according to

$$\Delta G = \Delta E - T \cdot \Delta S = U_{Coulomb} - \Delta E_{disorder} - T \cdot \Delta S \quad (3.13)$$

with $U_{Coulomb}$ being the Coulomb potential, $\Delta E_{disorder}$ being the energy reduction due to disorder at the interface, T being the temperature and ΔS being the entropic contribution. In contrast to earlier works considering entropy in the dissociation process,^{71,204} Hood and Kassal considered both electron and hole to be mobile and also took disorder at the interface into account. As a result, they point out that entropy depends on the dimensionality of the system and dominates in case of ordered systems, while disorder dominates the barrier reduction for larger values of static disorder σ . For $\sigma > 100 meV$ they find that the average free-energy landscape does not even feature a barrier at all. Yet, in this case there will be some low-lying traps that may hinder further charge separation, i.e. transport through the bulk of the material. These results are in general in agreement with the very recent theoretical work by Shi et al., who additionally emphasize the importance of non-equilibrium dynamics in the CT dissociation process,²⁰⁵ as well as the experimental studies by Nan et al. and Puttising et al. who also argue that a certain (descent) amount of disorder may actually be beneficial for charge separation from an entropic point of view.^{206,207} Nevertheless, it should be noted, that the current models by Hood et al., Gluchowski et al. or Shi et al. only explicitly consider CT dissociation dynamics without taking into account kinetic aspects like (non-)geminate recombination or the additional energy due to delocalization.^{110,175,205}

In the context of recombination, finally also the mobility of charge carriers may impact on the actual CT dissociation efficiency by influencing geminate recombination at the D/A interface. This aspect is shortly addressed in the next chapter (4).

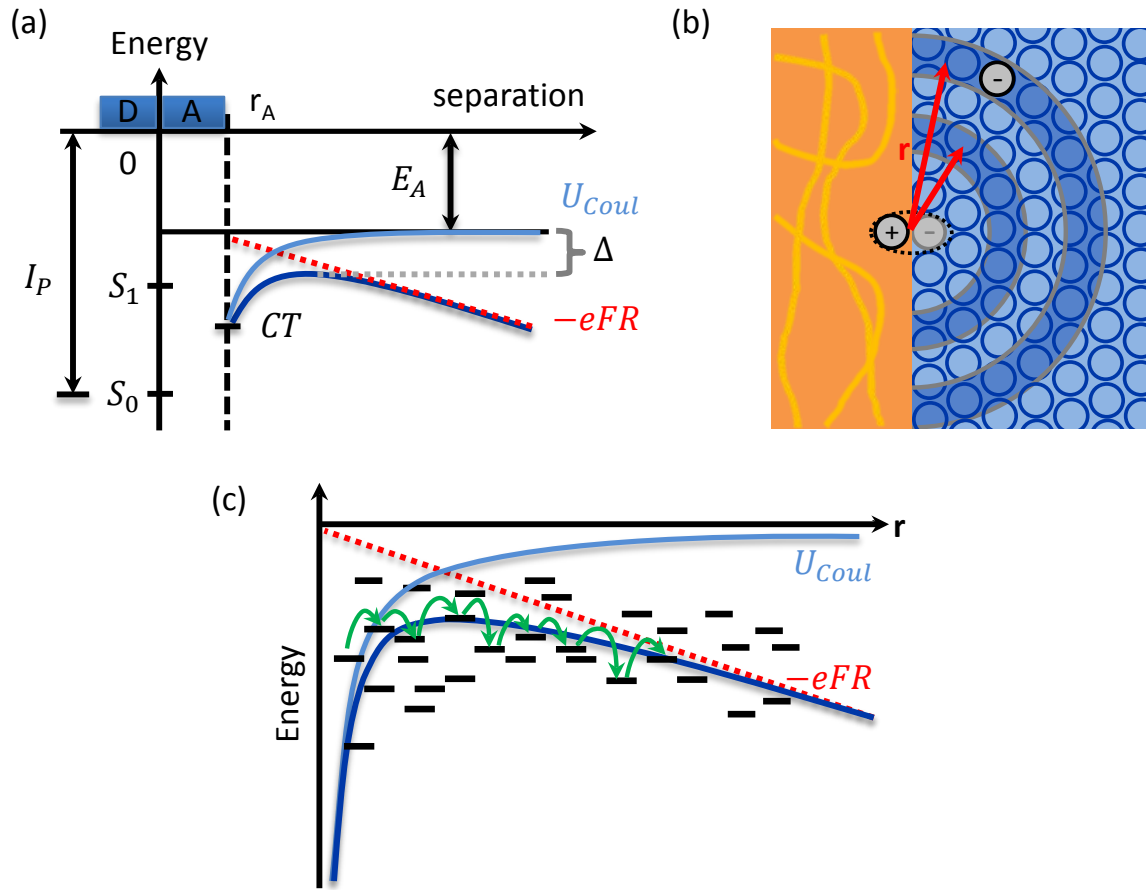


Figure 3.5.: (a) Modification of the Coulomb potential U_{Coul} by an electric field F . Δ illustrates the reduction of the potential barrier due to the electric field. The CT state is energetically lower than the first excited state S_1 (in this case of the donor D) and features an initial intra-pair separation r_A . I_P and E_A denote the ionization potential of the donor (D) and the electron affinity of the acceptor (A), respectively. (b) Schematic illustration of the concept of increasing entropy due a larger number of accessible sites (blue circles) with increasing distance r in an ordered system. The radial sum over all the shells gives the total number Ω of possible microstates the system can take. The associated change in entropy is then simply given by $\Delta S = -k_B \ln(\Omega)$. Therefore, a larger number of accessible states makes dissociation entropically favourable. (c) Illustration of the effect of disorder on charge separation. The presence of lower energy states and the possibility of smaller thermally activated jumps upward in energy enable a separation in several smaller steps instead of having to cross the potential barrier in one single step. This facilitates dissociation as long as disorder is not too large so that low energy states would act as deep traps.

4 Charge Transport and the role of mobility in the charge separation process

Charge transport in organic semiconductors is commonly described within the framework of the Gaussian Disorder Model (GDM).²⁰⁸ Energetic and positional disorder result in localization of charge carriers on their transport sites, be it a single molecule or a conjugated segment of a polymer chain. Due to the associated random fluctuations of intermolecular interactions charge transport takes place via hopping among (uncorrelated)¹ neighbouring sites in an inhomogeneously broadened density of states (DOS) of Gaussian shape $\rho(E)$:

$$\rho(E) = \frac{1}{\sqrt{2\pi\sigma^2}} \exp\left[-\frac{(E - E_0)^2}{2\sigma^2}\right] \quad (4.1)$$

with E_0 being the energy at the centre of the DOS and σ being its standard deviation. The hopping rate ν_{ij} among two sites i and j with energies E_i and E_j , respectively is usually expressed in terms of a Miller-Abrahams-rate if relaxation effects are small compared to disorder effects:

$$\nu_{ij} = \nu_0 \exp(-2\gamma r) \begin{cases} \exp\left(-\frac{E_j - E_i}{k_B T}\right) & E_j > E_i \\ 1 & E_j \leq E_i \end{cases} \quad (4.2)$$

where ν_0 denotes a frequency prefactor, γ the inverse localization length and r the intersite distance. The first exponential accounts for the electronic wavefunction overlap while the second one is simply a Boltzmann factor accounting for thermally activated jumps upward in energy. Downward jumps are not hindered. If relaxation effects are relevant, i.e. when electron-phonon coupling is significant, Marcus-type rates are often used instead of Miller-Abrahams hopping rates.²¹¹

According to this model injected or photogenerated charge carriers will execute a random walk inside DOS and subsequently relax energetically until they reach a quasi-equilibrium energy located at $\langle E_\infty \rangle = -\frac{\sigma^2}{k_B T} = -\sigma\hat{\sigma}$ below the centre of the DOS. This results in the formation of a so called *occupied DOS* centred at $\langle E_\infty \rangle$ with the same variance σ^2 as the DOS. Charge transport then takes place via thermal activation to a so called transport energy E_{tr} (figure 4.1(a)).²¹² Choosing the energy scale such that the transport energy is located at 0 eV and taking both energetic ($\hat{\sigma}$) and positional (Σ) disorder as well as the presence of an external electric field F into account, the charge carrier mobility $\mu(T, F)$ as a function of temperature T and field F then takes the form:^{208,213}

¹ This assumption is justified in case of amorphous (glassy) organic solids with small structural correlation lengths in the order of only a few nm.²⁰⁸ If energetic correlations are present, e.g. due to the presence of permanent or induced dipoles, more complex, extended models need to be considered.^{209,210}

$$\mu(T, F) = \mu_0 \exp \left[- \left(\frac{2\hat{\sigma}}{3} \right)^2 \right] \begin{cases} \exp \left[(\hat{\sigma}^2 - \Sigma^2) \sqrt{F} \right] & \Sigma \geq 1.5 \\ \exp \left[(\hat{\sigma}^2 - 2.25) \sqrt{F} \right] & \Sigma < 1.5 \end{cases} \quad (4.3)$$

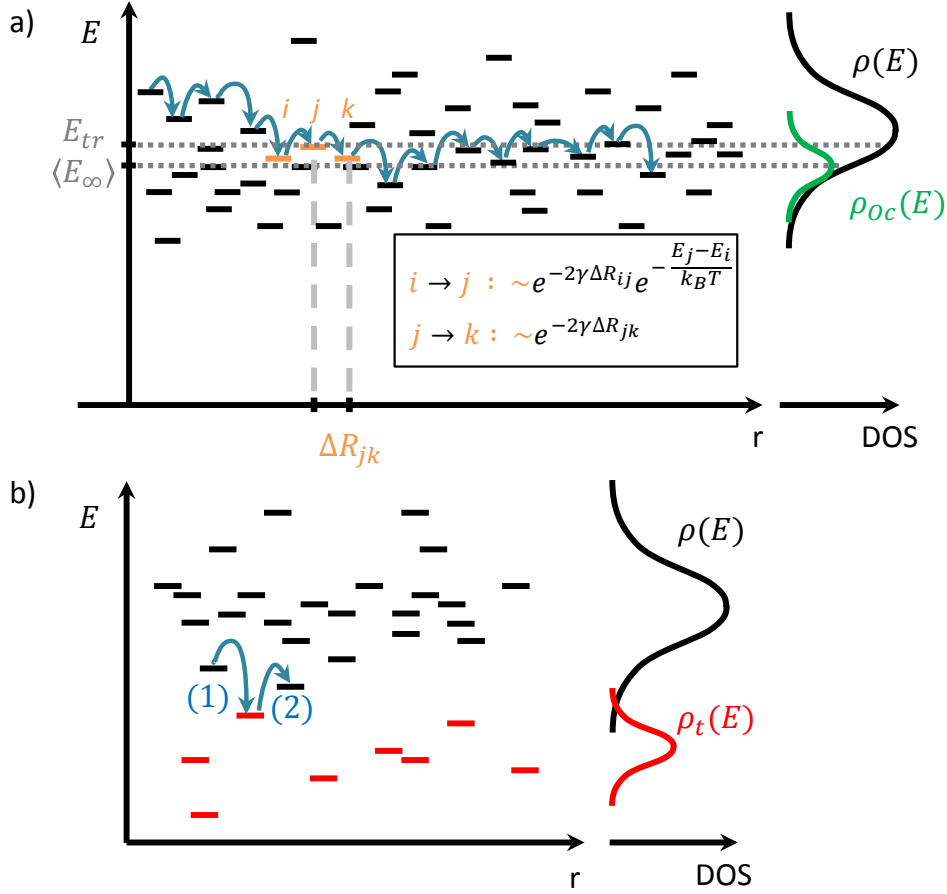


Figure 4.1.: (a) Illustration of charge transport via hopping in an inhomogeneously broadened DOS $\rho(E)$ according to the GDM. After initial relaxation to a quasi-equilibrium energy $\langle E_\infty \rangle$ establishing an occupied DOS $\rho_{Oc}(E)$ subsequent transport takes place via thermally activated hops to the transport energy E_{tr} ($i \rightarrow j$). Downward jumps in energy are not impeded ($j \rightarrow k$). ΔR_{jk} is the distance between two sites j and k . E and r denote energetic and spatial coordinates, respectively. (b) Hopping transport in a Gaussian DOS $\rho(E)$ in the presence of additional trapping sites. The associated trap DOS is assumed to be Gaussian, too. Charge transport is impeded due to repeated trapping (1) and release (2) of charge carriers.

Common methods to experimentally assess the mobility in organic semiconductors range from the early Time of Flight experiments (TOF)^{214–218} and the widely used Space-Charge-Limited-Current (SCLC) measurements,^{218–223} where relatively thick layers of several 100 nm up to 1 μm are needed, over the Charge Extraction by Linerally Increasing Voltage (CELIV) technique, which allows to measure in thickness and carrier density regimes relevant to actual devices,^{85,224–227} to highly sophisticated methods like Time Resolved Microwave Conductivity (TRMC)²²⁸ and Time Resolved Electric Field Induced Second Harmonic Generation (TREFISH),²²⁹ which enables systematic probing of mobility on different length and time scales, making it possible for example to directly study intra- and interchain transport in conjugated polymers. In the course of this

thesis, two selected methods are used to characterize the charge carrier mobility at low to medium as well as high charge carrier densities, respectively: MIS-CELIV and OFET measurements. The first technique is a modification of the original CELIV method where an additional insulating layer (I) is inserted into an OPV device or a single layer heterojunction between the organic semiconductor (S) and the metal electrode (M). By applying a prebias voltage charge carriers are selectively injected into the sample and accumulated at the semiconductor/insulator interface forming a charge reservoir that may subsequently be extracted by applying a voltage ramp.^{85,230} Mobility μ may then be determined from the current response of the sample according to^{85,230,231}

$$\mu = \frac{2d_s^2}{At_{tr}^2} \left(1 + \frac{\epsilon_s d_i}{\epsilon_i d_s} \right) \quad \text{with } t_{tr} = \frac{4}{\pi} t_{2j_0} \quad (4.4)$$

This is valid for sufficiently large signals, i.e. $j - j_0 \gg j_0$, where j and j_0 are the measured current densities with previously applied prebias and for pure capacitive response, respectively. The indices s and i refer to the organic semiconductor and the insulator, respectively, d denotes the layer thickness and ϵ the relative permittivity. $A = \frac{dV}{dt}$ is the slope of the applied voltage ramp, t_{tr} is the transit time of a charge carrier from the insulator/semiconductor interface to the opposite electrode and t_{2j_0} is the time at which the current density reaches two times of the capacitive plateau value j_0 . This technique allows to selectively study electron and hole mobilities depending on the position of the insulating layer. The measurement principle is illustrated in figure 4.2(a). Detailed descriptions of the method and the related data analysis are given in the works by Armin et al., Juška et al. and Sandberg et al.^{85,230,231}

In contrast to CELIV, OFET measurements yield mobility values characteristic for high charge carrier densities.^{9,232–234} The general principle for a bottom gate/top contact p-type OFET is shown in figure 4.2(b). An OFET features a three electrode architecture, with a gate electrode that is separated from the organic semiconductor via an insulating layer (*gate dielectric*) and two further electrodes, source and drain, that are in direct contact with the semiconductor. The current between source and drain is controlled via the gate voltage V_g applied between source and gate electrode, as above a certain threshold voltage V_T the associated field draws positive charges (for $V_g < 0V$) from the source into the semiconductor which then accumulate at the interface to the gate dielectric forming a conducting channel. This in turn allows a current flow between source and drain when a (drain) voltage V_d is applied between these two electrodes. For voltages $V_d \ll V_g$, the current I_d between source and drain (*drain current*) increases linearly with V_d . In this regime, the mobility may be determined according to^{9,233}

$$\mu_{lin} = \frac{L}{WC_i V_d} \frac{\partial I_d}{\partial V_g} \Big|_{V_d} \quad (4.5)$$

with L and W being the channel length and width, respectively and C_i being the capacitance per unit area. For voltages V_d higher than $V_g - V_T$, the accumulation layer will start to get depleted and the drain current will start to saturate. In this regime, the mobility may be determined according to^{9,233}

$$\mu_{sat} = \frac{2L}{WC_i} \left(\frac{\partial \sqrt{I_{d,sat}}}{\partial V_g} \Big|_{V_d} \right)^2 \quad (4.6)$$

Detailed information about the working principle and various aspects related to the operation of OFETs may especially be found in the works of Sirringhaus and coworkers.^{232–235}

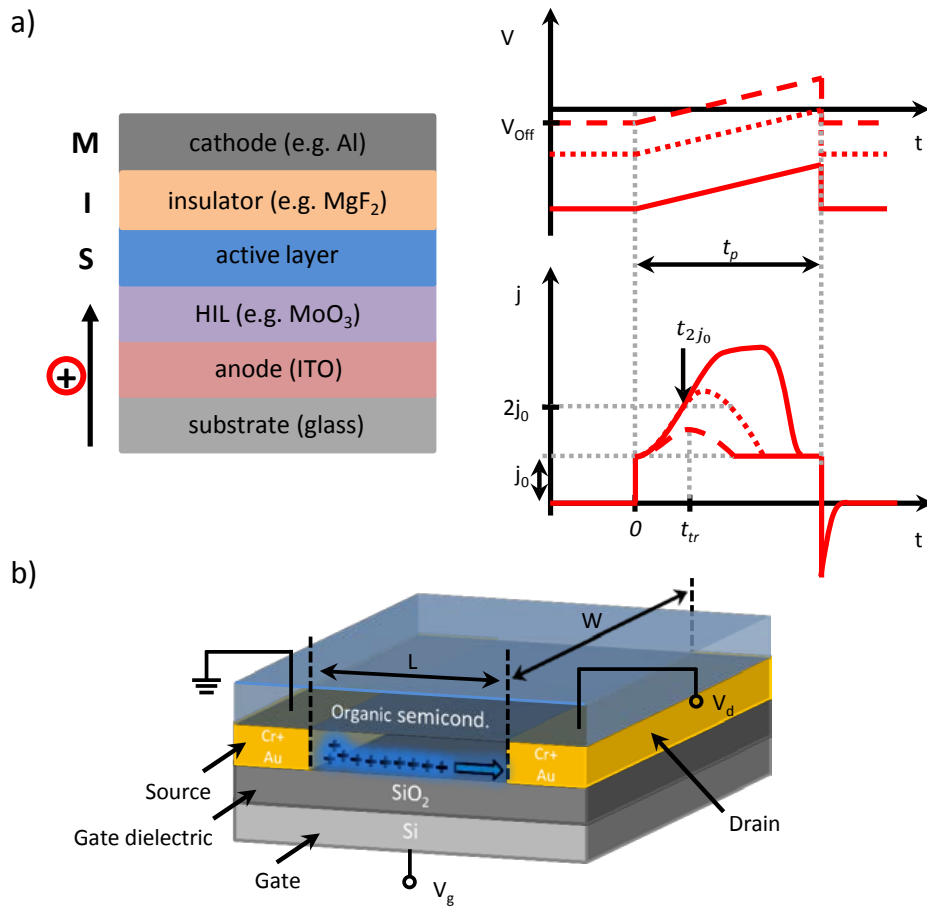


Figure 4.2.: (a) Illustration of a typical sample structure in a MIS-CELIV experiment (left) and the according measurement principle (right). Charge carriers, in this case holes, are injected from one electrode and accumulated at the semiconductor(S)/insulator(I) interface by applying a prebias voltage V_{off} . These charge carriers are then extracted by a subsequent voltage ramp of duration t_p . The mobility may finally be determined from the resulting current (density) response $j(t)$. The associated response is illustrated for low (dashed), medium (dotted) and high (solid) prebias voltages. j_0 denotes the current density due to pure capacitive response, t_{2j_0} the time at which $j(t) = 2j_0$ and t_{tr} the transit time of the charge carriers needed to travel through the device. Further details are given in the text. (b) Schematic of a typical bottom gate/top contact p-type OFET architecture. V_g and V_d denote gate and drain voltage, respectively.

An important issue of practical relevance in terms of charge transport is the presence of additional energy sites below the DOS that may impede the motion of charges via trapping.^{213,221,223,232,236,237} These *trap states* may be due to structural or chemical defects or impurities.^{43,221,238,239} Especially in the context of crosslinking polymers to form insoluble networks and stabilize morphologies the latter two aspects could play a role, as chemical crosslinks are formed and side products or remnants of initiators may remain in the organic film. This issue is addressed in the course of my publication on the influence of crosslinking on the hole mobility in a series PF2/6 derivatives (see chapter 8.2.3 and 11).

In the simplest way, one can think of traps effectively increasing the disorder parameter σ thereby broadening the DOS, as long as the concentration of traps is small compared to the number of states in the original DOS (figure 4.1(b)).^{236,240} The mobility is reduced in this case since charge carriers have to be released from trap states by thermal activation before they can con-

tinue their movement (*"trapping-and-release transport"*). In case of high trap concentrations, charge transport will rather take place within the trap DOS (*"trap transport"*).²⁴⁰ This may be the case in sufficiently doped organic semiconductors. The effect of traps on charge transport has been extensively studied by several groups, especially by Blom and coworkers.^{210,213,221,236,240-244} By investigating a wide range of semiconducting polymers Blom and coworkers found that the frequently observed inferiority of electron transport in organic semiconductors is related to the existence of a universal trap level located at about 3.6 eV below the vacuum level that is present in all the investigated compounds. As origin of these traps they suggest hydrated-oxygen complexes to be likely candidates.²²¹ As a consequence, trapping should not occur for acceptor materials with electron affinities larger than 3.6 eV, which is usually the case for the commonly used fullerene derivatives,^{32,34,179} meaning that their mobility should not be altered in a device.

In general, charge carrier mobility plays an important role concerning the overall performance of an organic solar cell as it governs the transport of charge carriers through the device and away from D/A interfaces thereby greatly affecting the probability of recombination of charges both geminately and non-geminately. Low mobilities in general increase the probability of geminate recombination (GR) as well as (NGR) because in this case charges are more likely to reside in the vicinity of a D/A interface for a longer time and it also takes longer for them to be extracted at a given electric field, thereby increasing the probability of an encounter between charges of different sign in the bulk. A straightforward indication of significant recombination in a device is the presence of a so called S-Shape (usually in the forth quadrant) of the J-V-characteristic (Figure 4.3), which is accompanied by a reduction of the Fill Factor (FF).^{83,245-247}

The effect of NGR due to low charge carrier mobility may be greatly reduced by using a PHJ architecture. In this case percolation paths to the electrodes for separated charge carriers of opposite sign are well defined and separated from each other. This makes it possible to decouple interface related effects from morphology related effects. Bimolecular recombination during extraction will not occur as long as the illumination intensity is low enough that recombination between charges stemming from different e-h-pairs is unlikely.^{43,44,75} Nevertheless, GR will still be enhanced for low mobilities as separated charges will on average stay in closer vicinity of the D/A interface during their lifetime τ . This situation is characterized by a small $\mu\tau$ -product. Furthermore, according to Tress et al. a space charge will built up in the complete device due to the slow extraction as compared to the fast generation giving rise to an increased carrier concentration at the D/A interface and therefore higher recombination probability.^{83,86}

In addition to that, Hahn et al. point out that also back diffusion to the D/A interface is connected to the mobility of the charge carriers via the Stokes-Einstein relation meaning that a lower charge carrier mobility also results in a lower diffusion coefficient.⁷⁵ Therefore, the probability of a charge carrier to recombine with a counter charge rather than being extracted at the electrode is increased for low mobilities. In this respect, charge carrier mobility also affects the photogenerated current near V_{OC} , i.e. at low internal electric fields, where charge carrier motion is dominated by diffusion instead of drift, and with this also the fill factor. This conclusion even holds for low illumination intensities and low carrier densities. In this respect, Hahn et al. found that even secondary geminate recombination may occur when charges diffuse back into the Coulomb capture radius of their sibling charge after they had already left it and that this process is mainly determined by charge carrier mobility.⁷⁵ The latter effect will also be more pronounced for larger layer thicknesses as in this case back diffusion of charge carriers to

the D/A interface becomes more probable as compared to extraction, especially at low electric fields close to V_{OC} . This leads to an enhanced S-Shape for thicker layers with low charge carrier mobility (see figure 4.3(a)).^{75,248,249} Smaller layer thicknesses will in this case be of advantage in terms of recombination although this will be at the cost of absorption ability in the device.

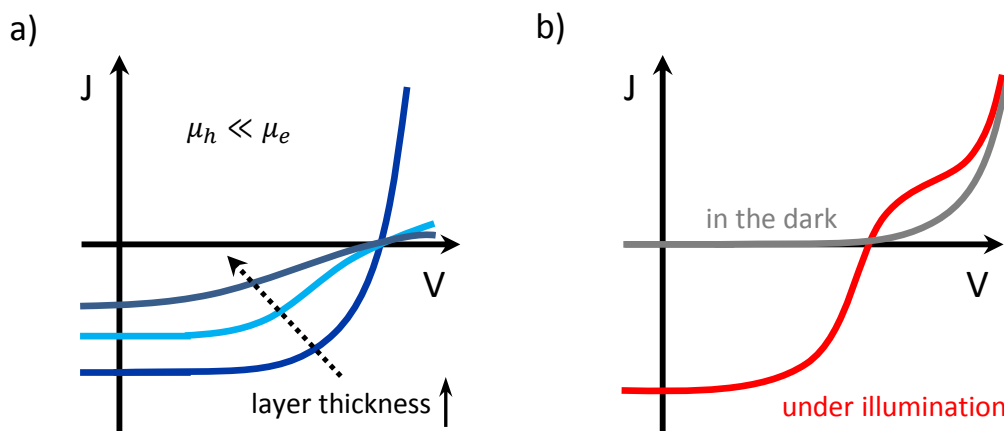


Figure 4.3.: (a) Formation of an S-Shape in the J-V-characteristic as function of layer thickness in PHJ for imbalanced mobilities, e.g. $\mu_h \ll \mu_e$. (b) Schematic showing a kink in forward direction as a result of the presence of an injection barrier. In this case, extraction is still more efficient than injection, leading to a crossing of J-V-characteristics under illumination and in the dark.

Imbalanced mobilities, which means a difference by a factor of more than 10-100,^{83,84,86} in addition result in the build up of a space charge at the side where charges with lower mobility are extracted. This in turn reduces the electric potential drop on the opposite side of the device in order to maintain overall charge neutrality and with this increases the probability of recombination.⁸⁶ In this respect also the presence of charge carrier traps may be interpreted in this way as they effectively lower charge carrier mobility towards the respective electrode.²⁴⁵ The same reasoning as given above concerning the impact of mobility on backdiffusion of charges to the D/A interface also applies to the layer with lower mobility in the case of imbalanced mobilities.⁷⁵

Also in this case, the effect of GR can be reduced in PHJ devices by decreasing the thickness of the layer with lower mobility, because this enhances the probability of extraction in relation to backdiffusion to the D/A interface⁷⁵ and reduces the electric potential drop over the layer with low mobility.⁸⁶ Hahn et al. for example showed that the FF may eventually become independent of illumination intensity up to 1 sun (at AM1.5 conditions) even for a mobility imbalance of $10^3 - 10^4$ when using a thin donor layer of only 14nm and a thickness ratio of 1:2 for donor as compared to acceptor. This also means that bimolecular processes are no longer important and recombination effects are purely geminate. Similar results were also obtained by Tress.⁸⁶ Therefore, using a proper design of the sample, limitations due to extraction and device geometry can be avoided. This renders PHJ solar cells useful model systems to study processes at the D/A interface like the dissociation of charge transfer states.⁸⁴ For this reason bilayer samples with small donor layer thickness were also used in my publication about the effect of electron delocalization on CT dissociation at D/A interfaces in organic solar cells (cf. chapters 8.2.1 and 9).

In line with the work by Tress et al.⁸³, Athanasopoulos et al.⁸⁴ also find that a mobility imbalance of up to two orders of magnitude is still bearable and only has a minor effect on charge separation efficiency. Yet, in addition, based on entropic arguments, they point out that transport dimensionality has a strong effect, so that filamentary 1D transport would deteriorate the charge separation yield. This is in line with several works on the role of entropy in the CT dissociation process as discussed in chapter 3.3.

Besides low or imbalanced mobilities also injection or extraction barriers can account for an S-shaped J-V-characteristic.^{245-247,250} In the case of hindered extraction charge carriers pile up at the barrier thereby generating a space charge that partially screens the internal electric field in the device. This in turn gives rise to enhanced recombination at a D/A interface and a larger reverse bias is needed to extract the charges as well.^{247,250} On the other hand, also an injection barrier may cause an S-shape. Here, the barrier decreases the built-in potential, so that at a certain voltage below V_{OC} the field becomes positive - e.g. in the donor layer in a PHJ in case of a hole injection barrier - and current is extracted against the internal electric field. Consequently, carrier motion is driven only by diffusion making extraction inefficient.²⁵⁰ An injection barrier may also cause a kink in forward direction (in the first quadrant), if extraction is still more efficient than injection (figure 4.3(b)). In this case the photogenerated current is larger than the injected current until the barrier is overcome and significant injection sets in.^{87,250} The presence of injection barriers may also be desired, if OPV materials are intended to be used as photosensors, where a low dark current is essential for the resulting on/off ratio of the device and concomitantly the sensitivity of the detector.²⁵¹⁻²⁵⁴ This concept is used in my fifth publication to realize organic bidirectional phototransistor-like devices capable of both electrical and optical switching (see chapters 8.2.5 and 13).

5

Fullerenes as electron acceptors in organic solar cells

Fullerenes have been (and still are) very successfully used as electron accepting materials in organic photovoltaics. This is mainly attributed to the spherical shape of these molecules and their fully conjugated structure,^{18,19} as these properties result in a strong electron accepting ability as well as an effective three-dimensional system. This is entropically favourable for CT dissociation (cf. chapter 3.3) and gives rise to isotropic electron transport ability with high mobility in the order of $10^{-2} \frac{\text{cm}^2}{\text{Vs}}$.^{84,110,204,255} The spherical aromaticity is also regarded to facilitate electron delocalization at D/A interfaces,^{131,171,174} yet there is still an ongoing discussion whether electron delocalization actually occurs in a fullerene aggregate and if so whether this delocalization helps in the CT dissociation process. This is discussed in detail in chapters 3.2, 8.2.1 and 9. Due to their isotropic interaction capability, fullerenes in addition have the advantage that there is no special need for a specific orientation with respect to the donor, so that they are compatible and efficient with a wide range of donor materials (be they polymers or small molecules).

A common drawback of C_{60} and its derivatives in solar cell applications is their limited absorption in the VIS-range. The singlet energy of C_{60} is located at 1.85 eV, but significant absorption only sets in around 2.25 eV.^{46,256–258} Unfortunately, the absorption range is only hardly tunable, as the core structure of the molecule is always the same, i.e. C_{60} fullerene, and side-chains have only small influence on the conjugation of the C_{60} core and thus on its electronic structure that in turn determines the optical properties.³ This is why a lot of effort was put into the development of low bandgap polymers to cover a larger portion of the red part of the electromagnetic spectrum and complement the absorption of C_{60} and its derivatives.^{20–24,49} To some extent the issue of weak absorption in the VIS range could be also addressed by using C_{70} or its derivatives instead of C_{60} based compounds, as C_{70} features a stronger absorption around 2.5 eV (figure 5.1(a)).^{257,259–261} Yet, C_{70} is more difficult to obtain and thus much more expensive making it less relevant to a possible commercial application.^{44,262} Thus, some groups suggested to use mixtures of C_{60} and C_{70} because these are the natural result of fullerene synthesis and would render additional separation steps unnecessary.^{44,262}

Apart from this drawback in absorption coefficient, C_{60} tends to crystallize and form aggregates.^{23,25,30,31,35,36,263} This is on the one hand a desired property, as a certain domain size of the acceptor phase is favourable in terms of CT dissociation and charge transport and too strong intermixing would increase charge carrier recombination during the extraction process. On the other hand, a morphology that is optimized concerning domain sizes and percolation is usually not thermodynamically stable and phase separation takes place under thermal stress like it is the case under operating conditions.^{23,35,36} As already noted in chapter 2, the driving force for this demixing is either crystallization of the polymeric donor, thereby expelling fullerenes from

the mixed phase, or Oswald ripening^{1,23,35,36,60} Over the last years a lot of effort has been and still is put into understanding the formation and temporal evolution of specific morphologies as well as the underlying thermodynamics.^{25–31,57–59} One possible approach to stabilize blend morphologies in fullerene based devices was found to be the deliberate formation of a densely linked network via chemical cross-linking. This mechanism is addressed in chapter 7.

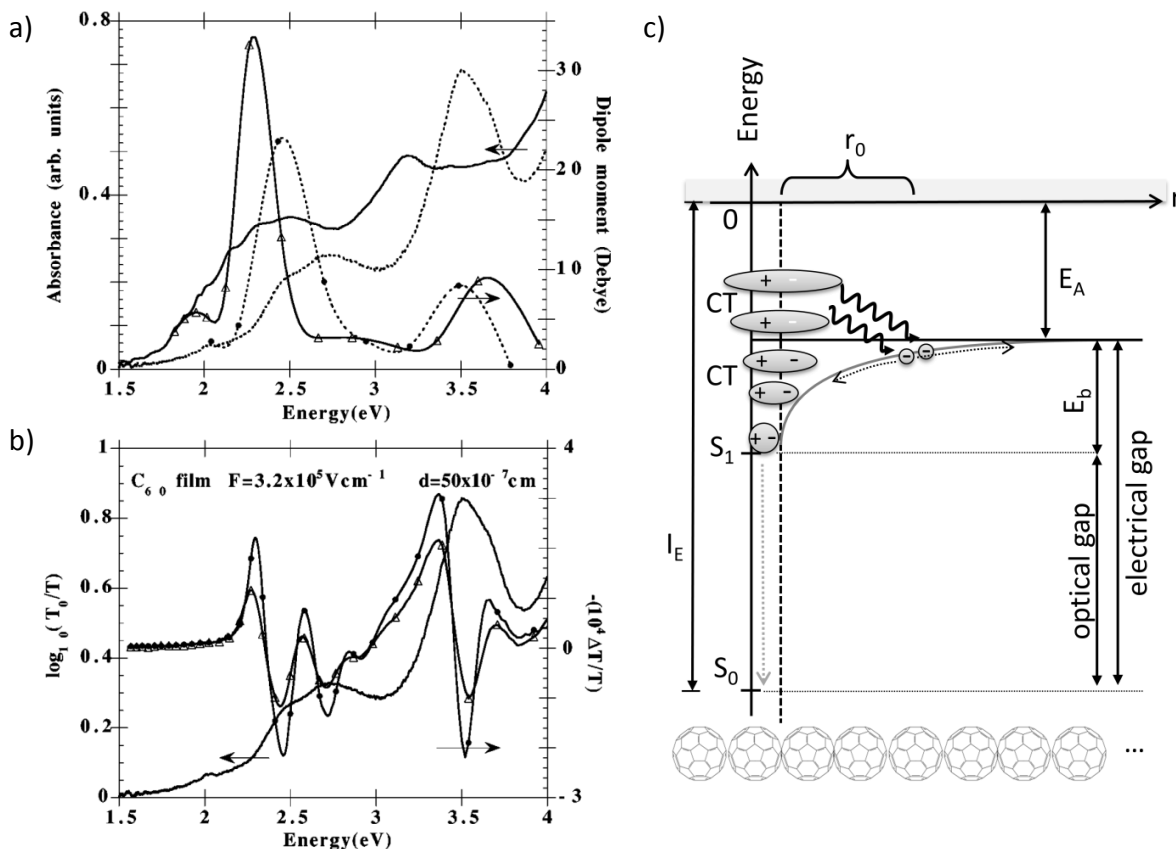


Figure 5.1.: (a) Absorption spectra of C₆₀ (---) and C₇₀-films (—), as well as dipole moment as function of energy for C₆₀ (••) and C₇₀ (—Δ—) measured at 77 K. Reprinted with permission from Kazaoui et al., *Phys. Rev. B* **58**, 7689 (1998). Copyright ©(1998) by the American Physical Society. (b) Absorption spectrum of a C₆₀ film measured at 77 K (—) and Electroabsorption spectra of C₆₀ films measured at 300 K (---) and 77 K (••). Reprinted with permission from Kazaoui et al., *Phys. Rev. B* **58**, 7689 (1998). Copyright ©(1998) by the American Physical Society. (c) Illustration of the autoionization mechanism of CT states in neat C₆₀ films. I_E and E_A are the ionization potential and the electron affinity of C₆₀, respectively. r₀ denotes the intrapair distance after thermalization. The latter process only occurs for excitation energies higher than the electrical gap. Adapted with permission from Hahn et al., *J. Phys. Chem. C*, **2016**, 120 (43), pp 25083–25091. Copyright ©(2016) American Chemical Society.

Another possibility to suppress the aggregation tendency of C₆₀ is to add bulky side chains to the molecule that prevent efficient clustering and mutual alignment. Beside this effect, additional side chains are usually designed to increase the solubility of the fullerene, as pure C₆₀ only features a very low solubility in common organic solvents used in device processing^{264,265}. Several

¹ Ostwald ripening is a thermodynamically-driven process that results in the growth of larger particles at the cost of smaller ones as a result of the tendency to minimize the surface area and achieve an energetically more favourable state.⁶⁰

derivatives with solubilizing side-chains were developed,^{32,33,179,266} with the most prominent one being PCBM.^{266,267} Common examples of higher adduct fullerenes are ICBA or ICTA.^{32,179}^{33,34} These fullerene derivatives enabled organic photovoltaic devices with V_{OC} exceeding 1 V, yet at the cost of j_{sc} and thus charge generation efficiency.^{33,34,179} The increase in V_{oc} may be attributed to the lower electron affinity (EA) as compared to C_{60} or monoadduct derivatives. A concomitant decrease in the EA- as well as ionization energy (IE)-difference between donor and acceptor results in increased exciton recycling to donor or acceptor and concomitantly inefficient CT dissociation as shown by Hoke et al. and Faist et al.^{33,34} Furthermore, the addition of side chains decreases electron mobility which in addition impedes efficient charge extraction and increases recombination.^{32,33} According to Faist et al., for these systems the donor has to be chosen carefully to compensate the drawbacks associated with higher adduct fullerenes.³³

Apart from aggregation, fullerenes may under certain conditions, especially photoexcitation and electrical bias, also form covalently bound dimers.^{268–273} This mechanism was thoroughly investigated by Heumüller et al.²⁶⁸ and found to represent a major contribution to the often observed burn-in loss as a result of a gradual reduction in short-circuit current J_{sc} in organic solar cell systems based on fullerene acceptors.^{274–277} According to their study, the light-induced dimerization process of PCBM depends on both film morphology and electrical bias of the respective organic solar cell. Concerning film morphology they found that a higher degree in fullerene crystallinity in neat fullerene phases as well as strong intermixing of fullerenes with amorphous polymeric donors inhibits or even prevents the dimerization reaction. This was attributed to geometric constraints in the first case and a lower probability of two fullerenes being in close proximity and aligned in the right way in the second case.²⁷⁸ Due to the observed clear correlation of PL quenching as well as changes in absorption with fullerene dimerization, they suggest the reaction mechanism to be based on the light induced presence of (triplet-) excitons.²⁷⁹

Meanwhile, it has been shown that fullerenes may not only be efficient acceptors in combination with another donor component, but that neat phases of fullerenes are able to contribute to the photogeneration process via autoionization of CT states in the bulk of C_{60} . The principal existence of excited states with CT character at energies above 2.2 eV has been already investigated before by Könenkamp et al. and Kazaoui et al. by spectroscopic means.^{256,258} Kazaoui et al. also performed electroabsorption measurements in order to assess polarizability Δp and dipole moment μ of the involved states and found that neat C_{60} already features a pronounced, extended CT-state at 2.43 eV that is characterized by $\Delta p = 880 \cdot 10^{-24} \text{ cm}^3$, $\mu = 22.9 \text{ D}$ and a fraction of transferred charge of 0.48 (figure 5.1(a) and (b)). An in-depth study about the role of such CT states in the charge generation process in organic solar cells as well as the underlying mechanism of their autoionization was finally conducted by Hahn et al.⁴⁶ In their work, they performed measurements on single layer devices of C_{60} and PCBM and investigated the photogeneration as a function of the internal electric field. They found that significant e-h-pair dissociation via autoionization of charge transfer states starts at about 2.25 eV, i.e. about 0.4 eV above the S_1 state of C_{60} . This process can be described and analysed in the framework of Onsager’s 1938 theory, yielding an initial intrapair distance of about 2 nm at the onset energy of 2.25 eV. At higher excitation energy, the resulting e-h-pairs are slightly more extended and generated incoherently via thermalization from higher energy states (figure 5.1(c)). Furthermore, Hahn et al. found that the coupling between charge transfer and charge transporting states is by

a factor of three lower in PCBM than in C_{60} . This was inferred from the fraction of generated charges in relation to the number of photoexcitations at a certain electric field. Apart from all this, their works also indirectly shows that C_{60} may also fairly well transport holes, albeit with a somewhat lower mobility in the order of $10^{-4} \frac{\text{cm}^2}{\text{Vs}}$ as shown by Könenkamp et al.²⁵⁶.

6 Diffusion of small molecules in a polymer matrix

Diffusive transport of small molecules through a polymer matrix can be described via a statistically random process known as random walk. The driving force behind diffusion is the presence of a gradient concerning the concentration - or more general, the chemical potential - of the diffusing species in the matrix as the system seeks to achieve a homogeneous distribution.^{280–282} Mathematically, the diffusion of small particles in a surrounding substance can be described via Fick's law, according to which the net flux \vec{J} of diffusion is proportional to the concentration gradient ∇c :^{280,283}

$$\vec{J} = -D \cdot \nabla c \quad (6.1)$$

The proportionality constant D is the so called diffusion coefficient. In general, this coefficient can be also a function of concentration c and spatial coordinates, if interactions between matrix and diffusing particle are significant or the system is not spatially homogenous.²⁸⁰ In order to describe dynamic processes where diffusion can vary with time, one additionally has to take into account mass conservation via the continuity equation:

$$\frac{\partial c}{\partial t} = -\nabla \cdot \vec{J} \quad (6.2)$$

Inserting this in eq. (6.1) one arrives at Fick's second law:

$$\frac{\partial c}{\partial t} = \nabla \cdot (D \cdot \nabla c) \quad (6.3)$$

In the case of an isotropic system and when D is not concentration dependent, this simplifies to:

$$\frac{\partial c}{\partial t} = D \cdot \Delta c \quad (6.4)$$

The simplification of assuming an isotropic system in case of a polymeric matrix is justified as long as there is no preferential orientation of the chains that would introduce anisotropy into the mass transport within the system.²⁸⁰ Consequently, this simplification can be applied mainly to amorphous polymers. Concentration dependence of the diffusion coefficient D on the other hand is often relevant for polymers when the interaction between the chains and the diffusing species becomes significant,^{280,281} which is strongly dependent on the kind of polymer and the diffusing particle. In the case of fullerenes, these interactions with typical polymers used in organic solar cells, like P3HT, PCDTBT or PTB7, become relevant for concentrations larger than about 10 – 20 wt%.^{26,31,57} This in turn means that for small concentrations in the range of only a few wt%, the diffusion coefficient can be regarded as constant. In this case, also the assumption of Fickian diffusion is usually justified, while at larger concentrations deviations may occur.^{26,280}

Wang et al.²⁶ for example found that PCBM diffusion into a PTB7 polymer matrix features two diffusion modes at higher PCBM concentrations (> 40 wt%): A normal Fickian diffusion front of PCBM is followed by a second concentration front of PTB7 saturated with PCBM that evolves linearly with time, i.e. that shows Case-II-like characteristics (=linear dependence of the mass uptake on time²⁸⁴).

Beside concentration, diffusion in polymers depends on several factors such as molecular weight, segmental mobility, side chain structure and functional groups (that might interact with the diffusing particle under certain conditions), as well as π - π -interactions as these influence the aggregation tendency of a polymer.^{281,285-287} All these factors impact on the temperature dependent behaviour of the polymer and its ability to deform and relax under externally applied stress.^{285,288} A crucial quantity in this respect is the so called glass transition temperature T_g . It is defined as the temperature, where "the transition from a liquid equilibrium state to a non-ergodic one, i.e. only partially equilibrated state takes place".²⁸⁸ It is well known that polymers can undergo a transition from a glassy to a rubbery state and finally to a viscous, fluid-like state when temperature is increased.^{288,289} The presence of a rubbery behaviour is determined by the entanglement of polymer chains and therefore structure, molecular weight and chain rigidity. It should be noted, though, that whether a polymer behaves like a glass or a rubber in a relaxation experiment depends on the measurement conditions (measurement time and applied frequency at a certain temperature), meaning that the transition from a glassy to a rubbery state - usually referred to as the " α -process"¹ - is a purely kinetic phenomenon and not an actual structural transition like a melting process. This is directly obvious from the observation that the time range of the glass-rubber transition shifts with temperature.²⁸⁸

The glass transition temperature T_g as such is associated with the occurrence of characteristic steps in expansion coefficient $\frac{d\rho^{-1}}{dT}$ and heat capacity $\frac{dH}{dT}$, respectively. Therefore, common methods to determine T_g are volumetric (DMA) or calorimetric measurements (DSC).^{285,288} In practice, the characteristic steps in these measurements appear at a temperature where the relaxation time for the α -process is in the order of minutes, i.e. $\tau_\alpha(T_g) \approx 10^2$ s.²⁸⁸ This corresponds to a heating/cooling rate of 10^{-2} $\frac{\text{K}}{\text{s}}$. For higher rates, the step shifts to shorter relaxation rates and hence slightly higher temperatures. This rate dependence and the fact that the steps are naturally broadened in a real experiment - with typical widths in the order of 10 K - implies that T_g should be rather viewed as a temperature range with a tolerance of a few degrees rather than a sharp, well-defined transition temperature. Consequently, for a direct comparison between different materials a fixed heating/cooling rate should be chosen.²⁸⁸

From a microscopic point of view, the observation of steps in $\frac{d\rho^{-1}}{dT}$ and $\frac{dH}{dT}$ is associated with an increased mobility and intensified motion of the chain segments above T_g . This in turn is accompanied by the increase of the so called "free volume" V_f in the sample, as a rising number of conformational states become populated in which the chains are not or no longer densely packed. V_f is referred to as the volume that is not occupied by the hard cores of the monomer units.²⁸⁸ This concept is usually used to explain the rapid increase in diffusivity above T_g .

In case of a mixture like polymer-fullerene blends, the associated T_g may be estimated from the empirical Fox-Flory equation:^{285,290}

¹ This process is related to segmental chain relaxation after externally applied stress.²⁸⁸

$$\frac{1}{T_g^{blend}} = \frac{w_1}{T_{g1}} + \frac{w_2}{T_{g2}} \quad (6.5)$$

where w_1 and w_2 are the weight fractions and T_{g1} and T_{g2} the glass transition temperatures of the respective component of the blend system. This simple relation does not take into account a possible presence of crystalline domains, but works for anticipating general trends especially in amorphous systems.^{285,288}

It should be emphasized, that T_g as defined above is a quantity that is related to the mobility of the polymer backbone. The side chains are still mobile below T_g and only stiffen at temperatures well below T_g .^{285,291} Xie et al. for example have shown that P3HT (rr: $T_g \approx 22$ °C, rra: $T_g \approx 6$ °C) features a second transition temperature at around -100 °C that can be associated with the relaxation of alkyl side chains.²⁹¹

Above T_g , the viscosity η of a polymer is usually described via the well-established empirical equation known as the Vogel-Fulcher-law:²⁹²⁻²⁹⁴

$$\eta(T) = B \cdot \exp\left(\frac{T_A}{T - T_V}\right) \quad (6.6)$$

where B is a system dependent prefactor, T_A denotes the activation temperature and T_V is referred to as Vogel temperature. This equation features a singularity at $T = T_V$. Consequently, according to the Stokes-Einstein relation

$$D = \frac{k_B T}{6\pi\eta R_v} \quad (6.7)$$

one would expect the diffusion coefficient D of a small spherical particle with hydrodynamic radius R_v to rapidly decrease when approaching T_V . T_V is typically located $30 - 70$ °C below T_g , yet whether η really diverges seems difficult to be checked by experiment as measurements are only possible down to about 50 K above T_V , because then η is already very large.²⁸⁸

Concerning diffusion in the vicinity of T_g and below there are several works reporting that diffusion of a particle and viscosity of the polymer matrix seem to decouple in a way²⁹⁵⁻²⁹⁸ and Vogel-Fulcher-Tammann (VFT)-like behaviour of $\eta(T)$ or equivalently a diffusion coefficient D obeying Stokes-Einstein relation is not necessarily observed for $T < T_g$.^{296,299-304} In a rather simple picture, one could think of mass transport rather taking place via thermally activated hopping^{281,300} like one would expect for interstitial diffusion of atoms or dopants in a solid,³⁰⁵ which is not an inconceivable picture when thinking of a rather stiff and brittle polymer matrix. Yet, one has to keep in mind that side chains are still mobile leading to continuous redistribution of "free-volume" in the material.³⁰⁶ The actual underlying mechanism and how to properly describe diffusion below T_g is still subject to research.^{26,307-310} In order to contribute to the discourse on this issue, this is also addressed in my third publication (see chapters 8.2.2 and 10).

Diffusion in general also plays an important role for device applications in terms of morphological stability of blend mixtures or interfaces between different materials in layered structures.^{23,25,30,31 311,312} Morphology in turn is crucial in terms of device efficiency, for example when considering percolation paths for charge carrier extraction or injection and dissociation or recombination efficiencies (cf. chapters 2 and 3). Consequently, this topic is of special interest to the or-

ganic electronics community and there are several studies dealing with approaches to either suppress diffusion and stabilize morphology^{23,35,36,274,312–315} or to understand the underlying mechanisms governing miscibility and diffusion in organic electronic devices.^{25,26,30,57,263,316,317} Special focus in this respect is laid on binary and even ternary blend systems^{26,31,318} for organic photovoltaics as well as doping of transport layers and at interfaces.^{319–324} An effective way to reduce diffusion and increase morphological stability is to perform crosslinking of the matrix material or even between two components of a system.^{23,35,36,274,312–315} This aspect is shortly addressed in chapter 7 and in more detail in the review in appendix A. Some important aspects about diffusion in organic electronic devices resulting from recent research are summarized shortly in the following. Several groups found that diffusion mainly takes place in amorphous regions.^{25,26,30,31,319,325} Crystalline phases are not affected when they have been already present before the mixing,^{30,326,327} but only when they are formed afterwards, for example when sequential deposition is applied.³²⁷ Furthermore, the degree of intermixing depends on the size and shape of the diffusing molecule, which also provides a means to design molecules for special purposes.^{319–321,323} For example when using a molecule as a dopant for a transport layer it should be bulky enough to prevent diffusion into the active layer, which in turn may deteriorate device efficiency. Concerning the relevance of T_g for morphological stability, McEwan et al.³²⁸ verified that materials with higher T_g tend to diffuse into adjacent layers that feature a lower T_g . So for an overall morphological stability one should only use materials together in a device that all feature a high T_g . Finally, Hartmeier et al.³¹⁸ emphasize that in complex systems like binary or even ternary blends, in which the components may also tend to crystallize or aggregate, the mixing behaviour is of course not only governed by diffusion kinetics but also thermodynamic aspects. These have to be taken into account when trying to understand the formation of microstructures in these devices.

7

Excursus: Crosslinking in organic solar cells

As already addressed shortly in chapter 2, morphologies in organic solar cells tend to be thermodynamically unstable. This results in phase separation in bulk-heterojunction structures or the intermixing of adjacent layers in stacked architectures over time due to diffusion of low molecular weight compounds like fullerene acceptors or dopants. Crosslinking has proven to be a promising approach to tackle these issues and a lot of investigations on the potential use of crosslinkable materials in organic solar cells have emerged in the last decade.^{23,35,36} In general, it can be defined as covalently linking molecules applying various stimuli like temperature, pressure or light and often using additional compounds as agents. The linkage is usually mediated by specific functional groups attached to the molecules that are to be crosslinked.^{23,35,36} Transferring this concept to organic solar cells allows "freezing" the initial morphology of a blend structure after optimization during processing and concomitantly suppressing the tendency of small molecules to diffuse within or into the active material. The latter has been nicely addressed for example in a work by Fischer et al.,³¹⁵ where the diffusion coefficient has been shown to be reduced by three orders of magnitude as compared to the non-crosslinked reference in the case where every repeat unit in a model polyfluorene derivative carried a crosslinkable group. Furthermore, crosslinking renders the respective layers insoluble. In general, it has been shown that it is not absolutely necessary to have a crosslinkable group attached to every side chain, but smaller amounts are already enough to obtain a densely linked and insoluble network.^{329–333} The aspect of insolubility additionally makes crosslinking a promising alternative to the use of orthogonal solvents³³⁴ or inorganic blocking layers^{49,335,336} when fabricating multilayer structures via solution processing^{315,337–347} and is of special importance for the model bilayer systems that are frequently used throughout this thesis.

In terms of organic solar cells it is possible to crosslink either donor or acceptor to form a stable matrix for the respective other component or to directly link them.^{23,35,36} Here we will focus on the donor-to-donor linkage as this is the method utilized in this thesis. In the majority of devices, polymers are used as electron donating species. In this case, functional groups are usually attached to the solubilizing side chains of the donor in order to retain the electronic properties of the polymer and not severely disrupt the backbone conjugation. The general principle of this crosslinking approach is illustrated schematically in figure 7.1(a). Possible functional groups that may and have been applied in organic solar cells are bromine, acrylate, oxetane, azide and vinyl groups.^{23,35,36} In the framework of this thesis two of these concepts were used: acrylate and oxetane (figure 7.1(b)).

Crosslinking of acrylate groups takes place via a free radical mechanism.^{313,348,349} This process usually requires the addition of a (photo-)initiator, which is split into fragments with unpaired electrons upon exposure to UV-light and heat, thereby creating the primary (free) radicals

which then transfer to the polymer chain forming secondary propagating radicals. These are then the reactive species mediating the crosslinking between the acrylate containing side chains of individual polymers. A possible drawback in terms of application to optoelectronic devices is that the residues of the photoinitiator decomposition remain in the device and may act traps for charge carrier transport or as exciton quenching sites.^{23,350,351} This can be circumvented by mere thermally activated crosslinking with accompanying illumination. Both aspects, thermally activated crosslinking and the influence on charge transport when adding photoinitiators are addressed in my publication about the impact of crosslinking on charge carrier mobility (chapters 8.2.3 and 11). Nevertheless, crosslinking via acrylate groups is restricted to the use in layered, sequentially deposited architectures when intended to be used in the presence of compounds with strong electron scavenging ability such as fullerenes^{352–355} because these will efficiently terminate the radical mediated reaction thereby preventing the formation of a network.

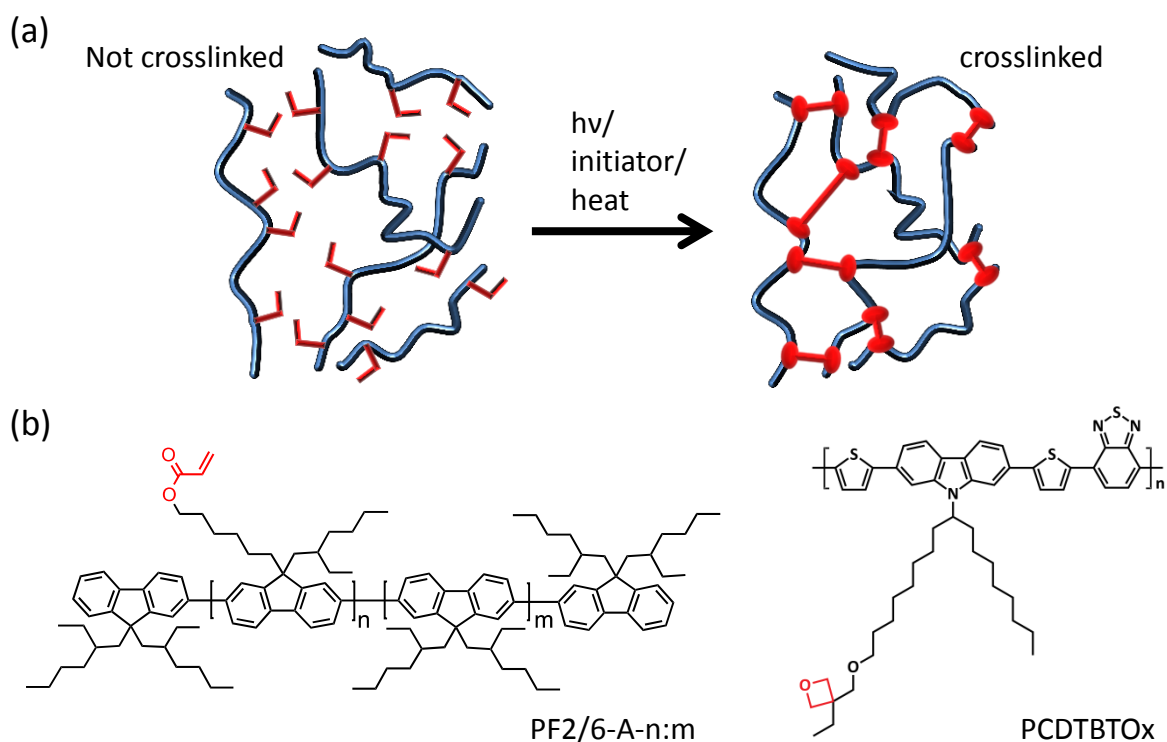


Figure 7.1.: (a) Schematic of the donor-to-donor crosslinking of a conjugated polymer. The process may be initiated via a (photo)initiator, heat and/or exposure to UV-light $h\nu$ resulting in a densely linked and insoluble network due to the formation of covalent bonds between the chains. (b) Structure formulas of the two crosslinkable polymers used in this thesis. The respective functional groups used for crosslinking (left: acrylate, right: oxetane) are highlighted in red.

To allow for crosslinking in the presence of fullerenes, e.g. in a bulk heterojunction, another mechanism has to be applied. In this respect, the use of oxetane groups instead of acrylates is a promising approach, because oxetane mediated crosslinking proceeds via a cationic ring opening process (CROP).³⁵⁶ The protons needed for the initiation are typically provided from so called photoacid generators (PAGs).^{351,357} However, the interplay between a PAG and the oxetane-functionalized compound may lead to a number of unwanted side reactions. Among others, photoinduced electron transfer from the PAG to the semiconductor additionally results in unintentional doping of the crosslinked layer, which in turn could deteriorate device

performance.³⁵¹ Also, residuals of the acid and the presence of counterions can cause problems in this respect.^{23,35,358} A very good alternative to the use of PAG is exposing the crosslinkable sample at elevated temperatures to trifluoroacetic acid (TFA) vapour, which is a very efficient initiator for the CROP process.³⁵⁹ TFA has the advantage of being very volatile with a boiling point of 72 °C and a high vapour pressure (97.5 mmHg @20 °C) so that residual acid may be easily removed after processing.³⁶⁰ In our case, we applied a combined thermal and vacuum treatment (90 °C, 90 min, 10⁻⁴ mbar) with a subsequent exposure to high vacuum (5 · 10⁻⁷ mbar) for several hours prior to deposition of additional layers via evaporation. Again it was found, that even crosslinking via oxetane groups may be achieved by mere thermal activation,³¹² but this requires to expose the sample to heat for several tens of hours in order to achieve a good crosslinking density.

A noteworthy example of crosslinking in an organic solar cell without addition of any further initiator has been shown by Peters et al. as well as Tourné et al.^{274,313,314} They found that in a bulk heterojunction of PCDTBT with PCBM a special mechanism is at work that results in an impressive long-term stability of the respective devices with expected average lifetimes of up to seven years while still retaining 4% PCE.^{274,314} The underlying process leads to the formation of actual covalent crosslinks between the polymer backbone and the fullerene, which is preceded by the photoinduced scission of the bond between the N-atom of the carbazole units of PCDTBT and the attached alkyl side chain.^{23,313}

As a side remark, it shall be mentioned that the concept of crosslinking may also be used to stabilize nanostructures fabricated by nanoimprinting.²³ This could be used to obtain a well-controlled morphology with defined phase intercalation and percolation pathways for organic solar cells.^{361–363} Unfortunately, Pfadler et al.³⁶⁴ have shown that the advantage of a larger interfacial area is finally outbalanced by increased recombination so that no net improvement of device performance could be achieved. For a more in-depth review about crosslinking in organic solar cells the reader is referred to chapter A in the appendix.

8

Overview over the publications

Before going into detail about the content of the individual publications in section 8.2, the first section of this chapter will present an overview about how the different works are linked or build up on each other and how they are embedded into the greater context of organic solar cells. A schematic overview over the relation between the publications and which processes in an organic solar cell they address is presented at the end of chapter 8.1 in figure 8.1.

8.1. Summary and overall context

As already noted in abstract and motivation, organic solar cells have regained a lot of research interest after the successful development of new non-fullerene acceptors.^{3,18,73} Before that, further improvements with the common systems based on fullerenes and low bandgap polymers seemed to be very hard to achieve and a lot of effort in the organic solar cell community has been put into morphology optimization and stabilization and the extension of the absorption range to the red to better match the solar spectrum.^{20-31,49,57-59} Although it is easier to tune the bandgap of the newer non-fullerene based systems and they have less tendency to aggregate and phase separate in a D/A blend - sometimes they even mix too well - they feature the same basic properties as all organic materials. Especially, they are still extrinsic semiconductors where excitations result in bound electron hole pairs instead of free charges as it is typically the case in inorganic semiconductors.³⁹ For this reason, the most important key factor for the performance of an organic solar cell is the dissociation efficiency of these e-h-pairs, preferably in the form of CT states formed at D/A interfaces. Understanding the relevant mechanisms and aspects of the dissociation process, including recombination before the actual separation, and the character of the CT states is a crucial requirement to further improve the properties of new systems and finally someday pave the way to actual commercial applicability.

Against this background, this thesis is devoted to contribute to a deeper understanding of the charge transfer state, the fundamental process of its dissociation as well as closely related aspects that are indivisibly connected with it and finally affect the overall device efficiency. These aspects include for example charge transport, which influences both geminate and non-geminate recombination (cf. chapter 4) and intermixing at the D/A interface via diffusion.

Chapter 9 addresses the key aspect of CT dissociation at a D/A interface. Several factors have been proposed to impact on this process, for example internal electric fields or charge carrier mobility.^{43,44,74} Heavily disputed especially in view of the new non-fullerene acceptors are on the one hand entropic aspects and in this context particularly disorder and on the other hand delocalization of charge carriers and the CT state as a whole (cf. chapters 3.2 and 3.3).^{71,110,204-207} The fundamental idea in the case of delocalization is that the CT binding energy is reduced thereby facilitating dissociation of the interfacial electron hole pair.^{162,163} It is easy to see and has been convincingly shown before, that in the case of conjugated polymers

delocalization of a hole along the conjugated segments is possible and helps the dissociation process.^{162,166} This is due to the high coupling strength within the chain segments. Yet, it is not so straightforward to transfer this concept to small molecular acceptors as they feature a smaller coupling between adjacent molecules,²¹¹ so that transport is rather expected to be incoherent.⁴³ Up to now, there is still no consensus but rather controversial discussion, whether electron delocalization is actually present in typical small molecular acceptor systems and if so, whether it is of similar significance as hole delocalization (see chapter 3.2). In chapter 9 I thus address this issue by performing photophysical, electrical as well as structural investigations on organic bilayer solar cells consisting of a crosslinked derivative of the well-known amorphous polymer PCDTBT (PCDTBTOx) combined with three different fullerene acceptors. These experiments are complemented by theoretical modelling according to the effective mass model under consideration of interfacial dipoles.^{162,163} Bilayer samples were chosen as model system to avoid additional effects due to morphology (i.e. bimolecular recombination, percolation, domain sizes), which otherwise would superimpose interfacial effects. The application of a crosslinked donor layer allows to deposit solution processable acceptors and suppresses interdiffusion into the donor thereby providing a well-defined interface.³¹⁵ This was also beneficial for the application of our theoretical simulations. As for all crosslinkable polymers used in this thesis, the functional groups were attached to the side chains to leave the electronic structure of the polymer backbone unchanged (cf. chapter 7).

As acceptors I chose three different fullerenes (C_{60} , *PCBM*, *ICBA*). The reason for the use of fullerenes is that they are well-conjugated systems with spherical aromaticity (cf. chapter 5), which makes them a suitable model system to study possible effects of electron delocalization in the acceptor phase on the overall CT dissociation efficiency. Apart from that, they are readily available and well characterized. The series of fullerene acceptors used here differ in their number of additional covalent bonds which are attached to the C_{60} core and thus in their degree of (local) order. These properties are expected to impact on the intermolecular coupling strength and thus delocalization of the electron wavefunction.^{32,173,365}

The combined experimental and theoretical analysis presented in chapter 9 reveals that a higher local structural order and concomitantly stronger intermolecular coupling in the acceptor phase can be associated with a higher degree of delocalization and a higher CT dissociation efficiency. This is especially substantiated by an increase in the effective mass m_{eff} of the CT state when replacing C_{60} with *PCBM*. Although m_{eff} as a measure of wave function delocalization in general refers to the entire CT state and contains contributions from both electron and hole, the observed change in effective mass can be unambiguously attributed to the electron because the donor is the same in all cases. In general, this result indicates that high local order is crucial for efficient dissociation in organic solar cells - an implication that is also particularly relevant for non-fullerene systems which are prone to feature ordered aggregates.^{3,18}

In the previously described work I had used a crosslinked donor polymer to allow the fabrication of bilayer devices with acceptors that are deposited from solution and to suppress interdiffusion of fullerenes into the donor layer. Intermixing at interfaces in multilayer architectures, but also phase segregation in blend morphologies as a result of diffusion of small molecular acceptors or dopants can severely affect dissociation and recombination and thus device efficiency in an organic solar cell. The latter results in coarsening of the morphology and with this deteriorates percolation of charge carriers to their respective electrode thus increasing recombination proba-

bility. Intermixing at an interface in turn may give rise to the formation of traps states for charge carriers. As this is a general problem when using small molecules in a device — especially with respect to (long-term) stability —, it is important to understand the mechanisms and factors governing diffusion in optoelectronic devices like organic solar cells.

The fact that crosslinking effectively reduces the diffusion coefficient of C_{60} in a polymer matrix had been verified before by Fischer et al.³¹⁵ In this case, diffusion was monitored via quenching of the photoluminescence (PL) of a sensor layer in a three-layer architecture. The quenching species is deposited on top of the investigated material and undergoes thermally activated diffusion towards the sensor. The underlying principle is inspired by the time-of-flight technique. The major disadvantage of this approach was the need for a sensor that absorbs at higher wavelengths than the investigated polymer to ensure selective detection of the sensor PL, which made the method unsuitable for state-of-the-art low bandgap polymers, because radiative efficiency drastically reduces when approaching the NIR region.³⁶⁶ To circumvent this problem T. Müller developed a modified, 2-layer based approach in his master thesis, where the investigated polymer itself serves as the sensor.³⁶⁷ In chapter 10 of this thesis, the underlying theoretical model of this method was extended to account for more realistic scenarios and further aspects concerning the initial concentration profile. In the extended framework, I introduced a self-consistent approach to determine an approximate initial concentration profile and may additionally take surface quenching into account. Before, the initial concentration of C_{60} at the beginning of the experiment at a certain temperature was always assumed to be homogeneous all over the sample. With this extension, I first compared the 2-layer and the previous 3-layer technique to verify the reliability and comparability of the results. To this end, I measured the temperature dependent diffusion coefficient of the crosslinked PF2/6-derivative PF2/6-A-75:25, which was also investigated in the work by Fischer et al.³¹⁵ Gratifyingly we also find an Arrhenius-type temperature dependence with the same activation energy of diffusion, although the absolute values differ slightly by a factor of 2-3. The latter could be related to the different models from which the diffusion coefficient is determined (arrival time vs. dynamic photoluminescence decay due to bulk quenching) but does not affect the physical meaning of the measurement, as evidenced by the coinciding activation energies for the same material.

Having verified the reliability of the new technique and the corresponding model, I then investigated an important aspect of diffusion affecting morphological stability and the tendency of intermixing at an interface in multilayer architectures.^{319,325,328} The relation between diffusivity in a polymer matrix and the glass transition temperature T_g of the backbone. A special focus in this respect was laid on the role of the side chains in the diffusion process as well as on the question whether diffusion may still appear below the glass transition temperature. The latter also has important implications on a possible device degradation during mere storage, e.g. due to interdiffusion of dopants from adjacent transport layers into the volume of the active layer. For this study I chose three different derivatives of the well-known low bandgap polymer PCDTBT ($PCDTBT$, $PCDTBT_{stat}$, $PCDHTBT$),^{274,313,314} the polymer I had also used as a donor in the first work discussed above (see chapter 9). These derivatives differed slightly concerning their molecular weight, the sequence of their building blocks and more importantly their side chains. This in turn results in a variation of the glass transition temperature T_g , which determines the mobility of the polymer backbone.²⁸⁵ Two of the derivatives featured a similar T_g which resulted in very similar diffusion coefficients as well as the same temperature dependence. This provides further evidence that the results obtained from the new 2-layer approach are reliable. In general,

I found very low diffusion coefficients for PCDTBT in the order of $\leq 10^{-15} \frac{\text{cm}^2}{\text{s}}$ at temperatures around 373 K, which is even lower than for the crosslinked PF2/6 derivative PF2/6-A-75:25. Consequently, we can safely assume that interdiffusion does not play a role in the bilayer samples used in the study about electron delocalization, especially as the donor layer is additionally crosslinked there. Interestingly, we do not observe a drastic decrease of the diffusion coefficient for temperatures $T < T_g$ as one would expect according to the Stokes-Einstein relation if the viscosity followed a Vogel-Fulcher-Tammann law (see chapter 6),^{288,368} but rather a continuous transition with an Arrhenius-type temperature dependence below T_g . Such a behaviour has indeed been observed before in polymer matrices but the microscopic origin of this process is still subject to research (see chapter 6). From our results, we could conclude that diffusion of C_{60} in the investigated systems is not governed by collective motion of glassy elements of the polymer backbone but rather determined by local motions mediated by the side chains. This seems plausible as they are still mobile below T_g and feature a much lower transition temperature (see chapter 6).^{285,291} Accordingly, with this study I could gain mechanistic insight into the role of the side chains in the diffusion process, especially for temperatures $T \leq T_g$. In terms of application — for example with respect to doping of interlayers in optoelectronic devices (e.g. OLEDs, OPVs, perovskite solar cells) — this implies that high glass transition temperatures are required to enhance morphological stability and suppress intermixing at interfaces.

In general, the information inferred from such temperature dependent diffusion measurements with respect to T_g can prove useful as guidance for device processing and material design for example with respect to annealing times and temperatures and thus also long-term stability under operating conditions.^{23,369}

A promising approach in the organic electronics community to address the issues of morphological instability and intermixing at interfaces in multilayer architectures, which was also applied in my study on electron delocalization, is to crosslink either of the active components to form a stable matrix or even directly link them.^{23,35,36} This is discussed in more detail in chapter 7 and appendix A. The main focus of research on the use of crosslinking in organic photovoltaics has been set on processing, material design and device architectures with respect to the overall device performance and long-term stability.^{23,35,36} However, in-depth studies about the impact of crosslinking on charge carrier mobility — a key parameter for device performance due to its influence on geminate and non-geminate charge carrier recombination and charge extraction — are sparse and particularly missing in the field of organic photovoltaic devices. In view of the above and because crosslinked polymer layers were applied in the work on the influence of electron delocalization on CT dissociation, I conducted a systematic study about the influence of crosslinking density on hole mobility in an amorphous polymeric system in chapter 11. Furthermore, as crosslinking often requires initiation from a curing agent, the impact of this additional compound or the respective byproducts of the reaction are also addressed.

For this investigation, I used the same series of crosslinkable PF2/6 derivatives like Fischer et al.³¹⁵ with different fractions of crosslinkable acrylate groups as model system. In their diffusion study, Fischer et al. had already shown convincingly that the diffusion coefficient significantly reduced with crosslinking density. Consequently, this material system showed the desired behaviour for our research purpose and was additionally amorphous just like the donor polymer used in the delocalization study (see chapter 9). The corresponding crosslinkable PCDTBT derivative was not suitable for the intended systematic study as function of crosslinking den-

sity, because its synthesis turned out to be very complex and time consuming so that different amounts of crosslinkable functional groups could not be realized easily. In contrast, PF2/6-A-m:n was much easier to fabricate in the desired fashion.

Mobility measurements are combined with spectroscopic investigations to characterize possible changes in the electronic structure upon crosslinking and the presence of traps. To assess the low to medium charge carrier density regime I carried out MIS-CELIV measurements. For high charge carrier densities I used p-type bottom-gate top-contact OFETs. Absorption and Photoluminescence spectra showed minor changes as a function of the fraction of acrylate containing side chains and thus crosslinking density, irrespective of the admixture of photoinitiators or crosslinking. These minor changes are attributed to conformational changes in the film structure induced by the additional functional groups in the side chains, e.g. due to increased chain torsions. Photoluminescence quantum yield (PL-QE) and mobility measurements, which are particularly sensitive to the presence of trapping sites, reveal that a larger amount of photoinitiator may induce traps in the system, either by its mere presence or by remaining decomposition products after the crosslinking reaction. This is especially pronounced for initiators containing heavy metals. Consequently, we could show that such compounds should be avoided in optoelectronic applications. Importantly, I showed that for the investigated crosslinking mechanism also mere thermal crosslinking in the presence of UV/VIS illumination is possible without the need for additional initiators, which is particularly advantageous for the fabrication of multi-layer devices like OLEDs or bilayer OSCs. Under proper crosslinking conditions, i.e. only small amounts of metal-free initiators or mere thermal crosslinking, hole mobility is not altered by the crosslinking process itself. What remains is a small mobility reduction as a result of the conformational changes in the network introduced by the increasing amount of crosslinkable groups. The decrease is at most about one order of magnitude in the case where every side chain carries a crosslinkable group in relation to the reference carrying no functional groups. To account for this and avoid a negative effect of imbalanced mobilities in the framework of my study on electron delocalization, the crosslinked donor layer was applied very thin (14 nm) with half the thickness of the acceptor and appropriate transport layers were incorporated additionally.

In view of the results of Fischer et al.,³¹⁵ who had shown that diffusivity is significantly reduced by crosslinking, I can now conclude that under appropriate conditions a compromise between mobility reduction and morphological stabilization is possible. This is because significant stabilization can be already achieved with only 25 % of crosslinkable groups,^{23,329–333,359} in which case mobility is just reduced by a factor of 2-3, and only due to morphological alterations, yet not due to defects.

In my work on the influence of electron delocalization on the dissociation of CT states I had found that local order is correlated with delocalization in the acceptor phase (chapter 9). Yet, commonly the aspect of order/disorder is neglected in the analysis of CT spectra according to the widely used approach by Vandewal et al.¹⁵⁷ These two aspects inspired me to aim for the development of an approach to consistently model absorption and fluorescence spectra of CT states under consideration of disorder as a function of temperature and thus get a deeper insight into the underlying mechanism of electron transfer processes in organic solar cells (chapter 12). Moreover, this is of particular interest as the discussion about the role of disorder for CT state splitting has gained momentum within the last years.^{110,205,206}

In chapter 12 we performed photocurrent (EQE) and time resolved PL spectroscopy as a func-

tion of temperature as well as EL measurements at room temperature, to identify the suitable framework to describe CT spectra consistently over a wide range of temperatures (5 – 295 K). This in turn allows to reliably characterize the associated CT states concerning their energy distribution and reorganization energy that is needed upon formation of a CT state. A special focus is set on the role of disorder in the determination of the spectral line shape and thus the correct extraction and interpretation of characteristic properties of the CT state. Commonly, in organic solar cells CT spectra or bands in EQE and EL are analysed in the framework of Marcus' electron transfer theory typically assuming a single absorber, i.e. neglecting energetic disorder (cf. equations (8.1) and (8.2)).¹⁵⁷ Notably, in a very recent work by Vandewal et al., the authors state that the CT lineshape is dominated by intra-molecular vibrations and that static disorder only gives a minor contribution.¹⁴⁶

Against this background, our work specifically addresses three questions: Is the simplified Marcus-type framework without consideration of disorder suitable to describe and analyse CT spectra reliably? Is a neglect of disorder in this context acceptable? Are intra-molecular vibrations indeed so important for the reorganization energy associated with an inter-molecular state?

To answer these questions, the temperature dependent spectra are analysed in terms of the often used Marcus-type framework, the extended theory of Marcus, Levich and Jortner (MLJ)^{143,145,151} with and without consideration of static disorder and finally the widely used Franck-Condon approach, that is commonly applied in spectral analysis. Even without a deeper analysis we find clear experimental evidence that disorder significantly contributes to the spectral line shape of the CT band. This conclusion is inferred from a time dependence of the photoluminescence decay in accordance with the Hong-Noolandi formalism indicating a distribution of CT energies and the spectral shift between EL and PL implying a contribution of spectral diffusion in a Gaussian DOS. Accordingly, the temperature dependent spectra could not be reproduced physically meaningful with models that neglected disorder. This is especially evidenced by the fact that the Marcus model as well as the MLJ framework without considering disorder theoretically predict significant line narrowing with decreasing temperature, which was not observed experimentally. In contrast to that, both MLJ with disorder and the Franck-Condon model were equally well able to reproduce the line shape of the spectra over the entire temperature range investigated here (5 – 295 K). The fact that both fits are practically indistinguishable is attributed to two factors: 1) The dominant contribution of disorder and 2) that the MLJ expression under consideration of disorder converges to the same form as the Franck-Condon expression at lower temperatures. A detailed analysis in the Franck-Condon framework further revealed that the major contribution to the reorganization energy comes from intermolecular vibrations, i.e. low-frequency phonon modes.

In conclusion we found that (i) disorder is essential to correctly describe the spectral line shape of a CT transition, (ii) the associated reorganization energy is rather determined by inter- than intra-molecular vibrations and that (iii) CT spectra may be consistently modelled over the entire investigated temperature range using the Franck-Condon approach. The latter indicates that electron transfer in disordered media takes place via tunneling. With these implications in mind, results obtained from the simple Marcus-type expressions neglecting disorder should be viewed with some caution.

Finally, in chapter 13 I made use of the pronounced ability of C_{60} to split bulk CT states via

autoionization to realize simple bilayer devices that behave like a bidirectional phototransistor where illumination takes the role of the gate voltage in a conventional OFET. This was inspired by the work of Hahn et al. on the role of intrinsic photogeneration in C_{60} and $PCBM$ ⁴⁶ and the work on electron delocalization in fullerene acceptors in chapter 9. Further ingredients to achieve a bidirectional characteristic dominated by photogeneration rather than injection of charge carriers are good charge transport to ensure efficient extraction of charges and the presence of an injection barrier to keep the dark current low in the device. The latter enhances the on/off ratio and is an important requirement to obtain a net photocurrent under forward bias.⁸⁷ The mechanism behind the phototransistor-like behaviour can be understood in terms of a photoenhanced recombination current close to the cathode and the Ph-TDPP-Ph/ C_{60} interface.^{87,88} To allow good charge transport in the donor phase, I used the DPP derivative *Ph-TDPP-Ph*. DPPs are a material class that typically feature good charge transport properties^{370–375} and may even be tuned to show ambipolar behaviour.^{370,375,376}

The combination of Ph-TDPP-Ph and C_{60} shows a voltage dependent photosensitivity between 1.85 and 2.25 eV which can be used as additional switching mechanism for the photocurrent apart from the voltage. I could exploit this behaviour to obtain fully organic hybrid optical and electrical logic elements like NOT-, AND- or OR-Gates, that form the basis for advanced analog and digital applications. This application eventually represents a remarkable example of how efficient dissociation of (delocalized) CT states in a fullerene phase can be used in an alternative way instead of the conventional organic solar cell.

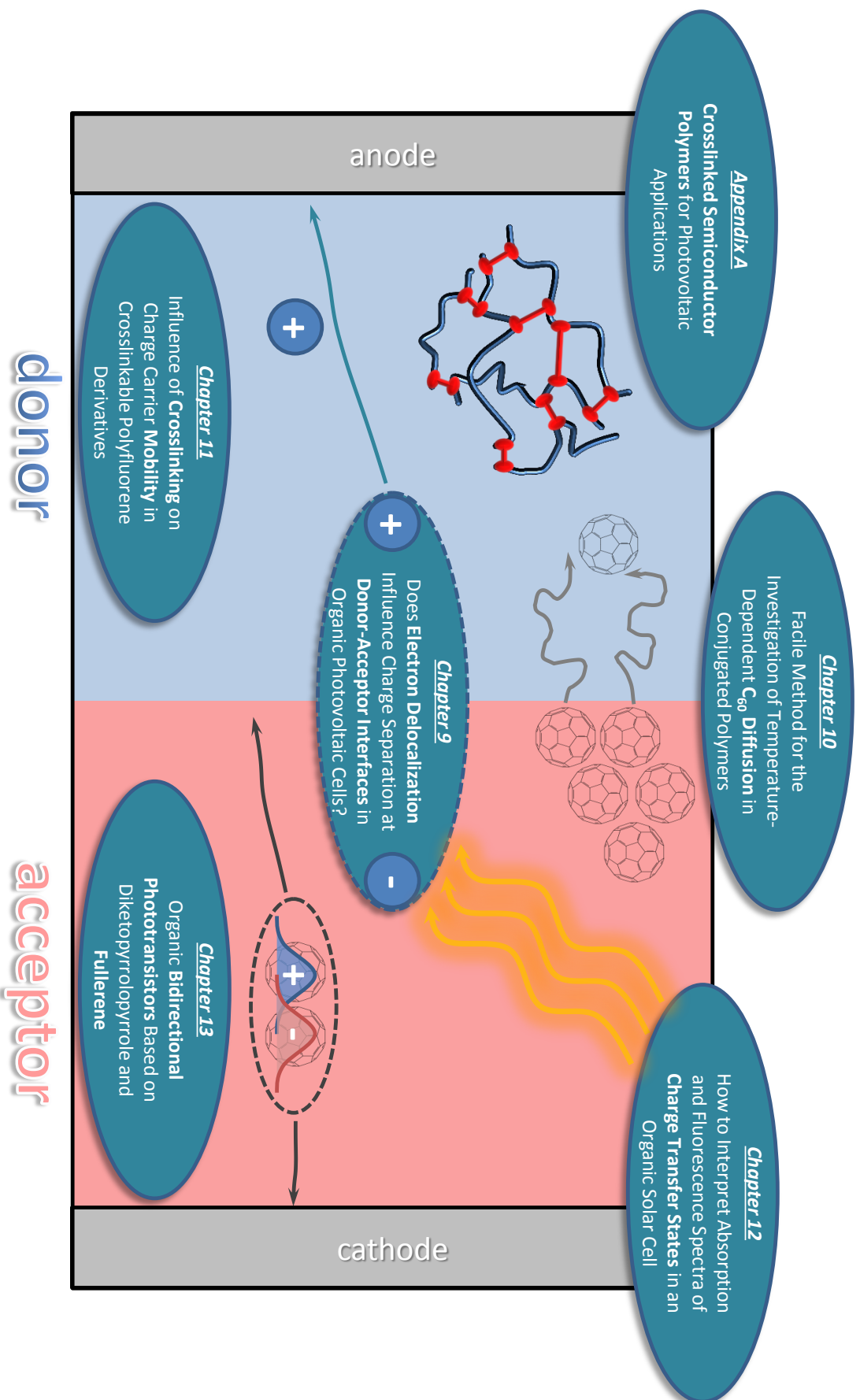


Figure 8.1.: Schematic overview over the relation between the publications in this thesis and which processes in an organic solar cell they address.

8.2. Contents of the individual publications

The following subsections provide detailed summaries of the publications that emerged in the course of my PhD project about dissociation, recombination and the character of charge transfer states in organic solar cells. A special focus will be laid on the significance of the respective results for the research on organic solar cells. The figures and captions presented here are reprinted or adapted from the respective publications (see part II). These were reprinted with permission of the respective publisher.

8.2.1. Does Electron Delocalization Influence Charge Separation at Donor-Acceptor Interfaces in Organic Photovoltaic Cells?

As detailed in chapter 3.1 there is currently a hot debate about what factors and mechanisms actually contribute substantially to the efficient dissociation of CT states in optimized and well-performing organic solar cell systems, with disorder, entropy and delocalization being promising candidates. The study presented here is devoted to the delocalization aspect and lays the focus on the controversially discussed role of electron delocalization on the charge separation process at D/A interfaces. Some works readily attribute an observed enhancement in the device efficiency to electron delocalization as a result of the presence of crystalline C_{60} domains or even merely aggregated phases of the more amorphous PCBM.^{131,171,174} Others in turn directly question the positive role of delocalization in general.¹⁷⁵ Here, I address this issue by studying CT-characteristics and dissociation in organic solar cells using a bilayer architecture. It consists of a crosslinked derivative of the well-known, well-performing amorphous donor polymer PCDTBT (PCDTBTOx, see chapter 7) and a series of three different fullerene acceptors (C_{60} , PCBM, ICBA) with increasing number of additional covalent bonds added to the C_{60} core. The respective structure impacts on the packing and crystallinity of the acceptor molecules (cf. chapter 5) and thus should change the degree of intermolecular coupling and delocalization in the acceptor phase.^{32,173,365} This is also reflected in electron mobility measured in the bulk.³² The use of a bilayer structure with a crosslinked donor layer has the advantage of providing a well-defined interface due to efficiently reduced diffusion.³¹⁵ This in turn effectively reduces morphology related aspects like non-geminate recombination, percolation problems or a distribution of acceptor domain sizes which otherwise would superimpose interface-related effects. Accordingly, theoretical modelling of interface-related processes such as CT dissociation is easier and more straightforward. Finally, the use of an amorphous polymer as a donor ensures that its energy levels are unlikely to change when different acceptors are deposited on top,¹³⁵ rendering the donor layer a good and stable reference. Consequently, observed changes in device properties may be assigned to the different acceptors.

In essence, the role of electron delocalization on CT dissociation is inferred from the analysis of photocurrent spectra and theoretical modelling of field dependent IV-data. For a profound interpretation and a proper analysis I first had to verify our expectations concerning the structure of the acceptor phase and the coupling between the molecules. Structural information are obtained from GIWAXS experiments. As expected, no indication of order is found for the PCDTBTOx donor proving the assumption of a purely amorphous layer. There is no distinct preferential orientation for any of the fullerenes, yet the amount of ordered domains clearly decreases in the sequence $C_{60} \rightarrow PCBM \rightarrow ICBA$, while the average intermolecular distance

increases in the same order. These observations imply a reduction in the intermolecular coupling strength in the same series, because electronic coupling between neighbouring fullerene molecules decreases exponentially with increasing distance.^{32,173,377–379} The trend in coupling strength is further confirmed by the consistent increase in electron mobility from ICBA $\left(10^{-5} \frac{\text{cm}^2}{\text{Vs}}\right)$ ³⁸⁰ over PCBM $\left(2 \cdot 10^{-3} \frac{\text{cm}^2}{\text{Vs}}\right)$ ^{380,381} to C₆₀ $\left(5 \cdot 10^{-2} \frac{\text{cm}^2}{\text{Vs}}\right)$ ²⁵⁵, a higher autoionization efficiency for C₆₀ in relation to PCBM (cf. chapter 5),⁴⁶ and the presence of extended CT states in the bulk of C₆₀²⁵⁸ that are much more localized in PCBM and ICBA as evidenced from additional electroabsorption measurements.

In addition to this I conducted UPS, IPES and Kelvin-Probe measurements to gain insight into the energy levels as well as interface energetics in the investigated systems, which are needed as input for our theoretical simulation. As expected, EA and IE values increase in the series $ICBA > PCBM > C_{60}$.^{382–384} From the work function shifts inferred from Kelvin-Probe measurements we basically find vacuum level alignment at the D/A interface for C₆₀ as acceptor, while ground state interfacial dipoles are present for PCBM and ICBA. These dipoles affect the dissociation efficiency at the interface and have to be taken into account when modelling the dissociation probability according to the effective mass model (cf. chapter 3.2)

To gain insight into the charge generation process at the D/A interface, photocurrent spectroscopy was performed under short circuit conditions on bilayer organic solar cells (figure 8.2(a), exemplary for PCDTBTOx/C₆₀). For a qualitative idea which of the components in the device contributes to the photocurrent at which energy, the absorption profiles of each layer were calculated according to the transfer matrix algorithm (dashed lines) to account for parasitic absorption and reflections.⁵⁰ This additionally allowed us to calculate the IQE (figure 8.2 (b)). Qualitative aspects are the same in case of all three fullerenes both in EQE and IQE (figures 8.2 (b) and (c)): Photocurrents decrease in the series $C_{60} > PCBM > ICBA$, the donor itself hardly contributes and the acceptors show some degree of autoionization above an excitation energy of 2.25 eV.^{46,258} Consequently, the signal below 2.25 eV is due to dissociation at the D/A interface as neat materials show no considerable photocurrent in this region.

An important factor in the context of CT dissociation efficiency is CT recombination. To assess this aspect, intensity dependent JV-measurements were carried out. These yielded fill factor (FF) values that are independent of irradiation intensity over three orders of magnitude up to $7 \frac{\text{mW}}{\text{cm}^2}$ irrespective of the excitation energy proving that only geminate recombination is present.⁷⁵ Notably, the FF values are the same for C₆₀ and PCBM indicating similar recombination rates in both cases. With the observed trend in IQE this implies a higher dissociation rate for C₆₀, as $IQE = \frac{k_{diss}}{k_{diss} + k_{rec}}$. The overall smaller FF (as well as considerably reduced EQE/IQE) for ICBA is related to inefficient exciton and charge transport in ICBA giving rise to enhanced geminate recombination (cf. chapter 4).^{32,83} Nevertheless, no s-shaped J-V-characteristics are observed in this case as hole and electron mobilities are rather balanced for PCDTBTOx and ICBA.⁸³ In general, all IV-characteristics show no s-shape indicating no extraction or injection problems. This further implies that imbalanced mobilities in the case of PCDTBTOx/C₆₀ and PCDTBTOx/PCBM do not play a role here, especially because I accounted for this aspect by using a thickness ratio of 1:2 for donor to acceptor layer, a small absolute donor thickness of only 14 nm and appropriate transport layers at the electrodes.^{75,86}

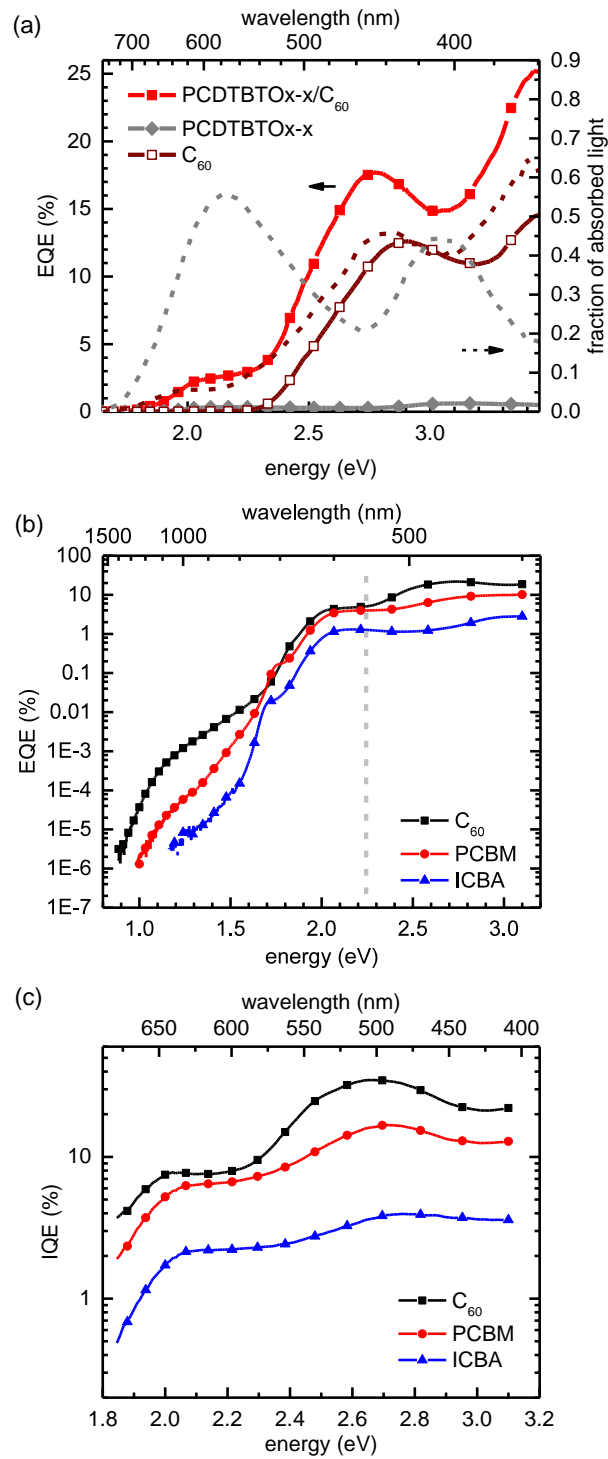


Figure 8.2.: (a) Left axis: EQE of a PCDTBTO_x/C₆₀ bilayer solar cell (red filled squares) and single layer devices with PCDTBTO_x (grey filled diamonds) or C₆₀ (dark red open squares). Right axis: Calculated fraction of absorbed light of PCDTBTO_x and C₆₀ in a bilayer solar cell (dashed lines). (b) Comparison of EQE for bilayer devices with C₆₀ (black squares), PCBM (red dots) or ICBA (blue triangles) as acceptor. The grey dashed line marks the autoionization threshold in fullerenes. (c) IQE for the bilayer devices in (b). The displayed range is limited by the literature values of the refractive index n and the extinction coefficient k used for the calculation of the absorption.

To finally assess the origin of different dissociation efficiencies in devices with C_{60} and $PCBM$, IV-data that are converted to field dependent EQE (figure 8.3 (a)) are analysed in terms of the effective mass model under consideration of the presence of interfacial dipoles (cf. chapter 3.2)^{162,163} as obtained from Kelvin-Probe measurements. A preliminary qualitative measure of the ease of dissociation that may be directly derived from the experimental data is the so called saturation field strength F_{sat} , at which basically all generated CT excitons are split (figure 8.3 (b)).¹⁶² As expected from the results obtained so far, F_{sat} increases in the order $C_{60} < PCBM < ICBA$. Now taking the interfacial dipoles inferred from Kelvin-Probe measurements into account as well as the literature values for the electron mobilities and a typical lifetime in the order of several tens of ns,^{162,186,255,380,381,385–387} the simulations according to the effective mass model eventually yield effective masses m_{eff} that are a factor of about three larger for PCBM than for C_{60} . In this context it is noteworthy that the experimental data could only be reproduced physically meaningful with a reasonable mobility and lifetime when differences in the effective mass m_{eff} are explicitly considered. This indicates that CT delocalization to certain degree contributes to the observed differences in dissociation probability. As the donor is the same in both cases, this difference has to be related to electron delocalization in the acceptor phase. Furthermore, this analysis implies that the high local order of C_{60} is an important ingredient for the realization of coherent delocalization in the acceptor phase, in accordance with the findings of Bernardo et al.¹³¹ This effect is less pronounced for the more disordered $PCBM$, which is reflected in a higher effective mass that implies a more incoherent coupling and more localized CT states. The latter aspect is especially true for ICBA as evidenced by a low electron mobility and weak inter-molecular coupling.³²

In previous work by Schwarz et al. it had been shown that the effective mass strongly depends on hole delocalization along the conjugated segments of polymer chains.¹⁶² In that study several different polymers of different stiffness and thus effective conjugation length — among others PCDTBT — were also investigated in a bilayer configuration in combination with C_{60} . Gratifyingly, I find the effective mass of the combination PCDTBTOx/ C_{60} obtained from my analysis to be consistent with the results of Schwarz et al. Notably, I still found a change in the effective mass when replacing C_{60} with $PCBM$. This indicates that electron delocalization to a certain degree also contributes to the effective mass associated with the CT state, although a significant part of it will surely be determined by the hole delocalization along the polymer backbone as evidenced by Schwarz et al. At this point it should be emphasized again that the effective mass of a CT state involves contributions from both hole and electron. The important message inferred from the comparison of the three different fullerenes C_{60} , $PCBM$ and $ICBA$ is that high local order in organic solar cells plays a crucial role to allow efficient dissociation of charge transfer states, because wavefunction delocalisation of the electron within such ordered aggregates may significantly contribute to this process. This is also an important notification for the newly emerged non-fullerene acceptors, which are actually prone to aggregate in an ordered way.^{3,18}

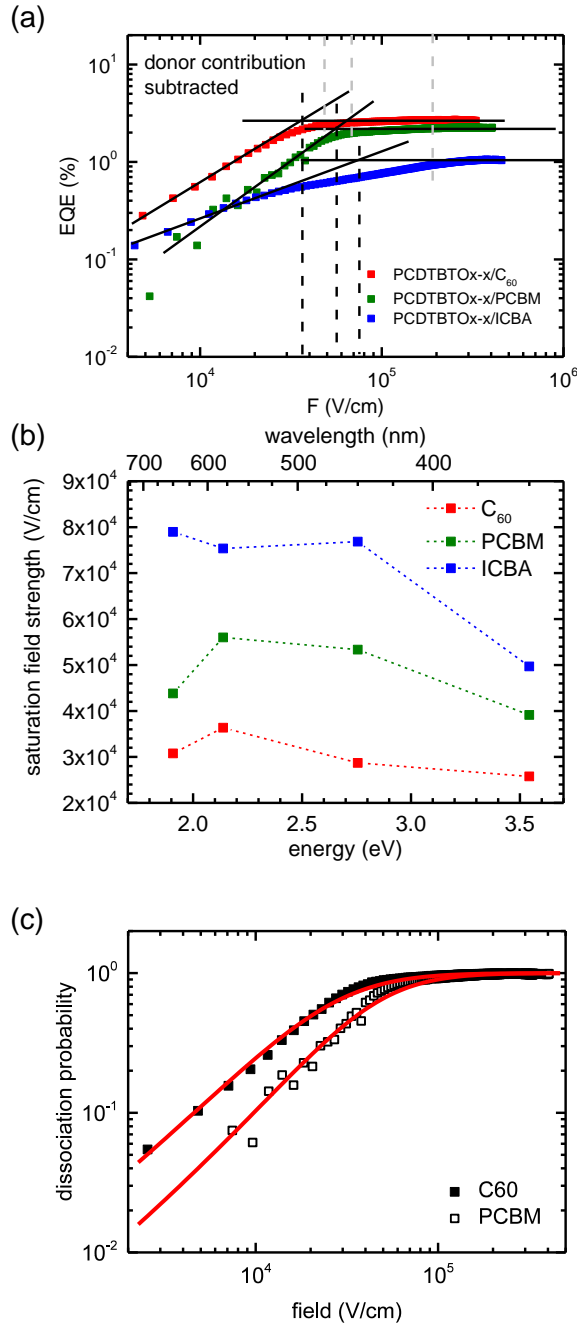


Figure 8.3.: (a) EQE of bilayer devices with C₆₀ (red squares), PCBM (green circles) or ICBA (blue triangles) as acceptors as function of the internal electric field for an excitation energy of 2.14 eV. The data were corrected for an intrinsic contribution from CT dissociation within the donor. F_{Sat} is given as the intersection of the tangents to the low and high field regime, respectively (black dashed lines) or alternatively as the value where the dissociation probability reached 90% of the saturation value. (b) F_{Sat} as function of excitation energy for C₆₀ (red squares), PCBM (green circles) or ICBA (blue triangles). (c) CT dissociation probability for PCDTBTO x /C₆₀ (filled squares) and PCDTBTO x /PCBM (open squares) bilayer devices as function of the internal electric field. Solid red lines are fits according to the effective mass model including interfacial dipoles. Details about the parameters used in the simulation are given in chapter 9.

8.2.2. Facile Method for the Investigation of Temperature-Dependent C_{60} Diffusion in Conjugated Polymers

In this work, we present an all-optical, spectrally versatile approach to measure the diffusion of small quencher molecules in the presence of a matrix material such as a polymer as a function of sample temperature. In our case, the diffusing species is the widely used acceptor molecule C_{60} . After verifying the reliability of the results using a previously studied model system based on PF2/6³¹⁵, the method is eventually applied to a series of three derivatives of the well-known low bandgap polymer PCDTBT, which is frequently used in efficient organic solar cells in combination with PCBM.^{274,313,314} The investigated compounds slightly differ in their structure regarding the sequence of the building blocks (alternating vs. statistical) and their sidechains (additional hexyl spacers) as well as in their molecular weight resulting in a variation of glass transition temperature T_g . T_g is an important quantity with respect to the morphological stability of organic electronic devices^{319,325}, as it governs the mobility of the polymer backbone.²⁸⁵ This in turn determines the degree of intermixing of donor and acceptor or, equivalently, matrix and dopant via interdiffusion and is especially relevant to interfaces in bilayer or multilayer architectures like they are used for example in OLED devices.^{319,328} In terms of application, the degree of intermixing determines the efficiency of charge generation as well as recombination, so studying the temperature dependence of diffusion with respect to T_g can provide valuable guidance for device processing procedures, e.g. with respect to annealing times and temperatures. In addition, one may gain deeper insight into the underlying microscopic processes governing the diffusion process in a PCDTBT-based polymer matrix from that temperature dependence as well as the associated activation energies. In this context, particularly the question of how the side chains and the local motions mediated by them impact on the diffusion process is addressed by studying diffusion below the glass transition temperature T_g (cf. chapter 6).

The methodology of the approach is based on the earlier work of Fischer et al.³¹⁵ where photoluminescence (PL) quenching was used to monitor diffusion in a vertical three-layer architecture. The diffusing (quencher) species is deposited on top of one half of the material of interest, which again rests on an additional fluorescing sensor layer. The arrival of the diffusing molecules after increasing the sample temperature is then detected via luminescence quenching of the sensor. In practice, the mean arrival time is derived from the onset of fluorescence quenching as compared to a reference beam illuminating the sample half where no quenchers are present. Consequently, the measuring principle is inspired by the time-of-flight technique. The use of a two beam layout consisting of sample and reference beam additionally allows to correct for temperature induced changes during the measurement. In the corresponding study, C_{60} diffusion was investigated as a function of crosslinking density of the polymer matrix (PF2/6 with different amounts of crosslinkable acrylate units) and found to be thermally activated and drastically reduced with increasing degree of crosslinking. This result provided a clear guideline towards a stabilization of bulk heterojunction morphologies in organic solar cells (cf. also appendix A). Unfortunately, this approach is not applicable to the more application relevant low bandgap polymers, because the sensor luminescence has to be considerably red-shifted compared to the investigated polymer to allow selective detection.

To account for the latter limitation, I developed a modified approach applying only two layers,

where the investigated polymer simultaneously takes the role of the sensor itself. A schematic of the sample geometry is shown in the top panel of fig. 8.4(a). As before, only a part of the investigated polymer layer is covered with the diffusing quencher molecule and a two beam measurement geometry is applied to account for temperature induced fluctuations of the photoluminescence signal (fig. 8.4(a), bottom). Upon temperature increase, the diffusion of C_{60} molecules is activated (or enhanced) and a new equilibrium concentration is established after a certain amount of time (fig. 8.4(b)). This results in a dynamic decrease of the PL ratio $PL_{C_{60}}/PL_0$, where $PL_{C_{60}}$ is the PL intensity of the C_{60} -covered half and PL_0 is the reference intensity (fig. 8.4(c)), until the final quenching level corresponding to the equilibrium concentration at the respective end temperature is reached.

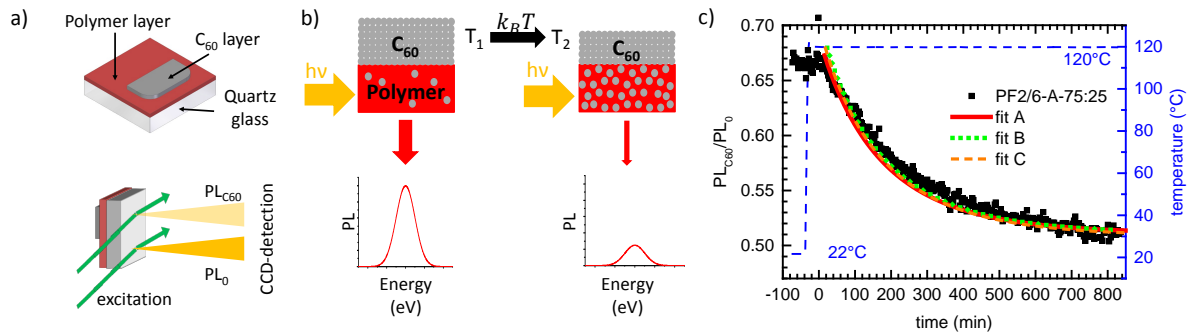


Figure 8.4.: (a) Schematic of the sample architecture (top) and the measurement geometry (bottom). (b) Principle of the measurement. The temperature activated diffusion of C_{60} molecules induces a dynamic reduction of the detected photoluminescence until a (new) temperature dependent equilibrium concentration is reached. (c) Exemplary time-dependent decrease of the relative PL intensity, $PL_{C_{60}}/PL_0$ (left axis). The investigated material was PF2/6-A-75:25. The right axis displays the temperature increase in the cryostat. The solid red line and the green dotted lines correspond to fits assuming different initial concentration profiles.

In contrast to the three-layer technique, it is not the arrival time that is derived from the experiment, but the dynamic photoluminescence decay due to diffusion of quencher molecules and the establishment of a new equilibrium concentration in the investigated material itself. This decay is then fitted using a theoretical model that connects the dynamic evolution of the quencher concentration with the concomitant quenching of the relative PL. It assumes purely Fickian diffusion, which is a reasonable assumption considering the minimum timescales of the experiment are in the order of minutes.³⁸⁸ In the simplest case, the model assumes a homogenous initial concentration of quencher molecules within the polymer matrix that is assigned to the equilibrium at room temperature (fit A in fig. 8.4(c)). Yet, in many cases when a second layer is deposited on top of another layer of material, the interface will not be ideal but a concentration gradient will likely prevail.^{327,389} For this reason, I slightly modified the fitting procedure to obtain an estimate for the initial concentration gradient (fit B in fig. 8.4(c)). In this case, the initial condition for the experiment is approximated from an iterative, self-consistent fitting procedure: The diffusion is simulated under the assumption that there is no quenching at a certain time $t < 0$ s corresponding to the situation right before the deposition of C_{60} . The simulated decay curve is then adjusted to fit the experimentally observed decay at later times. The concentration profile at the time $t = 0$ s, where the simulated quenching is equal to the

quenching level observed in the experiment before the temperature increase is then used as approximation for the initial concentration gradient caused by deposition of C_{60} . Finally, I slightly extended this self-consistent approach to account for a finite exciton diffusion length and the concomitant quenching at the polymer/ C_{60} interface even if it were an ideal interface by considering an additional quenching "channel" (fit C in fig. 8.4(c)).

For a first test of the model and the evaluation of the applicability and reliability of the approach I chose a crosslinkable model system that has already been investigated by Fischer et al. (PF2/6-A-75:25).³¹⁵ The variations between the diffusion coefficients derived from the three different initial conditions mentioned above vary by at most 20 %, meaning that the respective initial condition only has a minor impact on the extracted diffusion coefficient. Yet, the obtained concentration profile at early times may differ more or less significantly from the actual profile and should be considered with care. Nonetheless, they get increasingly reliable at later time ($> 1-2$ min) and few nm away from the interface. Moreover, the final equilibrium concentration that emerges at a certain temperature is well-defined as long as the relation between quencher concentration and PL quenching is properly calibrated. This calibration can be obtained from static quenching experiments to determine the Stern-Volmer constant¹ for the investigated system.

Satisfyingly, we also find an Arrhenius-type temperature dependence of the diffusion coefficient with the same activation energy as reported by Fischer et al for the respective polymer. The absolute values systematically deviate by a factor of 2-3 (fig. 8.5(a)). This difference could arise from the different protocols from which the diffusion coefficient is derived. Consistent with the expectation for a crosslinked polymer, the final equilibrium concentration of C_{60} is very low in the range of 0.2 – 0.5 wt %.

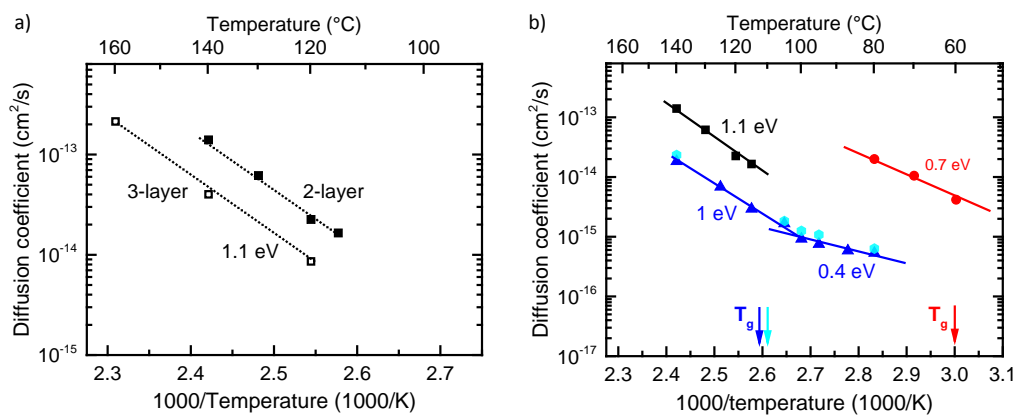


Figure 8.5.: Arrhenius representation of the temperature dependence of the diffusion coefficient. (a) Comparison for crosslinked PF2/6-A-75:25 measured in a three-layer architecture (open squares) and a two-layer architecture (filled squares). The slope, yielding the activation energy of diffusion is indicated by dotted lines. (b) PF2/6-A-75:25 (black squares), as well as PCDTBT (blue filled triangles), PCDHTBT (red filled circles) and PCDTBTstat (light blue filled hexagons) measured using the two-layer approach. The solid lines provide a guide to the eye, and colored arrows indicate the respective T_g .

¹ The Stern-Volmer constant is a measure of the relative PL reduction due to the presence of a certain concentration of quencher molecules.³⁹⁰

Having verified the reliability of the approach, I then applied the method to a series of three derivatives of the well-known and technologically relevant low-bandgap polymer PCDTBT (PCDTBT, PCDTBT_{stat}, PCDHTBT). PCDTBT is an efficient polymer system that is frequently used in organic photovoltaics in together with fullerenes resulting in long-term stable devices with estimated lifetimes of up to 7 years while still maintaining an efficiency of about 4.5%.^{274,313,314} As already mentioned in the first paragraph, the PCDTBT derivatives slightly differ in their structure and molecular weight and concomitantly their glass transition temperature T_g . While PCDTBT and PCDTBT_{stat} feature similar side chains, molecular weight and T_g , PCDHTBT has some additional hexyl spacer chains and a lower molecular weight, both resulting in a lower T_g . The results of the temperature dependent measurement of the diffusion coefficient D are summarized in fig. 8.5(b).

The fact that the two similar polymers show basically the same temperature dependence of the diffusion coefficient as well as similar activation energies is another proof for the appropriateness of the new approach. Overall, the order of the absolute values of $D(T_g)$ ($\approx 5 \times 10^{-15} \frac{\text{cm}^2}{\text{Vs}}$) is consistent with the diffusivities for small amounts of about 1 wt % of a diffusing quencher or dopant molecule in a polymer matrix. Under these conditions, also activation energies of $0.7 \pm 0.3 \text{ eV/molecule}$ are in line with literature.^{31,263,301,316,320} Interestingly, we find that diffusion still continues well below T_g and that D does not decrease drastically for $T < T_g$. As already discussed in chapter 6 one would usually expect the diffusion coefficient to reduce rapidly when approaching the glass transition temperature from higher temperatures according to the Stokes-Einstein relation (6.7), because of a considerable increase in the viscosity η of the matrix polymer, as long as η can be described in terms of a Vogel-Fulcher-Tammann equation (6.6) (or equivalently a Williams-Landel-Ferry law^{288,368}) and C_{60} diffusion is governed by the dynamics of free volume (see chapter 6). Instead, we rather observe an Arrhenius-type dependence, i.e. thermally activated diffusion both above and below T_g , yet with different activation energies. Below T_g the activation energy is considerably smaller than above T_g . Although, diffusion behaviour deviating from the Stokes-Einstein-relation with a Vogel-Fulcher-Tammann-type temperature dependence of viscosity has already been observed earlier in polymer matrices, the actual microscopic origin of this is not clear yet and still subject to research (see chapter 6)

In our interpretation, the temperature dependence of C_{60} diffusion in the investigated systems is not a direct reflection of collective motion of the glass elements but rather of local and simply activated motion mediated by the side chains of the polymer. The latter are still mobile below T_g and feature another transition temperature at way lower temperatures that are typically below the temperature range I investigated here (see chapter 6).^{285,291}

In conclusion, this publication introduced a facile and versatile approach to measure diffusion of small molecules in a polymer matrix by sole optical means. With this technique, it is possible to obtain not only the temperature dependent diffusion coefficient, but also dynamic information about the approximate evolution of the concentration profile inside the sample as well as the equilibrium concentration at a certain temperature. These data are useful as a guidance for material design and device engineering, e.g. when choosing appropriate annealing times and temperatures and might even prove helpful when thinking of morphological long-term stability under operating conditions, although other factors like degradation or thermal decomposition also play a major role in this issue.³⁶⁹

The method is particularly easy from a processing point of view, because it only requires a

simple bilayer structure, and can be adopted to a wide range of matrices and dopant/quencher molecules, as long as the matrix is luminescent and the diffusing molecules can act as quenchers. Applying this approach to different carbazole-based polymer matrices, I finally gained mechanistic insight into the role of the sidechains in the diffusion process, especially in the vicinity of T_g and even well below T_g in these systems.

8.2.3. Influence of Crosslinking on Charge Carrier Mobility in Crosslinkable Polyfluorene Derivatives

In the course of research regarding the long-term stability of morphology and efficiency of organic electronic devices crosslinking has been suggested as a means to stabilize blend morphologies in organic solar cells. Furthermore, it may be used to suppress interdiffusion of molecules from an adjacent layer in multilayer structures like they are commonly used in OLEDs both in the lab as well as in commercially available ones.^{312,315,341,391–396} In context of the latter application, crosslinking has been shown to effectively reduce diffusion³¹⁵ and being able to stabilize doping in transport or blocking layers under certain conditions^{345,397} and also prevent unintentional doping of adjacent layers.^{315,398} This possibility makes the approach also very interesting for the use in the recently evolved field of perovskite solar cells, where unintentional doping of the perovskite from the doped hole transport layer results in severe stability and degradation problems, that could be overcome by crosslinking the transport layer.^{399,400}

The general impact of crosslinking on the overall efficiency of organic devices has been addressed in the course of several studies dealing with crosslinking approaches applicable to organic solar cells.^{35,36,312,329–332,341,401–407} Observed differences were mainly attributed to morphological changes induced upon crosslinking. As charge carrier mobility is a key parameter for device performance (cf. chapter 4) and as such very sensitive to defects and charge carrier traps that might be introduced as a result of network formation, I investigated how crosslinking impacts on the charge carrier mobility in the respective layer. This aspect has been hardly addressed before and then only in case of OFETs and (liquid) crystalline materials.^{408,409} For a systematic investigation of the influence of crosslinking on mobility, I studied a series of five PF2/6 derivatives with different fractions of crosslinkable acrylate groups attached to the side chains. This has the advantage that the backbone of the polymer remains largely unaffected resulting in very similar electronic structure of all derivatives. Moreover, due to its bulky side chains, PF2/6 does not feature a crystalline phase^{410,411} thereby avoiding additional complication by possible morphological differences arising from sample processing. Since PF2/6 is typically applied as a hole transporting material, the investigations were focused on the measurement of hole mobilities. To gain insight into the character of possible traps and defects, the measurements were performed at both low and high charge carrier densities. In the former case, I used quite novel MIS-CELIV technique to selectively determine the hole mobility, in the latter case p-type OFETs were fabricated and measured. In the course of this work I also addressed the influence of adding further substances to the system that may be needed to activate the crosslinking process. This is of fundamental importance since residues of the initiators could act as electronic traps for charge carrier transport and are a major concern when considering crosslinkable layers or materials in an optoelectronic device.^{24,35,337,339,412} Here, I used two different photoinitiators, a purely organic one (IC651) as well as another one containing a heavy metal (IC784) in amounts of 0.1 wt% and 1.0 wt%

In the first place I carried out spectroscopic measurements, in order to get an idea about structural or morphological peculiarities of the PF2/6 derivatives themselves, which could then be correlated to trends observed in the mobility measurements. From the absorption spectra I got insight into the morphological similarities and differences of the compounds in the electronic

ground state.⁴¹³ In addition to films, I also investigated dilute solution spectra, as they are characteristic of the respective compound as it is and there is no additional influence of processing like it could happen in films. The spectra are unstructured and we find an increasing FWHM for PF2/6 with up to 50 % acrylate content that decreases again for higher contents (figures 8.6(a) [top] and (b) [top]). An according trend is also observed for the peak positions. They shift to the blue up to an acrylate content of 50 % and back to the red again for higher contents.

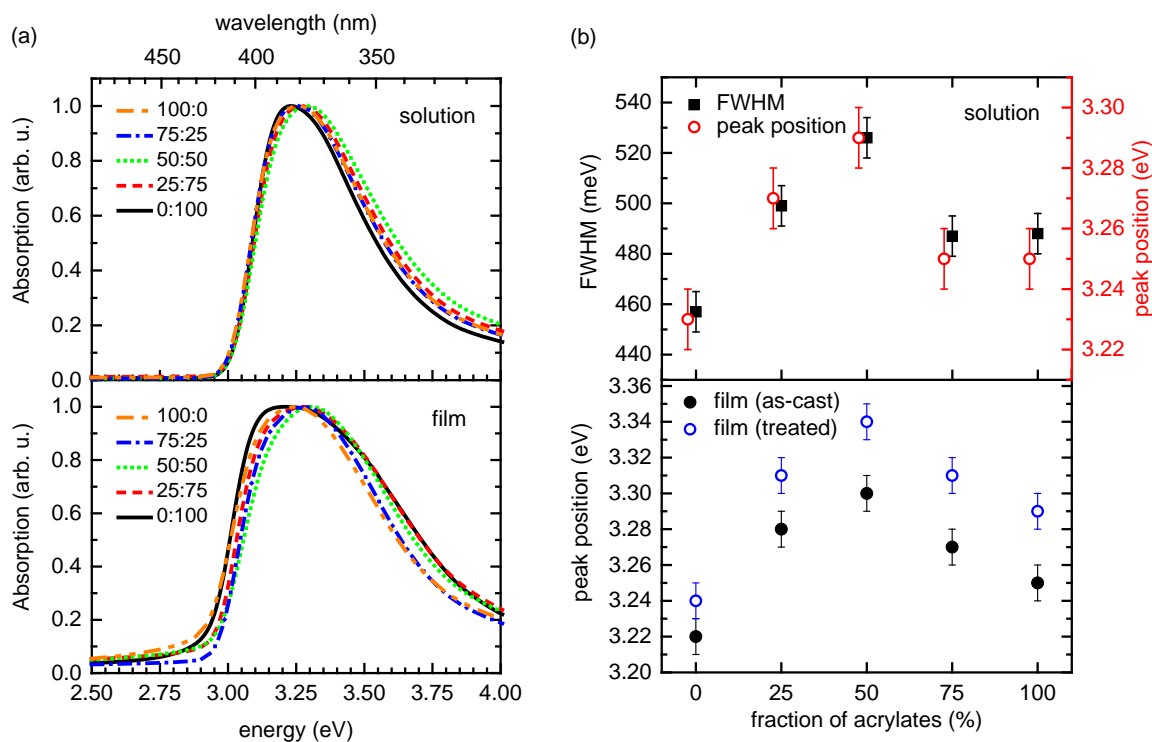


Figure 8.6.: (a) Absorption spectra of crosslinkable PF2/6 derivatives with different ratios ($n:m$) of acrylate containing repeat units (n) to unmodified fluorene repeat units (m) for dilute solutions (top) (0.017 mg/ml) and as-cast films (bottom). (b) top: FWHM (black squares) and peak positions (red circles) of dilute solution spectra as a function of acrylate content. bottom: Peak positions of as-cast (black filled circles) and thermally treated (red open circles) films without curing agent as a function of acrylate content.

The mentioned lack of structure in the absorption spectra applies to both dilute solution and thin films (figure 8.6(a)). It can be assigned to a distribution of conjugation lengths and the concomitant disorder due to torsions in the polymer backbone.^{410,413–415} The same trend of peak shifts that were observed for dilute solution spectra are also present in the absorption spectra of as-cast thin polymer films as well as crosslinked films irrespective of the applied photoinitiator or its amount (figure 8.6(b), bottom). In the latter case of crosslinked films, the spectra are only slightly broader and blue shifted compared to as-cast ones. This points to a small increase in disorder due to more torsions of the polymer backbone and accordingly a higher percentage of shorter chromophores induced by the crosslinking. Interestingly, I found that crosslinking of the films does not necessarily require the addition of another curing agent and can be achieved by mere thermal activation in combination with UV/VIS-illumination ($\lambda > 350$ nm), which is an advantage for a potential (commercial) application in optoelectronic devices. For details on the crosslinking process the reader is referred to the actual publication (chapter 11) or the short

excursus on crosslinking in chapter 7.

As the observed trend in peak position is correlated with the evolution of polydispersity of the compounds I additionally checked GPC data. Yet, I found no indication of significant differences in low molecular weight contributions, i.e. short chains which could account for blue shifted peak positions.^{414,416} Therefore, the differences observed in FWHM and peak positions are indeed of structural origin and intrinsic to the respective derivatives, irrespective of the treatment. Remarkably, the properties of the respective compounds are preserved in the film as well.

In order to gain a first insight into the defects that may be either present in the different compounds or introduced by sample processing, it is worth considering photoluminescence (PL) spectra and the even more sensitive photoluminescence quantum yield (PLQE). This is especially true for a film, where energy transfer to a defect site can readily occur via exciton diffusion. No changes of the spectral shape irrespective of the treatment and the acrylate content in the used PF2/6 derivative are observable, meaning that no additional emissive defects are induced upon crosslinking no matter which photoinitiator is applied. Yet, energy transfer could of course also take place to quenching sites thereby increasing the rate of non-emissive decay. This can be identified from absolute measurements of the PL in an integrating sphere, i.e. PLQE-measurements (figure 8.7). In accordance with literature we find $24 \pm 3\%$,^{415,417,418} which is only reduced when using the Ti-containing photoinitiator (IC784). This means that residual molecules or decomposition products of the latter compound act as quenching sites for singlet excitons enhancing the nonradiative decay rate. Consequently, curing agents containing heavy metals like Ti are not suitable for the use in optoelectronic devices.

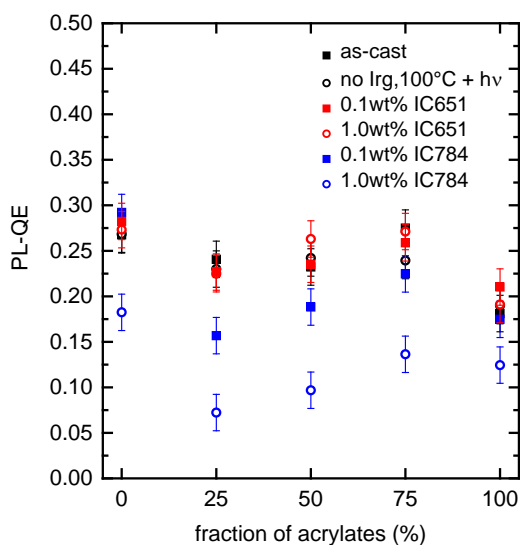


Figure 8.7.: *PL-QE as a function of the fraction of acrylate containing repeat units for different sample treatments.*

After the preparatory spectroscopic work I finally investigated the influence of the presence of additional functional groups, the addition of further curing agents and the crosslinking process itself on the hole transporting properties of PF2/6. Insight into the character of the traps and defects identified from spectroscopy can be gained from mobility measurements in the low to intermediate and the high carrier density regime. In the former case, I used MIS-CELIV.

In this approach, charge carriers are first selectively injected into the device and subsequently accumulated at an additional interface between the organic semiconductor and an insulating layer. This extractable charge reservoir is then depleted by applying a voltage ramp and mobility can be determined from the resulting current response. More details about the underlying principle of the MIS-CELIV measurement are given in chapters 4 and 11 as well as in references [85, 230]. Experimental conditions were chosen to be the same for all devices and compounds, so differences can be attributed to intrinsic properties of the respective compound or changes due to processing.

No significant difference between as-cast samples and crosslinked ones is observable when either no or only a small amount of organic initiator (IC651) is used (figure 8.8(a)). However, mobility reduces with increasing fraction of crosslinkable acrylate groups from about $2 \cdot 10^{-5} \frac{\text{cm}^2}{\text{Vs}}$ to $2 - 4 \cdot 10^{-6} \frac{\text{cm}^2}{\text{Vs}}$, even when no crosslinking is performed (dashed grey arrow in figure 8.8(a)). Finally, for larger amounts of initiator and especially when applying the Ti-complex IC784, mobility is drastically reduced, irrespective of acrylate content (figure 8.8(b)). In the case of high charge carrier densities determined from OFET measurements, the same decrease of mobility with increasing acrylate content is observed, yet no dependence on the treatment and the processing of the sample (figure 8.8(c)).

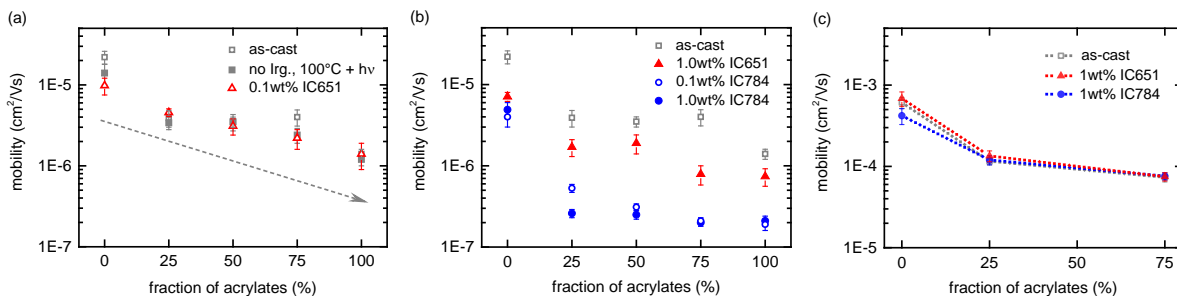


Figure 8.8.: (a) Hole mobility as a function of the fraction of acrylate containing repeat units for different sample treatments, that is, as cast without photoinitiator (open squares), crosslinked without photoinitiator (full grey squares), and crosslinked with 0.1 wt% of organic photoinitiator (IC651, red open triangles) determined via MIS-CELIV. The grey dotted arrow indicates the mobility trend for increasing acrylate content. (b) Mobility of samples for different treatments, that is, as cast without photoinitiator (open squares) for reference, crosslinked with 1.0 wt% of organic photoinitiator (IC651, red open triangles) and crosslinked with 0.1 or 1.0 wt% of metalorganic photoinitiator (IC784, blue circles). (c) OFET saturation mobility for selected PF2/6 derivatives without photoinitiator and crosslinking (as cast), crosslinked with 1 wt% organic photoinitiator (IC651) and crosslinked with 1 wt% metalorganic photoinitiator (IC784).

From these observations we find that the crosslinking process itself does not negatively influence mobility though our spectroscopic investigations have shown that disorder slightly increases upon network formation. Apparently, disorder is already sufficiently large in non-crosslinked films, meaning that a small increase does not further affect charge transport (see chapter 4) in these amorphous systems. Nevertheless, an intrinsic difference between the compounds induced by the addition of acrylate groups can still be seen: Changes in the microstructure due to chain torsions and possibly concomitant decreased coupling efficiency for charge transport between different chain segments result in a decrease of hole mobility with increasing acrylate content for both low and high charge carrier densities. Concerning traps induced by adding photoinitiator to the polymer I can conclude that traps are deeper for the metalorganic compound (IC784)

than for the purely organic one (IC651), because only larger amounts of organic IC651 reduce mobility while any addition of IC784 leads to a deterioration. Yet, additional traps induced by a curing agent are filled at high carrier densities, so that no difference to the pure polymer compounds prevails.

From this work, we learn that under optimized conditions crosslinking does not alter hole mobility in PF2/6, i.e. an amorphous polymer system. Yet, due to conformational changes upon introduction of acrylate groups in the polymer side chains mobility may be reduced by up to one order of magnitude. So in essence, one has to find a suitable compromise between mobility reduction (up to one order of magnitude) and morphological stabilization (up to three orders of magnitude reduction of diffusion³¹⁵). But as not necessarily 100% of crosslinkable groups are needed to achieve a densely linked stabilizing network (cf. also appendix A),^{23,329-333,359} a smaller fraction may be readily chosen to minimize negative effects on mobility. In all cases, special care has to be taken when choosing the crosslinking conditions whenever an application in optoelectronic devices is desired. With the possibility of mere thermal activation under UV/VIS-illumination, the network formation and concomitant stabilization via acrylate groups is a promising candidate in this respect, at least for multilayer processing (cf. chapter 7).

8.2.4. How to Interpret Absorption and Fluorescence Spectra of Charge Transfer States in an Organic Solar Cell

As detailed in chapters 2 and 3, (interfacial) charge transfer states and especially their dissociation play a crucial role in the photogeneration process of charges in organic solar cells. For this reason, it is important to understand the properties of these states and how their formation and behaviour can be properly described. A way to experimentally assess these aspects is to perform absorption and emission spectroscopy on CT states, yet the correct framework to extract reliable parameters characterizing these states is still under debate. The most important quantities in this respect are the CT energy E_{CT} , the reorganization energy λ related to the formation of the CT state and, as organic semiconductors are disordered systems, especially the energetic disorder σ associated with the DOS of the CT states. Nevertheless, the role of disorder in the analysis of CT spectra has often been neglected or was only regarded to be of minor importance as discussed in chapter 3.1.

In this work, I aimed for the identification of the suitable framework to analyse CT photoluminescence (PL) and EQE spectra of donor-acceptor blend solar cells with particular focus on the aspect of energetic disorder. Commonly, the well-known work by Vandewal et al on the relation between open-circuit voltage and interfacial molecular properties in BHJ solar cells is used as basis for the determination of CT and reorganization energies in organic solar cells from EQE and EL measurements.¹⁵⁷ The fits (equations (3.5) and (3.6) in chapter 3.1) to extract these quantities from the spectra are based on Marcus-type expressions which are inspired by the work of Gould et al. on radiative and non-radiative electron transfer in radical-ion pairs.¹⁵⁶ Yet, disorder is not explicitly included in this framework. Notably, in one of their latest works, Vandewal et al even claimed that the spectral shape of a CT transition is governed by the reorganization energy of the donor, that this energy is mainly related to intra-molecular vibrations and that static disorder is only of minor importance.¹⁴⁶

In view of this, I specifically intend to answer three conceptual questions here: i) Are the commonly used Marcus-type expressions appropriate to describe CT spectra and derive reliable characteristic quantities from them? ii) Is the neglect of disorder in this context acceptable? iii) What is the origin of the reorganization energy λ that is associated with the CT transition?

To address these issues, we carried out time resolved temperature dependent PL spectroscopy (5 – 295 K), temperature dependent EQE measurements (50 – 295 K), as well as Electroluminescence spectroscopy on 1:1 MeLPPP:PCBM blends (ratio by weight) and analysed the corresponding spectra in the framework of Marcus theory,^{144,156,157}

$$rEQE(E) = EQE(E) \cdot E \propto \frac{1}{\sqrt{4\pi\lambda k_B T}} \cdot \exp \left[-\frac{(E_{CT} - E + \lambda)^2}{4\lambda k_B T} \right] \quad (8.1)$$

$$rEL(E) = \frac{EL(E)}{E} \propto \frac{1}{\sqrt{4\pi\lambda k_B T}} \cdot \exp \left[-\frac{(E_{CT} - E - \lambda)^2}{4\lambda k_B T} \right] \quad (8.2)$$

the extended Marcus-Levich-Jortner (MLJ) model both with and without taking static disorder σ into account,^{145,151}

$$rEQE(E) = EQE(E) \cdot E \propto \sum_{n=0}^{\infty} \left[\frac{e^{-S} S^n}{n!} \cdot \exp \left(-\frac{(E_{CT} - E + \lambda_{low} + n\hbar\omega)^2}{4\lambda_{low}k_B T + 2\sigma^2} \right) \right] \quad (8.3)$$

$$rPL(E) = \frac{PL(E)}{E} \propto \sum_{n=0}^{\infty} \left[\frac{e^{-S} S^n}{n!} \cdot \exp \left(-\frac{(E_{CT} - E - \lambda_{low} - n\hbar\omega)^2}{4\lambda_{low}k_B T + 2\sigma^2} \right) \right] \quad (8.4)$$

as well as a modification of the common Franck-Condon expressions used in spectroscopy^{39,419}

$$rEQE(E) = EQE(E) \cdot E \propto \sum_{m_i} \prod_i \frac{S_i^{m_i} e^{-S_i}}{m_i!} \cdot \Gamma \cdot \delta \left[E - \left(E_0 + \sum_i m_i \hbar\omega_i \right) \right] \quad (8.5)$$

$$rPL(E) = \frac{PL(E)}{E} \propto \sum_{m_i} \prod_i \frac{S_i^{m_i} e^{-S_i}}{m_i!} \cdot \Gamma \cdot \delta \left[E - \left(E_0 - \sum_i m_i \hbar\omega_i \right) \right] \quad (8.6)$$

which explicitly consider inhomogeneous broadening usually in form of Gaussian linewidth function $\Gamma = \exp\left(-\frac{E^2}{2\sigma^2}\right)$ as well as a Poisson-distribution of high-energy vibrational modes. In all of these expressions we considered the electronic transition moment \tilde{M} to be energy dependent.¹⁵⁶ $rEQE$, rEL , and rPL are commonly referred to as *reduced* EQE, EL, and PL spectra.^{144,156} E is the photon energy, T the temperature S the Huang-Rhys-parameter and E_0 the 0-0 energy of the optical transition. Finally, $\hbar\omega$ are the vibrational quanta of frequency ω and $\lambda = \lambda_{low} + \lambda_{high} = S_{low} \cdot \hbar\omega_{low} + S_{high} \cdot \hbar\omega_{high}$ denotes the total reorganization energy consisting of the contributions of low (ω_{low}) and high (ω_{high}) frequencies. In the framework of Marcus' theory (equations (3.5) and (8.2)), all the vibrations are treated classically, assuming $k_B T \gg \hbar\omega$. In contrast to that, MLJ theory in the form of equations (8.3) and (8.4) assumes that $\hbar\omega_{low} \ll k_B T \ll \hbar\omega$, meaning that high frequency modes may still be treated classically, while the quantum mechanical nature of low frequency modes is explicitly taken into account.¹⁴⁵ Experimentally we find evidence that the spectral line shape of the CT spectra has to contain a contribution of inhomogeneous broadening due to the presence of a Gaussian DOS of the CT states. First, we do not observe a monoexponential but a power law decay of the CT emission band featuring an exponent very close to $-\frac{3}{2}$ and extending into the μs range (figure 8.9(a),(b)). According to the works by Hong and Noolandi this indicates geminate recombination with a broad distribution of recombination rates.^{420,421} As the rates depend exponentially on the intrapair distance this in turn implies the presence of an energetic distribution of the corresponding CT states. A second indication of a Gaussian DOS of the CT states and the importance to consider disorder is given by an observed red-shift of the EL with respect to the PL (figure 8.9(c),(d)).

In general, a photogenerated exciton or separate charge carriers may execute a random walk in an inhomogeneously broadened distribution of states thereby relaxing inside the DOS. This process is known as *spectral diffusion*.⁴³ In the case of EL, injected charge carriers recombine after a long path through the organic material giving rise to the possibility of significant energetic relaxation. In the case of PL on the other hand, photoexcitation generates a bound and thus correlated e-h-pair. This in combination with a low energy transfer rate due to the low transition dipole moment and the small overlap integral typically accompanying a CT transition results in only small spectral diffusion before recombination. In addition, this reasoning implies that the Stokes shift between absorption and EL emission contains a component of spectral relaxation.⁴²²⁻⁴²⁴

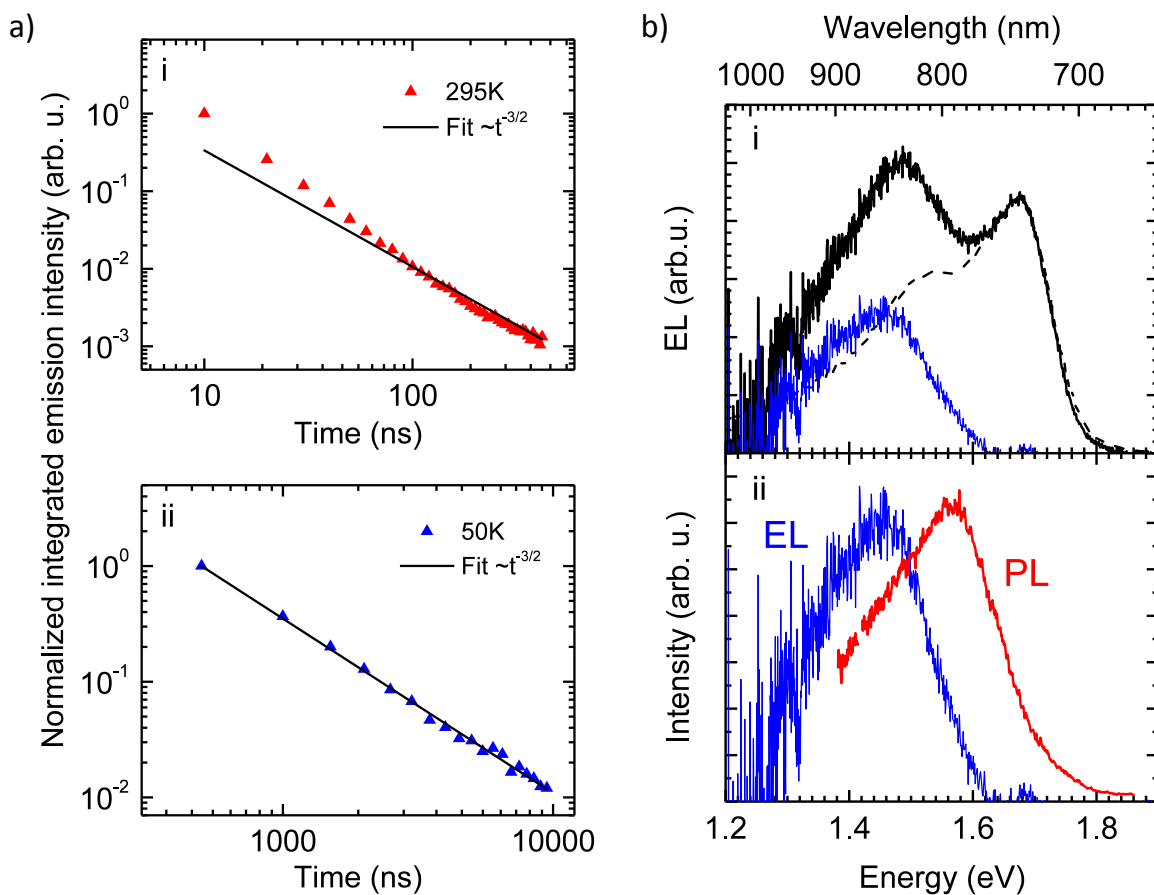


Figure 8.9.: (a) Normalized emission intensity measured at (i) 295 K and (ii) 50 K. Solid lines indicate fits according to a $t^{-3/2}$ power law. (b,i) EL spectra of MeLPPP:PCBM (1:1 by weight, black solid line) and pristine PCBM (black dashed line). The difference of the two spectra corresponds to the CT emission (blue solid line). EL spectra of PCBM were reprinted with permission from *J. Am. Chem. Soc.*, 2009, **131**(33), 11819–11824 Copyright (2009) American Chemical Society. (ii) Room temperature EL (blue) and PL (red) CT spectra of MeLPPP:PCBM (1:1 by weight).

Having confirmed that an inhomogeneously broadened DOS of CT states is present we show that the CT spectra may be convincingly analysed using a Franck-Condon progression as given by equations (8.5) and (8.6). Conceptually, in this picture absorption and fluorescence spectra are modelled to be vibronic progressions of high-frequency intramolecular modes built on the resonant 0-0 transition energy as long as $S \leq 1$. In a solid (or liquid) environment, polarizability effects introduce a bathochromic shift in both absorption and emission as well as additional inhomogeneous broadening if the surrounding medium of a chromophore is disordered.³⁹ Furthermore, in a solid, coupling of the excited (CT) state to phonons, i.e. low-frequency modes due to interaction with the environment, results in the appearance of low-frequency phonon wings for each vibronic (high-frequency) transition. These wings are characterized by an individual Poisson distribution with $S = S_{low}$. For Huang-Rhys parameters $S_{low} \geq 2$ a Stokes shift between absorption and emission occurs and the distribution is rather Gaussian than Poisson-type.⁴²⁵ The first exemplary analysis in this framework is performed on low temperature spectra (90 K) to reduce the effect of thermal broadening and facilitate spectral deconvolution of the CT feature from the PCBM singlet located at 1.76 eV.¹²¹ This is especially true for the EQE (figure 8.10),

where a narrowing of the PCBM singlet transition and a more pronounced CT feature is observed at lower temperature. An accompanying reduction of the absolute EQE with decreasing temperature is attributed to reduced mobility resulting in less effective charge extraction,^{75,178,426} as dissociation of geminate pairs in *MeLPPP/C₆₀* had been shown to be only slightly dependent on temperature.¹⁶³

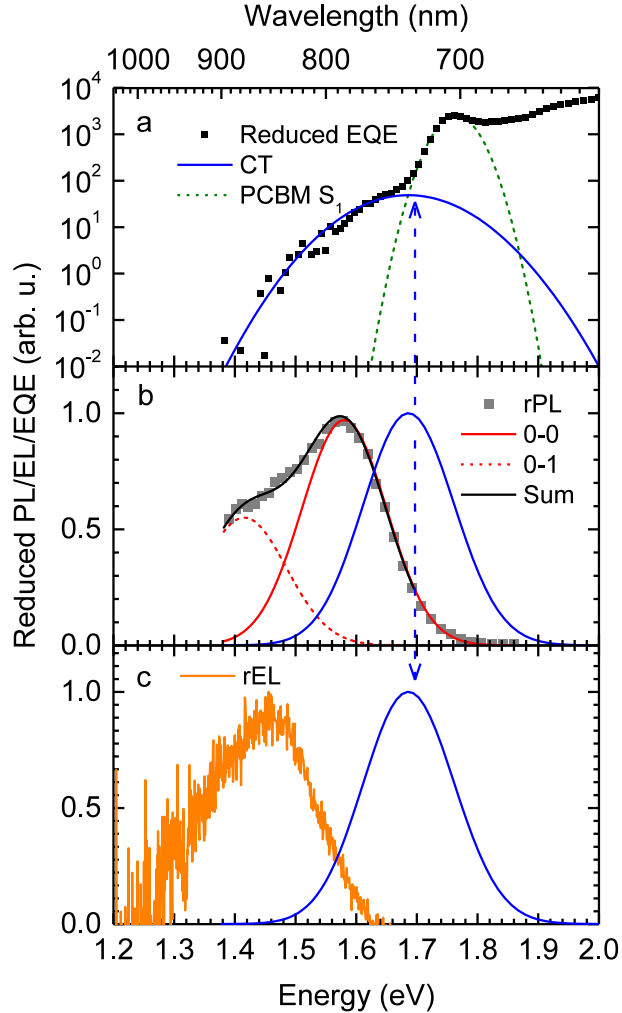


Figure 8.10.: (a) *rEQE* spectrum measured at 100 K (black squares). The CT state at 1.61 eV (blue solid line) is fitted according to the Franck-Condon approach, the PCBM singlet state (S_1) at 1.75 eV (green dashed line) is modelled with a Gaussian. (b) *rPL* measured at 90 K (grey squares) and fitted with a Franck-Condon progression (black solid line). The 0-0 transition and 0-1 vibronic peak are indicated by red solid and dashed lines, respectively. (c) *rEL* spectrum (orange line) along with the Franck-Condon fit (blue line) to the *rEQE* to further illustrate the red shift of *rEL* with respect to *rPL*.

In order to explicitly disentangle the contributions from inhomogeneous line broadening and low-frequency modes, we first focused only on the 0-0 peak without taking vibrational overtones into account (solid lines in figure 8.10(b)). Simultaneously fitting the high energy part of the PL spectrum and the low energy part of the EQE, gives sufficient confinement to determine CT energy E_{CT} (1.62 eV) and disorder parameter σ (67 meV) as well as the reorganization energies λ associated with absorption (60 meV) and emission (40 meV), which we expected to differ because

of a stronger bonding in the excited state due to a more ionic character. This was indeed the case. The sum of both reorganization energies is consistent with the observed Stokes shift (100 meV) between absorption and PL, meaning that it predominantly arises due to intermolecular, low-frequency modes. In order to additionally account for the observed first vibrational overtone in rPL, we considered further, (effective) high-frequency mode. Using the obtained parameter set, shifting the rPL fit by this high frequency mode to lower energies, weighting with a new Huang-Rhys-parameter S_{high} and finally adding both the original and the shifted fit an excellent match of the model to the experimental data could be obtained (figure 8.10(b)) Mathematically this is of course equivalent to directly considering two modes (a high and a low frequency one) in equations (8.5) and (8.6).⁴¹⁹

Consistent with the experimental observations of a power law decay of CT emission and the presence of an energy shift between PL and EL we also get an inhomogeneously broadened DOS from our Franck-Condon analysis. Moreover, the derived energy difference between CT states and PCBM singlet of about 150 meV makes the occurrence of TADF possible and indeed, we experimentally observe PCBM photoluminescence even after 30 ns at 295 K. The presence of this additional thermally activated non-radiative decay channel for CT states is further evidenced by an increase in CT emission with decreasing temperature.

Having shown, that a consistent description and analysis of CT spectra is possible using the Franck-Condon model, we finally address the issue of the appropriateness of the commonly used Marcus formalism especially by additionally considering the temperature dependence observed experimentally and predicted by the respective model. In the widely used approach by Vandewal et al. CT related parameters are extracted from rEQE and rEL spectra (equations (8.1) and (8.2)).¹⁵⁷ Yet, with the observed shift between rEL and rPL, this would imply a different reorganization energy λ depending on which emission is considered, which is unphysical. More strikingly, with decreasing temperature, the Marcus-type expression predicts a significant line narrowing which is not observed experimentally so that the temperature dependent spectra cannot be fitted with a consistent parameter set (figure 8.11). In addition to this, the observation of a power law decay and a red-shifted EL as compared to PL points to the inappropriateness of the assumption of a single absorber. The latter assumption was also addressed by Burke et al.⁴²⁷ In their work they pointed out that the parameters extracted from a Gaussian fit to temperature dependent rEQE and rEL measurements (E_{CT}^{exp} , λ^{exp}) have to be modified by $E_{CT}^{exp} = E_{CT} - \frac{\sigma^2}{2k_B T}$ and $\lambda^{exp} = \lambda + \frac{\sigma^2}{2k_B T}$ to account for static disorder in the system. This approach effectively results in a similar expression as the modified MLJ-fit (equations (8.3) and (8.4)), yet without explicit consideration of vibrational intermolecular low-frequency modes.

Considering the extended MLJ framework, the temperature dependent spectra can be equally well fitted consistently as with the Franck-Condon approach as long as disorder is taken into account (figure 8.12). The large degree of disorder makes it impossible to distinguish between the two fits. This again points to the important contribution of static disorder to the spectral line shape of the CT transition and that the requirements of a fully classical treatment of high- and low-frequency modes are not fulfilled. Given that typical low and high frequency modes in organics are in the range of 1 – 10 meV and 50 – 300 meV, respectively, the intermediate case that $\hbar\omega_{low} \ll k_B T \ll \hbar\omega$ for which equations (8.3) and (8.4) are derived is valid at room temperature. In the case of low temperatures, i.e. $k_B T \ll \hbar\omega_{low}$, the MLJ expression under consideration of disorder even converges to the same form as the Franck-Condon progression (equations (8.5) and (8.6))

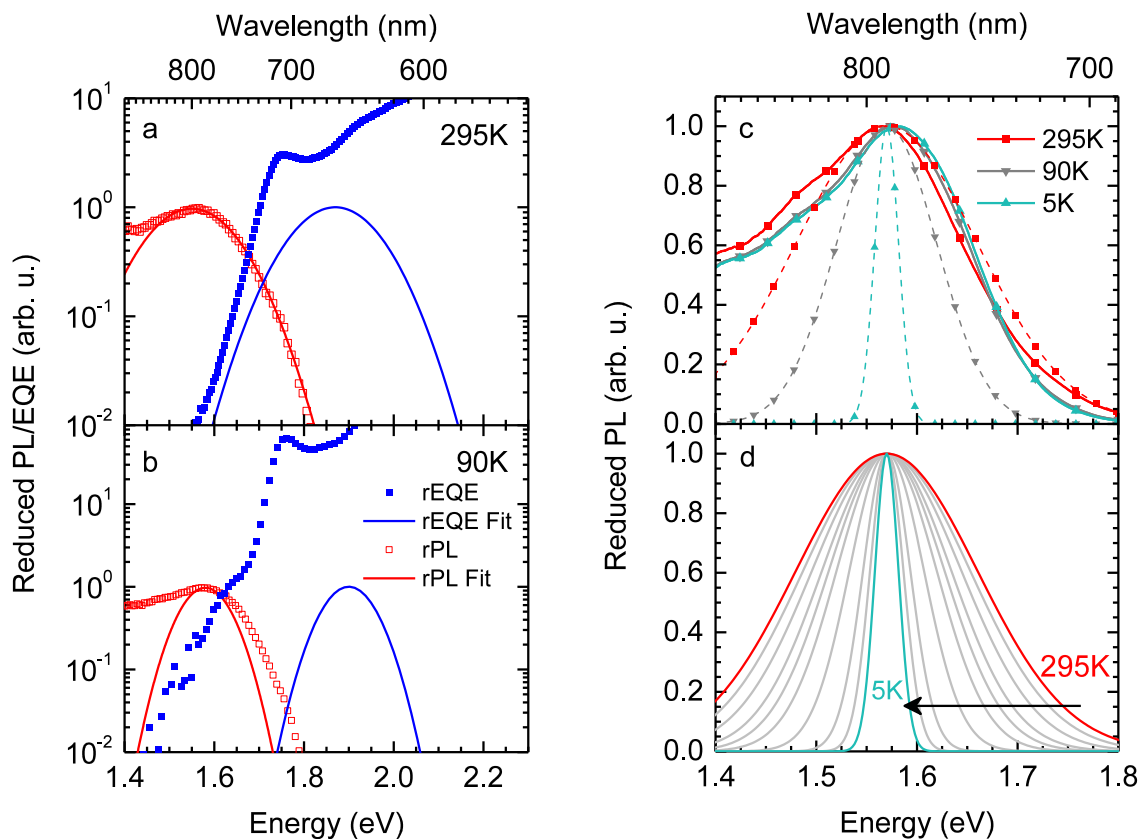


Figure 8.11.: *rPL* and *rEQE* measured at (a) 295 K and (b) 90 K (squares). The red solid lines corresponds to a fit according to equation (8.2), i.e. the simple Marcus-type expression. For comparison, the corresponding theoretically expected curve for the *rEQE* is also given (blue solid line, equation (8.1)). The fitting parameters for λ are the same for both temperatures. (c) Comparison of experimental *rPL* spectra (solid lines) with calculated line shapes (dashed lines) according to the Marcus framework (equations (8.1) and (8.2)) at 295 K, 90 K and 5 K. (d) Calculated narrowing of the line width as expected from Marcus theory when reducing temperature from 295 K to 5 K.

In conclusion, with this work it could be shown that the Franck-Condon approach can describe line shape and temperature dependence of the CT spectra over the entire temperature range (5 – 300 K) consistently with one closed-form expression. This in turn indicates that electron transfer can be described by a tunneling process, which is in accordance with the idea that quantum mechanical tunneling between adjacent sites is more important in disordered, organic systems than thermally activated transfer,^{148–150} Again, this is in line with several works where no actual barrier for charge transfer is observed.^{63,115,135,152–155} We conclude that the modes contributing to the reorganization process in the course of charge transfer are predominantly of inter-molecular instead of intra-molecular origin as stated by Vandewal et al.,¹⁴⁶ so that a Stokes shift can actually be associated with low-frequency phonons. Apart from these low-frequency vibrations, disorder is an essential contributor determining the CT line shape. With all this in mind, values for λ , E_{CT} as well as the Stokes' shift inferred from the simple Marcus-type expression (equations 8.1 and 8.2) should be viewed with caution.

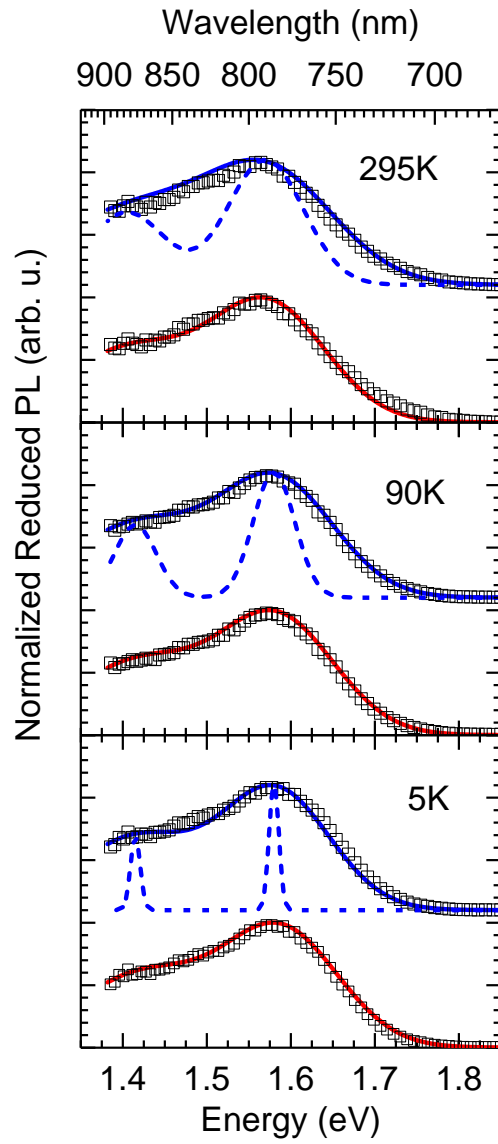


Figure 8.12.: Comparison of fits to the experimental spectra (open symbols) according to the Franck-Condon approach (red line) and the MLJ framework with (blue solid line) and without (blue dashed line) consideration of static disorder for 295 K, 90 K and 5 K.

8.2.5. Organic Bidirectional Phototransistors Based on Diketopyrrolopyrrole and Fullerene

In this work I demonstrate that a simple vertical D/A bilayer architecture is capable of featuring J-V-characteristics of a bidirectional organic phototransistor which may be switched by both electrical and optical means. The driving and switching voltages are in the order of 1 V. The microscopic origin for this behaviour is based on the good charge transport properties of the donor, a small DPP molecule (*Ph-TDPP-Ph*),³⁷⁰⁻³⁷⁵ and the efficient autoionization in the bulk of the acceptor C_{60} ⁴⁶ as well as its ability to transport both holes and electrons sufficiently well in this case (cf. chapter 5). Another important factor is the presence of an injection barrier to significantly reduce the dark current in the device. This behaviour is used to realize basic hybrid optical and electronic logic elements like NOT-, AND-, and OR-Gates with low driving voltage. Eventually, the corresponding set of logic operations is the basic requirement for the realization of advanced analog and digital applications. With this, the work demonstrates interesting applications of the light sensing ability of organic materials apart from the common use in standard organic solar cells.

An exemplary J-V characteristic of a ITO/MoO₃/Ph-TDPP-Ph/C₆₀/Al device under 1 sun illumination is shown in figure 8.13(a). Experimentally, I observe a very small current without illumination for devices with MoO₃ HTL and a pronounced photocurrent under forward bias. Due to these properties, the corresponding device can be regarded as a vertical asymmetric bidirectional phototransistor, because current flow is possible under forward and reverse bias and can be controlled via illumination of the device. The on/off ratio, i.e the difference between current under illumination and in the dark, is in the order of 10^5 (10^3) at -1 V ($+1$ V). Notably, due to the low dark current no corrections were needed to evaluate the photocurrent in forward direction correctly.⁸⁷ For monochromatic illumination above 2.25 eV I observe basically the same characteristic shape of the J-V curve as under sunlight conditions. Yet, when exciting below 2.25 eV the J-V characteristics feature a pronounced s-shape and very small current above V_{oc} (figure 8.13(b)). Consequently, the photocurrent is rather unidirectional under this condition. These observations indicate that the photosensitivity of the device is switchable via the applied voltage. This aspect becomes especially evident from EQE spectra as a function of bias (figure 8.13(c)) The photocurrent spectrum at $+1$ V resembles the spectrum of single layer C₆₀ devices and follows the absorption of C₆₀. This indicates that charge generation under these conditions is due to autoionization of CT states in the bulk of C₆₀ (cf. chapter 5).⁴⁶ At 0 V and -1 V an additional contribution appears at higher wavelengths in the region where Ph-TDPP-Ph absorbs (8.13(c)). As autoionization in neat Ph-TDPP-Ph is very weak (figure 8.13(d)), the additional photocurrent has to be due to CT dissociation at the D/A interface. This dissociation process is very efficient as evidenced from the presence of a well defined saturation. Good charge transport properties as well as possibly CT delocalization may be responsible for this.^{84,131,162,163,174,428,429} Due to the reproducibility of the samples, I could combine two devices in a back-to-back configuration to achieve symmetric characteristics under illumination with respect to the origin, and a current saturation plateau for voltages above ± 0.7 V, while the current is switched off in the dark. This results in a phototransistor like behaviour with an on/off ratio of 10^3 (figure 8.14(a)). As a first example of a logic gate, I used the tunability of the photosensitivity below 2.25 eV by the applied bias to realize a NOT-operation when the voltage is switched be-

tween 0 V (off state) and +1 V (on state) under constant illumination of a single device with monochromatic light in the region of 1.85 – 2.25 eV (figure 8.14(b)). Further applications that I successfully demonstrated in the work are AND- and OR-gates as well as a simple 4-bit analog output ADDER circuit (chapter 13). Consequently, the approach provides the full set of logic operations necessary to realize more complex analog and digital applications in future.

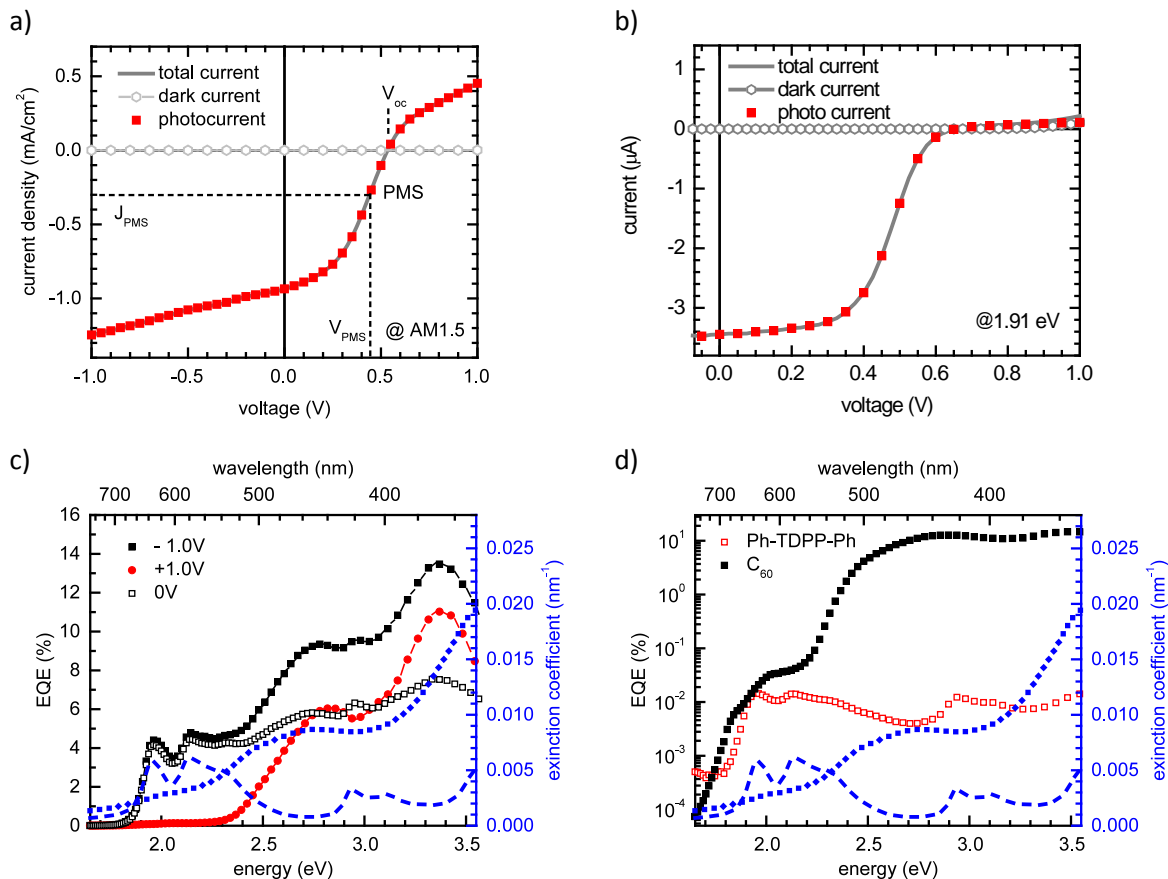


Figure 8.13.: (a) *J-V*-characteristic of a Ph-TDPP-Ph/C₆₀ bilayer device with a MoO₃ hole transport layer measured under AM1.5 conditions at 1 sun. (b) *I-V*-characteristic measured at $7 \frac{mW}{cm^2}$ and an excitation energy of 2.76 eV. The total current measured under illumination (grey solid line) is divided into its dark (light grey circles) and photocurrent contribution (red filled squares). EQE spectra of MoO₃/Ph-TDPP-Ph/C₆₀ devices as function of the applied voltage (left axis). Absorption spectra of the neat materials Ph-TDPP-Ph (dashed blue) and C₆₀ (solid line) (right axis). (c) EQE measured under short circuit conditions for Ph-TDPP-Ph and C₆₀ single layer devices (left axis). Absorption spectra of the neat materials Ph-TDPP-Ph (dashed blue) and C₆₀ (solid line) (right axis).

The details about the underlying mechanism behind the observed transistor behaviour are inferred from the analysis of photocurrent spectroscopy, intensity-dependent *J-V* measurements as well as energy level considerations with two different hole transport layers (HTL), MoO₃ and PEDOT:PSS.

When MoO₃ is replaced with PEDOT:PSS, the dark current is one to one and a half orders of magnitude higher. This indicates the presence of a considerable hole injection barrier in the case of an MoO₃ interlayer. It is further verified experimentally by the occurrence and characteristic intensity dependent evolution of an s-shape in the *J-V* characteristics measured

below 2.25 eV^{250,430} and explains the overall low dark current in the device. Furthermore, the analysis of the bias dependent EQE spectra revealed that (i) the photocurrent under forward bias is due to autoionization of charge transfer states in the bulk of C₆₀, (ii) Ph-TDPP-Ph does not feature any significant intrinsic photogeneration, and (iii) dissociation under reverse bias is efficient at the D/A interface, as further evidenced by a good saturation of J-V-characteristics recorded below 2.25 eV.

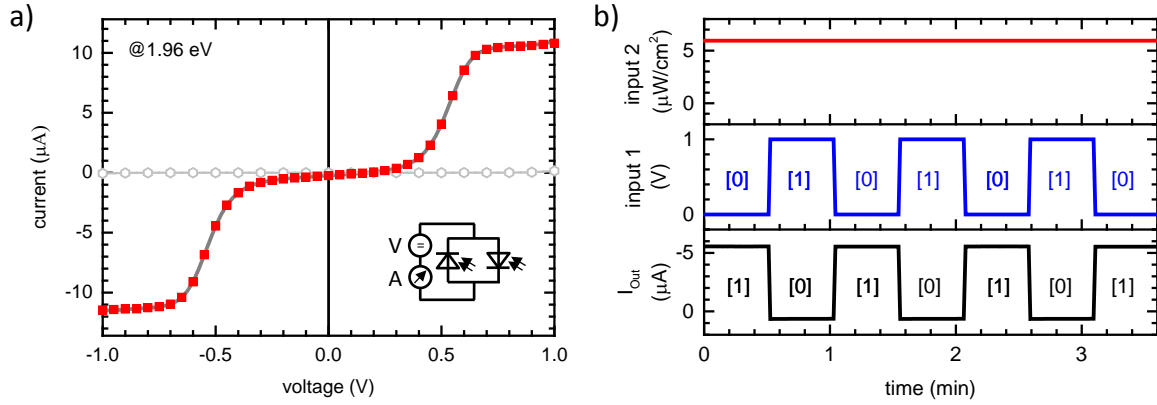


Figure 8.14.: (a) *J-V-characteristic of the back-to-back configuration of two Ph-TDPP-Ph/C₆₀ devices measured at an excitation energy of 1.96 eV ($\lambda = 632$ nm). The total current measured under illumination (grey solid line) is divided into its dark (light grey circles) and photocurrent contribution (red filled squares). A schematic circuit diagram is shown as inset. (b) Output current I_{Out} as a function of time for a NOT-Gate (black, bottom panel). The temporal course of the input voltage is displayed in blue (middle panel). The sample is constantly illuminated (red, top panel). Boolean states for input and output channels are indicated as binary numbers ([0]: off/low state, [1]: on/high state).*

In view of these results, the observed bidirectional behaviour can be explained in terms of a photoenhanced recombination current mediated by the autoionization of CT states and thus the photogeneration of charge carriers within the C₆₀ layer.^{87,88} Under reverse bias and excitation below 2.25 eV excitons are only generated in the donor (Ph-TDPP-Ph) and efficiently split at the D/A interface (figure 8.15 (a)). The generated charge then exit the device without encountering extraction barriers. At an excitation energy above 2.25 eV, the contribution from the autoionization in C₆₀ simply adds to the total photogenerated current. Under forward bias and excitation below 2.25 eV excitons generated in the donor can only be split via electron transfer to the ITO/MoO₃ electrode. The remaining holes feature an extraction barrier at the D/A interface and accumulate, thereby giving rise to a space charge, which additionally impedes extraction.^{86,429} This results in a very small photocurrent. When exciting above 2.25 eV, however, CT states are autoionized in the C₆₀ layer so that electrons can now recombine with the accumulated holes on the donor side of the D/A interface. The remaining holes in the C₆₀ layer can then drift to the Al electrode (figure 8.15). This mechanism results in an observable net photocurrent that is directly visible when the dark current is very small. To a certain extent, this mechanism resembles a tandem solar cell. In all cases, additional losses due to low or imbalanced mobilities⁴²⁹ are avoided due to good charge transport in both C₆₀^{255,256,381} and Ph-TDPP-Ph.⁴³¹

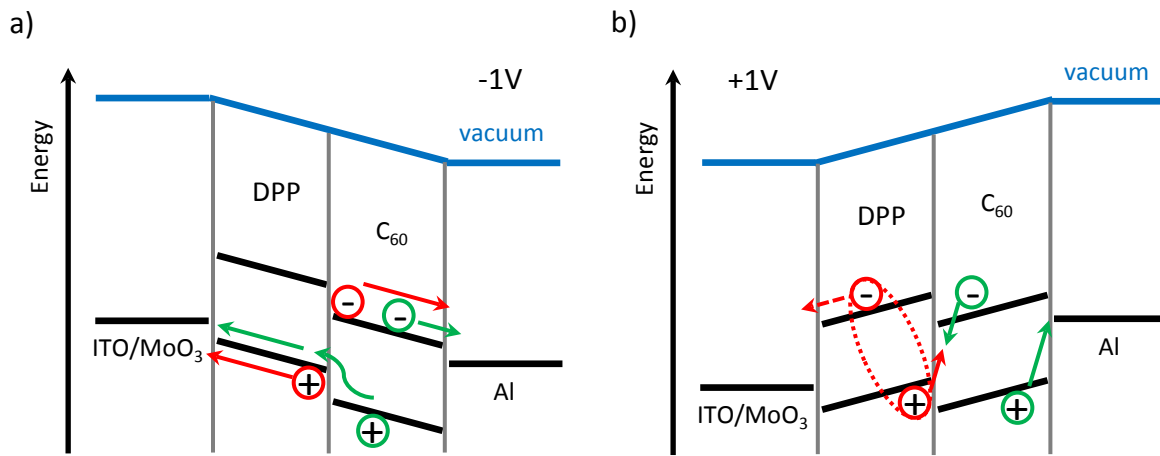


Figure 8.15.: a) Simplified energy level diagram for ITO/MoO₃/Ph-TDPP-Ph/C₆₀/Al devices under a) reverse bias and b) forward bias.

8.3. Author's contributions

The following publications form a part of this dissertation.

Does Electron Delocalization Influence Charge Separation at Donor-Acceptor Interfaces in Organic Photovoltaic Cells?

This publication is submitted to *The Journal of Physical Chemistry C* and reprinted in chapter 9. The authors are:

Frank-Julian Kahle, Christina Saller, Selina Olthof, Cheng Li, Jenny Lebert, Sebastian Weiß, Eva M. Herzig, Sven Hüttner, Klaus Meerholz, Peter Strohrriegl, and Anna Köhler

I prepared all the samples for the measurements performed in this study, conducted and analysed the photocurrent (EQE/IQE), J-V- and EL measurements and did the theoretical simulations according to the effective mass model as well as the optical modelling of the absorption spectra. Furthermore, I conducted and analysed the electroabsorption measurements on all three bilayer systems. Cheng Li measured the electroabsorption on the pure polymer and helped me with the initial interpretation of this measurement. Sven Hüttner provided the facility to measure electroabsorption. GIWAXS measurements were conducted by Jenny Lebert and Sebastian Weiß and analysed and interpreted by Eva M. Herzig. She also critically read and edited the GIWAXS part of the manuscript. Christina Saller synthesized and characterized the crosslinkable polymer PCDTBTOx and wrote the synthesis part of the manuscript. Selina Olthof measured UPS/IPES spectra and analysed and interpreted the data. Kelvin-Probe measurements were conducted and analysed by myself with the assistance of Selina Olthof. Klaus Meerholz provided the facility to measure UPS/IPES spectra and Kelvin-Probe. I finally evaluated and interpreted the full data set as a whole and wrote the manuscript. Peter Strohrriegl read and edited the synthesis part of the manuscript. Anna Köhler critically read and edited the whole manuscript and helped with the interpretation.

Facile Method for the Investigation of Temperature-Dependent C_{60} Diffusion in Conjugated Polymers

This work is published in *ACS Applied Materials and Interfaces* (*ACS Appl. Mater. Interfaces* **2018**, 10, 21499-21509) and reprinted in chapter 10. The authors are:

Christina Saller[‡], Frank-Julian Kahle[‡], Thomas Müller, Tobias Hahn, Steffen Tscheuschner, Denys Priadko, Peter Strohrriegl, Heinz Bässler, and Anna Köhler

[‡]Christina Saller and Frank-Julian Kahle contributed equally to this publication.

I prepared part of the samples, performed and analysed all the diffusion and spectroscopic calibration measurements, interpreted the data, extended the theoretical model and wrote the manuscript. Christina Saller synthesized and characterized (¹H-NMR, DSC, DMA, GPC) the three low bandgap polymers (*PCDTBT*, *PCDTBT_{stat}*, *PCDHTBT*), prepared some of the samples, helped with the diffusion measurement and wrote the synthesis part of the manuscript.

Thomas Müller originally developed the method and built the diffusion setup. Tobias Hahn supervised the thesis of Thomas Müller and helped with the development of the method and the design of the setup. Steffen Tscheuschner performed some initial calibration measurements and prepared some of the samples. Denys Priadko helped with the analysis of the data. Peter Strohriegl, Heinz Bässler and Anna Köhler critically read and edited the manuscript and helped with the interpretation.

Influence of Crosslinking on Charge Carrier Mobility in Crosslinkable Polyfluorene Derivatives

This work is published in the *Journal of Polymer Science, Part B: polymer physics (J. Polym. Sci. B Polym. Phys.* **2017**, *55*, 112-120) and reprinted in chapter 11. The authors are:

Frank-Julian Kahle, Irene Bauer, Peter Strohriegl, and Anna Köhler

I prepared the samples, performed, analysed and interpreted all measurements and wrote the manuscript. Irene Bauer synthesized the series of PF2/6 derivatives. Peter Strohriegl and Anna Köhler critically read and edited the manuscript and helped with the interpretation of the data.

How to Interpret Absorption and Fluorescence Spectra of Charge Transfer States in an Organic Solar Cell

This work is published in *Materials Horizons (Mater. Horiz.*, 2018, Advance Article, DOI: 10.1039/c8mh00564h) and reprinted in chapter 12. The authors are:

Frank-Julian Kahle, Alexander Rudnick, Heinz Bässler, and Anna Köhler

I prepared the samples for both spectroscopic measurements and solar cells, performed and analysed the solar cell measurements, interpreted the data, wrote part of the manuscript and critically revised the theoretical framework presented in the manuscript. Spectroscopic measurements were conducted together with Alexander Rudnick who also performed the fits and analysed the spectroscopic data. He also wrote part of the manuscript and interpreted the spectroscopic data together with me. Heinz Bässler and Anna Köhler wrote part of the manuscript and helped with the interpretation of the dataset.

Organic Bidirectional Phototransistors Based on Diketopyrrolopyrrole and Fullerene

This work is ready for submission. The draft of the manuscript is reprinted in chapter 13. The authors are:

Frank-Julian Kahle, Tobias Hahn, Tushita Mukhopadhyay, Boregowda Puttaraju, Satish Patil, and Anna Köhler

I prepared the samples, performed, analysed and interpreted all measurements and wrote the manuscript. Tobias Hahn helped with the interpretation. Tushita Mukhopadhyay and Boregowda Puttaraju synthesized the Ph-TDPP-Ph monomer and performed the CV measurements

to determine the energy levels of this compound. Satish Patil supervised the work of Tushita Mukhopadhyay and Boregowda Puttaraju and critically read the manuscript. Anna Köhler critically read and edited the manuscript.

8.4. Full list of Publications

Publications with major contributions (first author):

1. **Kahle, F.-J.**[†]; Saller, C.; Olthof, S.; Li, C.; Lebert, J.; Weiß, S., Herzig, E.M.; Hüttner, S.; Meerholz, K.; Strohrriegl, P.; Köhler, A. Does Electron Delocalization Influence Charge Separation at Donor-Acceptor Interfaces in Organic Photovoltaic Cells?. *J. Phys. Chem. C*, submitted. (chapter 9)
2. Saller[†], C.; **Kahle, F.-J.**[†]; Müller, T.; Hahn, T.; Tscheuschner, S.; Priadko, D.; Strohrriegl, P.; Bässler, H.; Köhler, A. Facile Method for the Investigation of Temperature-Dependent C_{60} Diffusion in Conjugated Polymers. *ACS Appl. Mater. Interfaces* **2018**, 10, 21499-21509. (chapter 10)
3. **Kahle, F.-J.**[†]; Bauer, I.; Strohrriegl, P.; Köhler, A. Influence of Crosslinking on Charge Carrier Mobility in Crosslinkable Polyfluorene Derivatives. *Journal of Polymer Science, Part B: Polymer Physics*, **2017**, 55, 112-120. (chapter 11)
4. **Kahle, F.-J.**[†]; Rudnick, A.; Bässler, H.; Köhler, A. How to Interpret Absorption and Fluorescence Spectra of Charge Transfer States in an Organic Solar Cell. *Mater. Horiz.*, **2018**, Advance Article, DOI: 10.1039/c8mh00564h. (chapter 12)
5. **Kahle, F.-J.**[†]; Hahn, T.; Mukhopadhyay, T.; Puttaraju, B.; Patil, S.; Köhler, A. Organic Bidirectional Phototransistors Based on Diketopyrrolopyrrole and Fullerene, prepared for submission. (chapter 13)
6. **Kahle, F.-J.**[†]; Saller, C.; Köhler, A.; Strohrriegl, P.; Crosslinked Semiconductor Polymers for Photovoltaic Applications. *Adv. Energy Mater.*, **2017**, 1700306. (appendix A)

Further publications with minor contribution:

7. Unger, T.[†]; Wedler, S.; **Kahle, F.-J.**; Scherf, U.; Bässler, H. Köhler, A. The Impact of Driving Force and Temperature on the Electron Transfer in Donor-Acceptor Blend Systems. *J. Phys. Chem. C*, **2017**, 121 (41), 22739-22752.
8. Mukhopadhyay, T.[†]; Puttaraju, B.; Roy, P.; Dasgupta, J.; Meyer, A.; Rudnick, A.; Tscheuschner, S.; **Kahle, F.-J.**, Köhler, A., Patil, S. Facile Synthesis and Chain-length Dependent Optical and Structural Properties of Diketopyrrolopyrrole-based Oligomers. *Chem. Eur. J.*, **2017**, 23, 13718-13723.
9. Hahn, T.[†]; Tscheuschner, S.; **Kahle, F.-J.**; Reichenberger, M.; Athanasopoulos, S.; Saller, C., Bazan, G.C.; Nguyen, T.-Q.; Strohrriegl, P.; Bässler, H.; Köhler, A. Monomolecular and Bimolecular Recombination of Electron-Hole Pairs at the Interface of a Bilayer Organic Solar Cell. *Adv. Funct. Mater.*, **2017**, 27, 1604906.

10. Panzer, F.[†]; Hanft, D.; Gujar, T.P.; **Kahle, F.-J.**; Thelakkat, M.; Köhler, A.; Moos, R.; Compact Layers of Hybrid Halide Perovskites Fabricated via the Aerosol Deposition Process—Uncoupling Material Synthesis and Layer Formation. *Materials*, **2016**, 9 (4), 277.

† indicates first author

Bibliography

- [1] NREL. *Photovoltaic Research*. <https://www.nrel.gov/pv/>, accessed: 2018-07-16, 10:42:19.
- [2] N. LI, I. MCCULLOCH, and C. J. BRABEC (2018). Analyzing the Efficiency, Stability and Cost Potential for Fullerene-Free Organic Photovoltaics in One Figure of Merit. *Energy & Environmental Science* **11** (6), 1355–1361. DOI: 10.1039/C8EE00151K.
- [3] C. B. NIELSEN, S. HOLLIDAY, H.-Y. CHEN, S. J. CRYER, and I. MCCULLOCH (2015). Non-Fullerene Electron Acceptors for Use in Organic Solar Cells. *Accounts of Chemical Research* **48** (11), 2803–2812. DOI: 10.1021/acs.accounts.5b00199.
- [4] S. YANG, W. FU, Z. ZHANG, H. CHEN, and C.-Z. LI (2017). Recent Advances in Perovskite Solar Cells: Efficiency, Stability and Lead-Free Perovskite. *Journal of Materials Chemistry A* **5** (23), 11462–11482. DOI: 10.1039/C7TA00366H.
- [5] N.-G. PARK, M. GRÄTZEL, T. MIYASAKA, K. ZHU, and K. EMERY (2016). Towards Stable and Commercially Available Perovskite Solar Cells. *Nature Energy* **1** (11), 16152. DOI: 10.1038/nenergy.2016.152.
- [6] M. A. GREEN and A. HO-BAILLIE (2017). Perovskite Solar Cells: The Birth of a New Era in Photovoltaics. *ACS Energy Letters* **2** (4), 822–830. DOI: 10.1021/acsenergylett.7b0137.
- [7] W. SHOCKLEY and H. J. QUEISSER (1961). Detailed Balance Limit of Efficiency of P - n Junction Solar Cells. *Journal of Applied Physics* **32** (3), 510–519. DOI: 10.1063/1.1736034.
- [8] E. O. LAWRENCE (1926). Transition Probabilities: Their Relation to Thermionic Emission and the Photo-Electric Effect. *Physical Review* **27** (5), 555–561. DOI: 10.1103/PhysRev.27.555.
- [9] A. KÖHLER and H. BÄSSLER (2015). Fundamentals of Organic Semiconductor Devices. In: *Electronic Processes in Organic Semiconductors*. Weinheim, Germany: Wiley-VCH Verlag GmbH & Co. KGaA, 307–388. DOI: 10.1002/9783527685172.ch4.
- [10] T. CASEY (2017). *Belgium’s IMEC Nails Coal-Killing Perovskite Solar Cell Record With 23.9% Efficiency*. <https://cleantechnica.com/2017/08/10/belgiums-imec-nails-coal-killing-perovskite-solar-cell-record-23-9-efficiency/>, accessed: 2018-07-16, 10:32:41.
- [11] L. CONTRERAS-BERNAL et al. (2018). Homeopathic Perovskite Solar Cells: Effect of Humidity during Fabrication on the Performance and Stability of the Device. *The Journal of Physical Chemistry C* **122** (10), 5341–5348. DOI: 10.1021/acs.jpcc.8b01558.
- [12] Z. SONG et al. (2016). In-Situ Observation of Moisture-Induced Degradation of Perovskite Solar Cells Using Laser-Beam Induced Current. In: *2016 IEEE 43rd Photovoltaic Specialists Conference (PVSC)*, 1202–1206. DOI: 10.1109/PVSC.2016.7749805.

- [13] N. K. ELUMALAI and A. UDDIN (2016). Hysteresis in Organic-Inorganic Hybrid Perovskite Solar Cells. *Solar Energy Materials and Solar Cells* **157**, 476–509. DOI: 10.1016/j.solmat.2016.06.025.
- [14] B. CHEN, M. YANG, S. PRIYA, and K. ZHU (2016). Origin of J–V Hysteresis in Perovskite Solar Cells. *The Journal of Physical Chemistry Letters* **7** (5), 905–917. DOI: 10.1021/acs.jpcllett.6b00215.
- [15] V. NANDAL and P. R. NAIR (2017). Predictive Modeling of Ion Migration Induced Degradation in Perovskite Solar Cells. *ACS Nano* **11** (11), 11505–11512. DOI: 10.1021/acsnano.7b06294.
- [16] P. V. KAMAT, J. BISQUERT, and J. BURIK (2017). Lead-Free Perovskite Solar Cells. *ACS Energy Letters* **2** (4), 904–905. DOI: 10.1021/acsenenergylett.7b00246.
- [17] R. ALI et al. (2018). Predicted Lead-Free Perovskites for Solar Cells. *Chemistry of Materials* **30** (3), 718–728. DOI: 10.1021/acs.chemmater.7b04036.
- [18] J. HOU, O. INGANÄS, R. H. FRIEND, and F. GAO (2018). Organic Solar Cells Based on Non-Fullerene Acceptors. *Nature Materials* **17** (2), 119–128. DOI: 10.1038/nmat5063.
- [19] M. BÜHL and A. HIRSCH (2001). Spherical Aromaticity of Fullerenes. *Chemical Reviews* **101** (5), 1153–1184. DOI: 10.1021/cr990332q.
- [20] C. CABANETOS et al. (2013). Linear Side Chains in Benzo[1,2-b:4,5-B']Dithiophene-Thieno [3,4-c]Pyrrole-4,6-Dione Polymers Direct Self-Assembly and Solar Cell Performance. *Journal of the American Chemical Society* **135** (12), 4656–4659. DOI: 10.1021/ja400365b.
- [21] Z. HE et al. (2015). Single-Junction Polymer Solar Cells with High Efficiency and Photovoltage. *Nature Photonics* **9** (3), 174–179. DOI: 10.1038/nphoton.2015.6.
- [22] L. LU and L. YU. Understanding Low Bandgap Polymer PTB7 and Optimizing Polymer Solar Cells Based on It. *Advanced Materials* **26** (26), 4413–4430. DOI: 10.1002/adma.201400384.
- [23] F.-J. KAHLE, C. SALLER, A. KÖHLER, and P. STROHRIEGL (2017). Crosslinked Semiconductor Polymers for Photovoltaic Applications. *Advanced Energy Materials* **7** (16), 1700306. DOI: 10.1002/aenm.201700306.
- [24] L. DERUE et al. (2014). Thermal Stabilisation of Polymer–Fullerene Bulk Heterojunction Morphology for Efficient Photovoltaic Solar Cells. *Advanced Materials* **26** (33), 5831–5838. DOI: 10.1002/adma.201401062.
- [25] B. A. COLLINS et al. (2010). Molecular Miscibility of Polymer-Fullerene Blends. *The Journal of Physical Chemistry Letters* **1** (21), 3160–3166. DOI: 10.1021/jz101276h.
- [26] D. WANG, K. NAKAJIMA, F. LIU, S. SHI, and T. P. RUSSELL (2017). Nanomechanical Imaging of the Diffusion of Fullerene into Conjugated Polymer. *ACS Nano* **11** (9), 8660–8667. DOI: 10.1021/acsnano.6b08456.
- [27] M. REICHENBERGER et al. Controlling Aggregate Formation in Conjugated Polymers by Spin-Coating below the Critical Temperature of the Disorder–Order Transition. *Journal of Polymer Science Part B: Polymer Physics* **56** (6), 532–542. DOI: 10.1002/polb.24562.

- [28] M. REICHENBERGER et al. (2016). The Effect of Intermolecular Interaction on Excited States in p - DTS(FBTTH2)2. *The Journal of Chemical Physics* **144** (7), 074904. DOI: 10.1063/1.4941700.
- [29] N. STINGELIN. On the Phase Behaviour of Organic Semiconductors. *Polymer International* **61** (6), 866–873. DOI: 10.1002/pi.4214.
- [30] N. D. TREAT et al. (2011). Interdiffusion of PCBM and P3HT Reveals Miscibility in a Photovoltaically Active Blend. *Advanced Energy Materials* **1** (1), 82–89. DOI: 10.1002/aenm.201000023.
- [31] N. D. TREAT, T. E. MATES, C. J. HAWKER, E. J. KRAMER, and M. L. CHABINYC (2013). Temperature Dependence of the Diffusion Coefficient of PCBM in Poly(3-Hexylthio Phene). *Macromolecules* **46** (3), 1002–1007. DOI: 10.1021/ma302337p.
- [32] B. W. LARSON et al. (2016). Inter-Fullerene Electronic Coupling Controls the Efficiency of Photoinduced Charge Generation in Organic Bulk Heterojunctions. *Advanced Energy Materials* **6** (24), 1601427. DOI: 10.1002/aenm.201601427.
- [33] M. A. FAIST et al. (2013). Understanding the Reduced Efficiencies of Organic Solar Cells Employing Fullerene Multiadducts as Acceptors. *Advanced Energy Materials* **3** (6), 744–752. DOI: 10.1002/aenm.201200673.
- [34] E. T. HOKE et al. (2013). Recombination in Polymer:Fullerene Solar Cells with Open-Circuit Voltages Approaching and Exceeding 1.0 V. *Advanced Energy Materials* **3** (2), 220–230. DOI: 10.1002/aenm.201200474.
- [35] J. W. RUMER and I. MCCULLOCH (2015). Organic Photovoltaics: Crosslinking for Optimal Morphology and Stability. *Materials Today* **18** (8), 425–435. DOI: 10.1016/j.mattod.2015.04.001.
- [36] G. WANTZ et al. (2014). Stabilizing Polymer-Based Bulk Heterojunction Solar Cells via Crosslinking. *Polymer International* **63** (8), 1346–1361. DOI: 10.1002/pi.4712.
- [37] A. WADSWORTH et al. (2018). Critical Review of the Molecular Design Progress in Non-Fullerene Electron Acceptors towards Commercially Viable Organic Solar Cells. *Chemical Society Reviews*. DOI: 10.1039/C7CS00892A.
- [38] G. ZHANG et al. (2018). Nonfullerene Acceptor Molecules for Bulk Heterojunction Organic Solar Cells. *Chemical Reviews* **118** (7), 3447–3507. DOI: 10.1021/acs.chemrev.7b00535.
- [39] A. KÖHLER and H. BÄSSLER (2015). The Electronic Structure of Organic Semiconductors. In: *Electronic Processes in Organic Semiconductors*. Weinheim: Wiley-VCH Verlag GmbH & Co. KGaA, 1–86. DOI: 10.1002/9783527685172.ch1.
- [40] K. DOMANSKI et al. (2016). Not All That Glitters Is Gold: Metal-Migration-Induced Degradation in Perovskite Solar Cells. *ACS Nano* **10** (6), 6306–6314. DOI: 10.1021/acsnano.6b02613.
- [41] Y. SHAO, Z. XIAO, C. BI, Y. YUAN, and J. HUANG (2014). Origin and Elimination of Photocurrent Hysteresis by Fullerene Passivation in CH₃NH₃PbI₃ Planar Heterojunction Solar Cells. *Nature Communications* **5**, 5784. DOI: 10.1038/ncomms6784.

- [42] L. XU, R. MOLAEI IMENABADI, W. G. VANDENBERGHE, and J. W. P. HSU (2018). Minimizing Performance Degradation Induced by Interfacial Recombination in Perovskite Solar Cells through Tailoring of the Transport Layer Electronic Properties. *APL Materials* **6** (3), 036104. DOI: 10.1063/1.5021138.
- [43] A. KÖHLER and H. BÄSSLER (2015). Electronic and Optical Processes of Organic Semiconductors. In: *Electronic Processes in Organic Semiconductors*. Weinheim: Wiley-VCH Verlag GmbH & Co. KGaA, 193–305. DOI: 10.1002/9783527685172.ch3.
- [44] W. TRESS (2014). Organic Solar Cells. In: *Organic Solar Cells*. Vol. 208. Springer Series in Materials Science. Cham: Springer, 67–214. DOI: 10.1007/978-3-319-10097-5_3.
- [45] (2006). Electronic Excited States, Excitons, Energy Transfer. In: *Organic Molecular Solids*. Ed. by M. SCHWOERER and H. C. WOLF. Weinheim: Wiley-VCH Verlag GmbH, 125–175. DOI: 10.1002/9783527618651.ch6.
- [46] T. HAHN et al. (2016). Role of Intrinsic Photogeneration in Single Layer and Bilayer Solar Cells with C60 and PCBM. *The Journal of Physical Chemistry C* **120** (43), 25083–25091. DOI: 10.1021/acs.jpcc.6b08471.
- [47] C. W. TANG (1986). Two-layer Organic Photovoltaic Cell. *Applied Physics Letters* **48** (2), 183–185. DOI: 10.1063/1.96937.
- [48] P. PEUMANS, A. YAKIMOV, and S. R. FORREST (2003). Small Molecular Weight Organic Thin-Film Photodetectors and Solar Cells. *Journal of Applied Physics* **93** (7), 3693–3723. DOI: 10.1063/1.1534621.
- [49] W. LI, A. FURLAN, K. H. HENDRIKS, M. M. WIENK, and R. A. J. JANSSEN (2013). Efficient Tandem and Triple-Junction Polymer Solar Cells. *Journal of the American Chemical Society* **135** (15), 5529–5532. DOI: 10.1021/ja401434x.
- [50] G. F. BURKHARD, E. T. HOKE, and M. D. MCGEHEE. Accounting for Interference, Scattering, and Electrode Absorption to Make Accurate Internal Quantum Efficiency Measurements in Organic and Other Thin Solar Cells. *Advanced Materials* **22** (30), 3293–3297. DOI: 10.1002/adma.201000883.
- [51] P. W. M. BLOM, V. D. MIHAILETCHI, L. J. A. KOSTER, and D. E. MARKOV. Device Physics of Polymer:Fullerene Bulk Heterojunction Solar Cells. *Advanced Materials* **19** (12), 1551–1566. DOI: 10.1002/adma.200601093.
- [52] J. J. M. HALLS et al. (1995). Efficient Photodiodes from Interpenetrating Polymer Networks. *Nature* **376** (6540), 498–500. DOI: 10.1038/376498a0.
- [53] M. ARIU et al. (2003). Exciton Migration in β -Phase Poly(9,9-Dioctylfluorene). *Physical Review B* **67** (19), 195333. DOI: 10.1103/PhysRevB.67.195333.
- [54] M. HIRAMOTO, H. FUJIWARA, and M. YOKOYAMA (1991). Three-layered Organic Solar Cell with a Photoactive Interlayer of Codeposited Pigments. *Applied Physics Letters* **58** (10), 1062–1064. DOI: 10.1063/1.104423.
- [55] G. YU, J. GAO, J. C. HUMMELEN, F. WUDL, and A. J. HEEGER (1995). Polymer Photovoltaic Cells: Enhanced Efficiencies via a Network of Internal Donor-Acceptor Heterojunctions. *Science* **270** (5243), 1789–1791. DOI: 10.1126/science.270.5243.1789.

- [56] C. J. BRABEC et al. (2001). Tracing Photoinduced Electron Transfer Process in Conjugated Polymer/Fullerene Bulk Heterojunctions in Real Time. *Chemical Physics Letters* **340** (3), 232–236. DOI: 10.1016/S0009-2614(01)00431-6.
- [57] A. J. CLULOW et al. (2014). Time-Resolved Neutron Reflectometry and Photovoltaic Device Studies on Sequentially Deposited PCDTBT-Fullerene Layers. *Langmuir* **30** (38), 11474–11484. DOI: 10.1021/la5020779.
- [58] J. MARTÍN et al. On the Effect of Confinement on the Structure and Properties of Small-Molecular Organic Semiconductors. *Advanced Electronic Materials* **4** (1), 1700308. DOI: 10.1002/aelm.201700308.
- [59] N. D. TREAT et al. (2018). Robust Processing of Small-Molecule:Fullerene Organic Solar Cells via Use of Nucleating Agents. *ACS Applied Energy Materials* **1** (5), 1973–1980. DOI: 10.1021/acsaem.8b00082.
- [60] W. OSTWALD (1887). *Lehrbuch der allgemeinen chemie*. Leipzig: W. Engelmann.
- [61] R. SCHUEPPEL et al. (2008). Optimizing Organic Photovoltaics Using Tailored Heterojunctions: A Photoinduced Absorption Study of Oligothiophenes with Low Band Gaps. *Physical Review B* **77** (8), 085311. DOI: 10.1103/PhysRevB.77.085311.
- [62] D. VELDMAN, S. C. J. MESKERS, and R. A. J. JANSSEN. The Energy of Charge-Transfer States in Electron Donor–Acceptor Blends: Insight into the Energy Losses in Organic Solar Cells. *Advanced Functional Materials* **19** (12), 1939–1948. DOI: 10.1002/adfm.200900090.
- [63] T. UNGER et al. (2017). The Impact of Driving Force and Temperature on the Electron Transfer in Donor–Acceptor Blend Systems. *The Journal of Physical Chemistry C* **121** (41), 22739–22752. DOI: 10.1021/acs.jpcc.7b09213.
- [64] N. S. SARICIFTCI, L. SMILOWITZ, A. J. HEEGER, and F. WUDL (1992). Photoinduced Electron Transfer from a Conducting Polymer to Buckminsterfullerene. *Science* **258** (5087), 1474–1476. DOI: 10.1126/science.258.5087.1474.
- [65] J. G. MÜLLER et al. (2005). Ultrafast Dynamics of Charge Carrier Photogeneration and Geminate Recombination in Conjugated Polymer:Fullerene Solar Cells. *Physical Review B* **72** (19). DOI: 10.1103/PhysRevB.72.195208.
- [66] A. A. BAKULIN, D. S. MARTYANOV, D. Y. PARASCHUK, M. S. PSHENICHNIKOV, and P. H. M. VAN LOOSDRECHT (2008). Ultrafast Charge Photogeneration Dynamics in Ground-State Charge-Transfer Complexes Based on Conjugated Polymers. *The Journal of Physical Chemistry B* **112** (44), 13730–13737. DOI: 10.1021/jp8048839.
- [67] S. COOK, R. KATOH, and A. FURUBE (2009). Ultrafast Studies of Charge Generation in PCBM:P3HT Blend Films Following Excitation of the Fullerene PCBM. *The Journal of Physical Chemistry C* **113** (6), 2547–2552. DOI: 10.1021/jp8050774.
- [68] F. ETZOLD et al. (2011). Ultrafast Exciton Dissociation Followed by Nongeminate Charge Recombination in PCDTBT:PCBM Photovoltaic Blends. *Journal of the American Chemical Society* **133** (24), 9469–9479. DOI: 10.1021/ja201837e.
- [69] G. GRANCINI et al. (2013). Hot Exciton Dissociation in Polymer Solar Cells. *Nature Materials* **12** (1), 29–33. DOI: 10.1038/nmat3502.

- [70] D. HERRMANN et al. (2011). Role of Structural Order and Excess Energy on Ultrafast Free Charge Generation in Hybrid Polythiophene/Si Photovoltaics Probed in Real Time by Near-Infrared Broadband Transient Absorption. *Journal of the American Chemical Society* **133** (45), 18220–18233. DOI: 10.1021/ja207887q.
- [71] T. M. CLARKE and J. R. DURRANT (2010). Charge Photogeneration in Organic Solar Cells. *Chemical Reviews* **110** (11), 6736–6767. DOI: 10.1021/cr900271s.
- [72] C. DEIBEL, T. STROBEL, and V. DYAKONOV. Role of the Charge Transfer State in Organic Donor–Acceptor Solar Cells. *Advanced Materials* **22** (37), 4097–4111. DOI: 10.1002/adma.201000376.
- [73] J. LIU et al. (2016). Fast Charge Separation in a Non-Fullerene Organic Solar Cell with a Small Driving Force. *Nature Energy* **1** (7), 16089. DOI: 10.1038/nenergy.2016.89.
- [74] S. FEW, J. M. FROST, and J. NELSON (2015). Models of Charge Pair Generation in Organic Solar Cells. *Physical Chemistry Chemical Physics* **17** (4), 2311–2325. DOI: 10.1039/C4CP03663H.
- [75] T. HAHN et al. Monomolecular and Bimolecular Recombination of Electron–Hole Pairs at the Interface of a Bilayer Organic Solar Cell. *Advanced Functional Materials* **27** (1), 1604906. DOI: 10.1002/adfm.201604906.
- [76] M. C. HEIBER, C. BAUMBACH, V. DYAKONOV, and C. DEIBEL (2015). Encounter-Limited Charge-Carrier Recombination in Phase-Separated Organic Semiconductor Blends. *Physical Review Letters* **114** (13), 136602. DOI: 10.1103/PhysRevLett.114.136602.
- [77] L. J. A. KOSTER, V. D. MIHAILETCHI, and P. W. M. BLOM (2006). Bimolecular Recombination in Polymer/Fullerene Bulk Heterojunction Solar Cells. *Applied Physics Letters* **88** (5), 052104. DOI: 10.1063/1.2170424.
- [78] A. PIVRIKAS et al. (2005). Bimolecular Recombination Coefficient as a Sensitive Testing Parameter for Low-Mobility Solar-Cell Materials. *Physical Review Letters* **94** (17), 176806. DOI: 10.1103/PhysRevLett.94.176806.
- [79] G. LAKHWANI, A. RAO, and R. H. FRIEND (2014). Bimolecular Recombination in Organic Photovoltaics. *Annual Review of Physical Chemistry* **65** (1), 557–581. DOI: 10.1146/annurev-physchem-040513-103615.
- [80] A. D. D. Z. MENDEZA et al. High-Entropy Mixtures of Pristine Fullerenes for Solution-Processed Transistors and Solar Cells. *Advanced Materials* **27** (45), 7325–7331. DOI: 10.1002/adma.201503530.
- [81] J. J. M. HALLS et al. (1999). Charge- and Energy-Transfer Processes at Polymer/Polymer Interfaces: A Joint Experimental and Theoretical Study. *Physical Review B* **60** (8), 5721–5727. DOI: 10.1103/PhysRevB.60.5721.
- [82] A. E. JAILAUBEKOV et al. (2013). Hot Charge-Transfer Excitons Set the Time Limit for Charge Separation at Donor/Acceptor Interfaces in Organic Photovoltaics. *Nature Materials* **12** (1), 66–73. DOI: 10.1038/nmat3500.
- [83] W. TRESS et al. (2011). Imbalanced Mobilities Causing S-Shaped IV Curves in Planar Heterojunction Organic Solar Cells. *Applied Physics Letters* **98** (6), 063301. DOI: 10.1063/1.3553764.

- [84] S. ATHANASOPOULOS, S. TSCHUSCHNER, H. BÄSSLER, and A. KÖHLER (2017). Efficient Charge Separation of Cold Charge-Transfer States in Organic Solar Cells Through Incoherent Hopping. *The Journal of Physical Chemistry Letters* **8**(9), 2093–2098. DOI: 10.1021/acs.jpcllett.7b00595.
- [85] A. ARMIN et al. (2014). Balanced Carrier Mobilities: Not a Necessary Condition for High-Efficiency Thin Organic Solar Cells as Determined by MIS-CELIV. *Advanced Energy Materials* **4**(4), 1300954. DOI: 10.1002/aenm.201300954.
- [86] W. TRESS (2014). Further Origins of S-Shaped J-V Curves. In: *Organic Solar Cells*. Vol. 208. Springer Series in Materials Science. Cham: Springer, 359–376. DOI: 10.1007/978-3-319-10097-5_7.
- [87] D. J. WEHENKEL, L. J. A. KOSTER, M. M. WIENK, and R. A. J. JANSSEN (2012). Influence of Injected Charge Carriers on Photocurrents in Polymer Solar Cells. *Physical Review B* **85**(12), 125203. DOI: 10.1103/PhysRevB.85.125203.
- [88] W. TRESS (2014). Simulation Study on Single-Layer Bulk-Heterojunction Solar Cells. In: *Organic Solar Cells*. Vol. 208. Springer Series in Materials Science. Cham: Springer, 277–312. DOI: 10.1007/978-3-319-10097-5_5.
- [89] R. A. STREET, K. W. SONG, and S. COWAN (2011). Influence of Series Resistance on the Photocurrent Analysis of Organic Solar Cells. *Organic Electronics* **12**(2), 244–248. DOI: 10.1016/j.orgel.2010.11.012.
- [90] B. KITCHEN et al. (2015). Tuning Open-Circuit Voltage in Organic Solar Cells with Molecular Orientation. *ACS Applied Materials & Interfaces* **7**(24), 13208–13216. DOI: 10.1021/am508855s.
- [91] C. M. RAMSDALE et al. (2002). The Origin of the Open-Circuit Voltage in Polyfluorene-Based Photovoltaic Devices. *Journal of Applied Physics* **92**(8), 4266–4270. DOI: 10.1063/1.1506385.
- [92] N. C. GIEBINK, G. P. WIEDERRECHT, M. R. WASIELEWSKI, and S. R. FORREST (2010). Ideal Diode Equation for Organic Heterojunctions. I. Derivation and Application. *Physical Review B* **82**(15), 155305. DOI: 10.1103/PhysRevB.82.155305.
- [93] G. GARCIA-BELMONTE (2010). Temperature Dependence of Open-Circuit Voltage in Organic Solar Cells from Generation–Recombination Kinetic Balance. *Solar Energy Materials and Solar Cells* **94**(12), 2166–2169. DOI: 10.1016/j.solmat.2010.07.006.
- [94] P. WÜRFEL and U. WÜRFEL (2016). *Physics of Solar Cells: From Basic Principles to Advanced Concepts*. 3rd ed. Weinheim: Wiley-VCH.
- [95] A. KÖHLER and H. BÄSSLER (2015). *Electronic Processes in Organic Semiconductors: An Introduction*. Weinheim: Wiley-VCH Verlag GmbH & Co. KGaA. DOI: 10.1002/9783527685172.
- [96] W. TRESS (2014). *Organic Solar Cells: Theory, Experiment, and Device Simulation*. Vol. 208. Springer series in materials science. Cham: Springer.
- [97] M. SCHWOERER, H. C. WOLF, and W. D. BREWER (2007). *Organic Molecular Solids*. Physics textbook. Weinheim: Wiley-VCH.

- [98] C. J. BRABEC, V. DYAKONOV, J. PARISI, and N. S. SARICIFTCI, eds. (2003). *Organic Photovoltaics: Concepts and Realization*. Springer Series in Materials Science. Berlin, Heidelberg: Springer-Verlag.
- [99] A. C. MORTEANI, R. H. FRIEND, and C. SILVA (2005). Exciton Trapping at Heterojunctions in Polymer Blends. *The Journal of Chemical Physics* **122** (24), 244906. DOI: 10.1063/1.1924504.
- [100] M. C. SCHARBER, N. A. SCHULTZ, N. S. SARICIFTCI, and C. J. BRABEC (2003). Optical- and Photocurrent-Detected Magnetic Resonance Studies on Conjugated Polymer/Fullerene Composites. *Physical Review B* **67** (8), 085202. DOI: 10.1103/PhysRevB.67.085202.
- [101] M. HALLERMANN et al. Charge Transfer Excitons in Polymer/Fullerene Blends: The Role of Morphology and Polymer Chain Conformation. *Advanced Functional Materials* **19** (22), 3662–3668. DOI: 10.1002/adfm.200901398.
- [102] T. OFFERMANS, P. A. VAN HAL, S. C. J. MESKERS, M. M. KOETSE, and R. A. J. JANSSEN (2005). Exciplex Dynamics in a Blend of π -Conjugated Polymers with Electron Donating and Accepting Properties: MDMO-PPV and PCNEPV. *Physical Review B* **72** (4), 045213. DOI: 10.1103/PhysRevB.72.045213.
- [103] K. VANDEWAL et al. The Relation Between Open-Circuit Voltage and the Onset of Photocurrent Generation by Charge-Transfer Absorption in Polymer : Fullerene Bulk Heterojunction Solar Cells. *Advanced Functional Materials* **18** (14), 2064–2070. DOI: 10.1002/adfm.200800056.
- [104] C. L. BRAUN (1984). Electric Field Assisted Dissociation of Charge Transfer States as a Mechanism of Photocarrier Production. *The Journal of Chemical Physics* **80** (9), 4157–4161. DOI: 10.1063/1.447243.
- [105] L. ONSAGER (1938). Initial Recombination of Ions. *Physical Review* **54** (8), 554–557. DOI: 10.1103/PhysRev.54.554.
- [106] L. ONSAGER (1934). Deviations from Ohm’s Law in Weak Electrolytes. *The Journal of Chemical Physics* **2** (9), 599–615. DOI: 10.1063/1.1749541.
- [107] M. POPE and C. E. SWENBERG (1999). *Electronic Processes in Organic Crystals and Polymers*. Second Edition. Monographs on the Physics and Chemistry of Materials. Oxford, New York: Oxford University Press.
- [108] P. LANGEVIN (1903). Recombinaison et Mobilites Des Ions Dans Les Gaz. **28**, 433–530.
- [109] R. M. FUOSS and F. ACCASCINA (1959). *Electrolytic Conductance*. New York: Interscience Publ.
- [110] S. N. HOOD and I. KASSAL (2016). Entropy and Disorder Enable Charge Separation in Organic Solar Cells. *The Journal of Physical Chemistry Letters* **7** (22), 4495–4500. DOI: 10.1021/acs.jpcllett.6b02178.
- [111] P. PEUMANS and S. R. FORREST (2004). Separation of Geminate Charge-Pairs at Donor–Acceptor Interfaces in Disordered Solids. *Chemical Physics Letters* **398** (1), 27–31. DOI: 10.1016/j.cpllett.2004.09.030.

- [112] T. OFFERMANS, S. C. J. MESKERS, and R. A. J. JANSSEN (2005). Monte-Carlo Simulations of Geminate Electron–Hole Pair Dissociation in a Molecular Heterojunction: A Two-Step Dissociation Mechanism. *Chemical Physics* **308** (1), 125–133. DOI: 10.1016/j.chemphys.2004.08.015.
- [113] I. G. SCHEBLYKIN, A. YARTSEV, T. PULLERITS, V. GULBINAS, and V. SUNDSTRÖM (2007). Excited State and Charge Photogeneration Dynamics in Conjugated Polymers. *The Journal of Physical Chemistry B* **111** (23), 6303–6321. DOI: 10.1021/jp068864f.
- [114] S. H. PARK et al. (2009). Bulk Heterojunction Solar Cells with Internal Quantum Efficiency Approaching 100%. *Nature Photonics* **3** (5), 297–302. DOI: 10.1038/nphoton.2009.69.
- [115] K. VANDEWAL et al. (2014). Efficient Charge Generation by Relaxed Charge-Transfer States at Organic Interfaces. *Nature Materials* **13** (1), 63–68. DOI: 10.1038/nmat3807.
- [116] J. LEE et al. (2010). Charge Transfer State Versus Hot Exciton Dissociation in Polymer–Fullerene Blended Solar Cells. *Journal of the American Chemical Society* **132** (34), 11878–11880. DOI: 10.1021/ja1045742.
- [117] L. GORIS et al. (2005). Absorption Phenomena in Organic Thin Films for Solar Cell Applications Investigated by Photothermal Deflection Spectroscopy. *Journal of Materials Science* **40** (6), 1413–1418. DOI: 10.1007/s10853-005-0576-0.
- [118] K. VANDEWAL et al. (2008). Fourier-Transform Photocurrent Spectroscopy for a Fast and Highly Sensitive Spectral Characterization of Organic and Hybrid Solar Cells. *Thin Solid Films*. Proceedings on Advanced Materials and Concepts for Photovoltaics EMRS 2007 Conference, Strasbourg, France **516** (20), 7135–7138. DOI: 10.1016/j.tsf.2007.12.056.
- [119] J. F. POWER (2006). Beam Deflection Photothermal Spectroscopy. In: *Handbook of Vibrational Spectroscopy*. Ed. by J. M. CHALMERS. Chichester: Wiley-VCH. DOI: 10.1002/0470027320.s3009.
- [120] E. BUCHACA-DOMINGO et al. (2015). Direct Correlation of Charge Transfer Absorption with Molecular Donor:Acceptor Interfacial Area via Photothermal Deflection Spectroscopy. *Journal of the American Chemical Society* **137** (16), 5256–5259. DOI: 10.1021/ja512410f.
- [121] W. J. D. BEENKEN et al. (2013). Sub-Bandgap Absorption in Organic Solar Cells: Experiment and Theory. *Physical Chemistry Chemical Physics* **15** (39), 16494. DOI: 10.1039/c3cp42236d.
- [122] S. M. MENKE, N. A. RAN, G. C. BAZAN, and R. H. FRIEND (2018). Understanding Energy Loss in Organic Solar Cells: Toward a New Efficiency Regime. *Joule* **2** (1), 25–35. DOI: 10.1016/j.joule.2017.09.020.
- [123] K. TVINGSTEDT et al. (2009). Electroluminescence from Charge Transfer States in Polymer Solar Cells. *Journal of the American Chemical Society* **131** (33), 11819–11824. DOI: 10.1021/ja903100p.
- [124] Y. ZHOU et al. Observation of a Charge Transfer State in Low-Bandgap Polymer/Fullerene Blend Systems by Photoluminescence and Electroluminescence Studies. *Advanced Functional Materials* **19** (20), 3293–3299. DOI: 10.1002/adfm.200900702.

- [125] H. KIM et al. (2005). Electroluminescence in Polymer-Fullerene Photovoltaic Cells. *Applied Physics Letters* **86** (18), 183502. DOI: 10.1063/1.1924869.
- [126] M. A. FAIST et al. (2012). Competition between the Charge Transfer State and the Singlet States of Donor or Acceptor Limiting the Efficiency in Polymer:Fullerene Solar Cells. *Journal of the American Chemical Society* **134** (1), 685–692. DOI: 10.1021/ja210029w.
- [127] G. RUANI, C. FONTANINI, M. MURGIA, and C. TALIANI (2002). Weak Intrinsic Charge Transfer Complexes: A New Route for Developing Wide Spectrum Organic Photovoltaic Cells. *The Journal of Chemical Physics* **116** (4), 1713–1719. DOI: 10.1063/1.1429235.
- [128] J. J. BENSON-SMITH et al. Formation of a Ground-State Charge-Transfer Complex in Polyfluorene//[6,6]-Phenyl-C61 Butyric Acid Methyl Ester (PCBM) Blend Films and Its Role in the Function of Polymer/PCBM Solar Cells. *Advanced Functional Materials* **17** (3), 451–457. DOI: 10.1002/adfm.200600484.
- [129] M. HALLERMANN, S. HANEDER, and E. DA COMO (2008). Charge-Transfer States in Conjugated Polymer/Fullerene Blends: Below-Gap Weakly Bound Excitons for Polymer Photovoltaics. *Applied Physics Letters* **93** (5), 053307. DOI: 10.1063/1.2969295.
- [130] M. GERHARD et al. (2017). Field-Induced Exciton Dissociation in PTB7-Based Organic Solar Cells. *Physical Review B* **95** (19). DOI: 10.1103/PhysRevB.95.195301.
- [131] B. BERNARDO et al. (2014). Delocalization and Dielectric Screening of Charge Transfer States in Organic Photovoltaic Cells. *Nature Communications* **5**, 3245. DOI: 10.1038/ncomms4245.
- [132] J. KERN, S. SCHWAB, C. DEIBEL, and V. DYAKONOV (2011). Binding Energy of Singlet Excitons and Charge Transfer Complexes in MDMO-PPV:PCBM Solar Cells. *physica status solidi (RRL) – Rapid Research Letters* **5** (10-11), 364–366. DOI: 10.1002/pssr.201105430.
- [133] N. A. RAN et al. Harvesting the Full Potential of Photons with Organic Solar Cells. *Advanced Materials* **28** (7), 1482–1488. DOI: 10.1002/adma.201504417.
- [134] T. ROLAND et al. (2011). Sub-100 Fs Charge Transfer in a Novel Donor–Acceptor–Donor Triad Organized in a Smectic Film. *Physical Chemistry Chemical Physics* **14** (1), 273–279. DOI: 10.1039/C1CP22122A.
- [135] A. C. JAKOWETZ et al. (2016). What Controls the Rate of Ultrafast Charge Transfer and Charge Separation Efficiency in Organic Photovoltaic Blends. *Journal of the American Chemical Society* **138** (36), 11672–11679. DOI: 10.1021/jacs.6b05131.
- [136] A. J. WARD et al. The Impact of Driving Force on Electron Transfer Rates in Photovoltaic Donor–Acceptor Blends. *Advanced Materials* **27** (15), 2496–2500. DOI: 10.1002/adma.201405623.
- [137] K. H. HENDRIKS, A. S. G. WIJPKEMA, J. J. VAN FRANEKER, M. M. WIENK, and R. A. J. JANSSEN (2016). Dichotomous Role of Exciting the Donor or the Acceptor on Charge Generation in Organic Solar Cells. *Journal of the American Chemical Society* **138** (31), 10026–10031. DOI: 10.1021/jacs.6b05868.

- [138] D. C. COFFEY et al. (2012). An Optimal Driving Force for Converting Excitons into Free Carriers in Excitonic Solar Cells. *The Journal of Physical Chemistry C* **116** (16), 8916–8923. DOI: 10.1021/jp302275z.
- [139] T. LIU and A. TROISI (2011). Absolute Rate of Charge Separation and Recombination in a Molecular Model of the P3HT/PCBM Interface. *The Journal of Physical Chemistry C* **115** (5), 2406–2415. DOI: 10.1021/jp109130y.
- [140] B. M. SAVOIE et al. (2014). Unequal Partnership: Asymmetric Roles of Polymeric Donor and Fullerene Acceptor in Generating Free Charge. *Journal of the American Chemical Society* **136** (7), 2876–2884. DOI: 10.1021/ja411859m.
- [141] A. WEU et al. (2018). Field-Assisted Exciton Dissociation in Highly Efficient PffBT4T-2OD:Fullerene Organic Solar Cells. *Chemistry of Materials* **30** (8), 2660–2667. DOI: 10.1021/acs.chemmater.8b00094.
- [142] R. A. MARCUS (1956). On the Theory of Oxidation-Reduction Reactions Involving Electron Transfer. I. *The Journal of Chemical Physics* **24** (5), 966–978. DOI: 10.1063/1.1742723.
- [143] R. A. MARCUS and N. SUTIN (1985). Electron Transfers in Chemistry and Biology. *Biochimica et Biophysica Acta (BBA) - Reviews on Bioenergetics* **811** (3), 265–322. DOI: 10.1016/0304-4173(85)90014-X.
- [144] R. A. MARCUS (1989). Relation between Charge Transfer Absorption and Fluorescence Spectra and the Inverted Region. *The Journal of Physical Chemistry* **93** (8), 3078–3086. DOI: 10.1021/j100345a040.
- [145] J. JORTNER (1976). Temperature Dependent Activation Energy for Electron Transfer between Biological Molecules. *The Journal of Chemical Physics* **64** (12), 4860–4867. DOI: 10.1063/1.432142.
- [146] K. VANDEWAL et al. (2017). Absorption Tails of Donor:C₆₀ Blends Provide Insight into Thermally Activated Charge-Transfer Processes and Polaron Relaxation. *Journal of the American Chemical Society* **139** (4), 1699–1704. DOI: 10.1021/jacs.6b12857.
- [147] K. KAWASHIMA, Y. TAMAI, H. OHKITA, I. OSAKA, and K. TAKIMIYA (2015). High-Efficiency Polymer Solar Cells with Small Photon Energy Loss. *Nature Communications* **6** (1), 10085. DOI: 10.1038/ncomms10085.
- [148] I. I. FISHCHUK et al. (2008). Triplet Energy Transfer in Conjugated Polymers. II. A Polaron Theory Description Addressing the Influence of Disorder. *Physical Review B* **78** (4), 045211. DOI: 10.1103/PhysRevB.78.045211.
- [149] I. I. FISHCHUK et al. (2013). Unified Description for Hopping Transport in Organic Semiconductors Including Both Energetic Disorder and Polaronic Contributions. *Physical Review B* **88** (12), 125202. DOI: 10.1103/PhysRevB.88.125202.
- [150] L. SUDHA DEVI et al. (2008). Triplet Energy Transfer in Conjugated Polymers. I. Experimental Investigation of a Weakly Disordered Compound. *Physical Review B* **78** (4), 045210. DOI: 10.1103/PhysRevB.78.045210.
- [151] V. LEVICH. Present State of the Theory of Oxidation-Reduction in Solution (Bulk and Electrode Reactions). *Advances in electrochemistry and electrochemical engineering* **4**, 249–371.

- [152] R. A. J. JANSSEN, J. C. HUMMELEN, and N. S. SARICIFTCI (2005). Polymer–Fullerene Bulk Heterojunction Solar Cells. *MRS Bulletin* **30** (1), 33–36. DOI: 10.1557/mrs2005.6.
- [153] P. CHENG et al. Alloy Acceptor: Superior Alternative to PCBM toward Efficient and Stable Organic Solar Cells. *Advanced Materials* **28** (36), 8021–8028. DOI: 10.1002/adma.201602067.
- [154] D. H. K. MURTHY, M. GAO, M. J. W. VERMEULEN, L. D. A. SIEBBELES, and T. J. SAVENIJE (2012). Mechanism of Mobile Charge Carrier Generation in Blends of Conjugated Polymers and Fullerenes: Significance of Charge Delocalization and Excess Free Energy. *The Journal of Physical Chemistry C* **116** (16), 9214–9220. DOI: 10.1021/jp3007014.
- [155] R. D. PENSACK and J. B. ASBURY (2009). Barrierless Free Carrier Formation in an Organic Photovoltaic Material Measured with Ultrafast Vibrational Spectroscopy. *Journal of the American Chemical Society* **131** (44), 15986–15987. DOI: 10.1021/ja906293q.
- [156] I. R. GOULD et al. (1993). Radiative and Nonradiative Electron Transfer in Contact Radical-Ion Pairs. *Chemical Physics* **176** (2), 439–456. DOI: 10.1016/0301-0104(93)80253-6.
- [157] K. VANDEWAL, K. TVINGSTEDT, A. GADISA, O. INGANÄS, and J. V. MANCA (2010). Relating the Open-Circuit Voltage to Interface Molecular Properties of Donor:Acceptor Bulk Heterojunction Solar Cells. *Physical Review B* **81** (12), 125204. DOI: 10.1103/PhysRevB.81.125204.
- [158] C. DEIBEL, T. STROBEL, and V. DYAKONOV (2009). Origin of the Efficient Polaron-Pair Dissociation in Polymer-Fullerene Blends. *Physical Review Letters* **103** (3), 036402. DOI: 10.1103/PhysRevLett.103.036402.
- [159] V. I. ARKHIPOV, E. V. EMELIANOVA, and H. BÄSSLER (2003). Dopant-Assisted Charge Carrier Photogeneration in Conjugated Polymers. *Chemical Physics Letters* **372** (5), 886–892. DOI: 10.1016/S0009-2614(03)00520-7.
- [160] V. I. ARKHIPOV, P. HEREMANS, and H. BÄSSLER (2003). Why Is Exciton Dissociation so Efficient at the Interface between a Conjugated Polymer and an Electron Acceptor? *Applied Physics Letters* **82** (25), 4605–4607. DOI: 10.1063/1.1586456.
- [161] A. V. NENASHEV et al. (2011). Theory of Exciton Dissociation at the Interface between a Conjugated Polymer and an Electron Acceptor. *Physical Review B* **84** (3), 035210. DOI: 10.1103/PhysRevB.84.035210.
- [162] C. SCHWARZ et al. (2013). Role of the Effective Mass and Interfacial Dipoles on Exciton Dissociation in Organic Donor-Acceptor Solar Cells. *Physical Review B* **87** (15), 155205. DOI: 10.1103/PhysRevB.87.155205.
- [163] S. TSCHAEUSCHNER, H. BÄSSLER, K. HUBER, and A. KÖHLER (2015). A Combined Theoretical and Experimental Study of Dissociation of Charge Transfer States at the Donor–Acceptor Interface of Organic Solar Cells. *The Journal of Physical Chemistry B* **119** (32), 10359–10371. DOI: 10.1021/acs.jpcc.5b05138.
- [164] J.-L. BRÉDAS, J. E. NORTON, J. CORNIL, and V. COROPCEANU (2009). Molecular Understanding of Organic Solar Cells: The Challenges. *Accounts of Chemical Research* **42** (11), 1691–1699. DOI: 10.1021/ar900099h.

- [165] M. WIEMER, A. V. NENASHEV, F. JANSSON, and S. D. BARANOVSKII (2011). On the Efficiency of Exciton Dissociation at the Interface between a Conjugated Polymer and an Electron Acceptor. *Applied Physics Letters* **99** (1), 013302. DOI: 10.1063/1.3607481.
- [166] X.-K. CHEN, M. K. RAVVA, H. LI, S. M. RYNO, and J.-L. BRÉDAS (2016). Effect of Molecular Packing and Charge Delocalization on the Nonradiative Recombination of Charge-Transfer States in Organic Solar Cells. *Advanced Energy Materials* **6** (24), 1601325. DOI: 10.1002/aenm.201601325.
- [167] Z. ZHENG, N. R. TUMMALA, Y.-T. FU, V. COROPCEANU, and J.-L. BRÉDAS (2017). Charge-Transfer States in Organic Solar Cells: Understanding the Impact of Polarization, Delocalization, and Disorder. *ACS Applied Materials & Interfaces* **9** (21), 18095–18102. DOI: 10.1021/acsami.7b02193.
- [168] S. ONO and K. OHNO (2018). Origin of Charge Transfer Exciton Dissociation in Organic Solar Cells. In: *Excitons*. Ed. by S. L. PYSHKIN. London: InTech. DOI: 10.5772/intechopen.69854.
- [169] D. CARUSO and A. TROISI (2012). Long-Range Exciton Dissociation in Organic Solar Cells. *Proceedings of the National Academy of Sciences* **109** (34), 13498–13502. DOI: 10.1073/pnas.1206172109.
- [170] A. A. BAKULIN et al. (2012). The Role of Driving Energy and Delocalized States for Charge Separation in Organic Semiconductors. *Science* **335** (6074), 1340–1344. DOI: 10.1126/science.1217745.
- [171] A. ZUSAN et al. (2014). The Crucial Influence of Fullerene Phases on Photogeneration in Organic Bulk Heterojunction Solar Cells. *Advanced Energy Materials* **4** (17), 1400922. DOI: 10.1002/aenm.201400922.
- [172] A. A. BAKULIN, Y. XIA, H. J. BAKKER, O. INGANÄS, and F. GAO (2016). Morphology, Temperature, and Field Dependence of Charge Separation in High-Efficiency Solar Cells Based on Alternating Polyquinoxaline Copolymer. *The Journal of Physical Chemistry C* **120** (8), 4219–4226. DOI: 10.1021/acs.jpcc.5b10801.
- [173] V. ABRAMAVICIUS et al. (2016). Role of Coherence and Delocalization in Photo-Induced Electron Transfer at Organic Interfaces. *Scientific Reports* **6** (1), 32914. DOI: 10.1038/srep32914.
- [174] S. GÉLINAS et al. (2014). Ultrafast Long-Range Charge Separation in Organic Semiconductor Photovoltaic Diodes. *Science* **343** (6170), 512–516. DOI: 10.1126/science.1246249.
- [175] A. GLUCHOWSKI, K. L. G. GRAY, S. N. HOOD, and I. KASSAL (2018). Increases in the Charge Separation Barrier in Organic Solar Cells Due to Delocalization. *The Journal of Physical Chemistry Letters* **9** (6), 1359–1364. DOI: 10.1021/acs.jpcllett.8b00292.
- [176] H. OHKITA et al. (2008). Charge Carrier Formation in Polythiophene/Fullerene Blend Films Studied by Transient Absorption Spectroscopy. *Journal of the American Chemical Society* **130** (10), 3030–3042. DOI: 10.1021/ja076568q.
- [177] C. SILVA (2013). Organic Photovoltaics: Some like It Hot. *Nature Materials* **12** (1), 5–6. DOI: 10.1038/nmat3523.

- [178] T. HAHN et al. (2015). Does Excess Energy Assist Photogeneration in an Organic Low-Bandgap Solar Cell? *Advanced Functional Materials* **25** (8), 1287–1295. DOI: 10.1002/adfm.201403784.
- [179] S. ALBRECHT et al. On the Efficiency of Charge Transfer State Splitting in Polymer:Fullerene Solar Cells. *Advanced Materials* **26** (16), 2533–2539. DOI: 10.1002/adma.201305283.
- [180] T. G. J. VAN DER HOFSTAD, D. D. NUZZO, M. VAN DEN BERG, R. A. J. JANSSEN, and S. C. J. MESKERS. Influence of Photon Excess Energy on Charge Carrier Dynamics in a Polymer-Fullerene Solar Cell. *Advanced Energy Materials* **2** (9), 1095–1099. DOI: 10.1002/aenm.201200030.
- [181] J. KURPIERS et al. (2018). Probing the Pathways of Free Charge Generation in Organic Bulk Heterojunction Solar Cells. *Nature Communications* **9** (1), 2038. DOI: 10.1038/s41467-018-04386-3.
- [182] K. TVINGSTEDT, K. VANDEWAL, F. ZHANG, and O. INGANÄS (2010). On the Dissociation Efficiency of Charge Transfer Excitons and Frenkel Excitons in Organic Solar Cells: A Luminescence Quenching Study. *The Journal of Physical Chemistry C* **114** (49), 21824–21832. DOI: 10.1021/jp107587h.
- [183] T. OFFERMANS, S. C. J. MESKERS, and R. A. J. JANSSEN (2006). Time Delayed Collection Field Experiments on Polymer: Fullerene Bulk-Heterojunction Solar Cells. *Journal of Applied Physics* **100** (7), 074509. DOI: 10.1063/1.2356783.
- [184] J. KNIEPERT, M. SCHUBERT, J. C. BLAKESLEY, and D. NEHER (2011). Photogeneration and Recombination in P3HT/PCBM Solar Cells Probed by Time-Delayed Collection Field Experiments. *The Journal of Physical Chemistry Letters* **2** (7), 700–705. DOI: 10.1021/jz200155b.
- [185] S. ALBRECHT et al. (2012). On the Field Dependence of Free Charge Carrier Generation and Recombination in Blends of PCPDTBT/PC70BM: Influence of Solvent Additives. *The Journal of Physical Chemistry Letters* **3** (5), 640–645. DOI: 10.1021/jz3000849.
- [186] R. A. MARSH, J. M. HODGKISS, and R. H. FRIEND (2010). Direct Measurement of Electric Field-Assisted Charge Separation in Polymer:Fullerene Photovoltaic Diodes. *Advanced Materials* **22** (33), 3672–3676. DOI: 10.1002/adma.201001010.
- [187] S. WESTENHOFF et al. (2008). Charge Recombination in Organic Photovoltaic Devices with High Open-Circuit Voltages. *Journal of the American Chemical Society* **130** (41), 13653–13658. DOI: 10.1021/ja803054g.
- [188] A. N. BRIGEMAN et al. (2016). Revealing the Full Charge Transfer State Absorption Spectrum of Organic Solar Cells. *Advanced Energy Materials* **6** (21), 1601001. DOI: 10.1002/aenm.201601001.
- [189] N. A. RAN et al. (2017). Impact of Interfacial Molecular Orientation on Radiative Recombination and Charge Generation Efficiency. *Nature Communications* **8** (1), 79. DOI: 10.1038/s41467-017-00107-4.
- [190] S. R. YOST and T. VAN VOORHIS (2013). Electrostatic Effects at Organic Semiconductor Interfaces: A Mechanism for “Cold” Exciton Breakup. *The Journal of Physical Chemistry C* **117** (11), 5617–5625. DOI: 10.1021/jp3125186.

- [191] S. DIFLEY, L.-P. WANG, S. YEGANEH, S. R. YOST, and T. V. VOORHIS (2010). Electronic Properties of Disordered Organic Semiconductors via QM/MM Simulations. *Accounts of Chemical Research* **43** (7), 995–1004. DOI: 10.1021/ar900246s.
- [192] S. VERLAAK et al. Electronic Structure and Geminate Pair Energetics at Organic–Organic Interfaces: The Case of Pentacene/C60 Heterojunctions. *Advanced Functional Materials* **19** (23), 3809–3814. DOI: 10.1002/adfm.200901233.
- [193] S. CANUTO, ed. (2010). *Solvation Effects on Molecules and Biomolecules: Computational Methods and Applications*. Vol. 6. Challenges and Advances in Computational Chemistry and Physics. Springer Science & Business Media.
- [194] H. ISHII, K. SUGIYAMA, E. ITO, and K. SEKI (1999). Energy Level Alignment and Interfacial Electronic Structures at Organic/Metal and Organic/Organic Interfaces. *Advanced Materials* **11** (8), 605–625. DOI: 10.1002/(SICI)1521-4095(199906)11:8<605::AID-ADMA605>3.0.CO;2-Q.
- [195] S. C. VEENSTRA and H. T. JONKMAN. Energy-Level Alignment at Metal–Organic and Organic–Organic Interfaces. *Journal of Polymer Science Part B: Polymer Physics* **41** (21), 2549–2560. DOI: 10.1002/polb.10658.
- [196] O. V. MOLODTSOVA, T. SCHWIEGER, and M. KNUPFER (2005). Electronic Properties of the Organic Semiconductor Hetero-Interface CuPc/C60. *Applied Surface Science*. 13th Applied Surface Analysis Workshop **252** (1), 143–147. DOI: 10.1016/j.apsusc.2005.02.023.
- [197] Y. GE and J. E. WHITTEN (2007). Energy Level Alignment between Sexithiophene and Buckminsterfullerene Films. *Chemical Physics Letters* **448** (1-3), 65–69. DOI: 10.1016/j.cplett.2007.09.075.
- [198] W. OSIKOWICZ, M. P. DE JONG, and W. R. SALANECK. Formation of the Interfacial Dipole at Organic–Organic Interfaces: C60/Polymer Interfaces. *Advanced Materials* **19** (23), 4213–4217. DOI: 10.1002/adma.200700622.
- [199] M. C. SCHARBER et al. (2006). Design Rules for Donors in Bulk-Heterojunction Solar Cells-Towards 10 % Energy-Conversion Efficiency. *Advanced Materials* **18** (6), 789–794. DOI: 10.1002/adma.200501717.
- [200] W. LI, K. H. HENDRIKS, A. FURLAN, M. M. WIENK, and R. A. J. JANSSEN (2015). High Quantum Efficiencies in Polymer Solar Cells at Energy Losses below 0.6 eV. *Journal of the American Chemical Society* **137** (6), 2231–2234. DOI: 10.1021/ja5131897.
- [201] K. VANDEWAL et al. (2012). Quantification of Quantum Efficiency and Energy Losses in Low Bandgap Polymer:Fullerene Solar Cells with High Open-Circuit Voltage. *Advanced Functional Materials* **22** (16), 3480–3490. DOI: 10.1002/adfm.201200608.
- [202] V. C. NIKOLIS et al. (2017). Reducing Voltage Losses in Cascade Organic Solar Cells While Maintaining High External Quantum Efficiencies. *Advanced Energy Materials* **7** (21), 00855. DOI: 10.1002/aenm.201700855.
- [203] W. ZHAO et al. Fullerene-Free Polymer Solar Cells with over 11% Efficiency and Excellent Thermal Stability. *Advanced Materials* **28** (23), 4734–4739. DOI: 10.1002/adma.201600281.

- [204] B. A. GREGG (2011). Entropy of Charge Separation in Organic Photovoltaic Cells: The Benefit of Higher Dimensionality. *The Journal of Physical Chemistry Letters* **2** (24), 3013–3015. DOI: 10.1021/jz2012403.
- [205] L. SHI, C. K. LEE, and A. P. WILLARD (2017). The Enhancement of Interfacial Exciton Dissociation by Energetic Disorder Is a Nonequilibrium Effect. *ACS Central Science* **3** (12), 1262–1270. DOI: 10.1021/acscentsci.7b00404.
- [206] Y. PUTTISONG et al. (2018). Charge Generation via Relaxed Charge-Transfer States in Organic Photovoltaics by an Energy-Disorder-Driven Entropy Gain. *The Journal of Physical Chemistry C*, 12640–12646. DOI: 10.1021/acs.jpcc.8b03432.
- [207] G. NAN, X. ZHANG, and G. LU (2016). The Lowest-Energy Charge-Transfer State and Its Role in Charge Separation in Organic Photovoltaics. *Physical Chemistry Chemical Physics* **18** (26), 17546–17556. DOI: 10.1039/C6CP01622G.
- [208] H. BÄSSLER. Charge Transport in Disordered Organic Photoconductors a Monte Carlo Simulation Study. *physica status solidi (b)* **175** (1), 15–56. DOI: 10.1002/pssb.2221750102.
- [209] D. H. DUNLAP, P. E. PARRIS, and V. M. KENKRE (1996). Charge-Dipole Model for the Universal Field Dependence of Mobilities in Molecularly Doped Polymers. *Physical Review Letters* **77** (3), 542–545. DOI: 10.1103/PhysRevLett.77.542.
- [210] R. COEHOORN and P. A. BOBBERT. Effects of Gaussian Disorder on Charge Carrier Transport and Recombination in Organic Semiconductors. *physica status solidi (a)* **209** (12), 2354–2377. DOI: 10.1002/pssa.201228387.
- [211] V. COROPCEANU et al. (2007). Charge Transport in Organic Semiconductors. *Chemical Reviews* **107** (4), 926–952. DOI: 10.1021/cr050140x.
- [212] V. I. ARKHIPOV, E. V. EMELIANOVA, and G. J. ADRIAENSSENS (2001). Effective Transport Energy versus the Energy of Most Probable Jumps in Disordered Hopping Systems. *Physical Review B* **64** (12), 125125. DOI: 10.1103/PhysRevB.64.125125.
- [213] BÄSSLER, HEINZ (2000). Charge Transport in Random Organic Semiconductors. In: *Semiconducting Polymers. Chemistry, Physics and Engineering*. Ed. by HADZIIOANNOU, G. and VAN HUTTEN, P. Weinheim: Wiley-VCH Verlag GmbH, 365–410.
- [214] R. G. KEPLER (1960). Charge Carrier Production and Mobility in Anthracene Crystals. *Physical Review* **119** (4), 1226–1229. DOI: 10.1103/PhysRev.119.1226.
- [215] O. H. LEBLANC (1960). Hole and Electron Drift Mobilities in Anthracene. *The Journal of Chemical Physics* **33** (2), 626–626. DOI: 10.1063/1.1731216.
- [216] N. KARL (1974). Organic Semiconductors. In: *Festkörperprobleme 14. Advances in Solid State Physics*. Berlin, Heidelberg: Springer, 261–290. DOI: 10.1007/BFb0108470.
- [217] J. P. J. MARKHAM et al. (2002). Nondispersive Hole Transport in a Spin-Coated Dendrimer Film Measured by the Charge-Generation-Layer Time-of-Flight Method. *Applied Physics Letters* **81** (17), 3266–3268. DOI: 10.1063/1.1514400.
- [218] A. KOKIL, K. YANG, and J. KUMAR. Techniques for Characterization of Charge Carrier Mobility in Organic Semiconductors. *Journal of Polymer Science Part B: Polymer Physics* **50** (15), 1130–1144. DOI: 10.1002/polb.23103.

- [219] J. A. GEURST. Theory of Space-Charge-Limited Currents in Thin Semiconductor Layers. *physica status solidi (b)* **15** (1), 107–118. DOI: 10.1002/pssb.19660150108.
- [220] M. ZUBAIR, Y. S. ANG, and L. K. ANG (2018). Thickness Dependence of Space-Charge-Limited Current in Spatially Disordered Organic Semiconductors. *IEEE Transactions on Electron Devices*, 1–9. DOI: 10.1109/TED.2018.2841920.
- [221] H. T. NICOLAI et al. (2012). Unification of Trap-Limited Electron Transport in Semiconducting Polymers. *Nature Materials* **11** (10), 882–887. DOI: 10.1038/nmat3384.
- [222] S. L. M. VAN MENSFOORT and R. COELHOORN (2008). Effect of Gaussian Disorder on the Voltage Dependence of the Current Density in Sandwich-Type Devices Based on Organic Semiconductors. *Physical Review B* **78** (8), 085207. DOI: 10.1103/PhysRevB.78.085207.
- [223] J. DACUÑA and A. SALLEO (2011). Modeling Space-Charge-Limited Currents in Organic Semiconductors: Extracting Trap Density and Mobility. *Physical Review B* **84** (19), 195209. DOI: 10.1103/PhysRevB.84.195209.
- [224] G. JUŠKA, K. ARLAUSKAS, M. VILIŪNAS, and J. KOČKA (2000). Extraction Current Transients: New Method of Study of Charge Transport in Microcrystalline Silicon. *Physical Review Letters* **84** (21), 4946–4949. DOI: 10.1103/PhysRevLett.84.4946.
- [225] J. LORRMANN, B. H. BADADA, O. INGANÄS, V. DYAKONOV, and C. DEIBEL (2010). Charge Carrier Extraction by Linearly Increasing Voltage: Analytic Framework and Ambipolar Transients. *Journal of Applied Physics* **108** (11), 113705. DOI: 10.1063/1.3516392. arXiv: 1006.4394.
- [226] S. BANGE, M. SCHUBERT, and D. NEHER (2010). Charge Mobility Determination by Current Extraction under Linear Increasing Voltages: Case of Nonequilibrium Charges and Field-Dependent Mobilities. *Physical Review B* **81** (3), 035209. DOI: 10.1103/PhysRevB.81.035209.
- [227] A. PIVRIKAS, N. S. SARICIFTCI, G. JUŠKA, and R. ÖSTERBACKA (2007). A Review of Charge Transport and Recombination in Polymer/Fullerene Organic Solar Cells. *Progress in Photovoltaics: Research and Applications* **15** (8), 677–696. DOI: 10.1002/pip.791.
- [228] G. H. GELINCK and J. M. WARMAN (1996). Charge Carrier Dynamics in Pulse-Irradiated Polyphenylenevinylenes: Effects of Broken Conjugation, Temperature, and Accumulated Dose. *The Journal of Physical Chemistry* **100** (51), 20035–20042. DOI: 10.1021/jp962051h.
- [229] A. DEVIŽIS, A. SERBENTA, K. MEERHOLZ, D. HERTEL, and V. GULBINAS (2009). Ultrafast Dynamics of Carrier Mobility in a Conjugated Polymer Probed at Molecular and Microscopic Length Scales. *Physical Review Letters* **103** (2), 027404. DOI: 10.1103/PhysRevLett.103.027404.
- [230] G. JUŠKA, N. NEKRAŠAS, and K. GENEVIČIUS (2012). Investigation of Charge Carriers Transport from Extraction Current Transients of Injected Charge Carriers. *Journal of Non-Crystalline Solids* **358** (4), 748–750. DOI: 10.1016/j.jnoncrysol.2011.12.016.
- [231] O. J. SANDBERG et al. (2017). On the Validity of MIS-CELIV for Mobility Determination in Organic Thin-Film Devices. *Applied Physics Letters* **110** (15), 153504. DOI: 10.1063/1.4980101.

- [232] H. SIRRINGHAUS (2009). Reliability of Organic Field-Effect Transistors. *Advanced Materials* **21** (38–39), 3859–3873. DOI: 10.1002/adma.200901136.
- [233] J. ZAUMSEIL and H. SIRRINGHAUS (2007). Electron and Ambipolar Transport in Organic Field-Effect Transistors. *Chemical Reviews* **107** (4), 1296–1323. DOI: 10.1021/cr0501543.
- [234] H. SIRRINGHAUS. 25th Anniversary Article: Organic Field-Effect Transistors: The Path Beyond Amorphous Silicon. *Advanced Materials* **26** (9), 1319–1335. DOI: 10.1002/adma.201304346.
- [235] E. C. P. SMITS et al. (2006). Ambipolar Charge Transport in Organic Field-Effect Transistors. *Physical Review B* **73** (20), 205316. DOI: 10.1103/PhysRevB.73.205316.
- [236] D. C. HOESTEREY and G. M. LETSON (1963). The Trapping of Photocarriers in Anthracene by Anthraquinone, Anthrone and Naphthacene. *Journal of Physics and Chemistry of Solids* **24** (12), 1609–1615. DOI: 10.1016/0022-3697(63)90104-5.
- [237] V. KUMAR, S. C. JAIN, A. K. KAPOOR, J. POORTMANS, and R. MERTENS (2003). Trap Density in Conducting Organic Semiconductors Determined from Temperature Dependence of J-V Characteristics. *Journal of Applied Physics* **94** (2), 1283–1285. DOI: 10.1063/1.1582552.
- [238] A. KADASHCHUK, R. SCHMECHEL, H. VON SEGGERN, U. SCHERF, and A. VAKHNIN (2005). Charge-Carrier Trapping in Polyfluorene-Type Conjugated Polymers. *Journal of Applied Physics* **98** (2), 024101. DOI: 10.1063/1.1953870.
- [239] E. LIST, R. GUENTNER, P. SCANDUCCI DE FREITAS, and U. SCHERF (2002). The Effect of Keto Defect Sites on the Emission Properties of Polyfluorene-Type Materials. *Advanced Materials* **14** (5), 374. DOI: 10.1002/1521-4095(20020304)14:5<374::AID-ADMA374>3.O.CO;2-U.
- [240] D. M. PAI, J. F. YANUS, and M. STOLKA (1984). Trap-Controlled Hopping Transport. *The Journal of Physical Chemistry* **88** (20), 4714–4717. DOI: 10.1021/j150664a054.
- [241] J. VERES and C. JUHASZ (1997). Trap-Controlled Hopping in Doubly Doped Organic Photoreceptor Layers. *Philosophical Magazine B* **75** (3), 377–387. DOI: 10.1080/13642819708202325.
- [242] O. V. MIKHENKO et al. Trap-Limited Exciton Diffusion in Organic Semiconductors. *Advanced Materials* **26** (12), 1912–1917. DOI: 10.1002/adma.201304162.
- [243] G. A. H. WETZELAER, M. KUIK, H. T. NICOLAI, and P. W. M. BLOM (2011). Trap-Assisted and Langevin-Type Recombination in Organic Light-Emitting Diodes. *Physical Review B* **83** (16), 165204. DOI: 10.1103/PhysRevB.83.165204.
- [244] E. KHODABAKHSHI, J. J. MICHELS, and P. W. M. BLOM (2017). Visualization of Trap Dilution in Polyfluorene Based Light-Emitting Diodes. *AIP Advances* **7** (7), 075209. DOI: 10.1063/1.4995381.
- [245] B. Y. FINCK and B. J. SCHWARTZ (2013). Understanding the Origin of the S-Curve in Conjugated Polymer/Fullerene Photovoltaics from Drift-Diffusion Simulations. *Applied Physics Letters* **103** (5), 053306. DOI: 10.1063/1.4817396.
- [246] B. QI and J. WANG (2013). Fill Factor in Organic Solar Cells. *Physical Chemistry Chemical Physics* **15** (23), 8972–8982. DOI: 10.1039/C3CP51383A.

- [247] J. WAGNER et al. (2012). Identification of Different Origins for S-Shaped Current Voltage Characteristics in Planar Heterojunction Organic Solar Cells. *Journal of Applied Physics* **111** (5), 054509. DOI: 10.1063/1.3692050.
- [248] A. PETERSEN et al. (2012). Field-Dependent Exciton Dissociation in Organic Heterojunction Solar Cells. *Physical Review B* **85** (24), 245208. DOI: 10.1103/PhysRevB.85.245208.
- [249] H. YU et al. (2016). Effect of Diffusion Current on Fill Factor in Organic Solar Cells. *Journal of Physics D: Applied Physics* **49** (20), 205105. DOI: 10.1088/0022-3727/49/20/205105.
- [250] W. TRESS (2014). Interplay Between Electrodes and Active Materials: The Open-Circuit Voltage and S-Shaped J-V Curves. In: *Organic Solar Cells*. Vol. 208. Springer Series in Materials Science. Cham: Springer, 315–357. DOI: 10.1007/978-3-319-10097-5_6.
- [251] D. NATALI and M. CAIRONI (2016). Organic Photodetectors. In: *Photodetectors*. Ed. by B. NABET. Woodhead Publishing, 195–254. DOI: 10.1016/B978-1-78242-445-1.00007-5.
- [252] M. KIELAR, O. DHEZ, G. PECASTAINGS, A. CURUTCHET, and L. HIRSCH (2016). Long-Term Stable Organic Photodetectors with Ultra Low Dark Currents for High Detectivity Applications. *Scientific Reports* **6** (1), 39201. DOI: 10.1038/srep39201.
- [253] R. NIE et al. (2017). Highly Sensitive and Broadband Organic Photodetectors with Fast Speed Gain and Large Linear Dynamic Range at Low Forward Bias. *Small* **13** (24), 1603260. DOI: 10.1002/smll.201603260.
- [254] H. ZHANG et al. (2015). Transparent Organic Photodetector Using a Near-Infrared Absorbing Cyanine Dye. *Scientific Reports* **5** (1), 09439. DOI: 10.1038/srep09439.
- [255] B. P. RAND, J. XUE, S. UCHIDA, and S. R. FORREST (2005). Mixed Donor-Acceptor Molecular Heterojunctions for Photovoltaic Applications. I. Material Properties. *Journal of Applied Physics* **98** (12), 124902. DOI: 10.1063/1.2142072.
- [256] R. KÖNENKAMP, G. PRIEBE, and B. PIETZAK (1999). Carrier Mobilities and Influence of Oxygen in C 60 Films. *Physical Review B* **60** (16), 11804–11808. DOI: 10.1103/PhysRevB.60.11804.
- [257] V. CAPOZZI et al. (1996). Optical Spectra and Photoluminescence of C60 Thin Films. *Solid State Communications* **98** (9), 853–858. DOI: 10.1016/0038-1098(96)00060-9.
- [258] S. KAZAOUI et al. (1998). Comprehensive Analysis of Intermolecular Charge-Transfer Excited States in C 60 and C 70 Films. *Physical Review B* **58** (12), 7689–7700. DOI: 10.1103/PhysRevB.58.7689.
- [259] M. M. WIENK et al. (2003). Efficient Methano[70]Fullerene/MDMO-PPV Bulk Heterojunction Photovoltaic Cells. *Angewandte Chemie International Edition* **42** (29), 3371–3375. DOI: 10.1002/anie.200351647.
- [260] M. E. EL-KHOULY (2007). Comparative Study of the Bimolecular Electron Transfer of Fullerenes (C60/C70) and 9,9-Disubstituted Fluorenes by Laser Flash Photolysis. *Photochemical & Photobiological Sciences* **6** (5), 539. DOI: 10.1039/b617814f.
- [261] H. DONG, H. ZHU, Q. MENG, X. GONG, and W. HU (2012). Organic Photoresponse Materials and Devices. *Chem. Soc. Rev.* **41** (5), 1754–1808. DOI: 10.1039/C1CS15205J.

- [262] A. DIAZ DE ZERIO MENDAZA et al. (2014). Neat C₆₀:C₇₀ Buckminsterfullerene Mixtures Enhance Polymer Solar Cell Performance. *J. Mater. Chem. A* **2** (35), 14354–14359. DOI: 10.1039/C4TA02515F.
- [263] G. A. BERRIMAN, J. L. HOLDSWORTH, X. ZHOU, W. J. BELCHER, and P. C. DASTOOR (2015). Molecular versus Crystallite PCBM Diffusion in P3HT:PCBM Blends. *AIP Advances* **5** (9), 097220. DOI: 10.1063/1.4932212.
- [264] R. S. RUOFF, D. S. TSE, R. MALHOTRA, and D. C. LORENTS (1993). Solubility of Fullerene (C₆₀) in a Variety of Solvents. *The Journal of Physical Chemistry* **97** (13), 3379–3383. DOI: 10.1021/j100115a049.
- [265] N. SIVARAMAN et al. (1992). Solubility of C₆₀ in Organic Solvents. *The Journal of Organic Chemistry* **57** (22), 6077–6079. DOI: 10.1021/jo00048a056.
- [266] B. W. LARSON et al. (2013). Electron Affinity of Phenyl–C₆₁–Butyric Acid Methyl Ester (PCBM). *The Journal of Physical Chemistry C* **117** (29), 14958–14964. DOI: 10.1021/jp403312g.
- [267] C. I. WANG and C. C. HUA (2015). Solubility of C₆₀ and PCBM in Organic Solvents. *The Journal of Physical Chemistry B* **119** (45), 14496–14504. DOI: 10.1021/acs.jpcc.5b07399.
- [268] T. HEUMUELLER et al. (2016). Morphological and Electrical Control of Fullerene Dimerization Determines Organic Photovoltaic Stability. *Energy & Environmental Science* **9** (1), 247–256. DOI: 10.1039/C5EE02912K.
- [269] E. F. SHEKA (2007). Donor–Acceptor Origin of Fullerene C₆₀ Dimerization. *International Journal of Quantum Chemistry* **107** (13), 2361–2371. DOI: 10.1002/qua.21420.
- [270] A. M. RAO et al. (1993). Photoinduced Polymerization of Solid C₆₀ Films. *Science* **259** (5097), 955–957. DOI: 10.1126/science.259.5097.955.
- [271] Y. B. ZHAO, D. M. POIRIER, R. J. PECHMAN, and J. H. WEAVER (1994). Electron Stimulated Polymerization of Solid C₆₀. *Applied Physics Letters* **64** (5), 577–579. DOI: 10.1063/1.111113.
- [272] A. DZWILEWSKI, T. WÅGBERG, and L. EDMAN (2009). Photo-Induced and Resist-Free Imprint Patterning of Fullerene Materials for Use in Functional Electronics. *Journal of the American Chemical Society* **131** (11), 4006–4011. DOI: 10.1021/ja807964x.
- [273] P. C. EKLUND, A. M. RAO, P. ZHOU, Y. WANG, and J. M. HOLDEN (1995). Photochemical Transformation of C₆₀ and C₇₀ Films. *Thin Solid Films* **257** (2), 185–203. DOI: 10.1016/0040-6090(94)05704-4.
- [274] C. H. PETERS et al. (2012). The Mechanism of Burn-in Loss in a High Efficiency Polymer Solar Cell. *Advanced Materials* **24** (5), 663–668. DOI: 10.1002/adma.201103010.
- [275] A. DISTLER et al. The Effect of PCBM Dimerization on the Performance of Bulk Heterojunction Solar Cells. *Advanced Energy Materials* **4** (4), 00171. DOI: 10.1002/aenm.201400171.
- [276] N. WANG, X. TONG, Q. BURLINGAME, J. YU, and S. R. FORREST (2014). Photodegradation of Small-Molecule Organic Photovoltaics. *Solar Energy Materials and Solar Cells* **125**, 170–175. DOI: 10.1016/j.solmat.2014.03.005.

- [277] Q. BURLINGAME et al. (2015). Photochemical Origins of Burn-in Degradation in Small Molecular Weight Organic Photovoltaic Cells. *Energy & Environmental Science* **8** (3), 1005–1010. DOI: 10.1039/C4EE03444A.
- [278] P. ZHOU, Z.-H. DONG, A. M. RAO, and P. C. EKLUND (1993). Reaction Mechanism for the Photopolymerization of Solid Fullerene C60. *Chemical Physics Letters* **211** (4), 337–340. DOI: 10.1016/0009-2614(93)87069-F.
- [279] G. E. MORSE et al. (2015). The Effect of Polymer Solubilizing Side-Chains on Solar Cell Stability. *Physical Chemistry Chemical Physics* **17** (17), 11884–11897. DOI: 10.1039/C5CP01158B.
- [280] J. CRANK (1975). *The Mathematics of Diffusion*. 2d ed. Oxford: Clarendon Press.
- [281] S. C. GEORGE and S. THOMAS (2001). Transport Phenomena through Polymeric Systems. *Progress in Polymer Science* **26** (6), 985–1017. DOI: 10.1016/S0079-6700(00)00036-8.
- [282] N. P. CHEREMISINOFF (1989). *Handbook of Polymer Science and Technology*. Boca Raton: CRC Press.
- [283] D. MESCHEDE, ed. (2006). *Gerthsen Physik*. 23rd ed. Springer-Lehrbuch. Berlin, Heidelberg: Springer-Verlag.
- [284] M. KARIMI (2011). Diffusion in Polymer Solids and Solutions. In: *Mass Transfer in Chemical Engineering Processes*. Ed. by J. MARKOŠ. London: InTechOpen, 25.
- [285] C. MÜLLER (2015). On the Glass Transition of Polymer Semiconductors and Its Impact on Polymer Solar Cell Stability. *Chemistry of Materials* **27** (8), 2740–2754. DOI: 10.1021/acs.chemmater.5b00024.
- [286] F. PANZER, H. BÄSSLER, R. LOHWASSER, M. THELAKKAT, and A. KÖHLER (2014). The Impact of Polydispersity and Molecular Weight on the Order–Disorder Transition in Poly(3-Hexylthiophene). *The Journal of Physical Chemistry Letters* **5** (15), 2742–2747. DOI: 10.1021/jz5009938.
- [287] F. PANZER, H. BÄSSLER, and A. KÖHLER (2017). Temperature Induced Order–Disorder Transition in Solutions of Conjugated Polymers Probed by Optical Spectroscopy. *The Journal of Physical Chemistry Letters* **8** (1), 114–125. DOI: 10.1021/acs.jpcllett.6b01641.
- [288] G. R. STROBL (2007). *The Physics of Polymers: Concepts for Understanding Their Structures and Behavior*. 3rd ed. Berlin, Heidelberg: Springer-Verlag.
- [289] W. HU (2013). Polymer Deformation. In: *Polymer Physics*. Vienna: Springer, 93–125. DOI: 10.1007/978-3-7091-0670-9_6.
- [290] T. FOX (1956). Influence of Diluent and of Copolymer Composition on the Glass Transition Temperature of a Polymer System. **1**, 123–132.
- [291] R. XIE et al. (2017). Glass Transition Temperature of Conjugated Polymers by Oscillatory Shear Rheometry. *Macromolecules* **50** (13), 5146–5154. DOI: 10.1021/acs.macromol.7b00712.
- [292] H. VOGEL (1921). Das Temperaturabhängigkeitsgesetz Der Viskosität von Flüssigkeiten. **22**, 645–646.

- [293] G. S. FULCHER (1925). Analysis of Recent Measurements of the Viscosity of Glasses. *Journal of the American Ceramic Society* **8** (6), 339–355. DOI: 10.1111/j.1151-2916.1925.tb16731.x.
- [294] G. TAMMANN (1925). Glasses as Supercooled Liquids. **9**, 166–185.
- [295] M. LOHFINK and H. SILLESCU (1992). Tracer Diffusion in Polymer and Organic Liquids Close to the Glass Transition. *AIP Conference Proceedings* **256** (1), 30–39. DOI: 10.1063/1.42374.
- [296] H. R. CORTI, G. A. FRANK, and M. C. MARCONI (2008). Diffusion-Viscosity Decoupling in Supercooled Aqueous Trehalose Solutions. *The Journal of Physical Chemistry B* **112** (41), 12899–12906. DOI: 10.1021/jp802806p.
- [297] M. T. CICERONE and M. D. EDIGER (1996). Enhanced Translation of Probe Molecules in Supercooled O-terphenyl: Signature of Spatially Heterogeneous Dynamics? *The Journal of Chemical Physics* **104** (18), 7210–7218. DOI: 10.1063/1.471433.
- [298] I. CHANG et al. (1994). Translational and Rotational Molecular Motion in Supercooled Liquids Studied by NMR and Forced Rayleigh Scattering. *Journal of Non-Crystalline Solids. Relaxations in Complex Systems* **172-174**, 248–255. DOI: 10.1016/0022-3093(94)90443-X.
- [299] F. MALLAMACE et al. (2010). Transport Properties of Glass-Forming Liquids Suggest That Dynamic Crossover Temperature Is as Important as the Glass Transition Temperature. *Proceedings of the National Academy of Sciences* **107** (52), 22457–22462. DOI: 10.1073/pnas.1015340107.
- [300] G. B. MCKENNA (2008). Diverging Views on Glass Transition: Glass Dynamics. *Nature Physics* **4** (9), 673–673. DOI: 10.1038/nphys1063.
- [301] D. EHLICH and H. SILLESCU (1990). Tracer Diffusion at the Glass Transition. *Macromolecules* **23** (6), 1600–1610. DOI: 10.1021/ma00208a008.
- [302] E. RÖSSLER and A. P. SOKOLOV (1996). The Dynamics of Strong and Fragile Glass Formers. *Chemical Geology. 5TH Silicate Melt Workshop* **128** (1), 143–153. DOI: 10.1016/0009-2541(95)00169-7.
- [303] G. HEUBERGER and H. SILLESCU (1996). Size Dependence of Tracer Diffusion in Supercooled Liquids. *The Journal of Physical Chemistry* **100** (37), 15255–15260. DOI: 10.1021/jp960968a.
- [304] M. D. EDIGER (1998). Can Density or Entropy Fluctuations Explain Enhanced Translational Diffusion in Glass-Forming Liquids? *Journal of Non-Crystalline Solids* **235-237**, 10–18. DOI: 10.1016/S0022-3093(98)00557-2.
- [305] C. KITTEL (2006). *Einführung in die Festkörperphysik*. München: Oldenbourg.
- [306] N. RAMESH and J. L. DUDA (2000). Diffusion in Polymers below the Glass Transition Temperature: Comparison of Two Approaches Based on Free Volume Concepts. *Korean Journal of Chemical Engineering* **17** (3), 310–317. DOI: 10.1007/BF02699046.
- [307] Q. LIU, S. HUANG, and Z. SUO (2015). Brownian Motion of Molecular Probes in Supercooled Liquids. *Physical Review Letters* **114** (22), 224301. DOI: 10.1103/PhysRevLett.114.224301.

- [308] W. GOTZE and L. SJOGREN (1992). Relaxation Processes in Supercooled Liquids. *Reports on Progress in Physics* **55** (3), 241. DOI: 10.1088/0034-4885/55/3/001.
- [309] L. BERTHIER and G. BIROLI (2011). Theoretical Perspective on the Glass Transition and Amorphous Materials. *Reviews of Modern Physics* **83** (2), 587–645. DOI: 10.1103/RevModPhys.83.587.
- [310] J. C. MARTINEZ-GARCIA, S. J. RZOSKA, A. DROZD-RZOSKA, and J. MARTINEZ-GARCIA (2013). A Universal Description of Ultraslow Glass Dynamics. *Nature Communications* **4**, 1823. DOI: 10.1038/ncomms2797.
- [311] S. D. COLLINS, N. A. RAN, M. C. HEIBER, and T.-Q. NGUYEN (2017). Small Is Powerful: Recent Progress in Solution-Processed Small Molecule Solar Cells. *Advanced Energy Materials* **7** (10), 1602242. DOI: 10.1002/aenm.201602242.
- [312] P. KNAUER, T. HAHN, A. KÖHLER, and P. STROHRIEGL (2016). Initiator-Free Crosslinking of Oxetane Functionalized Low Bandgap Polymers: An Approach towards Stabilized Bulk Heterojunction Solar Cells. *Journal of Materials Chemistry C* **4** (43), 10347–10357. DOI: 10.1039/C6TC03214A.
- [313] A. TOURNEBIZE et al. (2014). How Photoinduced Crosslinking Under Operating Conditions Can Reduce PCDTBT-Based Solar Cell Efficiency and Then Stabilize It. *Advanced Energy Materials* **4** (10), 1301530. DOI: 10.1002/aenm.201301530.
- [314] C. H. PETERS et al. (2011). High Efficiency Polymer Solar Cells with Long Operating Lifetimes. *Advanced Energy Materials* **1** (4), 491–494. DOI: 10.1002/aenm.201100138.
- [315] F. FISCHER et al. (2014). Measuring Reduced C60 Diffusion in Crosslinked Polymer Films by Optical Spectroscopy. *Advanced Functional Materials* **24** (39), 6172–6177. DOI: 10.1002/adfm.201401153.
- [316] J. G. LABRAM, J. KIRKPATRICK, D. D. C. BRADLEY, and T. D. ANTHOPOULOS (2011). Measurement of the Diffusivity of Fullerenes in Polymers Using Bilayer Organic Field Effect Transistors. *Physical Review B* **84** (7), 075344. DOI: 10.1103/PhysRevB.84.075344.
- [317] B. WATTS, W. J. BELCHER, L. THOMSEN, H. ADE, and P. C. DASTOOR (2009). A Quantitative Study of PCBM Diffusion during Annealing of P3HT:PCBM Blend Films. *Macromolecules* **42** (21), 8392–8397. DOI: 10.1021/ma901444u.
- [318] B. F. HARTMEIER et al. (2016). Significance of Miscibility in Multidonor Bulk Heterojunction Solar Cells. *Journal of Polymer Science Part B: Polymer Physics* **54** (2), 237–246. DOI: 10.1002/polb.23907.
- [319] I. E. JACOBS and A. J. MOULÉ (2017). Controlling Molecular Doping in Organic Semiconductors. *Advanced Materials* **29** (42), 1703063. DOI: 10.1002/adma.201703063.
- [320] J. LI et al. (2017). Quantitative Measurements of the Temperature-Dependent Microscopic and Macroscopic Dynamics of a Molecular Dopant in a Conjugated Polymer. *Macromolecules* **50** (14), 5476–5489. DOI: 10.1021/acs.macromol.7b00672.
- [321] M.-C. JUNG, H. KOJIMA, I. MATSUMURA, H. BENTEN, and M. NAKAMURA (2018). Diffusion and Influence on Photovoltaic Characteristics of P-Type Dopants in Organic Photovoltaics for Energy Harvesting from Blue-Light. *Organic Electronics* **52**, 17–21. DOI: 10.1016/j.orgel.2017.10.006.

- [322] L. ZHANG et al. (2015). Origin of Enhanced Hole Injection in Organic Light-Emitting Diodes with an Electron-Acceptor Doping Layer: P-Type Doping or Interfacial Diffusion? *ACS Applied Materials & Interfaces* **7** (22), 11965–11971. DOI: 10.1021/acsami.5b01989.
- [323] I. BRUDER et al. (2010). A Novel P-Dopant with Low Diffusion Tendency and Its Application to Organic Light-Emitting Diodes. *Organic Electronics* **11** (4), 589–593. DOI: 10.1016/j.orgel.2009.12.019.
- [324] A. DAI et al. (2015). Investigation of P-Dopant Diffusion in Polymer Films and Bulk Heterojunctions: Stable Spatially-Confined Doping for All-Solution Processed Solar Cells. *Organic Electronics* **23**, 151–157. DOI: 10.1016/j.orgel.2015.04.023.
- [325] D. CHEN, F. LIU, C. WANG, A. NAKAHARA, and T. P. RUSSELL (2011). Bulk Heterojunction Photovoltaic Active Layers via Bilayer Interdiffusion. *Nano Letters* **11** (5), 2071–2078. DOI: 10.1021/nl200552r.
- [326] G. M. PATERNÒ, M. W. A. SKODA, R. DALGLIESH, F. CACIALLI, and V. G. SAKAI (2016). Tuning Fullerene Intercalation in a Poly (Thiophene) Derivative by Controlling the Polymer Degree of Self-Organisation. *Scientific Reports* **6**, 34609. DOI: 10.1038/srep34609.
- [327] G. ZHANG et al. (2014). Crystallinity Effects in Sequentially Processed and Blend-Cast Bulk-Heterojunction Polymer/Fullerene Photovoltaics. *The Journal of Physical Chemistry C* **118** (32), 18424–18435. DOI: 10.1021/jp5054315.
- [328] J. A. MCEWAN et al. (2016). Diffusion at Interfaces in OLEDs Containing a Doped Phosphorescent Emissive Layer. *Advanced Materials Interfaces* **3** (17), 1600184. DOI: 10.1002/admi.201600184.
- [329] B. J. KIM, Y. MIYAMOTO, B. MA, and J. M. J. FRÉCHET (2009). Photocrosslinkable Polythiophenes for Efficient, Thermally Stable, Organic Photovoltaics. *Advanced Functional Materials* **19** (14), 2273–2281. DOI: 10.1002/adfm.200900043.
- [330] G. GRIFFINI et al. (2011). Long-Term Thermal Stability of High-Efficiency Polymer Solar Cells Based on Photocrosslinkable Donor-Acceptor Conjugated Polymers. *Advanced Materials* **23** (14), 1660–1664. DOI: 10.1002/adma.201004743.
- [331] J. E. CARLÉ et al. (2012). Comparative Studies of Photochemical Cross-Linking Methods for Stabilizing the Bulk Hetero-Junction Morphology in Polymer Solar Cells. *Journal of Materials Chemistry* **22** (46), 24417–24423. DOI: 10.1039/C2JM34284G.
- [332] C. J. MUELLER, T. KLEIN, E. GANN, C. R. MCNEILL, and M. THELAKKAT (2016). Azido-Functionalized Thiophene as a Versatile Building Block To Cross-Link Low-Bandgap Polymers. *Macromolecules* **49** (10), 3749–3760. DOI: 10.1021/acs.macromol.5b02659.
- [333] X.-Q. CHEN et al. (2016). Long-Term Thermally Stable Organic Solar Cells Based on Cross-Linkable Donor–Acceptor Conjugated Polymers. *Journal of Materials Chemistry A* **4** (23), 9286–9292. DOI: 10.1039/C6TA01450J.
- [334] H. KONG et al. (2013). Solution Processable Organic p–n Junction Bilayer Vertical Photodiodes. *Organic Electronics* **14** (3), 703–710. DOI: 10.1016/j.orgel.2012.12.008.
- [335] H. ZHOU et al. Polymer Homo-Tandem Solar Cells with Best Efficiency of 11.3%. *Advanced Materials* **27** (10), 1767–1773. DOI: 10.1002/adma.201404220.

- [336] A. PUETZ et al. (2012). Solution Processable, Precursor Based Zinc Oxide Buffer Layers for 4.5% Efficient Organic Tandem Solar Cells. *Organic Electronics* **13** (11), 2696–2701. DOI: 10.1016/j.orgel.2012.07.043.
- [337] R.-Q. PNG et al. (2010). High-Performance Polymer Semiconducting Heterostructure Devices by Nitrene-Mediated Photocrosslinking of Alkyl Side Chains. *Nature Materials* **9** (2), 152–158. DOI: 10.1038/nmat2594.
- [338] Z.-K. TAN et al. Suppressing Recombination in Polymer Photovoltaic Devices via Energy-Level Cascades. *Advanced Materials* **25** (30), 4131–4138. DOI: 10.1002/adma.201300243.
- [339] N. CHO et al. (2011). In-Situ Crosslinking and n-Doping of Semiconducting Polymers and Their Application as Efficient Electron-Transporting Materials in Inverted Polymer Solar Cells. *Advanced Energy Materials* **1** (6), 1148–1153. DOI: 10.1002/aenm.201100429.
- [340] C.-E. TSAI et al. (2015). Triarylamine-Based Crosslinked Hole-Transporting Material with an Ionic Dopant for High-Performance PEDOT:PSS-Free Polymer Solar Cells. *Journal of Materials Chemistry C* **3** (24), 6158–6165. DOI: 10.1039/C5TC00714C.
- [341] T. HAHN et al. (2015). Organic Solar Cells with Crosslinked Polymeric Exciton Blocking Layer. *physica status solidi (a)* **212** (10), 2162–2168. DOI: 10.1002/pssa.201532040.
- [342] B. MENG, Z. XIE, J. LIU, and L. WANG. A Bromo-Functionalized Conjugated Polymer as a Cross-Linkable Anode Interlayer of Polymer Solar Cells. *Chemistry – An Asian Journal* **11** (8), 1218–1222. DOI: 10.1002/asia.201501199.
- [343] Y.-J. CHENG, C.-H. HSIEH, Y. HE, C.-S. HSU, and Y. LI (2010). Combination of Indene-C-60 Bis-Adduct and Cross-Linked Fullerene Interlayer Leading to Highly Efficient Inverted Polymer Solar Cells. *Journal of the American Chemical Society* **132** (49), 17381–17383. DOI: 10.1021/ja108259n.
- [344] C.-H. HSIEH et al. (2010). Highly Efficient and Stable Inverted Polymer Solar Cells Integrated with a Cross-Linked Fullerene Material as an Interlayer. *Journal of the American Chemical Society* **132** (13), 4887–4893. DOI: 10.1021/ja100236b.
- [345] Y. SUN et al. (2011). Chemically Doped and Cross-Linked Hole-Transporting Materials as an Efficient Anode Buffer Layer for Polymer Solar Cells. *Chemistry of Materials* **23** (22), 5006–5015. DOI: 10.1021/cm2024235.
- [346] Q. XU et al. (2013). Construction of Planar and Bulk Integrated Heterojunction Polymer Solar Cells Using Cross-Linkable D-A Copolymer. *ACS Applied Materials & Interfaces* **5** (14), 6591–6597. DOI: 10.1021/am401263m.
- [347] K. ZHANG et al. (2014). Highly Efficient Inverted Polymer Solar Cells Based on a Cross-Linkable Water-/Alcohol-Soluble Conjugated Polymer Interlayer. *ACS Applied Materials & Interfaces* **6** (13), 10429–10435. DOI: 10.1021/am501920z.
- [348] C. BARNER-KOWOLLIK (2009). Acrylate Free Radical Polymerization: From Mechanism to Polymer Design. *Macromolecular Rapid Communications* **30** (23), 1961–1963. DOI: 10.1002/marc.200900676.
- [349] D. C. DOETSCHMAN, R. C. MEHLENBACHER, and D. CYWAR (1996). Stable Free Radicals Produced in Acrylate and Methacrylate Free Radical Polymerization: Comparative EPR Studies of Structure and the Effects of Cross-Linking. *Macromolecules* **29** (5), 1807–1816. DOI: 10.1021/ma951444w.

- [350] F.-J. KAHLE, I. BAUER, P. STROHRIEGL, and A. KÖHLER. Influence of Crosslinking on Charge Carrier Mobility in Crosslinkable Polyfluorene Derivatives. *Journal of Polymer Science Part B: Polymer Physics* **55** (1), 112–120. DOI: 10.1002/polb.24259.
- [351] S. FESER and K. MEERHOLZ (2011). Investigation of the Photocross-Linking Mechanism in Oxetane-Functionalized Semiconductors. *Chemistry of Materials* **23** (22), 5001–5005. DOI: 10.1021/cm202327c.
- [352] Y. CHEN and K.-C. LIN. Radical Polymerization of Styrene in the Presence of C60. *Journal of Polymer Science Part A: Polymer Chemistry* **37** (15), 2969–2975. DOI: 10.1002/(SICI)1099-0518(19990801)37:15<2969::AID-POLA30>3.0.CO;2-G.
- [353] S. CHAMBON, A. RIVATON, J.-L. GARDETTE, and M. FIRON (2007). Photo- and Thermal Degradation of MDMO-PPV:PCBM Blends. *Solar Energy Materials and Solar Cells*. Selected Papers from the European Conference on Hybrid and Organic Solar Cells – ECHOS '06 **91** (5), 394–398. DOI: 10.1016/j.solmat.2006.10.015.
- [354] S. CHAMBON, A. RIVATON, J.-L. GARDETTE, and M. FIRON (2008). Durability of MDMO-PPV and MDMO-PPV:PCBM Blends under Illumination in the Absence of Oxygen. *Solar Energy Materials and Solar Cells*. Degradation and Stability of Polymer and Organic Solar Cells **92** (7), 785–792. DOI: 10.1016/j.solmat.2007.12.003.
- [355] M. MANCEAU et al. (2010). Effects of Long-Term UV-Visible Light Irradiation in the Absence of Oxygen on P3HT and P3HT:PCBM Blend. *Solar Energy Materials and Solar Cells* **94** (10), 1572–1577. DOI: 10.1016/j.solmat.2010.03.012.
- [356] H. WATERS et al. (2013). Organic Photovoltaics Based on a Crosslinkable PCPDTBT Analogue; Synthesis, Morphological Studies, Solar Cell Performance and Enhanced Lifetime. *Journal of Materials Chemistry A* **1** (25), 7370–7378. DOI: 10.1039/C3TA11002H.
- [357] A. CHARAS et al. (2009). Insoluble Patterns of Cross-Linkable Conjugated Polymers from Blend Demixing in Spin Cast Films. *Macromolecules* **42** (20), 7903–7912. DOI: 10.1021/ma901329n.
- [358] C. D. MÜLLER et al. (2003). Multi-Colour Organic Light-Emitting Displays by Solution Processing. *Nature* **421** (6925), 829–833. DOI: 10.1038/nature01390.
- [359] C. P. YAU et al. (2015). Investigation of Radical and Cationic Cross-Linking in High-Efficiency, Low Band Gap Solar Cell Polymers. *Advanced Energy Materials* **5** (5), 1401228. DOI: 10.1002/aenm.201401228.
- [360] *Trifluoroacetic Acid 74564*. <https://www.sigmaaldrich.com/catalog/product/sial/74564>.
- [361] J. WEICKERT, R. B. DUNBAR, H. C. HESSE, W. WIEDEMANN, and L. SCHMIDT-MENDE (2011). Nanostructured Organic and Hybrid Solar Cells. *Advanced Materials* **23** (16), 1810–1828. DOI: 10.1002/adma.201003991.
- [362] P. K. WATKINS, A. B. WALKER, and G. L. B. VERSCHOOR (2005). Dynamical Monte Carlo Modelling of Organic Solar Cells: The Dependence of Internal Quantum Efficiency on Morphology. *Nano Letters* **5** (9), 1814–1818. DOI: 10.1021/nl051098o.
- [363] K. M. COAKLEY and M. D. MCGEHEE (2004). Conjugated Polymer Photovoltaic Cells. *Chemistry of Materials* **16** (23), 4533–4542. DOI: 10.1021/cm049654n.

- [364] T. PFADLER et al. (2014). Influence of Interfacial Area on Exciton Separation and Polaron Recombination in Nanostructured Bilayer All-Polymer Solar Cells. *ACS Nano* **8** (12), 12397–12409. DOI: 10.1021/nm5064166.
- [365] A. A. POPOV et al. (2007). Electrochemical, Spectroscopic, and DFT Study of C₆₀(CF₃)_n Frontier Orbitals (n = 2-18): The Link between Double Bonds in Pentagons and Reduction Potentials. *Journal of the American Chemical Society* **129** (37), 11551–11568. DOI: 10.1021/ja073181e.
- [366] J. S. WILSON et al. (2001). The Energy Gap Law for Triplet States in Pt-Containing Conjugated Polymers and Monomers. *Journal of the American Chemical Society* **123** (38), 9412–9417. DOI: 10.1021/ja010986s.
- [367] T. MÜLLER (2016). Diffusion Und Strukturbildung von C₆₀-Fullerenen in Vielschichtsystemen Organischer Halbleitermaterialien. Master Thesis. Bayreuth: Universität Bayreuth.
- [368] M. L. WILLIAMS, R. F. LANDEL, and J. D. FERRY (1955). The Temperature Dependence of Relaxation Mechanisms in Amorphous Polymers and Other Glass-Forming Liquids. *Journal of the American Chemical Society* **77** (14), 3701–3707. DOI: 10.1021/ja01619a008.
- [369] P. CHENG and X. ZHAN (2016). Stability of Organic Solar Cells: Challenges and Strategies. *Chemical Society Reviews* **45** (9), 2544–2582. DOI: 10.1039/C5CS00593K.
- [370] C. J. MUELLER, M. BRENDDEL, P. RUCKDESCHEL, J. PFLAUM, and M. THELAKKAT (2015). Diketopyrrolopyrroles with a Distinct Energy Level Cascade for Efficient Charge Carrier Generation in Organic Solar Cells. *Advanced Energy Materials* **5** (21), 00914. DOI: 10.1002/aenm.201500914.
- [371] C. J. MUELLER, C. R. SINGH, M. FRIED, S. HUETTNER, and M. THELAKKAT (2014). High Bulk Electron Mobility Diketopyrrolopyrrole Copolymers with Perfluorothiophene. *Advanced Functional Materials* **25** (18), 2725–2736. DOI: 10.1002/adfm.201404540.
- [372] M. GRZYBOWSKI and D. T. GRYSKO. Diketopyrrolopyrroles: Synthesis, Reactivity, and Optical Properties. *Advanced Optical Materials* **3** (3), 280–320. DOI: 10.1002/adom.201400559.
- [373] T. POTRAWA and H. LANGHALS (1987). Fluorescent Dyes with Large Stokes Shifts - Soluble Dihydropyrrolopyrrolediones. **120** (7), 1075–1078.
- [374] G. COLONNA, T. PILATI, F. RUSCONI, and G. ZECCHI (2007). Synthesis and Properties of Some New N,N'-Disubstituted 2,5-Dihydro-1,4-Dioxo-3,6-Diphenylpyrrolo[3,4-c]Pyrroles. *Dyes and Pigments* **75** (1), 125–129. DOI: 10.1016/j.dyepig.2006.05.024.
- [375] C. B. NIELSEN, M. TURBIEZ, and I. McCULLOCH (2013). Recent Advances in the Development of Semiconducting DPP-Containing Polymers for Transistor Applications. *Advanced Materials* **25** (13), 1859–1880. DOI: 10.1002/adma.201201795.
- [376] C. KANIMOSHI et al. (2014). Use of Side-Chain for Rational Design of n-Type Diketopyrrolo Pyrrole-Based Conjugated Polymers: What Did We Find Out? *Physical Chemistry Chemical Physics* **16** (32), 17253–17265. DOI: 10.1039/C4CP02322F.
- [377] R. C. I. MACKENZIE, J. M. FROST, and J. NELSON (2010). A Numerical Study of Mobility in Thin Films of Fullerene Derivatives. *The Journal of Chemical Physics* **132** (6), 064904. DOI: 10.1063/1.3315872.

- [378] F. GAJDOS, H. OBERHOFER, M. DUPUIS, and J. BLUMBERGER (2013). On the Inapplicability of Electron-Hopping Models for the Organic Semiconductor Phenyl-C61-Butyric Acid Methyl Ester (PCBM). *The Journal of Physical Chemistry Letters* **4** (6), 1012–1017. DOI: 10.1021/jz400227c.
- [379] D. L. CHEUNG and A. TROISI (2010). Theoretical Study of the Organic Photovoltaic Electron Acceptor PCBM: Morphology, Electronic Structure, and Charge Localization. *The Journal of Physical Chemistry C* **114** (48), 20479–20488. DOI: 10.1021/jp1049167.
- [380] S. ROLAND et al. (2017). Charge Generation and Mobility-Limited Performance of Bulk Heterojunction Solar Cells with a Higher Adduct Fullerene. *The Journal of Physical Chemistry C* **121** (19), 10305–10316. DOI: 10.1021/acs.jpcc.7b02288.
- [381] V. D. MICHAILETCHI (2005). Device Physics of Organic Bulk Heterojunction Solar Cells. PhD Thesis. Groningen: Groningen.
- [382] R. NAKANISHI, A. NOGIMURA, R. EGUCHI, and K. KANAI (2014). Electronic Structure of Fullerene Derivatives in Organic Photovoltaics. *Organic Electronics* **15** (11), 2912–2921. DOI: 10.1016/j.orgel.2014.08.013.
- [383] Z.-L. GUAN et al. (2010). Direct Determination of the Electronic Structure of the Poly(3-Hexylthiophene): Phenyl-[6,6]-C61 Butyric Acid Methyl Ester Blend. *Organic Electronics* **11** (11), 1779–1785. DOI: 10.1016/j.orgel.2010.07.023.
- [384] Z.-L. GUAN, J. BOK KIM, Y.-L. LOO, and A. KAHN (2011). Electronic Structure of the Poly(3-Hexylthiophene):Indene-C₆₀ Bisadduct Bulk Heterojunction. *Journal of Applied Physics* **110** (4), 043719. DOI: 10.1063/1.3626938.
- [385] D. VELDMAN et al. (2008). Compositional and Electric Field Dependence of the Dissociation of Charge Transfer Excitons in Alternating Polyfluorene Copolymer/Fullerene Blends. *Journal of the American Chemical Society* **130** (24), 7721–7735. DOI: 10.1021/ja8012598.
- [386] C. S. PONSECA et al. (2012). Ultrafast Terahertz Photoconductivity of Bulk Heterojunction Materials Reveals High Carrier Mobility up to Nanosecond Time Scale. *Journal of the American Chemical Society* **134** (29), 11836–11839. DOI: 10.1021/ja301757y.
- [387] J. KIRKPATRICK et al. (2011). Ultrafast Transient Optical Studies of Charge Pair Generation and Recombination in Poly-3-Hexylthiophene(P3ht):[6,6]Phenyl C61 Butyric Methyl Acid Ester (PCBM) Blend Films. *The Journal of Physical Chemistry B* **115** (51), 15174–15180. DOI: 10.1021/jp205731f.
- [388] I. V. VOLGIN, S. V. LARIN, E. ABAD, and S. V. LYULIN (2017). Molecular Dynamics Simulations of Fullerene Diffusion in Polymer Melts. *Macromolecules* **50** (5), 2207–2218. DOI: 10.1021/acs.macromol.6b02050.
- [389] S. TORABI et al. (2016). Deposition of LiF onto Films of Fullerene Derivatives Leads to Bulk Doping. *ACS Applied Materials & Interfaces* **8** (34), 22623–22628. DOI: 10.1021/acsami.6b05638.
- [390] J. R. LAKOWICZ and B. R. MASTERS (2008). Principles of Fluorescence Spectroscopy, Third Edition. *Journal of Biomedical Optics* **13** (2), 029901. DOI: 10.1117/1.2904580.
- [391] K. MEERHOLZ (2005). Device Physics: Enlightening Solutions. *Nature* **437** (7057), 327–328. DOI: 10.1038/437327a.

- [392] H.-K. SHIH et al. (2015). Photo-Crosslinking of Pendent Uracil Units Provides Supramolecular Hole Injection/Transport Conducting Polymers for Highly Efficient Light-Emitting Diodes. *Polymers* **7** (5), 804–818. DOI: 10.3390/polym7050804.
- [393] S. HO, S. LIU, Y. CHEN, and F. SO (2015). Review of Recent Progress in Multilayer Solution-Processed Organic Light-Emitting Diodes. *Journal of Photonics for Energy* **5** (1), 057611. DOI: 10.1117/1.JPE.5.057611.
- [394] J. LEE, H. HAN, J. LEE, S. C. YOON, and C. LEE (2014). Utilization of “Thiol–Ene” Photo Cross-Linkable Hole-Transporting Polymers for Solution-Processed Multilayer Organic Light-Emitting Diodes. *Journal of Materials Chemistry C* **2** (8), 1474–1481. DOI: 10.1039/C3TC32098G.
- [395] C. A. ZUNIGA, S. BARLOW, and S. R. MARDER (2011). Approaches to Solution-Processed Multilayer Organic Light-Emitting Diodes Based on Cross-Linking. *Chemistry of Materials* **23** (3), 658–681. DOI: 10.1021/cm102401k.
- [396] J. PARK et al. (2014). Facile Photo-Crosslinking of Azide-Containing Hole-Transporting Polymers for Highly Efficient, Solution-Processed, Multilayer Organic Light Emitting Devices. *Advanced Functional Materials* **24** (48), 7588–7596. DOI: 10.1002/adfm.201401958.
- [397] N. AIZAWA et al. (2016). Simultaneous Cross-Linking and p-Doping of a Polymeric Semiconductor Film by Immersion into a Phosphomolybdic Acid Solution for Use in Organic Solar Cells. *Chemical Communications* **52** (19), 3825–3827. DOI: 10.1039/C6CC01022A.
- [398] F. HERMERSCHMIDT et al. (2017). Influence of the Hole Transporting Layer on the Thermal Stability of Inverted Organic Photovoltaics Using Accelerated-Heat Lifetime Protocols. *ACS Applied Materials & Interfaces* **9** (16), 14136–14144. DOI: 10.1021/acsami.7b01183.
- [399] Y. BAI et al. (2016). Enhancing Stability and Efficiency of Perovskite Solar Cells with Crosslinkable Silane-Functionalized and Doped Fullerene. *Nature Communications* **7**, 12806. DOI: 10.1038/ncomms12806.
- [400] B. L. WATSON, N. ROLSTON, K. A. BUSH, L. TALEGHANI, and R. H. DAUSKARDT (2017). Synthesis and Use of a Hyper-Connecting Cross-Linking Agent in the Hole-Transporting Layer of Perovskite Solar Cells. *Journal of Materials Chemistry A* **5** (36), 19267–19279. DOI: 10.1039/C7TA05004F.
- [401] S. MIYANISHI, K. TAJIMA, and K. HASHIMOTO (2009). Morphological Stabilization of Polymer Photovoltaic Cells by Using Cross-Linkable Poly(3-(5-Hexenyl)Thiophene). *Macromolecules* **42** (5), 1610–1618. DOI: 10.1021/ma802839a.
- [402] F. OUHIB et al. (2013). Thermally Stable Bulk Heterojunction Solar Cells Based on Cross-Linkable Acrylate-Functionalized Polythiophene Diblock Copolymers. *Macromolecules* **46** (3), 785–795. DOI: 10.1021/ma3020905.
- [403] H. J. KIM et al. (2012). Solvent-Resistant Organic Transistors and Thermally Stable Organic Photovoltaics Based on Cross-Linkable Conjugated Polymers. *Chemistry of Materials* **24** (1), 215–221. DOI: 10.1021/cm203058p.

- [404] G. BROTHAS, J. FARINHAS, Q. FERREIRA, J. MORGADO, and A. CHARAS (2012). Nanostructured Layers of a New Cross-Linkable Poly(3-Hexylthiophene) in Organic Photovoltaic Cells. *Synthetic Metals* **162** (23), 2052–2058. DOI: 10.1016/j.synthmet.2012.10.007.
- [405] D. QIAN et al. (2013). Stabilization of the Film Morphology in Polymer: Fullerene Heterojunction Solar Cells with Photocrosslinkable Bromine-Functionalized Low-Bandgap Copolymers. *Journal of Polymer Science Part A: Polymer Chemistry* **51** (15), 3123–3131. DOI: 10.1002/pola.26695.
- [406] K. YAO, L. CHEN, T. HU, and Y. CHEN (2012). Photocrosslinkable Liquid-Crystalline Polymers for Stable Photovoltaics by Adjusting Side-Chains Spacing and Fullerene Size to Control Intercalation. *Organic Electronics* **13** (8), 1443–1455. DOI: 10.1016/j.orgel.2012.03.037.
- [407] X. CHEN, L. CHEN, and Y. CHEN (2013). The Effect of Photocrosslinkable Groups on Thermal Stability of Bulk Heterojunction Solar Cells Based on Donor-Acceptor-Conjugated Polymers. *Journal of Polymer Science Part A: Polymer Chemistry* **51** (19), 4156–4166. DOI: 10.1002/pola.26828.
- [408] I. MCCULLOCH et al. (2003). Polymerisable Liquid Crystalline Organic Semiconductors and Their Fabrication in Organic Field Effect Transistors. *Journal of Materials Chemistry* **13** (10), 2436–2444. DOI: 10.1039/B307764K.
- [409] S. R. FARRAR et al. (2002). Nondispersive Hole Transport of Liquid Crystalline Glasses and a Cross-Linked Network for Organic Electroluminescence. *Physical Review B* **66** (12), 125107. DOI: 10.1103/PhysRevB.66.125107.
- [410] G. LIESER et al. (2000). Ordering, Graphoepitaxial Orientation, and Conformation of a Polyfluorene Derivative of the “Hairy-Rod” Type on an Oriented Substrate of Polyimide. *Macromolecules* **33** (12), 4490–4495. DOI: 10.1021/ma9921652.
- [411] B. TANTO, S. GUHA, C. M. MARTIN, U. SCHERF, and M. J. WINOKUR (2004). Structural and Spectroscopic Investigations of Bulk Poly[Bis(2-Ethyl)Hexylfluorene]. *Macromolecules* **37** (25), 9438–9448. DOI: 10.1021/ma049006p.
- [412] B. LIU et al. (2012). High Internal Quantum Efficiency in Fullerene Solar Cells Based on Crosslinked Polymer Donor Networks. *Nature Communications* **3**, 1321. DOI: 10.1038/ncomms2211.
- [413] I. B. BERLMAN (1970). Empirical Correlation between Nuclear Conformation and Certain Fluorescence and Absorption Characteristics of Aromatic Compounds. *The Journal of Physical Chemistry* **74** (16), 3085–3093. DOI: 10.1021/j100710a012.
- [414] U. RAUSCHER, H. BÄSSLER, D. D. C. BRADLEY, and M. HENNECKE (1990). Exciton versus Band Description of the Absorption and Luminescence Spectra in Poly(*p*-Phenylenevinylene). *Physical Review B* **42** (16), 9830–9836. DOI: 10.1103/PhysRevB.42.9830.
- [415] A. MONKMAN, C. ROTHE, S. KING, and F. DIAS (2008). Polyfluorene Photophysics. In: *Polyfluorenes*. Ed. by U. SCHERF and D. NEHER. Berlin, Heidelberg: Springer, 187–225. DOI: 10.1007/12_2008_147.

- [416] J. GIERSCHNER, J. CORNIL, and H.-J. EGELHAAF (2007). Optical Bandgaps of π -Conjugated Organic Materials at the Polymer Limit: Experiment and Theory. *Advanced Materials* **19** (2), 173–191. DOI: 10.1002/adma.200600277.
- [417] L.-O. PÅLSSON and A. P. MONKMAN (2002). Measurements of Solid-State Photoluminescence Quantum Yields of Films Using a Fluorimeter. *Advanced Materials* **14** (10), 757–758. DOI: 10.1002/1521-4095(20020517)14:10<757::AID-ADMA757>3.0.CO;2-Y.
- [418] T. VIRGILI, D. G. LIDZEY, and D. D. C. BRADLEY (2000). Efficient Energy Transfer from Blue to Red in Tetraphenylporphyrin-Doped Poly(9,9-Dioctylfluorene) Light-Emitting Diodes. *Advanced Materials* **12** (1), 58–62. DOI: 10.1002/(SICI)1521-4095(200001)12:1<58::AID-ADMA58>3.0.CO;2-E.
- [419] P. K. H. HO, J.-S. KIM, N. TESSLER, and R. H. FRIEND (2001). Photoluminescence of Poly(*p*-Phenylenevinylene)–Silica Nanocomposites: Evidence for Dual Emission by Franck–Condon Analysis. *The Journal of Chemical Physics* **115** (6), 2709–2720. DOI: 10.1063/1.1372508.
- [420] K. M. HONG and J. NOOLANDI (1978). Solution of the Smoluchowski Equation with a Coulomb Potential. I. General Results. *The Journal of Chemical Physics* **68** (11), 5163–5171. DOI: 10.1063/1.435636.
- [421] K. M. HONG, J. NOOLANDI, and R. A. STREET (1981). Theory of Radiative Recombination by Diffusion and Tunneling in Amorphous Si:H. *Physical Review B* **23** (6), 2967–2976. DOI: 10.1103/PhysRevB.23.2967.
- [422] S. T. HOFFMANN et al. (2010). Triplet Energy Transfer in Conjugated Polymers. III. An Experimental Assessment Regarding the Influence of Disorder on Polaronic Transport. *Physical Review B* **81** (16). DOI: 10.1103/PhysRevB.81.165208.
- [423] R. JANKOWIAK, B. RIES, and H. BÄSSLER. Spectral Diffusion and Triplet Exciton Localization in an Organic Glass. *physica status solidi (b)* **124** (1), 363–371. DOI: 10.1002/pssb.2221240139.
- [424] B. MOVAGHAR, M. GRÜNEWALD, B. RIES, H. BASSLER, and D. WÜRTZ (1986). Diffusion and Relaxation of Energy in Disordered Organic and Inorganic Materials. *Physical Review B* **33** (8), 5545–5554. DOI: 10.1103/PhysRevB.33.5545.
- [425] R. F MAHRT and H BÄSSLER (1991). Light and Heavy Excitonic Polarons in Conjugated Polymers. *Synthetic Metals* **45** (1), 107–117. DOI: 10.1016/0379-6779(91)91850-A.
- [426] J. KURPIERS and D. NEHER (2016). Dispersive Non-Geminate Recombination in an Amorphous Polymer:Fullerene Blend. *Scientific Reports* **6** (1), 26832. DOI: 10.1038/srep26832.
- [427] T. M. BURKE, S. SWEETNAM, K. VANDEWAL, and M. D. MCGEHEE (2015). Beyond Langevin Recombination: How Equilibrium Between Free Carriers and Charge Transfer States Determines the Open-Circuit Voltage of Organic Solar Cells. *Advanced Energy Materials* **5** (11), 1500123. DOI: 10.1002/aenm.201500123.
- [428] SCHWARZ, CHRISTIAN et al. (2012). Does Conjugation Help Exciton Dissociation? A Study on Poly(P-phenylene)s in Planar Heterojunctions with C60 or TNF. *Advanced Materials* **24** (7), 922–925. DOI: 10.1002/adma.201104063.

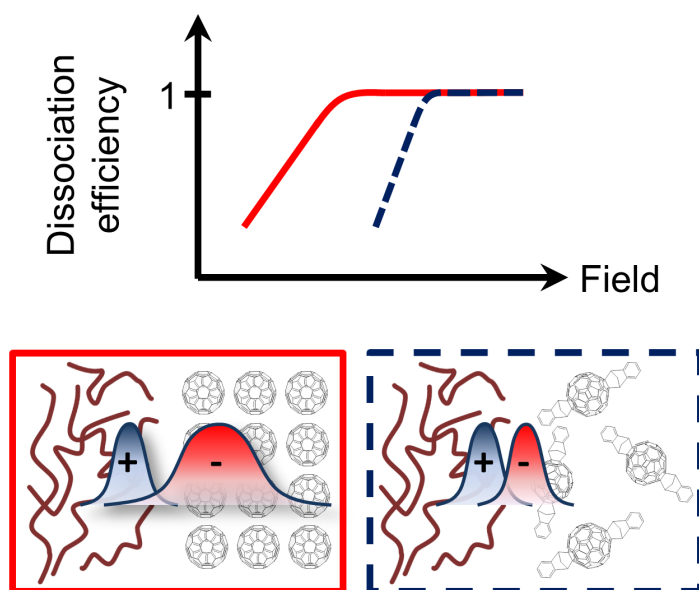
- [429] W. TRESS, K. LEO, and M. RIEDE (2012). Optimum Mobility, Contact Properties, and Open-Circuit Voltage of Organic Solar Cells: A Drift-Diffusion Simulation Study. *Physical Review B* **85** (15), 155201. DOI: 10.1103/PhysRevB.85.155201.
- [430] W. TRESS and O. INGANÄS (2013). Simple Experimental Test to Distinguish Extraction and Injection Barriers at the Electrodes of (Organic) Solar Cells with S-Shaped Current–Voltage Characteristics. *Solar Energy Materials and Solar Cells*. Dye Sensitized Solar Cells, Organic, Hybrid Solar Cells and New Concepts **117**, 599–603. DOI: 10.1016/j.solmat.2013.07.014.
- [431] A. PICKETT et al. (2018). Correlating Charge Transport with Structure in Deconstructed Diketopyrrolopyrrole Oligomers: A Case Study of a Monomer in Field-Effect Transistors. *ACS Applied Materials & Interfaces* **10** (23), 19844–19852. DOI: 10.1021/acsami.8b04711.

Part II.

Publications

9

Does Electron Delocalization Influence Charge Separation at Donor-Acceptor Interfaces in Organic Photovoltaic Cells?



Frank-Julian Kahle, Christina Saller, Selina Olthof, Cheng Li, Jenny Lebert, Sebastian Weiß, Eva M. Herzig, Sven Hüttner, Klaus Meerholz, Peter Strohrriegl, and Anna Köhler

Published in
J. Phys. Chem. C **2018**, *122*, 21792-21802.
(DOI: 10.1021/acs.jpcc.8b06429)

Reprinted with permission from *J. Phys. Chem. C* **2018**, *122*, 21792-21802.
Copyright ©(2018) American Chemical Society.

Does Electron Delocalization Influence Charge Separation at Donor–Acceptor Interfaces in Organic Photovoltaic Cells?

Frank-Julian Kahle,[†] Christina Saller,[‡] Selina Olthof,[§] Cheng Li,[‡] Jenny Lebert,^{||} Sebastian Weiß,^{||} Eva M. Herzig,[⊥] Sven Hüttner,[‡] Klaus Meerholz,[§] Peter Strohrriegl,[‡] and Anna Köhler^{*,†}

[†]Soft Matter Optoelectronics, Department of Physics, University of Bayreuth, 95447 Bayreuth, Germany

[‡]Macromolecular Chemistry I, Department of Chemistry, University of Bayreuth, 95447 Bayreuth, Germany

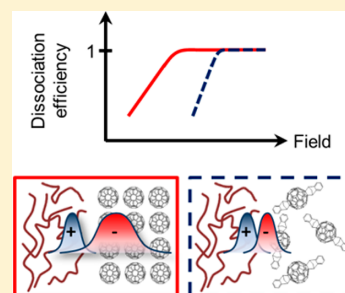
[§]Department of Chemistry, University of Cologne, 50939 Cologne, Germany

^{||}Herzig Group, Munich School of Engineering, Technical University Munich, 85748 Garching, Germany

[⊥]Dynamics and Structure Formation – Herzig Group, Department of Physics, University of Bayreuth, 95447 Bayreuth, Germany

Supporting Information

ABSTRACT: We use bilayer devices with a series of three fullerene acceptors differing in order and intermolecular coupling to systematically explore the influence of electron delocalization in the acceptor phase on the dissociation efficiency of charge transfer states. Structural information from GIWAXS measurements is combined with the results of optical and electrical characterization as well as theoretical modeling. Our results indicate that an increase in CT-dissociation efficiency is directly coupled to an enhancement in electron delocalization that is particularly prominent for C₆₀ which forms crystalline domains. Therefore, our results substantiate the concept of delocalization of electrons taking a positive role in the charge separation process, and of acceptor crystallinity being crucial in this respect.



1. INTRODUCTION

Organic solar cells (OSCs) have been an interesting topic to many research groups for decades now and especially gained remarkable attention again in recent years, as devices based on polymeric donors and small molecular acceptors have eventually reached efficiencies of more than 10% and even up to 14%.^{1–5} Much effort has been put into molecular design and device optimization, particularly with respect to layer structure and morphology. Yet, the fundamental mechanisms enabling such high efficiencies are still not fully understood. While the charge extraction process after the initially generated electron–hole (e–h) pairs are separated into free charge carriers is fairly well investigated,^{6–11} the exact mechanism by which Charge Transfer (CT) states are split at the donor–acceptor interface is still under debate. These states can be described as Coulombically bound (and therefore correlated) holes and electrons residing on neighboring donor and acceptor sites, respectively. In a classical picture, the Coulomb binding energy of a CT state would be around 500 meV,^{12,13} assuming a typical dielectric constant of 3–4 and a nearest neighbor separation of 1 nm, which is far above the available thermal energy of about 25 meV at room temperature. Nevertheless, there are reports showing that internal quantum efficiencies approaching 100% are possible in some organic solar cell systems,^{14,15} raising the question how the Coulomb barrier can actually be overcome.

Several factors influencing the efficiency of CT-state dissociation have been proposed and studied quite extensively to date, including aspects like mobility,^{16,17} entropy,^{12,18–20} driving force,^{12,21–23} and excess energy.^{14,21,24} Yet, another factor that has recently become a hot topic is the role of delocalization in the dissociation process of CT states, especially with respect to the electron in the acceptor phase.^{25–30} The basic idea behind this concept is that delocalization implies a reduction of the CT binding energy and an easier separation of electron and hole over larger distances.^{31,32} For holes being transported along a polymer chain, this is comparably easy to understand, because a high coupling strength along the conjugated segments of a polymer chain implies a larger bandwidth associated with an exciton or a charge carrier, meaning that such an excitation, be it an exciton or a charge carrier, can be coherently coupled (and thus delocalize) over several repeat units.³² A similar behavior is not so obvious for small molecular acceptors as the coupling between individual adjacent molecules is expected to be smaller (even if they formed a molecular crystal).³³ This in turn results in a bandwidth that is usually smaller than or comparable to the energetic disorder in the system. Consequently, transport in these systems is rather expected

Received: July 13, 2018

Revised: September 4, 2018

Published: September 4, 2018

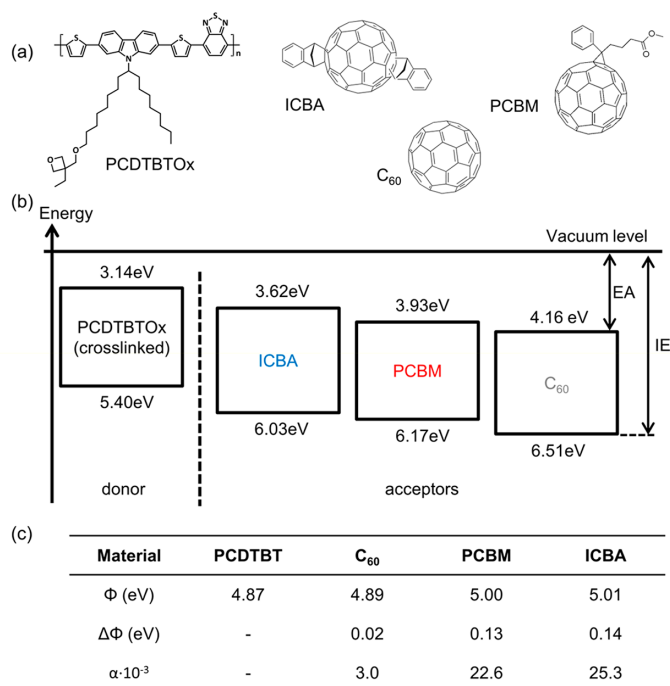


Figure 1. (a) Structure formula of the cross-linkable PCDTBTOx derivative (donor) as well as the structures of the three fullerene acceptors used in the bilayer solar cells. (b) Energy level diagrams for the donor and the three investigated fullerene acceptors. The values for ionization energies (IE) and electron affinities (EA) were measured via UPS and IPES, respectively. (c) Work functions Φ and calculated energy level displacement $\Delta\Phi$ in bilayer solar cells as determined via Kelvin-Probe measurements. α denotes the fractional interfacial dipole strengths calculated from $\Delta\Phi$ as detailed in the text.

to be incoherent.³⁴ While delocalization of the hole in the donor has been shown in several conjugated polymer systems as well as in crystalline donor materials and is accepted to affect the CT-dissociation efficiency,^{25,32} there is no full consensus up to now, whether electron delocalization is of similar significance. Some groups claim that delocalization of the electron in the acceptor is less important than of the hole in the donor,^{25,26} of equal importance,^{11,27,28,35,36} or even more important.²⁹ Others in turn state that only one of the components needs to feature a certain degree of delocalization.³⁰ A very recent theoretical study on the general effect of delocalization on the barrier height for charge separation by Gluchowski et al. even suggested that, from a thermodynamic point of view, delocalization would even increase the dissociation barrier.³⁷

With our current work, we aim to contribute to the clarification of this issue. We investigated bilayer solar cells as model systems to study CT characteristics and dissociation at a well-defined interface, thereby reducing morphology related effects such as bimolecular recombination, percolation problems, or varying domain sizes as present in bulk heterojunction systems. For the donor material, we chose a cross-linkable derivative of the well-known polymer PCDTBT for all investigated samples (PCDTBTOx, Figure 1a). As the functional group for cross-linking is attached to the side chain, we expect the properties of the main chain to remain unaffected.³⁸ The use of a cross-linkable donor allowed us to easily fabricate multilayer devices from solution without having to use orthogonal solvents. Furthermore, cross-linking the

donor layer effectively reduces interdiffusion of the subsequently deposited acceptor.³⁹ This results in a better defined donor/acceptor interface so that the layer structure is actually closer to an actual bilayer system, which facilitates theoretical modeling approaches. The use of the amorphous polymer PCDTBTOx as a donor additionally has the advantage that energy levels are likely to change little when in contact with different acceptor materials.⁴⁰

As acceptors we chose a series of three fullerenes (C₆₀, PCBM, ICBA) that feature a varying number of additional covalent bonds to the cage and different degrees of crystallinity and order. This should vary the degree of intermolecular coupling between acceptor sites and therefore also the degree of delocalization within the acceptor phase,^{27,29,41} which is also reflected in different bulk electron mobilities of the respective materials.²⁷ Furthermore, the chosen acceptors feature an energy level cascade (Figure 1b) which allows tuning the CT energy of the bilayer system.²¹

By performing photophysical, electrical, and structural investigations and combining the results with theoretical modeling, we find that higher structural order and intermolecular coupling in the acceptor phase substantiate the effect of delocalization of the CT state that enhances the CT-dissociation efficiency. A significant reduction of the effective mass of the CT state due to electron delocalization in the acceptor is found mainly with C₆₀ which forms crystalline domains.

II. EXPERIMENTAL SECTION

Materials and Sample Preparation. Cross-linkable PCDTBTOx was synthesized by C. Saller. The detailed synthesis route is given in the [Supporting Information](#). Molybdenum trioxide (MoO_3), Bathocuproine (BCP), and ICBA were purchased from Sigma-Aldrich. The product number of ICBA is 753955, and it contains a mixture of isomers. C_{60} and PCBM were purchased from ADS and TCI, respectively. All materials were used as received.

For solar cell measurements, we used cleaned patterned ITO glass substrates that were additionally covered with a patterned layer of photoresist to avoid spurious electrical breakdown effects at the electrode edges. After treating the substrates for 2 min inside an oxygen plasma chamber, a 6 nm layer of MoO_3 is vapor deposited using a shadow mask. After that, a 14 nm layer of PCDTBTOx is spin-cast on top inside a glovebox from a 3 g/L chlorobenzene solution (99.8% anhydrous, oxygen free). Cross-linking was then performed by cationic ring opening polymerization. Therefore, samples were transferred to an argon atmosphere and exposed to trifluoroacetic acid (TFA) vapor for 15 min at 100 °C. After this treatment, the samples were transferred to a vacuum chamber and kept in vacuum for 30 min at 90 °C, in order to remove possible volatile remnants of TFA. Subsequently, a 30 nm acceptor layer was deposited either by vacuum deposition (C_{60}) or by spin-coating (PCBM, ICBA) from a 5 g/L chloroform solution (99.8% anhydrous, oxygen free). In the end, BCP and Al are evaporated on top as a cathode. Samples for electroabsorption measurements were prepared the same way, but encapsulated to be measured under ambient conditions. In the case of the photoelectron spectroscopy and Kelvin-Probe measurements, samples were also prepared according to the above-mentioned protocol but without a cathode and with thinner acceptor layers.

For GIWAXS measurements, we used Si wafers as substrates. These were cleaned for 15 min in a piranha etch bath heated to 80 °C and subsequently rinsed with deionized water to remove acidic remnants. After cleaning, a 30 nm layer of PCDTBTOx was spin-cast on top from a 6 g/L chlorobenzene solution (99.8% anhydrous, oxygen free) and cross-linked according to the procedure described above. Following this, a 30 nm acceptor layer was deposited again as described above.

GIWAXS. Grazing incidence wide-angle X-ray scattering (GIWAXS) was carried out at the Sirius beamline of Soleil at 8 keV and a sample detector distance of 32.5 cm using a Pilatus 1M detector. The incident angle was set at 0.18° to penetrate the full bilayer. The data is flattened by an exponential background subtraction, and cuts are obtained using the GIXSGUI software.⁴²

Photoelectron Spectroscopy (PES) /Kelvin Probe. UV-photoelectron spectroscopy (UPS) measurements were done in ultrahigh vacuum using a helium based monochromatic microwave UV lamp (VUV 5000, Scienta Omicron). The measurements were performed using the much weaker He I β excitation at $h\nu = 23.087$ eV. This was done in order to minimize the light intensity illuminating the samples, which could lead to the creation of a photovoltage at the donor/acceptor interface and an unwanted shift of the vacuum levels. Furthermore, after the UPS measurements, the work functions were checked via a UHV based Kelvin-Probe system (McAllister KP6500) in the dark; this showed excellent agreement with the UPS measurements (within 20–40

meV). Finally, the LUMO levels were probed via inverse photoelectron spectroscopy using a low energy electron gun (ELG-2, Kimball) and a band-pass photon detector (IPES2000, Omnicvac).

Photocurrent and Electroluminescence Spectroscopy. External Quantum Efficiency (EQE) and current voltage (*IV*) measurements were performed under short circuit conditions using either a Keithley source-measure unit (SMU 238) and monochromatic illumination from a 450 W xenon lamp or, for more sensitive measurements, a Lock-In (SR830) at a reference frequency of 130 Hz and monochromatic illumination from a 150 W tungsten lamp (Osram). The sample was kept in an appropriate vacuum condition sample holder at room temperature. Absorption profiles used to convert EQE to IQE were calculated via the transfer matrix algorithm using the code provided online free of charge by McGehee and co-workers.⁴³ *n* and *k* values for the calculation were taken either from the library provided by McGehee and co-workers or from the literature.^{43–48}

In order to convert voltage-dependent measurements of the EQE into a field-dependent data set, the internal field in the active layer was taken as $(V_{\text{bi}} - V)/d$, where *d* is the thickness of the active layer, *V* is the applied voltage, and V_{bi} is the built-in voltage. The latter was approximated by the compensation voltage, i.e., the voltage at which the photocurrent vanishes.⁴⁹ The photocurrent is calculated from the difference between the current with and without illumination.

Electroabsorption. The light source was installed within a monochromator illuminator (Oriel). The light going through the monochromator (SPEX 1681B, Horiba Scientific) illuminated the device and was reflected back from the aluminum electrode onto a photodiode (HUV-4000B, EG&G Judson). A dual channel lock-in amplifier (SR 830 from Stanford Research Systems) was used to bias the device with a DC and an AC voltage and monitored the AC amplitude of the Electroabsorption (EA) signal from the photodiode. In parallel, the DC amplitude of the EA signal was recorded with a digital multimeter (HP34401A). For all the electrical experiment, the ITO electrode was connected to the ground and external voltages were applied to the Al electrode.

III. RESULTS

The role of electron delocalization in the CT-dissociation process will be inferred from the analysis of external and internal quantum efficiency spectra as well as theoretical modeling of field-dependent *IV* measurements. For a profound interpretation of the respective data, some fundamental information about the investigated systems is crucial. This includes knowledge about energy levels, interface energetics, and structural properties of the samples.

Energetics and Structural Properties. In order to address energetics, we performed UPS, IPES, and Kelvin-Probe measurements. The resulting energy levels for ionization energy (IE) and electron affinity (EA) for PCDTBTOx and the three acceptors C_{60} , PCBM, and ICBA are depicted in the schematic energy level diagram in [Figure 1b](#). For further details regarding the photoemission spectra, the reader is referred to the [Supporting Information](#). As expected and in agreement with the literature, we find a downward energy level cascade, i.e., increasing EA values, in the series ICBA > PCBM > C_{60} .^{50–52} The same trend is observed for the IE. The electrical band gap E_g of our donor polymer is around 2.3 eV.

Work function values Φ and interfacial vacuum level shifts $\Delta\Phi$ determined from Kelvin-Probe measurements (Figure S3) are summarized in the table in Figure 1c. We find that, within the accuracy of the measurement (10–20 meV, see SI), the work function of PCDTBTOx did not change when covered with C_{60} , indicating vacuum level alignment. In contrast to this, work function shifts of 130 and 140 meV for PCBM and ICBA are observed, respectively, indicating that Fermi-level pinning at the polymer/fullerene interface occurs for a work function of the fullerene film below ~ 4.9 eV. This implies the presence of ground state interfacial dipoles for PCBM and ICBA. The corresponding fractional interfacial dipole strengths α can be calculated from the measured vacuum level shifts $\Delta\Phi$ using the Helmholtz equation for interfacial dipoles. The strength of an interfacial dipole α can be calculated from $\epsilon_0\epsilon_r\Delta\Phi = p\sigma$, where $\Delta\Phi$ is measured in eV, $p = \alpha er$ is the dipole moment, and $\sigma = \frac{1}{r^2}$ the area density of dipoles. This yields $\alpha = \epsilon_0\epsilon_r\frac{\Delta\Phi}{e}$. Taking typical values $\epsilon_r = 3.5$ and $r = 0.92$ nm, we arrive at the α -values given in Figure 1c, which is $3 \cdot 10^{-3}$, $23 \cdot 10^{-3}$, and $25 \cdot 10^{-3}$ for C_{60} , PCBM, and ICBA, respectively.³² We attribute the reduced interfacial dipole for the C_{60} to its higher symmetry.⁵³

To characterize the order present in the three different types of fullerene top layers, grazing incidence wide-angle X-ray scattering (GIWAXS) experiments were carried out. This scattering technique is well suited for the examination of statistically averaged information on nearest neighbor ordering in thin films or thin multilayers. While highly ordered crystal structures will result in sharp strong peaks, such peaks will generally broaden with increasing disorder since the average separation of the scattering objects becomes less defined.

The GIWAXS pattern of the polymer layer shows no significant order throughout the film volume which is expected for the disordered PCDTBTOx bottom layer. The observed peaks in the 2D data can therefore be attributed to the respective fullerene layers. For all three cases, isotropic powder diffraction rings are observed, indicating no preferential orientation for all fullerenes. Figure 2 shows the azimuthally

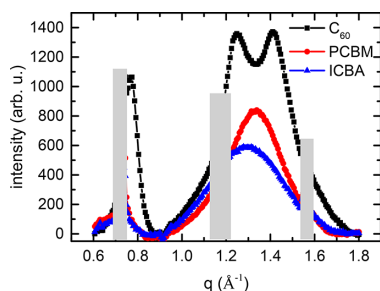


Figure 2. Azimuthally integrated GIWAXS cuts of C_{60} (black), PCBM (red), and ICBA (blue) layer on PCDTBTOx. Background signals not arising from the samples are shielded by the gray boxes to improve clarity of the data.

integrated intensity from 0° to 90° with increasing scattering vector q . The highest order is found for the evaporated C_{60} top layer. Peaks at $q = 0.77$, 1.25 , and 1.41 \AA^{-1} are found in good agreement with the literature for C_{60} in polycrystalline fcc configuration.^{54,55} For PCBM we find broad scattering rings at $q = 0.70$ and 1.33 \AA^{-1} , indicating short-range order but no

presence of larger crystals in agreement with the literature.⁵⁶ The scattering signal of the ICBA/PCDTBTOx bilayer also shows such a nearest neighbor ordering but is even broader in width than PCBM, indicating that the statistically averaged separation of ICBA is less well-defined than for PCBM. Additionally, the peak center of the main peak shifts to slightly smaller q -value (1.29 \AA^{-1}), implying an on average larger separation between ICBA than PCBM molecules. Since the fullerene top layers are prepared with the same thickness (30 ± 1 nm), the decreasing intensity of the signals shown in Figure 2 further indicates that the amount of ordered fullerenes in the layer decreases from C_{60} via PCBM to ICBA. These observations regarding crystalline order and average intermolecular spacing suggest that the strength of the intermolecular coupling within the acceptor phase is likely to decrease in the series $C_{60} > \text{PCBM} > \text{ICBA}$, as the electronic coupling between adjacent fullerenes decreases exponentially with increased cage–cage distance.^{27,29,57–59}

Photocurrent Spectroscopy and Charge Transfer

States. Having clarified fundamental properties of the used materials and material combinations, we now turn to the study of organic solar cells. Figure 3a exemplarily shows the EQE spectra of a bilayer device with a C_{60} acceptor layer on top of the cross-linked PCDTBTOx donor, together with spectra of single layer cells comprising only the donor or the acceptor (solid lines). The EQE was measured under short circuit conditions. A more detailed view of the sub-band-gap region relevant to direct CT absorption is shown in Figure 3b for all the different acceptors. In order to get a qualitative idea which of the two components contributes to the EQE at which energy, the absorption for the PCDTBTOx and C_{60} layers is also shown (dashed lines). Absorption profiles for PCDTBTOx and the fullerene were calculated using the transfer matrix algorithm.⁴³ n and k values for the different layers of the solar cell were taken from the literature.^{43–48} The accessible range of these values limited the calculation down to about 1.55 eV. The respective spectra for PCBM and ICBA can be found in the Supporting Information (Figure S4). The qualitative aspects are the same for all three fullerenes.

In Figure 3a, we see that the donor polymer itself (gray line) hardly contributes to the EQE, indicating that excitons are not split efficiently within the bulk of the donor. In contrast to that, single layer devices of C_{60} (dark red line) show a considerable EQE for energies above 2.25 eV, which is identified as the autoionization threshold of fullerenes, where bulk CT states can be split.^{60,61} This contribution is also present in the bilayer devices (light red line). The autoionization efficiency is smaller for PCBM and ICBA (see the Supporting Information). Below 2.25 eV, there is no significant intrinsic exciton dissociation in the neat materials, as can be inferred from the EQE of single layer devices. Nevertheless, we observe a considerable EQE in this region in the case of bilayer devices. Therefore, the EQE below 2.25 eV can be assigned to dissociation at the donor–acceptor interface.

From Figure 3b, we see that the overall EQE increases in the order $\text{ICBA} < \text{PCBM} < C_{60}$. To account for differences in absorption or reflection, we calculated the internal quantum efficiency (IQE) (Figure 3c). For this calculation, we were limited by the accuracy of the literature values for n and k from which absorption profiles were derived, so a reliable IQE could only be obtained down to about 1.85 eV. We still find the same trends as for the EQE, indicating that the observed differences

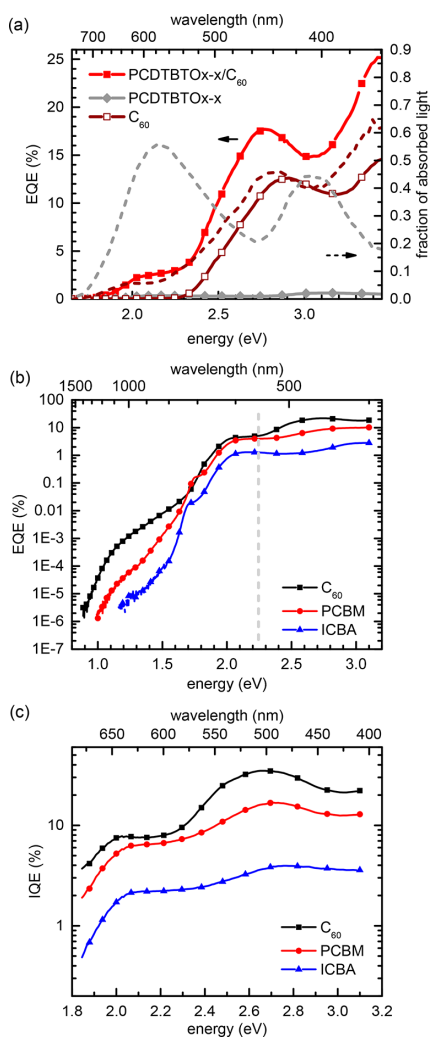


Figure 3. (a) Left axis: EQE of a PCDTBTOx/ C_{60} bilayer solar cell (red filled squares) along with the EQE of single layer devices of the pristine materials PCDTBTOx (gray filled diamonds) and C_{60} (dark red open squares). Right axis: Simulated fraction of absorbed light of the respective layer in a bilayer device using the transfer matrix algorithm (dashed lines). (b) Comparison of the EQE of bilayer devices with C_{60} (black squares), PCBM (red dots), or ICBA (blue triangles) on top of a cross-linked PCDTBTOx layer. The gray dashed line separates the different regions discussed in the text. (c) IQE of the devices in (b). It was calculated using the absorption as obtained from the transfer matrix algorithm.

may indeed be related to differences in dissociation efficiency at the donor–acceptor interface.

Another important aspect that needs to be addressed in addition to film morphology and photoinduced charge generation is the degree of CT-state recombination. For this reason, we performed intensity-dependent I – V measurements from which we extracted the Fill Factor (FF) as a function of irradiation intensity. According to Hahn et al., this provides information about the character and degree of recombination in organic solar cells.^{62,63} We measured I – V curves under

monochromatic excitation at four different energies, two above and two below the autoionization threshold of the fullerenes (1.91 eV, 2.14 eV, 2.76 eV, 3.54 eV). Exemplary I – V characteristics measured at $7 \frac{\text{mW}}{\text{cm}^2}$, that is, the intensity used in the EQE experiments, as well as the FF as a function of irradiation intensity are shown in Figure 4a,b for an excitation

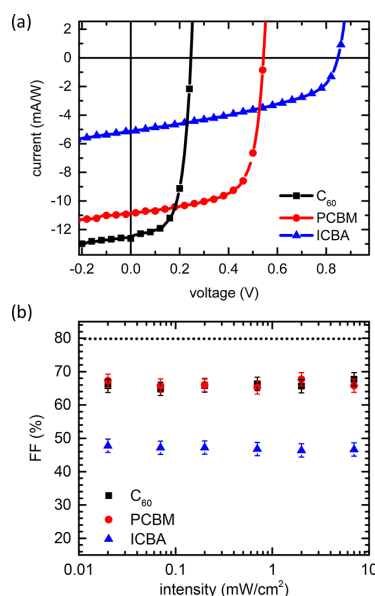


Figure 4. (a) Comparison of monochromatic current–voltage (I – V) characteristics of bilayer solar cells with varying acceptors on top of the cross-linked PCDTBTOx layer. The excitation energy was 2.14 eV. (b) Fill factor (FF) as a function of illumination intensity for the same devices as in (a). The excitation energy was also 2.14 eV.

energy of 2.14 eV. The corresponding graphs for the other excitation energies can be found in the Supporting Information (Figures S6 and S7). The dotted line in Figure 4b indicates the maximum obtainable fill factor according to the Shockley–Queisser limit, in agreement with simulations by Bartesaghi et al.⁶⁴ The difference to the FF measured in the limit of the lowest intensity can be ascribed to geminate recombination. The FF is the same for C_{60} and PCBM (66%), while it is overall smaller for ICBA (47%). The same behavior is also observed for excitation above 2.25 eV (Figure S7). The fact that both C_{60} and PCBM show the same FF implies similar recombination rates k_{rec} in these materials. Recalling that the IQE features an overall increase in the series ICBA < PCBM < C_{60} and taking into account that $\text{IQE} = k_{\text{diss}} / (k_{\text{diss}} + k_{\text{rec}})$, where k_{diss} denotes the rate of CT dissociation, this clearly proves a higher dissociation efficiency in C_{60} .

All I – V characteristics show no s-shape, as well as an increasing V_{OC} in combination with decreasing I_{SC} in the order $C_{60} \rightarrow \text{PCBM} \rightarrow \text{ICBA}$, irrespective of excitation energy (cf. also Figure S6). The trend in V_{OC} is consistent with the trend in built-in voltage as inferred from dark I – V measurements (Figure S6) and voltage-dependent electroabsorption (Figure S10b). The absence of an s-shape evidences that there are no injection or extraction problems in our devices.^{65,66} In terms of the FF, we find no dependence on the excitation energy over 3

orders of magnitude, indicating that nongeminate recombination processes are indeed absent.

Electroabsorption Spectroscopy. To gain further insight into the character of the CT states present in the different systems, we additionally performed electroabsorption spectroscopy on bilayer devices. In this technique, one applies a varying electric field $F = F_{DC} + F_{AC} \cos(\omega t)$ to the sample and measures the change in absorption $\Delta\alpha$ due to the quadratic Stark effect and the nonzero second-order term of the linear Stark effect.^{67–70} We measured electroabsorption from about 3.2 eV down to 1.2 eV to cover the full range of excitation, from bulk CT states in the fullerenes above 2.0 eV to the interfacial CT states in the sub-band-gap region.⁶¹ Figure 5

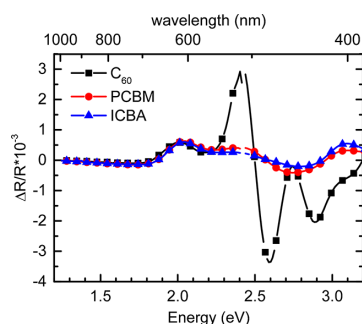


Figure 5. Electroabsorption spectra of bilayer devices using C_{60} (squares), PCBM (dots), or ICBA (triangles) as acceptor.

shows the spectra for all three acceptors in a bilayer device with PCDTBTOx measured at the same internal field. We find a pronounced peak at around 2.0 eV that is present in all three spectra. By comparison to electroabsorption measurements on pristine PCDTBTOx (Figure S10c), we can assign this peak to the polymer. Furthermore, we observe a second pronounced peak at around 2.4 eV that is very prominent for C_{60} and decreases significantly when going to PCBM and ICBA (For a more detailed view, see Figure S10a in the Supporting Information). This signal is known to be due to a delocalized CT state in the bulk of the fullerene phase,^{60,61} with a dipole moment and polarizability of 22.9 D and 880 Å³, respectively, for C_{60} .⁶¹ The features at higher energies (>2.4 eV) are related to higher energy CT states in the fullerenes and PCDTBTOx and will not be discussed here. For PCBM and ICBA, the signature of the delocalized CT state is also expected to be around 2.4 eV.^{60,71} As the contribution of the polymer at 2.0 eV is the same for all bilayer samples while the peak height at 2.4 eV decreases, we conclude that both dipole moment and polarizability increase in the order $C_{60} > PCBM = ICBA$. Since dipole moment and polarizability correlate with the extent of an excited state, this implies that the wave function delocalization is significantly larger in C_{60} compared to PCBM and ICBA.

Analysis of the Dissociation Efficiency. To further explore the underlying effects that can account for the observed increase in EQE and IQE in the series $ICBA < PCBM < C_{60}$, we now address the dissociation efficiency of the CT states in the different systems in more detail by analyzing field-dependent IV data in terms of the effective mass model.^{31,32} To this end, we convert the IV curves we had measured under monochromatic excitation (see above) into EQE as a function of internal electric field as detailed in the

Experimental Section. An example of a converted data set of EQE as a function of the internal electric field is shown in Figure 6a for an excitation energy of 2.14 eV. The data were

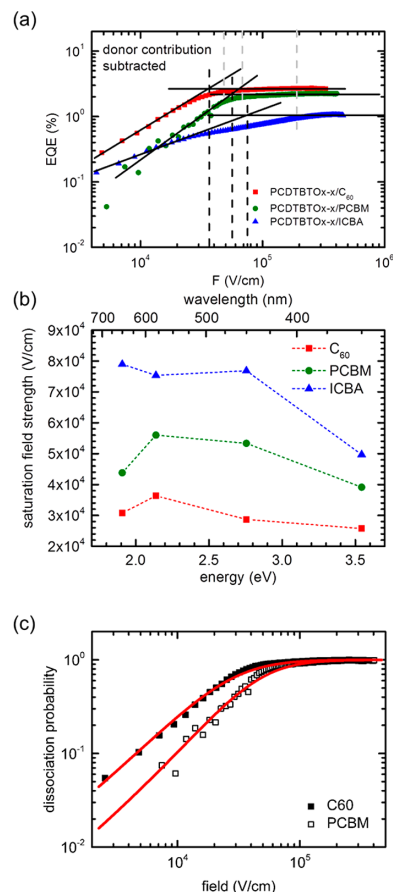


Figure 6. (a) EQE of bilayer devices with different acceptors as a function of the internal electric field. The excitation energy is 2.14 eV, i.e., below the autoionization threshold of the fullerenes. The data were corrected for an intrinsic contribution from CT dissociation within the donor. Black solid lines correspond to the tangents to the low and high field regime, respectively, with the intersection giving F_{sat} (black dashed lines). Gray dashed lines correspond to the F_{sat} values determined from the alternative 90% method. (b) F_{sat} as a function of excitation energy for all three acceptors. (c) Dissociation probability of a CT state in PCDTBTOx/ C_{60} (squares) and PCDTBTOx/PCBM (open squares) bilayer solar cells as a function of the internal electric field. Solid red lines correspond to the simulations according to the effective mass model taking interfacial dipoles into account. The used parameter set is summarized in Table 1.

corrected for the intrinsic contribution of the donor. This correction is only important for ICBA due to its low efficiency. For further details, the reader is referred to the Supporting Information. The key parameter derived from these data, which is accessible directly from experiment and which is a measure of the ease of CT dissociation at the donor–acceptor interface, is the so-called saturation field strength F_{sat} .³² We derive it from the intersection of the tangents to the

photocurrent in the regimes of low and high electric field (that is the saturation regime) in a log–log plot, respectively (Figure 6). Using an alternative approach by defining F_{sat} as the value where the EQE reached 90% of the plateau value, we qualitatively get the same results, though the exact values differ, especially for ICBA (Figure S9).

The saturation field strengths resulting from the above-mentioned tangent method are displayed in Figure 6b as a function of excitation energy. We observe no distinct trend with respect to excitation energy. However, the overall F_{sat} increases in the order $C_{60} < \text{PCBM} < \text{ICBA}$. In order to analyze the differences in dissociation efficiency implied by the variation of F_{sat} in more detail, we apply the effective mass model under consideration of interfacial dipoles as described in refs 31 and 32. The basic idea is that an electron can jump from site to site, perpendicular to the interface, and that, within its lifetime, it may take several jump attempts. Key features of the model are that the potential at the interface may be screened via interfacial dipoles,^{12,72} thereby facilitating CT dissociation, and that additional kinetic energy due to quantum mechanical zero point oscillations may reduce the binding energy of the CT state. This energy varies with the degree of delocalization of the electron or hole and is parametrized via an effective mass of the electron–hole pair. The results of the simulation are shown in Figure 6c, and the parameters set used is summarized in Table 1.

Table 1. Parameter Set That Is Used in the Simulations of Field-Dependent Data According to the Effective Mass Model under Consideration of Interfacial Dipoles^a

material	fixed input parameter		τ_0/ns	derived parameter	fitting parameter
	$\alpha \cdot 10^{-3}$	$\mu/\frac{\text{cm}^2}{\text{V s}}$			
C_{60}	3.0	$5 \cdot 10^{-2}$	25	$\tau_0 \nu_0 \cdot \exp(-2\gamma r)$	m_{eff}
PCBM	22.6	$2 \cdot 10^{-3}$	25	780	0.22

^aThe different quantities are explained in the main text.

From Kelvin-Probe measurements, we know that, for PCBM and ICBA, ground state interfacial dipoles α are present, while no such dipole is observed for C_{60} when in contact with PCDTBTOx (cf. Figure 1 and Figure S3). For the mobility, we used literature values and, for the lifetime, we assumed a typical value of 25 ns for the CT states of C_{60} and PCBM.^{73–79} We chose the same lifetime for both of them, as our intensity-dependent measurements of the FF indicated that the recombination rates should be comparable. The product of hopping rate ν_0 and lifetime τ was calculated using the Einstein relation between diffusivity and lifetime $eD = \mu k_B T$, and considering that in a 3D system, the diffusivity is given by $D = \frac{1}{6} a^2 \nu_0 \exp(-2\gamma r)$, where a is the jump distance and γ denotes the inverse localization length.³¹ Using this parameter set for our simulations, we find that a significantly smaller effective mass needs to be used for C_{60} than for PCBM to reproduce the field dependence of the photocurrent (Figure 6c). Notably, the data could only be reproduced with a reasonable mobility and lifetime when taking differences in m_{eff} into account, meaning that mobility and CT lifetime do not suffice to explain the observed difference in dissociation probability. For ICBA, it was not possible to reproduce the experimentally measured field-dependent data. We attribute

this to the overall low EQE in the samples with ICBA, which makes correction for the intrinsic donor contribution difficult and unreliable. Nevertheless, the observed trend in saturation field strengths in combination with our analysis of the effective mass in C_{60} and PCBM and the observation of weaker intermolecular coupling increased recombination and a fractional interfacial dipole comparable to PCBM ($\alpha = 25.3 \cdot 10^{-3}$) implies a stronger localization in ICBA than in C_{60} or PCBM. We recall that the effective mass is a parameter that is introduced to quantify electronic coupling within the geminately bound electron–hole pair comprising the CT state. With respect to the hole on the polymer chain, it comprises the coupling mainly within a conjugated segment of the chain. Regarding the electron in the fullerene phase, a lower effective mass (of the e–h pair) suggests a larger coherent spread of the electron wave function over adjacent fullerenes. Transport of the charges away from the interface, however, proceeds by noncoherent hopping between the sites over which the charge wave functions spread. In passing, we note that there was no need to include any additional doping effects to obtain a reasonable fit to the experimental data, indicating that the actual diffusion of fullerenes into the polymer layer is small.

IV. DISCUSSION

A currently intensively discussed question is the issue whether delocalization of the electron in the usually molecular acceptor phase contributes significantly to the dissociation of an interfacial electron–hole pair. Whereas for a hole, coherent wave function delocalization along a conjugated polymer backbone is undisputed, at least within a conjugated segment, it is not a priori obvious whether there is significant coherent delocalization of an electron across several adjacent molecules, nor, whether this is required for efficient electron–hole separation. Clearly, such electronic coupling will depend on the degree of order within the acceptor phase. In an earlier study on the impact of hole delocalization, we combined differently conjugated poly(*p*-phenylene) polymers with an identical acceptor (C_{60}) in a bilayer setup.³² Here, we used a similar approach to address the question of the impact of electron delocalization, that is combining a constant donor (PCDTBTOx) with a series of fullerenes that we expected to vary in intermolecular coupling strength. The cross-linkable donor allows for deposition of C_{60} by evaporation as well as of PCBM and ICBA by solution coating.

The GIWAXS measurements of Figure 2 indicate that the three fullerenes indeed form an acceptor set with increasing intermolecular coupling in the order $\text{ICBA} < \text{PCBM} < C_{60}$, in agreement with our expectation.^{27,29} This is further confirmed by the increase in electron mobility from about $10^{-5} \frac{\text{cm}^2}{\text{V s}}$ for ICBA⁷⁴ over $2 \cdot 10^{-3} \frac{\text{cm}^2}{\text{V s}}$ for PCBM^{74,75} to $5 \cdot 10^{-2} \frac{\text{cm}^2}{\text{V s}}$ for C_{60} ,⁷³ by the higher autoionization efficiency of C_{60} compared to PCBM and ICBA for energies above 2.3 eV (cf. Figure S4),⁶⁰ and by the electroabsorption measurements of Figure 4.

The EQE and IQE data in Figure 3 clearly indicate an increased photocurrent from the dissociation of interfacial CT states in the order $\text{ICBA} < \text{PCBM} < C_{60}$. The pertinent question is, whether this is mainly merely the result of the increasing electron mobility, and thus of the mobility–lifetime product, along the series, or whether an increasing wave function delocalization of the interfacial CT state along the

series plays a significant role in this higher photocurrent. Mobility affects the EQE in different ways. For example, mobility imbalance can lead to space charge buildup and thus increased bimolecular recombination, which manifests itself in an s-shape in the I - V curve.^{65,66} Even though hole mobility of PCDTBT is merely in the range of $3 \cdot 10^{-5}$ to $9 \cdot 10^{-5} \frac{\text{cm}^2}{\text{Vs}}$,⁸⁰ i.e., well below that of PCBM and C_{60} , mobility imbalance and bimolecular recombination does not play a role in our samples, as evidenced by the absence of an s-shape in the I - V curves (Figure 4a). This is because we accounted for the difference in mobilities by using a donor layer (14 nm) with only half the thickness of the acceptor (30 nm),^{62,66} incorporated appropriate transport layers at the electrodes (see the Experimental Section), and used thin layers, which has the further advantage of reducing nongeminate as well as secondary geminate recombination.⁶² We recall that the fill factor was independent of excitation intensity for all three fullerenes, suggesting that bimolecular recombination is indeed absent. Under these circumstances, the increase in I_{SC} in the order ICBA < PCBM < C_{60} is thus a direct reflection of better dissociation of electron-hole pairs rather than of charge carrier extraction.

In our view, the most convincing evidence that wave function delocalization contributes significantly to the CT-state dissociation lies in the simulation of the field dependence of the photocurrent by the effective mass model (Figure 6c). The increase in mobility along the series ICBA < PCBM < C_{60} is explicitly taken into account when modeling the data, yet it is insufficient to account for the observed improved field-dependent photocurrent in C_{60} compared to PCBM. Without consideration of wave function delocalization, our model is equivalent to an Onsager-Braun-type fit in a potential modified by the interfacial dipoles.⁸¹⁻⁸³ The fact that this fails to account for the difference (cf. Figure S11) indicates the necessity of explicitly considering the increased ease of dissociation due to an electron wave function that extends over more than one fullerene.

When considering the effective mass, one needs to bear in mind that this quantity actually refers to the entire CT state, i.e., the pair of electron and hole. A significant part of its low value will certainly result from the delocalization of the hole wave function along the polymer backbone. However, what is relevant here is not the absolute value (that should, in any case, be viewed with some caution due to the simplistic geometry assumed in the model), but that a *reduction* in the effective mass is required when replacing PCBM with C_{60} as acceptor, even when changes in mobility and interfacial dipole are taken into account. This result testifies to the critical role of high local order in organic solar cells. Many of the recently emerged non-fullerene acceptors are characterized by a tendency to aggregate in an ordered fashion,^{84,85} and our results suggest that the increased electron wave function delocalization within such aggregates may significantly contribute to the efficient CT-state dissociation that they show when processed appropriately.

V. CONCLUSION

In conclusion, we investigated three different fullerene acceptors (C_{60} , PCBM, ICBA) with varying degree of order and intermolecular coupling in a bilayer configuration with a cross-linked layer of PCDTBTOx as donor in order to reveal the influence of electron delocalization within the acceptor

phase on the dissociation efficiency of charge transfer states. The bilayer structure ensured a well-defined interface, providing an ideal model system to investigate interface effects without need to consider issues arising from inhomogeneous mixing, domain sizes, and bimolecular recombination. By correlating structural information with the results of optical and electrical characterization, we find that higher intermolecular coupling, evidenced by smaller inter-acceptor spacing and a higher degree of crystallinity and order, is correlated with higher electron delocalization of the CT states in accordance with the works of Larson et al., Abramavicius et al., and Forrest et al.²⁷⁻²⁹ Finally, by applying the effective mass model of Tscheuschner et al.³¹ and taking into account dipole effects at the donor-acceptor interface, as evidenced via Kelvin-Probe measurements, a clear correlation could be established between delocalization of the electron in the acceptor phase and a reduced barrier for CT dissociation, resulting in enhanced dissociation efficiency.

From the comparison of the three fullerenes C_{60} , PCBM, and ICBA, we found that, in this respect, quality of local order in C_{60} is a crucial ingredient to allow coherent delocalization in the acceptor phase, as also suggested by Bernardo et al.³⁰ This effect is much less pronounced in the less ordered PCBM, where a higher effective mass implies that coupling has a more incoherent character resulting in more localized CT states. This is especially true for ICBA, where weak inter-fullerene coupling and concomitantly low mobility additionally enhance geminate recombination at the interface. This is consistent with the results of Larson et al. that show that low mobility in fullerenes lowers charge generation efficiency at the interface.²⁷

Consequently, we find clear evidence that not only hole delocalization along the covalently bonded polymer chain but also electron delocalization plays a positive role in the charge separation process. In the context of our previous works on the delocalization of holes in the donor phase,^{31,32} our results support the model concept of delocalization of both electron and hole taking an important and positive role in the charge separation process. Yet, order and crystallinity are even more important in the case of electron delocalization due to the need for strong intermolecular coupling. All this should be taken into account when investigating and discussing the mechanisms leading to very efficient donor-acceptor systems, especially in the view of the use and design of the recently emerged non-fullerene acceptors.

■ ASSOCIATED CONTENT

Supporting Information

The Supporting Information is available free of charge on the ACS Publications website at DOI: 10.1021/acs.jpcc.8b06429.

Full synthetic details for PCDTBTOx; ¹H NMR spectrum of PCDTBTOx; UPS and IPES spectra; Kelvin-Probe measurements; exemplary derivation of IE, EA, and work function; additional EQE spectra of bilayer and single layer devices; discussion of IQE; calculated fractions of absorbed light; additional IV characteristics at different excitation energies; additional intensity-dependent FF diagrams at different excitation energies; comment on the intensity dependence of FF; comment on exciton recycling for ICBA; comment on the correction of field-dependent EQE data; alternative method to determine the saturation field strength; additional electroabsorption spectra; additional field-

dependent fits according to the effective mass model (PDF)

AUTHOR INFORMATION

Corresponding Author

*E-mail: anna.koehler@uni-bayreuth.de.

ORCID

Frank-Julian Kahle: 0000-0003-3416-0072

Selina Olthof: 0000-0002-8871-1549

Eva M. Herzig: 0000-0002-0151-5562

Anna Köhler: 0000-0001-5029-4420

Notes

The authors declare no competing financial interest.

ACKNOWLEDGMENTS

We acknowledge financial support by the German Science Foundation DFG through the doctoral training center "Photophysics of Synthetic and Biological Multichromophoric Systems" (GRK 1640), the Volkswagen foundation and by the Bavarian State Ministry of Education, Science and the Arts through the Collaborative Research Network "Solar Technologies go Hybrid" (SolTech). Moreover, we acknowledge SOLEIL for provision of synchrotron radiation facilities and we would like to thank Philippe Fontaine for assistance in using beamline Sirius. S.W. and E.M.H. are grateful for the support by Deutsche Forschungsgemeinschaft (DFG) through TUM International Graduate School of Science and Engineering (IGSSE). F.-J.K. was supported by the Elite Network Bavaria (ENB) in the framework of the Elite Study Program "Macromolecular Science". Finally, we want to thank Prof. Heinz Bässler, Dr. Tobias Hahn, and Dr. Steffen Tscheuschner for valuable discussions throughout the whole project.

REFERENCES

- (1) Li, Z. K.; Jiang, K.; Yang, G. F.; Lai, J. Y. L.; Ma, T. X.; Zhao, J. B.; Ma, W.; Yan, H. Donor Polymer Design Enables Efficient Non-Fullerene Organic Solar Cells. *Nat. Commun.* **2016**, *7*, 13094.
- (2) Zhao, W. C.; Qian, D. P.; Zhang, S. Q.; Li, S. S.; Inganäs, O.; Gao, F.; Hou, J. H. Fullerene-Free Polymer Solar Cells with over 11% Efficiency and Excellent Thermal Stability. *Adv. Mater.* **2016**, *28*, 4734–4739.
- (3) Zhao, W. C.; Li, S. S.; Yao, H. F.; Zhang, S. Q.; Zhang, Y.; Yang, B.; Hou, J. H. Molecular Optimization Enables over 13% Efficiency in Organic Solar Cells. *J. Am. Chem. Soc.* **2017**, *139*, 7148–7151.
- (4) Zheng, Z.; Awartani, O. M.; Gautam, B.; Liu, D. L.; Qin, Y. P.; Li, W. N.; Bataller, A.; Gundogdu, K.; Ade, H.; Hou, J. H. Efficient Charge Transfer and Fine-Tuned Energy Level Alignment in a Thf-Processed Fullerene-Free Organic Solar Cell with 11.3% Efficiency. *Adv. Mater.* **2017**, *29*, 1604241.
- (5) Zhang, S.; Qin, Y.; Zhu, J.; Hou, J. Over 14% Efficiency in Polymer Solar Cells Enabled by a Polymer Donor. *Adv. Mater.* **2018**, *30*, 1800868.
- (6) Castet, F.; D'Avino, G.; Muccioli, L.; Cornil, J.; Beljonne, D. Charge Separation Energetics at Organic Heterojunctions: On the Role of Structural and Electrostatic Disorder. *Phys. Chem. Chem. Phys.* **2014**, *16*, 20279–20290.
- (7) Gao, F.; Inganäs, O. Charge Generation in Polymer-Fullerene Bulk-Heterojunction Solar Cells. *Phys. Chem. Chem. Phys.* **2014**, *16*, 20291–20304.
- (8) Mangold, H.; Bakulin, A. A.; Howard, I. A.; Kästner, C.; Egbe, D. A. M.; Hoppe, H.; Laquai, F. Control of Charge Generation and Recombination in Ternary Polymer/Polymer:Fullerene Photovoltaic Blends Using Amorphous and Semi-Crystalline Copolymers as Donors. *Phys. Chem. Chem. Phys.* **2014**, *16*, 20329–20337.
- (9) Bittner, E. R.; Lankevich, V.; Gélinas, S.; Rao, A.; Ginger, D. A.; Friend, R. H. How Disorder Controls the Kinetics of Triplet Charge Recombination in Semiconducting Organic Polymer Photovoltaics. *Phys. Chem. Chem. Phys.* **2014**, *16*, 20321–20328.
- (10) Vithanage, D. A.; Devizis, A.; Abramavicius, V.; Infahsaeng, Y.; Abramavicius, D.; MacKenzie, R. C. I.; Keivanidis, P. E.; Yartsev, A.; Hertel, D.; Nelson, J.; et al. Visualizing Charge Separation in Bulk Heterojunction Organic Solar Cells. *Nat. Commun.* **2013**, *4*, 2334.
- (11) Athanasopoulos, S.; Tscheuschner, S.; Bässler, H.; Köhler, A. Efficient Charge Separation of Cold Charge-Transfer States in Organic Solar Cells through Incoherent Hopping. *J. Phys. Chem. Lett.* **2017**, *8*, 2093–2098.
- (12) Clarke, T. M.; Durrant, J. R. Charge Photogeneration in Organic Solar Cells. *Chem. Rev.* **2010**, *110*, 6736–6767.
- (13) Bässler, H.; Köhler, A. Charge Transport in Organic Semiconductors. *Top. Curr. Chem.* **2011**, *312*, 1–65.
- (14) Vandewal, K.; Albrecht, S.; Hoke, E. T.; Graham, K. R.; Widmer, J.; Douglas, J. D.; Schubert, M.; Mateker, W. R.; Bloking, J. T.; Burkhard, G. F.; et al. Efficient Charge Generation by Relaxed Charge-Transfer States at Organic Interfaces. *Nat. Mater.* **2014**, *13*, 63–68.
- (15) Park, S. H.; Roy, A.; Beaupre, S.; Cho, S.; Coates, N.; Moon, J. S.; Moses, D.; Leclerc, M.; Lee, K.; Heeger, A. J. Bulk Heterojunction Solar Cells with Internal Quantum Efficiency Approaching 100%. *Nat. Photonics* **2009**, *3*, 297–303.
- (16) Tress, W.; Leo, K.; Riede, M. Optimum Mobility, Contact Properties, and Open-Circuit Voltage of Organic Solar Cells: A Drift-Diffusion Simulation Study. *Phys. Rev. B: Condens. Matter Mater. Phys.* **2012**, *85*, 155201.
- (17) Deibel, C.; Wagenpfahl, A.; Dyakonov, V. Influence of Charge Carrier Mobility on the Performance of Organic Solar Cells. *Phys. Status Solidi RRL* **2008**, *2*, 175–177.
- (18) Hood, S. N.; Kassal, I. Entropy and Disorder Enable Charge Separation in Organic Solar Cells. *J. Phys. Chem. Lett.* **2016**, *7*, 4495–4500.
- (19) Gregg, B. A. Entropy of Charge Separation in Organic Photovoltaic Cells: The Benefit of Higher Dimensionality. *J. Phys. Chem. Lett.* **2011**, *2*, 3013–3015.
- (20) Puttison, Y.; Xia, Y.; Chen, X.; Gao, F.; Buyanova, I. A.; Inganäs, O.; Chen, W. M. Charge Generation Via Relaxed Charge-Transfer States in Organic Photovoltaics by an Energy-Disorder-Driven Entropy Gain. *J. Phys. Chem. C* **2018**, *122*, 12640–12646.
- (21) Albrecht, S.; Vandewal, K.; Tumbleston, J. R.; Fischer, F. S. U.; Douglas, J. D.; Frechet, J. M. J.; Ludwigs, S.; Ade, H.; Salteo, A.; Neher, D. On the Efficiency of Charge Transfer State Splitting in Polymer: Fullerene Solar Cells. *Adv. Mater.* **2014**, *26*, 2533–2539.
- (22) Coffey, D. C.; Larson, B. W.; Hains, A. W.; Whitaker, J. B.; Kopidakis, N.; Boltalina, O. V.; Strauss, S. H.; Rumbles, G. An Optimal Driving Force for Converting Excitons into Free Carriers in Excitonic Solar Cells. *J. Phys. Chem. C* **2012**, *116*, 8916–8923.
- (23) Ohkita, H.; Cook, S.; Astuti, Y.; Duffy, W.; Tierney, S.; Zhang, W.; Heeney, M.; McCulloch, I.; Nelson, J.; Bradley, D. D. C.; et al. Charge Carrier Formation in Polythiophene/Fullerene Blend Films Studied by Transient Absorption Spectroscopy. *J. Am. Chem. Soc.* **2008**, *130*, 3030–3042.
- (24) Hahn, T.; Geiger, J.; Blase, X.; Duchemin, I.; Niedzialek, D.; Tscheuschner, S.; Beljonne, D.; Bässler, H.; Köhler, A. Does Excess Energy Assist Photogeneration in an Organic Low-Bandgap Solar Cell? *Adv. Funct. Mater.* **2015**, *25*, 1287–1295.
- (25) Chen, X. K.; Ravva, M. K.; Li, H.; Ryno, S. M.; Brédas, J. L. Effect of Molecular Packing and Charge Delocalization on the Nonradiative Recombination of Charge-Transfer States in Organic Solar Cells. *Adv. Energy Mater.* **2016**, *6*, 1601325.
- (26) Zheng, Z. L.; Tummala, N. R.; Fu, Y. T.; Coropceanu, V.; Brédas, J. L. Charge-Transfer States in Organic Solar Cells: Understanding the Impact of Polarization, Delocalization, and Disorder. *ACS Appl. Mater. Interfaces* **2017**, *9*, 18095–18102.
- (27) Larson, B. W.; Reid, O. G.; Coffey, D. C.; Avdoshenko, S. M.; Popov, A. A.; Boltalina, O. V.; Strauss, S. H.; Kopidakis, N.; Rumbles,

- G. Inter-Fullerene Electronic Coupling Controls the Efficiency of Photoinduced Charge Generation in Organic Bulk Heterojunctions. *Adv. Energy Mater.* **2016**, *6*, 1601427.
- (28) Liu, X.; Ding, K.; Panda, A.; Forrest, S. R. Charge Transfer States in Dilute Donor-Acceptor Blend Organic Heterojunctions. *ACS Nano* **2016**, *10*, 7619–7626.
- (29) Abramavicius, V.; Pranculis, V.; Melianas, A.; Inganäs, O.; Gulbinas, V.; Abramavicius, D. Role of Coherence and Delocalization in Photo-Induced Electron Transfer at Organic Interfaces. *Sci. Rep.* **2016**, *6*, 32914.
- (30) Bernardo, B.; Cheyns, D.; Verreert, B.; Schaller, R. D.; Rand, B. P.; Giebink, N. C. Delocalization and Dielectric Screening of Charge Transfer States in Organic Photovoltaic Cells. *Nat. Commun.* **2014**, *5*, 3245.
- (31) Tscheuschner, S.; Bäessler, H.; Huber, K.; Köhler, A. A Combined Theoretical and Experimental Study of Dissociation of Charge Transfer States at the Donor-Acceptor Interface of Organic Solar Cells. *J. Phys. Chem. B* **2015**, *119*, 10359–10371.
- (32) Schwarz, C.; Tscheuschner, S.; Frisch, J.; Winkler, S.; Koch, N.; Bäessler, H.; Köhler, A. Role of the Effective Mass and Interfacial Dipoles on Exciton Dissociation in Organic Donor-Acceptor Solar Cells. *Phys. Rev. B: Condens. Matter Mater. Phys.* **2013**, *87*, 155205.
- (33) Coropceanu, V.; Cornil, J.; da Silva Filho, D. A.; Olivier, Y.; Silbey, R.; Brédas, J. L. Charge Transport in Organic Semiconductors. *Chem. Rev.* **2007**, *107*, 926–952.
- (34) Köhler, A.; Bäessler, H. Charges and Excited States in Organic Semiconductors. In *Electronic Processes in Organic Semiconductors: An Introduction*; Wiley-VCH: Weinheim, Germany, 2015; p 424.
- (35) Bakulin, A. A.; Xia, Y. X.; Bakker, H. J.; Inganäs, O.; Gao, F. Morphology, Temperature, and Field Dependence Separation in High-Efficiency Solar Cells Based on Polyquinoxaline Copolymer. *J. Phys. Chem. C* **2016**, *120*, 4219–4226.
- (36) Zusan, A.; Vandewal, K.; Allendorf, B.; Hansen, N. H.; Pfäum, J.; Salleo, A.; Dyakonov, V.; Deibel, C. The Crucial Influence of Fullerene Phases on Photogeneration in Organic Bulk Heterojunction Solar Cells. *Adv. Energy Mater.* **2014**, *4*, 1400922.
- (37) Gluchowski, A.; Gray, K. L. G.; Hood, S. N.; Kassal, I. Increases in the Charge Separation Barrier in Organic Solar Cells Due to Delocalization. *J. Phys. Chem. Lett.* **2018**, *9*, 1359–1364.
- (38) Kahle, F. J.; Bauer, I.; Stroehriegel, P.; Köhler, A. Influence of Crosslinking on Charge Carrier Mobility in Crosslinkable Polyfluorene Derivatives. *J. Polym. Sci., Part B: Polym. Phys.* **2017**, *55*, 112–120.
- (39) Fischer, F.; Hahn, T.; Bäessler, H.; Bauer, I.; Stroehriegel, P.; Köhler, A. Measuring Reduced C-60 Diffusion in Crosslinked Polymer Films by Optical Spectroscopy. *Adv. Funct. Mater.* **2014**, *24*, 6172–6177.
- (40) Jakowetz, A. C.; Bohm, M. L.; Zhang, J. B.; Sadhanala, A.; Huettner, S.; Bakulin, A. A.; Rao, A.; Friend, R. H. What Controls the Rate of Ultrafast Charge Transfer and Charge Separation Efficiency in Organic Photovoltaic Blends. *J. Am. Chem. Soc.* **2016**, *138*, 11672–11679.
- (41) Popov, A. A.; Kareev, I. E.; Shustova, N. B.; Stukalin, E. B.; Lebedkin, S. F.; Seppelt, K.; Strauss, S. H.; Boltalina, O. V.; Dunsch, L. Electrochemical, Spectroscopic, and Dft Study of C-60(Cf₃)_N Frontier Orbitals (N=2-18): The Link between Double Bonds in Pentagons and Reduction Potentials. *J. Am. Chem. Soc.* **2007**, *129*, 11551–11568.
- (42) Jiang, Z. Gixsgui: A Matlab Toolbox for Grazing-Incidence X-Ray Scattering Data Visualization and Reduction, and Indexing of Buried Three-Dimensional Periodic Nanostructured Films. *J. Appl. Crystallogr.* **2015**, *48*, 917–926.
- (43) Burkhard, G. F.; Hoke, E. T.; McGehee, M. D. Accounting for Interference, Scattering, and Electrode Absorption to Make Accurate Internal Quantum Efficiency Measurements in Organic and Other Thin Solar Cells. *Adv. Mater.* **2010**, *22*, 3293–3297.
- (44) Polyanskiy, M. N. *Refractive Index Database*. <https://refractiveindex.info> (accessed Aug 16, 2017).
- (45) Schmiedova, V.; Heinrichova, P.; Zmeskal, O.; Weiter, M. Characterization of Polymeric Thin Films for Photovoltaic Applications by Spectroscopic Ellipsometry. *Appl. Surf. Sci.* **2015**, *349*, 582–588.
- (46) Leman, D.; Kelly, M. A.; Ness, S.; Engmann, S.; Herzing, A.; Snyder, C.; Ro, H. W.; Kline, R. J.; DeLongchamp, D. M.; Richter, L. J. In Situ Characterization of Polymer-Fullerene Bilayer Stability. *Macromolecules* **2015**, *48*, 383–392.
- (47) Wynands, D.; Erber, M.; Rentenberger, R.; Levichkova, M.; Walzer, K.; Eichhorn, K. J.; Stamm, M. Spectroscopic Ellipsometry Characterization of Vacuum-Deposited Organic Films for the Application in Organic Solar Cells. *Org. Electron.* **2012**, *13*, 885–893.
- (48) Liu, Z. T.; Kwong, C. Y.; Cheung, C. H.; Djuricic, A. B.; Chan, Y.; Chui, P. C. The Characterization of the Optical Functions of Bcp and Cbp Thin Films by Spectroscopic Ellipsometry. *Synth. Met.* **2005**, *150*, 159–163.
- (49) Tress, W. Simulation Study on Single-Layer Bulk-Heterojunction Solar Cells. In *Organic Solar Cells: Theory, Experiment and Device Simulation*; Springer: New York, 2014; p 474.
- (50) Nakanishi, R.; Nogimura, A.; Eguchi, R.; Kanai, K. Electronic Structure of Fullerene Derivatives in Photovoltaics. *Org. Electron.* **2014**, *15*, 2912–2921.
- (51) Guan, Z. L.; Kim, J. B.; Wang, H.; Jaye, C.; Fischer, D. A.; Loo, Y. L.; Kahn, A. Direct Determination of the Electronic Structure of the Poly(3-Hexylthiophene):Phenyl-[6,6]-C61 Butyric Acid Methyl Ester Blend. *Org. Electron.* **2010**, *11*, 1779–1785.
- (52) Guan, Z. L.; Kim, J. B.; Loo, Y. L.; Kahn, A. Electronic Structure of the Poly(3-Hexylthiophene):Indene-C-60 Bisadduct Bulk Heterojunction. *J. Appl. Phys.* **2011**, *110*, 043719.
- (53) Linares, M.; Beljonne, D.; Cornil, J.; Lancaster, K.; Brédas, J. L.; Verlaak, S.; Mityashin, A.; Heremans, P.; Fuchs, A.; Lennartz, C.; et al. On the Interface Dipole at the Pentacene-Fullerene Heterojunction: A Theoretical Study. *J. Phys. Chem. C* **2010**, *114*, 3215–3224.
- (54) Czerwosz, E.; Byszewski, P.; Diduszko, R.; Wronka, H.; Dluzewski, P.; Mizera, E. The Structural Changes of Polycrystalline Film C-60/C-70:Ni Caused by Ni Diffusion. *J. Mater. Res.* **1996**, *11*, 3146–3151.
- (55) Skokan, E. V.; Arkhangel'skii, I. V.; Izotov, D. E.; Chelovskaya, N. V.; Nikulin, M. M.; Velikodnyi, Y. A. Stability of Hexagonal Modification of Fullerite C-60. *Carbon* **2005**, *43*, 803–808.
- (56) Erb, T.; Zhokhavets, U.; Gobsch, G.; Raleva, S.; Stuhn, B.; Schilinsky, P.; Waldauf, C.; Brabec, C. J. Correlation between Structural and Optical Properties of Composite Polymer/Fullerene Films for Organic Solar Cells. *Adv. Funct. Mater.* **2005**, *15*, 1193–1196.
- (57) MacKenzie, R. C. I.; Frost, J. M.; Nelson, J. A Numerical Study of Mobility in Thin Films of Fullerene Derivatives. *J. Chem. Phys.* **2010**, *132*, 064904.
- (58) Gajdos, F.; Oberhofer, H.; Dupuis, M.; Blumberger, J. On the Inapplicability of Electron-Hopping Models for the Organic Semiconductor Phenyl-C61-Butyric Acid Methyl Ester (Pcbm). *J. Phys. Chem. Lett.* **2013**, *4*, 1012–1017.
- (59) Cheung, D. L.; Troisi, A. Theoretical Study of the Organic Photovoltaic Electron Acceptor Pcbm: Morphology, Electronic Structure, and Charge Localization. *J. Phys. Chem. C* **2010**, *114*, 20479–20488.
- (60) Hahn, T.; Tscheuschner, S.; Saller, C.; Stroehriegel, P.; Boregowda, P.; Mukhopadhyay, T.; Patil, S.; Neher, D.; Bäessler, H.; Köhler, A. Role of Intrinsic Photogeneration in Single Layer and Bilayer Solar Cells with C-60 and Pcbm. *J. Phys. Chem. C* **2016**, *120*, 25083–25091.
- (61) Kazaoui, S.; Minami, N.; Tanabe, Y.; Byrne, H. J.; Eilmel, A.; Petelenz, P. Comprehensive Analysis of Intermolecular Charge-Transfer Excited States in C-60 and C-70 Films. *Phys. Rev. B: Condens. Matter Mater. Phys.* **1998**, *58*, 7689–7700.
- (62) Hahn, T.; Tscheuschner, S.; Kahle, F. J.; Reichenberger, M.; Athanasopoulos, S.; Saller, C.; Bazan, G. C.; Nguyen, T. Q.; Stroehriegel, P.; Bäessler, H.; et al. Monomolecular and Bimolecular Recombination of Electron-Hole Pairs at the Interface of a Bilayer Organic Solar Cell. *Adv. Funct. Mater.* **2017**, *27*, 1604906.

- (63) Tress, W. Interplay between Electrodes and Active Materials: The Open-Circuit Voltage and S-Shaped J-V Curves. In *Organic Solar Cells: Theory, Experiment, and Device Simulation*; Springer: New York, 2014; p 474.
- (64) Bartesaghi, D.; Perez, I. D.; Kniepert, J.; Roland, S.; Turbiez, M.; Neher, D.; Koster, L. J. A. Competition between Recombination and Extraction of Free Charges Determines the Fill Factor of Organic Solar Cells. *Nat. Commun.* **2015**, *6*, 7083.
- (65) Tress, W.; Petrich, A.; Hummert, M.; Hein, M.; Leo, K.; Riede, M. Imbalanced Mobilities Causing S-Shaped Iv Curves in Planar Heterojunction Organic Solar Cells. *Appl. Phys. Lett.* **2011**, *98*, 063301.
- (66) Tress, W. Further Origins of S-Shaped J-V Curves. In *Organic Solar Cells: Theory, Experiment, and Device Simulation*; Springer: New York, 2014; p 474.
- (67) Sebastian, L.; Weiser, G.; Bäessler, H. Charge-Transfer Transitions in Solid Tetracene and Pentacene Studied by Electro-Absorption. *Chem. Phys.* **1981**, *61*, 125–135.
- (68) Harrison, M. G.; Möller, S.; Weiser, G.; Urbasch, G.; Mahrt, R. F.; Bäessler, H.; Scherf, U. Electro-Optical Studies of a Soluble Conjugated Polymer with Particularly Low Intrachain Disorder. *Phys. Rev. B: Condens. Matter Mater. Phys.* **1999**, *60*, 8650–8658.
- (69) Singh, C. R.; Li, C.; Mueller, C. J.; Hüttner, S.; Thelakkat, M. Influence of Electron Extracting Interface Layers in Organic Bulk-Heterojunction Solar Cells. *Adv. Mater. Interfaces* **2016**, *3*, 1500422.
- (70) Li, C.; Credgington, D.; Ko, D. H.; Rong, Z. X.; Wang, J. P.; Greenham, N. C. Built-in Potential Shift and Schottky-Barrier Narrowing in Organic Solar Cells with Uv-Sensitive Electron Transport Layers. *Phys. Chem. Chem. Phys.* **2014**, *16*, 12131–12136.
- (71) Drori, T.; Holt, J.; Vardeny, Z. V. Optical Studies of the Charge Transfer Complex in Polythiophene/Fullerene Blends for Organic Photovoltaic Applications. *Phys. Rev. B: Condens. Matter Mater. Phys.* **2010**, *82*, 075207.
- (72) Bredas, J. L.; Norton, J. E.; Cornil, J.; Coropceanu, V. Molecular Understanding of Organic Solar Cells: The Challenges. *Acc. Chem. Res.* **2009**, *42*, 1691–1699.
- (73) Rand, B. P.; Xue, J. G.; Uchida, S.; Forrest, S. R. Mixed Donor-Acceptor Molecular Heterojunctions for Photovoltaic Applications. I. Material Properties. *J. Appl. Phys.* **2005**, *98*, 124902.
- (74) Roland, S.; Yan, L.; Zhang, Q. Q.; Jiao, X. C.; Hunt, A.; Ghasemi, M.; Ade, H.; You, W.; Neher, D. Charge Generation and Mobility-Limited Performance of Bulk Heterojunction Solar Cells with a Higher Adduct Fullerene. *J. Phys. Chem. C* **2017**, *121*, 10305–10316.
- (75) Mihailetchi, V. D. Device Physics of Organic Bulk Heterojunction Solar Cells. Ph.D. Thesis, University of Groningen, Groningen, The Netherlands, 2005.
- (76) Veldman, D.; Ipek, Ö.; Meskers, S. C. J.; Sweelssen, J.; Koetse, M. M.; Veenstra, S. C.; Kroon, J. M.; van Bavel, S. S.; Loos, J.; Janssen, R. A. J. Compositional and Electric Field Dependence of the Dissociation of Charge Transfer Excitons in Alternating Polyfluorene Copolymer/Fullerene Blends. *J. Am. Chem. Soc.* **2008**, *130*, 7721–7735.
- (77) Marsh, R. A.; Hodgkiss, J. M.; Friend, R. H. Direct Measurement of Electric Field-Assisted Charge Separation in Polymer: Fullerene Photovoltaic Diodes. *Adv. Mater.* **2010**, *22*, 3672–3676.
- (78) Ponceca, C. S.; Yartsev, A.; Wang, E.; Andersson, M. R.; Vithanage, D.; Sundström, V. Ultrafast Terahertz Photoconductivity of Bulk Heterojunction Materials Reveals High Carrier Mobility up to Nanosecond Time Scale. *J. Am. Chem. Soc.* **2012**, *134*, 11836–11839.
- (79) Kirkpatrick, J.; Keivanidis, P. E.; Bruno, A.; Ma, F.; Haque, S. A.; Yarstev, A.; Sundström, V.; Nelson, J. Ultrafast Transient Optical Studies of Charge Pair Generation and Recombination in Poly-3-Hexylthiophene(P3ht):[6,6]Phenyl C61 Butyric Methyl Acid Ester (Pcbm) Blend Films. *J. Phys. Chem. B* **2011**, *115*, 15174–15180.
- (80) Faist, M. A.; Shoaee, S.; Tuladhar, S.; Dibb, G. F. A.; Foster, S.; Gong, W.; Kirchartz, T.; Bradley, D. D. C.; Durrant, J. R.; Nelson, J. Understanding the Reduced Efficiencies of Organic Solar Cells Employing Fullerene Multiadducts as Acceptors. *Adv. Energy. Mater.* **2013**, *3*, 744–752.
- (81) Onsager, L. Deviations from Ohm's Law in Weak Electrolytes. *J. Chem. Phys.* **1934**, *2*, 599–615.
- (82) Onsager, L. Initial Recombination of Ions. *Phys. Rev.* **1938**, *54*, 554–557.
- (83) Braun, C. L. Electric-Field Assisted Dissociation of Charge-Transfer States as a Mechanism of Photocarrier Production. *J. Chem. Phys.* **1984**, *80*, 4157–4161.
- (84) Hou, J. H.; Inganäs, O.; Friend, R. H.; Gao, F. Organic Solar Cells Based on Non-Fullerene Acceptors. *Nat. Mater.* **2018**, *17*, 119–128.
- (85) Nielsen, C. B.; Holliday, S.; Chen, H. Y.; Cryer, S. J.; McCulloch, I. Non-Fullerene Electron Acceptors for Use in Organic Solar Cells. *Acc. Chem. Res.* **2015**, *48*, 2803–2812.

Supporting Information to

Does Electron Delocalization Influence Charge Separation At Donor-Acceptor Interfaces In Organic Photovoltaic Cells?

Frank-Julian Kahle¹⁾, Christina Saller²⁾, Selina Olthof³⁾, Cheng Li²⁾, Jenny Lebert⁴⁾, Sebastian Weiß⁴⁾, Eva M. Herzig⁵⁾, Sven Hüttner²⁾, Klaus Meerholz³⁾, Peter Strohriegl²⁾, Anna Köhler^{1,*)}

¹⁾ Soft Matter Optoelectronics, Department of Physics, University of Bayreuth, 95447 Bayreuth, Germany

²⁾ Macromolecular Chemistry I, Department of Chemistry, University of Bayreuth, 95447 Bayreuth, Germany

³⁾ Department of Chemistry, University of Cologne, 50939 Cologne, Germany

⁴⁾ Herzig Group, Munich School of Engineering, Technical University Munich, 85748 Garching, Germany

⁵⁾ Dynamics and Structure Formation – Herzig Group, Department of Physics, University of Bayreuth, 95447 Bayreuth, Germany

Synthesis of the polymer PCDTBOx:

Materials and methods

All chemicals and anhydrous solvents were purchased from commercial suppliers and used as received. Solvents needed for extraction and purification were distilled prior to use. The monomer 4,7-bis(4,4,5,5-tetramethyl-1,3,2-dioxaborolan-2-yl)-2,1,3-benzothiadiazole was delivered by SunaTech Inc. and used without further purification. ^1H NMR spectra at room temperature were recorded on a Bruker Avance 300 spectrometer in deuterated solvents at 300 MHz. High temperature ^1H NMR spectra were measured at 120 °C with a Varian INOVA 300 spectrometer in 1,1,2,2-tetrachloroethane as solvent. As internal references, the residual solvent peaks were used. Mass spectra were recorded on a Finnigan MAT 8500 via electron ionization.

9-Bromononanal

Oxalyl chloride (4.24 mL, 49.29 mmol) was dissolved in anhydrous dichloromethane (100 mL) and cooled to -78 °C under argon. A solution of anhydrous dimethyl sulfoxide (6.99 mL, 98.59 mmol) and anhydrous dichloromethane (20 mL) was added dropwise. After stirring for 5 min, a solution of 9-bromononanol (10.000 g, 44.81 mmol) in anhydrous dichloromethane (45 mL) was added dropwise over a short time and the reaction mixture was stirred for 30 min at -78 °C before triethylamine (31.23 mL, 224.06 mmol) was added dropwise. The reaction mixture was again stirred for 15 min at -78 °C, allowed to warm to room temperature and poured into water. After extraction with dichloromethane, the organic phase was washed twice with HCl solution (2%), twice with deionised water, twice with NaHCO_3 solution (5%) and again twice with deionised water. The organic phase was dried over Na_2SO_4 and the solvent was evaporated. Drying in vacuum overnight yielded 9-bromononanal (9.500 g, 42.96 mmol, 96%) as a colourless oil.

EI-MS: m/z (%) = 221 (M^+ , 4), 204 ($M^+ - \text{O}$, 23), 192 ($M^+ - \text{HCO}$, 17), 176 ($M^+ - \text{C}_2\text{H}_3\text{O}$, 100), 163 ($M^+ - \text{C}_3\text{H}_5\text{O}$, 5), 149 ($M^+ - \text{C}_4\text{H}_7\text{O}$, 7), 135 ($M^+ - \text{C}_5\text{H}_9\text{O}$, 22).

^1H NMR (300 MHz, CDCl_3): δ (ppm) = 1.18-1.49 (m, 8H, CH_2), 1.50-1.70 (m, 2H, $\text{HCO-CH}_2\text{-CH}_2$), 1.75-1.92 (m, 2H, $\text{CH}_2\text{-CH}_2\text{-Br}$), 2.33-2.48 (m, 2H, HCO-CH_2), 3.40 (t, $J = 6.8$ Hz, 2H, $\text{CH}_2\text{-Br}$), 9.67-9.76 (t, $J = 1.8$ Hz, 1H, HCO).

1-Bromoheptadecan-9-ol

Bromooctane (8.39 mL, 48.57 mmol) was dissolved in anhydrous THF (24 mL) and added slowly to magnesium chips (1.476 g, 60.71 mmol) under argon atmosphere. When the exothermic reaction has started, the remaining solution is added dropwise under stirring and cooling if necessary. The reaction mixture is heated to reflux and stirred for 1 h. After cooling to room temperature, anhydrous THF (8 mL) was added for dilution of the reaction mixture. A solution of 9-bromononanal (8.950 g, 221.13 mmol) in anhydrous THF (15 mL) was added slowly under intermittent cooling. The reaction mixture was stirred at room temperature overnight, poured into water and extracted with diethyl ether. After washing twice with saturated NaHCO₃ solution, twice with deionised water and twice with brine, the organic phase was dried over Na₂SO₄ and the solvent was evaporated. After purification via column chromatography (hexanes:ethyl acetate = 5:1), 1-bromoheptadecan-9-ol (9.318 g, 27.78 mmol, 69%) was obtained as a colourless solid.

EI-MS: m/z (%) = 334 (M^+ , 1), 318 ($M^+ - OH$, 19), 221 ($M^+ - C_8H_{17}$, 73), 143 ($M^+ - C_8H_{16}Br$, 59).

¹H NMR (300 MHz, CDCl₃): δ (ppm) = 0.88 (t, J = 6.5 Hz, 3H, CH₃), 1.19-1.52 (m, 26H, CH₂), 1.85 (qui, J = 7.3 Hz, 2H, CH₂-CH₂-Br), 3.41 (t, J = 6.8 Hz, 2H, CH₂-Br), 3.52-3.64 (br, CH-OH).

1-((3'-Ethylloxetan-3'-yl)-methoxy)-heptadecan-9-ol

Tetrabutylammonium bromide (0.448 g, 1.39 mmol) was dissolved in aqueous NaOH solution (48.624 g, 45 wt%). A solution of 1-bromoheptadecan-9-ol (9.318 g, 27.79 mmol) and (3-ethylloxetan-3-yl)-methanol (5.54 mL, 48.63 mmol) in distilled hexanes (160 mL) was added. The reaction mixture was stirred overnight under reflux. After cooling to room temperature, the reaction mixture was extracted with deionised water and hexanes. The organic phase was dried over Na₂SO₄ and the solvent was evaporated. 1-((3'-Ethylloxetan-3'-yl)-methoxy)-heptadecan-9-ol (6.530 g, 17.62 mmol, 63%) was obtained as a colourless oil after column chromatography (hexanes:ethylacetate = 5:1).

EI-MS: m/z (%) = 371 (M^+ , 1), 353 ($M^+ - OH$, 3), 340 ($M^+ - CH_2O$, 10), 322 ($M^+ - CH_2O - OH$, 8), 257 ($M^+ - C_6H_{11}O_2$, 22), 227 ($M^+ - C_8H_{15}O_2$, 8).

¹H NMR (300 MHz, CDCl₃): δ (ppm) = 0.88 (t, J = 7.5 Hz, 6H, CH₃), 1.16-1.49 (m, 26H, CH₂), 1.50-1.62 (m, 2H, CH₂-CH₂-O), 1.74 (q, J = 7.5 Hz, 2H, oxetane-CH₂-CH₃), 3.44 (t, J = 6.5 Hz, 2H, CH₂-O), 3.52 (s, 2H, O-CH₂-oxetane), 3.53-3.63 (br, CH), 4.41 (q, J = 5.8 Hz, 4H, oxetane).

(1'-((3''-Ethyloxetan-3''-yl)-methoxy)-heptadecan-9'-yl)-4-toluenesulfonate

A solution of 1-((3'-ethyloxetan-3'-yl)-methoxy)-heptadecan-9-ol (3.400 g, 9.17 mmol), triethylamine (2.312 g, 22.84 mmol), and trimethylammonium hydrochloride (0.877 g, 9.17 mmol) in anhydrous dichloromethane (20 mL) was cooled to 0 °C. Tosyl chloride (2.169 g, 11.38 mmol) was dissolved in anhydrous dichloromethane (20 mL) and added to the reaction mixture in a time range of 10 min. After stirring for 90 min at 0 °C, the reaction mixture was allowed to warm to room temperature and stirred overnight. Extraction was carried out with dichloromethane and water. The organic phase was washed with deionised water, dried over Na₂SO₄ and the solvent was evaporated. Column chromatography (hexanes:ethyl acetate = 5:1) yielded the spacer molecule (1'-((3''-ethyloxetan-3''-yl)-methoxy)-heptadecan-9'-yl)-4-toluenesulfonate (3.820 g, 7.28 mmol, 79%) as a colourless oil.

EI-MS: m/z (%) = 524 (M⁺, 1), 494 (M⁺ - CH₂O, 15), 353 (M⁺ - C₇H₇O₃S, 37), 322 (M⁺ - C₈H₉O₄S, 23), 255 (M⁺ - C₁₃H₁₈O₄S, 78).

¹H NMR (300 MHz, CDCl₃): δ (ppm) = 0.80-0.93 (m, 6H, CH₃), 1.06-1.37 (m, 26H, CH₂), 1.44-1.65 (m, 2H, CH₂-CH₂-O), 1.74 (q, J = 7.5 Hz, 2H, oxetane-CH₂-CH₃), 2.44 (s, 3H, tosylate-CH₃), 3.44 (t, J = 6.5 Hz, 2H, CH₂-O), 3.52 (s, 2H, O-CH₂-oxetane), 4.41 (q, J = 5.8 Hz, 4H, oxetane), 4.53 (qui, J = 6.0 Hz, 1H, CH), 7.19 (d, J = 8.0 Hz, 2H, tosylate), 7.79 (d, J = 8.3 Hz, 2H, tosylate).

2,7-Dibromo-N-(1'-((3''-ethyloxetan-3''-yl)-methoxy)-heptadecan-9'-yl)-carbazole

In an argon atmosphere, 2,7-dibromocarbazole (0.991 g, 3.05 mmol) and KOH (0.855 g, 15.24 mmol) were stirred in dimethyl sulfoxide (8 mL) at room temperature. A solution of (1'-((3''-ethyloxetan-3''-yl)-methoxy)-heptadecan-9'-yl)-4-toluenesulfonate (2.400 g, 4.57 mmol) in dimethyl sulfoxide (6 mL) was added slowly over a time range of 1 h. The reaction mixture was stirred at room temperature overnight and extracted with water and diethyl ether. After the organic phase was washed twice with deionised water and dried over Na₂SO₄, the solvent was evaporated. Purification was carried out via column chromatography (hexanes:toluene = 1:2). 2,7-dibromo-N-(1'-((3''-ethyloxetan-3''-yl)-methoxy)-heptadecan-9'-yl)-carbazole (1.400 g, 2.07 mmol, 68%) was obtained as a colourless oil.

EI-MS: m/z (%) = 677 (M⁺, 100), 647 (M⁺ - CH₂O, 9), 450 (M⁺ - C₁₄H₂₇O₂, 42), 322 (M⁺ - C₂₂H₄₃O₂, 12).

¹H NMR (300 MHz, CDCl₃): δ (ppm) = 0.77-0.91 (m, 6H, CH₃), 0.92-1.37 (m, 22H, CH₂), 1.42-1.56 (m, 2H, CH₂-CH₂-O), 1.72 (q, J = 7.5 Hz, 2H, oxetane-CH₂-CH₃), 1.77-1.97 (br, 2H, carbazole-CH-CH₂), 2.10-2.28 (br, 2H, carbazole-CH-CH₂), 3.39 (t, J = 6.6 Hz, 2H, CH₂-O), 3.49 (s, 2H, O-CH₂-oxetane), 4.40 (q, J = 5.8 Hz, 4H,

oxetane), 4.33-4.47 (br, 1H, CH), 7.28-7.37 (br, 2H, carbazole), 7.49-7.57 (br, 1H, carbazole), 7.64-7.73 (br, 1H, carbazole), 7.84-7.96 (br, 2H, carbazole). Broadened and multiple signals are due to atropisomerism.

2,7-Di(thiophen-2'-yl)-N-(1''-((3'''-ethyloxetan-3'''-yl)-methoxy)-heptadecan-9''-yl)-carbazole

2,7-dibromo-N-(1''-((3'''-ethyloxetan-3'''-yl)-methoxy)-heptadecan-9''-yl)-carbazole (0.500 g, 0.74 mmol) and 2-(4',4',5',5'-tetramethyl-1',3',2'-dioxaborolan-2'-yl)-thiophene (0.465 g, 2.21 mmol) were dissolved in toluene (20 mL). After addition of four drops of Aliquat 336 and aqueous Na₂CO₃ solution (24.95 mL, 2M), the reaction mixture was degassed by three freeze-thaw cycles. Tetrakis(triphenylphosphine)palladium(0) (0.028 g, 0.02 mmol) was added and the reaction mixture was again degassed by three freeze-thaw cycles before stirred under reflux for 90 h. The reaction mixture was poured into water and extracted with dichloromethane. The organic phase was washed twice with deionised water and dried over Na₂SO₄. After evaporation of the solvent, column chromatography (hexanes:THF = 10:1) was performed to remove the catalyst. 2,7-di(thiophen-2'-yl)-N-(1''-((3'''-ethyloxetan-3'''-yl)-methoxy)-heptadecan-9''-yl)-carbazole (0.485 g, 0.71 mmol, 96%) was yielded as a slightly yellowish oil.

EI-MS: m/z (%) = 684 (M⁺, 98), 654 (M⁺ - CH₂O, 10), 568 (M⁺ - C₆H₁₁O₂, 4), 457 (M⁺ - C₁₄H₂₇O₂, 40), 345 (M⁺ - C₂₂H₄₄O₂, 38), 332 (M⁺ - C₂₃H₄₅O₂, 28).

¹H NMR (300 MHz, CDCl₃): δ (ppm) = 0.74-0.89 (m, 6H, CH₃), 0.97-1.36 (m, 22H, CH₂), 1.38-1.51 (m, 2H, CH₂-CH₂-O), 1.70 (q, J = 7.5 Hz, 2H, oxetane-CH₂-CH₃), 1.88-2.04 (br, 2H, carbazole-CH-CH₂), 2.24-2.42 (br, 2H, carbazole-CH-CH₂), 3.34 (t, J = 6.6 Hz, 2H, CH₂-O), 3.46 (s, 2H, O-CH₂-oxetane), 4.38 (q, J = 5.8 Hz, 4H, oxetane), 4.54-4.67 (br, 1H, CH), 7.13 (dd, J = 5.1 Hz, J = 3.7 Hz, 2H, thiophene), 7.31 (dd, J = 5.1 Hz, J = 1.1 Hz, 2H, thiophene), 7.37-7.44 (br, 2H, carbazole), 7.50 (d, J = 8.0 Hz, 2H, thiophene), 7.56-7.62 (br, 1H, carbazole), 7.74-7.81 (br, 1H, carbazole), 8.01-8.11 (br, 2H, carbazole). Broadened and multiple signals are due to atropisomerism.

2,7-Bis(5'-bromothien-2'-yl)-N-(1''-((3'''-ethyloxetan-3'''-yl)-methoxy)-heptadecan-9''-yl)-carbazole

A solution of 2,7-di(thiophen-2'-yl)-N-(1''-((3'''-ethyloxetan-3'''-yl)-methoxy)-heptadecan-9''-yl)-carbazole (0.280 g, 0.41 mmol) in anhydrous chloroform (10 mL) was cooled to 0 °C. In the dark, N-bromosuccinimide (0.146 g, 0.82 mmol) was added in portions. The reaction mixture was stirred at room

temperature for 1 h in the dark, allowed to cool to room temperature and stirred overnight in the dark. NMR spectroscopy was used for reaction control and if required NBS is added to the reaction mixture. After the reaction was completed, the reaction mixture was extracted with water and dichloromethane and the organic phase was washed twice with deionised water. The organic phase was dried over Na₂SO₄ before the solvent was evaporated. After column chromatography (hexanes:THF = 20:1), 2,7-bis(5'-bromothien-2'-yl)-*N*-(1''-(3'''-ethyloxetan-3'''-yl)methoxy)-heptadecan-9''-yl)-carbazole (0.230 g, 0.27 mmol, 67%) was obtained as a yellowish oil.

EI-MS: *m/z* (%) = 841 (M⁺, 100), 811 (M⁺ - CH₂O, 9), 763 (M⁺ - Br, 13), 725 (M⁺ - C₆H₁₁O₂, 4), 647 (M⁺ C₆H₁₁O₂Br, 11), 614 (M⁺ - C₁₄H₂₇O₂, 23), 502 (M⁺ - C₂₂H₄₄O₂, 19), 488 (M⁺ - C₂₃H₄₅O₂, 12), 422 (M⁺ - C₂₂H₄₄O₂Br, 6), 408 (M⁺ - C₂₃H₄₅O₂Br, 5).

¹H NMR (300 MHz, CDCl₃): δ (ppm) = 0.76-0.93 (m, 6H, CH₃), 0.94-1.37 (m, 22H, CH₂), 1.39-1.53 (m, 2H, CH₂-CH₂-O), 1.71 (q, *J* = 7.4 Hz, 2H, oxetane-CH₂-CH₃), 1.89-2.03 (br, 2H, carbazole-CH-CH₂), 2.21-2.40 (br, 2H, carbazole-CH-CH₂), 3.35 (t, *J* = 6.6 Hz, 2H, CH₂-O), 3.47 (s, 2H, O-CH₂-oxetane), 4.39 (q, *J* = 5.8 Hz, 4H, oxetane), 4.50-4.64 (br, 1H, CH), 7.08 (d, *J* = 3.8 Hz, 2H, thiophene), 7.11-7.19 (br, 2H, carbazole), 7.39 (d, *J* = 8.0 Hz, 2H, thiophene), 7.45-7.55 (br, 1H, carbazole), 7.62-7.72 (br, 1H, carbazole), 7.98-8.11 (br, 2H, carbazole). Broadened and multiple signals are due to atropisomerism.

Poly-[(*N*-1'-((3''-ethyloxetan-3''-yl)-methoxy)-heptadecan-9'-yl)-2,7-carbazole-*alt*-5,5-(4',7'-bis(thien-2-yl)-2',1',3'-benzothiadiazole)] PCDTBTOx

The monomers 2,7-bis(5'-bromothien-2'-yl)-*N*-(1''-(3'''-ethyloxetan-3'''-yl)methoxy)-heptadecan-9''-yl)carbazole (0.137 g, 0.16 mmol) and 4,7-bis(4',4',5',5'-tetramethyl-1',3',2'-dioxaborolan-2'-yl)-2,1,3-benzothiadiazole (0.063 g, 0.16 mmol) were dissolved in toluene (7 mL) under argon. Four drops of Aliquat 336 and aqueous Na₂CO₃ solution (7.5 mL, 2 M) were added before degassing the reaction mixture by three freeze-thaw cycles. After adding tetrakis(triphenylphosphine)palladium(0) (0.003 g, 0.002 mmol), again three freeze-thaw cycles were conducted. The reaction mixture was stirred under reflux in an argon atmosphere for 90 h. Bromobenzene (0.017 g, 0.16 mmol) was added and the reaction mixture was stirred under reflux for 1 h. Subsequently, phenylboronic acid (0.020 g, 0.16 mmol) was added and the endcapping reaction was completed by stirring the reaction mixture under reflux overnight. After cooling to room temperature, the polymer was extracted with toluene and washed with water. The organic phase was reduced and the polymer was precipitated into cold methanol. Soxhlet extraction was carried out with acetone, hexanes and toluene as solvents. The toluene fraction was

evaporated to dryness, the polymer was dissolved in chlorobenzene and precipitated into cold methanol. Drying in vacuum overnight yielded PCDTBTOx (0.084 g, 0.10 mmol, 60%) as a dark-red powder.

^1H NMR (300 MHz, $\text{C}_2\text{D}_2\text{Cl}_4$, 120 $^\circ\text{C}$): δ (ppm) = 0.72-0.93 (m, 6H, CH_3), 1.09-1.56 (m, 26H, CH_2 , $\underline{\text{CH}_2\text{-CH}_2\text{-O}}$), 1.57-1.79 (m, 2H, oxetane- $\underline{\text{CH}_2\text{-CH}_3}$), 1.96-2.22 (br, 2H, carbazole- $\underline{\text{CH-CH}_2}$), 2.25-2.56 (br, 2H, carbazole- $\underline{\text{CH-CH}_2}$), 3.24-3.54 (m, 4H, $\text{CH}_2\text{-O}$, $-\text{O-CH}_2\text{-oxetane}$), 4.17-4.45 (m, 4H, oxetane), 4.54-4.77 (br, 1H, CH), 7.04 - 8.61 (m, 12H, ar-CH). Broadened and multiple signals are due to atropisomerism. (Figure S1)

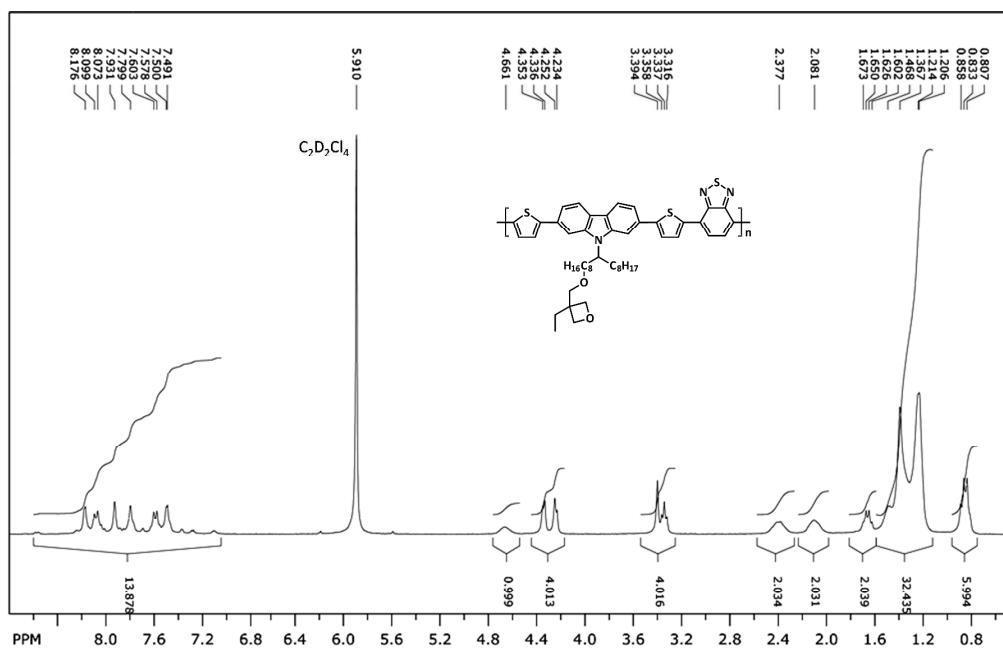


Figure S1: ^1H NMR spectrum of PCDTBTOx (300 MHz) in $\text{C}_2\text{D}_2\text{Cl}_4$ at 120 $^\circ\text{C}$.

Remarks on energy levels and work function:

The high binding energy cutoff (HBEC) and valence band spectra for UPS as well as the IPES spectra are displayed in **Figure S2**. The layer thicknesses of the acceptor were in the range of 10-13 nm. Valence spectra of bilayer samples consistently show the typical features of the molecular levels for the respective fullerenes.¹⁻² These spectra were used to determine IE and

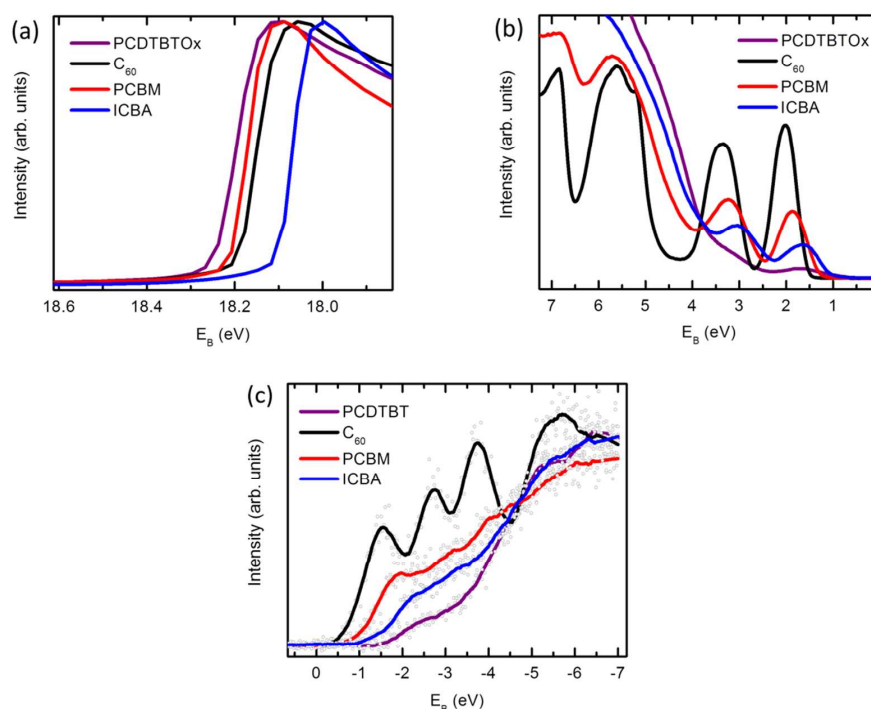


Figure S2: (a) UPS measured high binding energy cutoff (HBEC) and (b) low binding energy region of a pristine 14nm spin-coated and crosslinked PCDTBTOx film on an ITO/MoO₃-substrate (purple), as well as bilayer samples with an additional layer of C₆₀ (black), PCBM (red) or ICBA (blue) on top. Layer thicknesses are in the range of 10-13 nm. (c) IPES spectra of 14 nm thick pristine PCDTBTOx (purple) and samples with an additional layer of C₆₀ (black), PCBM (red) or ICBA (blue) on top. The layer thicknesses ranged from 10 to 13nm. Light grey open dots indicate raw data of the measurements.

EA values for the different materials. Their derivation from the experimental data is exemplary given for C₆₀ in the following. For the excitation a side band of the He I _{β} line with energy

23.09 eV was used. The difference between this energy and the high binding energy cutoff of the signal at (18.2 ± 0.05) eV gives the work function $\Phi = 23.09\text{eV} - 18.2\text{eV} = 4.89\text{eV}$. With a binding energy of (1.62 ± 0.1) eV as determined from the HOMO onset position this results in an ionization energy of $\text{IE} = 4.89\text{ eV} + 1.62\text{ eV} = 6.51\text{ eV} (\pm 0.1\text{ eV})$. With the known work function Φ from UPS and the “LUMO onset position” of -0.34 eV from IPES we can accordingly calculate the electron affinity $\text{EA} = 4.89\text{ eV} - 0.34\text{ eV} = 4.16\text{ eV}$. The respective values for PCBM, ICBA and PCDTBT are derived accordingly.

Deeper insight into the actual energy landscape may eventually be gained from our Kelvin-Probe measurements (**Figure S3**). Due to a well-defined interface and the use of a bilayer structure for our solar cells, we can directly study interface energetics which are identical to the situation in our actual devices. In order to allow for the determination of absolute workfunction values from the measured contact potential difference (CPD) between the measurement tip and the sample surface, the tip was calibrated using a well-characterized batch of PEDOT:PSS ($\Phi_{\text{PEDOT}} = 5.100\text{eV}$, $\Phi_{\text{tip}} = 4.828\text{ eV}$). The workfunction is then simply calculated according to $\Phi = \Phi_{\text{tip}} - \text{CPD}$. Film thicknesses of the acceptors were (4 ± 1) nm. The acceptors were deposited on top of a crosslinked layer of PCDTBTOx. The error in these measurements simply corresponds to the experimentally observed fluctuation of CPD values between different measurements (deviation from average) and is in the order of 10-20 meV.

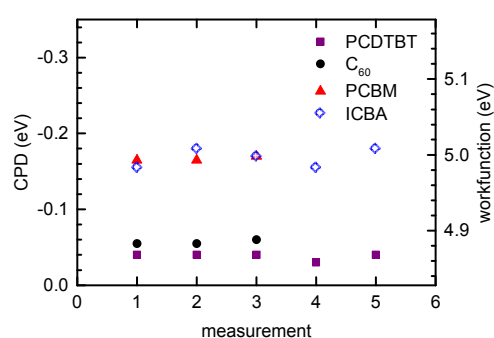


Figure S3: Measured Contact Potential Difference (CPD) between tip and sample surface (left axis) as well as derived work function values Φ for all the investigated materials (right axis).

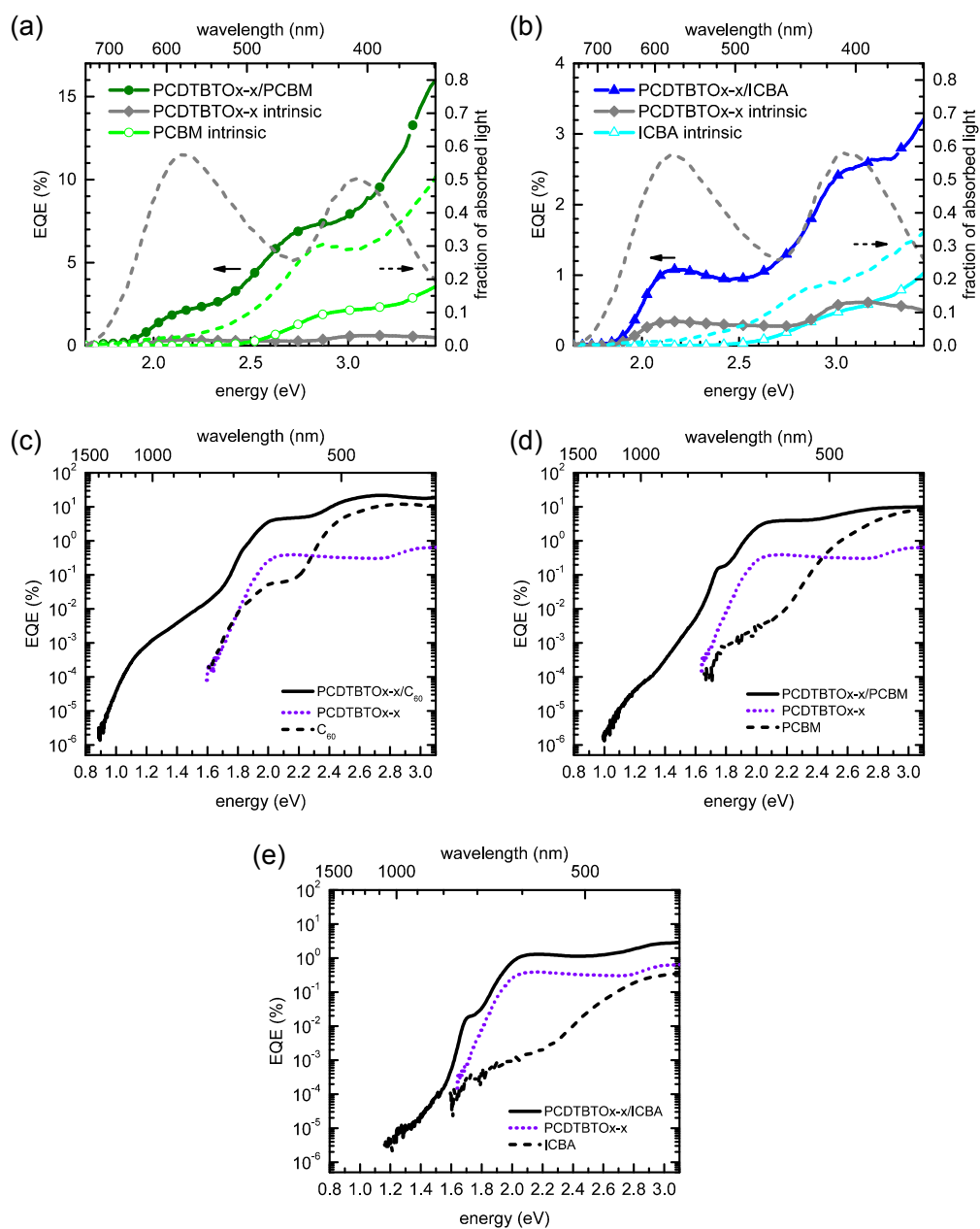


Figure S4: (a) Left axis: EQE of a PCDTBTOx-x/PCBM bilayer solar cell (green filled dots) in comparison to the EQE of single layer devices of the pristine materials PCDTBTOx-x (grey filled diamonds) and PCBM (light green open dots). The suffix -x refers to the fact, that the donor layer is crosslinked. EQE was measured under short circuit conditions. Right axis: Simulated

fraction of absorbed light of the respective layer in a bilayer device using the transfer matrix algorithm (dashed lines). (b) Left axis: EQE of a PCDTBT_x/ICBA bilayer solar cell (blue filled triangles) in comparison to the EQE of single layer devices of the pristine materials PCDTBT_x (grey filled diamonds) and ICBA (light blue open triangles). EQE was again measured under short circuit conditions. Right axis: Simulated fraction of absorbed light of the respective layer in a bilayer device using the transfer matrix algorithm (dashed lines). (c) Comparison of bilayer EQE with the EQE of single layer devices of the pristine materials for PCDTBT_x/C₆₀. The region below about 1.7 eV can be clearly identified to be related to CT-absorption. (d) Same as in (c) but for PCDTBT_x/PCBM. (e) Same as in (c) and (d) but for PCDTBT_x/ICBA.

Discussion of the internal quantum efficiency (Figure 3c):

To exclude the possibility, that the observed EQE differences between the acceptors are simply caused by differences in absorption or reflection, we calculated the internal quantum efficiency (IQE) using the absorption profiles we obtained via the transfer matrix algorithm (**Figure 3c**). The detailed deconvolution of the absorption contributions from different layers as well as the reflectance can be found in **Figure S5**.

The calculations were performed using the code provided free of charge by McGehee and coworkers.³ For n and k of glass, ITO, PCBM and Al we used the values already present in the library provided by McGehee. For MoO_3 we used the values from the free online library RefractiveIndex.INFO.⁴ Data for n and k of PCDTBTOx we took values from the work of Schmiedova et al.⁵ ICBA permittivity data were taken from the work of Leman et al. and converted to n and k values.⁶ Data for C_{60} and BCP were extracted from the work of Wynands et al. and Liu et al., respectively.⁷⁻⁸

We find the same trend in the IQE as in the EQE indicating that differences in the absorption profile and strength cannot account for the differences in quantum efficiency. The fact that the IQE decreases for energies below 2.0 eV can be explained by the bandgap of the materials. Below 2.0 eV (PCDTBTOx) and above 1.7-1.85 eV (fullerenes)⁹⁻¹⁰ mostly tightly bound Frenkel excitons are created, from which only a fraction reaches the interface due to an acceptor layer thickness larger than the exciton diffusion length of less than 10nm.¹¹ The rest of them will mostly recombine resulting in a low IQE. It is expected to rise again for direct CT excitation as then all the excited states already reside at the interface.¹²

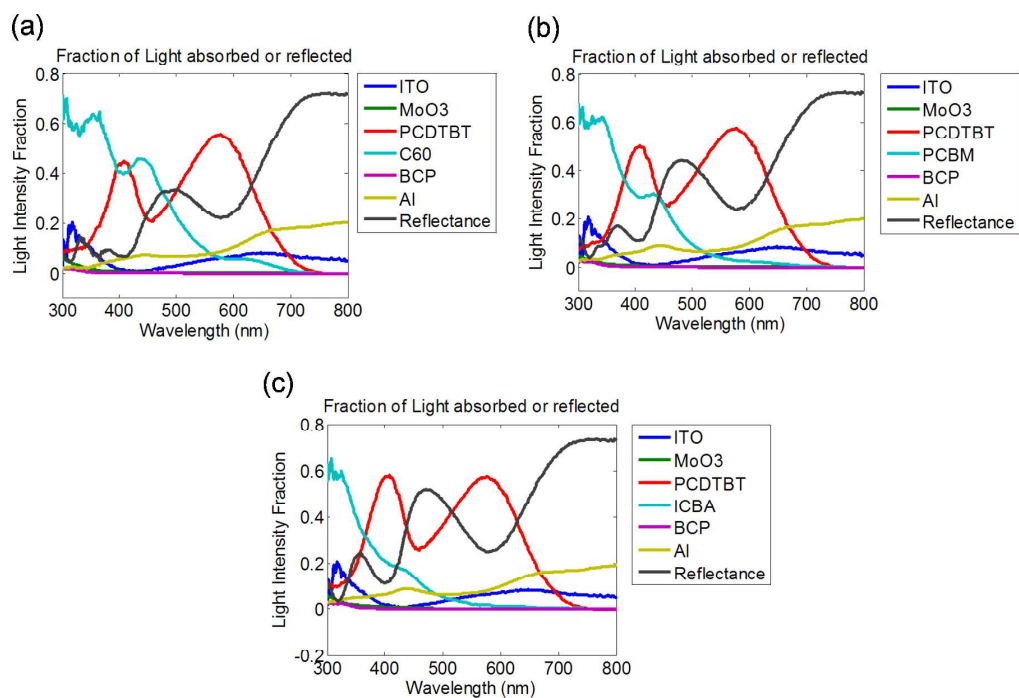


Figure S5: (a) Fraction of the incident light absorbed of each individual layer of a glass/ITO/MoO₃/PCDTBT_{x-x}/C₆₀/BCP/Al plotted together with the total reflectance (black). The calculation was performed using the transfer matrix algorithm. (b) Same as in (a) but with PCBM instead of C₆₀. (c) Same as in (a) but with ICBA instead of C₆₀.

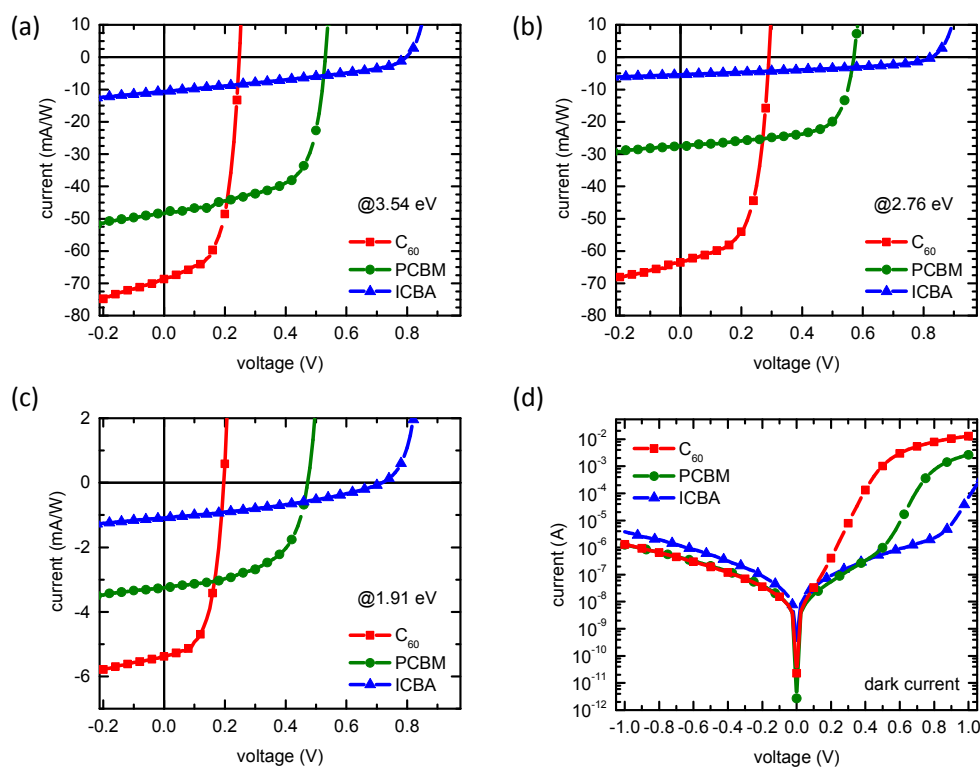


Figure S6: Comparison of monochromatic current-voltage (IV) characteristics of bilayer solar cells all with varying acceptors on top of the crosslinked PCDTBTOx layer. The excitation energies were (a) 3.54 eV, (b) 2.76 eV and (c) 1.91 eV. The observed trend in V_{OC} and I_{SC} is discussed in the main text. (d) Dark IV characteristics of the devices shown in (a). A difference in built-in potential is clearly visible from different onset voltages. This is also evidenced by voltage dependent electroabsorption measurements (Figure S10b)

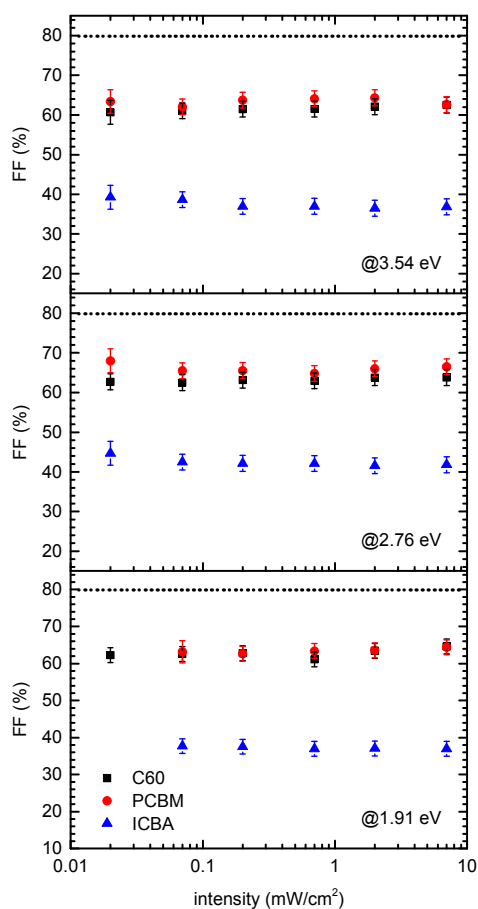


Figure S7: Fill Factor (FF) as function of illumination intensity for the same devices as in Figure 3b and c. The excitation energies were 3.54 eV (top), 2.76 eV (middle) and 1.91 eV (bottom).

Note:

Also for intensity dependent measurements of the FF above the autoionization threshold of fullerenes we find no intensity dependence of FF over three decades of illumination intensity. This again indicates that there is no bimolecular recombination present in our devices. Yet, the FF is a little bit lower than for excitation energies below 2.25 eV (see Figure 4a). This may be attributed to increased geminate recombination within the fullerene bulk due to the presence

of electrons and holes, that are the result of the splitting of bulk CT states of the neat fullerene (e.g. at 2.4 eV).^{9,13}

The overall smaller FF for ICBA indicates higher losses due to geminate recombination. This might in part be related to significantly more localized CT states that recombine with a higher rate k_{rec} . A major reason will surely be inefficient transport of excitons to the interface as well as charges away from it. The former is due to weak inter-fullerene coupling and the latter because of low electron mobility. As the mobilities of donor and acceptor are rather balanced in the case of ICBA we do not expect and also not observe an s-shape as discussed above.¹⁴ Nevertheless, geminate recombination probability will be enhanced for low mobilities¹⁴⁻¹⁵ (even if they are balanced). This is reflected in a lower FF for ICBA, a low J_{SC} and a considerable reduction of EQE and IQE in comparison to PCBM and C₆₀. With this interpretation, our results are in line with the work of Larson et al. who found that that low mobility in fullerenes also affects the charge generation at the interface.¹⁵

Another possible factor would be exciton recycling to the polymer due to the smaller EA offset for ICBA compared to PCDTBTOx, but as evidenced from voltage dependent electroluminescence measurements, this is not the case (see below).

Comment on exciton recycling:

Looking at the offsets of IE values between donor and acceptors, we find a difference of at least 0.63 eV, which should be sufficient to suppress large exciton recycling to the acceptor also in the case of ICBA. In the case of EA, ICBA only features a difference of 0.48eV. We therefore investigated by measuring electroluminescence (EL) whether there is any backtransfer of CT-excited to the polymer.¹⁶ If there was considerable exciton recycling in the PCDTBTOx/ICBA system, it should take place back to the polymer according to the energy levels obtained from UPS and IPES, and thus should emerge as a function of increasing drive voltage in forward direction. A corresponding behavior is not observed even for higher voltages (**Figure S8**). We rather see EL from ICBA, most likely due to recombination of excitons in the bulk of ICBA that do not reach the interface. Furthermore, we see dominant EL of a CT state at 1.4 eV and only a small contribution of ICBA itself, when biasing the device with only 1.5V. This also indicates that exciton recycling does not play a significant role in our devices.

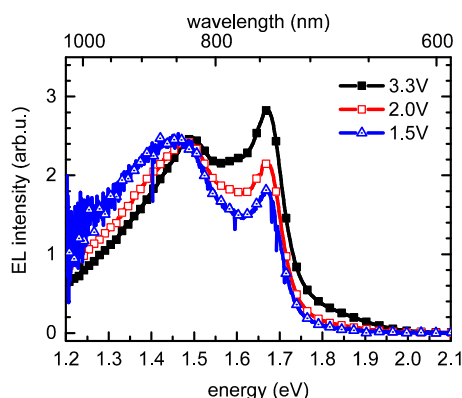


Figure S8: Voltage dependent EL spectra of PCDTBT/ICBA solar cells. A distinct shoulder at around 1.4 eV emerges upon decreasing voltage that is not related to emission from pristine ICBA or PCDTBT.

EL measurements: For Electroluminescence (EL) measurements, the solar cells were biased at 1.5 – 3.3V using a Keithley source-measure unit (SMU 237). The luminescence of the sample was recorded by a Si-CCD camera (Andor iDus420) coupled to a monochromator (Oriel MS125) or an IR-CCD camera (Andor iDus InGaAs 1.7 μm) also coupled to a monochromator (Andor

S17

Shamrock). The sample was kept in an appropriate vacuum condition sample holder at room temperature.

Comment on the correction of field dependent EQE data:

For 1.90 eV and 2.14 eV the field dependent EQE was corrected for the donor contribution by subtracting the field dependent EQE of a single layer PCDTBTOx device and taking the actual absorption profile in a bilayer device into account. This is mainly of importance for ICBA due to the low efficiency of the respective devices

For 2.76 eV and 3.54 eV (i.e. above autoionization threshold) saturation field strengths are determined after correcting for the intrinsic contribution in donor and acceptor, which were again corrected for differences in absorption in the actual bilayer. As this is only a simplified correction, the error is a bit higher compared to the data at 1.90 eV and 2.14 eV (i.e. below the threshold), but the qualitative trend is still reliable.

In order to study the dissociation efficiency at the interface quantitatively in terms of the effective mass model, we use data obtained from measurements below the autoionization threshold, because there dissociation at the interface is dominant. At higher energies there will be no distinct saturation regime due to the additional contribution from fullerene bulk CT-states at higher field strength, a factor that is not covered by the model we use. For our analysis, we therefore chose an excitation energy of 2.14 eV.

Alternative method to determine F_{Sat} : 90%-method

An alternative to the tangent method to determine F_{Sat} is to define it as the field strength at which EQE reaches 90% of the plateau value in the saturation regime. This method gives the same qualitative trend for F_{Sat} , but (slightly) different absolute values.

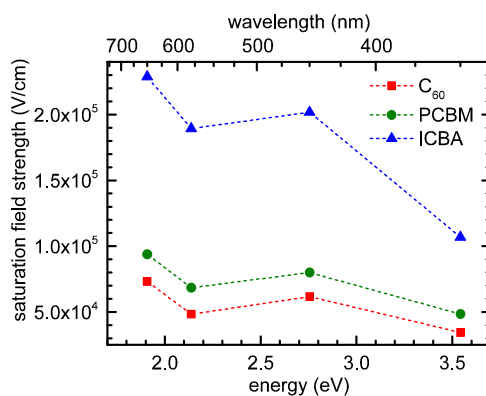


Figure S9: F_{Sat} as function of excitation energy for all three acceptors as obtained via the 90%-method.

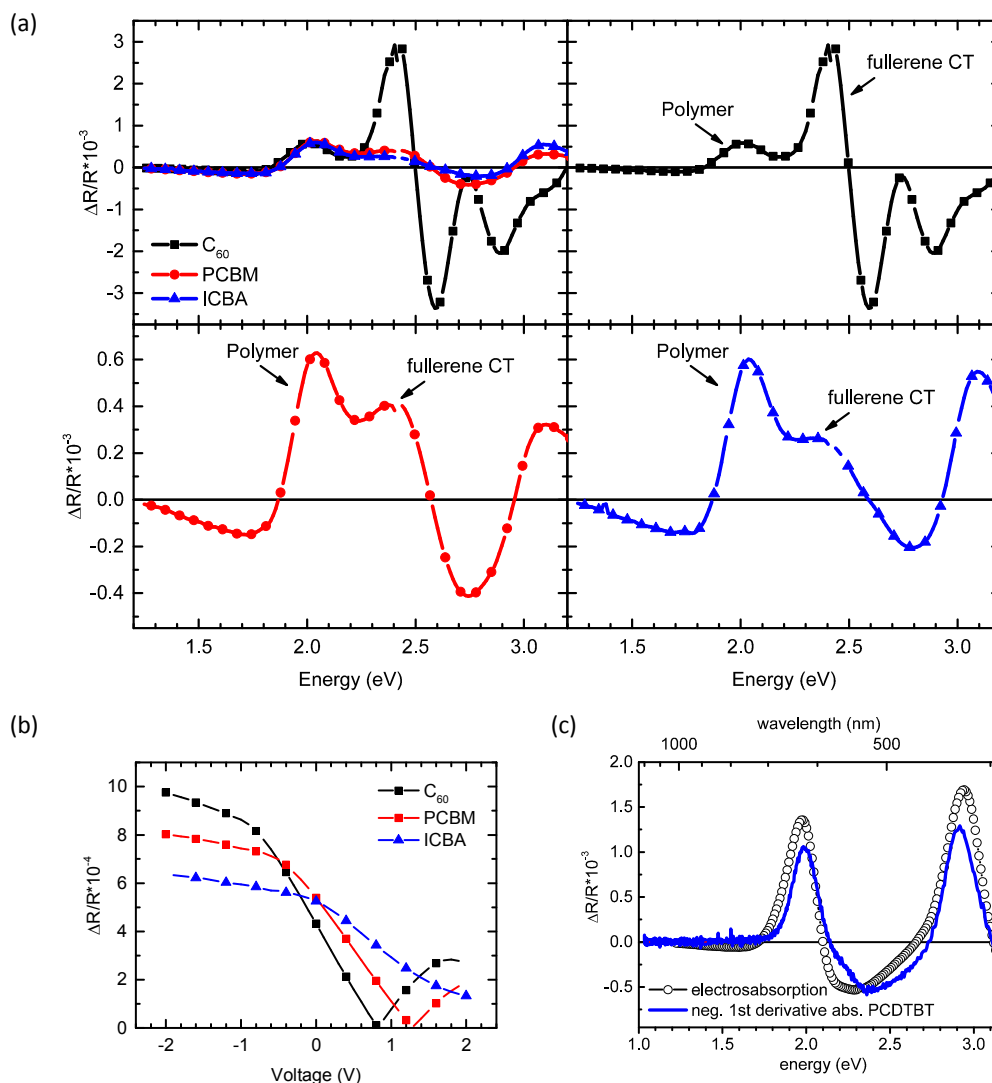


Figure S10: (a) Top left: Electroabsorption spectra of bilayer devices using C₆₀ (squares), PCBM (dots) or ICBA (triangles) as acceptor. The experimental conditions were chosen such, that the internal field is comparable among the samples. Top right to bottom right: Detailed view of the spectra shown in (a). The height of the polymer peak at around 2.0 eV is the same for all spectra, while the CT-related peak at around 2.2-2.3 eV (corresponding to the CT absorption peak at 2.4 eV)¹³ decreases in the order C₆₀ > PCBM > ICBA. (b) Voltage dependent Electroabsorption amplitude recorded at 1.9 eV. The (extrapolated) intersection of the linear

part of the curves at small changes $\Delta R/R$ with the abscissa is a measure of the built-in potential of the respective device.¹⁷⁻¹⁹ (c) Electroabsorption spectra of pristine crosslinked PCDTBTOx (open circles). It coincides very well with the first derivative of the steady state absorption spectrum (blue line), which is typical for an induced dipole momentum.¹⁸⁻²³ Furthermore, it shows a distinct peak at around 2.0 eV that is also present in the electroabsorption spectra of the bilayer devices shown in (a).

Field dependent fits:

Figure S11 illustrates the necessity to take wavefunction delocalization via effective masses into account in order to achieve reasonable fits to the experimental data. In the top panel of (a) and (b) we increased the effective mass up to a value of 10.0 - which corresponds to strongly localized charge carriers²⁴ - while keeping the other parameters at the same values as in the main text. This shows that when considering interfacial dipoles, the effect of charge carrier mobility and a reasonable value for the CT lifetime in the order of few tens of ns,²⁴ a reasonable fit may be only obtained, if a certain degree of wavefunction delocalization is taken into account. Numerically, a good fit may still be obtained for higher effective masses, yet at the cost of having to assume unphysically high values for the lifetime τ_0 (bottom panels of (a) and (b)). The used parameter set is summarized in **Table S1**.

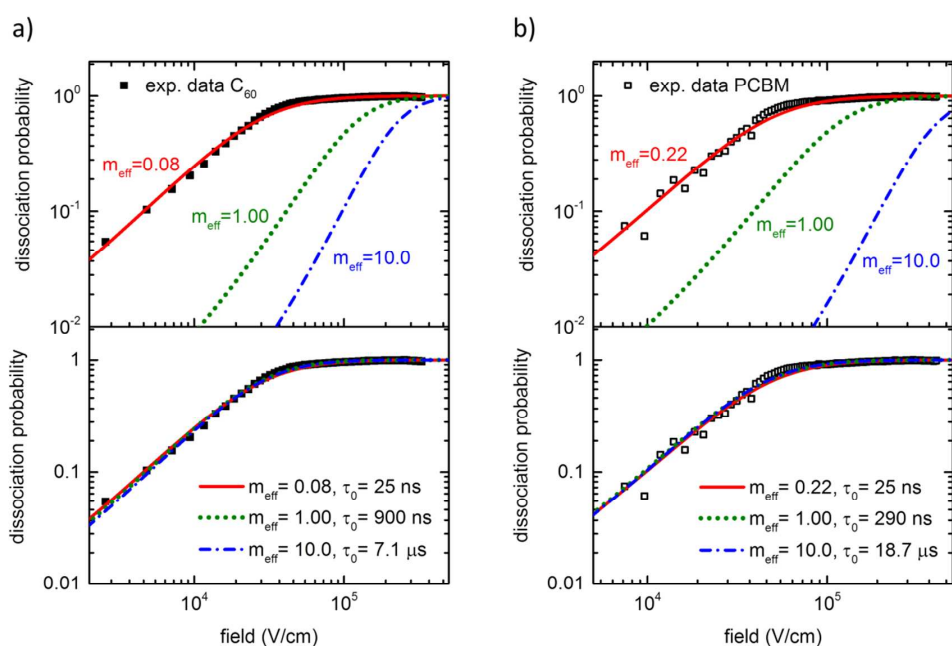


Figure S11: Dissociation probability of a CT-state in (a) PCDTBTOx/C₆₀ (squares) and (b) PCDTBTOx/PCBM (open squares) bilayer solar cells as function of the internal electric field. Solid red lines correspond to the simulations in the main text according to the effective mass model taking interfacial dipoles into account. In the top panels we varied the effective mass while

keeping all the other parameters constant. In the bottom panels, τ_0 was additionally adjusted to obtain numerically good fits for the different effective masses m_{eff} .

Table S1: Parameter set that is used in the simulations of field dependent data according to the effective mass model under consideration of interfacial dipoles. The different quantities are explained in the main text.

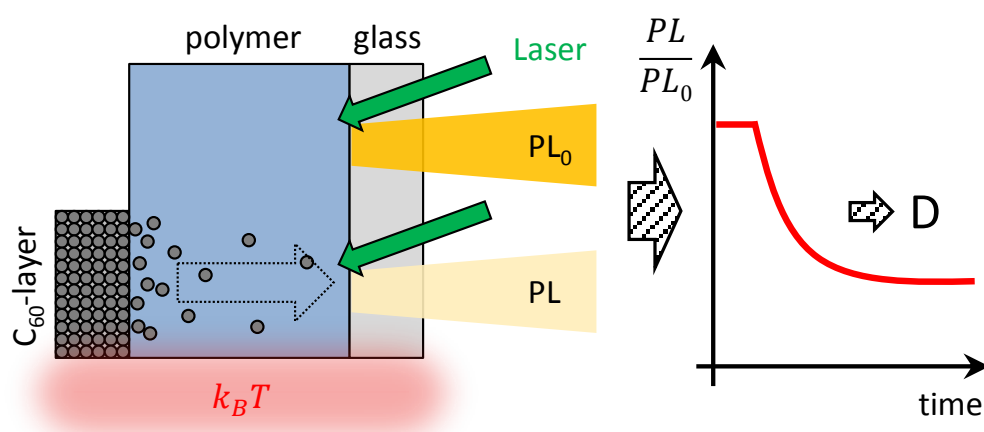
Material	$\alpha \cdot 10^{-3}$	$\mu / \frac{\text{cm}^2}{\text{Vs}}$	τ_0 / ns	$\tau_0 \nu_0 \cdot \exp(-2\gamma r)$	m_{eff}
C ₆₀	3.0	$5 \cdot 10^{-2}$	25	19406	0.08
	3.0	$5 \cdot 10^{-2}$	25	19406	1.00
	3.0	$5 \cdot 10^{-2}$	25	19406	10.0
	3.0	$5 \cdot 10^{-2}$	900	700000	1.0
	3.0	$5 \cdot 10^{-2}$	7100	5500000	10.0
PCBM	22.6	$2 \cdot 10^{-3}$	25	776	0.22
	22.6	$2 \cdot 10^{-3}$	25	776	1.00
	22.6	$2 \cdot 10^{-3}$	25	776	10.0
	22.6	$2 \cdot 10^{-3}$	290	580000	1.00
	22.6	$2 \cdot 10^{-3}$	18700	8500000	10.0

References:

1. Chase, S. J.; Bacsá, W. S.; Mitch, M. G.; Pilione, L. J.; Lannin, J. S., Surface-Enhanced Raman-Scattering and Photoemission of C-60 on Noble-Metal Surfaces. *Phys. Rev. B.* **1992**, *46*, 7873-7877.
2. Nakanishi, R.; Nogimura, A.; Eguchi, R.; Kanai, K., Electronic Structure of Fullerene Derivatives in Organic Photovoltaics. *Org. Electron.* **2014**, *15*, 2912-2921.
3. Burkhard, G. F.; Hoke, E. T.; McGehee, M. D., Accounting for Interference, Scattering, and Electrode Absorption to Make Accurate Internal Quantum Efficiency Measurements in Organic and Other Thin Solar Cells. *Adv. Mater.* **2010**, *22*, 3293-3297.
4. Polyanskiy, M. N. Refractive Index Database. <https://refractiveindex.info> (accessed Aug 16, 2017).
5. Schmiedova, V.; Heinrichova, P.; Zmeskal, O.; Weiter, M., Characterization of Polymeric Thin Films for Photovoltaic Applications by Spectroscopic Ellipsometry. *Appl. Surf. Sci.* **2015**, *349*, 582-588.
6. Leman, D.; Kelly, M. A.; Ness, S.; Engmann, S.; Herzing, A.; Snyder, C.; Ro, H. W.; Kline, R. J.; DeLongchamp, D. M.; Richter, L. J., In Situ Characterization of Polymer-Fullerene Bilayer Stability. *Macromolecules* **2015**, *48*, 383-392.
7. Wynands, D.; Erber, M.; Rentenberger, R.; Levichkova, M.; Walzer, K.; Eichhorn, K. J.; Stamm, M., Spectroscopic Ellipsometry Characterization of Vacuum-Deposited Organic Films for the Application in Organic Solar Cells. *Org. Electron.* **2012**, *13*, 885-893.
8. Liu, Z. T.; Kwong, C. Y.; Cheung, C. H.; Djuricic, A. B.; Chan, Y.; Chui, P. C., The Characterization of the Optical Functions of Bcp and Cbp Thin Films by Spectroscopic Ellipsometry. *Synthetic Met.* **2005**, *150*, 159-163.
9. Hahn, T.; Tscheuschner, S.; Saller, C.; Strohriegel, P.; Boregowda, P.; Mukhopadhyay, T.; Patil, S.; Neher, D.; Bäessler, H.; Köhler, A., Role of Intrinsic Photogeneration in Single Layer and Bilayer Solar Cells with C-60 and Pcbm. *J. Phys. Chem. C* **2016**, *120*, 25083-25091.
10. Coffey, D. C.; Larson, B. W.; Hains, A. W.; Whitaker, J. B.; Kopidakis, N.; Boltalina, O. V.; Strauss, S. H.; Rumbles, G., An Optimal Driving Force for Converting Excitons into Free Carriers in Excitonic Solar Cells. *J. Phys. Chem. C.* **2012**, *116*, 8916-8923.
11. Köhler, A.; Bäessler, H., Fundamentals of Organic Semiconductor Devices. In *Electronic Processes in Organic Semiconductors: An Introduction*, Wiley-VCH: Weinheim, Germany, 2015; p 424.
12. Vandewal, K.; Albrecht, S.; Hoke, E. T.; Graham, K. R.; Widmer, J.; Douglas, J. D.; Schubert, M.; Mateker, W. R.; Bloking, J. T.; Burkhard, G. F., et al., Efficient Charge Generation by Relaxed Charge-Transfer States at Organic Interfaces. *Nat. Mater.* **2014**, *13*, 63-68.
13. Kazaoui, S.; Minami, N.; Tanabe, Y.; Byrne, H. J.; Eilmes, A.; Petelenz, P., Comprehensive Analysis of Intermolecular Charge-Transfer Excited States in C-60 and C-70 Films. *Phys. Rev. B* **1998**, *58*, 7689-7700.
14. Tress, W., Further Origins of S-Shaped J-V Curves. In *Organic Solar Cells - Theory, Experiment, and Device Simulation*, Springer: New York, 2014; p 474.
15. Larson, B. W.; Reid, O. G.; Coffey, D. C.; Avdoshenko, S. M.; Popov, A. A.; Boltalina, O. V.; Strauss, S. H.; Kopidakis, N.; Rumbles, G., Inter-Fullerene Electronic Coupling Controls the Efficiency of Photoinduced Charge Generation in Organic Bulk Heterojunctions. *Adv. Energy Mater.* **2016**, *6*, 1601427.
16. Hoke, E. T.; Vandewal, K.; Bartelt, J. A.; Mateker, W. R.; Douglas, J. D.; Noriega, R.; Graham, K. R.; Fréchet, J. M. J.; Salleo, A.; McGehee, M. D., Recombination in Polymer:Fullerene Solar Cells with Open-Circuit Voltages Approaching and Exceeding 1.0 V. *Adv. Energy Mater.* **2013**, *3*, 220-230.
17. Nonomura, S.; Okamoto, H.; Hamakawa, Y., Determination of the Built-in Potential in a-Si Solar-Cells by Means of Electro-Absorption Method. *Jpn. J. Appl. Phys.* **2** **1982**, *21*, L464-L466.

18. Li, C.; Credginton, D.; Ko, D. H.; Rong, Z. X.; Wang, J. P.; Greenham, N. C., Built-in Potential Shift and Schottky-Barrier Narrowing in Organic Solar Cells with Uv-Sensitive Electron Transport Layers. *Phys. Chem. Chem. Phys.* **2014**, *16*, 12131-12136.
19. Singh, C. R.; Li, C.; Mueller, C. J.; Hüttner, S.; Thelakkat, M., Influence of Electron Extracting Interface Layers in Organic Bulk-Heterojunction Solar Cells. *Adv. Mater. Interfaces* **2016**, *3*, 1500422.
20. Bernardo, B.; Cheyns, D.; Verreert, B.; Schaller, R. D.; Rand, B. P.; Giebink, N. C., Delocalization and Dielectric Screening of Charge Transfer States in Organic Photovoltaic Cells. *Nat. Commun.* **2014**, *5*, 3245.
21. Sebastian, L.; Weiser, G.; Bäessler, H., Charge-Transfer Transitions in Solid Tetracene and Pentacene Studied by Electro-Absorption. *Chem. Phys.* **1981**, *61*, 125-135.
22. Bublitz, G. U.; Boxer, S. G., Stark Spectroscopy: Applications in Chemistry, Biology, and Materials Science. *Annu. Rev. Phys. Chem.* **1997**, *48*, 213-242.
23. Vance, F. W.; Williams, R. D.; Hupp, J. T., Electroabsorption Spectroscopy of Molecular Inorganic Compounds. *Int. Rev. Phys. Chem.* **1998**, *17*, 307-329.
24. Tscheuschner, S.; Bäessler, H.; Huber, K.; Köhler, A., A Combined Theoretical and Experimental Study of Dissociation of Charge Transfer States at the Donor-Acceptor Interface of Organic Solar Cells. *J. Phys. Chem. B* **2015**, *119*, 10359-10371.

10 Facile Method for the Investigation of Temperature-Dependent C_{60} Diffusion in Conjugated Polymers



Christina Saller, Frank-Julian Kahle, Thomas Müller, Tobias Hahn, Steffen Tscheuschner, Denys Priadko, Peter Strohrriegel, Heinz Bäessler, and Anna Köhler

Published in
ACS Appl. Mater. Interfaces **2018**, *10*, 21499-21509
(DOI: 10.1021/acsami.8b05520)

Reprinted by permission of *ACS Appl. Mater. Interfaces* **2018**, *10*, 21499-21509.
Copyright ©(2018) American Chemical Society.

Facile Method for the Investigation of Temperature-Dependent C₆₀ Diffusion in Conjugated Polymers

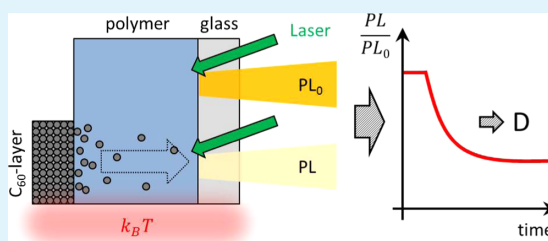
Christina Saller,^{†,‡} Frank-Julian Kahle,^{†,‡,⊥} Thomas Müller,[‡] Tobias Hahn,[‡] Steffen Tscheuschner,[‡] Denys Priadko,[‡] Peter Strohriegel,^{†,§,||} Heinz Bässler,[§] and Anna Köhler^{*,‡,§,⊥}

[†]Macromolecular Chemistry I, [‡]Soft Matter Optoelectronics, [§]Bayreuth Institute of Macromolecular Science (BIMF), and [⊥]Bavarian Polymer Institute (BPI), University of Bayreuth, 95440 Bayreuth, Germany

Supporting Information

ABSTRACT: We developed a novel all-optical method for monitoring the diffusion of a small quencher molecule through a polymer layer in a bilayer architecture. Experimentally, we injected C₆₀ molecules from a C₆₀ layer into the adjacent donor layer by stepwise heating, and we measured how the photoluminescence (PL) of the donor layer becomes gradually quenched by the incoming C₆₀ molecules. By analyzing the temporal evolution of the PL, the diffusion coefficient of C₆₀ can be extracted, as well as its activation energy and an approximate concentration profile in the film. We applied this technique to three carbazole-based low-bandgap polymers with different glass temperatures with a view to study the impact of structural changes of the polymer matrix on the diffusion process. We find that C₆₀ diffusion is thermally activated and not driven by WFL-type collective motion above T_g but rather by local motions mediated by the sidechains. The results are useful as guidance for material design and device engineering, and the approach can be adapted to a wide range of donor and acceptor materials.

KEYWORDS: diffusion, fullerene, low-bandgap polymer, fluorescence quenching, glass transition



1. INTRODUCTION

Molecular diffusion processes and associated changes in film composition and/or morphology are a critical factor in terms of performance, thermal stability, and degradation of organic semiconducting devices.^{1–3} For example, in an organic light-emitting diode (OLED), the active element is a stack of several transport and emitter layers including a large number of interfaces. Those interfaces can be sharp during the initial film preparation but may become more intermixed during the subsequent device operation because of molecular diffusion, which will alter the performance of the OLED.⁴ In fact, if well controlled, the diffusion process may be employed beneficially not only to determine the degree of interfacial intermixing but also to control doping processes in organic semiconductors.³ Similarly, for organic semiconductor devices such as organic solar cells (OSCs) annealing can induce morphological changes that improve the device performance.^{2,5} However, device optimization by annealing is often based on trial and error as too little is known about the temperature-dependent diffusivities of molecular dyes, acceptors, or dopants in the polymer matrix.

The diffusion of ions in inorganic glasses^{6–8} or of tracer molecules in polymers^{9–11} has been studied extensively. The results indicate that ion diffusion in inorganic glasses is a thermally assisted process featuring an Arrhenius-type temperature dependence, whereas molecular diffusion in polymers is usually controlled by Vogel–Fulcher–Tammann (or Wil-

liams–Landel–Ferry, WLF) law, applicable to glass dynamics near or above the glass transition temperature T_g, described by free volume concepts. The pertinent question is to which extent these conclusions apply for the diffusion of more bulky molecules such as C₆₀ in soft organic semiconductors such as conjugated polymers or glasses of organic oligomers. It seems plausible that in this case, molecular diffusion might indeed require free volume of the transporting matrix.^{12–15}

The diffusion of acceptor or dopant molecules in a polymeric or molecular matrix has only been addressed in the organic electronics community over the past decade, with the main concern being the morphological stability of films used in optoelectronic devices at elevated temperatures.^{3,16–18} In recent years, however, there have been an increasing number of studies that addressed molecular diffusion by various methods in a qualitative or quantitative way.^{2–4,14,16,19–27} Approaches employed include dynamic secondary ion-mass spectroscopy (DSIMS),^{2,14,19–21,25} scattering experiments (grazing-incidence small-angle scattering, grazing-incidence wide-angle X-ray scattering, resonant soft X-ray scattering, neutron reflectivity, near edge X-ray absorption fine structure, small-angle neutron scattering, grazing incidence X-ray diffraction),^{2,4,14,16,23,25,26} or spatially resolved optical, electron,

Received: April 5, 2018

Accepted: May 30, 2018

Published: May 30, 2018

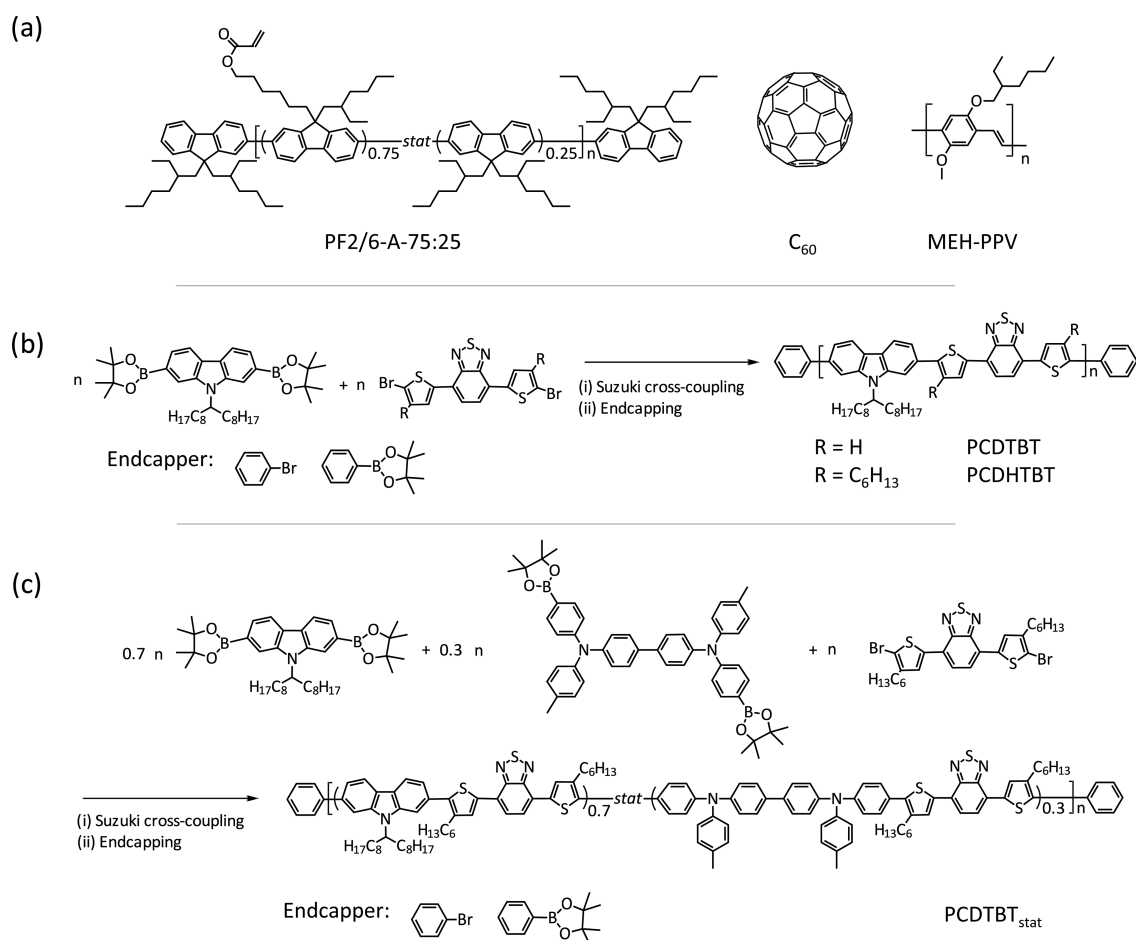


Figure 1. (a) Chemical structures of the PF2/6-A-75:25 polymer with cross-linkable acrylate groups, fullerene C_{60} , and poly(2-methoxy-5-(2-ethylhexyloxy)-1,4-phenylenevinylene) (MEH-PPV). (b) Synthetic route to the two donor-acceptor polymers PCDTBT and PCDHTBT: (i) toluene, aqueous NEt_4OH solution (20 wt %), Pd_2dba_3 , $P(o-tolyl)_3$, reflux, 72 h, (ii) bromobenzene, reflux, 1 h, phenylboronic acid, reflux, overnight. (c) Synthetic route to the donor-acceptor polymer $PCDTBT_{stat}$: (i) toluene, aqueous Na_2CO_3 solution (2 M), Aliquat 336, $Pd(PPh_3)_4$, reflux, 72 h, (ii) bromobenzene, reflux 1 h, phenylboronic acid, reflux, 1 h.

or X-ray microscopy as a tool to monitor diffusion.^{2,4,14,16,23–25,27}

In previous work, we introduced an approach to monitor diffusion and determine diffusion coefficients by comparatively simple photoluminescence (PL) measurements.²⁸ The approach was based on an adaptation of the time-of-flight-time technique, originally used to measure the mobility of charge carriers in organic semiconductor sandwiches between injecting and extracting electrodes.^{29–31} In that work, a polyfluorene derivative was sandwiched between a C_{60} layer on top and a fluorescent sensor layer at bottom. C_{60} molecules were “injected” from the C_{60} layer via stepwise increase of the temperature and diffused through the polymer layer to the sensor, where they accumulate and quench the sensor’s photoluminescence (PL). By recording the time until the PL quenching sets in, the diffusivity of the C_{60} molecules in the polymer could be derived. The essential result was that C_{60} diffusion is indeed thermally activated, and that the diffusion coefficient is reduced by 3 orders of magnitude upon cross-

linking the polyfluorene layer. This is a clear manifestation that the morphology of the transport layer is important and gives a guideline toward improved stability of polymer/ C_{60} devices. In our current work, we again apply an all-optical approach to study the diffusion of small quencher molecules, in our case C_{60} , in a polymer matrix but now applying a modified two-layer architecture. The advantage of our new approach is that the investigated material itself acts as a sensor for PL quenching, thus resulting in greater variability of investigable systems. The only requirement is its fluorescing ability.

This article is structured as follows. After introducing the materials in Section 2, Section 3 describes how the experiment is conducted and analyzed, and how it compares to our previous measurements. Section 4 illustrates how the novel approach can be employed to study fullerene diffusion in low-bandgap polymers such as PCDTBT and its derivatives previously spectrally not accessible to us. We show that our new method is capable of quantitatively determining the temperature-dependent diffusion coefficient and the associated

activation energy and equilibrium concentration of small molecules within a polymer matrix, both above and below the glass transition temperature. Interestingly, we find that diffusion is already present well below the glass transition temperature of the polymer backbone, T_g , and that all three PCDTBT derivatives feature similar diffusion coefficients at T_g . This means that below T_g , diffusion of small molecules in these polymers may be governed by local chain motion because of the mobility of the sidechains rather than by the collective motion of the chain backbone. In the end, because of its simplicity, our new approach may provide facile and valuable assistance in the engineering process of organic semiconducting devices.

2. SYNTHESIS AND MATERIALS

For the investigation of the diffusion process of C_{60} in a polymer matrix, we used two different material sets. For the comparison of the novel two-layer and three-layer methods, the cross-linkable polyfluorene PF2/6-A-75:25, already investigated in ref 28, was used. The chemical structures of PF2/6-A-75:25 with pendant acrylate units fullerene C_{60} and poly(2-methoxy-5-(2-ethylhexyloxy)-1,4-phenylenevinylene) (MEH-PPV) are shown in Figure 1a. In PF2/6-A-75:25, 75% of the sidechains contain acrylate moieties that were cross-linked by illumination with UV light at 40 °C for 10 min. In addition, a series of three donor–acceptor polymers including the well-known low-bandgap polymer PCDTBT was chosen (Figure 1b,c). This series exhibits fluorescence at longer wavelengths and allows studying the impact of small changes of the chemical structure on the diffusion behavior. The addition of hexyl spacers to the thiophene groups in the acceptor unit of PCDTBT yielded PCDHTBT. Another modification was the incorporation of a phenyl-substituted benzidine unit in the polymer backbone, resulting in PCDTBT_{stat}.

The synthesis of the three polymers is schematically depicted in Figure 1b,c. The donor monomer 2,7-bis-(4',4',5',5'-tetramethyl-1',3',2'-dioxaborolan-2'-yl)-N-(heptadecan-9"-yl)-carbazole and the acceptor monomers 4,7-bis(5'-bromothien-2'-yl)-2,1,3-benzothiadiazole and 4,7-bis(5'-bromo-4'-hexylthien-2'-yl)-2,1,3-benzothiadiazole are commercially available. For the synthesis of the second donor monomer *N,N'*-bis(4-methylphenyl)-*N,N'*-bis((4',4',5',5'-tetramethyl-1',3',2'-dioxaborolan-2'-yl)phenyl)benzidine, the corresponding dibromide is synthesized according to literature³² and converted into the bisborolane monomer via lithiation and reaction with 2-isopropoxy-4,4,5,5-tetramethyl-1,3,2-dioxaborolane, as shown in the Supporting Information.

The polymerizations are performed via Suzuki cross-coupling between bisborolane donor- and dibromide acceptor monomers. PCDTBT and PCDHTBT are synthesized similar to literature procedures.^{33,34} Endcapping of the polymers was carried out by subsequent addition of bromobenzene and phenylboronic acid after the polycondensation was finished. In the case of PCDTBT_{stat}, the donor monomer fraction was divided into a molar ratio of 0.7:0.3 for the carbazole and the phenyl-substituted benzidine monomer.³⁵ The composition was verified by NMR spectroscopy to be 0.7:0.3:1 for the carbazole, the benzidine, and the bithienyl benzothiadiazole moieties. The complete synthetic details are given in the Supporting Information.

Within this series of low-bandgap polymers, the glass transition temperature of the polymers varies. Table 1 includes the glass transition temperatures T_g and the molecular weights for the three polymers, as determined by differential scanning calorimetry (DSC) and (high-temperature) size-exclusion chromatography (SEC), respectively. We find that the reference polymer PCDTBT exhibits a T_g of 112 °C, whereas the glass transition temperature decreases to about 60 °C for PCDHTBT. We attribute this mainly to the addition of hexyl spacers to the thiophene units, which renders the PCDHTBT chains more flexible, and, to a minor extent, to the lower molecular weight of PCDHTBT. In contrast, the incorporation of the bulky phenyl-substituted benzidine units in PCDTBT_{stat} leads to a lower

Table 1. Glass Transition Temperatures T_g and Molecular Weights (Number-Average M_n and Weight-Average M_w) of the Three Polymers, as Determined by DSC and SEC Measurements

polymer	T_g /°C	M_n /g mol ⁻¹	M_w /g mol ⁻¹
PCDTBT	112	16 000 ^a	37 000 ^a
PCDHTBT	60	7000	14 000
PCDTBT _{stat}	110	18 000	47 000

^aHigh-temperature SEC at 150 °C in trichlorobenzene and polystyrene calibration.

flexibility. However, this is balanced by the hexyl spacers in the acceptor units. Thus, the glass transition of PCDTBT_{stat} is almost equal to that of PCDTBT, namely 110 °C. The DSC measurements are included in the Supporting Information. PF2/6-A-75:25 has a T_g of 80 °C,³⁶ which increases upon cross-linking.

3. ALL-OPTICAL MEASUREMENT OF C_{60} DIFFUSION BY A TWO-LAYER SETUP

3.1. Optical Two-Layer Setup. We prepared samples in a nitrogen-filled glovebox by first spin-coating a thin polymer layer onto a 2 × 2 cm² quartz substrate and then evaporating a 30 nm thick C_{60} layer with a shadow mask onto half of the polymer film. The general structure is shown in Figure 2a. Here, we used 200–270 nm thick films of PF2/6-A-75:25 that were cross-linked by UV-illumination at 40 °C (15 min at 50 W) prior to C_{60} deposition. This allows for a comparison to a previously used three-layer setup in which the same material was used.²⁸ The measurement is based on comparing the photoluminescence obtained from the half that is covered with C_{60} to that from the uncovered reference half after a temperature increase. As illustrated in Figure 2b, the technique is based on the premise that enhanced diffusion of C_{60} into the polymer layer takes place after a sudden temperature increase from T_1 to T_2 , which reduces the observed PL through quenching.

To this end, the polymer layer is excited through the quartz substrate on the C_{60} -covered half and on the reference half, using a continuous-wave diode laser at 405 nm for PF2/6-A-75:25 at an excitation density of ca. 15 mW cm⁻². The photoluminescence is recorded using a fiber-coupled spectrometer connected to a charge-coupled device camera (Andor-Solis). For the measurements, the samples are held under nitrogen in a heatable cryostat. The temperature was controlled with an ITC502 temperature controller. For the temperature rise, a high heating rate of 10 K min⁻¹ was chosen until the final temperature T_2 was reached. To record each data point, the reference half and the C_{60} -covered half of the sample were excited immediately after each other, and shutters were used to limit the exposure time of the sample in between recordings to the minimum. Figure 2c shows how the photoluminescence intensity of the C_{60} -covered half, normalized to that of the reference half, reduces as a function of time upon heating. For reference, the temperature in the cryostat is also indicated.

3.2. Theoretical Model. The diffusion coefficient $D(T_2)$ can be obtained from the photoluminescence transients using a suitable theoretical model. Consider the half that is initially covered with the C_{60} layer. As a result of the C_{60} coverage, we consider there to be an initial, uniformly distributed concentration of C_{60} sites in the film, $c(t = 0) = c_0(T_1)$, that may be finite or zero. We presume that photoluminescence (PL) quenching occurs upon contact between the polymer and

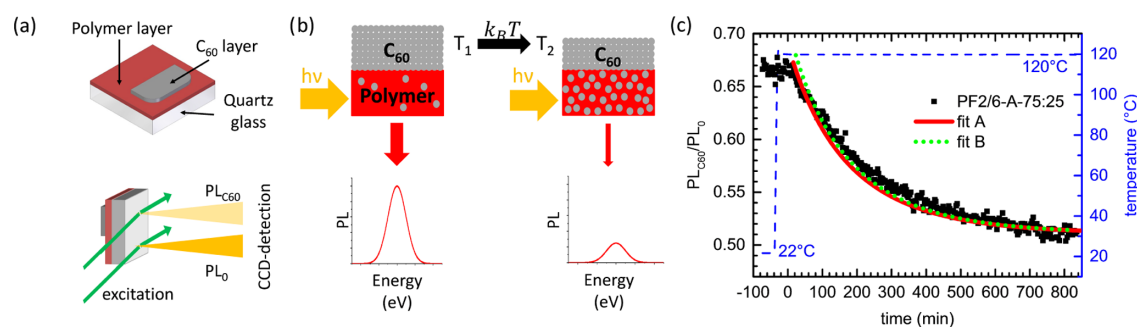


Figure 2. (a) Schematic of the sample and measurement geometry. (b) Schematic illustrating how the experiment is conducted. (c) Time-dependent decrease of the relative PL intensity, $PL_{C_{60}}/PL_0$ (left axis), measured on bilayer samples of cross-linked PF2/6-A-75:25 with C_{60} on top upon increasing the temperature from 22 to 120 °C (right axis). The solid red line and the green dotted lines correspond to different fits.

the C_{60} . Upon increasing the temperature from T_1 to T_2 , a new, larger equilibrium concentration $c_0(T_2) = c_0(T_1) + \Delta c_0(T_1, T_2)$ will establish at long times as a result of increased C_{60} diffusion from the top layer into the film. Concomitantly, the photoluminescence in the polymer film will reduce until a final equilibrium value is obtained at long times.

As the area of the polymer film (400 mm²) is large compared with its thickness (200–270 nm), it suffices to consider one-dimensional diffusion, on the basis of Fick's second law

$$\frac{\partial c(x, t)}{\partial t} = D \cdot \frac{\partial^2 c(x, t)}{\partial x^2} \quad (1)$$

where D is the diffusion coefficient, taken to be constant in time and space. We take $x = 0$ to be on the polymer side of the interface between the C_{60} layer and the polymer layer, and $x = d$ at the polymer-facing interface between the polymer and the quartz substrate, where no further diffusion is possible. For the boundary conditions $c(x = 0, t > 0) = c_0(T_2)$, and $\frac{\partial c(x = d, t)}{\partial x} = 0$, we use the known solution³⁷

$$c(x, t) = c_0(T_1) + \Delta c_0(T_1, T_2) \cdot f_c(x, t, T_2) \quad (2)$$

with $f(x, t, T_2) = \left(1 - \frac{4}{\pi} \sum_{n=0}^{\infty} \frac{(-1)^n}{2n+1} \exp\left(-D(T_2)(2n+1)^2 \pi^2 \frac{t}{4d^2}\right) \cos\left(\frac{(2n+1)\pi(d-x)}{2d}\right)\right)$

well as $0 \leq x \leq d$ and $\Delta c_0(T_1, T_2) = c_0(T_2) - c_0(T_1)$. This concentration of quenching sites leads to luminescence quenching with a rate $k_q(x, t)$. When a film of surface area A and thickness d is excited from the quartz side with a photon rate $k_0 = K_0 \exp(-\alpha(d-x))$, we thus find

$$PL(t) = A \cdot K_0 \int_0^d \exp(-\alpha(d-x)) \cdot \frac{k_r}{k_r + k_{nr} + k_q(x, t)} dx \quad (3)$$

for the film with the C_{60} quenchers, whereas

$$PL_0 = A \cdot K_0 \cdot \frac{k_r}{k_r + k_{nr}} \cdot \frac{1 - \exp(-\alpha d)}{\alpha} \quad (4)$$

applies for the part of the film that is not covered by C_{60} . α denotes the absorption coefficient, k_r the radiative, and k_{nr} the nonradiative decay rate of the excited state. The ratio between eqs 3 and 4 gives the evolution of the recorded normalized photoluminescence, that is,

$$\frac{PL}{PL_0}(t) = \frac{\alpha}{1 - \exp(-\alpha d)} \int_0^d \exp(-\alpha(d-x)) \cdot \left(1 + \frac{k_q(x, t)}{k_r + k_{nr}}\right)^{-1} dx \quad (5)$$

When the quenching rate depends linearly on the concentration of C_{60} molecules, $k_q(x, t) = K_D \cdot c(x, t)$, eq 5 reduces to

$$\frac{PL}{PL_0}(t) = \frac{\alpha}{1 - \exp(-\alpha d)} \int_0^d \exp(-\alpha(d-x)) \cdot (1 + K_D \cdot c(x, t))^{-1} dx \quad (6)$$

where $K_D = K_q/(k_r + k_{nr})$ is the Stern–Volmer constant that describes how strongly the PL of a material is reduced by a certain quencher.³⁸ At long times, a new equilibrium concentration $c_{max}(T_2)$ establishes so that quenching occurs with a constant rate $k_q(c_0(T_2)) = K_q \cdot c_0(T_2)$. This leads to a stationary value for the PL that is expressed by the Stern–Volmer equation

$$\frac{PL}{PL_0}(t \rightarrow \infty, T_2) = (1 + K_D \cdot c_0(T_2))^{-1} dx \quad (7)$$

The key equations to analyze the experimental data by numerical simulation are eqs 6 and 2. A more detailed derivation of eqs 6–5 can be found in the Supporting Information. There are two approaches to obtain the diffusion coefficient from this. A straightforward way (“fit A”) to obtain the diffusion coefficient is therefore to simulate the time-dependent decay of the luminescence using eq 6, with the C_{60} concentration given by eq 2. For this, the initial and final, spatially homogeneous equilibrium concentrations $c_0(T_1)$ and $c_0(T_2)$ are estimated on the basis of the experimental data using eq 7. The required Stern–Volmer constant K_D is taken from steady-state quenching experiments that we carried out as detailed in the Supporting Information. We determined the absorption coefficient, α , required to evaluate the data by measuring the absorption and the thickness of the films. In the simulation, the diffusion coefficient D is adjusted until the numerical simulation agrees with the experimentally observed luminescence decay. Figure 2c exemplary illustrates the good agreement between the PL quenching obtained for a 270 nm film of cross-linked PF2/6-A-75:25 and the simulated curve, using a value of $K_D = 4.81$ for the respective Stern–Volmer constant. This fitting procedure results in both a value for the

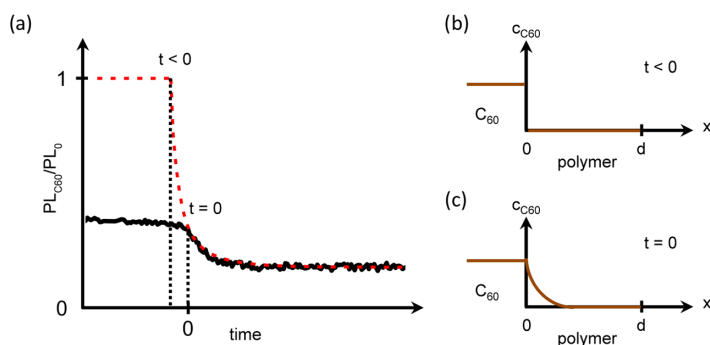


Figure 3. (a) Illustration of the fitting procedure using a self-consistent initial condition as described in the main text (fit B). The black solid line corresponds to experimental data, and the red dashed line is the result of a first simulation round starting nominally before the acceptor was deposited and ending at the final equilibrium concentration. (b) The concentration profiles assumed to prevail just before acceptor deposition at T_1 . This is used as the input to the first fitting round. (c) The concentration profile obtained from the first fitting round, assumed to prevail just before the heating step to T_2 . This is used as the initial condition for the second fitting round to the experimental data.

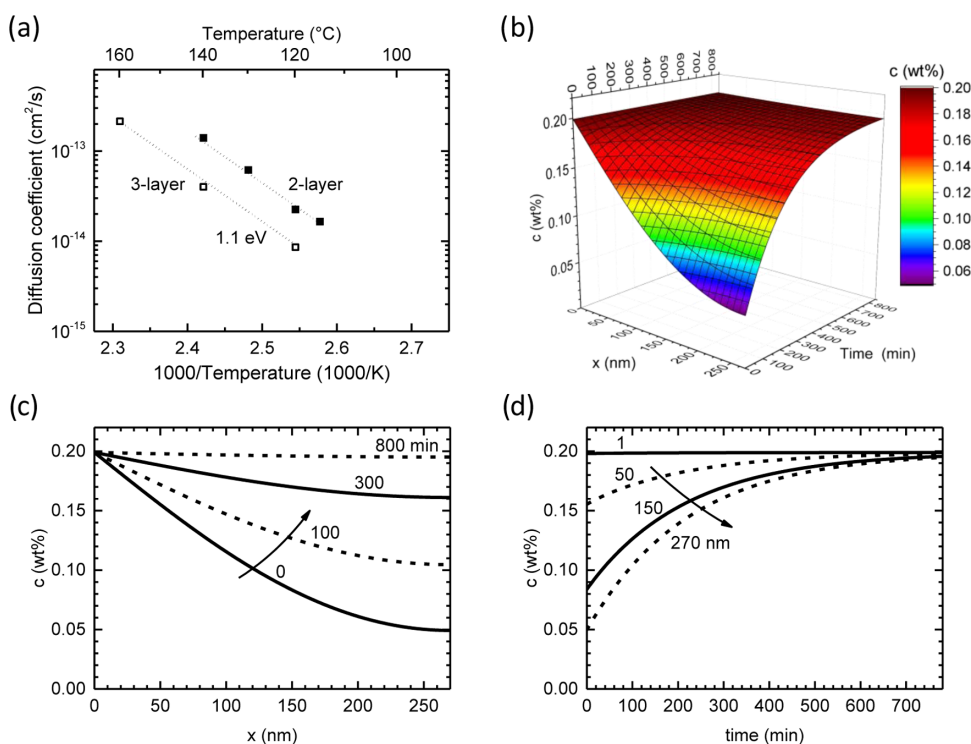


Figure 4. (a) Arrhenius representation of the temperature dependence of the diffusion coefficient for cross-linked PF2/6-A-75:25 measured in a three-layer architecture (open squares) and a two-layer architecture (filled squares). The slope yielding the activation energy, E_A , of diffusion is indicated by dotted lines. (b) Three-dimensional (3D) representation for the calculated time-dependent concentration, $c(x, t)$, of C_{60} . The positions $x = 0$ and 270 nm denote the interface to the C_{60} and the quartz substrate, respectively. (c) Distribution of $c(x, t)$ across the film thickness at different times. (d) Evolution of $c(x, t)$ with time at different positions in the film.

diffusion coefficient as well as a spatial and temporal concentration profile $c(x, t)$ after heating to T_2 .

Although fit A can be implemented easily, it assumes that the initial concentration of C_{60} in the film at T_1 be spatially homogeneous. However, this initial concentration of C_{60} after evaporation is not necessarily constant over the film thickness, and a concentration gradient can prevail. To account for this and to estimate the impact of this approximation, we also

explored an iterative, self-consistent approach ("fit B"). In the first step, we simulate the diffusion with the aim to obtain the approximate initial concentration profile in the experiment. For this, we apply eq 6 with the initial condition that there will be no C_{60} , and thus no PL-quenching in the film at a certain time $t < 0$. The diffusion coefficient, D , is adjusted until a reasonable fit to the experimental data is achieved, in particular at later times, as illustrated in Figure 3. From this simulation, we obtain

an initial spatial concentration profile $c(x, t)$. We use this profile at $t = 0$ in the second step as initial input concentration, nominally $c_0(T_1)$, to obtain an improved and more accurate diffusion coefficient. The quality of both fits is illustrated exemplarily in Figure 2c. Across all materials presented in this article, we found that the choice of initial conditions (spatially constant concentration, i.e., fit A, or spatial concentration gradient, i.e., fit B) affects the final value of the diffusion coefficient by less than 20%. This is illustrated and discussed in detail in the Supporting Information. All subsequent data presented in this article are based on fit B, which we consider to represent a more realistic scenario.

Our model has three premises that require discussing. (i) At first sight, the assumption of PL quenching upon C_{60} contact seems to neglect the exciton diffusion. This is, however, implicitly included through the value of the Stern–Volmer constant that was measured for each material in the solid film. (ii) Similarly, surface quenching at the interface to the C_{60} layer is not explicitly considered. This can be included through an additional surface quenching term in eq 6, but it has no significant effect on the diffusion coefficients as detailed in the Supporting Information. (iii) Equation 6 requires a linear dependence of the quenching rate on the quencher concentration. This is no longer warranted when C_{60} forms clusters. In that case, the effective quenching rate is smaller than that predicted on the basis of the Stern–Volmer constant measured for homogeneously distributed molecular C_{60} . In our measurements, the equilibrium concentrations of C_{60} in the cross-linked polyfluorene and the donor–acceptor polymers are 0.5 and 1–2%, respectively, as discussed in Sections 3.3 and 4.2. These low concentrations rule out cluster formation.

3.3. C_{60} Diffusion in Cross-Linked PF2/6. Figure 4 shows the diffusion coefficients and concentration profiles obtained when measuring a 270 nm film of cross-linked PF2/6-A-75:25 with the novel two-layer approach upon heating from $T_1 = 22$ °C to $T_2 = 120$ °C and fitting it as described above using fit B. Further transients and fits obtained when raising the temperature from room temperature up to 140 °C are displayed in the Supporting Information, along with a detailed table of input and output parameters for the simulations. The diffusion coefficients obtained by Fischer et al. for the three-layer approach for a 200 nm film of cross-linked PF2/6-A-75:25 are also indicated in Figure 4a for comparison.²⁸ We focus on the cross-linked PF2/6-A-75:25 as this will allow for a comparison with solution-processable acceptors, such as PCBM and nonfullerene acceptors, in future work. Over the measured temperature range from 100 °C to 160 °C, we observe an Arrhenius-like activation of the diffusion coefficient, as evidenced from the linear slope in the semilogarithmic plot. The activation energy evidently agrees with the observations made previously for the three-layer technique, though the absolute values for the diffusivity obtained by the two-layer technique are about 2–3 times larger than the values measured previously.

The simulations also yield concentration profiles $c(x, t)$ throughout the samples, as shown exemplarily in the 3D plot of Figure 4b for PF2/6-A-75:25 after heating from $T_1 = 22$ °C to $T_2 = 120$ °C. For the clarity of display, 2D slices along the time and thickness axes are shown in Figure 4c,d, respectively. From Figure 4d, we easily see that, for $t = 0$ s, a C_{60} concentration of 0.05 wt % was obtained at $x = 270$ nm, that is, at the quartz interface. The final, mean effective equilibrium concentration that establishes at long times at a temperature of 120 °C is 0.2

wt %. A total of 90% of the equilibrium concentration are reached at the quartz interface after 460 min. From Figure 4c, one can readily read off which effective concentration levels are obtained at certain positions through the film after some time. Obviously, the final equilibrium concentration obtained will depend on the solubility of the diffusing molecule in the polymer matrix at a given temperature.

The low final equilibrium concentration of about 0.2 wt % that we observe for the diffusion of C_{60} in cross-linked polyfluorene can be attributed to the fact that solubility of unsubstituted fullerene in a polymer matrix is generally rather limited,^{39,40} and this is impeded further by the cross-linking network. We point out that the cross-linking effectively suppresses clustering of C_{60} .⁴¹ Consequently, for this system, we can safely assume that the diffusing species is indeed molecular fullerene and that all of the assumptions made in our model in Section 3.2 are well met.

3.4. Evaluation of the Two-Layer Approach vs the Three-Layer Approach. It is worthwhile comparing the C_{60} diffusion coefficients derived from the two-layer and the three-layer measurements of the polyfluorene derivatives (Figure 4a). We briefly recall how the experiment is conducted with a three-layer sample.²⁸ The differences to the two-layer sample layout consist in using a thicker polymer layer, here 200 nm cross-linked PF2/6-A-75:25, and inserting a thin “sensor” layer in between the polymer and the quartz. The optical gap of the sensor material must be energetically lower than that of the polymer, so that it can be excited selectively. We used an 8 nm layer of MEH-PPV for this purpose. The experiment is conducted in the same way as for the two-layer setup, though with an excitation wavelength of 485 nm that excites only the MEH-PPV sensor layer and not the polyfluorene derivative. The sample is then heated to initiate the C_{60} diffusion. When the C_{60} molecules have traversed the PF2/6-A-75:25 layer and arrive at the MEH-PPV, PL intensity of the sample starts to reduce because of quenching. Neglecting exciton diffusion, the diffusion coefficient, D , for C_{60} could simply be evaluated according to $D = \frac{L^2}{2t}$, with L being the thickness of the PF2/6-A-75:25 layer. However, exciton diffusion in MEH-PPV toward the C_{60} quenching sites needs to be taken into account. As a result,²⁸ the diffusion coefficient is derived from fitting the normalized PL intensity using $\phi(t) = (1 + fp(t))^{-1}$, with $p(t) = 1 - \text{erf}(L(2\sqrt{Dt})^{-1})$ being the relative number of particles that diffused across the PF2/6-A-75:25 layer after time t and f being a dimensionless factor.

This three-layer setup is technologically simple, easy to implement, and data analysis is mathematically robust. However, the use of a lower-energy-emitting sensing layer that can be selectively excited limits this approach to higher energy materials that are typically green or blue emitting. To extend the spectral range of this approach, we developed the two-layer-based technique that can be applied to any photoluminescent material. It is satisfactory that two rather different approaches yield results that agree fully in the activation energy and within a factor of 2–3 as far as the absolute value is concerned.

In addition to allowing for using a larger range of materials, the two-layer method has the further advantage to give concentration profiles obtained from the simulations alongside of the diffusion coefficient (Figure 4b–d). They can be used as guidance when aiming to obtain a certain dopant concentration by annealing at a given temperature for a certain

time. Obviously, the approach can be applied to different diffusing molecules in various polymers, as long as the diffusing molecule quenches photoluminescence. It has to be noted though that the initial profiles are still approximations and may differ from the actual concentration gradients present in the samples, especially at short times and close to the dopant layer. Nevertheless, at later times ($>1-2$ min) and a few nanometer away from the interface, the profiles are increasingly reliable as the actual initial condition becomes less important (cf. SI). Evidently, the two-layer method may, in future work, also be applied to dopants that dissolve better in the polymer matrix, such as functionalized fullerenes or nonfullerene acceptors.

4. TEMPERATURE DEPENDENCE OF C_{60} DIFFUSION IN PCDTBT DERIVATIVES

4.1. Determining C_{60} Diffusion in PCDTBT Derivatives.

Having verified that both approaches give compatible results, we can apply the two-layer method to the low-bandgap polymer PCDTBT. It is a well-known and efficient polymer system that is frequently used in organic solar cells in combination with PCBM giving long-term stable devices with estimated lifetimes of up to 7 years while still maintaining an efficiency of about 4.5% after an initial burn-in loss of about 20%.⁴²⁻⁴⁴ Here, we use three different derivatives (PCDTBT, PCDTBT_{stat}, and PCDHTBT) to study the effect of different glass transition temperatures and small modifications of the chemical structure of the polymer on the C_{60} diffusion.

We recorded photoluminescence transients when heating the three low-bandgap polymers (PCDTBT, PCDTBT_{stat}, and PCDHTBT) to different temperatures in the range between 60 and 140 °C. For PCDHTBT, this range is entirely above its glass transition temperature, whereas for PCDTBT and PCDTBT_{stat}, this temperature range comprises measurements above and below T_g (cf. Table 1). Figure 5 shows the normalized photoluminescence transients with their fits, exemplary for PCDTBT, and the diffusion coefficients resulting from it, together with those obtained for PF2/6-A-7S:2S. The transients prior to normalization for all of the three polymers at all temperatures can be found in the Supporting Information, along with a table detailing all fitting parameters for fit A and fit B. Figure 5a illustrates how a higher final equilibrium temperature translates into an increasingly faster and more efficient quenching, which is attributed to an increased diffusion of C_{60} into the PCDTBT. We determined the absorption coefficients and Stern–Volmer constants for each material and fitted the data using fit B under the assumption that the quenching rate increases linearly with the quencher concentration, $k_q(x, t) = K_q \cdot c(x, t)$, as detailed in Section 3. With the increase in the final temperature, the equilibrium concentrations as well as the diffusion coefficients rise, as illustrated in Figure 5b,c, respectively. From the linear increase of the temperature-dependent diffusion coefficients in the Arrhenius plot, one can see that PCDHTBT features a thermally activated diffusion above its T_g of 60 °C, similar to the cross-linked polyfluorene derivative, yet with a lower activation energy of 0.70 ± 0.05 eV and about 1 order of magnitude lower absolute values. Despite their slightly different chemical structure, PCDTBT and PCDTBT_{stat} show very similar values, which we attribute to their similar molecular weight and T_g and which gives confidence in the reliability of our approach. For both materials, a temperature-activated diffusion process is also observed, yet the slope of the activation energy changes from 0.40 ± 0.05 eV below T_g to 1.00 ± 0.05 eV above T_g . The

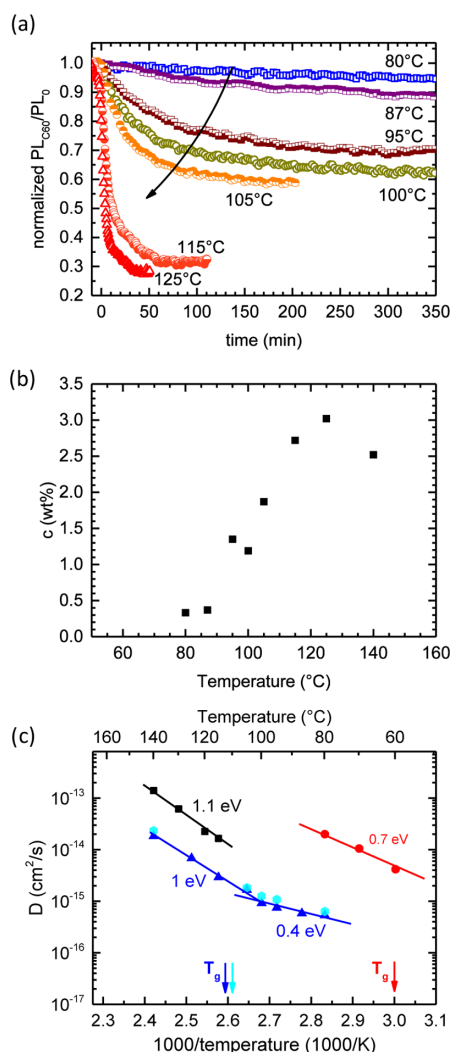


Figure 5. (a) Time dependence of $PL_{C_{60}}/PL_0$ for PCDTBT for different final temperatures after a one-step temperature increase. (b) Final concentration $c(T_2)$ of C_{60} in PCDTBT as a function of the final temperature T_2 , obtained from the measurements displayed in (a). (c) Arrhenius representation of the temperature dependence of the diffusion coefficient for cross-linked PF2/6-A-7S:2S (black squares), as well as for PCDTBT (blue filled triangles), PCDHTBT (red filled circles), and PCDTBT_{stat} (light blue filled hexagons). The solid lines provide a guide to the eye, and colored arrows indicate the respective T_g .

remarkable feature here is that the diffusion coefficient does not reduce drastically below T_g . The Stokes–Einstein equation that relates diffusion coefficient D , viscosity η , and particle radius r through $D = kT/6\pi\eta r$ would predict such a decrease in D because the viscosity η of polymers is known to strongly increase below T_g . When focussing on the temperature range above T_g , we find diffusion coefficients in the same range as that for PCDHTBT and about 1 order of magnitude below those of the cross-linked PF2/6-A-7S:2S.

4.2. Analyzing the Temperature Dependence of C_{60} Diffusion in PCDTBT Derivatives. We first assess the values and activation energies we obtain with our facile two-layer approach by comparison to values obtained for dye or dopant diffusion by other methods. To allow for comparison to other compounds despite the strong temperature dependence, we focus on the diffusivity at T_g . We find $D(T_g) = 3 \times 10^{-15} \text{ cm}^2 \text{ s}^{-1}$ for the diffusion of C_{60} in all three PCDTBT derivatives. This diffusivity is about 150 times lower than that determined for polyfluorene using the three-layer method, which extrapolates to $D(T_g = 80 \text{ }^\circ\text{C}) = 5 \times 10^{-13} \text{ cm}^2 \text{ s}^{-1}$,²⁸ and also lower than the values obtained for the cross-linked PF2/6-A-75:25. The equilibrium concentration of C_{60} at T_g was about 1–2 wt %. Our values for the diffusivities and activation energies of PCDTBT derivatives are in a similar range to those determined by rather different methods for other dyes/dopants at low concentrations in a polymer. This agreement is gratifying and supports the appropriateness of our approach.

For example, Ehlich and Sillescu investigated the diffusion of an indigo dye at less than 0.5 wt % in polymers such as polystyrene, poly(methyl methacrylate), and polycarbonate, which have glass transition temperatures of 100, 121, and 150 $^\circ\text{C}$, respectively.¹⁰ They use the holographic grating technique, where the diffusive decay of a photochemically produced grating is monitored by recording the intensity of forced Rayleigh scattering as a function of time, and they obtain values for the diffusion coefficient $D(T_g)$ at the glass transition of 8×10^{-15} , 1×10^{-14} , and $6.3 \times 10^{-12} \text{ cm}^2 \text{ s}^{-1}$, respectively. In a conceptually related way, the group of Moulé¹⁶ uses a confocal microscopy technique, where an acceptor dopant pattern is evaporated through a shadow mask onto a polymer film, and the spatial decay of the polymer luminescence due to the lateral diffusion of the dopant is monitored as a function of time and space before and after a heating step. They determined the diffusion of the acceptor molecules F4TCNQ and F4MCTCNQ in poly(3-hexylthiophene) (P3HT), which has a T_g of 10–14 $^\circ\text{C}$, and report values of $D(25 \text{ }^\circ\text{C}) \approx 5 \times 10^{-14} \text{ cm}^2 \text{ s}^{-1}$ for both compounds. The associated activation energy for an Arrhenius-like temperature dependence is 0.77 and 0.55 eV per molecule for F4TCNQ and F4MCTCNQ, respectively. Dynamic secondary ion-mass spectroscopy (DSIMS) was applied by Treat et al.²⁰ to a terraced bilayer–monolayer structure of PCBM covered with P3HT. Solving Fick's diffusion equation they arrive at D to be about 10^{-11} – $10^{-9} \text{ cm}^2 \text{ s}^{-1}$ for the range from 50 to 110 $^\circ\text{C}$ at a concentration of 1 vol % PCBM and at an activation energy of 0.7 eV per molecule. Extrapolation of their data to a T_g of about 10 $^\circ\text{C}$ gives $D(10 \text{ }^\circ\text{C}) = 1 \times 10^{-12} \text{ cm}^2 \text{ s}^{-1}$. Labram and co-workers²² use a bilayer structure of 40 nm PCBM on top of 8 nm P3HT. This bilayer is on top of a source and drain electrode, a hexamethyldisilazane layer, and a SiO_2 -covered silicon wafer, so as to form an organic field-effect transistor. They analyze the change in electron organic field-effect transistor mobility as a function of time after annealing and deduce $D(130 \text{ }^\circ\text{C}) = 5 \times 10^{-14} \text{ cm}^2 \text{ s}^{-1}$. Given that for very thin layers, T_g tends to be about 20 $^\circ\text{C}$ lower than that in the bulk,¹ this suggests a rather low value at T_g . Thus, overall, it seems that diffusivities for low amounts (≈ 1 wt %) of a diffusing dye/dopant molecule in a polymer at T_g range around 10^{-12} – $10^{-15} \text{ cm}^2 \text{ s}^{-1}$, with activation energies around 0.7 ± 0.3 eV per molecule. By the Stokes–Einstein relation, these variations between polymers even for the same dopant might result from differences in the viscosity of the

polymers, though we argue that they also reflect differences in local polymer motion (vide infra).

We point out that significantly higher diffusivities around 10^{-11} – $10^{-10} \text{ cm}^2 \text{ s}^{-1}$ are reported when the measurements are not concerned with a low dopant amount but rather with a blend of about equal ratios between the molecular and polymeric components, for example, of PCBM and P3HT.^{14,23,24} Although Treat reported only a weak dependence of the diffusivity on concentration,²⁰ results obtained on 1:1 blends are, at this stage, difficult to compare with our measurements as T_g changes, when half of the P3HT ($T_g = 12 \text{ }^\circ\text{C}$) is replaced by PCBM ($T_g = 131 \text{ }^\circ\text{C}$), and as it is not clear whether the diffusing entity then are PCBM molecules or 50 nm clusters, as suggested by Berriman et al.²⁴

We finally comment on the laws governing the observed C_{60} diffusion above and below the glass transition temperature. As mentioned above, according to the classical expectation based on the Stokes–Einstein relation, the diffusion should vanish below T_g ,^{9,45} yet, we observe a continuation of the diffusion process even at lower temperatures. The violation of the Stokes–Einstein relation below T_g has been observed before, for example, by Ehlich and Sillescu in 1990,¹⁰ and seem to occur particularly frequently for polymeric hosts.⁹ The reasons for this are a current subject of research in the area of polymer science.^{45–47} A crucial quantity for describing the dynamics of a glassy material is the free volume of the glass elements that provides motional freedom required for mechanical flow. The temperature dependence of the free volume follows a Williams–Landel–Ferry (WLF) (or, mathematically equivalent, the Vogel–Fulcher–Tammann law), which approaches zero near T_g . It is very different from Arrhenius-type dependence and is incompatible with the temperature dependence we observe. If the C_{60} diffusion was a direct reflection of the dynamics of free volume, it should be frozen out below T_g and the diffusivity should decrease drastically. However, for PCDTBT and PCDTBT_{stab} there is still diffusion well below T_g . On the basis of this observation, we argue that the temperature dependence of C_{60} diffusion is not a direct reflection of collective motion of the glass elements but rather of local and simply activated motion although both have a common origin.

In recent work, Xie et al. used oscillatory shear rheometry to investigate the glass transition temperature in regioregular (rr) and regiorandom (rra) poly(3-hexylthiophene) (P3HT), as well as in poly(bis(octyl)fluorene-dithiophene-benzothiadiazole) (PFTBT), which is structurally identical to PCDTBT, except that the carbazole moiety is exchanged by a fluorene moiety.⁴⁸ They pointed out that there is one glass transition temperature ($T_g = T_a$), for example, at 22 $^\circ\text{C}$ for region-regular P3HT, 6 $^\circ\text{C}$ for region-random P3HT, and 144 $^\circ\text{C}$ for PFTBT, that reflects the motion of the polymer backbone and that is also commonly observed in DSC measurements. In addition, there can be a second transition temperature ($=T_{\alpha\text{PE}}$), for example, near $-100 \text{ }^\circ\text{C}$ for P3HT, that is associated with the sidechain. The $T_{\alpha\text{PE}}$ that they observe for P3HT is in a temperature range similar to that observed for alkyl sidechain relaxations in other, nonconjugated polymers.⁴⁹ We therefore suggest that it is mainly the mobility of the sidechain that allows for the diffusion of C_{60} below T_g ($=T_a$) in the polymers we investigated and that this diffusion should, in general, be accelerated upon reaching T_g ($=T_a$) by the additional backbone motion. The importance of the sidechains for the diffusivity of the dopant, here the C_{60} molecule, is thus 2-fold. The

sidechains plasticize the backbone and so reduce the T_g ($=T_a$) of the backbone, as detailed in ref 48. In addition, the sidechains themselves enable local motion even below T_g ($=T_a$). As the investigated temperatures are far above the typical transition temperatures for sidechains,¹ as already pointed out above, all sidechains can be regarded to be mobile.

5. CONCLUSIONS

We developed a comparatively simple all-optical technique to monitor diffusion of a quenching dopant in a fluorescent organic layer that is based on monitoring the luminescence decay after inducing the dopant diffusion by heating. We found diffusion coefficients and activation energies that were consistent with earlier work by us and others. The advantage of the here presented two-layer-PL-quenching approach is its versatility. In principle, the method requires only that (i) a bilayer can be made, for example, by evaporation of the top layer, or by lamination¹⁴ and (ii) that the diffusing dopant induces a change in optical properties, for example, photoluminescence quenching. The analysis of the photoluminescence decay gives the diffusivity and its activation energy, as well as an approximation of the time-dependent concentration profile of the dopant. Notably, our approach allows for measurements several tens of degrees below T_g . In the present case, we utilized the extension of the detection range into the red part of the electromagnetic spectrum provided by the new architecture in contrast to the three-layer system to study low-bandgap materials relevant to state-of-the-art organic semiconducting devices, especially solar cells. We used three PCDTBT derivatives to explore the effect of structural variations on the diffusion of small molecules, in our case C_{60} . In these systems, diffusion already takes place well below the glass transition temperature related to the polymer main chain. This and the observation of an Arrhenius-type dependence of the diffusion coefficient on temperature indicate that C_{60} diffusion is not driven by WFL-type collective motion above T_g but rather by local motions mediated by the sidechains.

The method uses a planar heterojunction layout to determine the diffusion coefficient as well as the maximum soluble equilibrium concentration at a given temperature for a molecular acceptor in a polymer donor matrix. The knowledge of these two parameters is highly relevant for the controlled design as well as for estimations on morphological stability and thus lifetime of bulk heterojunction solar cells. For example, knowing the solubility limit as a function of temperature allows for predictions whether certain compositions will phase separate at room temperature and knowing the temperature-dependent diffusivity will allow estimating on what time scales this should occur. Evidently, knowing the diffusivities and solubilities of the components in binary or ternary blends as a function of temperature will assist the intelligent design of such devices. Our method may, for example, also be applied to the novel nonfullerene acceptor systems that attracted more and more attention in the recent years.⁵⁰ Clearly, for application to OSC materials, acceptors with higher solubility than C_{60} need to be considered. In future work, our method may be also applied to study the diffusion of dopants in OLED host or transport materials.

Up to now, our method relies on luminescence quenching by the diffusing molecule. Variations of this approach may include measuring changes in photoinduced absorption, charge-transfer-state absorption, electroabsorption, or PL lifetime instead of

PL intensity. In future work, the versatility of our approach should be used to further quantitatively explore the observed diffusion below T_g in device-relevant materials, which might impact the long-term morphological stability of devices.

6. EXPERIMENTAL SECTION

6.1. Sample Preparation. The samples were prepared in a nitrogen-filled glovebox by first spin-coating a thin polymer layer onto a 2×2 cm² quartz substrate from chlorobenzene solution and then evaporating a 30 nm thick C_{60} layer with a shadow mask onto half of the polymer film. For PF2/6-A-75:25, we used 200–270 nm thick films that were cross-linked by UV-illumination at 40 °C (15 min at 50 W) prior to C_{60} deposition. For the low-bandgap polymers, film thicknesses were in the range of 30–70 nm. To ensure that there is no residual solvent in the polymer film anymore, the samples were kept in the evaporation chamber for several hours before depositing C_{60} . It was evacuated down to a pressure of 5×10^{-7} mbar.

■ ASSOCIATED CONTENT

Supporting Information

The Supporting Information is available free of charge on the ACS Publications website at DOI: 10.1021/acsami.8b05520.

Synthetic details of the PCDTBT derivatives; ¹H NMR spectrum of PCDTBT_{stat}; DSC measurements of PCDTBT derivatives; additional experimental details, extensive explanation of the theoretical approach; time-dependent PL ratio decay curves and fits for all investigated polymers; and parameter set used for the simulations (PDF)

■ AUTHOR INFORMATION

Corresponding Author

*E-mail: anna.koehler@uni-bayreuth.de.

ORCID

Frank-Julian Kahle: 0000-0003-3416-0072

Anna Köhler: 0000-0001-5029-4420

Author Contributions

[†]C.S. and F.-J.K. contributed equally.

Notes

The authors declare no competing financial interest.

■ ACKNOWLEDGMENTS

We acknowledge financial support by the German Science Foundation DFG through the doctoral training center “Photophysics of Synthetic and Biological Multichromophoric Systems” (GRK 1640), the Bavarian State Ministry of Education, Science and the Arts through the Collaborative Research Network “Solar Technologies go Hybrid” (SolTech), and by the EU-Marie-Skłodowska-Curie-ITN Network IN-FORM. Furthermore, F.-J.K. was supported by the Elite Network Bavaria (ENB) in the framework of the Elite Study Program “Macromolecular Science”. We are also very grateful for helpful discussions with W. Köhler.

■ REFERENCES

- (1) Müller, C. On the Glass Transition of Polymer Semiconductors and Its Impact on Polymer Solar Cell Stability. *Chem. Mater.* **2015**, *27*, 2740–2754.
- (2) Chen, D.; Liu, F.; Wang, C.; Nakahara, A.; Russell, T. P. Bulk Heterojunction Photovoltaic Active Layers via Bilayer Interdiffusion. *Nano Lett.* **2011**, *11*, 2071–2078.
- (3) Jacobs, I. E.; Moule, A. J. Controlling Molecular Doping in Organic Semiconductors. *Adv. Mater.* **2017**, *29*, No. 1703063.

- (4) McEwan, J. A.; Clulow, A. J.; Shaw, P. E.; Nelson, A.; Darwish, T. A.; Burn, P. L.; Gentle, I. R. Diffusion at Interfaces in OLEDs Containing a Doped Phosphorescent Emissive Layer. *Adv. Mater. Interfaces* **2016**, *3*, No. 1600184.
- (5) Müller, C.; Ferenczi, T. A. M.; Campoy-Quiles, M.; Frost, J. M.; Bradley, D. D. C.; Smith, P.; Stingelin-Stutzmann, N.; Nelson, J. Binary organic photovoltaic blends: A simple rationale for optimum compositions. *Adv. Mater.* **2008**, *20*, 3510–3515.
- (6) Menezes, P. V.; Martin, J.; Schäfer, M.; Staesche, H.; Roling, B.; Weitzel, K. M. Bombardment induced ion transport-Part II. Experimental potassium ion conductivities in borosilicate glass. *Phys. Chem. Chem. Phys.* **2011**, *13*, 20123–20128.
- (7) Greaves, G. N.; Gurman, S. J.; Catlow, C. R. A.; Chadwick, A. V.; Houdewalter, S.; Henderson, C. M. B.; Dobson, B. R. A Structural Basis for Ionic-Diffusion in Oxide Glasses. *Philos. Mag. A* **1991**, *64*, 1059–1072.
- (8) Smedskjaer, M. M.; Zheng, Q. J.; Mauro, J. C.; Potuzak, M.; Morup, S.; Yue, Y. Z. Sodium diffusion in bororoaluminosilicate glasses. *J. Non-Cryst. Solids* **2011**, *357*, 3744–3750.
- (9) Ediger, M. D.; Harrowell, P. Perspective: Supercooled liquids and glasses. *J. Chem. Phys.* **2012**, *137*, No. 080901.
- (10) Ehlich, D.; Sillescu, H. Tracer Diffusion at the Glass-Transition. *Macromolecules* **1990**, *23*, 1600–1610.
- (11) Rössler, E. Indications for a Change of Diffusion Mechanism in Supercooled Liquids. *Phys. Rev. Lett.* **1990**, *65*, 1595–1598.
- (12) Obuchovsky, S.; Levin, M.; Levitsky, A.; Frey, G. L. Morphology visualization of P3HT: Fullerene blends by using subsurface atomic layer deposition. *Org. Electron.* **2017**, *49*, 234–241.
- (13) Maliakal, A. J. Characterization of Dopant Diffusion within Semiconducting Polymer and Small-Molecule Films Using Infrared-Active Vibrational Modes and Attenuated Total Reflectance Infrared Spectroscopy. *ACS Appl. Mater. Interfaces* **2013**, *5*, 8300–8307.
- (14) Treat, N. D.; Brady, M. A.; Smith, G.; Toney, M. F.; Kramer, E. J.; Hawker, C. J.; Chabiny, M. L. Interdiffusion of PCBM and P3HT Reveals Miscibility in a Photovoltaically Active Blend. *Adv. Energy Mater.* **2011**, *1*, 82–89.
- (15) Paternò, G. M.; Skoda, M. W. A.; Dalgliesh, R.; Cacialli, F.; Sakai, V. G. Tuning Fullerene Intercalation in a Poly (thiophene) derivative by Controlling the Polymer Degree of Self-Organisation. *Sci. Rep.* **2016**, *6*, No. 34609.
- (16) Li, J.; Koshnick, C.; Diallo, S. O.; Ackling, S.; Huang, D. M.; Jacobs, I. E.; Harrelson, T. F.; Hong, K.; Zhang, G.; Beckett, J.; Mascal, M.; Moulé, A. J. Quantitative Measurements of the Temperature-Dependent Microscopic and Macroscopic Dynamics of a Molecular Dopant in a Conjugated Polymer. *Macromolecules* **2017**, *50*, 5476–5489.
- (17) Jung, M. C.; Kojima, H.; Matsumura, I.; Bente, H.; Nakamura, M. Diffusion and influence on photovoltaic characteristics of p-type dopants in organic photovoltaics for energy harvesting from blue-light. *Org. Electron.* **2018**, *52*, 17–21.
- (18) Zhang, L.; Zu, F. S.; Deng, Y. L.; Igbari, F.; Wang, Z. K.; Liao, L. S. Origin of Enhanced Hole Injection in Organic Light-Emitting Diodes with an Electron-Acceptor Doping Layer: p-Type Doping or Interfacial Diffusion? *ACS Appl. Mater. Interfaces* **2015**, *7*, 11965–11971.
- (19) Hartmeier, B. F.; Brady, M. A.; Treat, N. D.; Robb, M. J.; Mates, T. E.; Hexemer, A.; Wang, C.; Hawker, C. J.; Kramer, E. J.; Chabiny, M. L. Significance of Miscibility in Multidonor Bulk Heterojunction Solar Cells. *J. Polym. Sci., Part B: Polym. Phys.* **2016**, *54*, 237–246.
- (20) Treat, N. D.; Mates, T. E.; Hawker, C. J.; Kramer, E. J.; Chabiny, M. L. Temperature Dependence of the Diffusion Coefficient of PCBM in Poly(3-hexylthiophene). *Macromolecules* **2013**, *46*, 1002–1007.
- (21) Dai, A.; Wan, A.; Magee, C.; Zhang, Y. D.; Barlow, S.; Marder, S. R.; Kahn, A. Investigation of p-dopant diffusion in polymer films and bulk heterojunctions: Stable spatially-confined doping for all-solution processed solar cells. *Org. Electron.* **2015**, *23*, 151–157.
- (22) Labram, J. G.; Kirkpatrick, J.; Bradley, D. D. C.; Anthopoulos, T. D. Measurement of the diffusivity of fullerenes in polymers using bilayer organic field effect transistors. *Phys. Rev. B* **2011**, *84*, No. 075344.
- (23) Watts, B.; Belcher, W. J.; Thomsen, L.; Ade, H.; Dastoor, P. C. A Quantitative Study of PCBM Diffusion during Annealing of P3HT: PCBM Blend Films. *Macromolecules* **2009**, *42*, 8392–8397.
- (24) Berriman, G. A.; Holdsworth, J. L.; Zhou, X. J.; Belcher, W. J.; Dastoor, P. C. Molecular versus crystallite PCBM diffusion in P3HT:PCBM blends. *AIP Adv.* **2015**, *5*, No. 097220.
- (25) Collins, B. A.; Gann, E.; Guignard, L.; He, X.; McNeill, C. R.; Ade, H. Molecular Miscibility of Polymer-Fullerene Blends. *J. Phys. Chem. Lett.* **2010**, *1*, 3160–3166.
- (26) Clulow, A. J.; Tao, C.; Lee, K. H.; Velusamy, M.; McEwan, J. A.; Shaw, P. E.; Yamada, N. L.; James, M.; Burn, P. L.; Gentle, I. R.; Meredith, P. Time-Resolved Neutron Reflectometry and Photovoltaic Device Studies on Sequentially Deposited PCDTBT-Fullerene Layers. *Langmuir* **2014**, *30*, 11474–11484.
- (27) Wang, D.; Nakajima, K.; Liu, F.; Shi, S. W.; Russell, T. P. Nanomechanical Imaging of the Diffusion of Fullerene into Conjugated Polymer. *ACS Nano* **2017**, *11*, 8660–8667.
- (28) Fischer, F.; Hahn, T.; Bäessler, H.; Bauer, I.; Strohrig, P.; Köhler, A. Measuring Reduced C_{60} Diffusion in Crosslinked Polymer Films by Optical Spectroscopy. *Adv. Funct. Mater.* **2014**, *24*, 6172–6177.
- (29) Köhler, A.; Bäessler, H. *Electronic Processes in Organic Semiconductors: An Introduction*; Wiley VCH, 2015.
- (30) Kepler, R. G. Charge Carrier Production and Mobility in Anthracene Crystals. *Phys. Rev.* **1960**, *119*, 1226–1229.
- (31) Leblanc, O. H. Hole and Electron Drift Mobilities in Anthracene. *J. Chem. Phys.* **1960**, *33*, 626.
- (32) Scheler, E.; Strohrig, P. Three Color Random Fluorene-Based Oligomers for Fast Micrometer-Scale Photopatterning. *Chem. Mater.* **2010**, *22*, 1410–1419.
- (33) Blouin, N.; Michaud, A.; Leclerc, M. A Low-Bandgap Poly(2,7-carbazole) Derivative for Use in High-Performance Solar Cells. *Adv. Mater.* **2007**, *19*, 2295–2300.
- (34) Kim, J.; Kwon, Y. S.; Shin, W. S.; Moon, S. J.; Park, T. Carbazole-Based Copolymers: Effects of Conjugation Breaks and Steric Hindrance. *Macromolecules* **2011**, *44*, 1909–1919.
- (35) Hahn, T.; Tscheuschner, S.; Kahle, F.-J.; Reichenberger, M.; Athanasopoulos, S.; Saller, C.; Bazan, G. C.; Nguyen, T.-Q.; Strohrig, P.; Bäessler, H.; Köhler, A. Monomolecular and Bimolecular Recombination of Electron-Hole Pairs at the Interface of a Bilayer Organic Solar Cell. *Adv. Funct. Mater.* **2016**, No. 1604906.
- (36) Tanto, B.; Guha, S.; Martin, C. M.; Scherf, U.; Winokur, M. J. Structural and spectroscopic investigations of bulk poly [bis(2-ethyl)hexylfluorene]. *Macromolecules* **2004**, *37*, 9438–9448.
- (37) Crank, J. Methods of Solution When the Diffusion Coefficient is Constant. In *The Mathematics of Diffusion*, 2nd ed., Crank, J., Ed.; Clarendon Press: Oxford, 1975.
- (38) Lakowicz, J. R. *Principles of Fluorescence Spectroscopy*, 3rd ed.; Springer, 2006.
- (39) Dattani, R.; Cabral, J. T. Polymer fullerene solution phase behaviour and film formation pathways. *Soft Matter* **2015**, *11*, 3125–3131.
- (40) Wong, H. C.; Sanz, A.; Douglas, J. F.; Cabral, J. T. Glass formation and stability of polystyrene-fullerene nanocomposites. *J. Mol. Liq.* **2010**, *153*, 79–87.
- (41) Kahle, F. J.; Saller, C.; Köhler, A.; Strohrig, P. Crosslinked Semiconductor Polymers for Photovoltaic Applications. *Adv. Energy Mater.* **2017**, *7*, No. 1700306.
- (42) Tournebise, A.; Rivaton, A.; Gardette, J. L.; Lombard, C.; Pepin-Donat, B.; Beaupre, S.; Leclerc, M. How Photoinduced Crosslinking Under Operating Conditions Can Reduce PCDTBT-Based Solar Cell Efficiency and then Stabilize It. *Adv. Energy Mater.* **2014**, *4*, No. 1301530.
- (43) Peters, C. H.; Sachs-Quintana, I. T.; Kastrop, J. P.; Beaupre, S.; Leclerc, M.; McGehee, M. D. High Efficiency Polymer Solar Cells with Long Operating Lifetimes. *Adv. Energy Mater.* **2011**, *1*, 491–494.

- (44) Peters, C. H.; Sachs-Quintana, I. T.; Mateker, W. R.; Heumueller, T.; Rivnay, J.; Noriega, R.; Beiley, Z. M.; Hoke, E. T.; Salleo, A.; McGehee, M. D. The Mechanism of Burn-in Loss in a High Efficiency Polymer Solar Cell. *Adv. Mater.* **2012**, *24*, 663–668.
- (45) Liu, Q.; Huang, S. C.; Suo, Z. G. Brownian Motion of Molecular Probes in Supercooled Liquids. *Phys. Rev. Lett.* **2015**, *114*, No. 224301.
- (46) Gotze, W.; Sjogren, L. Relaxation Processes in Supercooled Liquids. *Rep. Prog. Phys.* **1992**, *55*, 241–376.
- (47) Berthier, L.; Biroli, G. Theoretical perspective on the glass transition and amorphous materials. *Rev. Mod. Phys.* **2011**, *83*, 587–645.
- (48) Xie, R. X.; Lee, Y.; Aplan, M. P.; Caggiano, N. J.; Müller, C.; Colby, R. H.; Gomez, E. D. Glass Transition Temperature of Conjugated Polymers by Oscillatory Shear Rheometry. *Macromolecules* **2017**, *50*, 5146–5154.
- (49) Beiner, M.; Huth, H. Nanophase separation and hindered glass transition in side-chain polymers. *Nat. Mater.* **2003**, *2*, 595–599.
- (50) Hou, J.; Inganäs, O.; Friend, R. H.; Gao, F. Organic solar cells based on non-fullerene acceptors. *Nat. Mater.* **2018**, *17*, 119–128.

Supporting Information

A Facile Method for the Investigation of Temperature-Dependant C₆₀ Diffusion in Conjugated Polymers

Christina Saller^{1‡}, Frank-Julian Kahle^{2‡}, Thomas Müller², Tobias Hahn², Steffen Tscheuschner², Denys Priadko², Peter Strohriegl^{1,3,4}, Heinz Bäessler³, Anna Köhler^{2,3*}

¹ Macromolecular Chemistry I, University of Bayreuth, 95440 Bayreuth, Germany

² Soft Matter Optoelectronics, University of Bayreuth, 95440 Bayreuth, Germany

³ Bayreuth Institute of Macromolecular Science (BIMF), University of Bayreuth, 95440 Bayreuth, Germany

⁴ Bavarian Polymer Institute (BPI), University of Bayreuth, 95440 Bayreuth, Germany

‡ Both authors contributed equally

*anna.koehler@uni-bayreuth.de

Full synthetic details:

Materials

All chemicals and anhydrous THF were used as received from commercial suppliers. For purification, solvents were distilled prior to use. Argon inert gas atmosphere was used for air-sensitive and moisture-sensitive reactions. The monomers 2,7-bis(4',4',5',5'-tetramethyl-1',3',2'-dioxaborolan-2'-yl)-*N*-(heptadecan-9''-yl)carbazole, 4,7-bis(5'-bromothien-2'-yl)-2,1,3-benzothiadiazole, and 4,7-bis(5'-bromo-4'-hexylthien-2'-yl)-2,1,3-benzothiadiazole were delivered by SunaTech Inc. and used without further purification. The synthesis of *N,N'*-bis(4-bromophenyl)-*N,N'*-bis(4-methylphenyl)-benzidine was carried out as reported in literature.¹ C₆₀ was purchased by American Dye Source and used as received. Poly(2-methoxy-5-(2-ethylhexyloxy)-1,4-phenylenevinylene) (MEH-PPV) was purchased by Aldrich and also used as received. ¹H NMR spectra were recorded on a Bruker Avance 300 spectrometer in CDCl₃ at 300 MHz operated at room temperature. High temperature ¹H NMR spectra were obtained with a Varian INOVA 300 spectrometer at 120 °C in 1,1,2,2-tetrachloroethane as solvent. The residual solvent peaks were used as internal reference. Deuterated solvents were purchased from Deutero. Mass spectra were measured with a Finnigan MAT 8500. Size exclusion chromatography (SEC) was carried out with a Waters 515 pump with UV detector (UV WAT 2489) and refractive index detector (RI WAT 410) equipped with two Resipore columns (3 μm). As eluent, tetrahydrofuran was used at a flow rate of 0.5 mlmin⁻¹ and *o*-dichlorobenzene was used as internal standard. High temperature SEC was performed at PSS Polymer Standards Service GmbH. Differential scanning calorimetry (DSC) was performed on a Mettler Toledo DSC 2 with a temperature rate of 40 Kmin⁻¹ under nitrogen atmosphere. The absorption coefficient α required to evaluate the diffusion data was determined by measuring the absorption spectra using a Cary 5000 spectrometer.

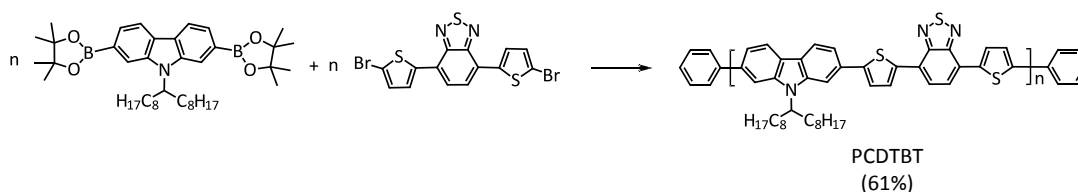


Figure S1: Synthesis scheme for Poly-(*N*-heptadecan-9'-yl)-2,7-carbazole-alt-5,5-(4',7'-bis(thien-2-yl)-2',1',3'-benzothia diazole): PCDTBT

Poly-(*N*-heptadecan-9'-yl)-2,7-carbazole-alt-5,5-(4',7'-bis(thien-2-yl)-2',1',3'-benzothiadiazole):

PCDTBT was synthesized similar to the procedure described by Leclerc.² In a Schlenk flask, 0.723 g (1.10 mmol) of 2,7-bis(4',4',5',5'-tetramethyl-1',3',2'-dioxaborolan-2'-yl)-*N*-(heptadecan-9''-yl)carba-

zole, 0.504 g (1.10 mmol) of 4,7-bis(5'-bromothien-2'-yl)-2,1,3-benzothiadiazole, 14 mL of toluene and 3.7 mL of an aqueous tetraethylammonium hydroxide solution (20 wt%) were mixed under argon. After degassing by three freeze-thaw cycles, 5.0 mg of tris(dibenzylideneacetone)dipalladium(0) and 6.7 mg of tri(*o*-tolyl)phosphine were added and again three freeze-thaw cycles were conducted before stirring the mixture under reflux for 72 h. Endcapping was performed by addition of 0.173 g (1.1 mmol) of bromobenzene, stirring for 1 h at reflux temperature and addition of 0.134 g (1.10 mmol) of phenylboronic acid. The mixture was allowed to cool to room temperature. After precipitation in methanol/water (10:1), the polymer was fractionated via Soxhlet extraction using acetone, hexane, and toluene. The reduced toluene fraction was precipitated in methanol/water (10:1) and dried in vacuum overnight. Yield: 0.468 g (61%) of a violet powder. A molecular weight of 37,000 g mol⁻¹ (M_w) and 16,000 g mol⁻¹ (M_n) was determined by high temperature polymer size exclusion chromatography in trichlorobenzene at 150 °C with a polydispersity index of 2.25 (polystyrene calibration). ¹H NMR (300 MHz, C₂D₂Cl₄, 120 °C): δ = 0.68-0.92 (m, CH₃), 1.07-1.59 (m, CH₂), 2.10 (br, carbazole-CH₂), 2.38 (br, carbazole-CH₂), 4.68 (br, CH), 7.04-8.37 (m, ar-CH).

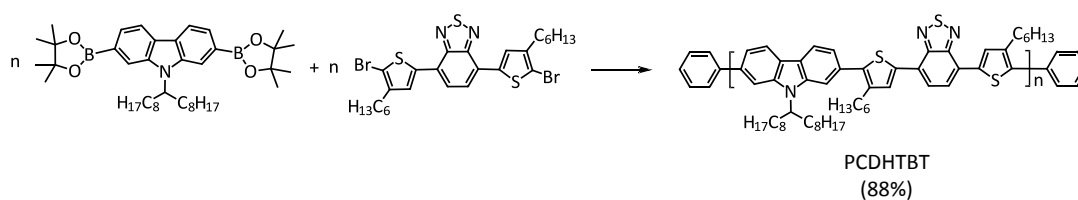


Figure S2: Synthesis scheme for Poly-(*N*-heptadecan-9'-yl)-2,7-carbazole-alt-5,5-(4',7'-bis(4-hexylthien-2-yl)-2',1',3'-benzothiadiazole): PCDHTBT

Poly-(*N*-heptadecan-9'-yl)-2,7-carbazole-alt-5,5-(4',7'-bis(4-hexylthien-2-yl)-2',1',3'-benzothiadiazole): The synthesis of PCDHTBT was carried out similar to the procedure described in literature, but with a different catalyst system.³ In a Schlenk flask, a mixture of 0.526 g (0.80 mmol) of 2,7-bis-(4',4',5',5'-tetramethyl1',3',2'-dioxaborolan-2'-yl)-*N*-(heptadecan-9''-yl)carbazole, 0.501 g (0.80 mmol) of 4,7-bis(5'-bromo-4'-hexylthien-2'-yl)-2,1,3-benzothiadiazole, 8 mL of toluene and 2.7 mL of an aqueous tetraethylammonium hydroxide solution (20 wt%) was degassed by three freeze-thaw cycles. After addition of 3.7 mg of tris(dibenzylideneacetone)dipalladium(0) and 4.9 mg of tri(*o*-tolyl)phosphine, the resulting mixture was degassed again by three freeze-thaw cycles and stirred at reflux temperature under argon for 72 h. 0.126 g (0.80 mmol) of bromobenzene were added and the mixture refluxed for 1 h under argon. Endcapping was finished by the addition of 0.098 g (0.80 mmol) of phenylboronic acid and stirring overnight at reflux temperature. Cooled to room temperature, the polymer was precipitated into methanol/water (10:1) and purified via Soxhlet extraction with acetone and hexane. The reduced hexane fraction was precipitated into

methanol/water (10:1) and the polymer was dried in vacuum overnight. Yield: 0.611 g (88%) of a dark-red powder. Size exclusion chromatography in THF solution at room temperature exhibits a molecular weight of $14,000 \text{ gmol}^{-1}$ (M_w) and $7,000 \text{ gmol}^{-1}$ (M_n) with a polydispersity index of 2.09 (polystyrene calibration). $^1\text{H NMR}$ (300 MHz, $\text{C}_2\text{D}_2\text{Cl}_4$, 120°C): $\delta = 0.75\text{-}0.94$ (m, CH_3), $1.05\text{-}1.50$ (m, CH_2), 1.75 (br, thiophene- CH_2), 2.04 (br, carbazole- CH_2), 2.32 (br, carbazole- CH_2), $2.67\text{-}2.93$ (m, thiophene- CH_2), 4.62 (br, CH), $7.02\text{-}8.19$ (m, ar-CH).

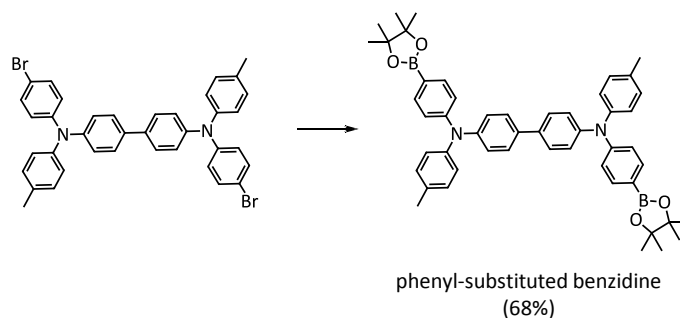


Figure S3: Synthesis scheme for *N,N'*-bis(4-methylphenyl)-*N,N'*-bis((4',4',5',5'-tetramethyl-1',3',2'-dioxaborolan-2'-yl)phenyl)benzidine

N,N'-bis(4-methylphenyl)-*N,N'*-bis((4',4',5',5'-tetramethyl-1',3',2'-dioxaborolan-2'-yl)phenyl)benzidine: In a three neck flask, 1.246 g (1.85 mmol) of *N,N'*-bis(4-bromophenyl)-*N,N'*-bis(4-methylphenyl)benzidine was dissolved in 18 mL of anhydrous THF under argon. The solution was cooled to -78°C and 2.54 mL (4.06 mmol) of *n*-butyllithium (1.6 M in hexane) were added dropwise. After stirring for 30 min at -78°C , 0.91 mL (4.43 mmol) of 2-isopropoxy-4,4,5,5-tetramethyl-1,3,2-dioxaborolane were added rapidly and stirred for 1 h. The reaction mixture was allowed to warm to room temperature and stirred overnight before it was poured into water. After extraction with diethyl ether, the organic phase was washed with brine, dried over Na_2SO_4 , and the solvent was evaporated. The crude product was purified via recrystallization in hot ethanol. Yield: 0.962 g (1.25 mmol, 68%) of a white solid. $^1\text{H NMR}$ (300 MHz, CDCl_3 , 20°C): δ (ppm) = 1.33 (s, borolane- CH_3), 2.33 (s, phenyl- CH_3), 7.01-7.16 (m, 16 H, ArH), 7.44 (d, 8.6 Hz, 4 H, ArH benzidine), 7.66 (d, 8.5 Hz, 4 H, ArH borolane). EI MS: m/z (%) = 768 (M^+ , 48), 642 (62), 516 (100), 384 (5), 321 (7), 258 (19).

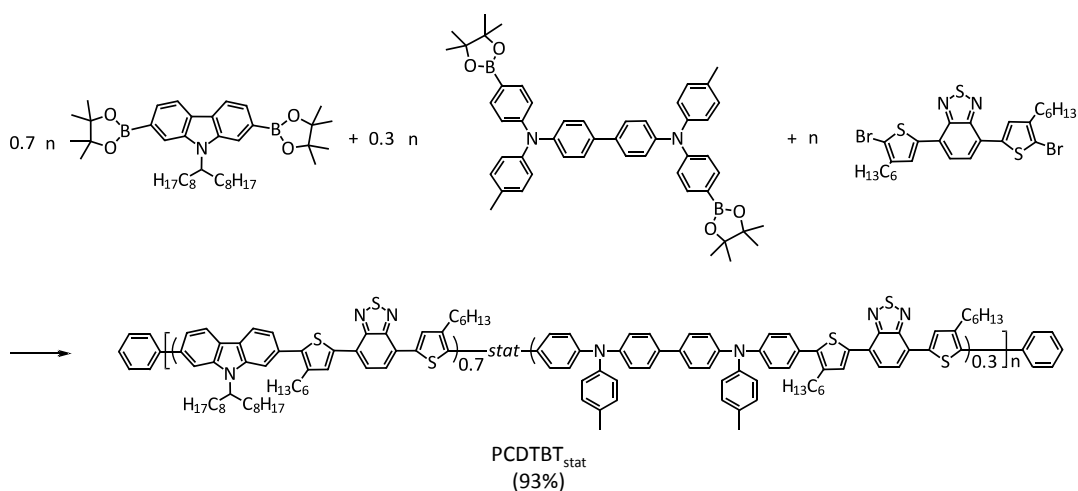


Figure S4: Synthesis scheme for Poly[(*N*-heptadecan-9'-yl)-2,7-carbazole-alt-5,5-(4',7'-bis(4-hexylthien-2-yl)-2',1',3'-benzothiadiazole)]_{0.7}-stat-[*N,N'*-bis(4-methylphenyl)-*N,N'*-diphenylbenzidine-alt-5,5-(4',7'-bis(4-hexylthien-2-yl)-2',1',3'-benzothiadiazole)]_{0.3}: PCDTBT_{stat}

Poly[(*N*-heptadecan-9'-yl)-2,7-carbazole-alt-5,5-(4',7'-bis(4-hexylthien-2-yl)-2',1',3'-benzothiadiazole)]_{0.7}-stat-[*N,N'*-bis(4-methylphenyl)-*N,N'*-diphenylbenzidine-alt-5,5-(4',7'-bis(4-hexylthien-2-yl)-2',1',3'-benzothiadiazole)]_{0.3}: PCDTBT_{stat} was synthesized via Suzuki coupling according to the following procedure:⁴ The molar ratio of the carbazole, the phenyl-substituted benzidine, and the bithienyl benzothiadiazole units in PCDTBT_{stat} is 0.7:0.3:1. A Schlenk flask was charged 0.368 g (0.56 mmol) of 2,7-bis(4',4',5',5'-tetramethyl-1',3',2'-dioxaborolan-2'-yl)-*N*-(heptadecan-9''-yl)carbazole, 0.184 g (0.24 mmol) of *N,N'*-bis(4-methylphenyl)-*N,N'*-bis((4',4',5',5'-tetramethyl-1',3',2'-dioxaborolan-2'-yl)phenyl)benzidine, 0.501 g (0.80 mmol) of 4,7-bis(5'-bromo-4'-hexylthien-2'-yl)-2,1,3-benzothiadiazole and 12 mL of toluene under argon. One drop of Aliquat 336 and 20 mL of 2 M Na₂CO₃ solution were added and the mixture was degassed by three freeze-thaw cycles. Afterwards, 14 mg of tetrakis(triphenylphosphine)palladium(0) were added and followed by again three freeze-thaw cycles. The reaction mixture was then stirred under reflux in an argon atmosphere for 90 h before 0.126 g (0.80 mmol) of bromobenzene was added. After stirring at reflux temperature for 2 h, 0.098 g (0.80 mmol) of phenylboronic acid was added and the reaction mixture was refluxed overnight before allowed to cool to room temperature. The polymer was precipitated into methanol/water (10:1). Soxhlet extraction was carried out using acetone and toluene. The reduced toluene fraction was precipitated into methanol/water (10:1) and dried in vacuum overnight. Yield: 0.669 g (93%) of a dark-red powder. A molecular weight of 47,000 gmol⁻¹ (M_w) and 18,000 gmol⁻¹ (M_n) was determined by size exclusion chromatography in THF solution with a polydispersity index of 2.56 (polystyrene calibration). ¹H NMR (300 MHz, C₂D₂Cl₄, 120 °C): δ = 0.75-0.95 (m, CH₃), 1.05-1.55 (m, CH₂), 1.75 (br, thiophene-CH₂), 2.04 (br, carbazole-CH₂), 2.23-2.44 (m, benzidine-CH₃, carbazole-

CH₂), 2.63-2.95 (m, thiophene-CH₂), 4.62 (br, CH), 6.92-8.22 (m, ar-CH). From the integration of the signal for the CH₂ group in the swallow-tail spacer of the carbazole unit (2.04 ppm), the combined signal for the methyl group in the benzidine units and the other CH₂ group in the carbazole spacer (2.23-2.44 ppm), and the signal for the CH₂ groups in the hexyl spacer of the thiophene (1.75 ppm), a molar ratio of 0.7:0.3:1 was calculated (**Figure S5**).

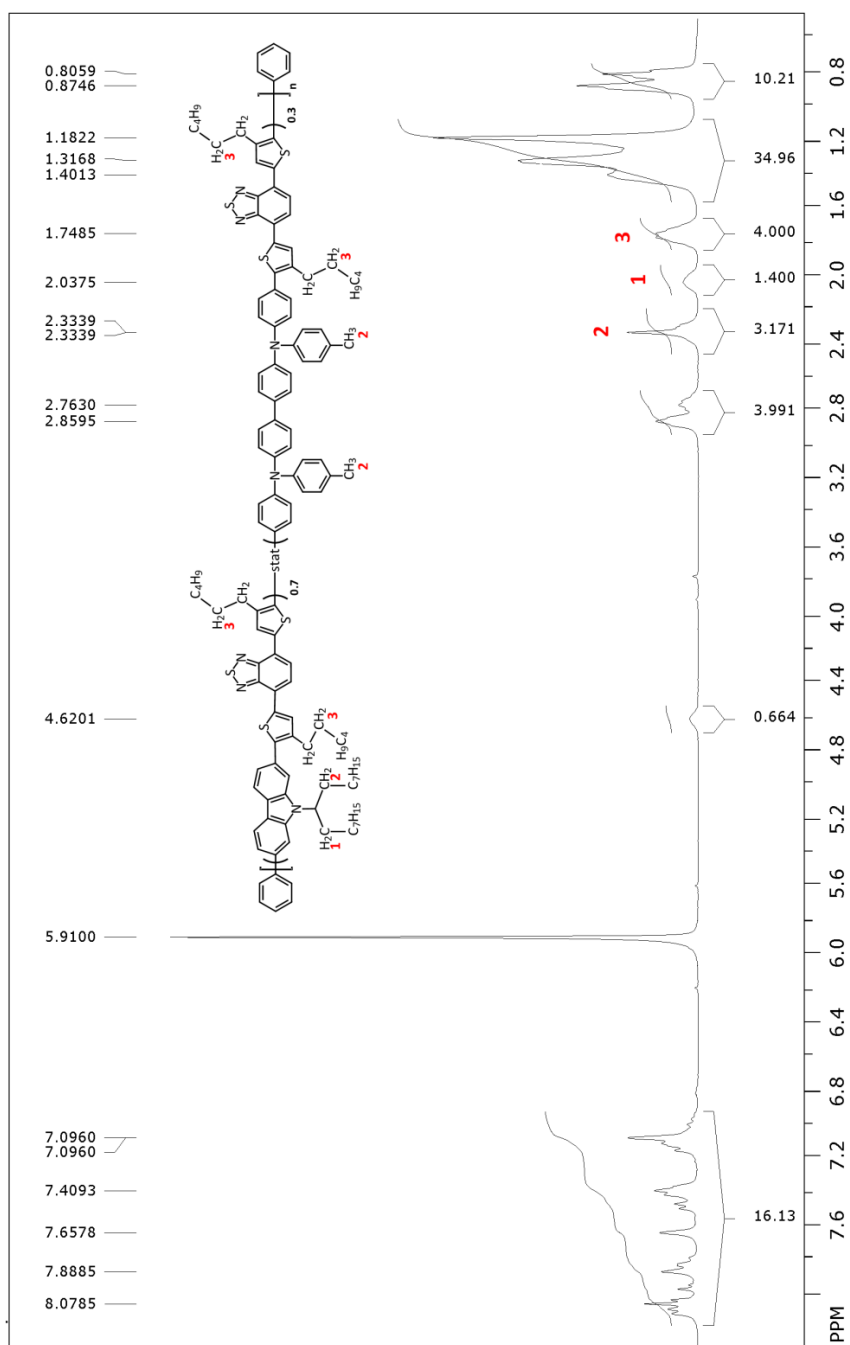


Figure S5: ¹H NMR spectrum of PCDTBT_{stat} (300 MHz) in C₂D₂Cl₄ at 120 °C. For the calculation of the molar ratio see text.

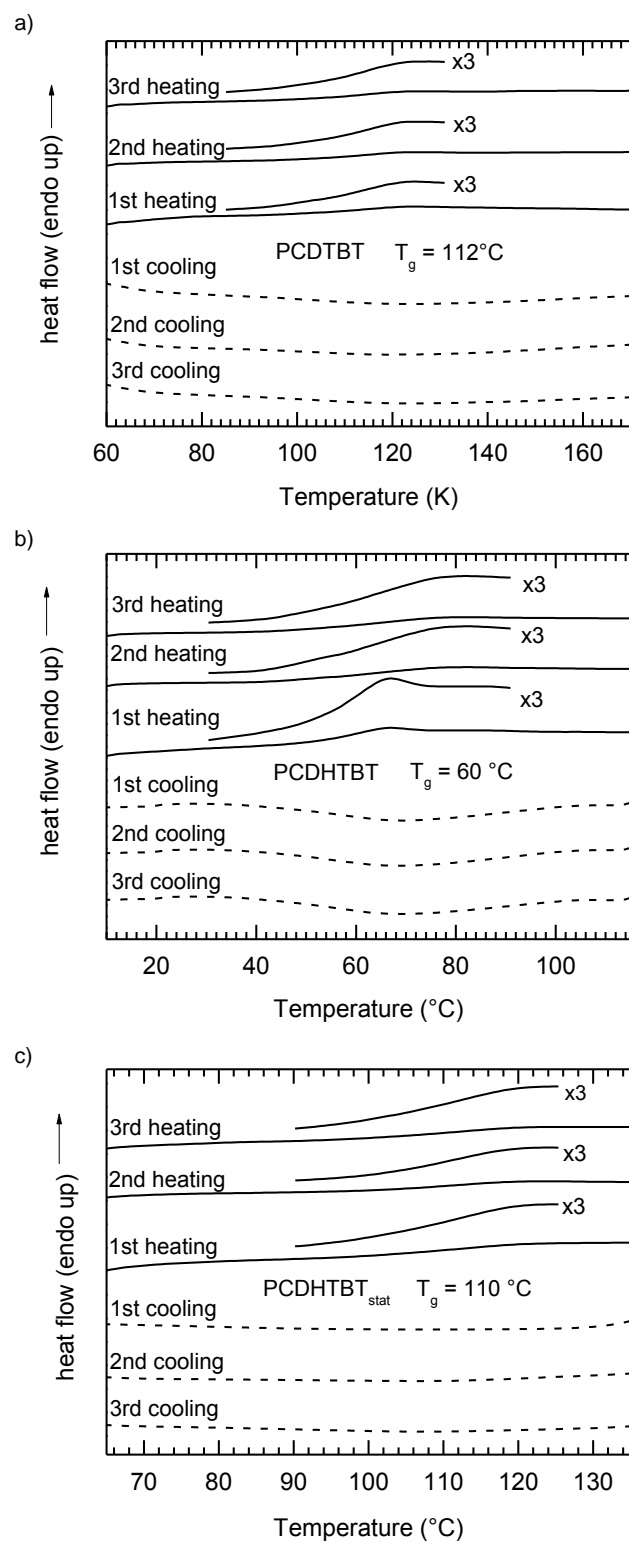


Figure S6: DSC measurements of a) PCDTBT, b) PCDHTBT, and c) PCDHTBT_{stat}. A heating and cooling rate of 40 Kmin⁻¹ under nitrogen atmosphere was used.

Determination of the Stern-Volmer constant K_d :

In order to determine the Stern-Volmer constant K_d we prepared i) neat films of the polymers PF2/6-A-25:75, PCDHTBT, PCDTBT and PCDTBT_{stat} and ii) blend films of the respective polymers with 2 wt% content of PC₆₀BM. PC₆₀BM was chosen to ensure proper solubility in the polymer solution from which the films were cast via spin-coating. To achieve a homogenous distribution of the fullerene within the polymer matrix we used only 2 wt% of PCBM.⁵⁻⁶ For each of the films we then carried out steady-state PL measurements. From the observed quenching in the PCBM containing samples as compared to the neat films we extracted the value of K_d for each polymer according to equation 7 from the main text. The resulting K_d values are given in **Table S1**.

Detailed derivation of equations (3)-(5):

In the following derivation, we assume a film of thickness d consisting of one fluorophore type. This layer will be denoted as sensor layer. The fluorophores shall have only one possible excited electronic state that decays either radiatively or non-radiatively in a film. The PL of a fluorophore is therefore given by

$$PL = \frac{k_0 \cdot k_r}{k_r + k_{nr}} \quad (1')$$

with k_0 being the excitation rate and k_r and k_{nr} being their radiative and non-radiative decay rate of the excited state, respectively. When exciting from the glass side of a sample, the excitation rate is

$$k_0(x) = K_0 \cdot \exp(-\alpha(d-x)) \quad (2')$$

Now we consider a fluorophore film that additionally features a concentration $c(x, t)$ of quenchers, e.g. C₆₀. For the PL of a fluorophore at position x in the sensor layer in the presence of quencher molecules, equation (1') changes to

$$PL(x, t) = \frac{k_0(x) \cdot k_r}{k_r + k_{nr} + k_q(x, t)} \quad (3')$$

k_q denotes the additional quenching rate caused by the presence of C₆₀. Self-absorption within the sensor layer as well as reflexions at the polymer/C₆₀-interface are neglected.

For the calculation of the fluorescence of the whole sensor layer consisting of several fluorophores,

equation (3') is regarded as a PL density by assuming the rates k to be rate densities ($[k] = \text{m}^{-3}\text{s}^{-1}$). Thus, the photoluminescence of the sensor layer PL_{total} with the area A and the thickness d at a time t can be calculated by inserting (2') into (3') and integrating over the layer volume:

$$PL_{\text{total}}(t) = A \int_0^d PL(x, t) dx = A \cdot K_0 \int_0^d \exp(-\alpha(d-x)) \cdot \frac{k_r}{k_r + k_{\text{nr}} + k_q(x, t)} dx \quad (4')$$

This is equation (3) of the main text.

If there is no quencher present in the sensor layer ($c = 0, k_q = 0$), PL_{total} is given by:

$$PL_{\text{total}}(c = 0) = A \cdot K_0 \cdot \frac{k_r}{k_r + k_{\text{nr}}} \cdot \frac{1 - \exp(-\alpha d)}{\alpha} \quad (5')$$

This is equation (4) of the main text.

Finally, the ratio of the PL from the sample half with C_{60} in relation to the PL from the reference half without C_{60} is then given by:

$$\frac{PL_{C_{60}}(t)}{PL_0} = \frac{PL_{\text{total}}(t)}{PL_{\text{total}}(c = 0)} = \frac{\alpha}{1 - \exp(-\alpha d)} \int_0^d \exp(-\alpha(d-x)) \cdot \left(1 + \frac{k_q(x, t)}{k_r + k_{\text{nr}}}\right)^{-1} dx \quad (6')$$

This is equation (5) of the main text.

Detailed explanation of the self-consistent approach (cf. section 3.2 in the main text):

To account for a possible concentration gradient at the beginning of the experiment, we took an iterative, self-consistent approach ("fit B", red dashed line in **Figure S7a**). In a first step, we simulate the diffusion with the aim to obtain the approximate initial concentration profile in the experiment. For this, we apply equation 6 with the initial condition that there will be no C_{60} , and thus no PL-quenching ($R_0 = 1$) at a certain time $t < 0$ (**Figure S7b**). The diffusion coefficient D is adjusted until a reasonable fit to the experimental data is achieved, in particular at later times, as illustrated in **Figure S7a**. From this simulation, we obtain an initial spatial concentration profile $c(x, t = 0)$ (**Figure S7c**). This is used in a second step as initial input concentration, nominally $c_0(T_1)$, to obtain an improved and more accurate diffusion coefficient.

Including surface quenching

To account for a possible influence of exciton quenching at the polymer/C₆₀ interface without the presence of C₆₀ in the polymer bulk we applied a slightly modified approach that is based on the self-consistent procedure discussed above. In this case we added another term in equation 6 of the main text:

$$\frac{PL}{PL_0}(t) = \frac{\alpha}{1 - \exp(-\alpha d)} \int_0^d \exp(-\alpha(d-x)) \cdot (1 + K_D \cdot c(x,t) + s(x,t) \cdot y_s)^{-1} dx. \quad (1^*)$$

where y_s is a measure of the initial quenching at the polymer/C₆₀ interface when no dopant is presented within the polymer bulk. This accounts for the fact that excitons may diffuse over a certain distance before they get finally quenched at said interface. s is defined as

$$s(x,t) = \exp\left(-\frac{x}{x_d} \cdot \exp\left(\frac{c(x,t)}{c_{char}}\right)\right) \quad (2^*)$$

Where x_D denotes the exciton diffusion length (typically in the order of 10 nm) and c_{char} defines the characteristic concentration at which the distance to the next interface has decayed to 1/e of the initial value of x_d (here assumed to be 1 wt%). From this concentration on the quenching is regarded to be dominated by the bulk effect characterized by $K_D \cdot c(x,t)$. The second exponential factor accounts for the fact that the distance to the next interface decreases with increasing concentration, effectively reducing the diffusion length of the exciton.

The value for y_s is determined from a quick calculation in which we take equation (1*) at $t = 0$ s and with no quencher molecules present in the bulk of the polymer. y_s is systematically varied until the calculated quenching level is equivalent to the expected quenching level for a given exciton diffusion length x_d , e.g. about 20 % for a film of thickness 70 nm.⁷ Apart from this modification, the fitting procedure is identical to the self-consistent approach discussed above and in the main text (see figure S7).

An exemplary comparison of all three approaches (effective concentration, self-consistent approach without initial quenching, self-consistent approach with initial surface quenching) is shown in **figure S8** for the case of crosslinked PF2/6-A-75:25. We find good agreement of all three fits with the experimental data and only small to no differences in the extracted diffusion coefficient (**cf. Table S1**). This again illustrates that in our case, an exact knowledge of the initial concentration profile is not required to obtain a reasonable value for the diffusion coefficient of a dopant in a polymer matrix.

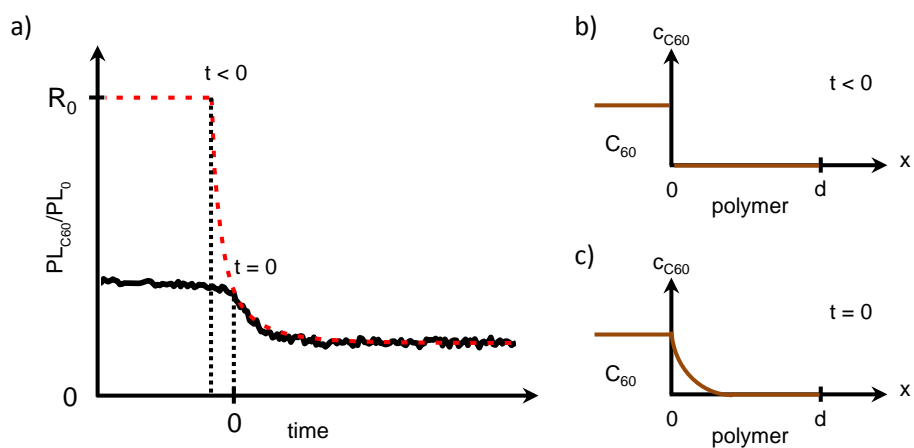


Figure S7: (a) Illustration of the fitting procedure using a self consistent initial condition as described in the main text. The black solid line corresponds to experimental data, the red dashed line is the result of a first simulation starting at zero initial concentration (i.e. right before evaporation) and ending at an equilibrium concentration corresponding to the experimentally observed final quenching level. (b) The concentration profiles assumed to prevail just before acceptor deposition at T_1 . This is used as input to the first fitting round. (c) The concentration profile obtained from the first fitting round, assumed to prevail just before the heating step to T_2 . This is used as initial condition for the second fitting round to the experimental data.

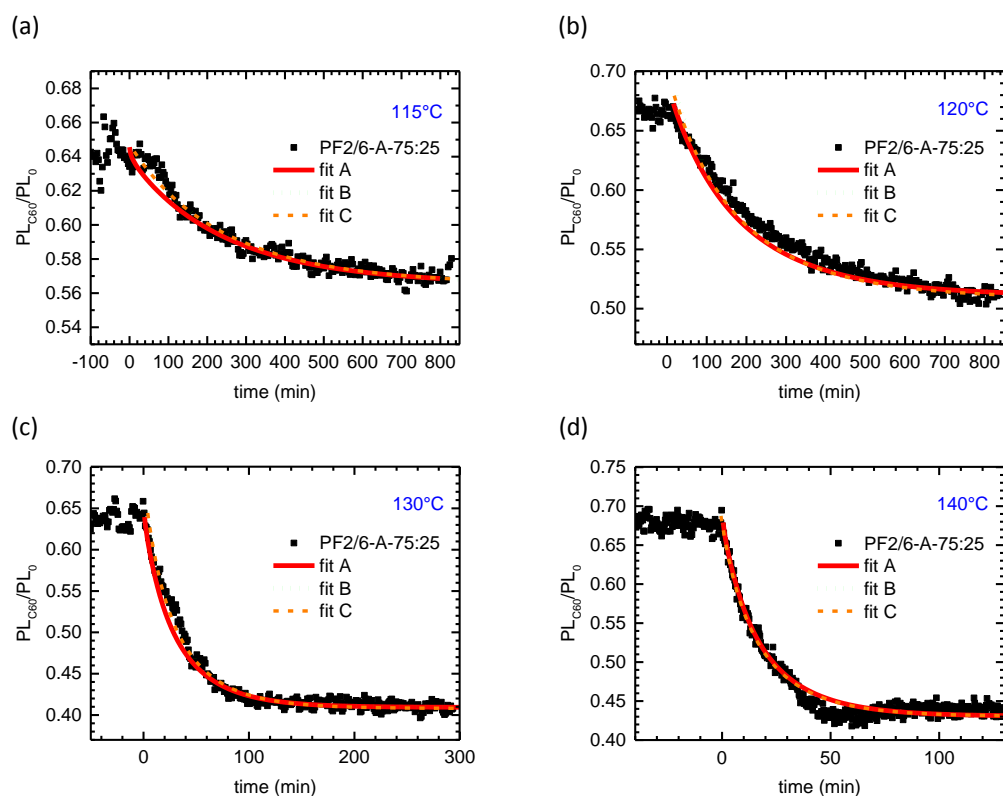


Figure S8: Time-dependence of $PL_{C_{60}}/PL_0$ measured on bilayer samples using crosslinked PF2/6-A-75:25 with C_{60} on top when increasing temperature to (a) 115°C, (b) 120°C, (c) 130°C and (d) 140°C. The red solid lines correspond to a fit according to eq. 6 of the main text using an effective homogeneous concentration as initial condition to extract the diffusion coefficient for C_{60} in PF2/6-A-75:25 as a function of temperature (fit A). The green dotted (fit B) and dashed orange lines (fit C) correspond to fits using a self-consistent initial concentration profile instead, as detailed in section 3.2 of the main text as well as the explanation given here in the supporting information.

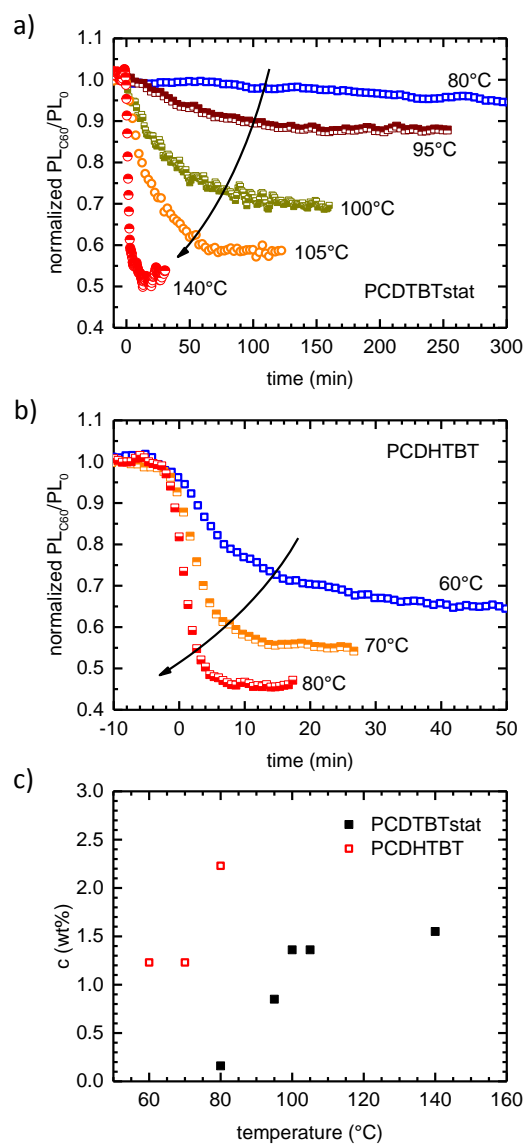


Figure S9: Time-dependence of $PL_{C_{60}}/PL_0$ for different final temperatures after a temperature increase for (a) PCDTBT_{stat} and (b) PCDHTBT. The data are normalized to the initial plateau value of $PL_{C_{60}}/PL_0$ in order to better visualize differences in decay dynamics. (c) Final concentration $c(T_2)$ as a function of the final temperature T_2 for PCDTBT_{stat} (filled symbols) and PCDHTBT (open symbols).

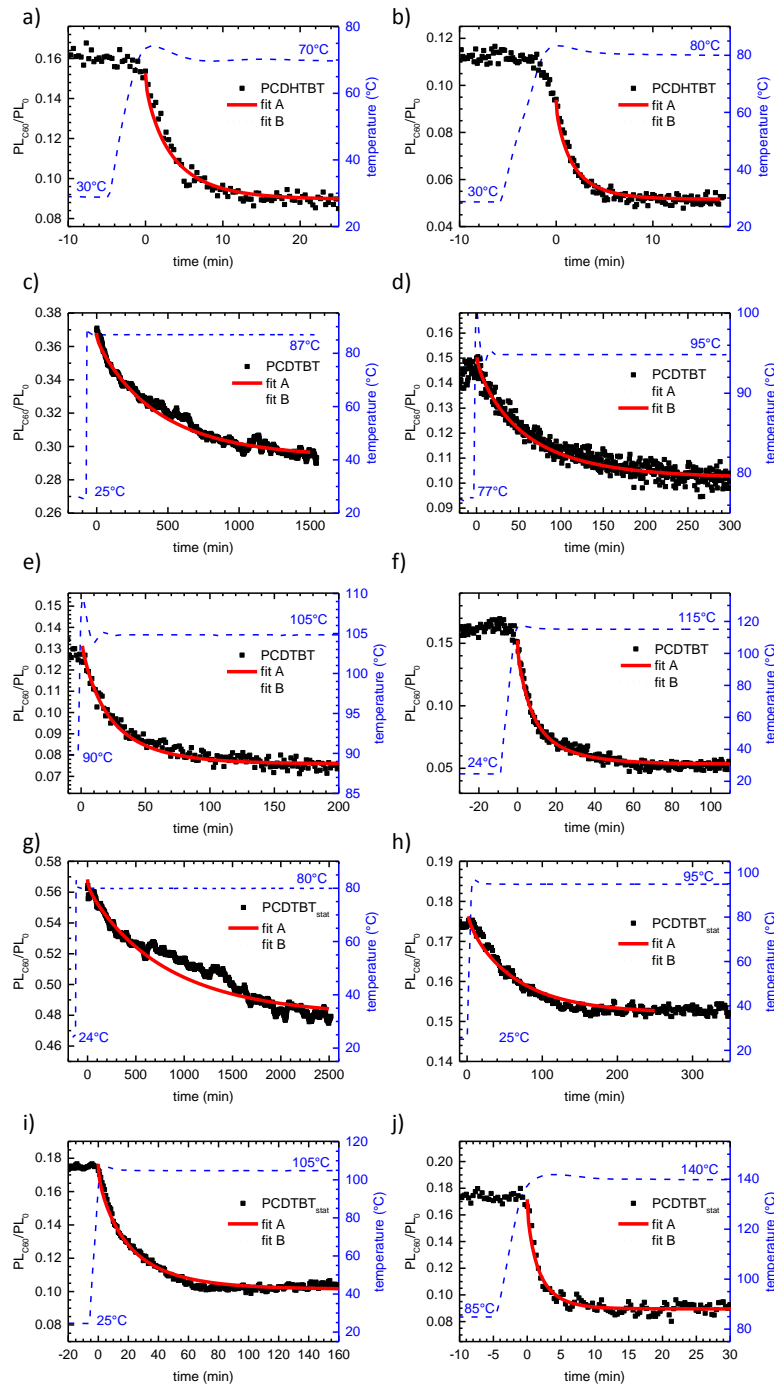


Figure S10: Time-dependence of $PL_{C_{60}}/PL_0$ (left axis) measured on bilayer samples using (a,b) PCDHTBT, (c-f) PCDTBT and (g-j) PCDTBT_{stat} with C₆₀ on top when applying a heating ramp as indicated by the dashed blue curve (right axis). The red solid and green dotted lines correspond to fits according to eq. 6 of the main text using an effective homogenous concentration (fit A) and a self-consistent initial condition (fit B) to extract the diffusion coefficient for C₆₀ (cf. figure 5c in the main text). The decay curves displayed here are the original data corresponding to some of the normalized data displayed in figure 5a in the main text and figure S9 above.

Table S1: Input and output parameters for the simulated PL decay due to quenching according to the model described in section 3.2 of the main text. T_1 and T_2 correspond to the initial and final temperature of the experimentally applied heating ramp, respectively. α denotes the absorption coefficient of the respective material at the indicated excitation wavelength. K_D is the Stern-Volmer constant as determined from steady state PL quenching experiments as detailed above. $c_0(T_1)$ denotes an effective homogenous initial concentration when evaluating the data according to the first approach outlined in section 3.2 of the main text (“fit A”). $c_0(T_2)$ corresponds to the final equilibrium concentration after the temperature has been raised from T_1 to T_2 . $D_A(T_2)$ refers to the diffusion coefficient for C_{60} diffusion at T_2 assuming an effective initial concentration. $D_B(T_2)$ denotes the diffusion coefficient for C_{60} diffusion at T_2 using a self-consistent initial condition and assuming no initial quenching. $D_C(T_2)$ is deduced from a self-consistent approach with the consideration of surface quenching.

Polymer	input				output				
	T_1 in °C	T_2 in °C	α in nm ⁻¹	K_D in wt% ⁻¹	$c_0(T_1)$ in wt%	$c_0(T_2)$ in wt%	$D_A(T_2)$ in cm ² s ⁻¹	$D_B(T_2)$ in cm ² s ⁻¹	$D_C(T_2)$ in cm ² s ⁻¹
PCDTBT	22	80	0.0157 ^a	6.51	0.28	0.33	5.50·10 ⁻¹⁶	5.33·10 ⁻¹⁶	5.37·10 ⁻¹⁶
	25	87	0.0157 ^a	6.51	0.26	0.37	6.33·10 ⁻¹⁶	5.83·10 ⁻¹⁶	6.17·10 ⁻¹⁶
	77	95	0.0157 ^a	6.51	0.85	1.35	7.50·10 ⁻¹⁶	7.50·10 ⁻¹⁶	7.83·10 ⁻¹⁶
	85	100	0.0157 ^a	6.51	0.72	1.19	9.17·10 ⁻¹⁶	9.17·10 ⁻¹⁶	9.17·10 ⁻¹⁶
	90	105	0.0157 ^a	6.51	0.95	1.87	1.66·10 ⁻¹⁵	1.66·10 ⁻¹⁵	1.75·10 ⁻¹⁵
	25	115	0.0157 ^a	6.51	0.85	2.72	2.83·10 ⁻¹⁵	2.92·10 ⁻¹⁵	2.92·10 ⁻¹⁵
	27	125	0.0157 ^a	6.51	1.00	3.02	7.00·10 ⁻¹⁵	6.83·10 ⁻¹⁵	6.92·10 ⁻¹⁵
	97	140	0.0157 ^a	6.51	1.12	2.52	1.83·10 ⁻¹⁴	1.83·10 ⁻¹⁴	1.87·10 ⁻¹⁴
PCDHTBT	32	60	0.0139 ^a	8.26	0.76	1.23	4.67·10 ⁻¹⁵	4.16·10 ⁻¹⁵	4.16·10 ⁻¹⁵
	30	70	0.0139 ^a	8.26	0.67	1.23	1.12·10 ⁻¹⁴	1.05·10 ⁻¹⁴	1.08·10 ⁻¹⁴
	30	80	0.0139 ^a	8.26	1.17	2.23	2.08·10 ⁻¹⁴	2.00·10 ⁻¹⁴	2.05·10 ⁻¹⁴
PCDTBT _{stat}	25	80	0.0117 ^a	6.56	0.12	0.16	5.83·10 ⁻¹⁶	6.33·10 ⁻¹⁶	5.83·10 ⁻¹⁶
	25	95	0.0117 ^a	6.56	0.70	0.85	8.66·10 ⁻¹⁶	1.08·10 ⁻¹⁵	1.03·10 ⁻¹⁵
	77	100	0.0117 ^a	6.56	0.90	1.36	1.25·10 ⁻¹⁵	1.25·10 ⁻¹⁵	1.33·10 ⁻¹⁵
	87	105	0.0117 ^a	6.56	0.78	1.36	1.83·10 ⁻¹⁵	1.83·10 ⁻¹⁵	1.92·10 ⁻¹⁵
	85	140	0.0117 ^a	6.56	0.73	1.55	2.00·10 ⁻¹⁴	2.33·10 ⁻¹⁴	2.17·10 ⁻¹⁴
PF2/6-	32	115	0.00357 ^b	4.81	0.11	0.16	1.62·10 ⁻¹⁴	1.65·10 ⁻¹⁴	1.65·10 ⁻¹⁴
A-75:25	22	120	0.00357 ^b	4.81	0.09	0.20	2.25·10 ⁻¹⁴	2.25·10 ⁻¹⁴	2.21·10 ⁻¹⁴
	25	130	0.00357 ^b	4.81	0.11	0.30	6.33·10 ⁻¹⁴	6.17·10 ⁻¹⁴	6.17·10 ⁻¹⁴
	35	140	0.00357 ^b	4.81	0.09	0.27	1.38·10 ⁻¹³	1.40·10 ⁻¹³	1.38·10 ⁻¹³

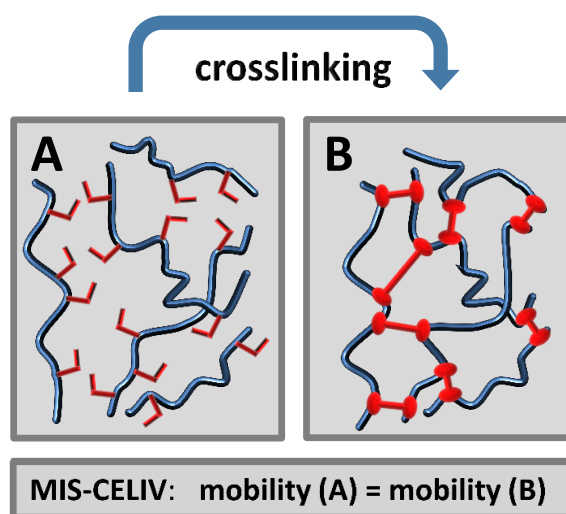
^a at 520 nm

^b at 405 nm

References

- (1) Scheler, E.; Strohriegl, P., Three Color Random Fluorene-Based Oligomers for Fast Micrometer-Scale Photopatterning. *Chem Mater* **2010**, *22*, 1410-1419.
- (2) Blouin, N.; Michaud, A.; Leclerc, M., A Low-Bandgap Poly(2,7-carbazole) Derivative for Use in High-Performance Solar Cells. *Adv Mater* **2007**, *19*, 2295–2300.
- (3) Kim, J.; Kwon, Y. S.; Shin, W. S.; Moon, S. J.; Park, T., Carbazole-Based Copolymers: Effects of Conjugation Breaks and Steric Hindrance. *Macromolecules* **2011**, *44*, 1909-1919.
- (4) Hahn, T.; Tscheuschner, S.; Kahle, F.-J.; Reichenberger, M.; Athanasopoulos, S.; Saller, C.; Bazan, G. C.; Nguyen, T.-Q.; Strohriegl, P.; Bäessler, H.; Köhler, A., Monomolecular and Bimolecular Recombination of Electron–Hole Pairs at the Interface of a Bilayer Organic Solar Cell. *Adv Funct Mater* **2016**, 1604906.
- (5) Wong, H. C.; Sanz, A.; Douglas, J. F.; Cabral, J. T., Glass formation and stability of polystyrene-fullerene nanocomposites. *J Mol Liq* **2010**, *153*, 79-87.
- (6) Dattani, R.; Cabral, J. T., Polymer fullerene solution phase behaviour and film formation pathways. *Soft Matter* **2015**, *11*, 3125-3131.
- (7) Lin, J. D. A.; Mikhnenko, O. V.; Chen, J. R.; Masri, Z.; Ruseckas, A.; Mikhailovsky, A.; Raab, R. P.; Liu, J. H.; Blom, P. W. M.; Loi, M. A.; Garcia-Cervera, C. J.; Samuel, I. D. W.; Nguyen, T. Q., Systematic study of exciton diffusion length in organic semiconductors by six experimental methods. *Mater Horizons* **2014**, *1*, 280-285.

11 Influence of Crosslinking on Charge Carrier Mobility in Crosslinkable Polyfluorene Derivatives



Frank-Julian Kahle, Irene Bauer, Peter Strohhriegl, and Anna Köhler

Published in
Journal of Polymer Science, Part B: Polymer Physics **2017**, *55*, 112-120
(DOI: 10.1002/polb.24259)

Copyright ©2017 by John Wiley Sons, Inc.
Reprinted by permission of John Wiley & Sons, Inc.

Influence of Crosslinking on Charge Carrier Mobility in Crosslinkable Polyfluorene Derivatives

Frank-Julian Kahle,¹ Irene Bauer,¹ Peter Strohriegel,^{2,3} Anna Köhler^{1,3}

¹Experimental Physics II, University of Bayreuth, Bayreuth, Germany

²Macromolecular Chemistry I, University of Bayreuth, Bayreuth, Germany

³Bayreuth Institute of Macromolecular Research (BIMF), University of Bayreuth, Bayreuth, Germany

Correspondence to: A. Köhler (E-mail: anna.koehler@uni-bayreuth.de)

Received 12 September 2016; accepted 30 September 2016; published online 26 October 2016

DOI: 10.1002/polb.24259

ABSTRACT: Carrier mobility is a key parameter for the application of conjugated polymers. In this work, a series of polyfluorenes (PF2/6) with different fractions of crosslinkable acrylate groups is investigated. Mobility measurements are carried out to assess the influence of crosslinking with different photoinitiators on the performance of the material. For the regime of low to medium charge carrier density, relevant for OLEDs and OPVs, we used a novel technique based on the injection of charge carriers from the electrodes of an optoelectronic device: MIS-CELIV (MIS: metal-insulator-semiconductor). For large charge carrier densities we performed OFET measurements. We find that using optimized conditions crosslinking does not

influence the hole mobility in the investigated system. Furthermore, we demonstrate that the crosslinking process may be triggered solely by thermal activation and UV-illumination without the need of any initiator. Thus, densely crosslinked networks are obtained without the formation of undesired decomposition products from added photoinitiator. © 2016 Wiley Periodicals, Inc. *J. Polym. Sci., Part B: Polym. Phys.* **2017**, *55*, 112–120

KEYWORDS: free radical polymerization; acrylate; MIS-CELIV; photoinitiator; polyfluorene (PF2/6)

INTRODUCTION Crosslinking provides a good means to fabricate optoelectronic devices, especially organic light emitting diodes (OLEDs) or organic solar cells (OSCs), with multiple layers via solution processing, or to stabilize certain morphologies in organic bulk heterojunction solar cells.^{1–8} In a previous work,⁹ we have shown that varying the crosslinking density of a polymer allows controlling the interdiffusion of “small molecules,” in our case C₆₀, in a polymer layer. The diffusion coefficient of C₆₀ could be reduced by three orders of magnitude in a highly crosslinked polyfluorene network. This is especially relevant for bulk heterojunction OSCs in order to maintain their morphology and to prevent crystallization. In the literature on crosslinkable conjugated polymers so far mainly processing issues and aspects of device architecture were addressed. However, another very important point is the actual performance of the material and its charge transport properties in optoelectronic devices, especially with respect to the question whether, or even how many, defects are induced by crosslinking or by adding additional substances needed for curing. A very sensitive quantity with respect to defects and a key parameter for device performance is charge carrier mobility. This is due to the

fact that defects may induce additional trapping states below or above the density of states (DOS) for electron or hole transport. Charge carriers travelling through the device will in this case be captured easily resulting in a reduced mobility.^{10–12} Up to now, only few investigations on the influence of crosslinking on charge carrier mobility were published and these were mainly focusing on charge transport in organic field effect transistors (OFETs) and (liquid) crystalline materials.^{13,14}

In this paper, we investigate a series of poly(9,9-bis(2-ethylhexyl)fluorene) derivatives with different fractions of crosslinkable acrylate groups [PF2/6-A, Fig. 1(a)]. The polymers have been prepared by Yamamoto coupling similar to the procedure given in ref. 15. A structurally similar polyfluorene with pendant acrylate groups has been described by Wu and crosslinking has been monitored by IR, UV/VIS, and PL spectroscopy, but no measurements of the carrier mobility have been reported.¹⁶ Due to the bulky side chains, PF2/6 films are amorphous at room temperature under the experimental conditions used in this work.^{17,18} In our case the polymer network is formed by free radical photopolymerization of polymers containing acrylate groups in their side

Additional Supporting Information may be found in the online version of this article.

© 2016 Wiley Periodicals, Inc.

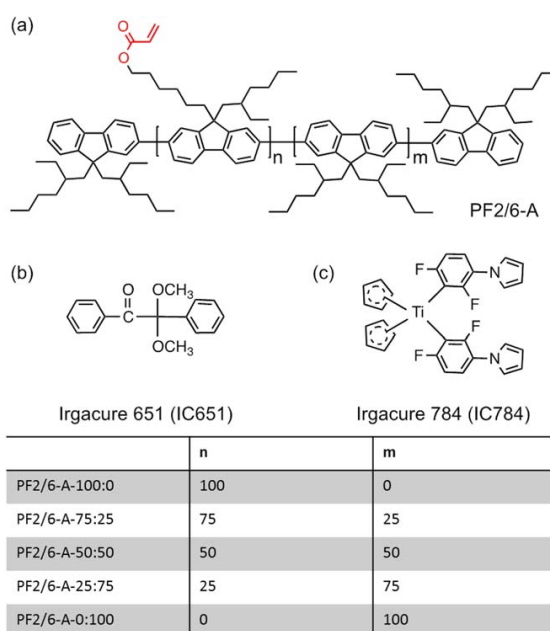


FIGURE 1 Chemical structure of the PF2/6-A polymers (a) and the photoinitiators Irgacure 651 (b) and Irgacure 784 (c). *n* and *m* denote the fractions of acrylate containing and unmodified fluorene repeating units, respectively. The crosslinkable acrylate group is highlighted in red. PF2/6-A-0:100 corresponds to unmodified PF2/6. [Color figure can be viewed at wileyonlinelibrary.com]

chains. The approach of incorporating the crosslinkable group into the side chain has the advantage that the polymer backbone is not directly affected, so that the electronic structure remains largely undisturbed. Furthermore, this approach may, in principle, be adapted to a wider range of polymer backbones. The acrylate based polymerization reaction may be performed at room temperature but can be accelerated using elevated temperatures. For this reaction, however, it is usually necessary to introduce photoinitiator into the polymer film.³ In order to investigate the effect of different initiators in the curing process, two different photoinitiators are used, the purely organic compound Irgacure 651 [Fig. 1(b)] and the Ti-complex Irgacure 784 [Fig. 1(c)]. In order to assess the influence of introducing acrylate groups and crosslinking with different crosslinking agents on the performance of the material, we performed spectroscopic measurements and determined mobility values in the low to medium and in the high charge carrier density regime. For the latter we measured OFETs, whereas for the former regime, which is more relevant for OLEDs and OSCs, we used a special CELIV technique called MIS-CELIV.^{19,20} Unlike in conventional CELIV it is possible to measure hole and electron mobility values separately. As PF2/6 is usually used as a hole conducting material, we focused on the measurement of hole mobility values.

By comparing crosslinked samples using either a Ti-complex or an organic compound as crosslinking agent with PF2/6 as reference, we found that the crosslinking process itself has no major influence on hole mobility. Nevertheless, a

reduction of around one order of magnitude is observed for the crosslinkable PF2/6 derivatives compared to PF2/6, even before crosslinking. This effect is attributed to conformational differences caused by the introduction of acrylate groups. Another important effect we observed is that the underlying crosslinking mechanism allows for network formation solely by thermal activation and UV-illumination without any additional photoinitiator. This is of special interest as it turned out that the decomposition products of the photoinitiator may introduce traps for charge carrier transport.

EXPERIMENTAL

Sample Preparation

Samples for spectroscopic characterization were prepared in a glovebox by spincoating the respective polyfluorene derivative from a 15 g/l chlorobenzene solution onto round spectro-sil B substrates. For mobility measurements we used cleaned patterned ITO glass substrates that were additionally covered with a patterned layer of photoresist to avoid spurious electrical breakdown effects at the electrode edges. After treating the substrates for 2 min inside a plasma chamber, a 15 nm layer of MoO₃ is vapor deposited using a shadow mask. After that the active layer of polyfluorene is spin-cast on top inside a glovebox again from a 15 g/l chlorobenzene solution. Layer thicknesses were around 80–100 nm as determined using a Veeco Dektak 150 profilometer. In case of crosslinking, samples were treated as described in the crosslinking procedure. For MIS-CELIV measurements, an additional layer of MgF₂

(40 nm) is evaporated on top of the polyfluorene layer before Al is deposited as cathode (100 nm). The resulting device area is around 2.1 mm². OFET samples were prepared on commercially available Fraunhofer IPMS end of line substrates (bottom gate/bottom contact). These were cleaned with acetone and isopropanol inside a cleanroom. Prior to HMDS deposition, the SiO₂ surface was first activated by treating the samples at 50 °C inside an ozone chamber for 15 min. SAMs of HMDS were deposited by exposing the substrates to HMDS vapor for 45 min. PF2/6 compounds were then spin-cast on top of the substrates from chlorobenzene solution (10 g/l) inside a glovebox.

Materials

Molybdenumtrioxide (MoO₃), magnesiumfluoride (MgF₂), and hexamethyldisilazane (HMDS) were purchased from Sigma Aldrich and used as received. The PF2/6 polymers with photo crosslinkable acrylate groups [Fig. 1(a)] were synthesized by Yamamoto coupling. The detailed synthesis route is given in the SI. In order to vary the degree of crosslinking, five derivatives are used, labelled as *n:m*, where *n* is the fraction of fluorene monomers with an acrylate group in the side chain and *m* is the fraction of unmodified, noncrosslinkable fluorene monomers. Due to the bulky side chains, PF2/6 films are amorphous at room temperature.^{17,18}

Crosslinking Procedure

Crosslinking of the acrylate groups is carried out by photopolymerization using either Irgacure 651 (IC651) or Irgacure 784 (IC784) from Ciba Specialty Chemicals in an amount of 0.1 or 1.0 wt%. Samples were tempered at 100 °C on a hot plate inside the glovebox and simultaneously exposed to UV-light of a 50W Xenon lamp at 20 cm distance with a UV-filter cutting off at 330 nm. For comparison, a series of samples was treated according to this procedure without using any photoinitiator. Success of crosslinking was checked by taking absorption spectra of spectroscopic samples before and after rinsing in THF for 1 min. The corresponding structures are shown in Figure 1(b,c).

Spectroscopic Characterization

Absorption spectra were taken using a Varian Cary 5000 UV-VIS-NIR Spectrophotometer. Photoluminescence (PL) spectra measurements were performed using a Jasco Spectrofluorometer FP8600. PL quantum yield values were determined using a Picoquant PDL 800-D Diode laser LDH-D-C-375 in combination with an integrating sphere. For detection we used a Andor DU420A-OE CCD camera.

MIS-CELIV Measurements

MIS-CELIV measurements were performed according to the procedure described in ref. 19,20. The voltage is supplied by a Rigol DG4102 function generator. The slope of the voltage ramp, the offset voltage and the length of the voltage pulse were fixed to 0.2 V/μs, 10 V, and 100 μs, respectively, for all measurements, to make sure that experimental conditions are identical for all compounds and samples. This ensures that observed trends and effects may be attributed to materials. The resulting current response signal was amplified

using a Femto DHPA-100 current amplifier and recorded with a Tektronix TDS3000 digital phosphor oscilloscope. In all the measurements we applied a prebias voltage of 10 V for several minutes to ensure equilibrium conditions.

OFET Measurements

OFETs were measured under inert conditions inside a glovebox using a PM5 Cascade Microtech measurement station and an Agilent B1500 A Semiconductor Device Analyzer. Mobility in the saturation regime was determined according to

$$\mu_{sat} = \frac{2L}{WC_i} \left(\frac{\partial \sqrt{I_{d,sat}}}{\partial V_g} \Big|_{V_d} \right)^2, \quad (1)$$

where *L* denotes the channel length, *W* the channel width (10 mm), *C_i* the capacitance per unit area ($1.4 \pm 0.1 \cdot 10^{-4} \text{ F m}^{-2}$), *I_{d,sat}* the source-drain-current in the saturation regime *V_g* the gate voltage and *V_d* the source-drain-voltage. Mobility in the linear regime was determined according to

$$\mu_{lin} = \frac{L}{WC_i V_d} \frac{\partial I_d}{\partial V_g} \Big|_{V_d}. \quad (2)$$

RESULTS AND DISCUSSION

Absorption Spectroscopy

In order to correlate findings in our mobility measurements to structural or morphological peculiarities of the investigated PF2/6 compounds, we performed spectroscopic measurements on dilute solutions and thin spin-cast films. First of all we consider absorption spectra, giving insight into structural and morphological properties of the investigated system in the ground state,²¹ such as to assess changes upon forming a crosslinked network structure.

The absorption spectra under different conditions are shown in Figures 2 and 3. We first consider spectra of dilute solutions (0.017 mg/ml) and as-cast films prior to the crosslinking procedure to assess the influence of different acrylate content on the optical properties of PF2/6 (Fig. 2). The spectra do not show a distinct structure. In solution, the absorption onset is the same irrespective of acrylate content [Fig. 2(a)], yet the FWHM increases up to 50% acrylate content and then decreases again [Fig. 2(b)]. Furthermore, increasing the acrylate content to 50% leads to a blue shift of the peak position, yet a further increase shifts the spectra back to the red again. The latter effect is observed for solution and as-cast films. Finally, comparing the spectra of thin films and dilute solutions one observes a spectral line broadening in the film [shown in Supporting Information Fig. S1(a)], a very commonly reported and well known effect attributed to an increased energetic disorder in the amorphous film compared to solution. It arises from the higher polarizability of the chromophores in the film compared to the solvent molecules surrounding a particular chromophore in solution.^{22,23}

The lack of structure in absorption spectra of both solution and film indicates that there is a distribution of conjugation

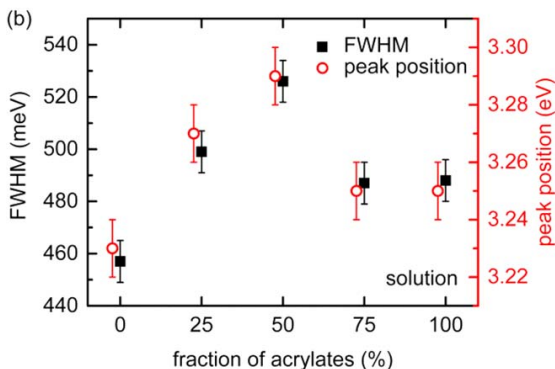
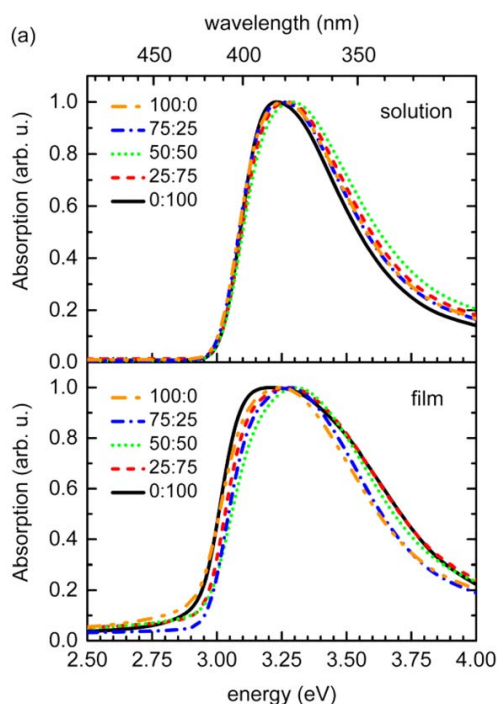


FIGURE 2 (a) Absorption spectra of crosslinkable PF2/6 compounds with different ratios of acrylate containing repeat units to unmodified fluorene repeat units for dilute solutions (0.017 mg/ml) and for as-cast films. (b) FWHM (black squares) and peak positions (red circles) of the solution spectra as a function of acrylate content. [Color figure can be viewed at wileyonlinelibrary.com]

lengths. This arises from the torsional degree of freedom between different fluorene units. We recall that in PF2/6 with its branched side chains, the backbone is not restricted by packing as would be the case for polyfluorene with linear side chains such as PFO (PF8).^{17,21,24,25} Evidently, the width of the distribution, indicated by the Full Width at Half Maximum (FWHM) and the peak position, changes with acrylate content in the sidechain, being largest when half of the repeat units features an acrylate moiety. This trend coincides with the evolution of polydispersity in the samples. For

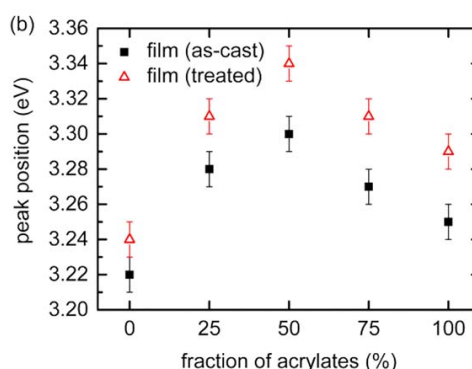
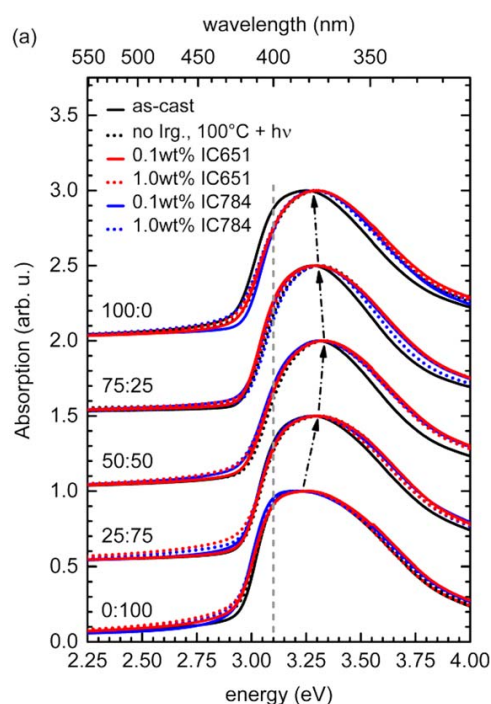


FIGURE 3 (a) Comparison of film absorption spectra for different sample treatments: as-cast (black solid line), thermally treated without photoinitiator (black dotted line), thermally treated with either 0.1 wt% (solid line) or 1.0 wt% (dotted) of photoinitiator Irgacure 651 (blue) or Irgacure 784 (red). The grey dashed line provides a guide to the eye for the spectral shifts indicated by the black arrows. (b) Peak positions of as-cast (black squares) and thermally treated (red triangles) films without Irgacure as a function of acrylate content. [Color figure can be viewed at wileyonlinelibrary.com]

samples with 0, 25, 50, 75, or 100% of acrylate containing polyfluorene units in the backbone, the polydispersity index (PDI) evolves as 2.4, 3.2, 4.1, 3.2, and 2.8. To examine whether this reflects a high fraction of short chains and concomitantly short conjugation lengths and blue-shifted peak positions,^{22,24} we considered the gel permeation

chromatography (GPC) data. We did not find any significant difference in the distribution for molecular weights below 4000 Daltons, corresponding to chains shorter than 10 repeat units. We therefore consider that the observed trend in blue-shift and FWHM arises from structural disorder; notably more torsions, that are introduced by the presence of different side chains to the same backbone and that slightly reduce the conjugation lengths in some chains, thus causing a small overall blue-shift and broadening. The very well coinciding onset in solution spectra is noteworthy. It points to a similar maximum intrinsic actual conjugation length of the chains, irrespective of acrylate content.²² As similar spectral shifts are observed for both dilute solution and as-cast films, we may state that despite of additional solid state effects such as packing and intermolecular interactions the basic properties of the respective compounds are preserved in the as-cast film.

So far we have discussed intrinsic properties of the polyfluorenes themselves. Figure 3a addresses what happens when the compounds are crosslinked. It shows the spectra of films made with the polymers containing different acrylate content and treated thermally at 100 °C for 15 min under UV/VIS-illumination inside a glovebox as described in the experimental section. Prior to the thermal treatment, 0.1 and 1.0 wt% of the organic (IC651) and the metalorganic (IC784) photoinitiator were added. Both amounts are sufficient to obtain fully crosslinked, insoluble films. For reference, the spectra of films without any photoinitiator, yet thermally treated in the same way, are included (“no Irg. 100 °C + hv”), as well as the spectra of as-cast films that have not undergone any thermal treatment (“as-cast”). We observe that (i) the spectra of the thermally treated samples coincide very well irrespective of the presence or the kind of photoinitiator, (ii) after thermal annealing, the spectra are slightly broadened and the peak shifts to the blue spectral range by about a 20 meV, and (iii) comparing the samples with different acrylate content, we find a blue shift with increasing acrylate content up to 50%, yet a backshift to the red for a further increase also for treated films, irrespective of the presence or the amount of photoinitiator [see Supporting Information Fig. S1(b) and arrows in Fig. 3(a)], just like in dilute solution and as-cast films.

Observation (i) hints at the possibility of mere thermally activated crosslinking. This was confirmed by taking UV/VIS absorption spectra before and after rinsing the sample in THF for 1 min observing no change in optical density [see Supporting Information Fig. S1(c)]. We further interpret the fact that the spectral shifts in the thermally treated samples show the same trend than the samples in solution (observation iii) yet in a slightly enhanced fashion (observation ii) to indicate that thermal treatment, and in particular the formation of crosslinks, increases the structural disorder; for example, by promoting twists of the fluorene.

Photoluminescence Spectroscopy

While absorption measurements yield information about the chromophore conformations in the ground state,

measurements of the photoluminescence (PL) spectra, and even more so of the photoluminescence quantum yield, are a sensitive indicator for possible defects. This applies in particular when the spectra are taken in a film where energy transfer to defect sites can occur readily by three-dimensional exciton diffusion in the dense medium. Figure 4(a) shows the PL spectra obtained in a thin film after different sample treatments, exemplary for the crosslinkable PF2/6 with 25% of acrylate containing repeat units. All spectra are normalized to the total area below the spectrum. In addition to the as-cast, untreated film, a spectrum is shown for the film after heating, in a glovebox, to 100 °C under illumination to UV light for 15 min (“no Irgacure, 100 °C + hv”). Further, films exposed to same treatment, yet with the photoinitiators IC651 and IC784, each at concentrations of 0.1 and 1.0 wt%, are also shown. Apart from some variation in the 0-0 peak intensity due to self-absorption in the film, we find that there are no changes of the spectral shape irrespective of the treatment. Importantly, the spectra of thermally treated films with and without photoinitiator are essentially identical, implying that the use of photoinitiators does not introduce any emissive defects. This behavior was found identical for all samples, irrespective of acrylate content (see Figs. S2 and S3 in Supporting Information).

While we do not observe any effect of the photoinitiator on the PL spectra, differences become evident when considering the PL-Quantum efficiency (PL-QE) measured in an integrating sphere. The PL-QE is a more sensitive measure to detect traps and quenching sites in the investigated system. The results are shown in Figure 4(b). The PL-QE is plotted as a function of the fraction of acrylate containing repeat units for different treatments. Error bars are estimated from a series of measurements of several samples. We find there is no difference in the PL-QE for untreated (as-cast) samples, for thermally treated samples without photoinitiator, and for thermally treated samples with the organic photoinitiator Irgacure 651. The PL-QE for these samples is about $(24 \pm 3)\%$, which is in good agreement to literature values measured for neat PF2/6.²⁵⁻²⁷ In contrast to the organic photoinitiator, a significant reduction of PL-QE occurs when using the metalorganic photoinitiator Irgacure 784, that is, the Ti-complex. These results imply that the (residual) organic photoinitiator Irgacure 651 or its decomposition products do not act as quencher for singlet excitons. In contrast to this, the Ti-complex Irgacure 784 or its reaction byproducts enhance nonradiative decay. This makes the latter compound unsuitable for applications in OLEDs and OSCs.

Impact on Mobility

MIS-CELIV Measurements

From absorption and photoluminescence spectroscopy we can conclude that the acrylate groups themselves only induce a small degree of structural disorder. Crosslinking without photoinitiator or with organic photoinitiator does not lead to noticeable defect sites. Crosslinking, in contrast, in the presence of *metalorganic* photoinitiator induces quenching sites for the photoluminescence. An even more sensitive technique

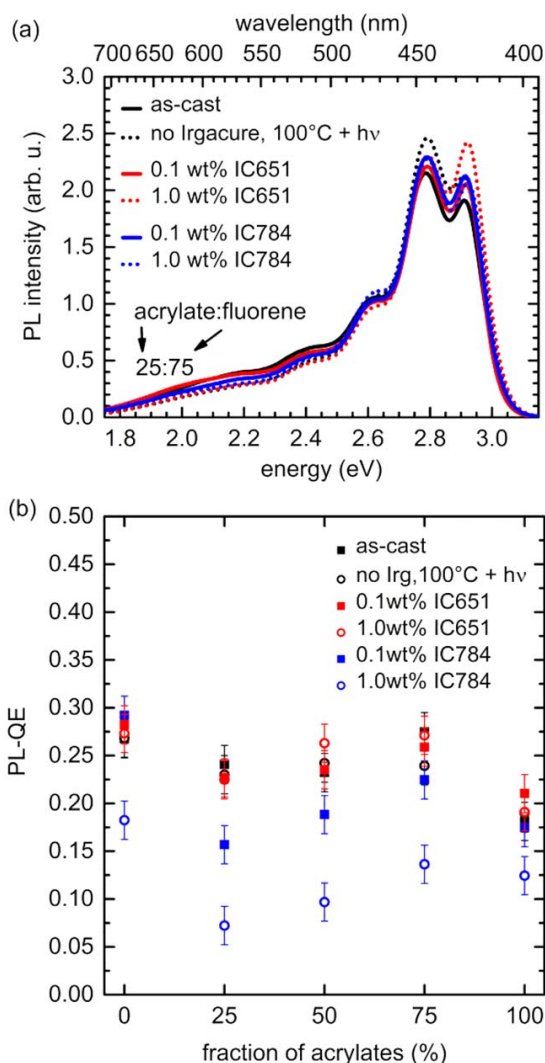


FIGURE 4 (a) Exemplary thin film photoluminescence spectra of crosslinkable PF2/6 with 25% of acrylate containing repeat units for different sample treatments (normalized to unit area). (b) Photoluminescence quantum yield as a function of the fraction of acrylate containing repeat units for different sample treatments. [Color figure can be viewed at wileyonlinelibrary.com]

to probe the presence of defect sites is measuring the charge carrier mobility. We focus here on hole mobility of PF2/6. First of all, we will discuss the results obtained for the low to medium charge carrier density regime using the MIS-CELIV technique.

The basic layer structure of a device employed in MIS-CELIV and an exemplary current response curve for a PF2/6 film of (98 ± 4) nm thickness are shown in Figure 5. In brief, charge carriers, in this case holes, are injected into the device from

the anode and the hole injection layer (HIL) by applying a constant offset voltage V_{off} to the sample. These charges are then accumulated at the interface between the investigated organic semiconductor (S), here PF2/6, and an insulating layer (I), here MgF_2 , forming an extractable charge carrier reservoir. This reservoir is then depleted by applying an oppositely biased voltage ramp. Mobility is determined from the current response of the sample according to²⁰

$$\mu = \frac{2d_s^2}{At_{\text{tr}}^2} \left(1 + \frac{\epsilon_s d_i}{\epsilon_i d_s} \right), \quad (3)$$

where the indices s and i refer to the organic semiconductor and the insulator, respectively. d denotes the layer thickness, ϵ the relative permittivity, A the slope of the voltage ramp, $A = dV/dt$, and t_{tr} the transit time of the charge carriers, that is, the time a charge carrier needs to travel from the semiconductor/insulator interface to the opposite electrode. ϵ_s and ϵ_i were assumed to be 3.5 and 5.5, respectively.^{23,28} For sufficiently large signals [$j - j_0 \gg j_0$, compare Fig. 5(b)], the transit time is given by

$$t_{\text{tr}} = \frac{4}{\pi} t_{2j_0}, \quad (4)$$

where t_{2j_0} refers to the time, where the current reaches two times the plateau value j_0 . The plateau value j_0 is determined separately by performing a second measurement at zero offset voltage, giving the pure capacitive response of the sample. Details about the parameters used are given in the experimental section. For all measurements we applied the same values for offset voltage, slope of the voltage ramp and pulse length so that experimental conditions are identical for different devices and compounds. Observed trends may therefore be attributed to intrinsic properties of the respective compounds or to changes induced by the respective treatment.

The results are shown in Figure 6. The mobility is plotted as a function of the fraction of acrylates in the chemical structure. Error bars reflect the statistical error obtained by measuring several samples prepared from the same material. At least 8 and up to 32 devices were measured for each of the data points. Figure 6(a) shows that for untreated, as-cast films of PF2/6-A-0:100, we find a mobility of about $2 \times 10^{-5} \text{ cm}^2/\text{Vs}$, which is in good agreement with the results obtained by Arif et al. by space-charge-limited current (SCLC) measurements.²⁹ Heating a PF2/6-A-0:100 sample at 100 °C for 15 min under UV-illumination only induces a small mobility reduction [Fig. 6(a)]. We also find no significant difference in the mobility for PF2/6-A-0:100 samples with 0.1 wt% of the organic photoinitiator Irgacure 651. The mobility reduces, however, from about 2×10^{-5} to $2\text{--}4 \times 10^{-6} \text{ cm}^2/\text{Vs}$ by introducing acrylate groups into the polymer structure, as indicated by the dashed grey arrow in Figure 6(a). This is independent on whether the polymer is used as cast, crosslinked without initiator or crosslinked with 0.1 wt% of organic initiator. In contrast to this, from Figure 6(b) it is evident that adding larger amounts of

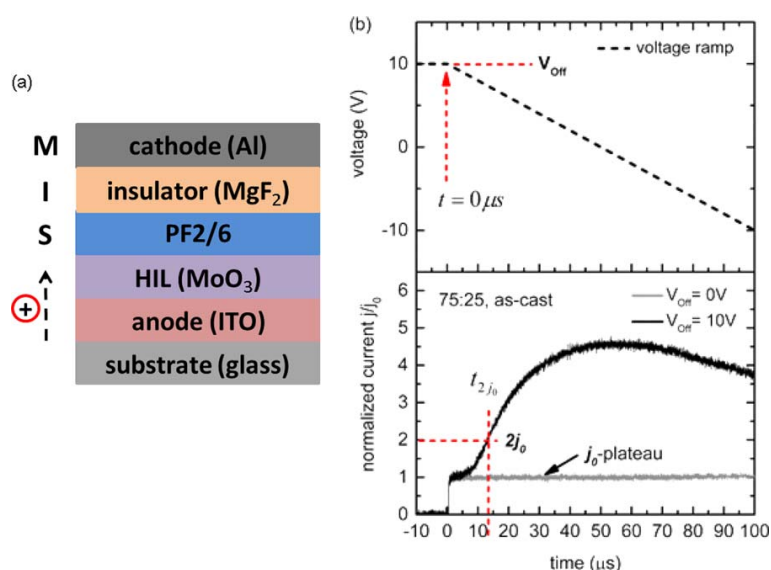


FIGURE 5 (a) Schematic representation of the layer structure used in the MIS-CELIV experiments. Holes are injected from the ITO anode into PF2/6 via a hole injection layer (HIL). (b) Typical voltage ramp (top) and current response curve (bottom) in a MIS-CELIV experiment (black curve). The grey curve is the pure capacitive response of the sample when no offset voltage is applied. [Color figure can be viewed at wileyonlinelibrary.com]

the organic photoinitiator (Irgacure 651) or, in particular, adding the metalorganic photoinitiator (the Ti-complex Irgacure 784) significantly reduces the hole mobility in a polymer. This is the case for both PF2/6 as well as the acrylate containing derivatives.

There are several conclusions we can draw from the data presented in Figure 6. First and most importantly, the fact that the hole mobility of a particular sample is not affected by crosslinking without photoinitiator or by crosslinking with 0.1 wt% of IC651 implies that *crosslinking itself* does not influence

mobility. In contrast, the mobility reduction caused by adding a larger amount (1.0 wt%) of organic photoinitiator Irgacure 651 or the metalorganic photoinitiator Irgacure 784 may be attributed to the introduction of traps for charge transport through the photoinitiator. It appears that the traps are deeper for the metalorganic photoinitiator than for the organic photoinitiator. We infer this from the fact that the hole mobility is only reduced upon adding larger amounts of organic photoinitiator (1.0 wt%), yet not upon adding small amounts (0.1 wt%), which would be consistent with the presence of shallow traps that are negligibly in small amounts. In contrast,

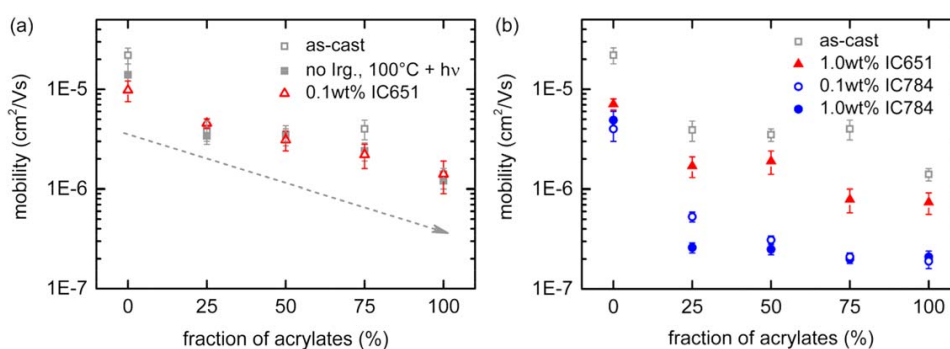


FIGURE 6 (a) Hole mobility as a function of the fraction of acrylate containing repeat units for different sample treatments, that is, as cast without photoinitiator (open squares), crosslinked without photoinitiator (full grey squares), crosslinked with 0.1 wt% of organic photoinitiator (Irg. 651, red open triangles). The grey dotted arrow indicates the mobility trend for increasing acrylate content. (b) Mobility of samples for different treatments, that is, as cast without photoinitiator (open squares) for reference, crosslinked with 1.0 wt% of organic photoinitiator (Irg. 651, red open triangles) and crosslinked with 0.1 or 1.0 wt% of metalorganic photoinitiator (Irg. 784, blue circles). [Color figure can be viewed at wileyonlinelibrary.com]

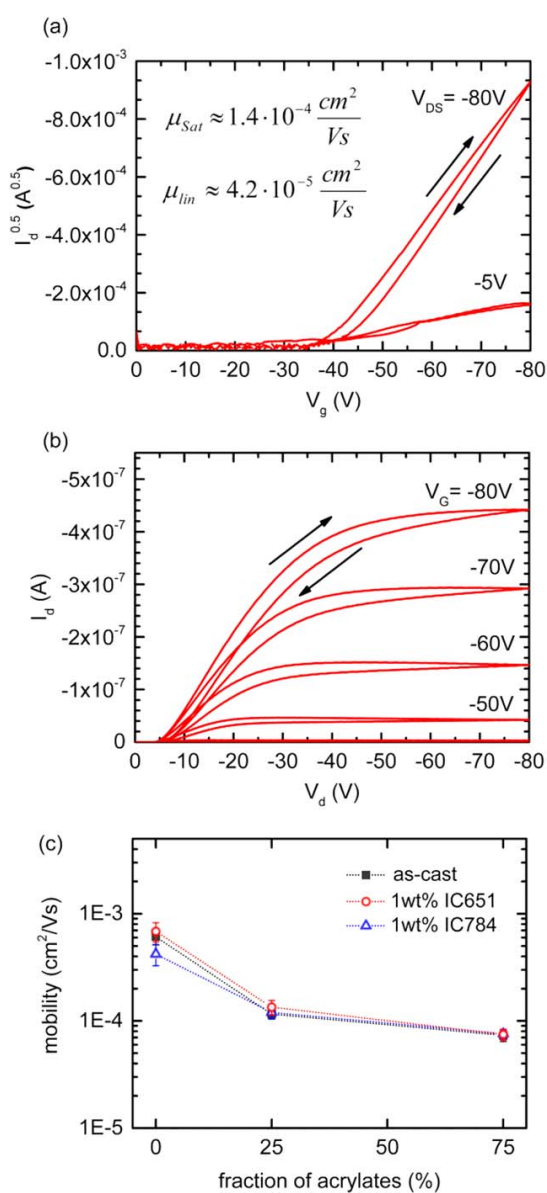


FIGURE 7 Typical (a) transfer and (b) output characteristics of a crosslinked PF2/6-A-25:75 OFET. Measurements were taken in forward and backward direction (arrows). (c) OFET mobility as a function of the fraction of acrylate containing repeat units for selected compounds without photoinitiator and crosslinking (as cast), crosslinked with 1 wt% organic photoinitiator (IC651) and crosslinked with 1 wt% metalorganic photoinitiator (IC784). The mobility was determined from the saturation regime. [Color figure can be viewed at wileyonlinelibrary.com]

the same small amounts of the metalorganic photoinitiator drastically reduce the mobility. The decrease in mobility by about one order of magnitude when introducing acrylate

groups into PF2/6 can be attributed to changes in the microstructure of the amorphous film resulting in slightly enhanced chain torsions as discussed in the context of the spectroscopic data presented in Figures 2 and 3.

OFET Measurements

We performed OFET measurements to assess the hole transport in the regime of large charge-carrier-density. The results are shown in Figure 7 and were obtained for channel lengths of 10 and 20 μm to reduce short channel effects.³⁰⁻³² Error bars are determined from measurements of at least 8 OFETs for each of the displayed fractions of acrylate. Typical transfer and output characteristics are shown in Figure 7(a,b), respectively. For the output characteristics, we find a clear saturation of the drain current I_d for larger drain voltage V_d . In the transfer characteristics, the threshold voltage is quite high (40–50 V) and, for both characteristics, a small hysteresis occurs between forward and backward scans, indicating trapping and a some disorder at the interface between dielectric and organic layer.^{23,33} The clear linear dependence in the saturation regime in a $\sqrt{I_d}$ versus V_g plot, indicating no nonlinear effects at high V_d and V_g , allows us to determine the saturation (linear) mobility from the slope of the transfer characteristic according to eq 1 (2) given in the experimental section. We find a roughly 2–3 times smaller mobility in the linear regime compared to the saturation values. We attribute this, as well as a small bending of the output characteristics to nonlinear contact resistances.³⁴

Considering the mobility as a function of acrylate content in the active layer polymer [Fig. 7(c)], we observe that (i) the mobility reduces markedly with increasing content of acrylate and (ii) the mobility values are independent of the sample treatment, even for large amounts (1 wt%) of organic or metalorganic photoinitiator. The first observation confirms the conclusions drawn above, that is, that the introduction of acrylate groups promotes structural disorder such as torsions in the respective compound thus reducing its mobility. The second observation reflects the higher charge density regime of the OFET measurements compared to the MIS-CELIV measurement. Whereas in regime of low carrier density, deep traps or large amounts of shallow traps affect the overall mobility measured in the sample, in the regime of high carrier density such traps are filled, so that the mobility in a sample with and without traps are identical. This result thus confirms that the metalorganic photoinitiator, the Ti-complex Irgacure 784, induces deep traps, which are, however, only relevant in the low to medium charge carrier density regime.

CONCLUSIONS

Crosslinking allows for facile fabrication of multilayer polymer devices as well as stabilization of the morphology in optoelectronic device such as bulk heterojunction solar cells. From our study of crosslinkable PF2/6 derivatives we have seen that crosslinking induces only minor structural changes and has no effect on the hole mobility, provided that the crosslinking conditions are chosen properly. The acrylate-

substituted PF2/6 derivatives may be crosslinked to a dense network without any initiator merely by exposing the sample to heat and UV illumination. The reaction can be accelerated by using organic or metalorganic photoinitiators. The organic photoinitiator Irgacure 651 introduces only shallow traps. Small amounts such as 0.1 wt% are sufficient to obtain a fully crosslinked, insoluble film and, most importantly, do not affect the hole mobility. This applies to both, the regime of low-to-medium charge carrier density typically encountered in OLED or solar cell applications as well as for high carrier densities characteristic for OFETs. In contrast, we found that the titanium-containing photoinitiator Irgacure 784 introduces deep traps. By MIS-CELIV measurements we could demonstrate that this reduces the mobility in the low-to-medium charge carrier density regime, so that this photoinitiator is not suitable for use in OLED or solar cell applications. It can, however, be used for OFET applications where the high carrier density implies that these deep traps do not affect mobility. Overall, these results show that polymers can be efficiently crosslinked for use in complex OLED and OSC architectures without compromising charge carrier mobility, if initiator-free conditions or only small amounts of organic photoinitiators are used.

ACKNOWLEDGMENTS

We acknowledge financial support by the German Science Foundation DFG through the doctoral training center "Photophysics of Synthetic and Biological Multichromophoric Systems" (GRK 1640), the Elitenetzwerk Bayern (ENB), Macromolecular Science, the Volkswagen foundation and by the Bavarian State Ministry of Education, Science and the Arts through the Collaborative Research Network "Solar Technologies go Hybrid" (SolTech). We want to thank Cheng Li and Sven Hüttner for assistance with the OFET measurements.

REFERENCES

- H. K. Shih, Y. H. Chen, Y. L. Chu, C. C. Cheng, F. C. Chang, C. Y. Zhu, S. W. Kuo, *Polymers Basel* **2015**, *7*, 804–818.
- J. Lee, H. Han, J. Lee, S. C. Yoon, C. Lee, *J. Mater. Chem. C* **2014**, *2*, 1474–1481.
- C. A. Zuniga, S. Barlow, S. R. Marder, *Chem. Mater.* **2011**, *23*, 658–681.
- J. Park, C. Lee, J. Jung, H. Kang, K. H. Kim, B. W. Ma, B. J. Kim, *Adv. Funct. Mater.* **2014**, *24*, 7588–7596.
- S. H. Ho, S. Y. Liu, Y. Chen, F. So, *J. Photon Energy* **2015**, *5*, 057611.
- G. Wantz, L. Derue, O. Dautel, A. Rivaton, P. Hudhomme, C. Dagron-Lartigau, *Polym. Int.* **2014**, *63*, 1346–1361.
- J. W. Rumer, I. McCulloch, *Mater. Today* **2015**, *18*, 425–435.
- T. Hahn, C. Saller, M. Weigl, I. Bauer, T. Unger, A. Köhler, P. Strohriegel, *Phys. Status Solidi A* **2015**, *212*, 2162–2168.
- F. Fischer, T. Hahn, H. Bässler, I. Bauer, P. Strohriegel, A. Köhler, *Adv. Funct. Mater.* **2014**, *24*, 6172–6177.
- H. Bässler, *Phys. Status Solidi B* **1993**, *175*, 15–56.
- A. Köhler, *Nat. Mater.* **2012**, *11*, 836–837.
- H. T. Nicolai, M. Kuik, G. A. H. Wetzelaer, B. de Boer, C. Campbell, C. Risko, J. L. Bredas, P. W. M. Blom, *Nat. Mater.* **2012**, *11*, 882–887.
- I. McCulloch, W. M. Zhang, M. Heeney, C. Bailey, M. Giles, D. Graham, M. Shkunov, D. Sparrowe, S. Tierney, *J. Mater. Chem.* **2003**, *13*, 2436–2444.
- S. R. Farrar, A. E. A. Contoret, M. O'Neill, J. E. Nicholls, G. J. Richards, S. M. Kelly, *Phys. Rev. B* **2002**, *66*, 125107.
- E. Scheler, P. Strohriegel, *J. Mater. Chem.* **2009**, *19*, 3207–3212.
- G. L. Wu, C. H. Yang, B. H. Fan, B. Zhang, X. M. Chen, Y. F. Li, *J. Appl. Polym. Sci.* **2006**, *100*, 2336–2342.
- G. Lieser, M. Oda, T. Miteva, A. Meisel, H. G. Nothofer, U. Scherf, D. Neher, *Macromolecules* **2000**, *33*, 4490–4495.
- B. Tanto, S. Guha, C. M. Martin, U. Scherf, M. J. Winokur, *Macromolecules* **2004**, *37*, 9438–9448.
- G. Juska, N. Nekrasas, K. Genevicius, *J. Non-Cryst. Solids* **2012**, *358*, 748–750.
- A. Armin, G. Juska, M. Ullah, M. Velusamy, P. L. Burn, P. Meredith, A. Pivrikas, *Adv. Energy Mater.* **2014**, *4*, 1300954.
- I. B. Berlman, *J. Phys. Chem.* **1970**, *74*, 3085–3093.
- J. Gierschner, J. Cornil, H. J. Egelhaaf, *Adv. Mater.* **2007**, *19*, 173–191.
- H. Bässler, A. Köhler, In *Electronic Processes in Organic Semiconductors - An Introduction*, Wiley-VCH: Weinheim, **2015**.
- U. Rauscher, H. Bässler, D. D. C. Bradley, M. Hennecke, *Phys. Rev. B* **1990**, *42*, 9830–9836.
- A. Monkman, C. Rothe, S. King, F. Dias, *Adv. Polym. Sci.* **2008**, *212*, 187–225.
- L. O. Palsson, A. P. Monkman, *Adv. Mater.* **2002**, *14*, 757–758.
- T. Virgili, D. G. Lidzey, D. D. C. Bradley, *Adv. Mater.* **2000**, *12*, 58–62.
- M. V. Jacob, J. Mazierska, J. Krupka, *Asia-Pacific Microwave Conference Proceedings*, 4–7 Dec. **2005**, pp 3455–3458.
- M. Arif, M. Yun, S. Gangopadhyay, K. Ghosh, L. Fadiga, F. Galbrecht, U. Scherf, S. Guha, *Phys. Rev. B* **2007**, *75*, 195202.
- B. H. Hamadani, J. L. LeBoeuf, R. J. Kline, I. McCulloch, M. Heeney, C. A. Richter, L. J. Richter, D. J. Gundlach, *Proc. SPIE*, San Diego, CA, September, **2007**, pp 66580V.
- E. J. Meijer, G. H. Gelinck, E. van Veenendaal, B. H. Huisman, D. M. de Leeuw, T. M. Klapwijk, *Appl. Phys. Lett.* **2003**, *82*, 4576–4578.
- M. L. Chabiny, J. P. Lu, R. A. Street, Y. L. Wu, P. Liu, B. S. Ong, *J. Appl. Phys.* **2004**, *96*, 2063–2070.
- H. Sirringhaus, *Adv Mater.* **2009**, *21*, 3859–3873.
- M. G. Kane, In *Flexible Electronics: Materials and Applications*, S. W. Wong; A. Salleo, Eds.; Springer Science & Business Media: New York, **2009**.

Supporting Information

**Influence of Crosslinking on Charge Carrier Mobility in Crosslinkable
Polyfluorene Derivatives**

*Frank-Julian Kahle, Irene Bauer, Peter Strohhriegl, Anna Köhler**

**Corresponding author: anna.koehler@uni-bayreuth.de*

Supporting Information to:

Influence of Crosslinking on Charge Carrier Mobility in Crosslinkable Polyfluorene Derivatives

By Frank-Julian Kahle, Irene Bauer, Peter Stroehriegl, Anna Köhler

Synthesis of poly(9-(2-ethylhexyl)-9-((6-acryloyloxy)hexyl)-fluorene-2,7-diyl) (PF2/6-A-n:m) by Yamamoto coupling

For (PF2/6-A-100:0)

A Schlenk flask was charged with nickel dicyclooctadiene (Ni(COD), 0.668 g, 2.43 mmol), cyclooctadiene (COD, 0.263 g, 2.43 mmol), 2,2'-bipyridyl (0.380 g, 2.43 mmol) and 15 mL dry DMF under argon. The mixture was degassed by three freeze–thaw cycles before it was heated to 80°C for 30 min while stirring. The monomer 2,7-dibromo-9-(2-ethylhexyl)-9-((6-acryloyloxy)hexyl)-fluorene (0.602 g, 1.02 mmol) was weighed into a separate flask under argon. A trace of BHT and 30 mL of dry toluene were added and the mixture was degassed by three freeze–thaw cycles. Subsequently, the monomer mixture was added to the catalyst mixture using a syringe. The reaction mixture was stirred at 80°C for five days in the dark before 2-bromo-9,9-bis-(2-ethylhexyl)-fluorene (0.09 g, 0.18 mmol) was added as endcapper. After stirring for 24 hours at 80 °C the mixture was poured into methanol–HCl (conc.) 1 : 1 and stirred at room temperature for 2 h. The organic layer was separated from the HCl layer, which was then washed with ether. The combined organic layers were washed with an alkaline EDTA solution (5%) and water and the solvent was evaporated. The crude product was reprecipitated twice from THF into methanol and dried under vacuum, yielding 0.146 g (33%) of PF2/6-A-100:0 as a pale yellow powder.

PF2/6-A-75:25, PF2/6-A-50:50, PF2/6-A-25:75 and PF2/6-A-0:100 (= PF2/6) were prepared according to the same procedure.

The molecular weights of the copolymers were measured by size exclusion chromatography (SEC) in THF solution and are given in Table S1.

Table S1: Molecular weights of the crosslinkable polyfluorenes

	Yield	$M_w^{1)}$	$M_n^{1)}$	M_w/M_n
PF2/6-A-100:0	33%	24.900	8.900	2.8
PF2/6-A-75:25	55%	34.700	10.900	3.2
PF2/6-A-50:50	79%	35.400	8.500	4.1
PF2/6-A-25:75	84%	23.200	7.300	3.2
PF2/6-A-0:100	93%	45.300	19.200	2.4

¹⁾ The weight average M_w and the number average M_n of the molecular weight were determined from SEC measurements using a polystyrene calibration

Absorption spectroscopy

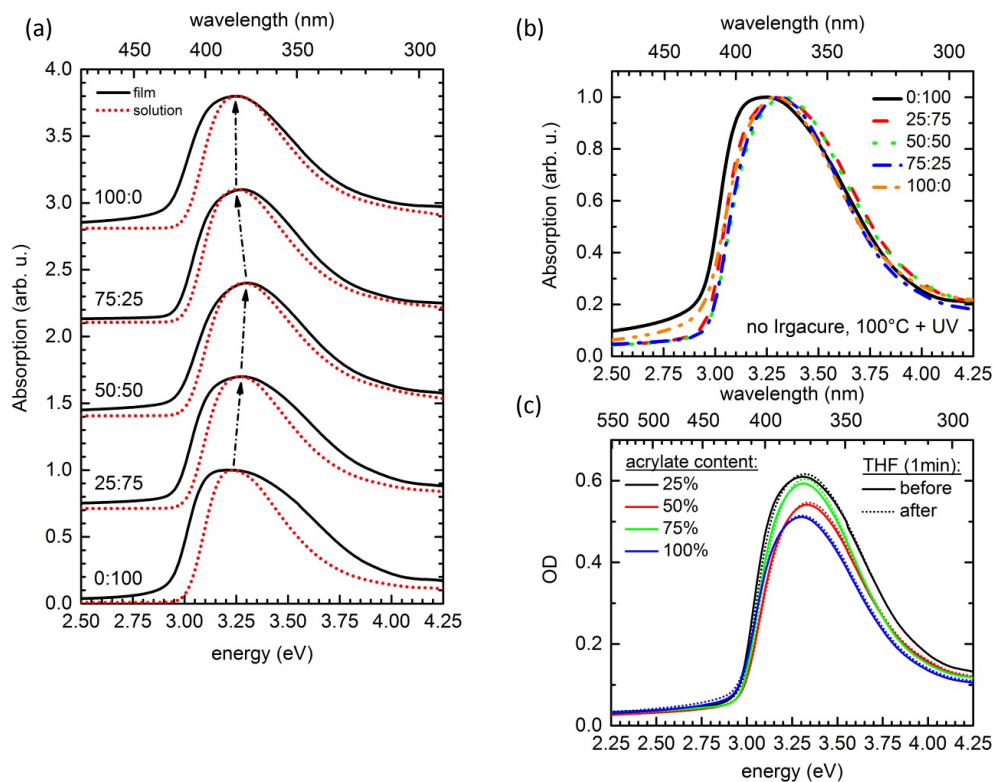


Figure S1: (a) Absorption spectra of crosslinkable PF2/6 compounds with different ratios $n:m$ of acrylate containing (n) to pure fluorene (m) repeat units for dilute solution (0.017 g/l) and as-cast films. The arrows indicate the observed spectral shift. (b) Thin film spectra of treated samples containing no photoinitiator (Irgacure). (c) Absorption spectra of acrylate containing, treated samples without photoinitiator before (solid lines) and after (dotted lines) rinsing in THF for 1 min.

Photoluminescence spectroscopy

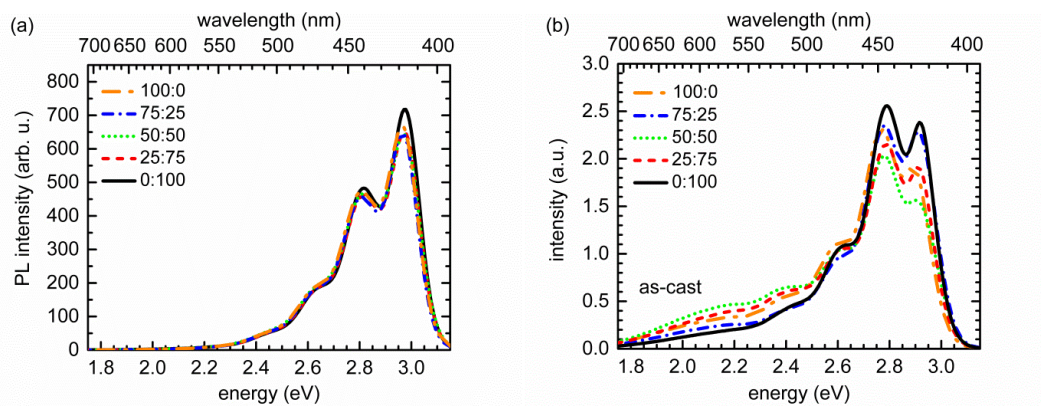


Figure S2: (a) Comparison of dilute solution (0.017 g/l) photoluminescence spectra (not normalized) for all the investigated compounds. (b) Comparison of photoluminescence spectra of as-cast thin films (normalized to area).

Figure S2a shows that in dilute solution, the PL of all samples is identical, independent of acrylate content. In thin film, shown in Figure S2b, there are small, yet statistical, variations concerning the 0-0 peak intensity and concerning the low-energy tail. The latter is characteristic for a small, statistical, inherent amount of fluorenone sites that are populated efficiently by energy transfer in the thin film.^[1]

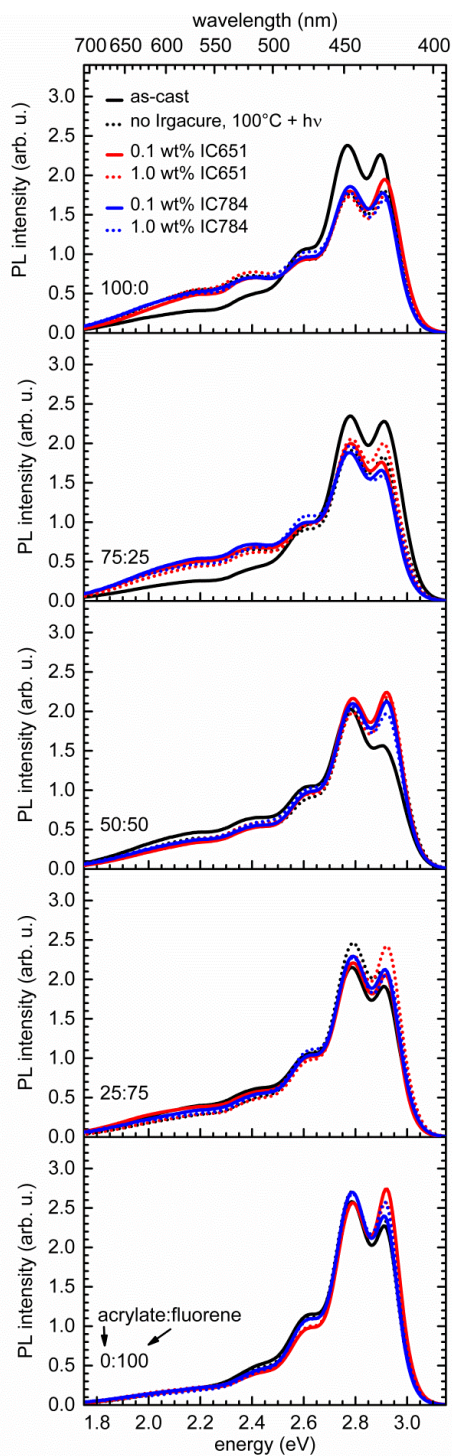


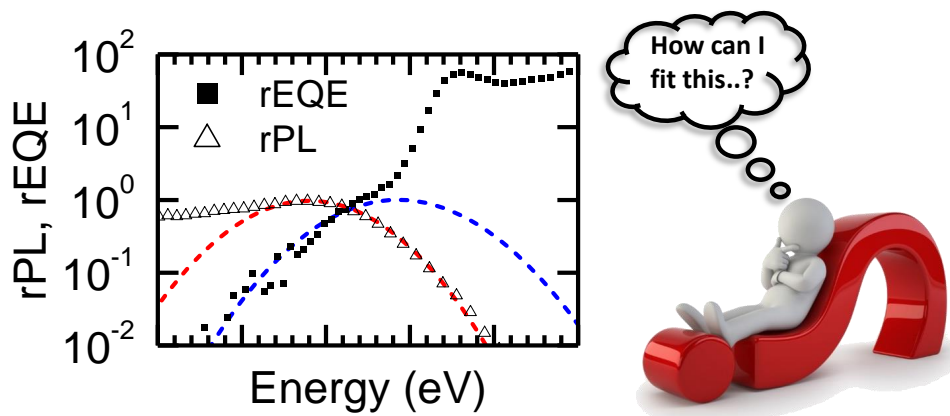
Figure S3: Thin film photoluminescence spectra of crosslinkable PF2/6 compounds with different ratios of acrylate containing repeat units to unmodified fluorene repeat units for different sample treatments. Spectra are normalized to unit area.

In Figure S3, the thin films are shown for different treatments, analogous to Figure 4 in the manuscript. In the same way as for Figure 4, we find that for all samples, the addition of photoinitiator does not result in a spectrum that differs from that obtained by heating under UV-light without photoinitiator.

References for supporting information

[1] a) F. B. Dias, M. Maiti, S. I. Hintschich, A. P. Monkman, *J Chem Phys* **2005**, *122*; b) T. Virgili, D. G. Lidzey, D. D. C. Bradley, *Adv Mater* **2000**, *12*, 58; c) X. O. Gong, P. K. Iyer, D. Moses, G. C. Bazan, A. J. Heeger, S. S. Xiao, *Adv Funct Mater* **2003**, *13*, 325; d) C. Y. Chi, C. Im, V. Enkelmann, A. Ziegler, G. Lieser, G. Wegner, *Chem-Eur J* **2005**, *11*, 6833; e) A. Monkman, C. Rothe, S. King, F. Dias, *Adv Polym Sci* **2008**, *212*, 187; f) U. Scherf, E. J. W. List, *Adv Mater* **2002**, *14*, 477.

12 How to Interpret Absorption and Fluorescence Spectra of Charge Transfer States in an Organic Solar Cell



Frank-Julian Kahle, Alexander Rudnick, Heinz Bässler, and Anna Köhler

Published in
Mater. Horiz., **2018**, *5*, 837
(DOI: 10.1039/c8mh00564h)

Reproduced by permission of The Royal Society of Chemistry



Cite this: *Mater. Horiz.*, 2018, 5, 837

Received 14th May 2018,
Accepted 27th June 2018

DOI: 10.1039/c8mh00564h

rsc.li/materials-horizons

How to interpret absorption and fluorescence spectra of charge transfer states in an organic solar cell†

Frank-Julian Kahle,^a Alexander Rudnick,^a Heinz Bässler^b and Anna Köhler^{a,b}

The aim of the present work is to identify the appropriate framework for analyzing photoluminescence and photocurrent (EQE) spectra of charge transfer (CT) states in donor–acceptor blends used as active materials for organic solar cells. It was stimulated by the work of Vandewal *et al.* (*J. Am. Chem. Soc.*, 2017, 139(4), 1699–1704) who analyzed EQE spectra of CT states of a series of blend systems in terms of Marcus theory assuming that, first, the spectral shape reflects the reorganization energy of the donor upon ionization and, second, that disorder effects are unimportant. To test this assumption we applied gated photoluminescence (PL) spectroscopy within a temperature range from 5 to 295 K combined with EQE as well as electroluminescence (EL) experiments on 1 : 1 Me-LPPP : PCBM blends by weight. We find that the PL spectra are virtually temperature independent and the temporal decay of the emission features a power law with an exponent close to $-3/2$ as Hong and Noolandi predicted for distributed geminately bound electron–holes pairs. The EL spectrum reveals a red-shift by 100 meV relative to the PL spectrum. The results are inconsistent with both Marcus' electron transfer theory and the original Marcus–Levich–Jortner (MLJ) theory, and they prove that disorder effects are crucial. Both PL and EQE spectra can be rationalized in terms of the classic Franck–Condon picture of electronic transitions that couple to intra-molecular vibrations as well as low frequency modes of the donor–acceptor pair that forms the CT state.

1. Introduction

Research into the spectroscopy of charge transfer (CT) states is basically an old subject^{1–4} but it receives currently a renaissance. The reason is related to the current endeavor to convert light to

^a Soft Matter Optoelectronics, University of Bayreuth, 95440 Bayreuth, Germany.

E-mail: anna.koehler@uni-bayreuth.de

^b Bayreuth Institute of Macromolecular Science (BIMF), University of Bayreuth, 95440 Bayreuth, Germany

† Electronic supplementary information (ESI) available. See DOI: 10.1039/c8mh00564h

Conceptual insights

The generation of charges in organic solar cells occurs by the dissociation of interfacial charge transfer (CT) states. It is therefore crucial to understand the properties of these states. Spectroscopy of CT state emission and absorption (inferred from the photocurrent) can yield pertinent information, provided one knows how to extract it. We demonstrate that the interpretation of CT spectra in thin films requires due consideration of the inhomogeneously broadened density of states. If energetic disorder is included, the spectra can be analysed in a conventional Franck–Condon or a Marcus–Levich–Jortner type picture, with the Stokes' shift between the maxima of absorption and emission reflecting the reorganization energy of the donor–acceptor pair. This advances beyond the currently applied method, where a classical Marcus-type approach is used without consideration of the energetic inhomogeneity of the film, and where the Stokes' shift is associated predominantly with the intra-molecular reorganization energy of the donor. In contrast to the classical Marcus-type approach, our model correctly reproduces the spectra over the entire temperature range from 5 to 300 K. Conceptually, it implies that the CT state emission or absorption can be described as a process dominated by quantum mechanical tunnelling rather than by strong thermal activation.

electrical power using an organic solar cell (OSC). The active material in an OSC is either a blend or a bilayer of two components that act as electron donors and electron acceptors. When the donor – or equivalently the acceptor – is optically excited, there is charge transfer in whose course a pair of free charge carriers is generated. Understanding how this process proceeds is the subject of current research. There is firm evidence that the process is sequential. Upon exciting the donor (or the acceptor) phase an exciton is created that diffuses towards the acceptor and transfers an electron. This interfacial transfer is an ultra-fast process, completed within typically 100 fs.^{5–11} Meanwhile there is growing evidence that the initial electron transfer step creates first a – more or less delocalized – CT state at the donor–acceptor interface.^{12–20} To contribute to a photocurrent, this CT state has to escape from the coulomb well to be converted into a charge-separated state. It turns out that in efficient OSCs this escape process is quite effective. The reason

for this is currently heavily disputed.^{15,21–28} Evidently, the dynamics of the CT state plays a crucial role. Other factors include the magnitude of the charge carrier mobility, the delocalization of charge carriers comprising the CT state, the topology of interface and the entropy of the diffusive random walk that the geminately bound electron–hole pair execute prior to complete dissociation.

Usually the CT state at the donor–acceptor interface of an OSC is generated by optically exciting the donor (or, equivalently, the acceptor) to the first singlet state. The electron in the LUMO of the donor is then transferred to the acceptor. Since this is an electron transfer process, it appeared straightforward to apply Marcus' electron transfer theory for quantitative description. However, Marcus theory is based on thermal equilibrium assuming that the quantum nature of the vibrations that drive the thermally activated transition from the precursor state to the final state does not need to be considered explicitly. Our recent study showed that this assumption is indeed questionable, notably on a time scale of 100 fs that is typical for photo-induced electron transfer in thin films of donor–acceptor composites.⁵ There is growing evidence that fast electron transfer is accomplished *via* quantum tunneling.

Energetically, the CT state of the donor–acceptor complex is the lowest state in the system. It can also be generated optically by photons below the absorption edge of either donor or acceptor, yet the oscillator strength of such a transition is quite low. This precludes simple absorption spectroscopy of CT states, though more sophisticated techniques such as photothermal deflection measurements can reveal its absorption spectrum.^{24,29} Similarly, the low energy tail of the action spectrum of the photocurrent is a reflection of optical CT state generation. It is usually manifested as weak feature, usually of Gaussian character, in the low energy tail of the external quantum efficiency (EQE) spectrum. In principle, a direct optical formation of a CT state, *i.e.* not *via* an excited donor or acceptor state, is also an electron transfer process, as is the emission of the CT state. This led Gould *et al.*³⁰ to use the Strickler–Berg relationship to connect the intensity of the reduced emission spectrum $rPL(E)$ to the transfer rate for electron transfer by

$$rPL(E) = \frac{PL(E)}{E} \propto V^2 \Delta\mu^2 FC(g) \quad (1)$$

with V being the electronic coupling matrix element, $\Delta\mu$ the change in dipole moment when returning from the CT state (A^-D^+) to a neutral donor–acceptor pair (AD), and $FC(g)$ being the Franck–Condon weighted density of states, that depends on the driving force for the charge transfer reaction, g . E is the photon energy, and the emission spectra, $PL(E)$, are given as photons per unit spectral energy. For the thermally averaged Franck–Condon weighted density of states, Gould uses the expression derived by Marcus, Jortner, Bixon and Levich,^{31–36}

$$FC(g) = \frac{1}{\sqrt{4\pi\lambda_{low}k_B T}} \sum_{n=0}^{\infty} \frac{e^{-S} S^n}{n!} \times \exp\left(-\frac{(g + \lambda_{low} + n\hbar\omega)^2}{4\lambda_{low}k_B T}\right), \quad (2)$$

where $g = E_{CT} - E$ is identified as the driving force of the transition in terms of original Marcus rate equation, λ_{low} is the reorganization energy associated with the low-energy phonons due to inter-molecular vibrational motion (we shall below use λ_{high} for that associated with intramolecular, high-energy modes), S and $\hbar\omega$ are the Huang–Rhys parameter and the vibrational quantum energy for the high-frequency intramolecular vibrations. We refer to eqn (2) henceforth as MLJ-equation. Gould applied eqn (1) and (2) to analyze room temperature absorption and photoluminescence spectra of CT complexes in various solvents using methyl-substituted benzene as an electron donor and tetra-cyanobenzene and tetra-cyanoanthracene as electron acceptors and found good agreement between measured and calculated values.

This work prompted Vandewal *et al.* to apply a similar formalism to analyze OSCs with different donor materials combined with PCBM as an acceptor that feature Gaussian tails below the dominant absorption of both donor and acceptor.^{37–40} Analogous to Gould, Vandewal used a modified Marcus expression taking an energy dependence of the electronic transition moment M into account, *i.e.* $M = \frac{V\Delta\mu}{\hbar\nu} = \frac{V\Delta\mu}{E}$, thus arriving at the expressions for the reduced external quantum efficiency $rEQE(E)$ and the reduced emission spectra $rEL(E)$ of the OSCs, that is,^{37,38}

$$rEQE(E) = EQE(E) \cdot E \propto \frac{1}{\sqrt{4\pi\lambda k_B T}} \exp\left(-\frac{(-E + E_{CT} + \lambda)^2}{4\lambda k_B T}\right) \quad (3a)$$

$$rEL(E) = \frac{EL(E)}{E} \propto \frac{1}{\sqrt{4\pi\lambda k_B T}} \exp\left(-\frac{(-E + E_{CT} - \lambda)^2}{4\lambda k_B T}\right) \quad (3b)$$

The “reduced” emission spectrum is given in photons per unit spectral energy, divided by energy, *i.e.* if the emission was measured as photon per unit time per unit wavelength, it needs to be divided by E^3 . The emission spectrum is taken from the electroluminescence when the diode is operated in forward direction, so that charge carriers are injected from the electrodes and recombine in the diode. In theory, the reorganization energy λ here comprises both, the contribution from low-frequency and from high-frequency phonons, so that $\lambda = \lambda_{low} + \lambda_{high}$. Vandewal *et al.* found the reorganization energy correlates linearly with the calculated relaxation energy of a hole on the donor.

The analysis of the CT spectra according to Gould *et al.* [eqn (1) + (2)] and according to Vandewal *et al.* [eqn (3)] differs from the approach usually taken in the spectroscopy of thin amorphous organic films. To describe the shape of absorption or emission spectra, it is common to consider a Franck–Condon progression in form of a Poisson-distribution of high-energy vibrational modes, that is multiplied by a Gaussian linewidth function, *e.g.* to account for the inhomogeneous broadening that is characteristic for amorphous thin films. This results in expressions such as⁴¹

$$PL(E) \propto \tilde{M}^2 [n(E)E]^3 \times \sum_m \frac{S^m}{m!} e^{-S} \cdot \Gamma \cdot \delta(E - (E_0 - m\hbar\omega)) \quad (4a)$$

$$\text{Abs}(E) \propto \tilde{M}^2 [n(E)E] \times \sum_m \frac{S^m}{m!} e^{-S} \cdot \Gamma \cdot \delta(E - (E_0 + m\hbar\omega)), \quad (4b)$$

when it suffices to consider a dominant effective high-frequency mode. Similar expressions exist when several high-frequency modes need to be considered explicitly.^{41,42} Here, $m = 0, 1, 2, \dots$ denotes the number of vibrational levels considered for the high-frequency intramolecular vibration with vibrational energy $\hbar\omega$. E_0 is the 0-0 energy of the optical transition. δ is the Delta-function, and for the lineshape function Γ , a Gaussian profile is usually taken, *i.e.*

$$\Gamma = \exp\left(-\frac{(E)^2}{2\sigma^2}\right) \quad (5)$$

with σ^2 being the variance. The electronic transition moment \tilde{M} is usually considered to be constant. In this representation, the effect of low-frequency modes is usually subsumed in the linewidth function. $\text{PL}(E)$ and $\text{Abs}(E)$ are given in photons per unit energy. Here, the relaxation energy associated with the transition is $\lambda_{\text{high}} = S \cdot \hbar\omega$. $n(E)$ is the refractive index of the medium. To allow for facile comparison with the work of Gould, we shall also consider the electronic transition moment to be energy dependent in this work. Eqn (4) can then be rewritten in a reduced form:

$$\text{rPL}(E) = \frac{\text{PL}(E)}{E} \propto \sum_m \frac{S^m}{m!} e^{-S} \cdot \Gamma \cdot \delta(E - (E_0 - m\hbar\omega)) \quad (6a)$$

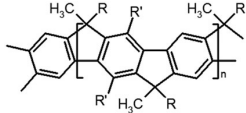
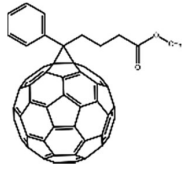
$$\text{rAbs}(E) = \text{Abs}(E) \cdot E \propto \sum_m \frac{S^m}{m!} e^{-S} \cdot \Gamma \cdot \delta(E - (E_0 + m\hbar\omega)) \quad (6b)$$

The present work has several goals. The role of CT state disorder is receiving increasing attention in the community,⁴³⁻⁴⁶ and here we aim to find out if the neglect of inhomogeneous broadening in eqn (1)-(3) is acceptable when describing CT states in thin donor-acceptor films. By comparison with experiment, we shall explore whether a Marcus-type description or a description based upon conventional molecular spectroscopy is more appropriate to rationalize the spectroscopy of CT states in an OSC. Associated with this question, we will discuss the relation between eqn (1), (2), (3) and (6) in the framework of earlier work,^{30,35,41,47} and the Stokes' shift and the reorganization energy associated with the CT transition. The experimental system we chose for evaluation and illustration is a blend of the rigid conjugated polymer MeLPPP (methyl-substituted ladder-type poly(*para*-phenylene)) and PCBM ([6,6]-phenyl C61 butyric acid methyl ester) (see Table 1 below). We carried out steady state as well as time-gated fluorescence spectroscopy in combination with photocurrent excitation spectroscopy to determine the EQE on related OSCs.

2. Experimental section

Bulk heterojunction solar cells devices using MeLPPP:PCBM blends (1:1 by weight) were fabricated on structured ITO-coated

Table 1 Structure formulas as well as ionisation potential I_p , electron affinity E_a and S_1 energy levels for MeLPPP and PCBM

	MeLPPP	PCBM
		
E_a (eV)	-2.60 ⁴⁸	-3.70 ⁴⁹
I_p (eV)	-5.20 ⁴⁸	-6.10 ⁴⁹
S_1 (eV)	2.70 ⁵⁰	1.75 ⁵¹

glass substrates. A 15 nm thick layer of MoO_3 was used on top of the ITO to improve hole extraction. The active blend layer was spun from chloroform solution (15 mg ml^{-1}) and had a thickness of 110 nm. Finally, a 100 nm thick aluminum cathode was evaporated. For reference, solar cells with pristine MeLPPP (in chloroform, 7.5 mg ml^{-1}) and PCBM layers (in chloroform, 15 mg ml^{-1}), respectively, were fabricated accordingly. The thickness of MeLPPP and PCBM were 60 nm and 30 nm, respectively. The thicknesses of the active layer of the solar cells were controlled with a Dektak (Veeco) profilometer directly on a device. Structure formulas and relevant literature values for the energy levels (ionisation potential I_p , electron affinity E_a , S_1 energy) of MeLPPP and PCBM are summarized in Table 1. For ease of reference, the absorption and emission of both compounds are shown in the ESI.†

EQE measurements were performed using a Lock-In-Amplifier (SR830) at a reference frequency of 130 Hz and monochromatic illumination from a 150 W tungsten lamp (Osram). For EL measurements, the solar cells were biased at 3 V using a Keithley source-measure unit (SMU 237). The luminescence of the sample was recorded by a CCD-camera (Andor iDus) coupled to a monochromator (Oriel). For both EQE and EL measurements, the sample was kept in a sample holder under vacuum at room temperature.

For time-gated emission spectroscopy, the sample was excited at 355 nm, using the frequency-tripled output from a Nd-YAG laser with variable pulse frequency. To record spectra with distinct delay and integration time an intensified charged coupled device camera from Andor was used. For exact time correlation the iCCD camera was triggered by the laser. All experiments were done with the sample being kept under vacuum in a temperature controlled cryostat.

3. Results

Fig. 1a shows gated photoluminescence spectra of a Me-LPPP:PCBM blend with zero delay and integration time of 10 ns excited at 3.49 eV and recorded in a temperature range of 5 K to 295 K. The spectra reveal two main features with maxima at 1.68 eV and near 1.55 eV.

Spectra recorded with a variable delay time indicate that the higher energy feature gradually disappears (Fig. 1b). It is straightforward to associate the 1.68 eV feature with

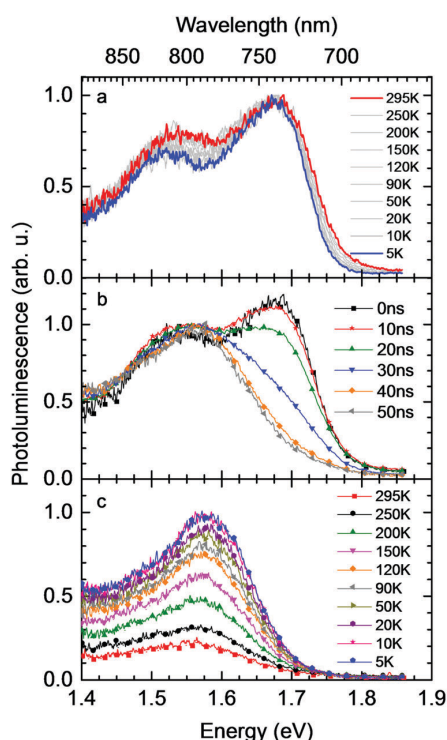


Fig. 1 (a) Photoluminescence spectra of a MeLPPP:PCBM blend recorded at different temperatures with zero delay and 10 ns gate width, normalized to maximum intensity (b) emission spectra of a MeLPPP:PCBM blend at room temperature with different delay times and 10 ns integration time, normalized to about 1.55 eV (c) evolution of the emission spectrum with temperature 90 ns after excitation. While the 5 K spectrum is normalized to unity, all spectra show the correct relative intensity.

fluorescence from large PCBM domains that are formed during the spin coating process based on comparison with emission spectra from neat PCBM films (shown in the ESI,† Fig. S1). Evidently, domains with a size that exceeds the exciton diffusion lengths are being formed at such a high PCBM loading (≥ 50 wt%) in MeLPPP. We note that the PCBM emission is still noticeable after a delay time of 30 ns although the lifetime of C_{60} is known to be around 1 ns. In the following discussion only the 1.55 eV feature of the PL spectrum will be considered that we assign to the CT emission of a Me-LPPP:PCBM complex. This is consistent with the fact that the energy difference between the E_a of the acceptor and the I_p of the donor is about 1.5 eV (*cf.* Table 1).

In Fig. 1c we show how the CT emission spectra, recorded after a delay time of 90 ns, evolve as a function of temperature. The key observation is that there is a 5-fold increase in intensity when lowering the temperature from 295 K to 5 K while the shape of the emission spectrum is preserved (see also Fig. S2, ESI†). There is only a marginal hypsochromic shift of the spectra upon cooling. The high energy wing of the spectrum is close to a Gaussian lineshape.

Next we measured the temporal decay of the CT emission. It turns out the decay is highly non-exponential and extends

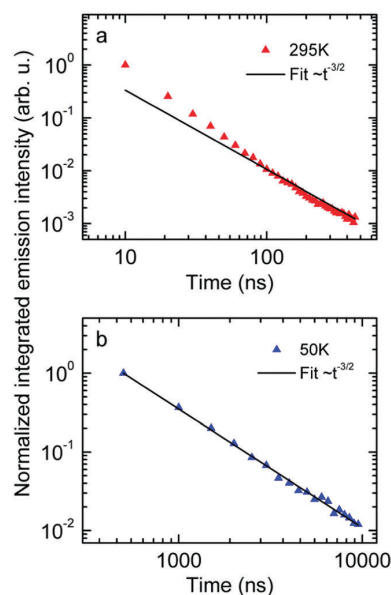


Fig. 2 Normalized emission intensity at (a) 295 K and (b) 50 K along with fits following a $t^{-3/2}$ power law.

into μ s range. This is documented by Fig. 2(a and b), in which the emissions, recorded at 295 K with a gate width of 10 ns (at 5 K with a gate width of 500 ns) are plotted on a double logarithmic scale. The decay follows a power law with an exponent very close to $-3/2$.

Finally we measured the EQE as well as the electroluminescence (EL) of the diode with a 1 : 1 blend of Me-LPPP : PCBM at selected temperatures. The EQE spectra, shown in Fig. 3a, reveal a broad tail with a weak shoulder below 1.7 eV that is associated with the generation of CT states, followed by a weak local maximum at the S_1-S_0 0-0 transition of PCBM at about 1.75 eV (*cf.* Table 1) and a smooth increase at higher photon energies. Upon sample cooling from the 300 K to 50 K the EQE decreases by two orders of magnitude (Fig. 3b), yet the character of the spectra is largely retained. Normalization of the EQE to the PCBM S_1 energy (1.75 eV) identifies two small spectral changes (Fig. 3c). First, the linewidth close to S_1 increases with temperature, and second, the relative intensity of the EQE signal at the CT energy reduces, so that the tail of S_1 and the CT state merge into one indistinguishable feature.

The EL spectrum (Fig. 4a), is a superposition of the electroluminescence from the CT state (EL_{CT}) and the EL-spectrum of PCBM. By subtracting the EL-spectrum of pristine PCBM, known from the literature,⁴⁰ the EL_{CT} spectrum can be recovered. It is noteworthy that the EL_{CT} spectrum is bathochromically shifted relative to the PL_{CT} spectrum (Fig. 4b).

4. Analysis

Before embarking on an analysis and discussion of results it is appropriate to summarize the essential experimental facts:

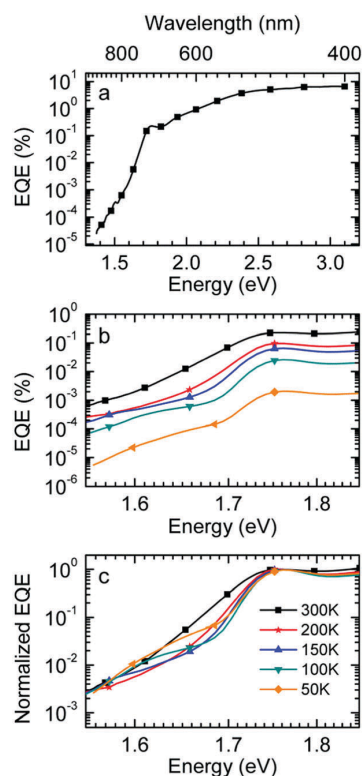


Fig. 3 (a) External quantum efficiency of MeLPPP:PCBM (1:1) bulk heterojunction devices measured at 300 K over the whole VIS-range down to the sub-bandgap region below 1.7 eV. (b) Temperature dependent EQE for MeLPPP:PCBM (1:1 by weight) blends in the range from room temperature (300 K) to 50 K, shown for the red spectral range. (c) EQE spectra normalized to the S_1 transition peak of PCBM at about 1.76 eV.

(i) upon lowering the temperature from 295 K to 5 K the intensity of the CT emission increases by a factor of 5 while the spectrum shifts slightly to the blue, yet it retains its spectral shape (Fig. 1c). (ii) When cooling from 295 K to 50 K, the EQE-decreases by two orders of magnitude while the spectral shape is preserved (Fig. 3b). (iii) The electroluminescence spectrum is off-set from the PL spectrum by roughly 100 meV (Fig. 4b). (iv) The decay of the optically generated CT spectrum features a power law and extends into the μ s range (Fig. 2).

We shall first argue that there is not a single, well-defined CT state, but rather a broad distribution of them that gives rise to significant energetic disorder.⁴⁶ In general, OSCs are made of disordered materials as evidenced by the inhomogeneous broadening of the absorption and photoluminescence spectra of the singlet excited states. Likewise, charge transport occurs *via* incoherent hopping among energetically disordered chromophores or conjugated segments of a polymer chain. Therefore, CT spectra are likely to be affected by disorder.^{43,46} There are two features in the experimental data that testify to it.

First, the CT-emission decays in power law fashion rather than exponentially (Fig. 2). This is firm evidence that there is a broad distribution of states that have their own transition rates

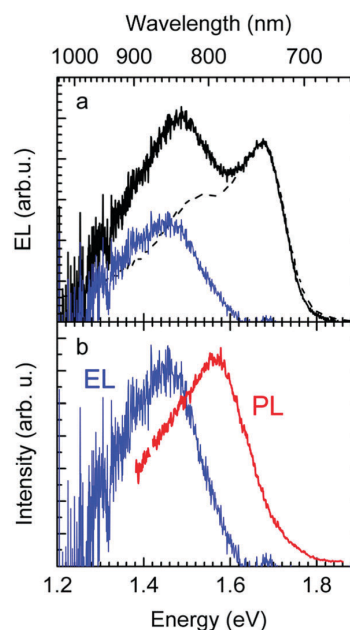


Fig. 4 (a) Electroluminescence spectra of MeLPPP:PCBM (1:1 by weight, black solid line) and pristine PCBM (black dashed line). The difference of the two spectra corresponds to the CT emission (blue solid line). The spectra of pristine PCBM was reprinted with permission from *J. Am. Chem. Soc.*, 2009, **131**(33), 11819–11824 Copyright (2009) American Chemical Society. (b) Comparison of electroluminescence (blue) and photoluminescence spectra (red) of the CT-state in MeLPPP:PCBM (1:1 by weight), measured at room temperature.

and emission energies. The observation that the CT decay follows a power law with an exponent of $-3/2$ up to a microsecond is suggestive of geminate recombination as has been described by Hong and Noolandi.⁵² In their original work these authors calculated how an electron-hole pair within its Coulomb capture radius recombines with constant, temperature dependent, diffusivity, and they found that the recombination rate follows a power law with exponent $-3/2$. Later on they extended their formalism by including the possibility that the recombination event is a tunneling process that does not require thermal activation, yet the functional dependences are the same.⁵³ It is a straightforward conjecture that this formalism can explain the observed non-exponential decay of optically generated CT states evidenced in Fig. 2. Since donor and acceptor moieties are distributed in energy it is likely that CT states also form a distribution. It is also likely that the hole that has been transferred from an excited PCBM molecule can make another jump to a nearby but energetically lower state at the expense of electron-hole separation. Considering that the recombination of the pair depends exponentially on their distance this gives rise to a broad distribution of recombination rates and the premises for the Hong-Noolandi formalism are fulfilled.

Second, the observation that the EL spectrum is red-shifted relative to the PL spectrum of CT states is also a signature of the

importance of disorder. If one generates an exciton or a charge carrier in a bulk organic solid in which the distribution of sites is inhomogeneously broadened, it will execute a random walk and thereby, on average, jump to lower states of the distribution. Such a spectral relaxation of an exciton is amenable by time resolved fluorescence spectroscopy. In an EL experiment, the recombining electrons and holes are injected from the electrodes, and thus experience a long journey until their decay during which significant energetic relaxation in the DOS occurs. However, when a CT state is generated by direct optical excitation, electron and hole are correlated. In addition, the transition dipole moment and overlap integral, controlling the rate of energy transfer, are low. Thus, spectral diffusion is greatly reduced. Accordingly, EL spectra are red-shifted relative to PL spectra of CT states, and this redshift is a signature of the broadened DOS. This implies, by the way, that the Stokes shift between absorption and EL emission includes a contribution from spectral relaxation.^{54–56}

Having confirmed that the CT states form a broad DOS, we now proceed to analyze the spectra in terms of the classic Franck–Condon picture. In this concept, absorption and fluorescence spectra of a chromophore are vibronic progressions of high-frequency intramolecular modes built on a resonant 0–0 origin. The coupling strength is controlled by a Huang–Rhys factor S . In rigid chromophores S is usually < 1 . In this case, the 0–0 transitions in absorption and emission are the dominant spectral features, and they are resonant. If the chromophore is embedded in a solid or liquid environment both, absorption and emission, experience a bathochromic shift because the excited state polarizes its environment. If the environment is non-crystalline, the inter-molecular distances, and concomitantly the polarization energies, vary randomly, and this effect leads to inhomogeneous line broadening and an associated Gaussian lineshape.⁴² Nevertheless, the 0–0 features in absorption and emission remain being resonant provided that $S \leq 1$ and that there is no spectral diffusion, *e.g.* due to energy transfer. In a condensed medium, such as a thin film, there is an additional coupling of the excited state to low energy modes of the molecular environment, *i.e.* phonons. As a consequence, each vibronic (high-frequency) transition carries a so-called phonon wing. This wing can be described by a Poisson distribution characterized by Huang–Rhys factor S_{low} and an average (low-frequency) phonon energy $\hbar\omega_{\text{low}}$. If $S_{\text{low}} > 2$, the maxima of the 0–0 transition are no longer resonant as evidenced by the appearance of a Stokes shift.⁵⁷ For large values of S_{low} , *e.g.* $S_{\text{low}} \gtrsim 4$ the Poisson distribution merges into a Gaussian distribution (*cf.* ESI,† Fig. S3). In consequence, a Gaussian lineshape results that adds to the Gaussian linewidth obtained by the inhomogeneous broadening.

The reduced EQE spectrum (Fig. 5a), plotted on a logarithmic scale, is composed of a Gaussian low energy tail and a strong feature that is associated with S_1-S_0 0–0 transition of PCBM. The width of the PCBM feature decreases upon sample cooling which facilitates spectral deconvolution (Fig. 3c). For this reason and since at lower temperatures thermal broadening plays a lesser role, we present an analysis of the reduced PL and EQE spectra

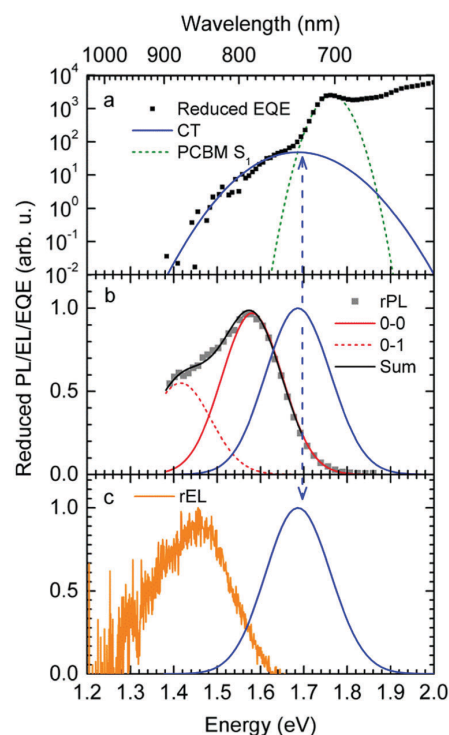


Fig. 5 (a) Reduced EQE spectrum at 100 K (black squares), together with a Franck–Condon fit to the CT state at about 1.61 eV (blue solid line) and a Gaussian fit to the PCBM S_1 state at about 1.75 eV (green dashed line). (b) Reduced Photoluminescence at 90 K (grey squares) along with a Franck–Condon fit (black line) as described in the text. The 0–0 and 0–1 vibronic overtones are indicated by red solid and dashed lines, respectively (c) Reduced EL spectrum (orange dots). The FC fit to the CT state from the EQE is also indicated in parts (b) and (c) for ease of comparison.

recorded at 90 K. At that temperature, the origin of the PCBM feature is at 1.77 eV with a standard deviation of 20 meV. The rPL spectra of the CT state show a Gaussian high energy edge followed by a low energy tail that we interpret as a vibrational overtone (Fig. 5b). In the rEQE spectra, the vibrational overtone cannot be differentiated from those pertaining to the S_1 state of the PCBM.

We therefore analyze the rEQE and rPL spectra with eqn (6) for only the 0–0 and, in the case of the rPL, also the 0–1 peak, *i.e.* $m = 0$ to 1. As already mentioned, the Gaussian linewidth function Γ usually includes contributions from both, the inhomogeneous line broadening as well as the low-frequency phonon wing. Here, we wish to explicitly differentiate between the two contributions. Focusing first only on the 0–0 transition of the CT state ($m = 0$), we thus use the product of the Poisson distribution for the low-frequency intermolecular modes with the Gaussian lineshape function of variance σ^2 characterizing the inhomogeneous broadening to fit the 0–0 peak. This corresponds to using eqn (6) with $S = S_{\text{low}}$ and $\omega = \omega_{\text{low}}$ (and $m = 0$).

To fit both, rEQE and rPL, $E_0 = E_{\text{CT}}$ is determined by the intersection of the rEQE and rPL spectra. It may, at first, seem that with 3 parameters, S_{low} , $\hbar\omega_{\text{low}}$ and σ , the problem is

overparametrized. However, the high energy tail of the rPL (the low energy tail of the rEQE) needs to be reproduced, thus determining the inhomogeneous broadening captured in σ^2 , and the maxima of rEQE and rPL are at fixed positions, which defines combination of S_{low} and $\hbar\omega_{\text{low}}$. (We recall that any contribution to the PL at energies above the 0–0 transition can only arise from inhomogeneous broadening and not from a phonon wing that, by definition, is below the 0–0 transition.)

The rPL spectrum can be reproduced by invoking a 0–0 feature of the CT transition at $E_{\text{CT}} = 1.62$ eV and an inhomogeneous broadening (standard deviation σ) of 67 meV. The coupling to low-frequency phonons can be expressed, *e.g.*, by considering 10 meV phonons with a Huang Rhys factor of $S_{\text{low}} = 4.0$, corresponding to a reorganization energy of $\lambda_{\text{low}} = S_{\text{low}} \cdot \hbar\omega_{\text{low}} = 40$ meV. Equally good fits can be obtained by considering phonons of a lower or higher energy, with correspondingly higher or lower Huang–Rhys parameter (in the range of $S = 3–7$), as long as the reorganization energy is kept at 40 meV.‡ The peaks pertaining to rPL and rEQE are not fully mirror-symmetric but differ slightly. However, the pertinent parameters to fit the rEQE are kept at a σ of 67 meV, and a E_{CT} of 1.62 eV. For the rEQE, a reorganization energy of $\lambda_{\text{low}} = 60$ meV results, *e.g.* obtained by $S_{\text{low}} = 4$ and $\hbar\omega_{\text{low}} = 15$ meV. The sum of both reorganization energies is 40 meV + 60 meV = 100 meV. This is the observed Stokes' shift. The parameters used for the fits of rEQE and rPL are summarized in Table 2.

We can now continue to also include the first vibrational overtone observed in the PL. The easiest way to do this is to shift the obtained rPL fit by an effective high frequency mode, here $\hbar\omega_{\text{high}} = 165$ meV, multiply it by an appropriate high-frequency Huang–Rhys factor, here $S_{\text{high}} = 0.58$, and add the two peaks (0–0 and 0–1). The excellent match of the fit to the experimental data is shown in Fig. 5b. Mathematically, this is equivalent to performing one multi-mode fit, taking both modes into account simultaneously, according to⁴¹

$$\begin{aligned} \text{rPL}(E) &= \frac{\text{PL}(E)}{E} \\ &\propto \sum_{m_i} \prod_i \frac{S_i^{m_i}}{m_i!} e^{-S_i} \cdot \Gamma \cdot \delta\left(E - \left(E_0 - \sum_i m_i \hbar\omega_i\right)\right) \end{aligned} \quad (7)$$

with i ranging from 0 to 1 in our case, as detailed in the ESI† (cf. Fig. S4), and the two modes being $\hbar\omega_0 = 10$ meV and $\hbar\omega_1 = 165$ meV.

We can summarize the result of our analysis as follows. The rPL and rEQE of the CT state can be modelled as a Franck–Condon progression with a 0–0 transition at $E_{\text{CT}} = 1.62$ eV. It is characterized by an inhomogeneous broadening of 67 meV.

Table 2 Parameter set used in the fits to rEQE and rPL spectra at 90 K according to eqn (6)

	E_{CT} (eV)	σ (meV)	λ_{low} (meV)	S_{low}	$\hbar\omega$ (meV)
rEQE	1.62	67	60	4	15
rPL	1.62	67	40	4	10

The Stokes' shift of 100 meV between the peaks of CT emission and rEQE arises only due to low-frequency phonon modes. The asymmetry between the CT part of the rEQE and the rPL results in a higher reorganization energy for the CT state D^+A^- than for the associated ground state pair DA. This is illustrated in Fig. 6. It implies a steeper curve of the potential energy for D^+A^- than for DA, in agreement with the intuitive notion that there should be a stronger bonding, *i.e.* force constant k , for the ionic pair where coulomb forces prevail than for the neutral pair that is only held together by van der Waals forces. We suggest that the low-frequency modes be predominantly of inter-molecular nature. The transfer of an electron from donor to acceptor creates an inter-molecular coulomb attraction that is likely to couple strongly to inter-molecular motion. Moreover, coupling of the rigid MeLPPP or the fullerene to low-frequency torsional or librational modes can only be weak due to their geometric constraints.

The above analysis is consistent with all experimentally observed features. In Fig. 1, we noticed a surprisingly long-lived fluorescence from PCBM that still prevails after 30 ns at room temperature, and concomitantly, the CT emission increases upon cooling by a factor of 5. Given the moderately small energy difference between the 0–0 peaks of the CT state (1.62 meV) and that of the PCBM S_1 state (1.77 meV) of 150 meV, the part of PCBM emission that we still observe at 30 ns after excitation is likely to arise from thermally activated delayed fluorescence (TADF), and this is also the most likely non-radiative decay channel of the CT state that is frozen out upon cooling. The power-law decay with exponent $-3/2$ we reported in Fig. 2 testifies to the existence of a broad DOS of CT states. Our analysis shows that the CT DOS ($\sigma = 67$ meV) is about 3.5 times as broad as that of the S_1 state of PCBM ($\sigma = 20$ meV). This broad CT DOS is fully consistent with the observed energy difference between EL and PL (Fig. 4b), as detailed above. The fact that the EQE of the diode decreases strongly upon cooling as documented by Fig. 3b can be understood by considering that the EQE is the product of the probability for creating a CT state, the probability that it dissociates into a pair of free charge

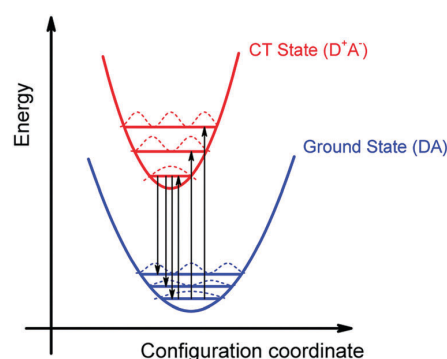


Fig. 6 Schematic illustration of the energy surface of S_0 and CT state. The general configuration coordinate reflects mostly the distance and orientation between donor and acceptor. Note the steeper potential and thus higher vibrational frequencies in the excited state.

carriers, and the probability that these free carriers are extracted at the electrode. From earlier work we know that the dissociation probability of the MeLPPP-fullerene CT state under short-circuit conditions depends only weakly on temperature.⁵⁸ This is because the degree of delocalization of the hole on the conjugated polymer of Me-LPPP is large, which substantially reduces the binding energy of the CT state with fullerenes.⁵⁸ The probability for charge extraction is controlled by the mobility of the charge carriers, which has a strong dependence on temperature.^{25,59,60} Thus, the overall decrease of the EQE reflects mostly the charge transport properties of the film. The subtle change in shape of the EQE reflects mostly the increase in inhomogeneous line broadening for the S_0 - S_1 transition of the PCBM with temperature.

5. Discussion

It appears appropriate to briefly comment on the results of the analysis of the rEQE that Vandewal *et al.* carried out on a series of donor-acceptor systems with C_{60} as an acceptor.³⁹ Using the Marcus-formalism [eqn (3)], they identified the standard deviation of the Gaussian tail of the reduced EQE spectrum with the structural relaxation of the CT state thus ignoring inhomogeneous spectral broadening. They suggest (i) that the most important contributor to the line-shape be low-frequency intramolecular vibrations and that static disorder played no role, and (ii) that these vibrations be thermally activated, so that the lineshape be reasonably well described in terms of a Marcus-type expression. In their definition, “low-frequency” reaches up

to 125 meV, which differs from the range *e.g.* Jortner³⁵ refers to as “low-frequency”, which is up to about 10 meV. Moreover, they compared the inferred reorganization energy with that of the donor upon ionization thus arguing (iii) that the EQE spectrum is an experimental probe of this intramolecular reorganization energy.

In certain cases, it can indeed be useful to consider the optical excitation as a charge-transfer reaction,^{30,61} and this approach, cast into eqn (1) by Gould, is undoubtedly valid. However, we question whether the use of a classical Marcus expression [eqn (3)] is appropriate, and whether the neglect of inhomogeneous broadening can be justified, and we doubt to the direct association of the Stokes' shift with a reorganization energy that mostly reflects the intramolecular reorganization energy of the donor cation.

We first point out that the observations presented in Fig. 2 and 4 cannot be accounted for when presuming a single CT-state energy without energetic disorder. Moreover, when using the rEL instead of the rPL to obtain a simultaneous fit of reduced emission and reduced EQE, a different Stokes' shift is obtained, which would suggest a different reorganization energy, depending on the mode of excitation, which is unphysical. When using the rPL spectra, the Gaussian shape of the 0-0 peak at room temperature can readily be reproduced using the classical Marcus expression of eqn (3), which is also a Gaussian function, albeit with $E_{CT} = 1.71$ and $\lambda = 160$ meV at 295 K, as shown in Fig. 7a. However, neither the low-energy tail of the rPL nor the experimental rEQE are reproduced. Rather, the fit suggests the absorption of the CT state to peak at an energy above the S_1 energy of PCBM, which is also unphysical. More important,

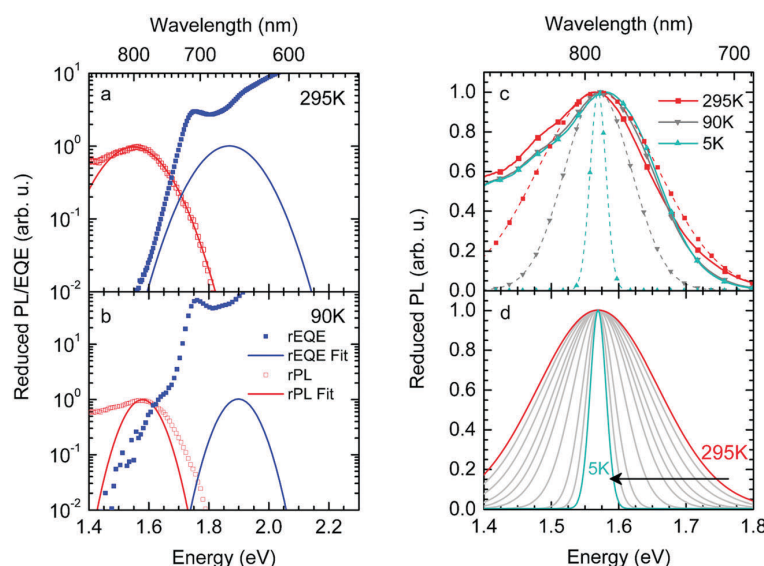


Fig. 7 (a) Reduced PL and EQE recorded at (a) 295 K and (b) 90 K (squares), along with a fit (blue solid lines) to the rPL according to the Marcus model, *i.e.* eqn (3b). The concomitant resulting curve for the rEQE (blue curve) according to eqn (3a) is also shown. The fit parameters are at $E_{CT} = 1.71$ (1.74) meV and $\lambda = 160$ meV at 295 K (90 K). (c) Comparison of the rPL data at 295 K, 90 K and 5 K (solid lines) with the spectra calculated (dashed lines) according to Marcus' theory [eqn (3)] at corresponding temperatures. (d) Spectra calculated according to Marcus theory [eqn (3)] over a temperature range from 295 K down to 5 K.

however, is that the temperature evolution of the rPL spectra of Fig. 1c cannot be rendered correctly in the classical Marcus framework of eqn (3). When reducing the temperature, eqn (3) predicts a narrowing of the Gaussian shape that is not observed experimentally, as evident in Fig. 7b. Fig. 7c compares the intensity-normalized rPL spectra with the fit to eqn (3) for different temperatures. In the same way, the shape of the EQE around the CT transition hardly narrows upon cooling (Fig. 3 and 7b), and is thus not compatible with the Marcus-type description.

To understand why the classical Marcus expression falls short here, it is worthwhile reconsidering eqn (1). As Jortner pointed out some time ago,³⁵ the Franck–Condon-weighted density of states, $FC(g)$, can be evaluated for different limiting cases, such as at low, intermediate and high temperature, where the thermal energy is compared to the energy of the vibrational modes involved. The classical Marcus expression that is used for eqn (3), with $\lambda = \lambda_{\text{low}} + \lambda_{\text{high}}$, presumes that the thermal energy be large compared to both low-frequency and high-frequency phonons, *i.e.* $k_{\text{B}}T \gg \hbar\omega$. For MeLPPP and PCBM, the dominant high-frequency mode is associated with the CC stretching motion and is around 160 meV. The highest temperature, at which the measurements are carried out, is room temperature, where $k_{\text{B}}T$ is about 25 meV. Thus, the requirements for the classic case are not fulfilled. $k_{\text{B}}T$ is even smaller than the “low-frequency” cut-off of 125 meV of Vandewal *et al.*

In his evaluation of CT-states, Gould used the MLJ-expression to account for $FC(g)$. This is the intermediate case, where the thermal energy is large compared to the low-frequency modes, yet small compared to the high-frequency modes, $\hbar\omega_{\text{low}} \ll k_{\text{B}}T \ll \hbar\omega$. Given that for organic thin films, low frequency modes usually range from about 1–10 meV,³⁵ and high-frequency ones from about 50–300 meV, this appears to be the appropriate range for a description at room temperature. To test whether this works, we have fitted the PL and EQE using the MLJ expression, multiplied with a Gaussian lineshape function of standard deviation σ to account for inhomogeneous broadening. The pertinent expression is thus

$$rQE(E) = EQE(E) \cdot E$$

$$\propto \sum_{n=0}^{\infty} \left(\frac{e^{-S} S^n}{n!} \times \exp \left(-\frac{(E_{\text{CT}} - E + \lambda_{\text{low}} + n\hbar\omega)^2}{4\lambda_{\text{low}}k_{\text{B}}T + 2\sigma^2} \right) \right) \quad (8a)$$

$$rPL(E) = \frac{PL(E)}{E}$$

$$\propto \sum_{n=0}^{\infty} \left(\frac{e^{-S} S^n}{n!} \times \exp \left(-\frac{(E_{\text{CT}} - E - \lambda_{\text{low}} - n\hbar\omega)^2}{4\lambda_{\text{low}}k_{\text{B}}T + 2\sigma^2} \right) \right) \quad (8b)$$

To illustrate the effect of disorder we performed fits both with and without considering disorder in eqn (8). Fig. 8 displays exemplary rPL spectra recorded at three different temperatures, *i.e.* 295 K, 90 K and 5 K. They are compared to fits once according to eqn (7) (“FC-Fits”) and once according to eqn (8) (“MLJ-Fits”). The fit-parameters are summarized in Table 3.

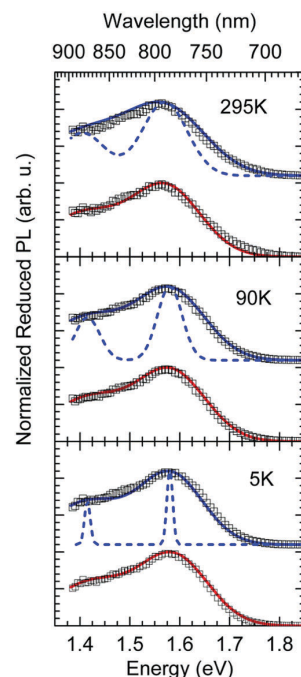


Fig. 8 Comparison of Franck–Condon-Fit (red line) and MLJ-Fit with (solid blue line) and without (dashed blue line) inhomogeneous broadening due to disorder for 295 K, 90 K and 5 K. Open symbols represent the measured data at distinct temperature. The parameters used in the fits are mentioned in the text.

Fig. 8 shows that the FC-Fits reproduce the experimental data well at all temperatures. An equally good reproduction is obtained for the MLJ-fits, when disorder is taken into account. However, the MLJ-equation without disorder cannot reproduce the lineshape of the rPL, neither at room temperature and especially not at lower temperature, where the associated linewidth narrows to an extent that is not compatible with experiment. Similarly, good fits according to eqn (8a) are obtained for the same parameters with respect to the rEQE, as illustrated in the ESI† (*cf.* Fig. S5), when disorder is taken into account, yet not without it.

What do we learn from this? Evidently, a FC-Fit and a MLJ-Fit work equally well, as long as inhomogeneous line broadening due to energetic disorder is taken into account. In fact, the large degree of disorder ($\sigma = 65$ meV) compared to the reorganization energy of the low-frequency phonons (40 meV) makes it impossible to differentiate between two fits.

Formally, at very low temperatures where $k_{\text{B}}T \ll \hbar\omega_{\text{low}}$, according to Jortner’s work it would be necessary to use a different expression for the Franck–Condon-weighted density of states instead of eqn (2) or (8). It is

$$FC(g) = \sum_{n=0}^{\infty} \frac{e^{-S_{\text{low}}} \times S_{\text{low}}^{k(n)}}{k(n)!} \times \frac{e^{-S} S^n}{n!} \quad (9)$$

with a certain relation between k and n as detailed in ref. 35. It is easy to see that, when incorporating inhomogeneous line

Table 3 Parameter set used for the fits to the PL spectra recorded at 295 K, 90 K and 5 K according to eqn (7) and (8)

	σ (meV)	$\hbar\omega$ (meV)	S	λ_{low} (meV)	E_{CT} (eV) (295 K)	E_{CT} (eV) (90 K)	E_{CT} (eV) (5 K)
FC-Fit	67	165	0.58	40	1.61	1.62	1.625
MLJ-Fit with σ	65	165	0.58	40	1.61	1.62	1.62
MLJ-Fit $\sigma = 0$ meV	0	165	0.58	40	1.61	1.62	1.62

broadening into this and truncating the sum over n in eqn (9) at $n = 1$, one arrives at the same expression for $\text{FC}(g)$ as was used in eqn (7), or equivalently at the procedure we adopted in eqn (6) and the accompanying text. Thus, eqn (9), combined with eqn (1), is evidently the expression that reproduces the line shape and temperature dependence of the CT state emission and absorption from 5 to 300 K. As Jortner points out, eqn (9) “corresponds to temperature independent nuclear tunneling between the zero point of the nuclear configuration of the initial state to the vibronic states of the final nuclear surface, which are nearly degenerate with it”. Poignantly, this is exactly the case described by the common evaluation of the Franck–Condon overlap integral, from which the common Franck–Condon analysis derives, and implies that electron transfer can be consistently described by a tunneling process. With increasing temperature, *e.g.* above about 100 K, the evaluation of the Franck–Condon-weighted density of states then results in eqn (2), where some (small) thermal activation of the transfer by low-frequency photons is included. In practice, however, the broad DOS removes any distinction between the two modes of transfer.

6. Conclusion

Thus, in summary we find that the lineshape of the CT state, in PL and EQE, is determined by the effects of static disorder and low-frequency vibrations by about equal contributions. Vandewal *et al.* attribute the modes involved in the reorganization process entirely to an intramolecular origin. We question this and suggest that the transfer of a charge, that changes a neutral DA pair into a charged D^+A^- pair, is likely to couple strongly to inter-molecular vibrations, so that the low-frequency reorganization energy is predominantly an inter-molecular quantity that reflects the structural displacement between donor and acceptor upon excitation like in an excimer state. Even so, Vandewal *et al.* have convincingly shown that the Gaussian linewidth, and thus the Stokes’ shift, correlate linearly with the reorganization energy calculated for the formation of the donor cation. It is conceivable that this correlation is accidental. We suspect that the static disorder, which contributes to about half of the Gaussian linewidth, may actually correlate with the flexibility or rigidity of the chromophores. For a satisfying description of the CT state spectra, we found that the inclusion of static disorder is essential. As already noted by Burke *et al.*, the neglect of disorder in the treatment of CT states leads to values that implicitly contain a contribution from disorder, and the

associated values for λ , ECT and the Stokes’ shift need to be viewed with some caution, keeping this implication in mind.^{46,62} With disorder included, the spectra may be modelled using a MLJ-based or a FC-based fit [eqn (8) or (7), respectively]. In our interpretation, the resulting Stokes’ shift gives the reorganization energy associated with low-frequency phonons.

Conflicts of interest

There are no conflicts to declare.

Acknowledgements

We acknowledge financial support by the German Science Foundation DFG through the doctoral training center “Photo-physics of Synthetic and Biological Multichromophoric Systems” (GRK 1640) and the Bavarian State Ministry of Education, Science and the Arts through the Collaborative Research Network “Solar Technologies go Hybrid” (SolTech). Furthermore, F.-J. K. was supported by the Elite Network Bavaria (ENB) in the framework of the Elite Study Program “Macromolecular Science”. We thank S. Athanasopoulos for critical reading of the manuscript.

Notes and references

‡ As a criterion for the appropriateness of a fit, we choose a maximum deviation from the experimental data of 5% (significance level) at half of the maximum peak height at the high energy edge of the spectrum. To determine the according parameter range we varied the Huang–Rhys-parameter S while keeping the reorganization energy fixed.

- 1 H. Leonhardt and A. Weller, *Ber. Bunsen-Ges.*, 1963, **67**, 791–795.
- 2 D. Rehm and A. Weller, *Z. Phys. Chem.*, 1970, **69**, 183–200.
- 3 A. Weller, *Z. Phys. Chem.*, 1982, **130**, 129–138.
- 4 A. Weller, *Z. Phys. Chem.*, 1982, **133**, 93–98.
- 5 T. Unger, S. Wedler, F. J. Kahle, U. Scherf, H. Bässler and A. Köhler, *J. Phys. Chem. C*, 2017, **121**, 22739–22752.
- 6 S. M. Falke, C. A. Rozzi, D. Brida, M. Maiuri, M. Amato, E. Sommer, A. De Sio, A. Rubio, G. Cerullo, E. Molinari and C. Lienau, *Science*, 2014, **344**, 1001–1005.
- 7 J. L. Brédas, E. H. Sargent and G. D. Scholes, *Nat. Mater.*, 2017, **16**, 35–44.
- 8 E. R. Bittner and C. Silva, *Nat. Commun.*, 2014, **5**, 3119.
- 9 H. Tamura, I. Burghardt and M. Tsukada, *J. Phys. Chem. C*, 2011, **115**, 10205–10210.

- 10 H. Tamura, R. Martinazzo, M. Ruckebauer and I. Burghardt, *J. Chem. Phys.*, 2012, **137**, 22A540.
- 11 H. Tamura and I. Burghardt, *J. Phys. Chem. C*, 2013, **117**, 15020–15025.
- 12 G. Grancini, M. Maiuri, D. Fazzi, A. Petrozza, H. J. Egelhaaf, D. Brida, G. Cerullo and G. Lanzani, *Nat. Mater.*, 2013, **12**, 29–33.
- 13 J. M. Szarko, B. S. Rolczynski, S. J. Lou, T. Xu, J. Strzalka, T. J. Marks, L. P. Yu and L. X. Chen, *Adv. Funct. Mater.*, 2014, **24**, 10–26.
- 14 A. C. Jakowetz, M. L. Bohm, J. B. Zhang, A. Sadhanala, S. Huettner, A. A. Bakulin, A. Rao and R. H. Friend, *J. Am. Chem. Soc.*, 2016, **138**, 11672–11679.
- 15 M. Gerhard, A. P. Arndt, M. Bilal, U. Lemmer, M. Koch and I. A. Howard, *Phys. Rev. B*, 2017, **95**, 195301.
- 16 C. Schwarz, S. Tscheuschner, J. Frisch, S. Winkler, N. Koch, H. Bässler and A. Köhler, *Phys. Rev. B*, 2013, **87**, 155205.
- 17 B. Bernardo, D. Cheyns, B. Verreet, R. D. Schaller, B. P. Rand and N. C. Giebink, *Nat. Commun.*, 2014, **5**, 3245.
- 18 V. Abramavicius, V. Pranculis, A. Melianas, O. Inganäs, V. Gulbinas and D. Abramavicius, *Sci. Rep.*, 2016, **6**, 32914.
- 19 X. Liu, K. Ding, A. Panda and S. R. Forrest, *ACS Nano*, 2016, **10**, 7619–7626.
- 20 B. W. Larson, O. G. Reid, D. C. Coffey, S. M. Avdoshenko, A. A. Popov, O. V. Boltalina, S. H. Strauss, N. Kopidakis and G. Rumbles, *Adv. Energy Mater.*, 2016, **6**, 1601427.
- 21 S. N. Hood and I. Kassal, *J. Phys. Chem. Lett.*, 2016, **7**, 4495–4500.
- 22 S. Albrecht, K. Vandewal, J. R. Tumbleston, F. S. U. Fischer, J. D. Douglas, J. M. J. Frechet, S. Ludwigs, H. Ade, A. Salleo and D. Neher, *Adv. Mater.*, 2014, **26**, 2533–2539.
- 23 D. C. Coffey, B. W. Larson, A. W. Hains, J. B. Whitaker, N. Kopidakis, O. V. Boltalina, S. H. Strauss and G. Rumbles, *J. Phys. Chem. C*, 2012, **116**, 8916–8923.
- 24 K. Vandewal, S. Albrecht, E. T. Hoke, K. R. Graham, J. Widmer, J. D. Douglas, M. Schubert, W. R. Mateker, J. T. Bloking, G. F. Burkhard, A. Sellinger, J. M. J. Frechet, A. Amassian, M. K. Riede, M. D. McGehee, D. Neher and A. Salleo, *Nat. Mater.*, 2014, **13**, 63–68.
- 25 T. Hahn, J. Geiger, X. Blase, I. Duchemin, D. Niedzialek, S. Tscheuschner, D. Beljonne, H. Bässler and A. Köhler, *Adv. Funct. Mater.*, 2015, **25**, 1287–1295.
- 26 C. Deibel, A. Wagenpfahl and V. Dyakonov, *Phys. Status Solidi RRL*, 2008, **2**, 175–177.
- 27 W. Tress, K. Leo and M. Riede, *Phys. Rev. B*, 2012, **85**, 155201.
- 28 J. Liu, S. S. Chen, D. P. Qian, B. Gautam, G. F. Yang, J. B. Zhao, J. Bergqvist, F. L. Zhang, W. Ma, H. Ade, O. Inganäs, K. Gundogdu, F. Gao and H. Yan, *Nat. Energy*, 2016, **1**, 16089.
- 29 N. A. Ran, J. A. Love, C. J. Takacs, A. Sadhanala, J. K. Beavers, S. D. Collins, Y. Huang, M. Wang, R. H. Friend, G. C. Bazan and T. Q. Nguyen, *Adv. Mater.*, 2016, **28**, 1482–1488.
- 30 I. R. Gould, D. Noukakis, L. Gomezjahn, R. H. Young, J. L. Goodman and S. Farid, *Chem. Phys.*, 1993, **176**, 439–456.
- 31 R. A. Marcus, *J. Chem. Phys.*, 1956, **24**, 966–978.
- 32 R. A. Marcus, *Discuss. Faraday Soc.*, 1960, 21–31.
- 33 V. G. Levich, *Adv. Electrochem. Electrochem. Eng.*, 1966, **4**, 249–371.
- 34 R. R. Dogonadze, in *Reactions of Molecules at Electrodes*, ed. M. S. Hush, Wiley-Interscience, London, 1971.
- 35 J. Jortner, *J. Chem. Phys.*, 1976, **64**, 4860–4867.
- 36 M. Bixon and J. Jortner, *Faraday Discuss.*, 1982, **74**, 17–29.
- 37 K. Vandewal, K. Tvingstedt, A. Gadisa, O. Inganäs and J. V. Manca, *Phys. Rev. B*, 2010, **81**, 125204.
- 38 K. Vandewal, *Annu. Rev. Phys. Chem.*, 2016, **67**, 113–133.
- 39 K. Vandewal, J. Benduhn, K. S. Schellhammer, T. Vangerven, J. E. Rückert, F. Piersimoni, R. Scholz, O. Zeika, Y. L. Fan, S. Barlow, D. Neher, S. R. Marder, J. Manca, D. Spoltore, G. Cuniberti and F. Ortman, *J. Am. Chem. Soc.*, 2017, **139**, 1699–1704.
- 40 K. Tvingstedt, K. Vandewal, A. Gadisa, F. L. Zhang, J. Manca and O. Inganäs, *J. Am. Chem. Soc.*, 2009, **131**, 11819–11824.
- 41 P. K. H. Ho, J. S. Kim, N. Tessler and R. H. Friend, *J. Chem. Phys.*, 2001, **115**, 2709–2720.
- 42 A. Köhler and H. Bässler, *Electronic Processes in Organic Semiconductors: An Introduction*, Wiley, 2015.
- 43 R. A. Street, K. W. Song, J. E. Northrup and S. Cowan, *Phys. Rev. B*, 2011, **83**, 165207.
- 44 N. Jain, N. Chandrasekaran, A. Sadhanala, R. H. Friend, C. R. McNeill and D. Kabra, *J. Mater. Chem. A*, 2017, **5**, 24749–24757.
- 45 A. N. Brigeman, M. A. Fusella, Y. X. Yan, G. E. Purdum, Y. L. Loo, B. P. Rand and N. C. Giebink, *Adv. Energy Mater.*, 2016, **6**, 1601001.
- 46 T. M. Burke, S. Sweetnam, K. Vandewal and M. D. McGehee, *Adv. Energy Mater.*, 2015, **5**, 1500123.
- 47 R. A. Marcus, *J. Phys. Chem.*, 1989, **93**, 3078–3086.
- 48 C. Schwarz, H. Bässler, I. Bauer, J. M. Koenen, E. Preis, U. Scherf and A. Köhler, *Adv. Mater.*, 2012, **24**, 922–925.
- 49 J. J. Benson-Smith, L. Goris, K. Vandewal, K. Haenen, J. V. Manca, D. Vandezande, D. D. C. Bradley and J. Nelson, *Adv. Funct. Mater.*, 2007, **17**, 451–457.
- 50 D. Hertel, S. Setayesh, H. G. Nothofer, U. Scherf, K. Müllen and H. Bässler, *Adv. Mater.*, 2001, **13**, 65–70.
- 51 W. J. D. Beenken, F. Herrmann, M. Presselt, H. Hoppe, S. Shokhovets, G. Gobsch and E. Runge, *Phys. Chem. Chem. Phys.*, 2013, **15**, 16494–16502.
- 52 K. M. Hong and J. Noolandi, *J. Chem. Phys.*, 1978, **68**, 5163–5171.
- 53 K. M. Hong, J. Noolandi and R. A. Street, *Phys. Rev. B*, 1981, **23**, 2967–2976.
- 54 S. T. Hoffmann, H. Bässler, J. M. Koenen, M. Forster, U. Scherf, E. Scheler, P. Strohriegel and A. Köhler, *Phys. Rev. B*, 2010, **81**, 115103.
- 55 R. Jankowiak, B. Ries and H. Bässler, *Phys. Status Solidi B*, 1984, **124**, 363–371.
- 56 B. Movaghar, M. Grünwald, B. Ries, H. Bässler and D. Wurtz, *Phys. Rev. B*, 1986, **33**, 5545–5554.
- 57 R. F. Mahrt and H. Bässler, *Synth. Methods*, 1991, **45**, 107–117.
- 58 S. Tscheuschner, H. Bässler, K. Huber and A. Köhler, *J. Phys. Chem. B*, 2015, **119**, 10359–10371.

- 59 J. Kurpiers and D. Neher, *Sci. Rep.*, 2016, **6**, 26832.
- 60 T. Hahn, S. Tscheuschner, F. J. Kahle, M. Reichenberger, S. Athanasopoulos, C. Saller, G. C. Bazan, T. Q. Nguyen, P. Strohriegel, H. Bässler and A. Köhler, *Adv. Funct. Mater.*, 2017, **27**, 1604906.
- 61 V. May and O. Kühn, *Charge and Energy Transfer Dynamics in Molecular Systems*, Wiley-VCH, Weinheim, 3rd edn, 2011.
- 62 N. A. Ran, S. Roland, J. A. Love, V. Savikhin, C. J. Takacs, Y. T. Fu, H. Li, V. Coropceanu, X. F. Liu, J. L. Brédas, G. C. Bazan, M. F. Toney, D. Neher and T. Q. Nguyen, *Nat. Commun.*, 2017, **8**, 79.

Supporting information

How to interpret absorption and fluorescence spectra of charge transfer states in an organic solar cell

Frank-Julian Kahle¹, Alexander Rudnick¹, Heinz Bässler², Anna Köhler^{1,2*}

¹ Soft Matter Optoelectronics, University of Bayreuth, 95440 Bayreuth, Germany

² Bayreuth Institute of Macromolecular Science (BIMF), University of Bayreuth, 95440 Bayreuth, Germany

*anna.koehler@uni-bayreuth.de

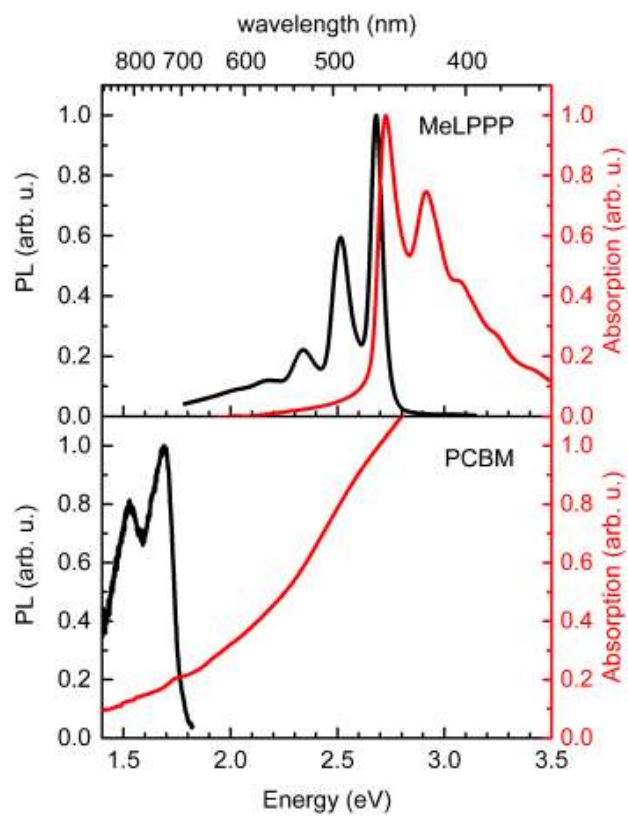


Figure S1: Absorption (red) and emission (black) spectra of pristine MeLPPP (top) and pristine PCBM (bottom) measured in a neat film. For PL spectra, the films were excited at 355 nm and 375 nm, respectively.

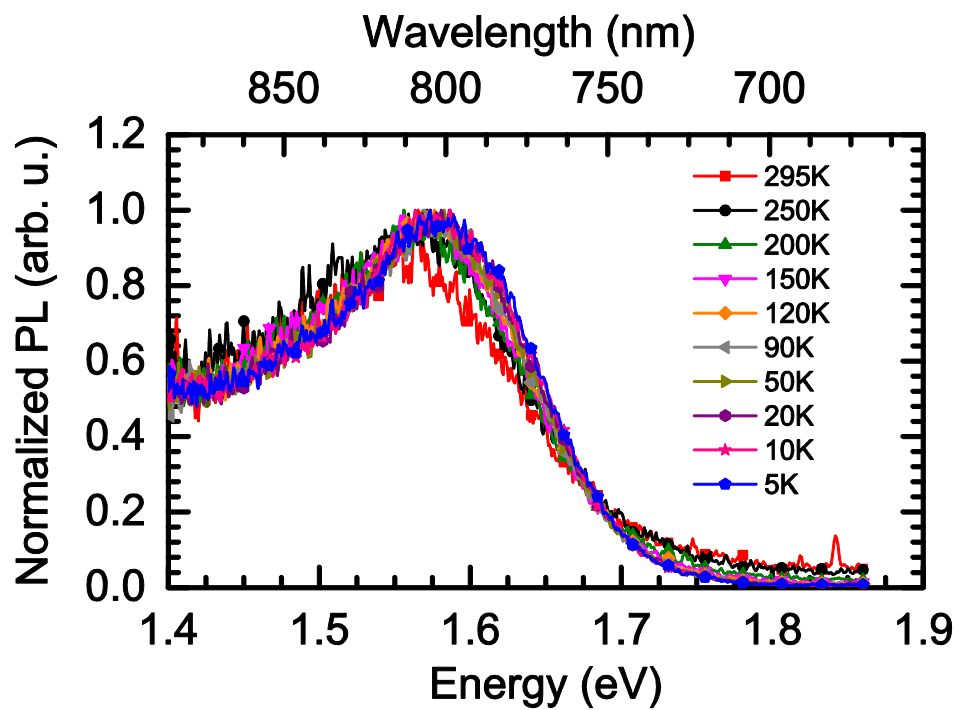


Figure S2: Normalized CT emission spectra from Figure 1c

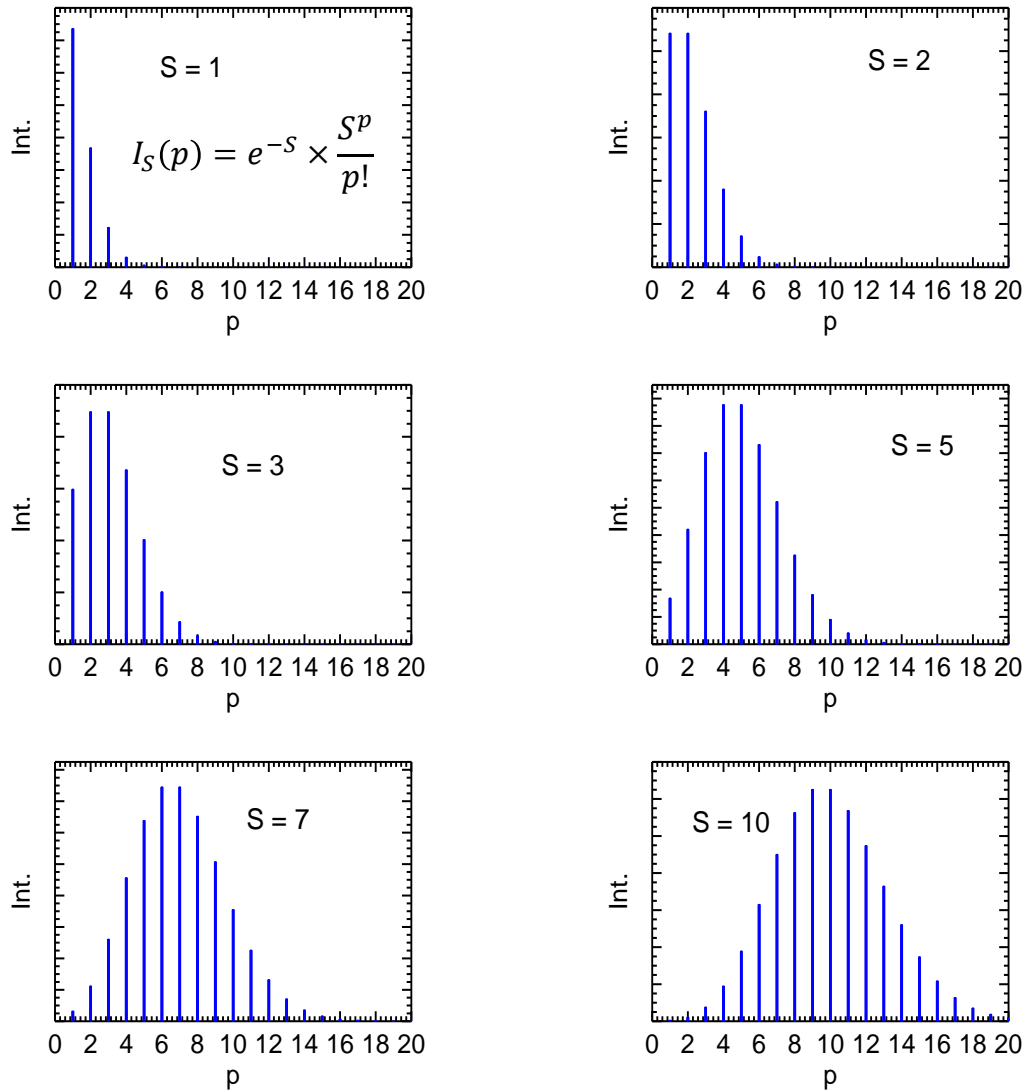


Figure S3: Schematic illustration of how a Poisson distribution becomes a Gaussian one for large values of S (underlying formula is shown in the upper left plot)

Mathematically, the procedure used in the manuscript to obtain the fit in Figure 5b is equivalent to performing one multi-mode fit, taking both modes into account simultaneously, according to¹

$$rPL(E) = \frac{PL(E)}{E} \propto \sum_{m_i} \prod_i \frac{S_i^{m_i}}{m_i!} e^{-S_i} \cdot \Gamma \cdot \delta(E - (E_0 - \sum_i m_i \hbar\omega_i)) \quad (7)$$

with the number of modes, i , ranging from 0 to 1 in our case. We used $\hbar\omega_0 = 10 \text{ meV}$ and $\hbar\omega_1 = 165 \text{ meV}$. The number of overtones, m_i , was running from 0 to 20 for m_0 , and from 0 to 1 for m_1 . In equation (7) we again considered the electronic transition moment M to be dependent on energy, i.e. $M = \frac{V \Delta \mu}{\hbar\nu} = \frac{V \Delta \mu}{E}$. The resulting fit, according to equation (7) is shown in Figure S4. Just like the fit presented in Figure 5a, it gives an excellent match to the experimental data. Also, the values for S_i and $\hbar\omega_i$ are in line with the values obtained from the method presented in the paper, therefore validating that both approaches are equivalent.

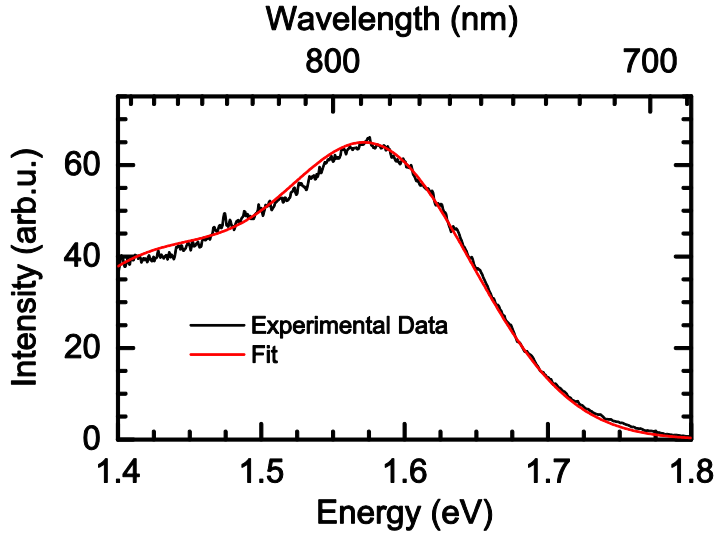


Figure S4: Franck-Condon fit with two vibronic modes according to eq. (7) with $\hbar\omega_0 = 10 \text{ meV}$ and $\hbar\omega_1 = 165 \text{ meV}$ of the 90K reduced PL recorded after a delay of 90ns with respect to the excitation pulse

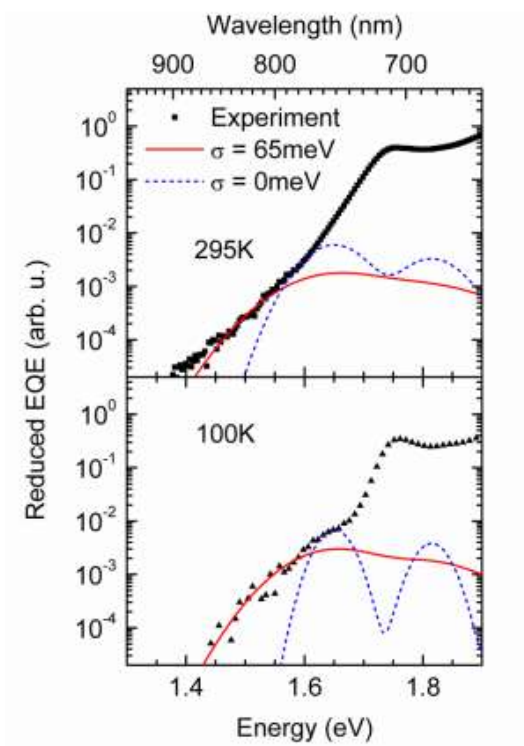
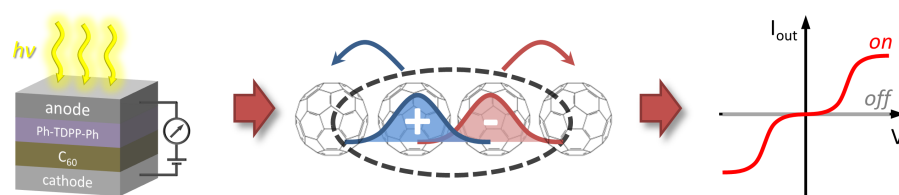


Figure S5: Reduced EQE (symbols) of a MeLPPP:PCBM blend at room temperature and at 100 K, along with MLJ fits with (solid line) and without (dashed line) disorder. The fit parameters are listed in Table 3 of the manuscript.

References

1. P. K. H. Ho, J. S. Kim, N. Tessler and R. H. Friend, *J Chem Phys*, 2001, **115**, 2709-2720.

13 Organic Bidirectional Phototransistors Based on Diketopyrrolopyrrole and Fullerene



Frank-Julian Kahle, Tobias Hahn, Tushita Mukhopadhyay, Boregowda Puttaraju, Satish Patil, and Anna Köhler

Published in
Adv. Funct. Mater., **2018**, 1805684
(DOI: 10.1002/adfm.201805684)

Copyright ©2018 by John Wiley Sons, Inc.
Reprinted by permission of John Wiley & Sons, Inc.

Organic Bidirectional Phototransistors Based on Diketopyrrolopyrrole and Fullerene

Frank-Julian Kahle, Tobias Hahn, Tushita Mukhopadhyay, Boregowda Puttaraju, Satish Patil, and Anna Köhler*

It is shown that simple bilayer devices consisting of the diketopyrrolopyrrole (DPP) monomer Ph-TDPP-Ph as donor and C₆₀ as acceptor feature *J*-*V*-characteristics of a bidirectional organic phototransistor where illumination intensity plays the role of the gate voltage as compared to a conventional field-effect transistor. The output current may therefore be controlled both electrically and optically. The underlying mechanism is based on the good charge transport in Ph-TDPP-Ph and C₆₀, the intrinsic dissociation properties of C₆₀, and the presence of an injection barrier for holes. In addition to this, it is demonstrated that the observed behavior of the DPP/C₆₀ system allows the realization of basic logic elements like NOT-, AND-, and OR-Gates, which may provide the basis for advanced analog and digital applications.

1. Introduction

Diketopyrrolopyrrole (DPP) materials are commonly used as pigments in inks and paints due to their good stability.^[1–4] Furthermore, DPPs can be tuned to feature excellent fluorescent properties as well as good charge transport.^[5–11] In the context of optoelectronic applications, the DPP chromophore has been widely used in a plenty of π -conjugated donor–acceptor polymers and oligomers for excitonic organic solar cells.^[5,12] This is due to the fact that DPP-based materials have high molar extinction coefficients and easy synthetic tunability.^[7] Moreover, there are several reports on a good performance in ambipolar organic field effect transistors (OFETs).^[6,10,13] It is a quite obvious attempt to use these devices in a conventional way as voltage-driven field-effect transistors (FETs) in logic circuits.^[14,15]

F.-J. Kahle, Dr. T. Hahn, Prof. A. Köhler
Soft Matter Optoelectronics
University of Bayreuth
95440 Bayreuth, Germany
E-mail: anna.koehler@uni-bayreuth.de

Dr. T. Mukhopadhyay, Dr. B. Puttaraju, Prof. S. Patil
Solid State and Structural Chemistry Unit
Indian Institute of Science
Bangalore 560012, India

Prof. A. Köhler
Bayreuth Institute of Macromolecular Science (BIMF)
University of Bayreuth
95440 Bayreuth, Germany

The ORCID identification number(s) for the author(s) of this article can be found under <https://doi.org/10.1002/adfm.201805684>.

DOI: 10.1002/adfm.201805684

Recently, organic materials have demonstrated potential for light sensing and memory applications in so called phototransistors.^[16,17] Yet, these devices mostly rely on the basic FET structure using three electrical contacts. Here, we show that by combining a DPP monomer with C₆₀ (Figure 1) in a simple vertical sandwich-type bilayer structure we obtain a fully organic device capable of both switching mechanisms at the same time, that is, optical and electrical (voltage-driven) switching. This can be employed to realize basic organic hybrid optical and electronic logic elements (AND-, OR-, NOT-Gates), therefore providing the

basic set of operations necessary for various optically controlled analog and digital applications.

Up to now, there are few studies demonstrating logical elements using a combination of optical and electrical inputs, and those studies are often of an organic–inorganic device structure.^[17–20] One of the first works reporting on this topic is the study by Kim et al.^[19] In their work, they used single-walled carbon nanotube–silicon junctions to obtain scalable devices with voltage-switchable photocurrent output and switching ratios in the order of 10⁴–10⁵. In a more recent study, Lin et al.^[18] aimed for this application using the evolving materials class of hybrid organic–inorganic perovskites. They successfully demonstrated memristor activity and logic OR operation using a simple sandwich architecture and employing an electric field and illumination as input to control the output current. An on/off ratio of about 10³ could be achieved. Anthopoulos had already addressed the fabrication of organic electro-optical switches based on blends of poly[2-methoxy-5-(3',7'-dimethyloctyloxy)-*p*-phenylene vinylene (OC₁C₁₀PPV) and [6,6]-phenyl-C₆₁-butyric acid methyl ester (PC₆₀BM) on a silicon substrate.^[21] In his study, he used light-sensing ambipolar FETs in a conventional organic FET architecture on Si-wafers and demonstrated the realization of logic circuits like NOT and OR gates with response times of about 65 μ s by combining up to two FETs, albeit requiring driving voltages typically exceeding 10 V. In contrast to these earlier reports, we demonstrate the realization of low-voltage drivable, optically controlled vertical phototransistors, and logic circuits made only of organic semiconductors. We show that the photophysical mechanism involves mainly efficient autoionization of the C₆₀ and a hole injection barrier at the anode.

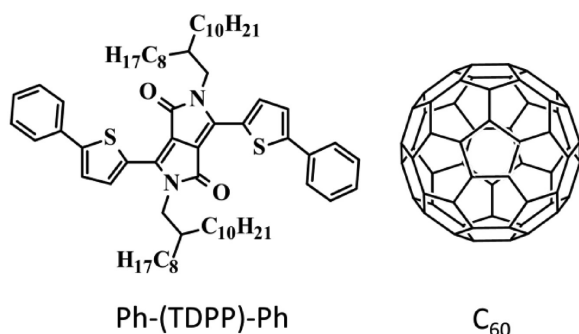


Figure 1. Chemical structures of Ph-(TDPP)-Ph and C₆₀.

2. Electrical Characterization and Logic Circuits

We fabricated photocells in a conventional layer structure of indium tin oxide (ITO)/MoO₃ (15 nm)/Ph-TDPP-Ph (15 nm)/C₆₀ (30 nm)/Al as described in the Experimental Section below. The results of current voltage (*J*-*V*) measurement on these devices under AM1.5 conditions are shown in Figure 2a. We observe a *J*-*V* characteristic that has a low dark current and a fill factor (FF) of 45% under illumination. Unusually, it is symmetric with respect to a certain point of maximum symmetry at $V_{PMS} = 0.44$ V and $J_{PMS} = -0.3$ mA cm⁻² and exhibits a net photocurrent in either direction, independent on whether forward or reverse bias is applied. One may therefore regard the device as a vertical asymmetric bidirectional phototransistor because i) current flow is possible in forward and reverse direction and ii) this current flow may be controlled and turned on and off via illumination of the device. The illumination in this case has the same function as the gate voltage in a conventional FET. At -1 V (+1 V) the on/off ratio, i.e., the difference between the current with and without illumination, is about 10⁵ (10³) (Figure S1a, Supporting Information).

Qualitatively the same *I*-*V* characteristics is obtained when the device is illuminated with monochromatic light at a wavelength above 2.25 eV, e.g., at 2.76 eV, as shown in the supporting information (Figure S1b, Supporting Information). In contrast, the bidirectional photocurrent disappears to yield to a “usual” unidirectional photocurrent for excitation below 2.25 eV, e.g., at 1.91 eV (Figure 2b). A more extended voltage range can be found in the Figure S1c in the Supporting Information. We point out that the dark current remains low, so that also the total current is very small above V_{oc} . The devices are very well reproducible. It is therefore possible to combine two devices in a back-to-back configuration to obtain a symmetric bidirectional phototransistor. An exemplary *J*-*V* curve of such a configuration is shown in Figure 2c for monochromatic illumination with 1.96 eV ($\lambda = 632$ nm) at 5.94 mW cm⁻². We observe a vanishing current at zero applied bias and a symmetric characteristic with respect to the origin. With increasing bias, the current remains low in the dark. Yet, under illumination, the current strongly increases above a threshold voltage of about ± 0.35 V and saturates at ± 0.70 V. The on/off ratio at ± 1.0 V is around 2×10^2 . Although the on/off ratio is low compared to conventional

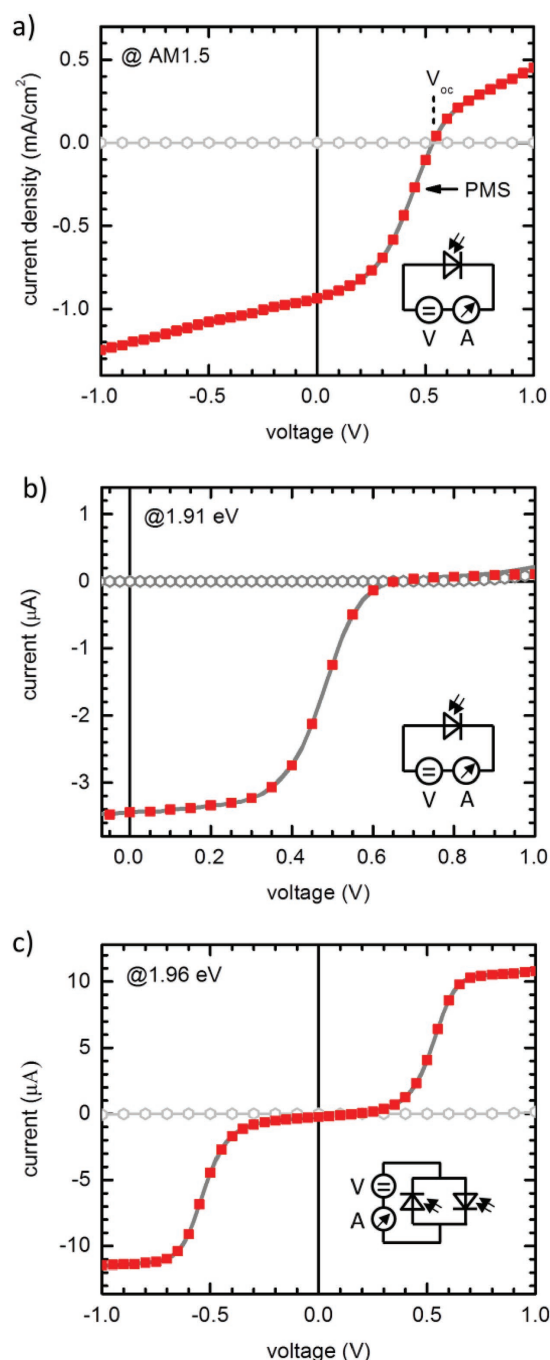


Figure 2. a) Exemplary *J*-*V* characteristic of a Ph-TDPP-Ph/C₆₀ device with MoO₃ interlayer measured at 1 sun illumination. b) *I*-*V* characteristic measured at 7 mW cm⁻² and an excitation energy of 1.91 eV. c) Exemplary *J*-*V* characteristic of a back-to-back configuration of two Ph-TDPP-Ph/C₆₀ devices recorded at an excitation energy of 1.96 eV ($\lambda = 632$ nm). Dark (light gray circles) and photocurrent contribution (red filled squares) to the total current (grey solid line) are explicitly shown. Schematic circuit diagrams are shown as insets.

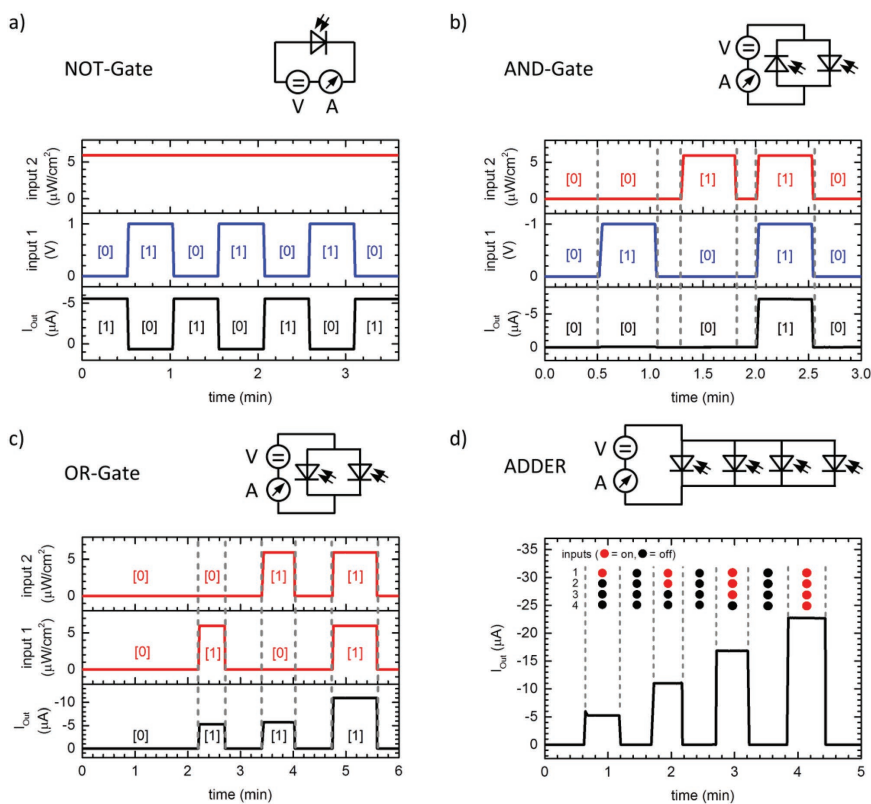


Figure 3. Output current I_{out} (black) for different input logic states as a function of time for various logic elements ([0]: off/low state, [1]: on/high state). a) NOT-Gate; The temporal course of the input voltage (input 1) is depicted in blue. The device is constantly illuminated (red, input 2). b) AND-Gate; voltage (input 1) and irradiation intensity (input 2) serve as two different input channels (back-to-back configuration). c) OR-Gate; Two devices in a parallel circuit are either illuminated ([1]) or not ([0]). d) 4-bit analog output ADDER; The number of red dots in a column indicates the number of simultaneously illuminated devices (parallel circuit). The corresponding circuit diagrams are also shown.

OFETs ($\geq 10^3$),^[22–24] it is nonetheless satisfying that a simple bilayer approach is capable of achieving the basic properties of a phototransistor.

This opens up the possibility to realize basic hybrid optical and electronic logic elements such as AND-, OR-, and especially also NOT-Gates, therefore providing the basic set of operations necessary for applications in logic algebra. As first logic element we consider the NOT-Gate (Figure 3a). A single phototransistor is constantly irradiated with the monochromatic light of a He-Ne-laser (1.96 eV, red), and the voltage (blue) is switched from 0 V (off state) to +1 V (on state). The resulting output current, depicted in black, is the typical response of a NOT-Gate. The current is in the Off [0] state (= low current) when the input voltage is in the On [1] state (= +1 V) and vice versa. With the low-intensity monochromatic illumination used here, the switching ratio is about a factor of 10, but nevertheless the basic requirements for a NOT-Gate are fulfilled. The ratio can be increased by using a higher illumination intensity, for example, to a factor of 500 for AM 1.5 (see Figure S1a in the Supporting Information).

The next logic element we realize is the AND-Gate, using i) the externally applied voltage and ii) the incident light on the

device as input parameters to control the current flow. For a working AND-Gate, there must be an output current response (on state) only, if both inputs are in the on-state. Due to the high reproducibility of our devices, we could easily obtain this behavior by combining two devices in a back-to-back configuration. The response resulting using a bias of -1 V as input 1 and monochromatic light of 1.96 eV as input 2 is displayed in Figure 3b together with an illustration of both input states. As desired, an output response is only present if both inputs are in the on state. The on/off ratio for the output current is in the range of 10^2 – 10^3 and the response time is about 80 μ s, corresponding to an operating frequency of about 12.5 kHz (Figure S2, Supporting Information).

Other possible applications are the OR-Gate and closely related to it, an analog output ADDER circuit. In the case of an OR-Gate, an output is required if any of the input channels is in the high state, with no output only if both inputs are in the off state. This function is realized with our system by using two devices in a parallel circuit that are biased at -1 V and either irradiated with monochromatic light for the on-state, [1], or not (off-state, [0]). Figure 3c shows the output current for every combination of the two inputs. As expected, an on state of the

output is achieved as long as any of the two devices or both of them are illuminated. Otherwise there is no significant current flow. The fact that the current output is twice as high when both devices instead of one are exposed to light at the same time already shows the possible application as a 2-bit analog output ADDER circuit. By using more devices, more bits are available for ADDER operations. This is illustrated in Figure 3d for four devices and thus 4 bits. Due to the good reproducibility of the samples the current output is proportional to the number of illuminated devices.

3. Optoelectronic Mechanism

In order to unravel the mechanism behind this special behavior of the investigated devices, we consider the external quantum efficiency (EQE) spectra at three different voltages (-1 , 0 , and $+1$ V). The EQE spectra are displayed in Figure 4a together with the respective absorption spectra of the pristine materials. For forward bias, at $+1$ V, we observe a significant photocurrent only for excitation above 2.25 eV. In contrast, under short-circuit condition and for reverse bias at -1 V, we observe a similar spectral response. The response for forward bias matches the absorption of C_{60} and in particular, it is almost identical to the photocurrent observed from autoionization of C_{60} by Hahn et al.^[25] Comparison of the donor absorption spectrum and the photocurrent spectrum for short-circuit and reverse bias shows that the contribution below 2.25 eV can be assigned to photoexcitation of the donor and subsequent dissociation at the donor/acceptor (D/A) interface, because neither C_{60} nor Ph-TDPP-Ph shows considerable autoionization of photogenerated excitons there. For reference, the EQE of single layer devices of pristine Ph-TDPP-Ph and C_{60} is given in Figure S1d in the Supporting Information.

Figure 4b,c shows simplified schemes of the energy levels for the bilayer devices under forward and reverse bias. Detailed values of the energy levels of C_{60} and Ph-TDPP-Ph are given in Figure S7 in the Supporting Information. We shall consider first the expected photoresponse for excitation below 2.25 eV. Under reverse bias (Figure 4b), excitons photogenerated in the donor dissociate at the interface and the carriers (shown in red color in Figure 4b) leave the device without encountering any extraction barriers, thus giving rise to a photoresponse. Under forward bias (Figure 4c), photogenerated excitons may only dissociate by electron transfer to the ITO. However, the remaining holes (still shown in red color) experience an extraction barrier at the Ph-TDPP-Ph/ C_{60} interface, so that photocurrent ceases. Furthermore, a space charge will build up at the Ph-TDPP-Ph/ C_{60} interface that additionally impedes charge extraction.^[26,27] This changes upon illumination above 2.25 eV. At these photon energies, CT states in C_{60} are excited that autoionize into charges (shown in green color) with significant yield.^[25,28] The holes accumulating on the donor side of the D/A junction can now recombine with the electrons provided from the autoionized C_{60} molecules, and the remaining hole on the C_{60} drifts to the cathode.^[29,30] In this way, a photocurrent is maintained under forward bias. To a certain extent, this mechanism resembles a tandem solar cell. In view of this, the observed net photocurrent under forward bias (above V_{oc} of the junction) can be interpreted in terms of an enhanced recombination

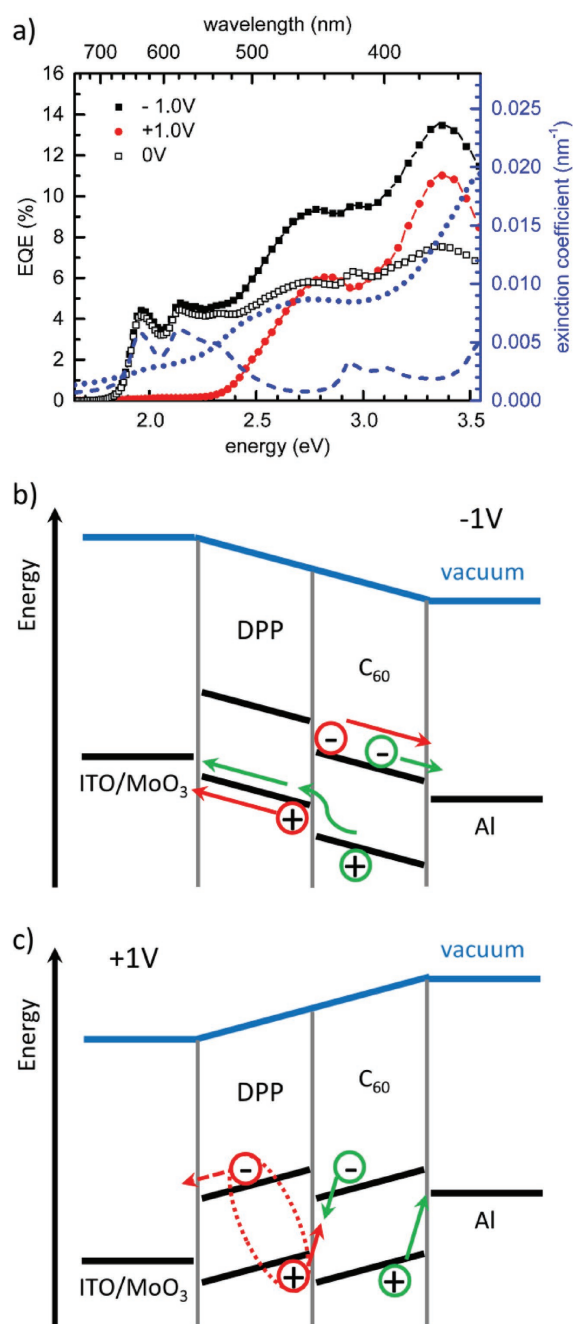


Figure 4. a) Left axis: series of voltage-dependent EQE spectra of MoO₃/Ph-TDPP-Ph/ C_{60} -devices. Right axis: absorption spectra of Ph-TDPP-Ph (dashed blue) and C_{60} (dotted blue). Simplified energy level diagram under b) reverse bias (-1 V) and c) forward bias ($+1$ V). Red and green color indicate charges resulting from photoexcitation in DPP and C_{60} , respectively.

current close to the cathode and the D/A interface, which eventually enables a hole current flow to the conventional cathode and an electron current flow to the conventional anode.^[27,31]

Under reverse bias and excitation above 2.25 eV, the photocurrent from the autoionized C₆₀, or C₆₀ excitons dissociated at the D/A interface simply adds to the total current (Figure 4b). In all these cases, good charge transport properties of both C₆₀^[32–34] and Ph-TDPP-Ph^[11] ensure that no additional losses are introduced due to low or imbalanced mobilities.^[26]

The overall mechanism is further supported by the independence of the FF on the illumination intensity, by the observation of a clear saturation field for exciton dissociation when exciting below 2.25 eV, yet not above 2.25 eV, and by the two orders of magnitude higher dark current observed when MoO₃ is replaced by PEDOT:PSS, as detailed further in the Supporting Information. The latter indicates the presence of a considerable hole injection barrier in the case of MoO₃, which accounts for the low dark current in our devices. Thus, this barrier is an important prerequisite for the total current above V_{oc} to be dominated by its photogenerated component.

4. Conclusion

To conclude, we are able to obtain the characteristics of an asymmetric vertical bidirectional phototransistor with on/off-ratios of up to 10³ at an applied bias of –1 V in a simple Ph-TDPP-Ph/C₆₀ bilayer structure. The underlying mechanism for this behavior is identified to be based on the efficient autoionization of CT states in C₆₀ and presence of an injection barrier at the anode to keep the dark current low, while at the same time charge carrier extraction is not inhibited. The net photocurrent in forward direction can be understood in terms of an enhanced recombination current close to the cathode and the D/A-interface.^[27,31]

The observed behavior of our bilayer devices allows the combination of switching operations with light and voltage independent from each other. These features make them capable of being used as hybrid optical/electronic logic elements. We have shown that the basic set of logic operations comprising NOT, AND, and OR-operations are possible using either a single phototransistor or two of them in a back-to-back configuration. The latter features a symmetric *J–V* characteristic with an on/off ratio of about 2 × 10². An improvement of this ratio could be achieved by further optimization of the injection barriers or illumination intensity.

With all the basic logic operations possible, our system – or the underlying approach – may in principle be used for various analog and digital applications. As a simple example we have shown the function of a 4-bit analog output ADDER. With this, we hope that our work will give new impulses toward further development of multifunctional organic logic elements.

5. Experimental Section

Sample Preparation: All samples were fabricated by spin coating the DPP-monomer Ph-TDPP-Ph^[35] from a chlorobenzene/chloroform-(2:3) solution (15 mg mL⁻¹) onto patterned glass/ITO/MoO₃ (15 nm) substrates. ITO was ozone treated prior to the evaporation of MoO₃. For some reference measurements, MoO₃ was replaced by a layer of PEDOT:PSS (30 nm). In a subsequent evaporation step, 30 nm of C₆₀ (Sigma-Aldrich) and 100 nm of Al were evaporated on top as

acceptor layer and cathode, respectively. Single layer devices with either Ph-TDPP-Ph or C₆₀ were fabricated accordingly by simply omitting the respective other layer.

Electrical and Optical Characterization: Current–voltage characteristics and current transients were recorded under vacuum conditions using Keithley source-measure units (SMU236/238). Illumination under AM1.5 sun light conditions was provided by a Newport sun simulator. Monochromatic light incidence for EQE measurements was generated by a 450W xenon lamp in combination with a monochromator. For the current transients, a HeNe-laser (3.9 mW) was used instead. In order to avoid heating of the sample due to illumination, light exposure time during the measurement was minimized using a shutter and alternately recording the current with and without illumination at each voltage step. The photocurrent was defined as the difference between the total current measured with and without light exposure. Absorption spectra were recorded using a Cary 5000 (Varian) absorption spectrometer. Response times for AND-Gates were measured using an optical chopper operated at 485 Hz and a 300 MHz oscilloscope (Tektronix). For this, response currents were converted to voltages using a FEMTO DHPA-100 amplifier.

Supporting Information

Supporting Information is available from the Wiley Online Library or from the author.

Acknowledgements

The authors acknowledge financial support by the German Science Foundation (DFG) through the doctoral training center “Photophysics of Synthetic and Biological Multichromophoric Systems” (GRK1640), the Bavarian State Ministry of Education, Science and the Arts through the Collaborative Research Network “Solar Technologies go Hybrid” (SolTech), and by the EU-Marie-Sklodowska-Curie-ITN Network INFORM. S.P. thanks IISc for MALDI and NMR Research Centre facility. T.M. thanks IISc for a Senior Research Fellowship. S.P. thanks Department of Science and Technology, India for Swarnajayanti fellowship. Furthermore, F.-J.K. was supported by the Elite Network Bavaria (ENB) in the framework of the Elite Study Program “Macromolecular Science”. The authors are also very grateful for helpful discussions with Dr. S. Tscheuschner.

Conflict of Interest

The authors declare no conflict of interest.

Keywords

autoionization, C₆₀, charge transfer states, logic operations, thin films

Received: August 15, 2018

Revised: September 7, 2018

Published online:

- [1] A. Iqbal, M. Jost, R. Kirchmayr, J. Pfenninger, A. Rochat, O. Wallquist, *Bull. Soc. Chim. Belg.* **1988**, 97, 615.
- [2] Z. M. Hao, A. Iqbal, *Chem. Soc. Rev.* **1997**, 26, 203.
- [3] R. Lenz, O. Wallquist, *Surf. Coat. Int., Part B* **2002**, 85, 19.
- [4] O. Wallquist, R. Lenz, *High Performance Pigments*, Wiley-VCH, Germany **2009**.

- [5] C. J. Mueller, M. Brendel, P. Ruckdeschel, J. Pflaum, M. Thelakkat, *Adv. Energy Mater.* **2015**, *5*, 1500914.
- [6] C. J. Mueller, C. R. Singh, M. Fried, S. Huettnner, M. Thelakkat, *Adv. Funct. Mater.* **2015**, *25*, 2725.
- [7] M. Grzybowski, D. T. Gryko, *Adv. Opt. Mater.* **2015**, *3*, 280.
- [8] T. Potrawa, H. Langhals, *Chem. Ber.* **1987**, *120*, 1075.
- [9] G. Colonna, T. Pilati, F. Rusconi, G. Zecchi, *Dyes Pigm.* **2007**, *75*, 125.
- [10] C. B. Nielsen, M. Turbiez, I. McCulloch, *Adv. Mater.* **2013**, *25*, 1859.
- [11] A. Pickett, M. Torkkeli, T. Mukhopadhyay, B. Puttaraju, A. Laudari, A. E. Lauritzen, O. Bikondoa, J. Kjølstrup-Hansen, M. Knaapila, S. Patil, S. Guha, *ACS Appl. Mater. Interfaces* **2018**, *10*, 19844.
- [12] W. W. Li, K. H. Hendriks, M. M. Wienk, R. A. J. Janssen, *Acc. Chem. Res.* **2016**, *49*, 78.
- [13] C. Kanimozhi, N. Yaacobi-Gross, E. K. Burnett, A. L. Briseno, T. D. Anthopoulos, U. Salzner, S. Patil, *Phys. Chem. Chem. Phys.* **2014**, *16*, 17253.
- [14] G. Gelinck, P. Heremans, K. Nomoto, T. D. Anthopoulos, *Adv. Mater.* **2010**, *22*, 3778.
- [15] A. J. Kronemeijer, E. Gili, M. Shahid, J. Rivnay, A. Salleo, M. Heeney, H. Sirringhaus, *Adv. Mater.* **2012**, *24*, 1558.
- [16] X. H. Liu, G. F. Dong, L. Duan, L. D. Wang, Y. Qiu, *J. Mater. Chem.* **2012**, *22*, 11836.
- [17] H. H. Xu, J. Li, B. H. K. Leung, C. C. Y. Poon, B. S. Ong, Y. T. Zhang, N. Zhao, *Nanoscale* **2013**, *5*, 11850.
- [18] G. M. Lin, Y. W. Lin, R. L. Cui, H. Huang, X. H. Guo, C. Li, J. Q. Dong, X. F. Guo, B. Y. Sun, *J. Mater. Chem. C* **2015**, *3*, 10793.
- [19] Y. L. Kim, H. Y. Jung, S. Park, B. Li, F. Z. Liu, J. Hao, Y. K. Kwon, Y. J. Jung, S. Kar, *Nat. Photonics* **2014**, *8*, 239.
- [20] X. D. Gao, G. T. Fei, Y. Zhang, L. D. Zhang, Z. M. Hu, *Adv. Funct. Mater.* **2018**, 1802288.
- [21] T. D. Anthopoulos, *Appl. Phys. Lett.* **2007**, *91*, 113513.
- [22] H. Sirringhaus, *Adv. Mater.* **2009**, *21*, 3859.
- [23] A. Salleo, M. L. Chabinyc, M. S. Yang, R. A. Street, *Appl. Phys. Lett.* **2002**, *81*, 4383.
- [24] J. Zaumseil, H. Sirringhaus, *Chem. Rev.* **2007**, *107*, 1296.
- [25] T. Hahn, S. Tscheuschner, C. Saller, P. Strohriegel, P. Boregowda, T. Mukhopadhyay, S. Patil, D. Neher, H. Bässler, A. Köhler, *J. Phys. Chem. C* **2016**, *120*, 25083.
- [26] W. Tress, K. Leo, M. Riede, *Phys. Rev. B* **2012**, *85*, 155201.
- [27] W. Tress, in *Organic Solar Cells – Theory, Experiment and Device Simulation*, (Eds: R. Hull, C. Jagadish, R. M. Osgood, J. Parisi, T.-Y. Seong, S.-i. Uchida, Z. M. Wang), Springer, New York **2014**, p. 474.
- [28] S. Kazaoui, N. Minami, Y. Tanabe, H. J. Byrne, A. Eilmers, P. Petelenz, *Phys. Rev. B* **1998**, *58*, 7689.
- [29] J. Meyer, S. Hamwi, M. Kroger, W. Kowalsky, T. Riedl, A. Kahn, *Adv. Mater.* **2012**, *24*, 5408.
- [30] M. Kröger, S. Hamwi, J. Meyer, T. Riedl, W. Kowalsky, A. Kahn, *Appl. Phys. Lett.* **2009**, *95*, 123301.
- [31] D. J. Wehenkel, L. J. A. Koster, M. M. Wienk, R. A. J. Janssen, *Phys. Rev. B* **2012**, *85*, 125203.
- [32] R. Könenkamp, G. Priebe, B. Pietzak, *Phys. Rev. B* **1999**, *60*, 11804.
- [33] V. D. Mihailtchi, *Vol. Doctoral Thesis*, University of Gronigen, **2005**.
- [34] B. P. Rand, J. G. Xue, S. Uchida, S. R. Forrest, *J. Appl. Phys.* **2005**, *98*, 124902.
- [35] T. Mukhopadhyay, B. Puttaraju, P. Roy, J. Dasgupta, A. Meyer, A. Rudnick, S. Tscheuschner, F. J. Kahle, A. Köhler, S. Patil, *Chem. - Eur. J.* **2017**, *23*, 13718.

**ADVANCED
FUNCTIONAL
MATERIALS**

Supporting Information

for *Adv. Funct. Mater.*, DOI: 10.1002/adfm.201805684

**Organic Bidirectional Phototransistors Based on
Diketopyrrolopyrrole and Fullerene**

*Frank-Julian Kahle, Tobias Hahn, Tushita Mukhopadhyay,
Boregowda Puttaraju, Satish Patil, and Anna Köhler**

Supporting Information

Organic Bidirectional Phototransistors Based on Diketopyrrolopyrrole and Fullerene

Frank-Julian Kahle¹, Tobias Hahn¹, Tushita Mukhopadhyay², Boregowda Puttaraju², Satish Patil², and Anna Köhler^{1,3}*

¹ *Soft Matter Optoelectronics, University of Bayreuth, 95440 Bayreuth, Germany*

² *Solid State and Structural Chemistry Unit, Indian Institute of Science, Bangalore-560012, India*

³ *Bayreuth Institute of Macromolecular Science (BIMF), University of Bayreuth, 95440 Bayreuth, Germany*

**anna.koehler@uni-bayreuth.de*

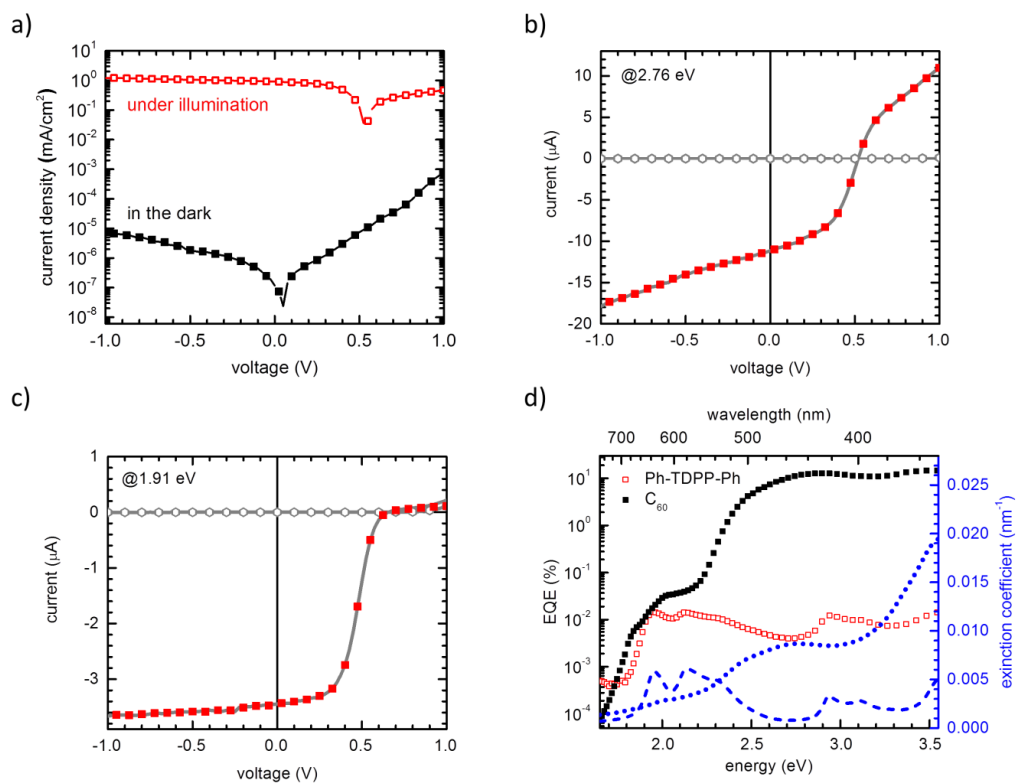


Figure S1: a) Exemplary J-V-characteristic of a Ph-TDPP-Ph/C₆₀ device with MoO₃ interlayer measured under 1 sun illumination (red open symbols) and in the dark (black filled squares). b) I-V-characteristic measured at $7 \frac{mW}{cm^2}$ and an excitation energy of 2.76 eV. c) Same as in b) but at an excitation energy of 1.91 eV. Dark (light grey circles) and photocurrent contribution (red filled squares) to the total current (grey solid line) are explicitly shown. c) Left axis: EQE spectra of Ph-TDPP-Ph and C₆₀ single layer devices measured under short circuit conditions. Right axis: Absorption spectra of Ph-TDPP-Ph (dashed blue) and C₆₀ (dotted blue).

Comment on the definition of the photocurrent

In this study, the term “photocurrent” is defined as the difference between the total current measured with and without light exposure. According to Wehenkel et al.¹, the direct identification of the difference between the current under illumination and in the dark with a photogenerated current is only justified, when the voltage drop across the series resistance R_s of the electrodes can be neglected. This is the case for low injection currents which are typical under reverse bias. Under forward bias, however, injection usually dominates the current above V_{oc} and the effective voltage across the active layer may actually be lower due to the voltage drop across R_s . Yet, as in our case the dark current is much lower than the current under illumination, no further correction is needed here.

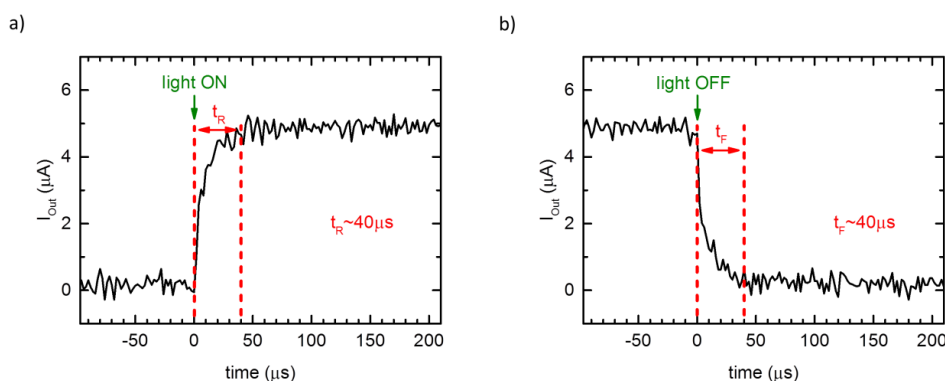


Figure S2: Response times for an AND-Gate when the light is turned a) ON and b) OFF. The total response time is given by the sum of rise (t_R) and fall time (t_F).

Further details about the optoelectronic mechanism

Intensity dependent I-V-measurements

Figure S3a-c display intensity dependent I-V-characteristics of devices with MoO₃ interlayer recorded at a) 3.54 eV, b) 2.76 eV, and c) 1.91 eV, i.e. above and below 2.25 eV, respectively. While the shape of the curves measured at 2.76 eV and 3.54 eV does not change with illumination intensity, a pronounced S-shape emerges with increasing intensity at 1.91 eV. Furthermore, a considerable net photocurrent is present when illuminating the device with 2.76 eV or 3.54 eV light, whereas it is nearly vanishing for 1.91 eV (see also Figure 2b, S1b and S1c).

In order to get an idea about the dissociation processes happening in the device it is convenient to convert the monochromatic I-V-data into field dependent EQE (**Figure S3d**).²⁻⁴ An estimation of the electric field E is simply calculated via $E = \frac{V_{appl} - V_0}{d}$, where V_{appl} is the externally applied voltage, V_0 denotes the compensation voltage and d is the thickness of the active layer of the device. Following the approach of Schwarz et al. presented in Ref.³ we obtain saturation field strengths F_{sat} in the range of $3 \cdot 10^4 - 5 \cdot 10^4 \frac{V}{cm}$. According to the work of Schwarz et al., F_{sat} can be regarded as a measure of the ease of dissociation of charge transfer (CT) states at the D/A interface.³ For 1.91 eV, i.e. below 2.25 eV, we obtain a very well defined saturation regime, as already expected from EQE data, whereas at energies above 2.25 eV an additional field dependence emerges at higher electric fields, implying a further exciton dissociation process. The same observations regarding the shape of the I-V-curves and the saturation field strength for different energies also apply to devices with PEDOT:PSS instead of MoO₃ (**Figure S4**).

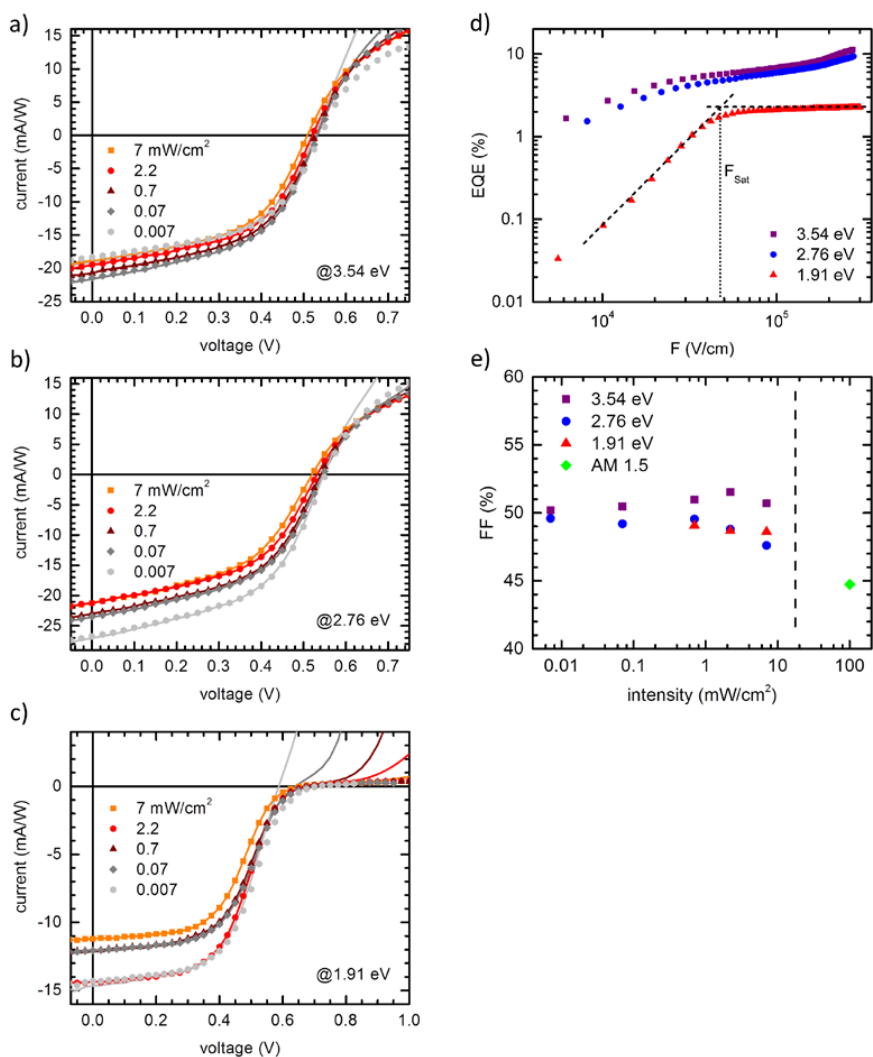


Figure S3: Intensity dependent I-V-characteristics of Ph-TDPP-Ph/C₆₀ bilayer devices with MoO₃ interlayer measured at a) 3.54 eV, b) 2.76 eV, and c) 1.91 eV. The respective total currents at the indicated intensities are drawn as solid lines, whereas the associated photocurrents are depicted as filled symbols of the same colour. d) Field dependent EQE for excitation energies of 3.54 eV, 2.76 eV and 1.91 eV. The intersection of the two dashed tangents indicates the saturation field strength F_{Sat} . e) Intensity dependence of the FF for the same energies as in d).

Finally, the degree and kind of recombination present in the device may be addressed via the intensity dependence of the fill factor (FF).⁵ The FF as function of illumination intensity is displayed in **Figure S3e** for excitation energies of 3.54 eV, 2.76 eV and 1.91 eV. For reference

also the FF obtained under AM1.5 conditions is given (see also main text). Due to the very low current at 1.91 eV, the FF for the two lowest intensities was omitted, as V_{oc} is largely dominated by the dark current in this case. Overall, we observe only small changes in the range of $\pm 2\%$, meaning that the FF is basically independent of intensity for all three wavelengths. The absolute value is about 50% up to an intensity of $7 \frac{mW}{cm^2}$. Under solar conditions (AM1.5) the FF is slightly lower (45%). Devices with PEDOT:PSS as HIL/HTL feature overall smaller values for FF under both monochromatic illumination as well as sunlight conditions (Figures S1a and S4b-d).

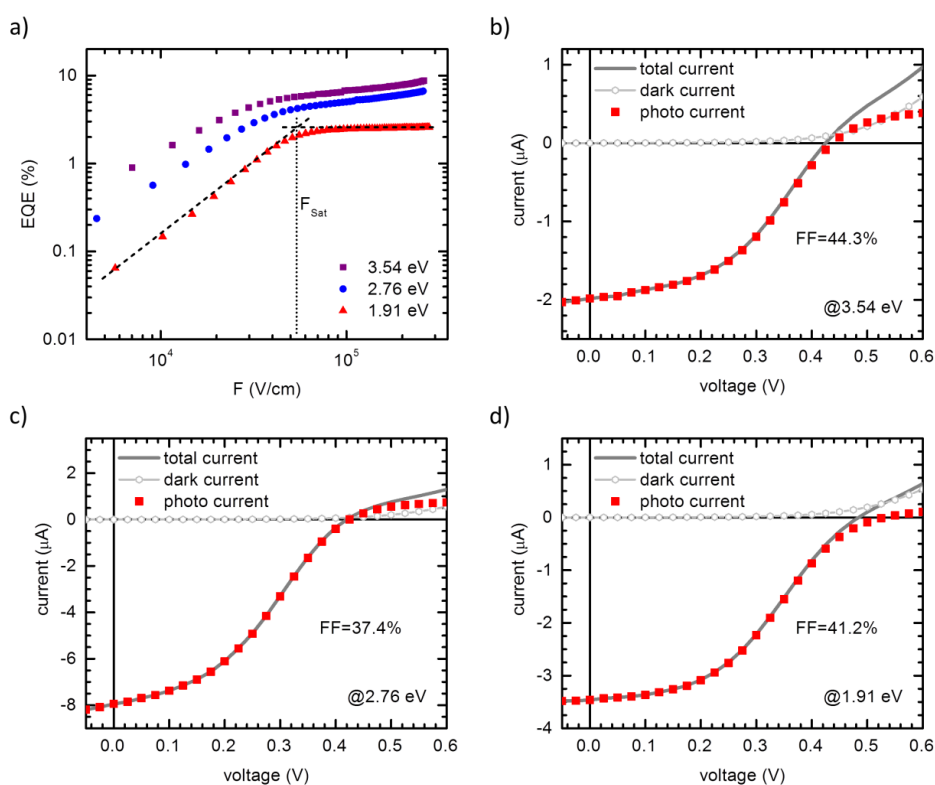


Figure S4: a) Field dependent EQE for excitation energies of 3.54 eV, 2.76 eV and 1.91 eV for PEDOT:PSS/Ph-TDPP-Ph/ C_{60} devices. The intersection of the two dashed tangents indicates the saturation field strength F_{Sat} . b) Corresponding I-V-characteristic measured at $7 \frac{mW}{cm^2}$ and an excitation energy of b) 3.54 eV, c) 2.76 eV, and d) 1.91 eV. Dark (light grey circles) and photocurrent contribution (red filled squares) to the total current (grey solid line) are explicitly shown.

From the presence of a defined saturation regime and the small F_{Sat} derived from field dependent EQE at 1.91 eV, we can conclude that all CT states are easily dissociated at the D/A interface and the resulting charges are separated efficiently. This is a result of good transport properties as well as maybe delocalization of the charge carriers in the donor or the acceptor or even both.^{3-4, 6-10} Unlike for 1.91 eV, an additional field dependence appeared at higher electric fields at excitation energies above 2.25 eV. According to Hahn et al. this can be attributed to an additional splitting of CT states generated in the bulk of C_{60} .¹¹ This autoionization process is also the reason for the considerable EQE observed for C_{60} single layer devices. With this in mind, the EQE spectrum at +1 V can be easily assigned to the intrinsic charge carrier generation in C_{60} .¹¹ The independence of the FF on illumination intensity for devices with MoO_3 interlayer indicates that no bimolecular recombination is present in these devices.⁵

Presence of a hole injection barrier

When replacing MoO_3 with PEDOT:PSS, the dark current is overall at least two orders of magnitude higher (**Figure S5**). Undoubtedly, this effect is related to the presence of a considerable hole injection barrier in the case of MoO_3 .

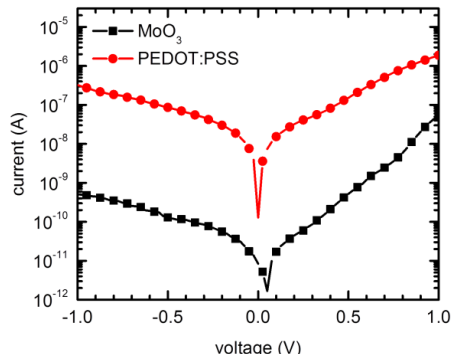


Figure S5: Dark current characteristics of Ph-TDPP-Ph/ C_{60} devices with either MoO_3 (black squares) or PEDOT:PSS (red circles) as anode interlayer.

Moreover, the presence of an injection barrier in the case of a MoO_3 interlayer is experimentally verified by the characteristic intensity dependent behavior of the J-V curves measured at 1.91 eV (Figure S3c).¹²⁻¹³ A similar effect is not observed for energies above 2.25 eV, as in this case the behavior is dominated by a considerable net photocurrent in forward direction that is still present at intensities as low as $0.007 \frac{\text{mW}}{\text{cm}^2}$. Both observations, explain the low dark current in

devices with MoO₃ interlayer compared to those with PEDOT:PSS interlayer, where the barrier is obviously considerably lower. The latter is also reflected in the overall smaller EQE (**Figure S6a**) and the lower FF (**Figure S4b-d** and **S6b**) in samples with PEDOT:PSS, because a larger density of injected charge carriers enhances bimolecular recombination .

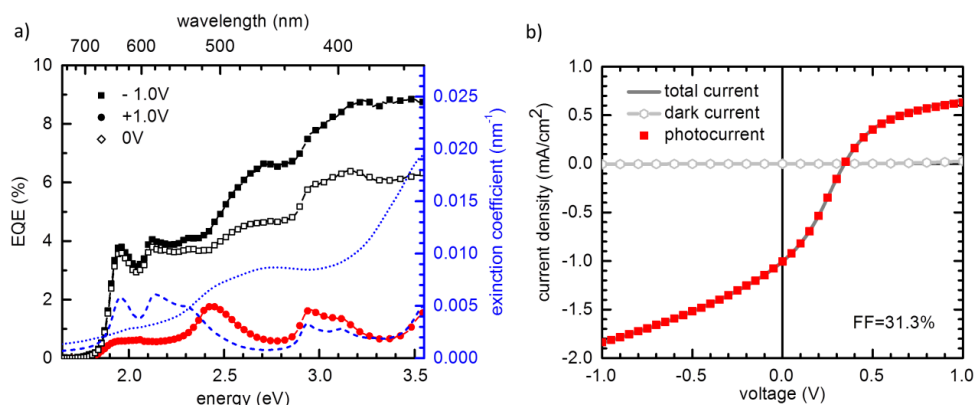


Figure S6: a) Left axis: Series of voltage dependent EQE spectra of PEDOT:PSS/Ph-TDPP-Ph/C₆₀-Devices; Right axis: Absorption spectra of Ph-TDPP-Ph (dashed blue) and C₆₀ (dotted blue). b) Exemplary J-V-characteristic of a Ph-TDPP-Ph/C₆₀ device with PEDOT:PSS interlayer measured at 1 sun illumination. Dark (light grey circles) and photocurrent contribution (red filled squares) to the total current (grey solid line) are explicitly shown.

Summary

We had seen that

- (1) A significant photocurrent in forward direction is only observed for energies above 2.25 eV, i.e. when charge carriers are generated within the C₆₀ bulk due to autoionization of CT-states.
- (2) Ph-TDPP-Ph does not feature any significant intrinsic photogeneration ability.
- (3) Ph-TDPP-Ph¹⁴⁻¹⁶ and C₆₀¹⁷ feature sufficiently good charge transport properties to ensure good extraction and avoid additional losses due to low or imbalanced mobilities between donor and acceptor.⁸
- (4) Under reverse bias, dissociation of CT states at the D/A interface is efficient.
- (5) A significant hole injection barrier is present in the case of a MoO₃ interlayer, which effectively suppresses the dark current in the devices.

In view of these observations, the presence of a net photocurrent can be explained in terms of an enhanced recombination current close to the cathode and the D/A-interface due to the photoinduced increase of minority charge carrier densities at the respective interface (holes at the cathode, electrons at the acceptor side of the D/A-interface),^{1, 18} as discussed in the main text.

In the light of this explanation, the significantly reduced photocurrent at +1V for devices with PEDOT:PSS interlayer (Figure S6a) compared to those with MoO₃ interlayer (Figure 4a) can be attributed to a higher dark injection current for PEDOT:PSS because of a lower injection barrier for holes. This in turn leads to increased bimolecular recombination due to the higher charge carrier density. In contrary, for MoO₃ interlayers, that introduce a larger hole injection barrier, the dark current is much lower resulting in significantly less bimolecular recombination so that photogenerated charge carriers in the C₆₀ bulk can effectively contribute to the measured photocurrent.¹ A slightly more detailed discussion of the EQE at +1V of PEDOT:PSS containing devices is given below.

Comment on the EQE spectra recorded at +1V (with PEDOT:PSS interlayer)

The EQE spectrum at +1V follows the absorption of Ph-TDPP-Ph down to about 2.4eV, i.e. close the autoionization threshold of CTS in the C₆₀ bulk at 2.25 eV (Figure S6a). Below this energy, the extracted EQE values have to be treated with caution, as the measured current in the dark and under illumination were of the same order. This fact results in larger errors when calculating the photo current from the difference between the illumination current and the dark current, particularly below 2.25 eV.

The fact that the EQE roughly follows the absorption spectrum of Ph-TDPP-Ph indicates the presence of a displacement current that is caused by the recombination of charge carriers, especially electrons, from the C₆₀ side at the D/A-interface with excitons generated by photon absorption in the bulk of Ph-TDPP-Ph. The remaining electron from Ph-TDPP-Ph may then be transported to PEDOT:PSS, where it can recombine with an injected hole or be extracted. Consequently, the additional recombination between excitons in Ph-TDPP-Ph and electrons from C₆₀ is limited on the one hand by the number of excitons generated in Ph-TDPP-Ph, as well as the number of charges generated from CT states in the C₆₀ bulk via autoionization. This mechanism may explain the fact that the additional displacement current only follows the absorption of Ph-TDPP-Ph down to an energy where autoionization of CT states in the C₆₀ bulk is still possible.

The remaining contribution below 2.25 eV could be due to exciton diffusion to the D/A-interface or the ITO/MoO₃ electrode and a subsequent (inefficient) splitting, as no significant intrinsic dissociation was observed in single devices of Ph-TDPP-Ph.

Energy levels of Ph-TDPP-Ph and C₆₀

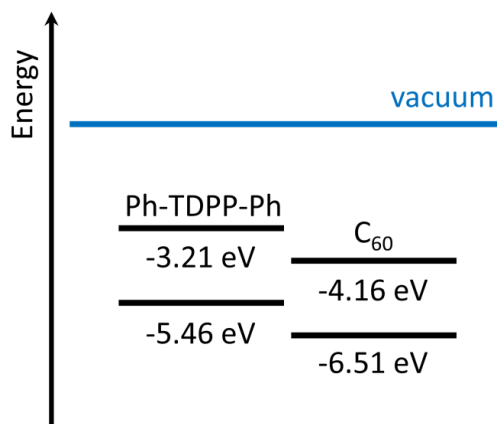


Figure S7: Energy levels of Ph-TDPP-Ph and C₆₀

The variation in frontier molecular orbital energy levels of Ph-TDPP-Ph was investigated by cyclic voltammetry measurements (CV) at a scan rate of 0.1 V/s. Platinum electrodes were used as working and counter electrode; where Ag/ Ag⁺ have been employed as the reference electrode. Energy levels have been calibrated with respect to an internal standard ferrocene/ferrocenium redox couple. Energy levels of C₆₀ are taken from literature and were measured via UPS/IPES.¹⁹

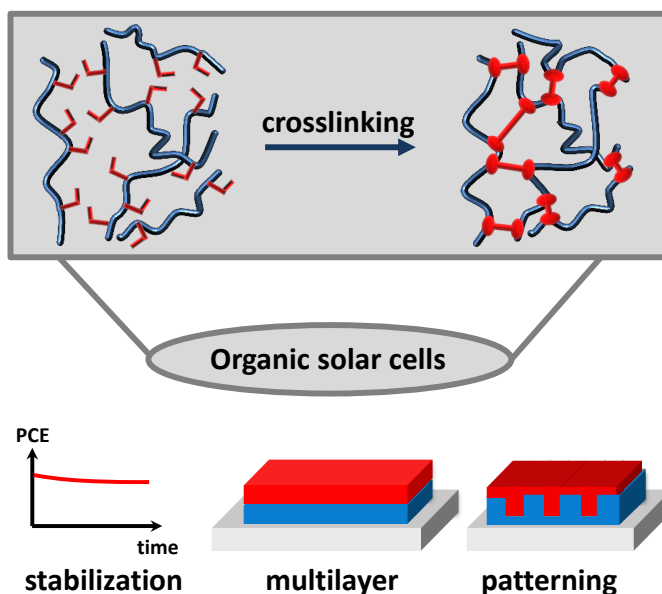
References

- 1 D. J. Wehenkel, L. J. A. Koster, M. M. Wienk, R. A. J. Janssen, *Phys Rev B* **2012**, *85*, 125203.
- 2 T. Hahn, J. Geiger, X. Blase, I. Duchemin, D. Niedzialek, S. Tscheuschner, D. Beljonne, H. Bässler, A. Köhler, *Adv Funct Mater* **2015**, *25*, 1287.
- 3 C. Schwarz, H. Bässler, I. Bauer, J. M. Koenen, E. Preis, U. Scherf, A. Köhler, *Adv Mater* **2012**, *24*, 922.
- 4 C. Schwarz, S. Tscheuschner, J. Frisch, S. Winkler, N. Koch, H. Bässler, A. Köhler, *Phys Rev B* **2013**, *87*, 155205.
- 5 T. Hahn, S. Tscheuschner, F. J. Kahle, M. Reichenberger, S. Athanasopoulos, C. Saller, G. C. Bazan, T. Q. Nguyen, P. Strohriegl, H. Bässler, A. Köhler, *Adv Funct Mater* **2017**, *27*, 1604906.
- 6 S. Tscheuschner, H. Bässler, K. Huber, A. Köhler, *J Phys Chem B* **2015**, *119*, 10359.
- 7 S. Athanasopoulos, S. Tscheuschner, H. Bässler, A. Köhler, *J Phys Chem Lett* **2017**, *8*, 2093.
- 8 W. Tress, K. Leo, M. Riede, *Phys Rev B* **2012**, *85*, 155201.
- 9 S. Gélinas, A. Rao, A. Kumar, S. L. Smith, A. W. Chin, J. Clark, T. S. van der Poll, G. C. Bazan, R. H. Friend, *Science* **2014**, *343*, 512.
- 10 B. Bernardo, D. Cheyns, B. Verreert, R. D. Schaller, B. P. Rand, N. C. Giebink, *Nat Commun* **2014**, *5*, 3245.
- 11 T. Hahn, S. Tscheuschner, C. Saller, P. Strohriegl, P. Boregowda, T. Mukhopadhyay, S. Patil, D. Neher, H. Bässler, A. Köhler, *J Phys Chem C* **2016**, *120*, 25083.
- 12 W. Tress, in *Organic Solar Cells: Theory, Experiment, and Device Simulation*, Springer, New York 2014, 474.
- 13 W. Tress, O. Inganäs, *Sol Energ Mat Sol C* **2013**, *117*, 599.
- 14 R. Könenkamp, G. Priebe, B. Pietzak, *Phys Rev B* **1999**, *60*, 11804.
- 15 V. D. Mihailetschi, Vol. Doctoral Thesis, University of Gronigen, 2005.
- 16 B. P. Rand, J. G. Xue, S. Uchida, S. R. Forrest, *J Appl Phys* **2005**, *98*, 124902.
- 17 A. Pickett, M. Torkkeli, T. Mukhopadhyay, B. Puttaraju, A. Laudari, A. E. Lauritzen, O. Bikondoa, J. Kjelstrup-Hansen, M. Knaapila, S. Patil, S. Guha, *Acs Appl Mater Inter* **2018**, *10*, 19844.
- 18 W. Tress, in *Organic Solar Cells - Theory, Experiment and Device Simulation*, Springer, New York 2014, 474.
- 19 F. J. Kahle, C. Saller, S. Olthof, C. Li, J. Lebert, S. Weiß, E. M. Herzig, S. Hüttner, K. Meerholz, P. Strohriegl, A. Köhler, *J Phys Chem C* **2018**, accepted.

Appendix

A

Crosslinked Semiconductor Polymers for Photovoltaic Applications



Frank-Julian Kahle, Christina Saller, Anna Köhler, and Peter Strohriegl

Published in
Adv. Energy Mater., **2017**, 7, 1700306
(DOI: 10.1002/aenm.201700306)

Copyright ©2017 by John Wiley Sons, Inc.
Reprinted by permission of John Wiley & Sons, Inc.

Crosslinked Semiconductor Polymers for Photovoltaic Applications

Frank-Julian Kahle, Christina Saller, Anna Köhler, and Peter Strohrriegl*

Organic solar cells (OSCs) have achieved much attention and meanwhile reach efficiencies above 10%. One problem yet to be solved is the lack of long term stability. Crosslinking is presented as a tool to increase the stability of OSCs. A number of materials used for the crosslinking of bulk heterojunction cells are presented. These include the crosslinking of low bandgap polymers used as donors in bulk heterojunction cells, as well as the crosslinking of fullerene acceptors and crosslinking between donor and acceptor. External crosslinkers often based on multifunctional azides are also discussed. In the second part, some work either leading to OSCs with high efficiencies or giving insight into the chemistry and physics of crosslinking are highlighted. The diffusion of low molar mass fullerenes in a crosslinked matrix of a conjugated polymer and the influence of crosslinking on the carrier mobility is discussed. Finally, the use of crosslinking to make stable interlayers and the solution processing of multilayer OSCs are discussed in addition to presentation of a novel approach to stabilize nanoimprinted patterns for OSCs by crosslinking.

1. Introduction

In recent years, the research on solar cells from organic semiconducting materials has made fast progress.^[1] Organic solar cells (OSCs) are an interesting alternative to the widely used silicon solar cells because of their unique properties. These include low weight, cost-efficient fabrication via solution processing, and the ability for application on flexible substrates.^[2] The active layer of an OSC is composed of an electron donor and an electron acceptor. The most promising approach is the bulk heterojunction (BHJ) solar cell that is composed of a blend of the two materials. In many cases, electron-donating polymers and electron-accepting fullerenes are applied.^[1b] Using different low bandgap polymers like NT812/PC₇₁BM^[3] and

PTB7-Th/PC₇₁BM,^[4] high efficiencies of 10.33% and 10.95% could be achieved, respectively.

Most BHJ solar cells containing a donor polymer and a fullerene acceptor are realized by solution processing. In contrast, vacuum evaporation allows the fabrication of solar cells with a large number of layers by subsequent deposition of different small molecules. Using this technique, BHJ as well as planar heterojunction (PHJ) solar cells, multilayer solar cells, and tandem solar cells can be fabricated. The advantage of this method is the possibility to optimize the properties of the different layers separately. The highest reported efficiency of a polymer tandem solar cell made under laboratory conditions is 11.3%.^[5] Companies announced multilayer OSCs with efficiencies up to 13.2%.^[6]

As the exciton diffusion length in OSCs is about 10 nm, a controlled morphology of the active layer in combination with direct charge percolation paths towards the electrodes is of vital importance for the performance of organic solar cells. One possible solution for that issue are nanostructured active layers, for example realized by nanoimprinting.^[7] By means of this method, an efficiency of 4.4% could be achieved with a nanostructured poly-3-hexylthiophene (P3HT) layer and [6,6]-phenyl-C61-butyric acid methyl ester (PCBM).^[8] In this case, the nanoimprinting additionally enforces a favorable chain alignment of the polymer.

However, a major disadvantage of OSCs is their lack of stability. Device instability arises from different reasons such as thermal, chemical or mechanical stress, and light exposure.^[9] Encapsulation of the device can prevent degradation by water or oxygen.^[10] One major issue regarding thermal degradation of BHJ solar cells is the diffusion of low molecular weight fullerenes and subsequent formation of large fullerene aggregates. This results in a decreased device performance.^[11]

Extending the concept of multilayer structures from evaporated low molar mass compounds to polymers is difficult as they are solution processed. The underlying polymer layer would be dissolved by the deposition of a second polymer solution on top. This can be prevented by the use of orthogonal solvents^[12] or the introduction of inorganic interlayers, especially in the field of tandem devices.^[5a,13] Orthogonal solvents are also used to prevent nanoimprinted patterns from dissolution.^[7,8]

One approach to overcome the problems mentioned above is the application of crosslinkable materials.^[14] The basic advantage applying crosslinkable materials is the “freezing”

F.-J. Kahle, Prof. A. Köhler
Experimental Physics II
University of Bayreuth
95440 Bayreuth, Germany
C. Saller, Prof. P. Strohrriegl
Macromolecular Chemistry I
University of Bayreuth
95440 Bayreuth, Germany
E-mail: peter.strohrriegl@uni-bayreuth.de

Prof. A. Köhler, Prof. P. Strohrriegl
Bayreuth Institute of Macromolecular Science (BIMF)
University of Bayreuth
95440 Bayreuth, Germany

DOI: 10.1002/aenm.201700306

of the initial morphology. This principle is illustrated using the example of a crosslinkable polymer in **Figure 1a**. Before crosslinking, the conjugated polymer is soluble and can be solution processed. Upon crosslinking, covalent bonds, which

connect the polymer chains, are formed. The resulting densely crosslinked conjugated polymer network is insoluble and its morphology is frozen. Initiation of the crosslinking process is possible via a (photo)initiator, exposure to UV-light or heat.

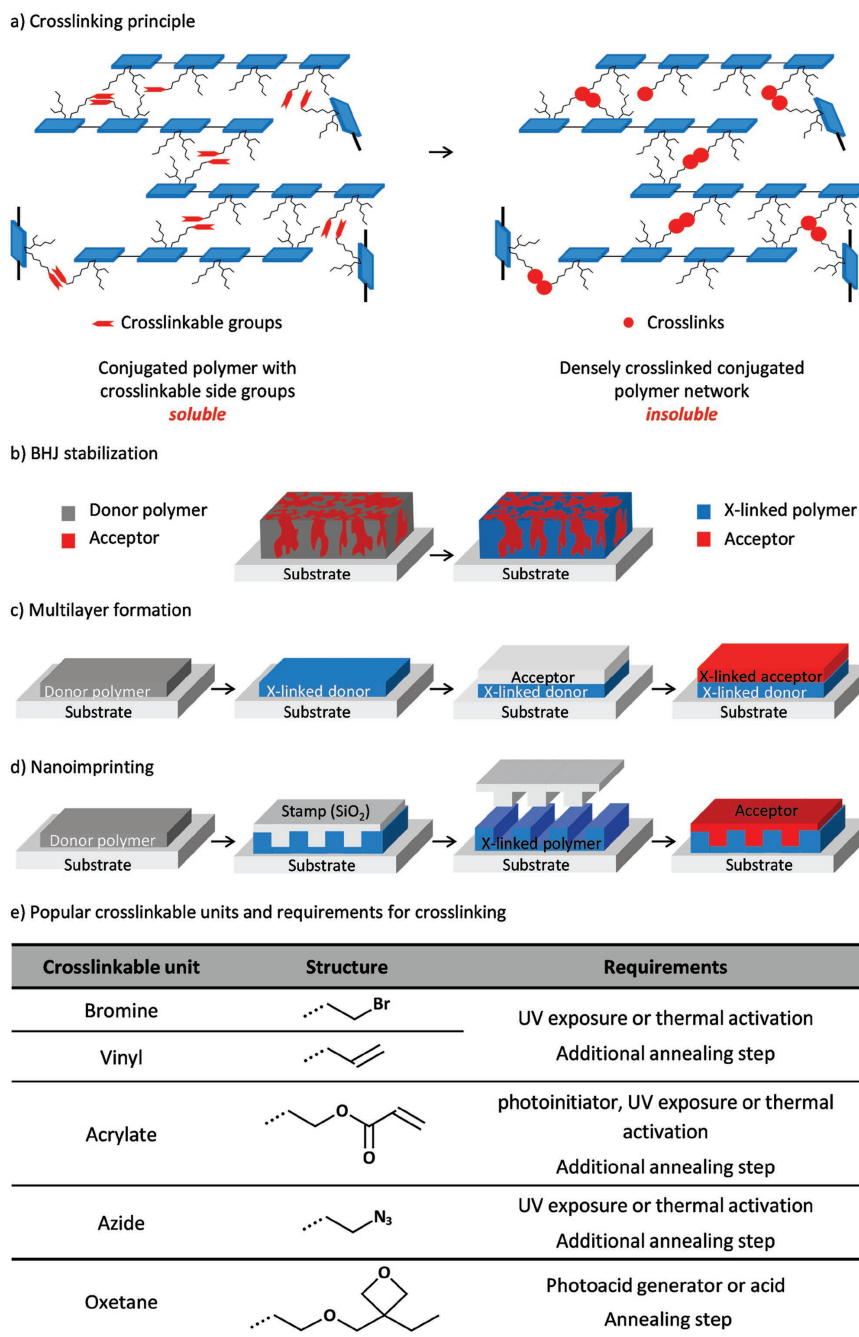


Figure 1. a) Schematic drawing of the formation of an insoluble network by crosslinking chains of a conjugated polymer. b) Stabilization of a BHJ morphology by crosslinking of the donor polymer. c) Multilayer formation by application of a crosslinkable donor and a crosslinkable acceptor. d) Patterning via nanoimprinting of a crosslinkable donor polymer. e) Popular crosslinkable units and requirements for crosslinking.

Crosslinking enables the realization of different concepts regarding organic solar cells. The first one is the stabilization of BHJ morphologies and is shown in Figure 1b. In this example, the blend is made up of a crosslinkable donor polymer. After crosslinking, the donor polymer has become insoluble and the morphology is locked. Thus, the migration of low molecular mass acceptors such as PCBM is reduced, leading to a stabilization of the OSC. A second concept concerns the multilayer formation from solution-processed materials. Figure 1c depicts the process applying two crosslinkable materials. First, the crosslinkable donor polymer is spin-coated onto a substrate. Subsequent crosslinking in presence of an initiator renders the donor polymer insoluble. This allows the spin-coating of an acceptor solution on top of the donor layer without damaging or dissolving the underlying layer. More complex stacks can also be realized by applying further crosslinkable functional materials. Finally, the realization of patterned structures by nanoimprinting is presented in Figure 1d. The first step in this process is the deposition of a crosslinkable donor polymer on a substrate. The pattern is transferred to the polymer layer with a stamp. Subsequent crosslinking of the donor polymer leads to a pattern that is stabilized and completely insoluble. After removal of the stamp, an acceptor can be deposited via solution processing or vacuum evaporation on top of the pattern without damaging it.

In the following, the design strategies for crosslinkable materials as well as the most popular crosslinking units are presented.

2. Overview of the Chemistry of Crosslinkable Materials

Three approaches can be discriminated for the crosslinking of active layers. These include the crosslinking of the donor material or the acceptor material as well as crosslinking both the donor and acceptor.

A lot of research effort has been put into crosslinkable donor materials over the last years. In organic solar cells, polymers are frequently used as electron donor. The general approach is to attach crosslinkable units to the solubilizing side chains of the polymers. Bromine, vinyl, acrylate, azide, and oxetane groups are commonly used. Their molecular structure and requirements for the crosslinking procedure are summarized in Figure 1e.^[14b] Bromine, vinyl, acrylate, and azide functionalities are activated upon UV-light exposure or thermally and the crosslinking procedure can additionally implement an annealing step to ensure complete crosslinking. In addition to its benefits, crosslinking may cause some problems that differ between the functional units. Remaining bromine groups can negatively influence device properties such as the charge carrier mobility. For the crosslinking of acrylates, photoinitiators are often used. The residues of the photoinitiator decomposition remain in the polymer layer. The activation of azides results in the release of nitrogen and very reactive nitrene species are formed. Because of the high reactivity, the nitrenes may not only attack the polymer side chains, but also insert into the conjugated backbone. Oxetane crosslinking requires the presence of an acid source or prolonged thermal activation.^[15] An

annealing step is necessary to ensure complete crosslinking. The problems with acid activated crosslinking are acid residues or the counterions of the photoacid generators. In contrast to the radical crosslinking process applying for bromine, vinyl and acrylate, the cationic mechanism of oxetane allows crosslinking in the presence of radical scavenging materials such as fullerene.

The crosslinking groups shown in Figure 1e have been attached to a number of polymers. P3HT, a widely used conjugated donor polymer, has been modified with several crosslinkable units. Kim et al. presented the derivative P3HT-Br containing up to 20% of bromine units that can be photocrosslinked via UV-exposure.^[16] The chemical structure is shown in Figure 2. Both planar heterojunction (PHJ) and BHJ solar cells were prepared. An efficiency of 2.2% was reached for a polymer with 10% bromine in a PHJ geometry and 3.4% efficiency for the 5% bromine derivative in a BHJ geometry. Stability tests at 150 °C showed that the efficiency is stable upon crosslinking for PHJ solar cells for up to three days and for BHJ solar cells for up to two days. Vinyl functionalized P3HTNT that can be crosslinked thermally was used to realize BHJ cells and the stability was tested by annealing at 150 °C for 10 h (Figure 2).^[17] The crosslinked devices showed a better thermal stability than the non-crosslinked reference devices. This is confirmed by optical microscopy yet the formation of PCBM crystals could not be fully suppressed. A P3HT diblock copolymer consisting of a P3HT block and a polythiophene block with pendent acrylate units was synthesized by Ouhib et al. and crosslinked thermally (Figure 2).^[18] BHJ cells with the crosslinked polymer retained 85% of their initial efficiency after 165 h at 110 °C. In contrast, the P3HT reference devices exhibited a decrease to 65%. Kim et al. demonstrated the synthesis of a photo-crosslinkable P3HT-azide copolymer (Figure 2).^[19] Annealing at 150 °C for 40 h yielded thermally stable BHJ solar cells with 3.3% efficiency. Another crosslinking chemistry was presented by Brotas et al. who synthesized a P3HT copolymer with 10% oxetane functionalization (P3HT-oxetane, Figure 2).^[20] The oxetane group was crosslinked using UV-light in presence of a photoacid generator and a subsequent annealing step. The incorporation of the oxetane unit decreased the performance of BHJ cells to 1.1% compared to 1.9% for the non-functionalized P3HT cell. Crosslinking of the blend led to a further drop to 0.2%. However, this is balanced by an improved stability of the cells during illumination for 40 min.

Recently, the interest shifted from P3HT to low bandgap polymers that can harvest a large part of the sun's spectrum. Griffini et al. presented a crosslinkable PBDTTPD derivative with 16% and 33% bromine in the side chains, respectively (Figure 2).^[21] This was the first crosslinkable low bandgap polymer applied in BHJ solar cells. The devices composed of the polymer with 16% bromine containing repeat units were annealed for 72 h at 150 °C and finally exhibited a remarkably high efficiency of 4.6%, while the efficiency of the reference cell dropped from 5.2% to 3.9%. In 2012, the Krebs group presented a study in which the performances of OSCs from the low bandgap polymers TQ-x (Figure 2) with different crosslinkable groups were compared.^[22] TQ1 was modified either with an alkyl chain, a bromine, a vinyl, or an oxetane functionality. This work is discussed in more detail in the next

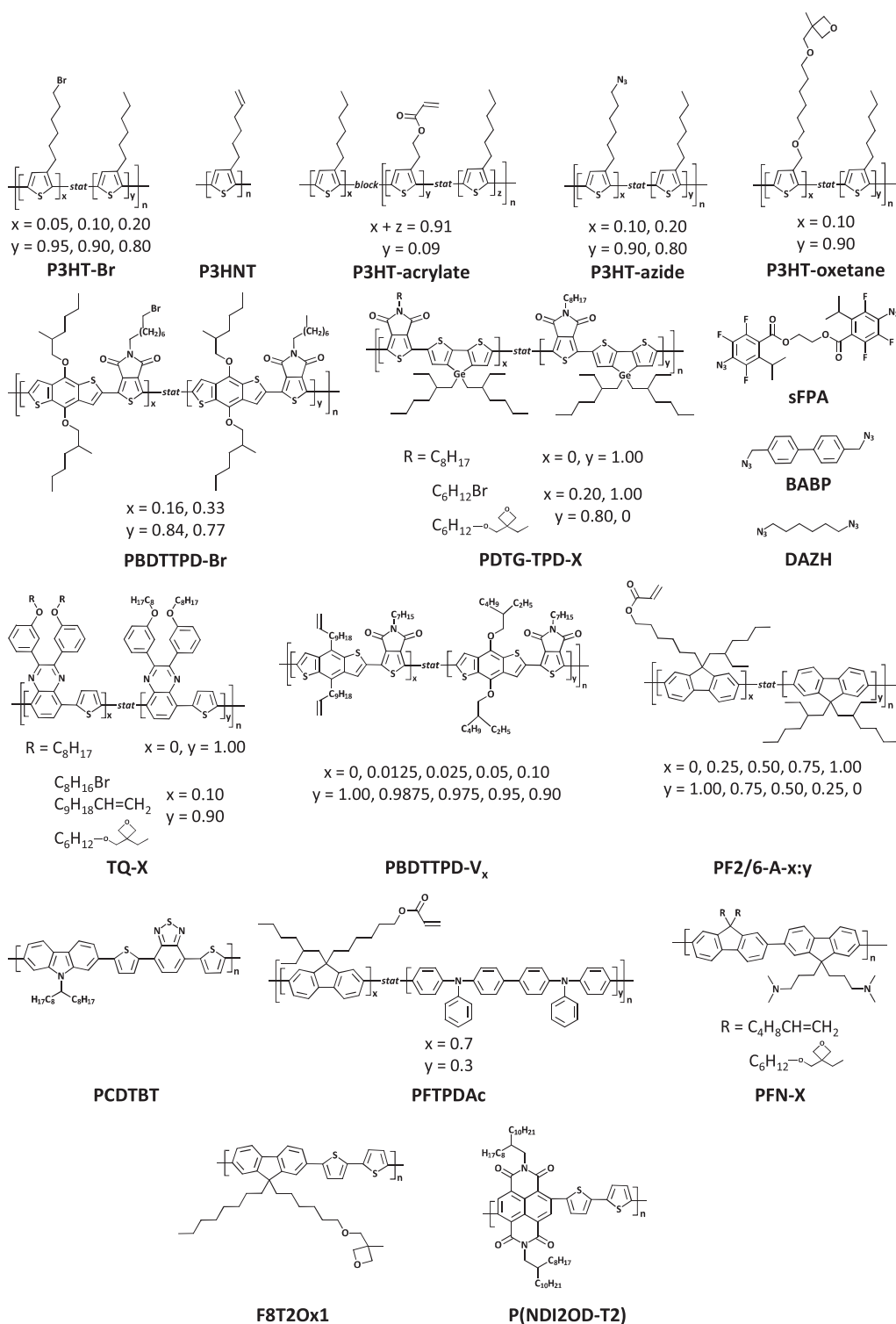


Figure 2. Crosslinkable semiconducting polymers and low molar mass crosslinkers. The chemical structures of the copolymers are drawn according to the IUPAC nomenclature, where -stat- means statistical and -block- denotes block copolymers.

section. Further work was performed on bromine containing low bandgap polymers,^[23] azide functionalized copolymers^[24] as well as on a series of PBT derivatives including bromine, azide, and vinyl units.^[25]

In the polymers discussed above, the crosslinkable groups are attached to the polymer side chain. Another option for the incorporation of a crosslinkable unit is the backbone itself. Bui et al. reported three different copolymers containing triple bonds in the polymer backbone.^[26] Two of them were tested as buffer layers in inverted OSCs for the interface modification of zinc oxide. Thereby, the crosslinking was performed by exposure of the polymer layers to UV-light. The increase of the hydrophobicity of the zinc oxide layer due to the crosslinked interlayer resulted in an improved efficiency of 3.1% compared to 2.7% for the reference cell.

A versatile approach for crosslinking without the need of functional groups is the use of small molecule crosslinkers. A prominent example was presented by Friend and co-workers. They added the reactive bis-nitrene crosslinker sFPA (Figure 2) to non-functionalized conjugated polymers.^[27] With this method, a PHJ solar cell with three polymer layers on top of each other was realized.^[28] The materials featured cascaded energy levels achieving an efficiency of 0.45%. In addition, P3HT was also crosslinked by the use of sFPA. Bilayer cells with PCBM as acceptor yielded 3.0% efficiency in comparison to 3.3% efficiency for the non-crosslinked reference.^[29] Derue et al. studied the crosslinking of fullerenes in blends with different donor polymers under mild conditions using the bis-azide BABP (Figure 2).^[30] 3.3% efficiency was achieved for a cell with P3HT. After 120 days at 85 °C, 90% of the initial efficiency could be retained. Regarding PTB7, an efficiency decrease from 5.8% to 4.6% was observed upon annealing for 16 h at 150 °C. PDPPTBT^[30] exhibited an initial value of 4.5%, which dropped to 3.0% when the cell was annealed for 15 h at 150 °C. In the group of McCulloch, SiDT-BT was crosslinked using the bis-azide DAZH (Figure 2), which improves the efficiency from 6.0% to 7.0%.^[31] Thermal aging for 130 h at 85 °C resulted in an efficiency of 4.1% for the crosslinked cell compared to 3.5% for the reference cell.

In addition to the crosslinking of donor polymers, crosslinkable fullerene derivatives were also investigated in the last years and are discussed in the reviews of Wantz et al. and Rumer et al.^[14]

3. Application of Crosslinking in Organic Photovoltaics

In the preceding section a number of polymers and different reactive groups used to make OSCs with crosslinked layers were presented. In a short review, however, it is not possible to cover all the work on crosslinked OSCs.^[14] Instead, we decided to highlight work that leads to efficient OSCs or that we believe is important for the understanding and the development of crosslinked solar cells. We begin with work on the stabilization of BHJ solar cells followed by a section on the use of crosslinked layers and multilayer OSCs and end with a short section on patterning.

As discussed above, there are several approaches of crosslinking in organic solar cells: donor to donor, acceptor

to acceptor, or donor to acceptor. In principal, all of the three approaches are capable of stabilizing the blend morphology in BHJ solar cells. Crosslinking of the donor is often used, as it is relatively easy and versatile and may be applied to a variety of material classes.^[14,18,22,25]

In an attempt to systematically assess the relation between different functional groups and the stability of the crosslinked OSCs, comparative studies were performed by several groups.^[22,25,32] Krebs and co-workers^[22] compared bromine-, azide-, vinyl-, and oxetane- functionalized derivatives of the low bandgap polymer TQ1 (Figure 2). Crosslinking via UV-illumination resulted in solvent resistant films and did not change the optical absorption spectra, therefore excluding damage to the π -conjugated polymer backbone. Photochemical and thermal stability was investigated using different experimental conditions for aging: dark versus illumination under 1 sun and ambient versus inert atmosphere. The observed stability enhancement was attributed to the suppression of morphological changes, that is fullerene aggregation, as confirmed by optical microscopy. Yet, the analysis of stability under the different experimental conditions did not result in a consistent correlation between polymer stability and the different functional groups used for crosslinking.

Heeney and co-workers^[32] compared derivatives of the low bandgap polymer PDTG-TPD with both bromine and oxetane functional groups (Figure 2). The pure polymers can both readily be crosslinked. Yet, in blends with fullerenes, crosslinking was only successful for the oxetane-containing PDTG-TPD derivative. This might be attributed to the radical scavenging ability of fullerenes^[33] preventing radical polymerization in the case of bromine. Moreover, efficiencies as high as 5.02% could be obtained with a relatively small number of oxetane units (20%). Finally, Heeney and co-workers found an increased thermal stability of the crosslinked BHJ cells on the timescale of 30 min.

Similar observations with regard to small amounts of functional groups were also made by several other groups.^[16,21,22,24,34] A noteworthy example is the work by Chen et al., who obtained a PCE of 6.06% using only 2.5% of crosslinkable vinyl-groups in PBDTPD- V_x (Figure 2) combined with PC₇₁BM, still retaining 91% of the efficiency after 40 h of annealing at 150 °C. This is among the highest PCEs reported for OPVs using crosslinked active layers.^[34]

In the context of oxetane functionalization, it is noteworthy that, although it is generally assumed that this mechanism requires the exposure to an acid,^[14,35] Knauer et al.^[15] showed that crosslinking via oxetane groups can be achieved by prolonged heating, yielding a fully crosslinked and long-term stable BHJ cell.

In general, this possibility of crosslinking without crosslinking additives is a great benefit, as possible remnant by-products, which could be detrimental for device performance, are avoided.^[14b,36] This issue was addressed by Kahle et al., who investigated the effect of crosslinking on the charge carrier mobility of acrylate functionalized PF2/6-A-xy (Figure 2) using MIS-CELIV measurements.^[36b] They showed that an amount of photoinitiator of 1 wt% could deteriorate charge transport in a PF2/6 polymer layer. This effect was especially pronounced in the case of a Ti-based initiator, leading to a reduction of hole

mobility by over two orders of magnitude due to the introduction of traps. On the other hand, when choosing appropriate conditions such as a small amount of Ti-free photoiniator (0.1 wt%) or even purely thermal crosslinking, no reduction in mobility compared to the respective non-crosslinked reference was observed.

In addition, Kahle et al. found a reduction of the mobility with increasing content of functional groups because of steric effects, implying that a smaller amount of functional groups may be advantageous for devices. This is in agreement with the results of Heeney and co-workers^[32] discussed above, who have shown that just 20% of crosslinkable groups result in sufficient device stabilization.

Apart from creating a 3D network of the donor polymer as a stable matrix for the fullerene acceptor, one can also follow the approach of directly crosslinking donor to acceptor. In this case, there are only a limited number of functional groups^[14a] available due to the electron scavenging properties of fullerene. The most suitable and common pathway to perform a controlled reaction between the donor and the acceptor is thermal crosslinking using azide-functionalized donor polymers.^[19,37]

A remarkable exception is the work of Tournebize and co-workers,^[38] who managed to link donor and acceptor without any additional functionalization using a blend of PCDTBT (Figure 2) and PC₇₁BM. The underlying mechanism was identified to be of photochemical origin and studied via accelerated artificial photoaging. It proceeds via scission of the bond between the N-atom of the carbazole units of PCDTBT and the alkyl side chain followed by reaction of the macroradicals with the fullerene. The formation of the covalent crosslinks first results in a decrease in PCE (“burn-in”) of about 25% of the initial value,^[39] but then leads to an impressive long-term stability and an expected average lifetime of PCDTBT/PCBM solar cells of about seven years, as reported by McGehee and co-workers (Figure 3).^[39] To the best of our knowledge this is the best long-term stability of polymer:fullerene blends reported to date. By performing additional thermal annealing and measuring

(light-induced) electron paramagnetic resonance ([L]EPR), it was shown that the crosslinking is mainly related to polymer crosslinking and not only due to a thermally reversible PCBM oligomerization.^[38]

The last possibility to suppress fullerene crystallization in a blend morphology is to directly crosslink functionalized fullerene derivatives.^[40] Yet, due to the electron scavenging properties of fullerenes and their ability to terminate radical reactions, only a limited number of functional groups may be used, and this approach is only rarely applied in BHJ stabilization.^[14a] In the emerging class of non-fullerene acceptors,^[41] no crosslinkable materials have been reported yet. We believe that such materials would be an interesting perspective for further research.

Instead of being a component of the BHJ layer, functionalized fullerenes are more often used as thin self-assembled layers at an electrode for passivating interfacial trap states and lowering the contact resistance,^[42] which leads to another possible application of crosslinking in organic photovoltaics: the formation of stable, insoluble interlayers. In general, this approach allows the fabrication of multilayer devices or even tandem or triple junction solar cells from solution without the use of orthogonal solvents^[43] or relying on materials that have to be evaporated. More specifically, crosslinked layers may be used as exciton blocking or transport layers at the electrodes allowing for subsequent deposition of further layers from solution or preventing materials from diffusing into each other.^[27,28,44]

However, to date, to best of our knowledge there is no report about advanced multilayer organic solar cell devices that are fully processed from solution using several crosslinked layers. Well-known examples such as the work by Janssen and co-workers^[13a] or Leo and co-workers^[45] still rely on solution-processed inorganic interlayers or vacuum-deposited small molecules. Nevertheless, there is some recent work demonstrating the successful application of polymeric interlayers in multilayer devices.^[27,28,44c,d,g-i] Hahn et al. were able to improve the efficiency of a PCDTBT/C₆₀ bilayer cell by introducing an additional

layer of crosslinked PFTPDAC (Figure 2) that reduced exciton quenching at the donor–anode interface leading to an increase of 25% in efficiency.^[44c] Wang et al. demonstrated an efficiency improvement of 195% using PFN-V (Figure 2) as an additional interlayer at the cathode of an inverted PTB7-Th/PC₇₁BM solar cell reaching a remarkable PCE of 9.18%. The improvement was attributed to enhanced vertical phase separation due to a favorable surface energy of the polymer interlayer.^[46] A 204% increase of the efficiency to 9.28% was achieved with a crosslinked interlayer of PFN-Ox in an inverted PTB7/PC₇₁BM cell.^[44]

The general ability of crosslinking to slow down or suppress the diffusion of fullerenes in BHJ cells is commonly accepted, but rather difficult to address experimentally. Therefore, this topic has only rarely been dealt with in the literature up to now.^[11,47] Recently an experimentally simple approach

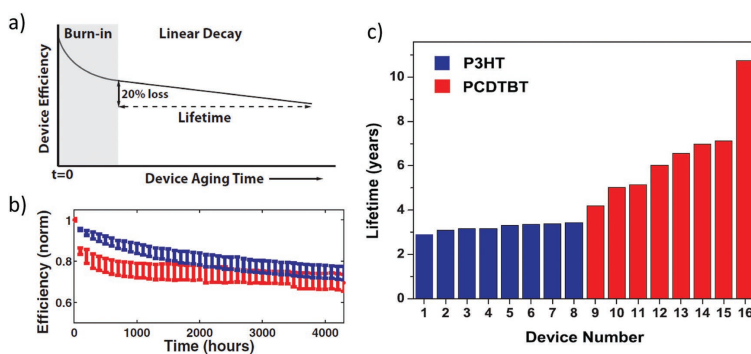


Figure 3. a) Definition of the OSC lifetime according to McGehee and co-workers. It is defined as the point at which the efficiency has dropped to 80% of the value at the start of the linear decay period. Both axes are linear. b) Normalized device efficiency for PCDTBT (red) and P3HT (blue) solar cells over a time span of 4400 h of continuous testing. Each point is the average of the efficiency for 8 individual solar cells of each type. c) Estimated lifetimes of eight P3HT and eight PCDTBT devices. The latter show, on average, significantly longer lifetimes. The wider spread of the PCDTBT data compared to P3HT is attributed to less experience with the PCDTBT system. Reproduced with permission.^[39a] Copyright 2011, John Wiley Sons, Inc.

to assess diffusivity of fullerenes in a polymer matrix by optical means was presented by Fischer et al.^[44] The method is based on photoluminescence quenching in a sensing layer (here: MEH-PPV) induced by electron transfer from the excited singlet exciton of the sensor to the fullerene after the fullerene has diffused through a polymer matrix starting from the top of the polymer layer (Figure 4a–c). In the accompanying work, Fischer et al. demonstrated a reduction of three orders of magnitude in the diffusion coefficient of C_{60} at 140 °C when using a densely crosslinked polyfluorene derivative (PF2/6-A-x:y) compared to a non-crosslinked reference sample (Figure 4d).

Finally, the stability and insolubility of crosslinked layers may be exploited in a third possible application: nanostructuring of layers and interfaces in optoelectronic devices. Structuring allows controlled tuning of donor–acceptor interfaces, phase intercalation, and percolation pathways and therefore is an approach to achieve an optimal spatial morphology on a nanometer scale.^[7,48] In addition to conventional photopatterning^[49] using crosslinkable conjugated polymers as negative photoresists, it is also

possible to apply nanotemplating to a blend mixture^[35,50] or even to use mold–assisted mechanical imprinting techniques.^[51] The latter even allows resolution beyond the limits imposed by light diffraction or beam scattering, that is even sub-10 nm accuracy,^[7] which is on the order of the exciton diffusion length. The templating approach was used, for example, by Farinhas et al., who processed a mixture of F8T2Ox1 (Figure 2), a conjugated polymer, and polystyrene, utilizing the tendency of both polymers to demix. After crosslinking F8T2Ox, polystyrene was removed, leading to columnar structures of F8T2Ox, which were then filled with PCBM. Unfortunately, the resulting PCEs were smaller than 1%.^[50b] A promising approach to get a spatially very well-defined interface morphology, allowing the systematic study of the influence of the interface on device performance, was presented by Schmidt-Mende and co-workers.^[51b] They applied nanoimprinting lithography (NIL)^[52] to process a comb-like bilayer all-polymer structure from the non-fullerene acceptor P(NDI2OD-T2) (Figure 2) and P3HT with exact control over spacing, dimensions and pattern of the

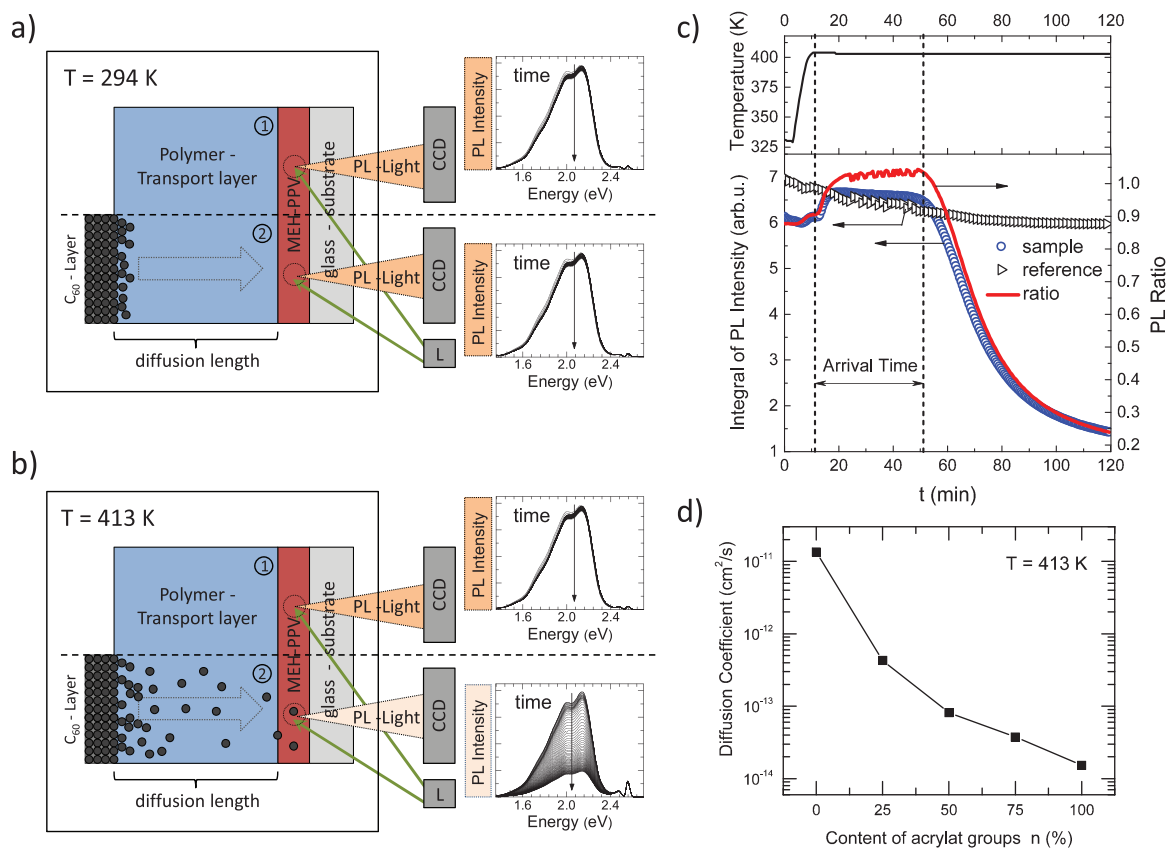


Figure 4. Illustration of the diffusion experiment from ref. [44]. a) In the reference cell (1) and the sample cell (2) the fluorescence of the sensor layer (MEH-PPV), excited by a laser-shutter unit (L-S), is recorded using a charge-coupled detector (CCD) camera. At 294 K the fluorescence is almost constant with time. b,c) After heating the sample to 413 K, C_{60} molecules diffuse leading to a decrease in the fluorescence of the sample cell at a certain time (blue circles). The corresponding kink is assigned to the arrival time of C_{60} in the sensor layer. The red solid line gives the temporal evolution of the sensor fluorescence in the sample cell (blue circles) normalized to that of the reference cell (black triangles). d) Diffusion coefficient of C_{60} as a function of the fraction of crosslinked polymer repeat units for PF2/6-A-x:y at 413 K. The structure formula of PF2/6-A-x:y is shown in Figure 2. Reproduced with permission.^[44] Copyright 2014, John Wiley Sons, Inc.

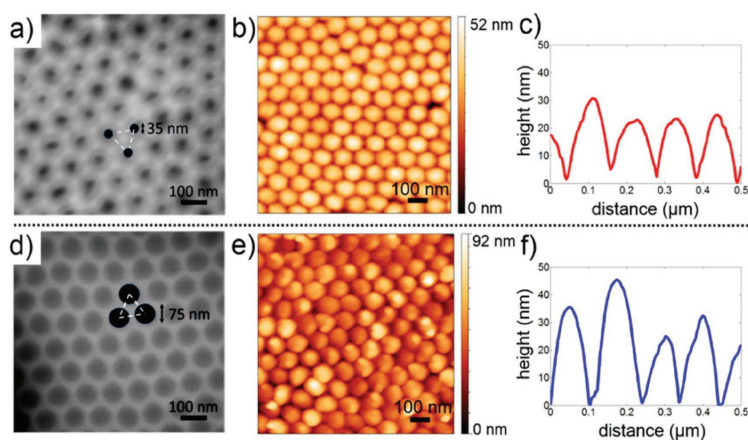


Figure 5. Comparison of nanoimprinting topographies with pore parameters of 35 nm (first row) and 75 nm (second row). The honeycomb lattice has a periodicity of 100 nm. a,d) SEM images of the master mold structures used in the NIL process. b,e) AFM height profiles of imprinted P(NDI2OD-T2) films. c,f) Exemplary AFM line sections. Adapted with permission.^[51b] Copyright 2014, American Chemical Society.

structure and therefore the resulting donor-acceptor interface (Figure 5). Photoinduced crosslinking of the P(NDI2OD-T2) layer was used to additionally stabilize the printed template and allow for the subsequent deposition of P3HT from solution. Schmidt-Mende and co-workers found that the enhanced harvesting of photoexcitations due to a larger interfacial area is outbalanced by increased polaron recombination losses. This results in efficiencies smaller than 1%. Consequently, morphology must be spatially and energetically optimized to achieve good efficiencies.

4. Conclusion and Outlook

One major problem concerned with OSCs is the lack of long-term stability. An important issue regarding the degradation in particular of BHJ solar cells is the diffusion of low molecular weight electron acceptors, for example fullerenes, followed by the formation of aggregates accompanied with a decrease in performance. In this article, crosslinking of the organic layers in OSCs is presented as a tool to overcome problems concerned with diffusion. According to the chosen synthetic strategy, crosslinking can take place within the donor polymer, between donor and acceptor, and within the acceptor. Until now, crosslinking the donor polymer is the most popular strategy. Nevertheless, the two other options will lead to an even stronger decrease in the diffusion of the acceptors and should be investigated intensively in the future. Different reactive groups such as bromine, vinyl, acrylate, azide, and oxetane have been used to crosslink OSC materials. As discussed in detail in Section 2, all reactive groups have certain advantages and disadvantages, for example with respect to their crosslinking ability in the presence of fullerenes. Consequently, up to now no final decision can be made as to which reactive unit is best suited to crosslink certain OSC materials. Here, some fundamental studies to clarify how the process of crosslinking influences the

basic properties of the crosslinked layers and finally the OSCs have already been carried out by several groups. Apart from comparing different functional groups concerning device stability, lifetime, and efficiency, such studies include investigations on the influence of crosslinking on the charge carrier mobility and on the diffusion coefficient of low molar mass electron acceptors in a crosslinked polymer matrix, including the effect of the resulting crosslink density on both charge carrier mobility and diffusion.

In the crosslinked materials mentioned above the reactive group is part of the low bandgap polymers or of a low molar mass molecule, normally the electron acceptor. An alternative concept uses external crosslinkers that are added to an existing low bandgap polymer and lead to crosslinking upon UV-irradiation or heating. The most popular materials from this class are bis-nitrenes.

For both crosslinkable polymers and low molar mass crosslinkers, the following design rules can be established. In general, it is important that crosslinking is carried out in a way that minimizes changes in the conjugated material. Therefore, the functional groups must be situated in the solubilizing spacer group or flexible low molar mass crosslinkers must be used. The chemistry of crosslinking has to be selective, meaning that crosslinking has to take place solely in the side chains and the conjugated system should not be affected. In the case that initiators are used, fragments of the initiating species remain in the polymer. By the choice of appropriate initiators, one has to make sure that these fragments do not negatively influence the material properties such as the charge carrier mobility. If possible, crosslinkable groups such as acrylates that can be crosslinked thermally or by UV-light without any initiator should be used.

Crosslinking of the active layer in BHJ solar cells has become rather popular and it has to be mentioned that unintentional crosslinking of PCDTBT/PCBM layers resulted in OSCs with the, to our knowledge, best long term stability.^[39a] Nevertheless, crosslinking can be used not only in BHJ solar cells but also to get crosslinked, insoluble layers of a single material, which are used as interlayers or to obtain multilayer OSCs by solution processing. This concept has been successfully used in the solution processing of OLEDs^[43] and, to our opinion, is a promising concept also in the field of OSCs.

Recently, crosslinking has been used for the stabilization of nanoscale polymer structures obtained by imprinting. Such small structures are prone to degradation and crosslinking seems to be a promising way to stable nanostructures.^[51b]

Acknowledgements

F.-J.K. and C.S. contributed equally to this work. Financial support by the Bavarian State Ministry of Science, Research, and the Arts through the Collaborative Research Network "Solar Technologies go Hybrid" and by the German Science Foundation DFG through the doctoral training center "GRK 1640" is acknowledged.

Conflict of Interest

The authors declare no conflict of interest.

Keywords

bulk heterojunctions, cross-linking, multilayer materials organic solar cells, stability

Received: February 3, 2017
Revised: February 27, 2017
Published online:

- [1] a) H. Bente, D. Mori, H. Ohkita, S. Ito, *J. Mater. Chem. A* **2016**, *4*, 5340; b) J. W. Jung, J. W. Jo, E. H. Jung, W. H. Jo, *Org. Electron.* **2016**, *31*, 149.
- [2] H. Kang, G. Kim, J. Kim, S. Kwon, H. Kim, K. Lee, *Adv. Mater.* **2016**, *28*, 7821.
- [3] Y. Jin, Z. Chen, S. Dong, N. Zheng, L. Ying, X.-F. Jiang, F. Liu, F. Huang, Y. Cao, *Adv. Mater.* **2016**, *28*, 9811.
- [4] J. Huang, J. H. Carpenter, C. Z. Li, J. S. Yu, H. Ade, A. K. Y. Jen, *Adv. Mater.* **2016**, *28*, 967.
- [5] a) H. Q. Zhou, Y. Zhang, C. K. Mai, S. D. Collins, G. C. Bazan, T. Q. Nguyen, A. J. Heeger, *Adv. Mater.* **2015**, *27*, 1767; b) X. Z. Che, X. Xiao, J. D. Zimmerman, D. J. Fan, S. R. Forrest, *Adv. Energy Mater.* **2014**, *4*, 1400568.
- [6] heliatek, *Technical Data*, <http://www.heliatek.com/de/heliainfilm/technische-daten> (accessed December 2016).
- [7] J. Weickert, R. B. Dunbar, H. C. Hesse, W. Wiedemann, L. Schmidt-Mende, *Adv. Mater.* **2011**, *23*, 1810.
- [8] Y. Yang, K. Mielczarek, A. Zakhidov, W. Hu, *ACS Appl. Mater. Interfaces* **2016**, *8*, 7300.
- [9] P. Cheng, X. W. Zhan, *Chem. Soc. Rev.* **2016**, *45*, 2544.
- [10] D. Yu, Y. Q. Yang, Z. Chen, Y. Tao, Y. F. Liu, *Opt. Commun.* **2016**, *362*, 43.
- [11] a) N. D. Treat, T. E. Mates, C. J. Hawker, E. J. Kramer, M. L. Chabiny, *Macromolecules* **2013**, *46*, 1002; b) N. D. Treat, M. A. Brady, G. Smith, M. F. Toney, E. J. Kramer, C. J. Hawker, M. L. Chabiny, *Adv. Energy Mater.* **2011**, *1*, 82; c) B. A. Collins, E. Gann, L. Guignard, X. He, C. R. McNeill, H. Ade, *J. Phys. Chem. Lett.* **2010**, *1*, 3160.
- [12] H. Kong, J. Sinha, D. Hoefl, S. B. Kirschner, D. H. Reich, H. E. Katz, *Org. Electron.* **2013**, *14*, 703.
- [13] a) W. W. Li, A. Furlan, K. H. Hendriks, M. M. Wien, R. A. J. Janssen, *J. Am. Chem. Soc.* **2013**, *135*, 5529; b) A. Puetz, F. Steiner, J. Mescher, M. Reinhard, N. Christ, D. Kutsarov, H. Kalt, U. Lemmer, A. Colmann, *Org. Electron.* **2012**, *13*, 2696.
- [14] a) G. Wantz, L. Derue, O. Dautel, A. Rivaton, P. Hudhomme, C. Dagron-Lartigau, *Polym. Int.* **2014**, *63*, 1346; b) J. W. Rumer, I. McCulloch, *Mater. Today* **2015**, *18*, 425.
- [15] P. Knauer, T. Hahn, A. Köhler, P. Strohrig, *J. Mater. Chem. C* **2016**, *4*, 10347.
- [16] B. J. Kim, Y. Miyamoto, B. W. Ma, J. M. J. Fréchet, *Adv. Funct. Mater.* **2009**, *19*, 2273.
- [17] S. Miyaniishi, K. Tajima, K. Hashimoto, *Macromolecules* **2009**, *42*, 1610.
- [18] F. Ouhib, M. Tomassetti, J. Manca, F. Piersimoni, D. Spoltore, S. Bertho, H. Moons, R. Lazzaroni, S. Desbief, C. Jerome, C. Detrembleur, *Macromolecules* **2013**, *46*, 785.
- [19] H. J. Kim, A. R. Han, C. H. Cho, H. Kang, H. H. Cho, M. Y. Lee, J. M. J. Fréchet, J. H. Oh, B. J. Kim, *Chem. Mater.* **2012**, *24*, 215.
- [20] G. Brotas, J. Farinhas, Q. Ferreira, J. Morgado, A. Charas, *Synth. Met.* **2012**, *162*, 2052.
- [21] G. Griffini, J. D. Douglas, C. Piliago, T. W. Holcombe, S. Turri, J. M. J. Fréchet, J. L. Mynar, *Adv. Mater.* **2011**, *23*, 1660.
- [22] J. E. Carlé, B. Andreasen, T. Tromholt, M. V. Madsen, K. Norrman, M. Jorgensen, F. C. Krebs, *J. Mater. Chem.* **2012**, *22*, 24417.
- [23] a) D. P. Qian, Q. Xu, X. L. Hou, F. Z. Wang, J. J. Hou, Z. A. Tan, *J. Polym. Sci. Pol. Chem.* **2013**, *51*, 3123; b) K. Yao, L. Chen, T. Hu, Y. W. Chen, *Org. Electron.* **2012**, *13*, 1443.
- [24] C. J. Mueller, T. Klein, E. Gann, C. R. McNeill, M. Thelakkt, *Macromolecules* **2016**, *49*, 3749.
- [25] X. Chen, L. Chen, Y. W. Chen, *J. Polym. Sci. Pol. Chem.* **2013**, *51*, 4156.
- [26] T. T. T. Bui, S. Park, M. Jahandar, C. E. Song, S. K. Lee, J. C. Lee, S. J. Moon, W. S. Shin, *RSC Adv.* **2016**, *6*, 61284.
- [27] R. Q. Png, P. J. Chia, J. C. Tang, B. Liu, S. Sivaramakrishnan, M. Zhou, S. H. Khong, H. S. O. Chan, J. H. Burroughes, L. L. Chua, R. H. Friend, P. K. H. Ho, *Nat. Mater.* **2010**, *9*, 152.
- [28] Z. K. Tan, K. Johnson, Y. Vaynzof, A. A. Bakulin, L. L. Chua, P. K. H. Ho, R. H. Friend, *Adv. Mater.* **2013**, *25*, 4131.
- [29] C. Tao, M. Aljada, P. E. Shaw, K. H. Lee, H. Cavaye, M. N. Balfour, R. J. Borthwick, M. James, P. L. Burn, I. R. Gentle, P. Meredith, *Adv. Energy Mater.* **2013**, *3*, 105.
- [30] L. Derue, O. Dautel, A. Tournebize, M. Drees, H. L. Pan, S. Berthumeyrie, B. Pavageau, E. Cloutet, S. Chambon, L. Hirsch, A. Rivaton, P. Hudhomme, A. Facchetti, G. Wantz, *Adv. Mater.* **2014**, *26*, 5831.
- [31] J. W. Rumer, R. S. Ashraf, N. D. Eisenmenger, Z. G. Huang, I. Meager, C. B. Nielsen, B. C. Schroeder, M. L. Chabiny, I. McCulloch, *Adv. Energy Mater.* **2015**, *5*, 1401426.
- [32] C. P. Yau, S. Wang, N. D. Treat, Z. P. Fei, B. J. T. de Villers, M. L. Chabiny, M. Heeney, *Adv. Energy Mater.* **2015**, *5*, 1401228.
- [33] a) Y. Chen, K. C. Lin, *J. Polym. Sci. Pol. Chem.* **1999**, *37*, 2969; b) S. Chambon, A. Rivaton, J. L. Gardette, M. Firon, *Sol. Energy Mater. Sol. Cells* **2007**, *91*, 394; c) S. Chambon, A. Rivaton, J. L. Gardette, M. Firon, *Sol. Energy Mater. Sol. Cells* **2008**, *92*, 785; d) M. Manceau, S. Chambon, A. Rivaton, J. L. Gardette, S. Guillerez, N. Lemaître, *Sol. Energy Mater. Sol. Cells* **2010**, *94*, 1572.
- [34] X. Q. Chen, X. Yao, X. Xiang, L. Liang, W. Shao, F. G. Zhao, Z. Q. Lu, W. W. Wang, J. J. Lic, W. S. Li, *J. Mater. Chem. A* **2016**, *4*, 9286.
- [35] A. Charas, Q. Ferreira, J. Farinhas, M. Matos, L. Alcácer, J. Morgado, *Macromolecules* **2009**, *42*, 7903.
- [36] a) S. Feser, K. Meerholz, *Chem. Mater.* **2011**, *23*, 5001; b) F.-J. Kahle, I. Bauer, P. Strohrig, A. Köhler, *J. Polym. Sci. B Polym. Phys.* **2017**, *55*, 112.
- [37] a) B. Gholamkhash, S. Holdcroft, *Chem. Mater.* **2010**, *22*, 5371; b) C. Y. Nam, Y. Qin, Y. S. Park, H. Hlaing, X. H. Lu, B. M. Ocko, C. T. Black, R. B. Grubbs, *Macromolecules* **2012**, *45*, 2338.
- [38] A. Tournebize, A. Rivaton, J. L. Gardette, C. Lombard, B. Pépin-Donat, S. Beaupré, M. Leclerc, *Adv. Energy Mater.* **2014**, *4*, 1301530.
- [39] a) C. H. Peters, I. T. Sachs-Quintana, J. P. Kastrop, S. Beaupré, M. Leclerc, M. D. McGehee, *Adv. Energy Mater.* **2011**, *1*, 491; b) C. H. Peters, I. T. Sachs-Quintana, W. R. Mateker, T. Heumüller, J. Rivnay, R. Noriega, Z. M. Beiley, E. T. Hoke, A. Salleo, M. D. McGehee, *Adv. Mater.* **2012**, *24*, 663.
- [40] a) C. P. Chen, C. Y. Huang, S. C. Chuang, *Adv. Funct. Mater.* **2015**, *25*, 207; b) N. Deb, R. R. Dasari, K. Moudgil, J. L. Hernandez, S. R. Marder, Y. Sun, A. Karim, D. G. Bucknall, *J. Mater. Chem. A* **2015**, *3*, 21856; c) C. Z. Li, H. L. Yip, A. K. Y. Jen, *J. Mater. Chem.* **2012**, *22*, 4161; d) J. F. Nierengarten, S. Setayesh, *New J. Chem.* **2006**, *30*, 313; e) Y. J. Cheng, C. H. Hsieh, P. J. Li, C. S. Hsu, *Adv. Funct. Mater.* **2011**, *21*, 1723; f) M. Drees, H. Hoppe, C. Winder, H. Neugebauer, N. S. Sariciftci, W. Schwinger, F. Schaffler, C. Topf, M. C. Scharber, Z. G. Zhu, R. Gaudiana, *J. Mater. Chem.* **2005**, *15*, 5158.
- [41] C. B. Nielsen, S. Holliday, H. Y. Chen, S. J. Cryer, I. McCulloch, *Acc. Chem. Res.* **2015**, *48*, 2803.
- [42] a) Y. J. Cheng, F. Y. Cao, W. C. Lin, C. H. Chen, C. H. Hsieh, *Chem. Mater.* **2011**, *23*, 1512; b) W. W. Liang, C. Y. Chang, Y. Y. Lai,

- S. W. Cheng, H. H. Chang, Y. Y. Lai, Y. J. Cheng, C. L. Wang, C. S. Hsu, *Macromolecules* **2013**, *46*, 4781.
- [43] K. Meerholz, *Nature* **2005**, *437*, 327.
- [44] a) N. Cho, H. L. Yip, J. A. Davies, P. D. Kazarinoff, D. F. Zeigler, M. M. Durban, Y. Segawa, K. M. O'Malley, C. K. Luscombe, A. K. Y. Jen, *Adv. Energy Mater.* **2011**, *1*, 1148; b) C. E. Tsai, M. H. Liao, Y. L. Chen, S. W. Cheng, Y. Y. Lai, Y. J. Cheng, C. S. Hsu, *J. Mater. Chem. C* **2015**, *3*, 6158; c) T. Hahn, C. Saller, M. Weigl, I. Bauer, T. Unger, A. Köhler, P. Strohhriegl, *Phys. Status Solidi A* **2015**, *212*, 2162; d) B. Meng, Z. Y. Xie, J. Liu, L. X. Wang, *Chem.-Asian J.* **2016**, *11*, 1218; e) Y. J. Cheng, C. H. Hsieh, Y. J. He, C. S. Hsu, Y. F. Li, *J. Am. Chem. Soc.* **2010**, *132*, 17381; f) C. H. Hsieh, Y. J. Cheng, P. J. Li, C. H. Chen, M. Dubosc, R. M. Liang, C. S. Hsu, *J. Am. Chem. Soc.* **2010**, *132*, 4887; g) Y. Sun, S. C. Chien, H. L. Yip, Y. Zhang, K. S. Chen, D. F. Zeigler, F. C. Chen, B. P. Lin, A. K. Y. Jen, *Chem. Mater.* **2011**, *23*, 5006; h) Q. Xu, F. Z. Wang, D. P. Qian, Z. A. Tan, L. J. Li, S. S. Li, X. H. Tu, G. Sun, X. L. Hou, J. H. Hou, Y. F. Li, *ACS Appl. Mater. Interfaces* **2013**, *5*, 6591; i) K. Zhang, C. M. Zhong, S. J. Liu, C. Mu, Z. K. Li, H. Yan, F. Huang, Y. Cao, *ACS Appl. Mater. Interfaces* **2014**, *6*, 10429; j) F. Fischer, T. Hahn, H. Bässler, I. Bauer, P. Strohhriegl, A. Köhler, *Adv. Funct. Mater.* **2014**, *24*, 6172.
- [45] R. Meerheim, C. Körner, B. Oesen, K. Leo, *Appl. Phys. Lett.* **2016**, *108*, 103302.
- [46] J. Wang, K. Lin, K. Zhang, X. F. Jiang, K. Mahmood, L. Ying, F. Huang, Y. Cao, *Adv. Energy Mater.* **2016**, *6*, 1502563.
- [47] D. Chen, F. Liu, C. Wang, A. Nakahara, T. P. Russell, *Nano Lett.* **2011**, *11*, 2071.
- [48] a) P. K. Watkins, A. B. Walker, G. L. B. Verschoor, *Nano Lett.* **2005**, *5*, 1814; b) K. M. Coakley, M. D. McGehee, *Chem. Mater.* **2004**, *16*, 4533.
- [49] a) E. Scheler, P. Strohhriegl, *J. Mater. Chem.* **2009**, *19*, 3207; b) E. Scheler, P. Strohhriegl, *Chem. Mater.* **2010**, *22*, 1410.
- [50] a) B. Liu, R. Q. Png, L. H. Zhao, L. L. Chua, R. H. Friend, P. K. H. Ho, *Nat. Commun.* **2012**, *3*, 1321; b) J. Farinhas, Q. Ferreira, R. E. Di Paolo, L. Alcacer, J. Morgado, A. Charas, *J. Mater. Chem.* **2011**, *21*, 12511.
- [51] a) H. C. Hesse, D. Lembke, L. Dossel, X. Feng, K. Müllen, L. Schmidt-Mende, *Nanotechnology* **2011**, *22*, 055303; b) T. Pfadler, M. Coric, C. M. Palumbiny, A. C. Jakowetz, K. P. Strunk, J. A. Dorman, P. Ehrenreich, C. Wang, A. Hexemer, R. Q. Png, P. K. H. Ho, P. Müller-Buschbaum, J. Weickert, L. Schmidt-Mende, *ACS Nano* **2014**, *8*, 12397; c) C. Y. Chang, C. E. Wu, S. Y. Chen, C. H. Cui, Y. J. Cheng, C. S. Hsu, Y. L. Wang, Y. F. Li, *Angew. Chem. Int. Ed.* **2011**, *50*, 9386; d) X. M. He, F. Gao, G. L. Tu, D. Hasko, S. Hüttner, U. Steiner, N. C. Greenham, R. H. Friend, W. T. S. Huck, *Nano Lett.* **2010**, *10*, 1302; e) N. Haberkorn, J. S. Gutmann, P. Theato, *ACS Nano* **2009**, *3*, 1415; f) R. Bai, M. Ouyang, R. J. Zhou, M. M. Shi, M. Wang, H. Z. Chen, *Nanotechnology* **2008**, *19*, 055604.
- [52] L. J. Guo, *Adv. Mater.* **2007**, *19*, 495.

B List of abbreviations

abbreviation	full name
BHJ	Bulk Heterojunction
CELIV	Charge Extraction by Linearly Increasing Voltage
CS (State)	Charge Separated State
CT (State)	Charge Transfer State
DFT	Density Functional Theory
DMA	Dynamic Mechanical Analysis
DOS	Density of States
DPP	Diketopyrrolopyrrole
DSC	Differential Scanning Calorimetry
EA	Electron Affinity
EQE	External Quantum Efficiency
FF	Fill Factor
FHJ	Flat Heterojunction
F_{sat}	Saturation Field
FWHM	Full Width at Half Maximum
GIWAXS	Grazing Incidence Wide Angle X-ray Scattering
HOMO	Highest Occupied Molecular Orbital
ICBA	indene- C_{60} -bisadduct
ICTA	indene- C_{60} -tris-adduct
IE	Ionization Potential
IPCE	Incident Photon to Current Efficiency
IPES	Inverse Photoelectron Spectroscopy
IQE	Internal Quantum Efficiency
I_{sc}	Short-Circuit Current
LUMO	Lowest Unoccupied Molecular Orbital
MD	Molecular Dynamics (Simulation)
m_{eff}	Effective Mass
MeLPPP	methyl-substituted ladder-type poly(p-phenylene)
MIS-CELIV	Metal-Insulator-Semiconductor Charge Extraction by Linearly Increasing Voltage
OFET	Organic Field Effect Transistor
P3HT	Poly(3-hexylthiophen-2,5-diyl)
PCBM	Phenyl- C_{61} -butyric acid methyl ester
PCDHTBT	Poly-(N-heptadecan-9'-yl)-2,7-carbazole-alt-5,5-(4',7'-bis(4-hexylthien-2-yl)-2',1',3'-benzothiadiazole)

abbreviation	full name
PCDTBT	Poly-(N-heptadecan-9'-yl)-2,7-carbazole-alt-5,5-(4',7'-bis
PCDTBT _{ox}	(thien-2-yl)-2',1',3'-benzothia diazole) Poly-[(N-1'-((3''-ethyloxetan-3''-yl)-methoxy)-heptadecan-9'-yl)-2,7-carbazole-alt-5,5-(4',7'-bis-(thien-2-yl)-2',1',3'-
PCDTBT _{stat}	-benzothiadiazole)] Poly[(N-heptadecan-9'-yl)-2,7-carbazole-alt-5,5-(4',7'-bis(4-hexylthien-2-yl)-2',1',3'-benzothiadiazole)] _{0.7} -stat-[N,N'-bis(4-methylphenyl)-N,N'-diphenylbenzidine-alt-5,5-(4',7'-bis-(4-hexylthien-2-yl)-2',1',3'-benzothiadiazole)] _{0.3}
PCE	Power Conversion Efficiency
PF2/6	poly[9,9-bis(2-ethylhexyl)fluorene]
PF2/6-A-n:m	poly(9-(2-ethylhexyl)-9-((6-acryloyloxy)hexyl)-fluorene-2,7-diyl)
PHJ	Planar Heterojunction
Ph-TDPP-Ph	2,5-bis(2-octyldodecyl)-3,6-bis(5-phenylthiophen-2-yl)pyrrolo
PTB7	[3,4-c]pyrrole-1,4(2H,5H)-dione Poly(4,8-bis[(2-ethylhexyl)oxy]benzo[1,2-b:4,5-b']dithiophene-2,6-diyl 3-fluoro-2-[(2-ethylhexyl)carbonyl]thieno[3,4-b]thiophenediyl)
SCLC	Space-Charge-Limited Current
TDCE	Time-Delayed Collection Field
TOF	Time of Flight
TRMC	Time Resolved Microwave Conductivity
TREFISH	Time Resolved Electric Field Induced Second Harmonic (Generation)
UPS	Ultraviolet Photoelectron Spectroscopy
V _{oc}	Open-Circuit Voltage

C Acknowledgements

In the end I would like to acknowledge all the people who supported me during my doctoral thesis and without whom this work would have never been possible. First of all I want to thank Prof. Anna Köhler for giving me the opportunity to do my PhD at the chair for Softmatter Optoelectronics (Experimental physics II), allowing me to get a much deeper insight into the micro-processes being at work in organic semiconductors. During my time at the chair I gained a lot of experimental and theoretical experience as well as broad insight into various topics and techniques. I am very grateful for her trust in my abilities and for her kind assistance as my supervisor. Furthermore, I am very grateful for the numerous interesting conferences I was allowed to attend all over Europe and even down to Arabia.

Special thanks go to Prof. Heinz Bässler for several valuable discussions and the chance to learn from his knowledge and years of experience in the field of organic semiconductors. I am especially grateful for his support of my work, his help in complex theoretical interpretations and his professional guidance during my studies, without which some projects would have never been realized.

Next I would like to thank Prof. Peter Strohriegl with whom I had some interesting interdisciplinary collaboration projects on crosslinkable polymers, which gave me the opportunity to think out of the box and work at the interface between chemistry and physics. The knowledge and experience I gained in the course of these studies even qualified me to be decisively involved in a review article about the use of crosslinkable polymers in organic solar cells. This was a real honour for me and I am still thankful for this experience. Apart from this, I had numerous fruitful, uncomplicated and often casual discussions with Prof. Strohriegl, which I really enjoyed.

In this context, I want to express my thanks to my main contact person in Prof. Strohriegl's group, Christina Saller, for giving me the chance to use her crosslinkable polymers in my studies and for sharing her chemical competence with me. Due to her enduring kindness and helpfulness during all the years of my PhD thesis it was really a pleasure to collaborate with her and it was kind of a sad moment when she left university. I wish her all the best in her new job and her further life in general.

I owe my special gratitude to my dear friend Tobias Hahn, with whom I had a great time at the chair both concerning the studies on organic solar cells but especially also personally. Apart from fruitful professional discussions and helpful advice, Tobi would always stand up for me in difficult situations and always encourage me to carry on especially in phases of frustration and discouragement. I am really thankful that he believed in me, especially in times when I did not. From the bottom of my heart I wish him all the best with his job and especially his personal future with his "own" family.

Moreover, I want to express my gratitude to my dear former colleague Steffen Tscheuschner for valuable discussions and helpful advice in any issues related to organic solar cells, be it experimentally or theoretically. I really appreciated his professional opinion and technical expertise. With him, the chair also lost a great table soccer player and reliable participant in the "Feierabendbier". I wish him all the best for the further course of his life with his wife and son.

Personal thanks also go to my dear colleagues Alexander Rudnick, Stefan Wedler and Fabian Panzer. Alex was a very pleasant coeval to work together with and I really appreciate his kind and courteous nature. We only got to work really together during the last year of my PhD thesis, but the joint work was really fun and finally we both got rid of the persisting "negation field". Next, gratitude is owed to Stefan Wedler for sharing his spectroscopic expertise, his readiness to help at nearly any time and for the great time we had at conferences, the daily table football matches or the construction of doctoral carts and hats. Eventually, I would like to thank Fabian Panzer for his advice, help- and insightful conversations and encouraging words at the right time. All three of them offered me great personal support during my PhD thesis and I am grateful that I had the chance to get acquainted with them. I wish them well and success with all their future plans.

My former roommates and colleagues Marcus Reichenberger, Thomas Unger, Konstantin Schötz and Tobias Meier should not remain unmentioned for their kind helpfulness in many respects and for being pleasant mates in various "free time activities". I would also like to give thanks to my other two colleagues from the chemistry department, Martina Schmidt and Julia Wollmann. Martina especially helped me in chemistry related questions regarding fullerenes and kept me informed about the latest gossip. Julia Wollmann needs to be owed gratitude for the fruitful cooperation and her diligence as student's representative in the SolTech network together with me. Unfortunately, we only got to work together for a comparably short period of time, but she has always been a pleasant partner to work with and to talk to.

Moreover, I want to thank the regular members of staff at the chair for their help and assistance in many respects. Michaela Fischer was a reliable, courteous and helpful person concerning any administrative problems. Without her help many things would have been much more complicated. Frank Schirmer and Irene Bauer helped me in many technical and chemical issues and quickly found a solution to whatever problem I came across in this respect. I owe them special thanks for the fabrication of hundreds of device substrates which really relieved me during my studies. Moreover, I am grateful for their immediate readiness to help and the many pleasant conversations we had. Next, I want to express my thanks to Melanie Kummer and particularly Thomas Dabisch for their assistance in any technical question, their kindness and general helpfulness and their willingness to provide the room, material and personal help in the construction of many doctoral carts. Special thanks also goes to Thomas Dabisch and Frank Schirmer for organizing the amazing hiking trips at the chair. Eventually, I want to thank Dr. Thomas Vogtman for his assistance in any laser related issues.

I would also like to thank the doctoral training programme "GRK 1640", the "SolTech" network and "University of Bayreuth Graduate School" and the Elite studies programme "Macromolecular Science" for their financial and non-material support. These networks allowed me make

a lot of interdisciplinary experiences and to get to know several interesting and nice people. I especially enjoyed the membership in the doctoral training programme "GRK 1640" due its nearly familial yet still highly professional character as well as the good supervision, intimate collaborations between the members and the valuable training offers.

At large, I am very grateful to be part of such a helpful and kind working group treating me as an equivalent member. The good working atmosphere repeatedly helped me to overcome failures throughout my work. Eventually I would like to thank the table football team (Steffen, Simon, Dani, Stefan), especially my most enduring partner Stefan Wedler for demanding matches in the lunch break, and the members of our "Schafkopfstammtisch" (Alex, Stefan, Thomas).

In addition to this I want to give special thanks to my dear friends Achim Guckenberger, Bernd Feist and Dominik Sieder for their help and advice during my studies and especially for the cheerful and uplifting long-standing games evenings. I really enjoyed the time we spent together and wish all of them well for the future course of their lives.

Finally and most importantly, I owe my very special, heartfelt gratitude to my parents, Roland and Christa Kahle, and my sister, Felicitas Kahle, for their enduring support in any respect during the time of my PhD thesis and my whole studies at the university. They always believed in me even when things did not go according to plan and helped me to overcome hard times and also longer lasting phases of frustration. I am really thankful for the opportunities my parents opened for me. This thesis is particularly devoted to them.

D Erklärung und Eidesstattliche Versicherung

Einverständniserklärung

Hiermit erkläre ich mich einverstanden, dass die elektronische Fassung meiner Dissertation unter Wahrung meiner Urheberrechte und des Datenschutzes einer gesonderten Überprüfung unterzogen werden kann.

Des Weiteren erkläre ich mich einverstanden, dass bei Verdacht wissenschaftlichen Fehlverhaltens Ermittlungen durch universitätsinterne Organe der wissenschaftlichen Selbstkontrolle stattfinden können.

Eidesstattliche Versicherung

Hiermit versichere ich an Eides statt, dass ich die vorliegende Arbeit selbständig verfasst und keine anderen als die von mir angegebenen Quellen und Hilfsmittel verwendet habe.

Weiterhin erkläre ich, dass ich die Hilfe von gewerblichen Promotionsberatern bzw. -vermittlern oder ähnlichen Dienstleistern weder bisher in Anspruch genommen habe, noch künftig in Anspruch nehmen werde.

Zusätzlich erkläre ich hiermit, dass ich keinerlei frühere Promotionsversuche unternommen habe.

Bayreuth, den 15.08.2018

Frank-Julian Kahle